UNIVERSITY OF CALIFORNIA, SAN DIEGO

SAN DIEGO STATE UNIVERSITY

Nonlinear Aeroelastic Analysis of Joined-Wing Configurations

A dissertation submitted in partial satisfaction of the
requirements for the degree
Doctor of Philosophy

in

Engineering Science (Structural Engineering)

by

Rauno Cavallaro

Committee in charge:

Professor David J. Benson, Co-Chair
Professor Luciano Demasi, Co-Chair
Professor Yuri Bazilevs
Professor Philip E. Gill
Professor Satchi Venkataraman

2014

The dissertation of Rauno Cavallaro is approved, and it is acceptable in quality and form for publication on microfilm and electronically:

_____

_____

_____

_____
Co-Chair

_____
Co-Chair

University of California, San Diego
San Diego State University

2014

DEDICATION

A chi mi guarda da lassù...
Alla mia famiglia.
Ai miei amici.
A tutti coloro i quali
antepongono i valori ai soldi.

EPIGRAPH

"O frati," dissi, "che per cento milia
perigli siete giunti a l'occidente,
a questa tanto picciola vigilia

d'i nostri sensi ch'è del rimanente
non vogliate negar l'esperïenza,
di retro al sol, del mondo sanza gente.

Considerate la vostra semenza:
fatti non foste a viver come bruti,
ma per seguir virtute e canoscenza".

'O brothers, who amid a hundred thousand
Perils,' I said, 'have come unto the West,
To this so inconsiderable vigil

Which is remaining of your senses still
Be ye unwilling to deny the knowledge,
Following the sun, of the unpeopled world.

Consider ye the seed from which ye sprang;
Ye were not made to live like unto brutes,
But for pursuit of virtue and of knowledge.'

Canto XXVI, Inferno, La Divina Commedia
Dante Alighieri

TABLE OF CONTENTS

LIST OF FIGURES

ACKNOWLEDGEMENTS

Chapter 3, in full, is a reprint of the journal paper: "*Postcritical Analysis of PrandtlPlane Joined-Wing Configurations*, AIAA Journal, Vol. 51, No. 1, 2013." The dissertation author was the primary investigator and author of this paper. Coauthors were Luciano Demasi and Alan Márquez Razón.

Chapter 4, in full, is a reprint of the journal paper: "*Nonlinear Analysis of PrandtlPlane Joined Wings: Effects of Anisotropy*, AIAA Journal, Vol. 52, No. 5, 2014." The dissertation author was the primary investigator and author of this paper. Coauthors were Luciano Demasi and Andrea Passariello.

Chapter 5, in full, is a reprint of the journal paper: "*Risks of Linear Design of Joined Wings: a Nonlinear Dynamic Perspective in the Presence of Follower Forces*, CEAS Aeronautical Journal, November 2014." The dissertation author was the primary investigator and author of this paper. Coauthors were Luciano Demasi, Federica Bertuccelli and David J. Benson.

Chapter 6, in part, is a reprint of the conference paper: "*Post-Critical Analysis of Joined Wings: the Concept of Snap-Divergence as a Characterization of the Instability*, AIAA 2013-1559." The dissertation author was the primary investigator and author of this paper. Coauthors were Luciano Demasi and Federica Bertuccelli.

Chapter 7, in part, is a reprint of the journal paper: "*Phenomenology of Nonlinear Aeroelastic Responses of Highly Deformable Joined Wings*, Advances in Aircraft and Spacecraft Science, An International Journal, *In press*, 2014." The dissertation author was the primary investigator and author of this paper. Coauthors were Andrea Iannelli, Luciano Demasi and Alan Márquez Razón.

Chapter 8, in part, is a reprint of the conference paper that will be soon presented (AIAA SciTech 2015): "*PrandtlPlane Joined Wing: Body Freedom Flutter, Limit Cycle Oscillation and Freeplay Studies.*" The dissertation author was the primary investigator and author of this paper. Coauthors were Rocco Bombardieri, Luciano Demasi and Andrea Iannelli.

VITA

2004	B. S. in Aerospace Engineering, University of Pisa, Pisa
2009	M. S. in Aerospace Engineering, University of Pisa, Pisa
2014	Ph. D. in Engineering Science (Structural Engineering), University of California San Diego and San Diego State University

PUBLICATIONS

R.Cavallaro, A.Iannelli, L.Demasi, A.M.Razon, "Phenomenology of Nonlinear Aeroelastic Responses of Highly Deformable Joined Wings", *Advances in Aircraft and Spacecraft Science, An International Journal*, 2014. **In Press**.

R.Cavallaro, L.Demasi, F.Bertuccelli, D.J.Benson, "Risks of linear design of joined wings: a non-linear dynamic perspective in the presence of follower forces", *CEAS Aeronautical Journal*, November 2014.

L.Demasi, G.Monegato, A.Dipace, **R.Cavallaro**, "Invariant Formulation for the Minimum Induced Drag Conditions of Non-planar Wing Systems". *AIAA Journal*, Vol.52, No.10, 2014.

R.Cavallaro, L.Demasi, A.Passariello, "Nonlinear Analysis of PrandtlPlane Joined Wings: Effects of Anisotropy", *AIAA Journal*, Vol.52, No.5, 2014. [**Winner of the *AIAA Structures Best Paper Award***]

L.Demasi, **R.Cavallaro**, A.M. Razon, "Post-critical Analysis of PrandtlPlane Joined-Wing Configurations", *AIAA Journal*, Vol.51, No.1, 2013.

L.Demasi, A.N.Palazotto, A.Hollenbeck, **R.Cavallaro**, "Exploratory Structural Investigation of a Hawkmoth-Inspired MAV's", *International Journal of Micro Air Vehicles*, Vol.4, No.4, 2012.

R.Cavallaro, A.Frediani, "A Code for Shape Generation and Aerodynamic Design of Aircraft", Book Chapter - *Variational Analysis and Aerospace Engineering: Mathematical Challenges for Aerospace Design*, Springer, 2012.

R.Cavallaro, L.Demasi, "Challenges, Ideas, and Innovations of Joined-Wing Configurations: A Concept from the Past, an Opportunity for the Future", Invited: *Progress in Aerospace Sciences*, 2014 **Invited**.

ABSTRACT OF THE DISSERTATION

Nonlinear Aeroelastic Analysis of Joined-Wing Configurations

by

Rauno Cavallaro

Doctor of Philosophy in Engineering Science (Structural Engineering)

University of California, San Diego, 2014
San Diego State University, 2014

Professor David J. Benson, Co-Chair
Professor Luciano Demasi, Co-Chair

Aeroelastic design of joined-wing configurations is yet a relatively unexplored topic which poses several difficulties. Due to the overconstrained nature of the system combined with structural geometric nonlinearities, the behavior of Joined Wings is often counterintuitive and presents challenges not seen in standard layouts.

In particular, instability observed on detailed aircraft models but never thoroughly investigated, is here studied with the aid of a theoretical/computational framework. Snap-type of instabilities are shown for both pure structural and aeroelastic cases. The concept of *snap-divergence* is introduced to clearly identify the true aeroelastic instability, as opposed to the usual aeroelastic divergence evaluated through eigenvalue approach.

Multi-stable regions and isola-type of bifurcations are possible characterizations of the nonlinear response of Joined Wings, and may lead to branch-jumping phenomena well below nominal critical load condition. Within this picture, sensitivity to (unavoidable) manufacturing defects could have potential catastrophic effects.

The phenomena studied in this work suggest that the design process for Joined Wings needs to be revisited and should focus, when instability is concerned, on nonlinear post-critical analysis since linear methods may provide wrong trend indications and also hide potentially catastrophical situations.

Dynamic aeroelastic analyses are also performed. Flutter occurrence is critically analyzed with frequency and time-domain capabilities. Sensitivity to different-fidelity aeroelastic modeling (fluid-structure interface algorithm, aerodynamic solvers) is assessed showing that, for some configurations, wake modeling (rigid versus free) has a strong impact on the results.

Post-flutter regimes are also explored. Limit cycle oscillations are observed, followed, in some cases, by flip bifurcations (period doubling) and loss of periodicity of the solution.

Aeroelastic analyses are then carried out on a realistic *PrantlPlane* to understand effects induced by freeplay of mobile surfaces. Conclusive work is also performed to study the interaction between rigid body and elastic modes, assessing the occurrence of body-freedom flutter.

Part I

Introductory Part

Chapter 1

Introduction

It is a controversial task to clearly identify the born of joined-wing concept. If, on the one hand, the first aircraft showed some sort of connection between the wings (mainly for structural reasons), on the other hand it is also true that this was a necessity more than a choice. However, without any doubt, the first documented and organic examination of joined-wing layout (in particular a box-wing) was given by *Ludwig Prandtl* [7]. The German scientist clearly stated that such a configuration was the one showing the lowest level of induced drag for a given lift and span. This concept was later further investigated and developed [8, 9], some other variants were studied [10] especially in the '70s. Those years could be considered as a departure decade from which a significant amount of current research originated.

The complexity of design of Joined Wings was early ascertained, see for example reference [11]. In particular, the following primary points were made:

- design presents difficult-to-predict situations, in which intuition built on traditional layout sizing is often contradicted;
- methodologies based, developed and used for decades may fail to give reasonable guidelines for the design of Joined Wings. In particular this invalidates the use of fast, low-order tools, used with confidence on traditional architectures. On the contrary, a novel approach is sought, suggesting that higher fidelity tools are needed since the early stages;
- integration between the different disciplines is strongly inherent. It is not obvious to slightly change a design for improvement in one discipline without affecting

(and most often decreasing) overall performances. This is particularly true for the lifting surface: the classical coupling between aero-structural design is enhanced due to the hyperstatic system and strong aerodynamic interactions; moreover flight mechanics/dynamics need to be considered early since the possibility of fine-tuning given by a tail/canard is lost (at least for pure Joined Wings);

- geometric nonlinearities seem to be relevant already for very small deformations, region traditionally considered as linear [12].

Further sources of difficulties were also detected, the reader is referred to the excellent works of Wolkovitch [10] and Frediani [9] for a first significant review of the topic. Most of literature efforts about Joined Wings will be reviewed in Chapter 2.

With the advent of High Altitude Long Endurance (HALE) and Unmanned Air Vehicle (UAV) concepts, design was pushed to lighter (and thus, very deformable) solutions. Large deflections amplified the role played by geometric nonlinearities. This was especially the case for the *SensorCraft*, a concept of HALE with ISR (intelligence, surveillance and recognition) role developed by the US Air Force. Researches noticed early difficulties connected to these nonlinearities, and investigated the topic for more than a decade. Research is still in progress and although scaled models have been built and flown, the nonlinearities have never been studied from a theoretical point of view and in the framework of Joined Wings. They remain, at the moment, far from being understood.

1.1 Motivation of the Present Study

What originally inspired this work was an attempt to study the nonlinear (the here considered nonlinearities are of the structural geometrical type) aeroelastic response of Joined Wings and capture the essence of physics. However, a large number of unresolved keypoints needed to be assessed and the groundwork to be laid before further aeroelastic analyses could be carried out.

In literature, a large number of contributions mentioned the importance of *nonlinearity*. It was observed, its importance was shown and its intrinsic difficulty in being captured by lower order models was proven. Thus, part of this study aims to *fill this gap*.

At the same time, the terminology *buckling of the aft wing* was always used

to describe instability issues related to some Joined Wings, whereas, years later the instability was described as having a more global flavour (overall configuration rather than buckling of the aft wing due to compressive loads). This work then, intends to explore the meaning of instability applied to Joined Wings in order to shed some light on this regard.

A further point to be clarified was the real meaning of the instability from an aeroelastic point of view. In fact, the same terminology *buckling of the aft wing* refers to a mechanical loading case, whereas, an aircraft in flight experiences aeroelastic loads. Thus, it is not clear how reliable is to express stability property of a flying configuration with a purely mechanical analysis.

A critical discussion of the above points was felt as a necessary intermediate step before moving to nonlinear dynamic aeroelasticity. However, the big question was about which approach needed to be chosen to efficiently tackle this problem.

1.1.1 The virtues of conceptual approach

A good scientific approach, as the universally recognized one proposed by *Galileo Galilei* cannot prescind from phenomenology. Likewise, to be able to capture a broad scenario, nonlinearities need to be studied for a wide number of different and significative cases. In other words, if one aims to see the manifestations of nonlinearities in Joined Wings, he/she should not restrict the analysis to very specific cases and configurations. On the contrary, one should ideally try to *explore* as much as possible the *design space* to unveil most of the phenomena inherent to the examined layout.

At this point, a question to answer would be what are the commonalities governing the behaviors of all different joined-wing cases. Observing the typical layout, it is straightforward to assess that the hyperstatic (overconstrained) nature of the structures is inherent to all the configurations and represents then a distinctive trait. This suggests that simplified models retain the most important peculiarity, and thus, are significative for the purposes. Obviously, with the term *overconstrained* the author is here referring to a macro-geometrical level, since a true realization of a monoplane wing is also overconstrained, though at small scale level (just think about the wing-box typical layout).

If it is true that a realistic aircraft configuration is not usually available for research purposes, the issue is ways more complicated for aircraft that have never been

flown before. Moreover, even with an airplane layout as Joined Wings, there are very different realization and classes: a civil-transport vehicle and a High Altitude Long Endurance configuration are completely different concepts, sharing only the macro-geometrical layout (monoplane for example), but having completely different mass and stiffness distributions. This supports even more the necessity of generality and the appropriateness of conceptual approach.

This is exactly the method pursued in this work. By means of different simplified models different phenomena are shown and described. The final aim is not to warn the joined-wing designers that all the configurations will experience the here presented instabilities. On the contrary, the objective is to (strongly) suggest that a safe-design of Joined Wings needs to incorporate some particular nonlinear investigations (as, for example, the post-critical ones) in order to assess that some typical instabilities or related catastrophical phenomena are not occurring. This theoretical support for the designer is one of the main contributions of this research.

Beside observing and classifying the behavior, a physical understanding of the phenomena has to be sought too. Unfortunately it is not always possible to give an in-depth explanation. For the case of Joined Wings, this has proven to be the case, at least so far. Disappointing performances of reduced order models reinforce the above statement. In the literature [13–16], common approaches successful on a wide range of problems, were not able to capture nonlinearities or well reproduce the response. There is clearly a relation between these low performances and the physical understanding of the nonlinearities. As a consequence, it can be speculated that the nonlinear behavior for Joined Wings is really complicated and need to be properly understood.

1.1.2 Contributions of the present study

In the following the main contributions of this work are presented, divided by thematic areas.

Review A review of past works on Joined Wing is given. After Wolkovitch's work [10], no effort was made to have a unique vision about Joined Wings. Moreover, American and European researches were not completely and in-depth aware of each other, leading to some independent results that needed to be associated one with the other one. The present extensive review represents a step toward filling this gap.

Computational tools In-house aeroelastic code has been developed for carrying out the analyses. The fundamental modules (structural, aerodynamics, etc) rely on well-known ad accepted methods (finite and boundary element methods). However, the particular pursued coupling between aerodynamics and structures, although not theoretically novel, is not widely used and has never been shown in detail in previous works. The merit of this effort is to present in detail some theoretical parts and discuss issues related to the different formulations.

Structural conceptual work This work shows for the first time snap-buckling phenomena observed on simplified models of Joined Wings when loaded with mechanical forces. It can be considered as a theoretical effort independently giving insight and completing an experimental campaign carried out by the Air Force Research Lab (AFRL) in which effects of nonfollower and follower type of loading were observed.

In this work complete post-critical response is also tracked, and a study on possible parameters driving the instability is performed, proving valuable indications. In particular, importance of bending stiffness, bending/torsion coupling and the moment transferred through the joint is critically analyzed.

Presence of snap-buckling induces, however, issues that may manifest well before the critical load is reached. In fact, bi-stable regions are inherent, and are a potential danger for promoting branch-jumping when an appropriate perturbation is applied. More complicate scenario may arise: a so-called *isola* (fully detached and close equilibrium branch) is found for particular combination of parameters. Such a picture is very worrying in terms of design perspective, since it implies multi-stable regions that cannot be easily detected through the common path-tracking continuation methods.

Finally, within this complex bifurcation scenario, the sensitivity to manufacturing defects is enhanced: sudden shifts in behavior may arise from small changes in parameters.

Static aeroelastic conceptual work Aeroelastic static analysis potentially demonstrated the same instability phenomena observed above. In the same framework, for the first time the concept of *snap-divergence* is formulated, as opposed to the classic definition of aeroelastic divergence evaluated thorough eigenvalue analysis. Thus, the same concerns expressed above apply also for the aeroelastic case.

The eigenvalue approach is found to give very unsatisfactory trends, even when

enhanced by successive linearizations. Good estimates of the real critical speed are given only after tracking most of the nonlinear response, jeopardizing then the computational advantages inherent to the eigenvalue approach.

Reliability of mechanical loading as a surrogate of aerodynamic loading is assessed. It is shown that this approach can hide important instabilities: although the structure may show very similar stiffness (to be intended as load versus deformation ratio), an infinitesimal increase in wind speed may cause a finite variation of aerodynamic loads, de-facto, an instability.

This part is not a self-standing effort, but should be read as a completion of some experimental works carried out by the AFRL and collaborators mimicking the aerodynamic actions with mechanical follower loads.

Dynamic aeroelastic conceptual work Aeroelastic dynamic phenomena are then observed, using multi-fidelity approaches. As for the previous settings, classic flutter analysis carried out on initial/undeformed configurations does not provide accurate results.

Effects of modeling techniques are examined: for some joined-wing layouts results are strongly sensitive to the modeling of the wake shed by the wing. Traditionally, effects of neglecting the wake roll-up are considered to be of the second order.

A stability diagram, traced for one particular configuration, shows the rich picture: multi-stability in static regimes, multi-stability in mixed static/dynamic regimes, Hopf's and flip's bifurcations give an idea of the complexity of the nonlinear behaviour.

Dynamic aeroelasticity: effects induced by freeplay of control surfaces Effect of freeplay of mobile surfaces are investigated for a typical *PrandtlPlane*, a civil aviation realization of the joined-wing (box-wing) concept. Low speed flutter occurrences are observed that can be dominated with dampers. These instabilities usually involve higher frequency modes, whereas, the main dynamic instability is observed to preserve in all cases its mechanism (involving low frequency modes) as in the configuration without any freeplay.

In some cases freeplay may also increase this main instability speed, providing possible design indication for passive flutter suppression. On the contrary, in some other cases, a different violent flutter mechanism is triggered by the freeplay at lower-than-reference critical speed.

Dynamic aeroelasticity: free flying analysis Since the first natural frequencies show relative low values on the above PrandtlPlane configuration, the elastic modes may theoretically strongly interact with the rigid body motion. Thus, a free-flying flutter analysis is carried out. Unexpectedly, flutter issues are alleviated by a large extent for the particular configuration under examination.

Design directions The conceptual work carried out on simplified models predicted instabilities which were practically observed (although never studied) in literature efforts on detailed HALE models employing realistic stiffness distributions and also a detailed structural description (spars, ribs, etc). Thus, all the difficulties and complexities shown for the models presented in this thesis may have a practical impact on real design of Joined Wings, at least for the highly flexible cases. Design directions could then be formulated, as summarized by the following list:

- Stability analysis should not be pursued with linear eigenvalue analysis. In fact, such an approach can lead to unsafe predictions and costly re-design computations.
- The static analysis should not be stopped when the maximum load is reached. On the contrary, it should be continued to track the response also in the *non-feasible* regions to assess if a snap-instability (with consequent bi-stable region) occurs.
- The operative conditions should be designed to avoid bi-stable regions.
- Even if no snap-instability is observed with path tracking techniques (arc length methods), there is no guarantee that branch jumping does not occur: a detached branch (*isola*) can exist.
- Joined Wings should be approached with a *global* perspective, and be thought as a unique whole system. Local actions or modifications may have a strong effect at large scales.
- Sensitivity to manufacturing defects needs to be carefully assessed.
- Even within the same modeling approach, different approximations and submodeling that are demonstrated not to be important (e.g., wake shape for aeroelastic studies) for traditional configurations, can lead to different results.

1.2 Layout of the Thesis

The thesis is organized in *three main parts*. The *first part*, constituted by Chapters 1 and 2, is preparatory for a in depth understanding of the rest of the work. Chapter 2 gives a literature review of works related to Joined Wings, indirectly highlighting the areas that need further development and studies.

The *second part* is constituted by Chapters 3 through 7. It regards all the conceptual work on Joined Wings. In Chapter 3, and for the first time, the snap-instability is shown to occur for different layouts when mechanical loads are applied. A parametric study is given in order to assess the influence of macro-geometrical parameters (joint's height, sweep angle) or load repartition between the two wings on the instability occurrence. Moreover, the nonlinear analysis is compared to the linear eigenvalue approach, widely used in literature, clearly showing the discrepancies between the two methods. This is even more evident since not only quantitative predictions but also qualitative trends may not match.

Chapter 4 presents an attempt to better understand the snap-phenomenon. Through the employment of different materials (isotropic or composite) effects of bending and torsion are assessed, with emphasis on the bending-torsion coupling at material level. In such a framework, the ratio of the bending stiffness of the lower and upper wing played the main driving instability role. However, torsional stiffness has an important contribution too, whereas extensional stiffness did not prove to be very relevant. Effects of moment transmission through the joint are also considered, showing its strong influence on instability onset. When the coupling is also present at geometrical level (sweep angles of the wing different than zero) the variety of the response becomes extremely difficult to be interpreted and predicted.

Chapter 5 introduces mechanical loads of the follower type. With such a loading condition, partially better resembling aerodynamic loading, the instabilities are exacerbated. However, the most relevant results are on the branch-jumping phenomena. In fact, a snap response is associated to a bi-stable region concept. Thus, a vanishing perturbation may lead to a transient and the configuration can settle to an equilibrium state very far from the initial one. As a consequence, the use of nonlinear tool is suggested to track also the post-critical response, in order to define these bi-stable regions and operate outside of them. Finally, cases in which this approach is not enough to avoid catastrophical consequences are presented: equilibrium states forming a detached (isola)

from the main branch are born. All these situations are studied from a dynamical system approach, showing the different bifurcations.

In Chapter 6, the aerodynamic loads are finally introduced. The instability phenomenon is again observed, and is formally defined and called snap-divergence. A classic divergence analysis through eigenvalue approach is carried out and compared to the nonlinear one. This is done for successive linearizations about deformed configurations, showing that the eigenvalue analysis overpredicts the true instability speed even when updating the "initial" configuration. A very important fact is shown regarding the instability and lifting capability: these are necessarily not coincident, thus, a true instability may happen but the configuration may continue to produce lift.

Chapter 7 describes the dynamic aeroelastic phenomena. First, a comparison between flutter as predicted with linear and linearized analyses and with different levels of fidelity nonlinear analyses is given. In some cases a large difference in the results is found, also between alternative nonlinear approaches. For example, it appears that considering the wake flexible does have a strong impact. Post-flutter response as limit cycle oscillations (LCOs) are shown and studied, considering the different fidelity approaches. The motion shows interesting features, as an asynchronous behavior of different areas of the wing. Finally, a dynamical system perspective is offered. Complex bifurcations take place. Tri-stable regions are present. Moreover, after a LCO develops, further increasing the speed, a flip-bifurcation (or period-doubling) is observed.

The *third part* is constituted by Chapter 8 and regards an application of the aeroelastic framework to a realistic configurations. Differently than the previous cases, the application is towards a civil aircraft concept featuring joined wings (called PrantlPlane) designed to operate in the small deformation field. Chapter 8 gives an overview of how the model is obtained through an optimization process aiming to aeroelastically match a model provided by a partner University (Università di Pisa). Then, dynamic aeroelastic instabilities are studied when the model is constrained (not free to rigidly move in the space). Moreover, an LCO is depicted and a critical discussion of flutter mechanism is attempted from a structure-fluid exchanged-energy perspective. The rigid-body motions are finally taken into account, flutter analysis repeated, and differences with the previous case outlined.

The same chapter studies effects of free-play of mobile surfaces in inducing flutter phenomena. In some cases the main flutter mechanisms is posticipated at higher speeds

(suggesting then an approach for a passive flutter suppression), in other cases different interaction with the rigid surface rotation induces a different mode to become unstable at lower speed. For almost all cases, high frequency modes become unstable for a reduced interval of velocities in the lower range. These situations, however, can be easily dominated adding some source of damping, e.g., rotational dampers acting on the hinge line.

Chapter 2

Joined Wings: an Historical Perspective

A complete and detailed review of all the previous theoretical and experimental works on Joined Wings would go far beyond the scope of this thesis. On the contrary, this chapter aims at giving an overview on the major past and current researches, and providing insight into the difficulties, the open questions and the main achieved results.

2.1 Prandtl's Best Wing System

It is a controversial task to clearly identify the born of joined-wing concept. If, on the one hand, the first biplane aircraft showed some sort of connection between the wings (mainly for structural reasons), on the other hand it is also true that this was a necessity more than a choice. However, without any doubt, the first documented and organic examination of joined-wing layout (in particular a box-wing) was given by *Ludwig Prandtl* [7]. The German scientist clearly stated that such a configuration was the one showing the lowest level of induced drag for a given lift and span. He called this layout performing in optimal condition the *Best Wing System* (BWS).

Without giving any explanation, he also proposed an approximated formula for evaluating the optimum induced drag as function of the vertical-to-wing span (h/b) ratio. Recently a few efforts [17, 18] have studied this topic from a mathematical point of view. In particular, with arguments about the circulation distribution on the two wings being a superposition of a constant and an elliptic function, they found that as

the above parameter (h/b) approaches an infinite value, the asymptotic behavior predicts an optimum induced drag equal to half of the correspondent optimum monoplane (same wingspan lift). More recent works however, [19, 20], approximating the corner with an hyper elliptical formula [21], show that in the limit induced drag approaches zero. Moreover, although the constant plus elliptical distribution is a good approximation for a wide range of values of h/b, the real distribution is different.

A very relevant point discussed in these last references is the lift repartition between the two wings. Considering most papers on the topic, the assumption that under optimal condition the two wings carry the same lift was done, see for example [8, 22]. However, this was first questioned in [23], and then, finally, shown with more rigour in efforts [19, 20].

2.2 The Seventies

Although some wind tunnel investigations were carried out, in early years, it is in the seventies that research on Joined Wings flourished. Some aerodynamic experimental activity [24] was investigating Box-Wing plane, under Lockheed suggestions. The main objectives were to confirm the theoretical advantages, especially after some previous tests [25] delivered contradictory results. This was, also in recent years, a very delicate topic: in different experimental but also numerical investigations results were not encouraging in terms of competitiveness of Joined Wings, because of conceptual errors in the approach (as the ones above, or also [26]) . For example, several wind tunnel tests were experiencing premature separated flows due to the inadequate design of the configuration based on methods fined-tuned on classic monoplane layout. In some other cases, comparisons with biplane (without joints) was attempted simply adding/removing the lateral joints. Such an approach is a conceptual mistake, since a biplane or a Box Wing performing under optimal conditions have different circulation distributions (on the wings), see references [19, 20].

In 1974, Miranda took out a patent [27], describing the application of a Box Wing to military aircraft; he stated that the concepts were general and could be applied to civil transport aircraft too. As primary advantages lower induced drag and close combat maneuverability were claimed. It was the first patent featuring a Boxplane, although the use of multiwings was as old as the field of aircraft. Among others, controllability aspects, maneuvering with direct force control, reduction of trim drag, reduction of aerodynamic

interference at transonic operation and wave drag at supersonic ones, exploitation of compact design, increased structural efficiency (stiffer) and increase of high roll capability were claimed.

In the same year, Lockheed in collaboration with NASA, conducted the first in-depth conceptual design of a civil transport aircraft based on box-wing paradigm [8]. A traditional layout was chosen as reference, and an exhaustive process was carried out considering all the most important aspects related to aircraft design, e.g., aerodynamics, flight mechanics, structures, landing gear integration, operative conditions. Unfortunately, for all the different obtained box-wing layouts flutter problems were inherent, with both a symmetric and antisymmetric low-frequency mode well below the acceptable speed. The anti-symmetric mode was similar to the classic T-tail flutter, in which yawing, rolling and lateral translation with the aft wing were associated with lateral bending and torsion of the vertical stabilizer. For this reason, increase in stiffness of the vertical tail design were later prospected (for example, as proposed by Frediani with the PrandtlPlane [28]). The symmetric mode was inherent to the Box Wing: fuselage pitching about a point near its nose with out-of-phase bending of the wings and vertical stabilizer, with relative little motions occuring at the wing tips. This mode resembled a highly modified, flexible, short-period mode. Because of the very low frequency they could probably be effectively stabilized by an active control system. Further studies tried to change the configuration in order to overcome flutter problems without significant benefits.

In the same decade, Dr. Julian Wolkovitch started investigating a different class of Joined Wings: the so called diamond-wing layouts, [29]. Contrary to Box Wings the wings were directly (and not through a small wing) connected, at the tip or inboard. This configuration was the main considered joined-wing layout for at least the two-three successive decades.

2.3 The Eighties and Nineties

2.3.1 The Eighties

The eighties were characterized by a very large and extensive effort in studying the diamond-wing typical layout: the wings were joined either directly on the tip, or at about 70% of the front wing. Structural optimization studies (pursuing the fully stressed

paradigm) [30] were suggesting large structural weight reduction when the wing-box was adequately designed, pursuing a nontraditional layout. It fact, it was noticed that in the optimal design the material was concentrated as far as possible from the line connecting the two wing roots. This was a particular consequence of the primary and secondary bending moment, inherent to joined-wing layouts.

Further investigations on the structural side were carried out in [31–33], where design space was explored and a preliminary weigh estimation procedure was set up. Overall, configurations lighter-than-reference one (monoplane) were found. Some other works focused on the *Joint* area, e.g. [34, 35].

Wind tunnel campaigns were also set up to investigate more in depth Diamond Wings potentials [36]. Results were in good agreement with theoretical findings. Some specific issues, mainly confined to high angle of attack regime were also noticed. Transonic regime investigations [37] were also carried out. Results were contradictory since the wind-tunnel model was not stiff enough. This difficulty was noticed also in other experimental activities, and was a flaw consequence of not pursuing a structural design enhancing stiffness (for example with an appropriate wing-box layout). On the other hand, devoting such a level of sophistication in the design of the wind-tunnel model was not always feasible, and the structural design was often not carefully considered due to relatively inexperience with the joined-wing configuration.

In the second half of the decade, further wind tunnel assessment studies were carried out [38]. Results showed very good aerodynamic performance and acceptable stability and control throughout the flight envelope. Interesting application of vortilons was pursued, producing a profound improvement in the stall and post-stall regimes without adversely impacting cruise performances. These last results were part of a study for a joined-wing flight demonstrator model, as explained in reference [39].

Original applications of the layout were also studied for cruise missiles [40] or tiltrotor [41].

The review proposed by Wolkovitch [10, 42] represents a milestone for Joined Wings. Nowadays, the need for such a review encompassing the last decades is strongly felt. The author is currently working to fill this gap [43].

Regarding box-wing layouts, the amount of research was not as large as the one for Diamond Wings. Some aerodynamic analyses were presented in reference [44], a review of past work in [45].

2.3.2 The Nineties

This decade too was characterized by a preponderance of works on diamond-wings layout. Aircraft synthesis approaches were pursued, in order to better assess practical potentials of Joined Wings, instead of separately focusing on one subject (like aerodynamics, structures, for example). A first step in this direction was shown in reference [46], followed later by [47, 48], featuring a multidisciplinary optimization. Interesting results were found. In particular, from a direct operative cost (DOC) perspective, gains were smaller than expected. However, results were obtained considering the former price of the fuel. Nowadays, the price of the fuel is higher, and this suggests that DOCs could be significantly reduced when compared to a reference traditional configuration (increasing fuel costs enhances the importance of having an aerodynamic efficient configuration).

A further result that needed more investigations concerned the role played by buckling of the aft wing. In fact, this constraint was found to be active during the optimization, and represented an important weight penalty.

Some of the above results are controversial considering last efforts and researches. To mention one, the low speed requirements were met with more powerful engine unit. In fact, in such conditions, to trim the aircraft, the rear wing was required to produce a very large downforce. This is evidently a design issue, since, to completely exploit Joined Wings advantages, trim needs to be achieved having both wings producing lift: the reduced drag would, contrary with what found, would lead to smaller power units.

2.4 The Noughties and Current Research

In these years, two main research projects can be clearly identified: work led by US AirForce (USAF) about diamond-wing layout applied to *SensorCraft* concept, and research carried out by University of Pisa (Aerospace Engineering Department) on a box-wing configuration called *PrandtlPlane*. Other researches were devoted to the concept of Strut-Braced Wing and Truss-Braced Wing, see references [49, 50]. However they won't considered in this thesis.

2.4.1 SensorCraft

As consequence of investigations started in the nineties as possible application of Joined Wings to replace the Navy E-2C Hawkeye, in 2000 the NASA's Office of AeroSpace

Technology selected 9 aeronautical concepts in its initial *RevCon* program. Participants were: NASA Langley (team leader), NASA Dryden, Boeing Phantom Works, Naval Air System Command (NAVAIR) and AFRL for the development of joined-wing flight demonstrator. The effort was a 4-plus-year project with the following three main objectives:

- enable the integration of large radar apertures into smaller aircraft for improved detection range and resolution;
- reduced drag and weight for improved aircraft speed and endurance;
- reduced system cost.

Notice that, Air Force interest was due to the rapidly growing in surveillance unmanned air vehicles (UAVs) [51]. In 2001 funding priorities within the participating government agencies were directed elsewhere. The Navy and Airforce were unable to meet their shares of the required funding commitment. For a detailed story refer to [11].

Air Force, however, continued to investigate the topic. Some efforts on the general concept of SensorCraft were discussed in [52], underlining the emerging technologies to produce unmanned air vehicle configured and optimized to conduct multiple advanced sensing modalities integrated into an airframe that sustains an enduring theater presence.

One of the difficulties with SensorCraft was the relevance of geometric nonlinear structures, see [12, 53]. Later works were strongly devoted to this topic [54, 55], see for example [56] where a stochastic approach was used. In [54, 57] an optimization was carried out. In work [58], an integrated design process for generating high-fidelity analytical configurations and weight estimation of JW concepts was described. Effectiveness of using control surfaces for lift and roll was determined. The most appropriate placement of control surface and their effectiveness at end of the mission profile was also discussed.

Reference [59] described the load testing, structural failure, and redesign of the Air Vehicle Joined Wing Technology Demonstrator, a 7% scaled version of the SensorCraft proposed in reference [60].

With the goal of weight minimization, different Joined Wings were investigated [61–63] by changing several design variables. The cited papers showed the importance of vertical offset as far a buckling on the aft wing was concerned. In particular, it was found that when there was no vertical offset panel buckling, rather than global buckling, became critical. In [64, 65] dynamic response optimization of a JW was carried out by

using equivalent static loads, which were made to generate the same displacement field as the one from dynamic loads at each time-step of dynamic analysis. Gust loads were also included.

Several efforts were focusing on aeroelastic scaling of Joined Wings. Reference [66] presented a scaling technique aimed to reproduce the aeroelastic equations of motion of a full scale aircraft by adopting a wind tunnel model. The scaled model matched flight Mach numbers and reduced natural frequencies. The research achieved a matching of the scaled natural frequencies and flutter speed and the ground vibration test was in excellent correlation. The paper [67] presented design plans for a low cost aeroelastically scaled flight test concept. Reference [68] reported additional studies towards the achievements of experimental characterization of aeroelastic nonlinearities in flight. Primary subjects of the research were ground tests, instrumentation and flight testing of 1/9th geometrically scaled model but with rigid wings (the flexible aeroelastically tailored wings were planned to be adopted in subsequent studies). The challenge of nonlinear aeroelastic scaling of a Joined-Wing SensorCraft was further addressed in reference [69]. Past studies from the same research group showed the difficulties in having a satisfactory nonlinear response when the nonlinearities were not included in the scaling procedure or when the matching involved only the buckling mode and eigenvalue (in addition to the vibration modes). Thus, reference [69] considered trim-like loads and matched the nonlinear static deflections. Reference [70] focused on a methodology to scale the *linear* aeroelastic response (flutter) of the full scale model. Six vibration modes were matched. In some modes an extraneous rigid pitch rotation was visible. The results provided good agreement for the flutter speed but the actual involved modes were incorrect. Moreover, damping did not match. Reference [71] continued a multi-institution effort aimed towards the creation of an aeroelastically scaled RPV with the final goal of experimentally demonstrating the nonlinear response of a Joined-Wing SensorCraft [68, 72–74]. The goal was to investigate if the existing forward wing could be reused with an aeroelastically tuned aft wing to demonstrate the geometric nonlinearities. The finite element analysis showed that the aft wing, required to support the existing forward wing, would need to be overly stiff, making the corresponding nonlinear response too small to be measured in flight. New algorithms designed to overcome the difficulties when the nonlinear aeroelastic scaling was pursued were discussed in references [75, 76]. Linear and nonlinear static responses were matched with the satisfaction

of modal frequency constraints. The computational cost was reduced by adopting the equivalent static loads, previously studied by the same research group.

In references [77, 78] the issue of gust-load analysis in the framework of design and certification of novel-configurations was addressed.

In [79, 80] the longitudinal control (pitch) of a SensorCraft model was achieved by using aft wing twist. In particular, wind tunnel tests were conducted to assess the effectiveness of this technique to achieve the pitch control.

References [81, 82] presented an experimental set up for Joined Wings. The model was designed so that the wing experienced nonlinearity without material failure. Main contribution was the publication of experimental data for comparison of analytical models. The applied forces were not of a follower type. Reference [83] conducted an experimental study and a joined-wing model was subjected to both conservative and follower forces. The obtained displacements were then compared.

Following the contract FA8650-05-C-3500 granted by AFRL, called Aerodynamic Efficiency Improvements (AEI), collaborative efforts between AFRL, NASA, Boeing, Lockheed Martin, Northrop Grumman were performed. In reference [84] transonic cruise design and optimization were investigated with the constraints required for antenna thickness and fixed planform. In paper [85] the activities carried out to mature the structural design of JWs were reviewed. Of particular interest was the description of the aeroservoelastic wind tunnel test campaign emphasizing the challenges represented by the statically unstable vehicle with low frequency structural modes. A fullspan model, with 13 active control surfaces was built. A particular support system was to be designed to appropriately simulate the free-flying condition (in pitch and plunge). The practical realization of the model was very complicated and full of novel solutions. According to [86] in phase1 aerodynamic optimization and structural sizing verified the potentials of meeting required performances, and found that the airframe structural design was mainly driven by gust loads: actively reducing these loads would have led to a 20% weight savings.

Phase2 was driven by experimental investigations about the active gust load alleviation performing an aeroservoelastic wind tunnel test by NASA Langley facilities with the aim of demonstrating controlled flight of the flexible model at CG positions ranging from +5% to −10% static margin, a 50% reduction in significant airframe gust loads at fundamental airframe symmetric mode frequency through the gust load alleviation and

validate the flexible aircraft design process. A completely redesigned support allowing a complete freedom of motion in pitch and plunge was then pursued. It proved to be very involving (for details see [87]). Relevant was the contribution of *Millenium Dynamics Corporation*. The article [88] described systems, software and procedures developed to perform experimental tests on a full-span aeroelastically scaled JWs. Details about the practical design of the model were offered in [89]. They were mainly carried out by *NextGen Aeronautics* company. Overall, during this AEI program a very large amount of numerical and experimental work was conducted.

2.4.2 PrandtlPlane

Several US/EU (and also German and Italian) patents [28,90–92] were taken out by Aldo Frediani in the last years of the nineties and first decade of the 21th century. The concept was recalling the *Best Wing System* introduced by Prandtl in [7] and already studied in the seventies. However, Frediani was strongly focusing on the aerodynamic advantages trying first an application to a large dimension aircraft (MTOW larger than 400000 Kg). The novelty in respect of previous work was also in the the different level of integration: a design to pursue the potential advantages needed to be different also in the fuselage layout (both inside, with a multideck arrangement, and outside, with a more enlarged horizontally solution). Later he extended the concept to a wide range of aircraft, from very large to very light machines. A double fin-rear wing connection was favoured in order both to not deteriorate the aerodynamics in that region (which could have led to flight mechanic instabilities) and also to dominate aeroelastic problems. The configuration was called *PrandtlPlane* in honour of the German aerodynamicist. Work conducted by him (at department Aerospace Engineering Department of University of Pisa) and partner universities about the PrandtlPlane are summarized in the following.

Work [9] represents a milestone as a general paper on the PrandtlPlane configuration, summarizing the motivations for such an architecture, its possible applications and the experience gained in more than a decade of studies on the topic. The need for a more sustainable aviation, enhanced by the expected increase in air traffic, is the driving reason for interest towards innovative aircraft. Documents as Vision2020 and Vision2050 (see [93]) set very ambitious goals concerning quality and affordability, safety, environment, efficiency and security of air transport system. In particular, cut of 30% of Direct Operative Costs (DOCs) while increasing safety level (with an expected increase in air

traffic), consistent reduction (larger than 50%) of noxious emissions and perceived external noise were indicated as objectives (defined in [93] as *Sustainable Growth* concept). An in depth analysis of the challenges related to the above documents are summarized in [94].

Observing the history of aviation, in the second part of the 20th century it has been registered a decrease of costs of a three factor. One approach to reduced the operative costs is to increase size or capacity, strategy that has culminated with the A380 (capable of hosting 700-800 passengers), whose dimensions almost reach the maximum allowable 80 m x 80 m value, constraint of compatibility with airports' infrastructures.

Improvements in aerodynamics seem to be then the most impacting for fuel efficiency increase, pollution and noise emissions reduction. Overall drag is dominated by friction and induced drag. Whereas studies on reducing the first source (boundary layer ingestion, turbulent flow control, etc) can approximately apply to every configuration, the induced drag is specifically related to the lift distribution. Its share (generally in the in $40-45\%$) can arrive to $80-90\%$ of the total drag during take-off. However, on current configurations the induced drag is so optimized, that significant gains are probably not possible without a "revolutionaty" layout.

Here is where PrandtlPlane concept comes into play: exploiting the BWS concept, consistent reductions of induced drag are then theoretically possible. However, possible advantages are not limited to aerodynamics, as it will be clear in the following.

PrandtlPlane concept has been studied for a wide variety of applications. Some of them will be briefly outlined in the following.

Very/Ultra Large Aircraft Considering the infrastructural constraint on maximum dimensions, and the need to cut down direct operative costs increasing aircraft capacity, PrandtlPlane concept was originally thought for very large aircraft [90]. In efforts [95–97] results of a two year project (2000-2001) co-financed by the Italian Ministry of University were summarized. The joint team was led by the aerospace engineering department of University of Pisa, and composed by aerospace engineering departments of University of Roma La Sapienza, Technical University of Torino, Technical University of Milano and department of mechanical engineering and automation of University of Roma Tre.

The project successfully set up tools and methods for the design and the multidisciplinary optimization of the PrandtlPlane configuration and, in parallel, developed the aerodynamic design of a very large PrantlPlane aicraft.

An extreme example of a PrandtlPlane concept applied to large configuration was presented in [9], for an over 1000 seats aircraft. Such a concept well highlighted the advantages of PrandtlPlane concept in respect of the traditional layout. Fuselage layout and structural analysis were carried out in [98], showing potential significant reductions of empty structural weight per passenger.

Very Large Freighter PrandtlPlane concept was applied to Freighter configurations in [99, 100]. More in detail, decreasing the operative Mach number made favourable the use of large open rotor, with milder impact on flight speed if also the cruise altitude was decreased. PrandtlPlane architecture was particularly well suited to integrate such efficient propulsion system, favouring, the economical competitiveness of airfreight. The horizontally elongated fuselage offered also noteworthy prospective advantages in terms of storage capability and structural efficiency of the design.

Ultralight Aircraft Motivations for adopting PrandtlPlane layout for Light Sport Aircraft (LSA) and Ultra Light Machine (ULM) categories were elaborated in [9, 94]. In particular, it was noticed how the majority of accidents for these aircraft were mainly consequences of human errors. Thirty percent of these events were related to stall, and became fatal for the fire provoked by contact of fuel and hot components (engines). The PrandtlPlane configuration offered ad-hoc solutions to increase safety in this regard.

Design featured a layout with a lower front wing and an higher rear wing connected with a single vertical fin, and was discussed in [101]. A scaled model was realized, enabling wind tunnel and also flight tests to be carried out, see [95, 101]. Also a full scale prototype was built, but never operated.

Positions of engines and propellers were accurately chosen (different options were possible) and passenger cabin was separated from engine and fuel tank by an anti-fire protection (for the above safety reasons). In particular, fuel tank was located close to the center of gravity, inside the fuselage in a protected position, to alleviate inertial (and thus margin of stability) variations. To counteract the likelihood of impacts close to the runaway (a large number of accidents were correlated with a lack of visibility) engines were positioning behind the cabin, enhancing visibility.

Pitch control was achieved by two control surfaces (elevators) in the inner part of the two wings working in opposition of phase, so to exploit the pure pitch control. Both wings also mounted flaps, whereas ailerons were just located on the rear wing. An

interesting point, as stated in [101], was that differently than a traditional configuration where flaps produce a large pitch down moment to be counteracted by a negative force of the tail, in the PrandtlPlane the design pursued positive lift on both wings.

The design strongly relied on an optimization tool described in [102, 103]. However, parallel strategies were also pursued in [104,105]. The high-speed regime sizing was characterized by trim and stability constraints, in a process that led to successive modifications of the aerodynamic surfaces and structural inertial properties. Aerodynamic evaluations were carried out by means of a Vortex-lattice method (VLM), results were corrected with some CFD runs and procedures suggested by the experience gained in the process. As far as low speed conditions were concerned, pure pitch control was pursued (taking into account command saturation), whereas for stall verification a procedure studied in [106] (for a mid-range commercial civil concept) was adopted.

Stall quality represented also one of the most interesting properties of the configuration: wind tunnel testing [95] showed a very flat stall and post stall curve, with great benefits on safety. As final note, the typical high pitch damping increased the flight comfort especially in turbulence presence. Short period eigenvalues were both negative and larger than one, indicating an overdamped response (no oscillatory behaviour).

A one-to-five scaled model of the optimized design was manufactured and flight tests were carried out. All the main features inherent to PrandtlPlane configurations were demonstrated (high pitch damping and stability, difficulty in reaching stall, good lateral stability). Moreover, the flight confirmed all the theoretical calculations and mathematical models. The same model was also presented at the Aerodays2006 exhibition in Vienna.

Medium Size Civil Transport PrandtlPlane Aircraft Efforts [94, 107] based in part on work [108] were first showing an application of the PrandtlPlane concept in the medium size class (200-300 passengers), with a layout featuring a 47 m wingspan and 46 m length. Other than early/conceptual analyses, successive studies pursued a more detailed and in-depth design. Thorough investigations and solutions of the innovative fuselages were proposed in [108–111], with possible weight estimations based on analytical arguments, and not on statistical data (which, considering the novel layout, could not be reliable). After different options were examined, the chosen fuselage layout had reduced vertical dimensions, promoting a reduction in weight and wetted surfaces, combined with a better load and comfort indices. Thanks to the continuous cargo deck (lower

wing under the cargo deck) a very efficient loading/unloading operation could be set up.

High-lift design method was studied and applied in [106], suggesting that common low-speed architecture systems (flaps and slats) were adequate. In particular, pursuing a BWS-like optimum lift distribution, a plain flap and single Fowler were preliminary found to be sufficient.

Structural design was tackled with a multilevel multi disciplinary optimization process, taking into account also aeroelastic constraints [5, 112] in collaborative efforts with Politecnico di Milano. Lifting system-to-total weight ratio was within typical traditional configuration values, if an appropriate design was pursued (asymmetric wing box concept). Use of a full composite wing solution was studied in [113].

Since flutter was found to give most of the penalty in terms of weight, a detailed study was dedicated to this topic in [114, 115].

Flight mechanics and dynamics, control architecture and engine integration were tackled in collaborative efforts with Delft University of Technology, in [6, 116, 117]. Most of these studies gave very important indications, suggesting that prospective advantages could be practically carry over into real design.

Liquid Hydrogen Propelled Aircraft Driven by the prospective increase of the already high level of pollution and CO2 emissions due to the rise in transport aviation numbers, efforts [9, 118] studied an environmental-friendly liquid hydrogen propelled PrandtlPlane concept. The fuel was stored in tanks placed at the tip of the front wing for keeping it far from the passengers and also to improve flutter qualities. In fact, previous aeroelastic analyses showed positive effects of placing an inertial element in such a location, see [114].

UAV As described in reference [9], an application of the PrandtlPlane concept was pursued for an UAV, with enhancement in range, maneuverability, installation and performances of sensors and observation devices (thanks to the high aerodynamic damping). In the studied case, the model had a VTOL capability: the vertical take-off propulsion system (ducted fans or one helicopter-like rotor) was perfectly integrated in the PrandtlPlane layout, maintaining a position close to the center of gravity .

***IDINTOS* - Amphibious Aircraft** IDINTOS (in Italian, acronyms of Tuscan Innovative Seaplane) is a project in which an amphibious seaplane featuring a PrandtlPlane

layout was designed and manufactured. References [119–122] describe the different phases of the design. The early stages were characterized by the same preliminary tools fine tuned in more than a decade of experience on the topic. However, later, extensive use of CFD for low speed operations (from ground or water) was done, and experimental investigations (wind and water tunnel) were carried out.

Recently, a prototype has been officially presented, and a flight test campaign on a scaled one-to-four model is underway.

Part II

Conceptual Analysis

Chapter 3

Post-critical Analysis of PrandtlPlane Joined-Wing Configurations

This chapter is a reproduction of the following paper:
Postcritical Analysis of PrandtlPlane Joined-Wing Configurations, AIAA Journal, Vol. 51, No. 1, 2013.

3.1 Introduction

STRUCTURAL design of Joined Wings (JW),[5, 6, 8–10, 60, 82, 103, 114, 123–130] Strut-Braced Wings (SBW) [131, 132], and Truss-Braced Wings (TBW) [133] presents significant difficulties due to the highly nonlinear geometric effects typical of these configurations. Strong in-plane forces determine important structural nonlinearity [126,134] which must be properly accounted for since the early stages of design. Low fidelity linear analyses are not sufficiently accurate and could not be used even for a preliminary estimation of the main configuration parameters [11]. Realistic optimization analysis [60] must take into account buckling phenomena, which could be of particular significance in typical joined-wing configurations. However, as it will be shown in this work, an eigenvalue analysis about undeformed state (trivial steady state) of JW is *not* acceptable for a proper simulation of the critical and post-critical conditions.
An accurate structural post-buckling analysis of Joined Wings has never been attempted

before and this paper will address this topic. It is true that actual Sensorcrafts and other Joined Wings will be designed to avoid static and dynamic aeroelastic instabilities, but the understanding of the leading mechanisms of these phenomena is crucial for an appropriate and safe design. The high degree of nonlinearity typical of these configurations makes the use of reduced order models extremely difficult [13] and not sufficiently accurate for this task. Only a full-order and detailed nonlinear analysis should be used to avoid large errors in the prediction of the static and dynamic aeroelastic responses. With the goal of a full and accurate geometrically nonlinear investigation of PrandtlPlane Joined Wings in mind, in the present paper and for the first time, the static full-order nonlinear post-critical response is studied for different configurations. The present effort adopts a nonlinear finite element code based on the theoretical work presented in References [135] and [136] and the results are validated with leading commercial software. To overcome limit points and accurately predict the post-buckling response (including *snap-through* phenomena) a continuation technique called *arc length* has been implemented [137–139] with the possibility of automatic switching between different arc length formulations to facilitate the numerical convergence of the most challenging joined-wing configurations.

It should be noted that the occurrence of this kind of instability is for most of the applications not acceptable, and thus, it is usually considered as a failure condition for the structure.

Comparison between the nonlinear and the linear buckling analysis results is presented. It is demonstrated that linear buckling analysis is not an accurate prediction of the true limit point. This has important practical implications and consequences in the multi-disciplinary optimization: the buckling constraint for the wings should appropriately be considered to avoid unnecessary weight penalty or, even worse, an unsafe design.

The study is carried out on one main JW layout, called *Box Wing* [27] or *PrandtlPlane* [28, 91, 92]. Effects of macro geometrical parameters are taken into account, in order to understand which modification could be detrimental or beneficial for the onset of structural instabilities. Different partitions of forces between the two wings are also considered, in order to asses which load condition is more demanding. This could be particularly interesting considering that for a typical box-wing configuration, the induced drag does not change when a constant lift distribution is added to an ex-

isting one [23]. Thus, the desired lift partition can be obtained without penalty on the induced drag, and could be actually fine tuned for better trim, stability and structural performances. [8, 102] However, an accurate nonlinear structural analysis is required to fully understand all the possible implications from a structural stability point of view. This paper will focus on this important aspect of the JW design.

3.1.1 Contributions of the Present Study

Thorough post-critical analyses of Joined Wing have not been presented in previous studies. Common practice in the conceptual design phase of cantilevered classic airplanes is to rely on low fidelity tools to size the structures and have a first educated guess estimation. For example, to assess a buckling load a linear eigenvalue analysis may be adequately precise. However, for the JW this approach cannot be successfully pursued [11].

The strong nonlinear behavior of the inherently overconstrained system gives rise in practice to a complete different scenario from the linear one. The progressive softening or stiffening cannot be predicted by linear investigations. Under certain conditions *snap* phenomena could be observed. In this case when the critical load is reached, the structure's configuration is no longer able to carry any increment in load, being this possible only in a configuration which is not continuously adjacent to the critical one. Thus, what practically occurs is a dynamic snap through to the new configuration which is able to carry the load more efficiently. This new configuration is usually stiffer.

Tracking the unstable branch of the response shows how the structure progressively deforms and how its stiffness changes.

The analyses presented in this work are performed for different geometrical configurations and for different load conditions. The physical mechanism leading to the instability conditions is investigated with particular emphasis on the geometric sensitivity to get useful insights and avoid the buckling.

Studying the structural response for different loading scenarios provides an important indication of the different possible cruise conditions and, for some architecture of the control surfaces [6], these forces could resemble also maneuvering loads. Therefore, significant indications on which is the most critical (sizing) load condition during cruise (for onset of buckling) could be drawn.

This work will answer the following questions:

- When the joint's height is changed what happens to the buckling load? Is it increased or reduced? It will be shown that a counter-intuitive phenomenon is observed.

- What happens when the sweep angle is changed? How sensitive is the nonlinear-buckling load to this parameter?

- How is the nonlinear response of the PrandlPlane Joined Wing for applied loads in the range of interest? Does it always follow a softening, unstable branch, stiffening type of path or this changes case by case? It is desirable to have a nonlinear load-curve path which presents an immediate stiffnening effect rather than a softening phenomenon followed by an unstable branch and a consequent snap-through type of instability.

- How reliable is the linear buckling analysis? Is it conservative with respect to the true nonlinear computations? Does it predict the correct sensitivity of the buckling load with respect to design parameters like the joint's size?

The paper first presents the theoretical background on the structural analysis (Newton-Raphson and arc length techniques). Then the nonlinear buckling analysis of several PrandtlPlane Joined Wings will try to answer the questions presented above.

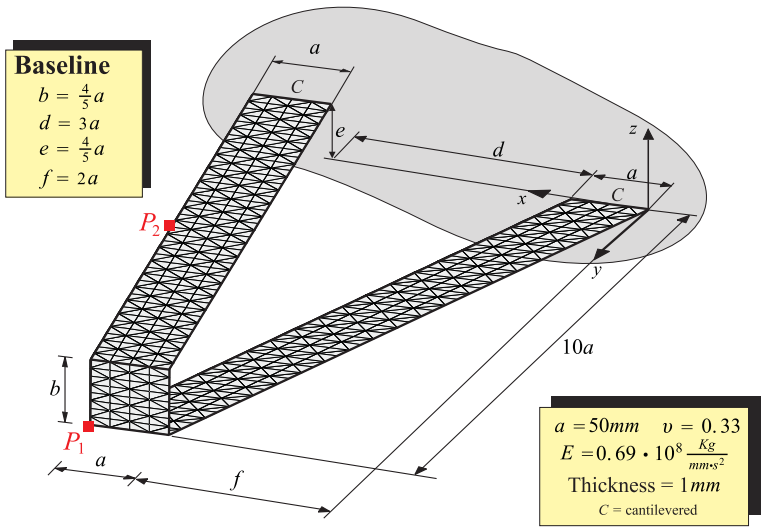

Figure 3.1: Possible wind-tunnel-type model of a PrantlPlane. Baseline configuration.

3.2 Nonlinear Structural Model: Updated Lagrangian Formulation

3.2.1 Newton-Raphson Procedure

In this work the wing is loaded with conservative loads indicated with $\boldsymbol{P}_{\text{ext}}$. The Newton-Raphson solution procedure is now described.First, an increment of external nodal loads can be defined. The applied loads (of the non-follower force type) is calculated by using the following expression:

$$\boldsymbol{P}_{\text{str}}^{\text{step}\,\mu} = \Lambda \cdot \boldsymbol{P}_{\text{ext}} \tag{3.1}$$

where the *dimensionless* parameter Λ indicates the applied fraction of the external loads (if this parameter is equal to 1 it means that all load $\boldsymbol{P}_{\text{ext}}$ has been applied to the structure). μ indicates the load step and n indicates the iteration in a determined load step. The number of iterations required to reach the convergence is in general different if a different load step is analyzed. The internal forces $\boldsymbol{F}_{\text{int}}^{\text{step}\,\mu\,\text{iter}\,n}$ are known from the previous iteration (if the very first iteration of the first load step is considered, there are no internal forces because the structure is initially assumed to be stress-free). So the unbalanced loads $\boldsymbol{P}_{\text{unb}}^{\text{step}\,\mu\,\text{iter n}}$ can be calculated:

$$\boldsymbol{P}_{\text{unb}}^{\text{step}\,\mu\,\text{iter n}} = \boldsymbol{P}_{\text{str}}^{\text{step}\,\mu} - \boldsymbol{F}_{\text{int}}^{\text{step}\,\mu\,\text{iter}\,n} \tag{3.2}$$

The structural tangent matrix $\boldsymbol{K}_T^{\text{step}\,\mu\,\text{iter}\,n}$ is calculated by adding the elastic stiffness matrix $\boldsymbol{K}_E^{\text{step}\,\mu\,\text{iter}\,n}$ (calculated considering the coordinates at the beginning of the n^{th} iteration) and the geometric stiffness matrix $\boldsymbol{K}_G^{\text{step}\,\mu\,\text{iter}\,n}$. In practice it is convenient to perform this operation at element level and then assemble the resulting matrix:

$$\boldsymbol{K}_T^{\text{step}\,\mu\,\text{iter}\,n} = \boldsymbol{K}_E^{\text{step}\,\mu\,\text{iter}\,n} + \boldsymbol{K}_G^{\text{step}\,\mu\,\text{iter}\,n} \tag{3.3}$$

The structural tangent matrix is updated at each iteration of the procedure.
The term iteration used here refers to the repetitive refinement of a nonlinear solution for an incremental load step.
In the standard Newton-Raphson procedure the following linear system is solved and the

displacement vector $\boldsymbol{u}^{\text{step}\,\mu\,\text{iter}\,n}$ can be found:

$$\boldsymbol{K}_{T}^{\text{step}\,\mu\,\text{iter}\,n} \cdot \boldsymbol{u}^{\text{step}\,\mu\,\text{iter}\,n} = \boldsymbol{P}_{\text{unb}}^{\text{step}\,\mu\,\text{iter}\,n} \tag{3.4}$$

Node location coordinates are updated for the next iteration (Updated Lagrangian Formulation):

$$\boldsymbol{x}^{\text{step}\,\mu\,\text{iter}\,(n+1)} = \boldsymbol{x}^{\text{step}\,\mu\,\text{iter}\,n} + \boldsymbol{u}_{d}^{\text{step}\,\mu\,\text{iter}\,n} \tag{3.5}$$

where $\boldsymbol{u}_{d}^{\text{step}\,\mu\,\text{iter}\,n}$ is the vector which contains only the translational degrees of freedom, and it is obtained from the vector of displacements $\boldsymbol{u}^{\text{step}\,\mu\,\text{iter}\,n}$ by eliminating the rows corresponding to the rotations. If the last iteration of the load step μ has been performed, then the left hand side of the previous equation is $\boldsymbol{x}^{\text{step}\,(\mu+1)\,\text{iter}\,1}$ instead of $\boldsymbol{x}^{\text{step}\,\mu\,\text{iter}\,(n+1)}$.

Rigid body motion is eliminated from elements according to the Levy-Gal's [136] procedure and the pure elastic rotations and strains are found. Using these quantities the internal forces are updated for the next iteration and, therefore, the vector $\boldsymbol{F}_{\text{int}}^{\text{step}\,\mu\,\text{iter}\,(n+1)}$ is created (in the case in which the last iteration of load step μ has been performed the term $\boldsymbol{F}_{\text{int}}^{\text{step}\,\mu\,\text{iter}\,(n+1)}$ has to be replaced by $\boldsymbol{F}_{\text{int}}^{\text{step}\,(\mu+1)\,\text{iter}\,1}$).

The cumulative displacement vector is updated next:

$$\boldsymbol{U}^{\text{step}\,\mu\,\text{iter}\,(n+1)} = \boldsymbol{U}^{\text{step}\,\mu\,\text{iter}\,n} + \boldsymbol{u}^{\text{step}\,\mu\,\text{iter}\,n} \tag{3.6}$$

The procedure is repeated until a desired convergence tolerance is reached.

3.2.2 Post-Critical Analysis and Arc Length Methods

In the standard Newton-Raphson method the linear equation 3.4 is solved at each iteration of a generic load step. However, in some cases the convergence can be difficult due to the vicinity of critical [139, 140] points. This problem can be overcome with the well known technique of arc length methods which are briefly explained below with a unified notation consistent with the present work.

Differently from the Newton-Raphson case, now the increment of the applied load is not directly set, but it is an unknown. The problem is then closed by adding a constraint equation on the displacement and (eventually) applied load fraction too. For example, according to *Crisfield*'s method [138], the new converged status is sought

on the (hyper)sphere surface centered on the previous converged status and having a predefined (hyper)radius, where the dimensions of the space here considered are just the displacement of each degree of freedom and the load fraction. As said, the parameter Λ is generally varying for each iteration and load step (thus now the superscript $\text{step}\,\mu\,\text{iter}\,n$ is used in the definition of Λ):

$$\boldsymbol{P}_{\text{str}}^{\text{step}\,\mu\,\text{iter}\,n} = \Lambda^{\text{step}\,\mu\,\text{iter}\,n} \cdot \boldsymbol{P}_{\text{ext}} \tag{3.7}$$

The *linear* system that needs to be solved at each iteration n to find the incremental displacement vector $\boldsymbol{u}^{\text{step}\,\mu\,\text{iter}\,n}$ is the following:

$$\boldsymbol{K}_{T}^{\text{step}\,\mu\,\text{iter}\,n} \cdot \boldsymbol{u}^{\text{step}\,\mu\,\text{iter}\,n} = \boldsymbol{P}_{\text{str}}^{\text{step}\,\mu\,\text{iter}\,(n+1)} - \boldsymbol{F}_{\text{int}}^{\text{step}\,\mu\,\text{iter}\,n} \tag{3.8}$$

$\boldsymbol{P}_{\text{str}}^{\text{step}\,\mu\,\text{iter}\,(n+1)}$ could be expressed using equation 3.7 written for load step μ and iteration $n+1$:

$$\boldsymbol{P}_{\text{str}}^{\text{step}\,\mu\,\text{iter}\,(n+1)} = \Lambda^{\text{step}\,\mu\,\text{iter}\,(n+1)} \cdot \boldsymbol{P}_{\text{ext}} \tag{3.9}$$

Substituting equation 3.9 into equation 3.8:

$$\boldsymbol{K}_{T}^{\text{step}\,\mu\,\text{iter}\,n} \cdot \boldsymbol{u}^{\text{step}\,\mu\,\text{iter}\,n} = \Lambda^{\text{step}\,\mu\,\text{iter}\,(n+1)} \cdot \boldsymbol{P}_{\text{ext}} - \boldsymbol{F}_{\text{int}}^{\text{step}\,\mu\,\text{iter}\,n} \tag{3.10}$$

The counterpart of equation 3.2 is now:

$$\boldsymbol{P}_{\text{unb}}^{\text{step}\,\mu\,\text{iter}\,n} = \boldsymbol{P}_{\text{str}}^{\text{step}\,\mu\,\text{iter}\,n} - \boldsymbol{F}_{\text{int}}^{\text{step}\,\mu\,\text{iter}\,n} \Rightarrow \boldsymbol{F}_{\text{int}}^{\text{step}\,\mu\,\text{iter}\,n} = \boldsymbol{P}_{\text{str}}^{\text{step}\,\mu\,\text{iter}\,n} - \boldsymbol{P}_{\text{unb}}^{\text{step}\,\mu\,\text{iter}\,n} \tag{3.11}$$

$\boldsymbol{P}_{\text{str}}^{\text{step}\,\mu\,\text{iter}\,n}$ in equation 3.11 can be expressed as shown in equation 3.7. This means that equation 3.11 can be simplified as follows:

$$\boldsymbol{F}_{\text{int}}^{\text{step}\,\mu\,\text{iter}\,n} = \Lambda^{\text{step}\,\mu\,\text{iter}\,n} \cdot \boldsymbol{P}_{\text{ext}} - \boldsymbol{P}_{\text{unb}}^{\text{step}\,\mu\,\text{iter}\,n} \tag{3.12}$$

which substituted into equation 3.10 leads to

$$\boldsymbol{K}_{T}^{\text{step}\,\mu\,\text{iter}\,n} \cdot \boldsymbol{u}^{\text{step}\,\mu\,\text{iter}\,n} = \underbrace{(\Lambda^{\text{step}\,\mu\,\text{iter}\,(n+1)} - \Lambda^{\text{step}\,\mu\,\text{iter}\,n})}_{\lambda^{\text{step}\,\mu\,\text{iter}\,n}} \boldsymbol{P}_{\text{ext}} + \boldsymbol{P}_{\text{unb}}^{\text{step}\,\mu\,\text{iter}\,n} \tag{3.13}$$

The unknowns are both the displacement $\boldsymbol{u}$ and the applied load increment λ for the iteration n at the load step μ. Application of Crisfield's cylindrical arc length method

[139] leads to the following constraint:

$$\|\boldsymbol{u}^{\text{step}\,\mu\,\text{iter}\,n} + \boldsymbol{U}^{\text{step}\,\mu\,\text{iter}\,n} - \boldsymbol{U}^{\text{step}\,\mu\,\text{iter}\,1}\|^2 = \Delta l^2 \tag{3.14}$$

where Δl has been previously fixed. Equations 3.13 and 3.14 give raise to a second order algebraic equation which contains the term $\lambda^{\text{step}\,\mu\,\text{iter}\,n}$. Different closing constraint equations could be employed, leading to different arc length methods, as for example the *Riks-Wempner* or *Ramm*'s method [137, 139, 141, 142]. The present computational tool gives the possibility to switch between one of these arc length methods. This proves to be very useful, especially when convergence is troublesome or one of the methods fails, as could for example happen with Crisfield's algorithm when equation 3.14 does not have real roots.

The formal procedure as for the Newton-Raphson case is employed for structural tangent matrix assembling and rigid body elimination.

3.3 Post-Critical Analysis

3.3.1 Baseline Configuration

The Box-Wing or PrandtlPlane [8, 9] presented in Figure 3.1 is the *baseline* configuration adopted in this work. The joint is located at the tip of the wings. The lower wing is swept-back, whereas the upper one is swept-forward. The sweep angles are exactly opposite, and the value is 11.3°. Both the two wings are untapered and present no dihedral angle.

The applied load is a constant conservative non-aerodynamic vertical pressure (direction $+z$) acting on the wings' surfaces (the joint is unloaded). The value of this pressure is equal to $p_z = 0.55125[\frac{Kg}{mms^2}]$ and corresponds to a dynamic pressure relative to a speed of $V_\infty = 30\ [m/s]$.

For all considered configurations a realistic failure criteria could been implemented with the present nonlinear capability and is a plan for future work. Investigation on the maximum stress level in the structure showed that the structure can withstand the applied load without structural failure. The details of this analysis are outside the scope of this paper and for the sake of brevity are omitted.

In a PrandtlPlane Joined Wing the total aerodynamic load can be freely redistributed between the upper and lower wings without penalty on the induced drag.

However, this repartition affects other important aspects which cannot be excluded in the design of these configurations. Aeroelastic performance and stability are two possible examples.

Holding constant the value of total load determined by the aforementioned pressure, it is possible to set different values of the pressures acting on the upper or lower wing in order to simulate different load partitions and investigate their consequences on buckling response, as showed in Section 3.6.

Starting from the baseline's layout a whole family of configurations could be obtained varying some geometrical parameters as the joint's height or the sweep angles. Studies about the effects of these geometrical parameters on the static response of the structure are carried out in Sections 3.4 and 3.5.

It can be shown [7, 8, 10, 94] that the PrandtlPlane configuration presents several aerodynamic benefits with respect to the classical cantilevered wing configurations with the same wing span and total lift. Moreover, this innovative airplane design could be highly beneficial in other areas such as structures, flight mechanics, and engine integration.[8–10, 94]

3.3.2 Post-buckling Response of the Baseline Configuration

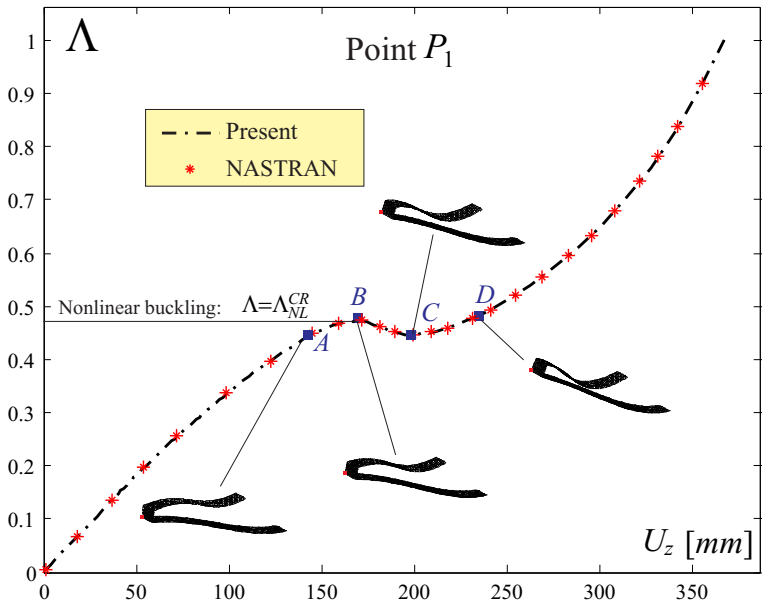

Figure 3.2: Load parameter Λ vs vertical displacement U_z for lower wing tip point P_1. Baseline configuration, front and rear wing carrying the same load.

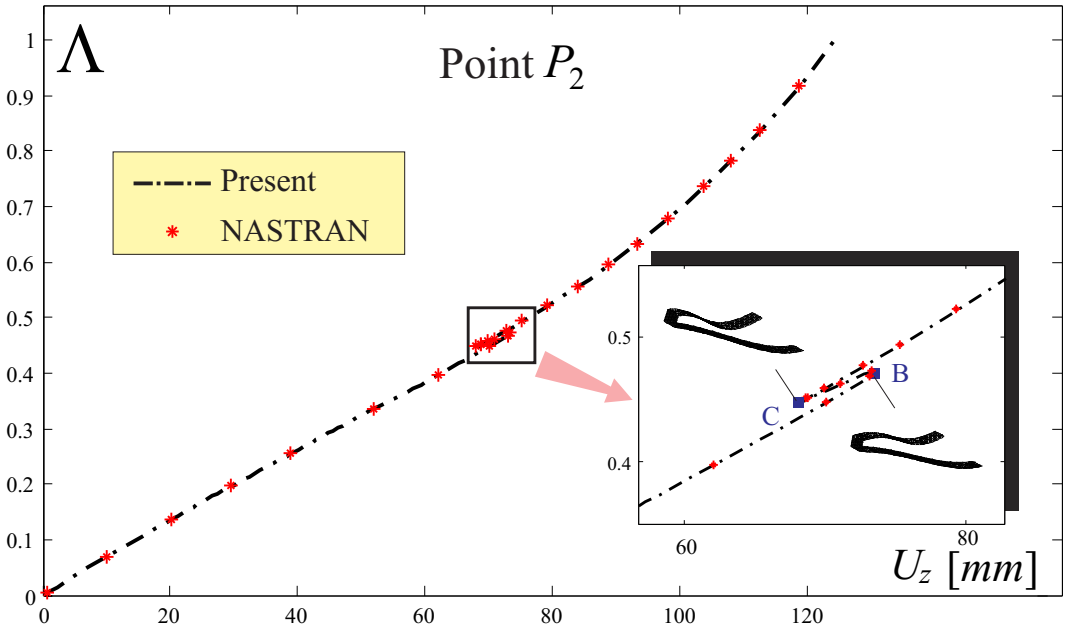

Figure 3.3: Load parameter Λ vs vertical displacement U_z for upper wing midspan point P_2. Baseline configuration, front and rear wing carrying the same load.

The load-displacement responses for point $P_1 \equiv [a+f, 10a, 0]$, at the tip of the lower wing, and point $P_2 \equiv [3/2a + (d+f)/2, 5a, e]$, at the midspan of the upper wing (see Figure 3.1 for the graphical location of these two points) are presented in Figures 3.2 and 3.3 respectively. The dimensionless parameter Λ represents the fraction of the current load level to the external applied load.

From these figures it can be seen that state B corresponds to a load parameter Λ equal to 0.47. Therefore, it can be inferred that applying roughly 47% of the total load, the structure experiences an instability (state B). The shapes of the structure at different positions in the load-displacement curves (see the indicated states A, B, C and D in Figures 3.2 and 3.3) are also presented.

It is not straightforward to track the evolution of deformations identifying characteristic shapes. However, it could be observed that the joint's rigid rotation continuously increases following the path. This does not necessarily correspond to an increase in the load. For example, in the portion of path delimited by states B and C although the rotation is continuously increasing, the structure is decreasing the ability of carrying load. For this reason, there exist distinct deformation shapes as the ones at states A and C, as well as those at states B and D, corresponding to the same applied load levels. This analysis is supported by Figure 3.4, where the parameter $\Theta_x = \frac{y_L - y_U}{z_U - z_L}$ is taken as

an index of the rotation of the joint along the x axis and its evolution is plotted versus the load level. The subscripts U and L refer to the downstream points on the tip of the upper and lower wing. What practically happens when the load is applied, is that after

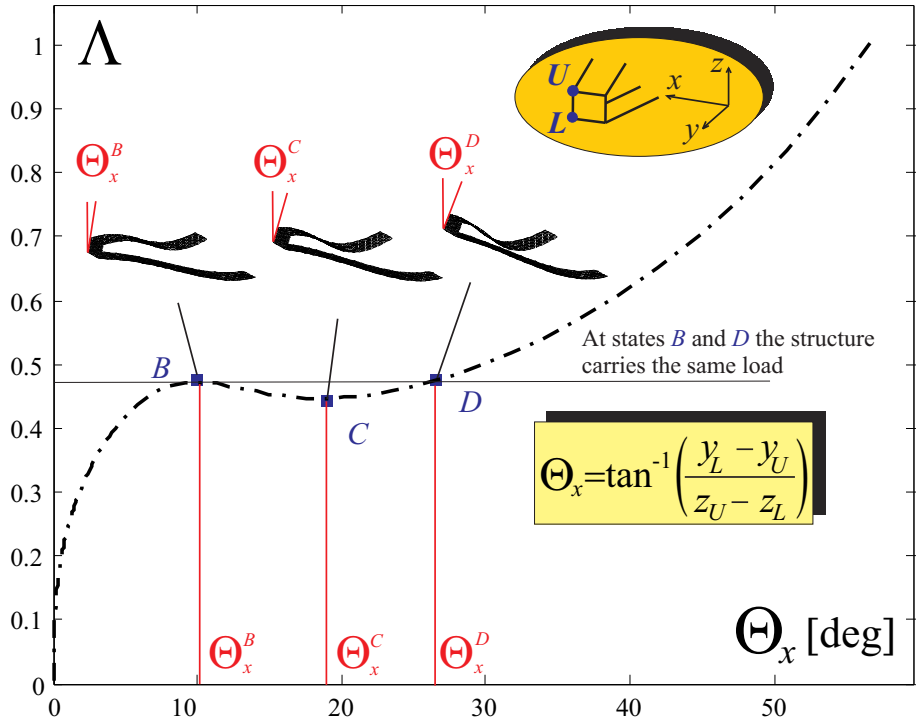

Figure 3.4: The parameter Θ_x, index of the rigid rotation of the joint along x axis, is plotted against the load parameter Λ for the baseline configuration.

the *limit point* B has been reached, a *snap* to state D occurs. The configuration at the limit point B is not able to carry any more load (descending branch), being this instead accomplished by configuration at state D. The fact that the two corresponding configurations are not continuously adjacent to each other creates the dynamic instability called *snap*.

Although the dynamic nature of the instability requires a dynamic analysis in order to properly simulate the response, the snap phenomenon could be hardly accepted in the aeronautical field, and thus, the critical load could be identified with the *buckling load* (state B, see Figure 3.2). As it could be inferred from both the Figures 3.2 and 3.3, there is an excellent agreement between the present capability and the commercial software NASTRAN. For this and next analyzed cases NASTRAN has been used on mesh employing CTRIA 3 elements.

The linear buckling analysis (eigenvalue approach) has been carried out with

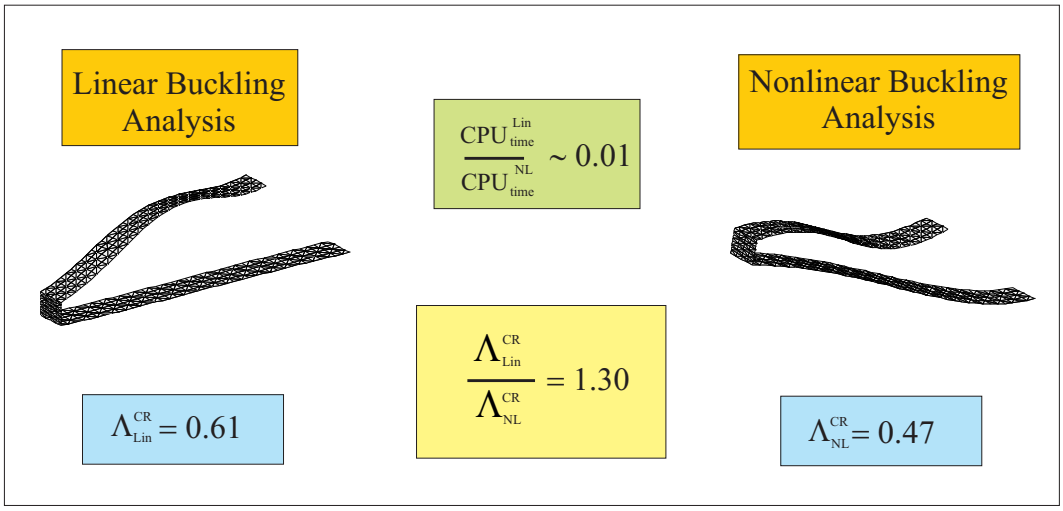

Figure 3.5: Comparison between the buckling loads assessed with the linear and nonlinear analyses, and relative mode shapes at buckling.

NASTRAN. The CPU time required for this simulation is in the order of one hundredth of the CPU time required for the nonlinear analysis. However, the buckling load is overpredicted of about 30%, as is depicted in Figure 3.5. Thus, although the linear simulation is computationally inexpensive, it proves to be unreliable for this particular case.

It can also be observed that there is a significant difference between the mode shapes at the respective buckling points (see Figure 3.5). This is a clear indication of the different physics caught by the two analyses.

3.4 Effects of Joint's Height to Post-buckling Behavior

It is well known that increasing the distance between the wings enhances the aerodynamic performances of PrandtlPlane Joined Wing configurations in terms of induced drag reduction. This has been demonstrated by Prandtl in his original work [7] which represents a milestone for the aerodynamic analysis of box wings, and has been verified in Reference [18].

Driven by these facts, the baseline configuration (Figure 3.1) is modified by changing the joint's height and rigidly translating one of the two wings along the z coordinate. The the new obtained configuration does not present a dihedral angle. Referring to the geometric parameters depicted in (Figure 3.1), b and e are varied by the same

amount.

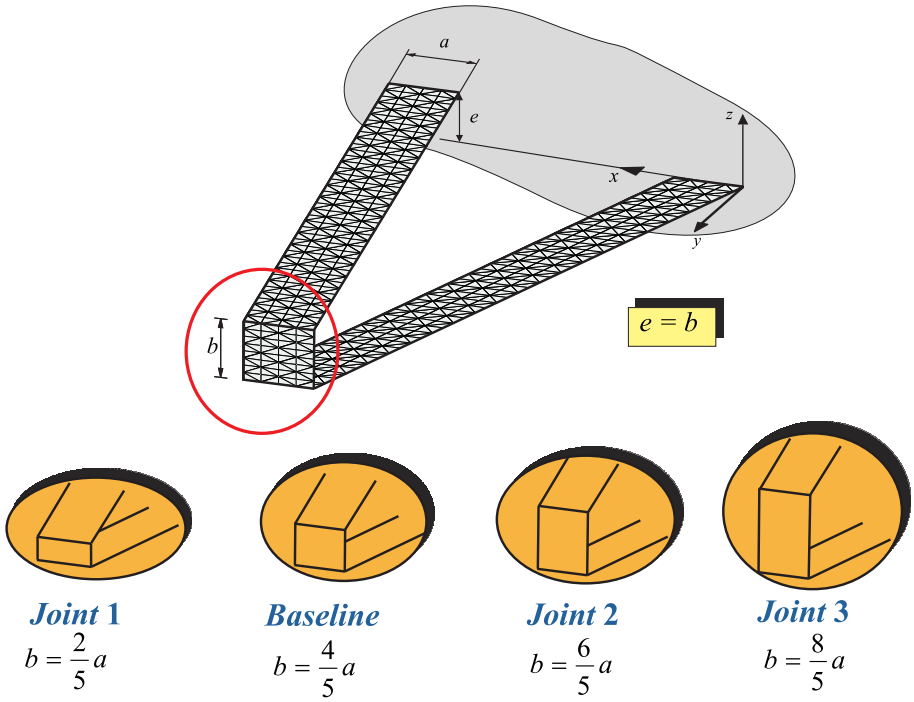

Figure 3.6: Family of configurations obtained varying the joint's height b and maintaining $e = b$ (no dihedral angle is present).

The family of configurations obtained by modifying the parameters in the aforementioned way is sketched in Figure 3.6. It could be recognized that starting from the baseline configuration, a layout with shorter joint, called Joint 1 configuration, and two layouts with longer joints, Joint 2 and Joint 3 configurations, are taken into consideration. The loads and the remaining geometric parameters remain unchanged to the corresponding values adopted for the baseline configuration case. The post-critical behavior of each of these configurations is then studied.

3.4.1 Joint 1 Configuration

In this first case, the height of the joint has been set to be $\frac{2}{5}a$, corresponding to a value of 20 mm. Thus, due to the small joint's height to wing span ratio this configuration carries negligible advantages in terms of induced drag as compared to the classical cantilevered wing with same span and producing the same total lift.[7]

As done for the baseline configuration, post-critical response has been traced for this case. The load parameter Λ versus the displacement response U_z is traced for the

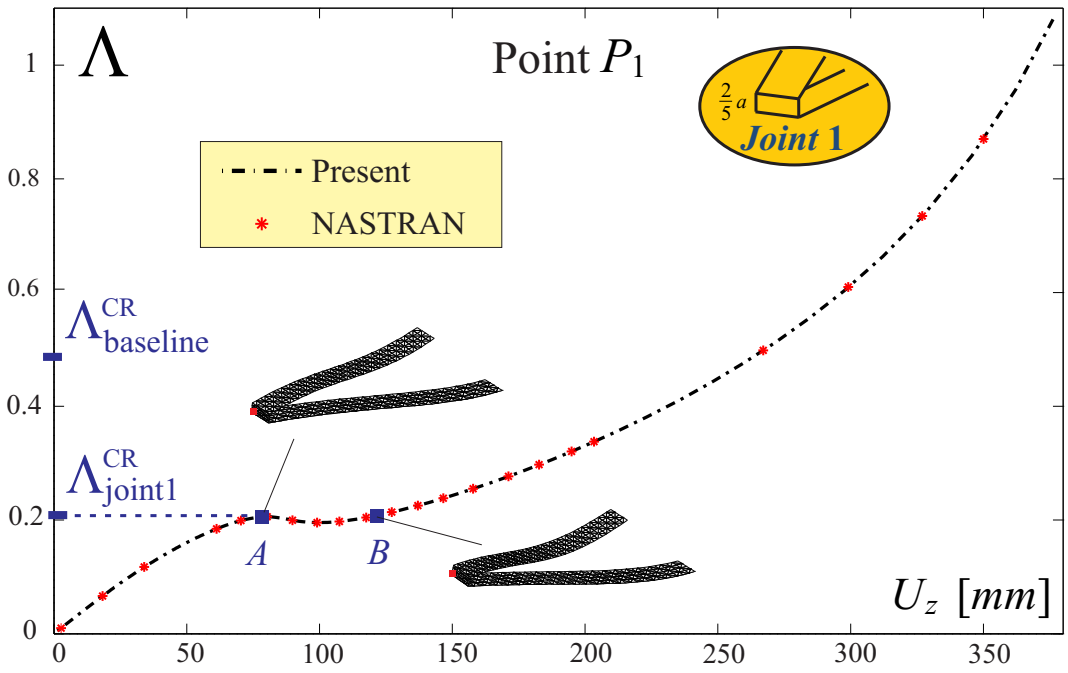

Figure 3.7: Load parameter Λ versus vertical displacement U_z for lower wing tip point P_1. Joint 1 configuration with $b = e = \frac{2}{5}\,a$. The buckling load levels for the Baseline ($\Lambda^{\text{CR}}_{\text{baseline}}$) and actual ($\Lambda^{\text{CR}}_{\text{joint1}}$) configurations are indicated.

two locations, P_1 at the tip of the front wing (see Figure 3.7), and P_2 located at the midspan of the rear wing (see Figure 3.8).

It can be inferred that a similar buckling phenomenon occurs as in the baseline case. The configuration corresponding to state A is the critical one snapping to configuration corresponding to state B. The differences between these two deformation shapes could be properly understood observing the significant increment in the joint's rotation.

In term of convenience of this layout from a structural point of view, it should be observed that buckling occurs at much lower load level, Figure 3.7. This may appear counter intuitive, since the reduction of the joint's height could erroneously be assumed to provide a stiffer structural design. However, a more thorough analysis shows that the joint is responsible of complex transferring of internal forces on the two wings, and this may lead to an equilibrium configuration in which the system does not react optimally to the loads, see for example [130].

The linear and nonlinear analyses show significant differences (see Figure 3.9). As for the Baseline configuration, the linear buckling analysis overpredicts the critical load. However, this overprediction is more pronounced. Examinations of the mode shapes (see

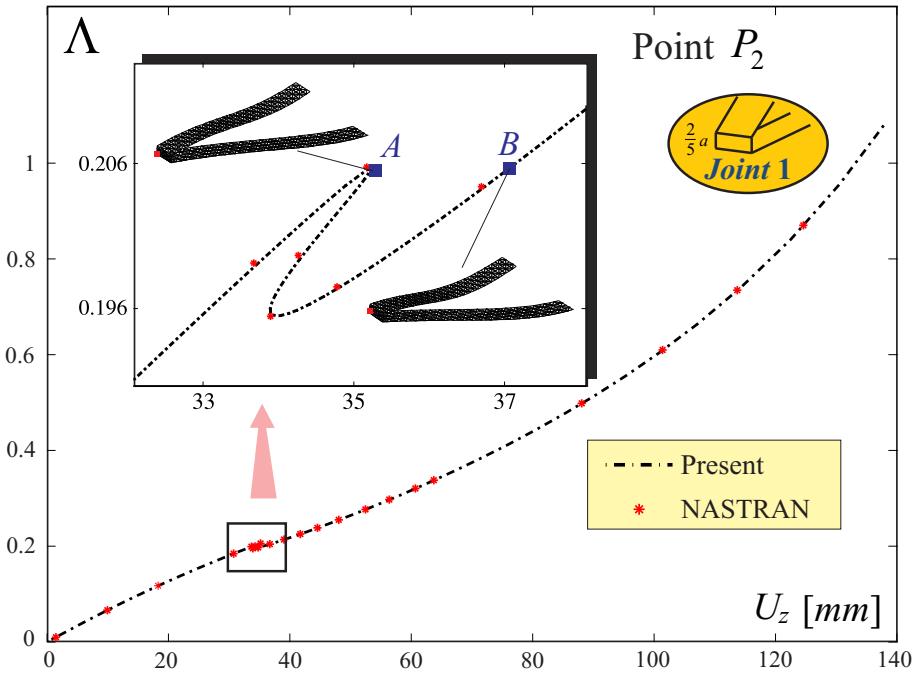

Figure 3.8: Load parameter Λ versus vertical displacement U_z for upper wing midspan point P_2. Joint 1 configuration with $b = e = \frac{2}{5}a$.

Figure 3.9) reveals that the linear analysis could not capture the proper physics of the problem.

The analysis discussed here showed that the Joint 1 configuration, which presents a smaller joint, has a significant lower buckling load (besides the induced drag penalty not considered in this analysis).

3.4.2 Joint 2 Configuration

In this configuration (see Figure 3.6), the joint is higher than the one in the Baseline configuration, being $b = \frac{6}{5}a$, or $b = 60\ mm$. This layout is more performing in terms of aerodynamic induced drag. On the structural side, the responses for the same points P_1, on the tip of the lower wing, and P_2, on the midspan of the upper wing, are depicted in Figure 3.10 and 3.11 in terms of vertical displacement against load level. As it can be noticed, the behavior for Joint 2 follows qualitatively the previous test cases quite closely. This could be supported by means of the shape of the deformed configurations shown in Figures 3.10 and 3.11 (states A, B, C, and D). However, the buckling load, state B, is now occurring at approximately 85% of the nominal load, a consistent increase in respect of the ones found for configurations with shorter joint.

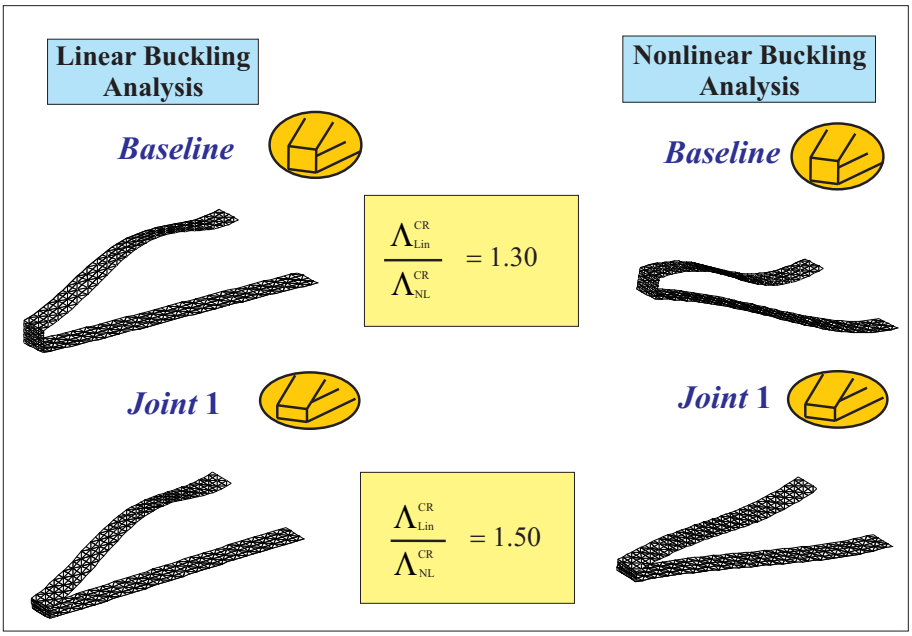

Figure 3.9: Comparison between the buckling loads assessed with the linear and nonlinear analysis, and relative mode shapes at buckling, for the Baseline and Joint 1 configurations.

Considering the significant improvements on the structural stability performance and remembering that a larger distance between the two wings increase the aerodynamic efficiency, it can be inferred that this layout with higher joint is a better choice in the design of PrandtlPlane configurations. Despite the reduction in stiffness consequence of a slender joint, the structure reacts more efficiently.

As for previous analyses, it could be noted the excellent agreement with the commercial software NASTRAN. The linear analysis gives a more reliable prediction of the buckling load with respect to the previously analyzed cases, Figure 3.12. However, it may be misleading to infer that for this particular layout the nonlinearities are of smaller entity compared to the investigations earlier presented. In fact, it is incorrect to compare the physics caught by the linear buckling analysis and the nonlinear one featuring a snap-buckling. This deficiency is reflected in the different mode shapes (see Figure 3.12) provided by the two analyses.

The fact that the buckling load is overpredicted by a minor extent for this configuration where the joint is higher, pose the question if, for this layouts' family, the linear prediction is going to be more conservative with higher joints. An attempt to answer this question is presented in the following sections.

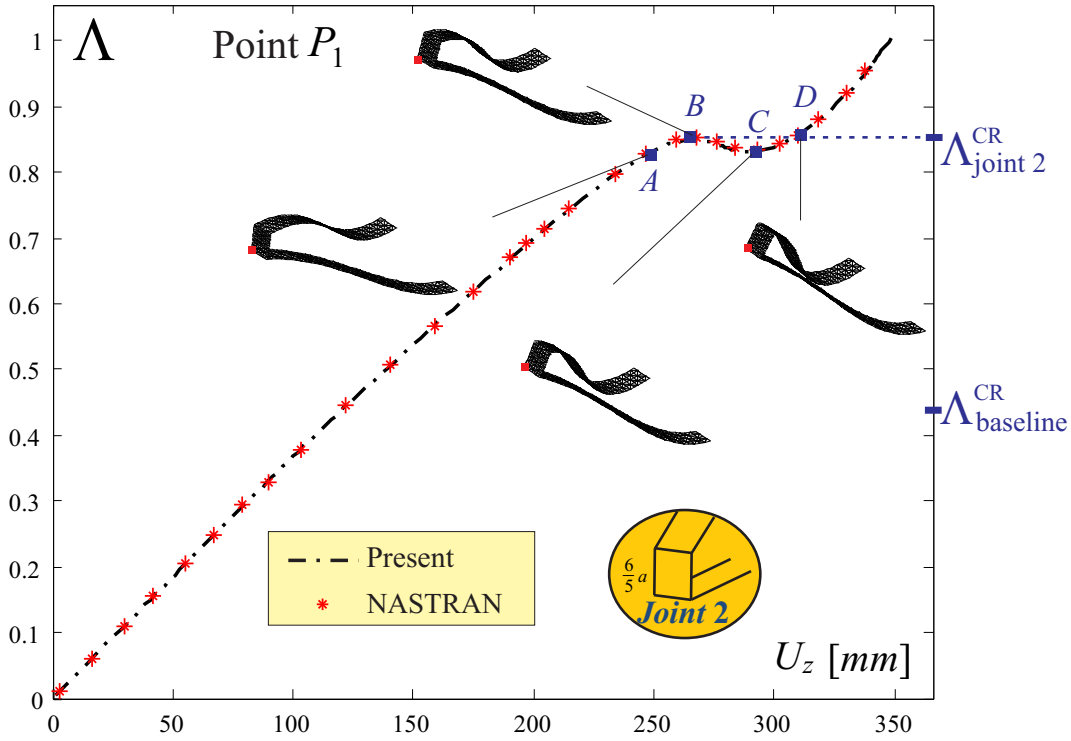

Figure 3.10: Load parameter Λ vs vertical displacement U_z for lower wing tip point P_1. Joint 2 configuration with $b = e = \frac{6}{5}a$. The buckling load levels for the Baseline ($\Lambda^{CR}_{baseline}$) and actual ($\Lambda^{CR}_{joint\ 2}$) configurations are indicated.

3.4.3 Joint 3 Configuration

The Joint 3 layout features a joint's height of $b = e = \frac{8}{5}$, corresponding to 80 mm, and represents the most aerodynamic efficient choice among the four so far considered configurations (see Figure 3.6).

The responses for the point P_1 on the lower wing's tip is depicted in Figure 3.13. It can be observed that *snap-buckling phenomenon does not occur*. The response also follows a close-to-linear pattern for most of the curve (see also the small window in Figure 3.13), before a stiffening behavior is observable. The analysis conducted doubling the nominal load showed that there is a significant stiffening effect and thus no critical instability phenomenon appears.

The excellent agreement with the commercial software NASTRAN validates the analysis.

It is then deduced that increasing the joint's heights is beneficial not only from an aerodynamic view point but also from a structural one with elimination of the buckling instability and a close-to-linear behavior for a large extent of the load fraction Λ. This

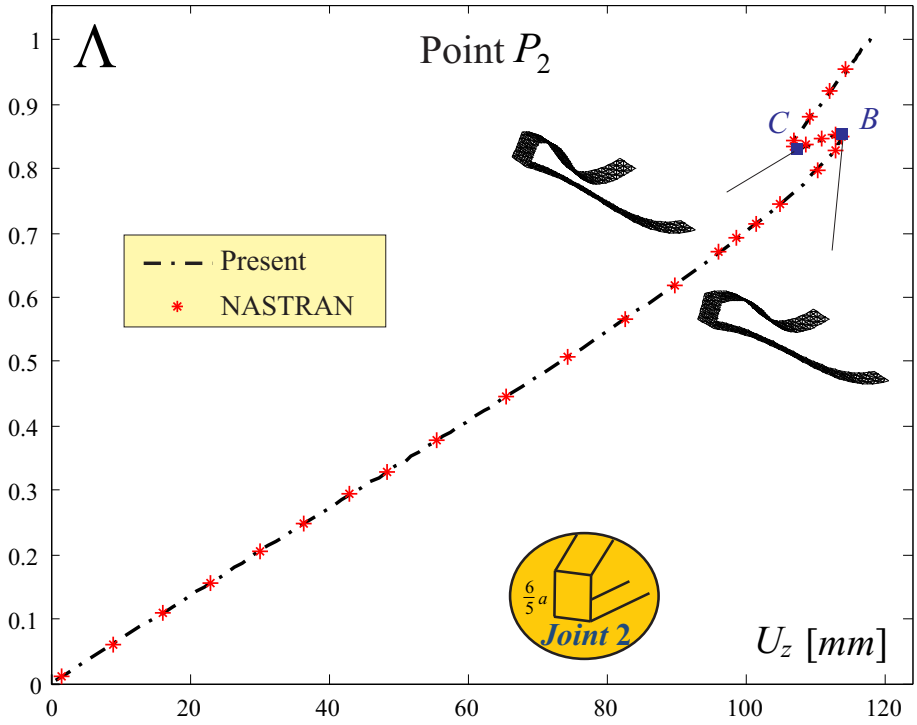

Figure 3.11: Load parameter Λ vs vertical displacement U_z for upper wing midspan point P_2. Joint 2 configuration with $b = e = \frac{6}{5}a$.

statement is valid only for configurations relatively far from joint's heights which could induce buckling of the joint itself. The linear analysis provides a buckling load higher than the nominal applied load (see Figure 3.14). Thus, for the given load condition, no buckling is predicted by the linear model as well.

3.4.4 Interpretation of the Effects of Joint's Height

A qualitative nonlinear displacement-load path for a PrandtlPlane joined-wing configuration is presented in Figure 3.15. A "softening" region has the characteristic of presenting increasingly larger displacements for given increments of the loads. In other words, the *slope* $\frac{\partial \Lambda}{\partial U_z}$ decreases its value. A "stiffening" region has the exact opposite feature: further increments of the applied load correspond to increasingly smaller increments of the cumulative displacement U_z. This is mathematically defined by observing that in the "stiffening" regions $\frac{\partial \Lambda}{\partial U_z}$ increases its value. Not all configuration present all the branches depicted in Figure 3.15. Changing the parameters of the system (for example the joint's height) dramatically affects the nonlinear response.

Next, focus on the different Joined Wings obtained from the baseline configuration by

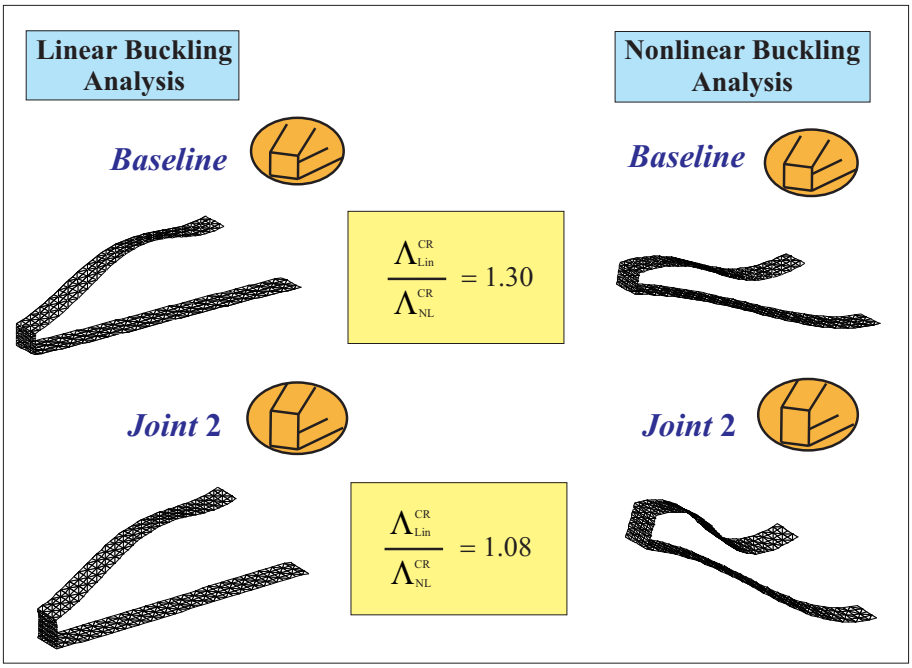

Figure 3.12: Comparison between the buckling loads assessed with the linear and nonlinear analysis, and relative mode shapes at buckling, for the Baseline and Joint 2 configurations.

changing the joint's size b. The vertical displacement of point P_1 as a function of the load level Λ is plotted in Figure 3.16. For the analyzed configurations the buckling load tend to increase with the joint's height. Starting from a certain value, the buckling no longer occurs. Looking more in depth at the responses reported in Figure 3.16, it could be inferred that there is a range of joint's heights where the response shows a typical softening region followed by an unstable branch and a stiffening region as qualitatively introduced in Figure 3.15.

However, for higher joints the response does not show this pattern. To find the configuration which represents the transition between the two different types of behaviors the joint's height is gradually increased. It is found that the configuration with $b = 69\ mm = \frac{5}{69}a$ is the first one which does not show any buckling, as depicted in Figure 3.17. The nonlinear load-displacement curve corresponding to this configuration is called the *Upper Limit Snap Buckling Region* (ULSBR) (see Figure 3.17). More in detail, for the ULSBR the softening branch is immediately followed by the stiffening branch, without any snap occurring in between. All the configurations featuring higher joints don't show any buckling. If the response relative to the Joint 3 configuration (Figure

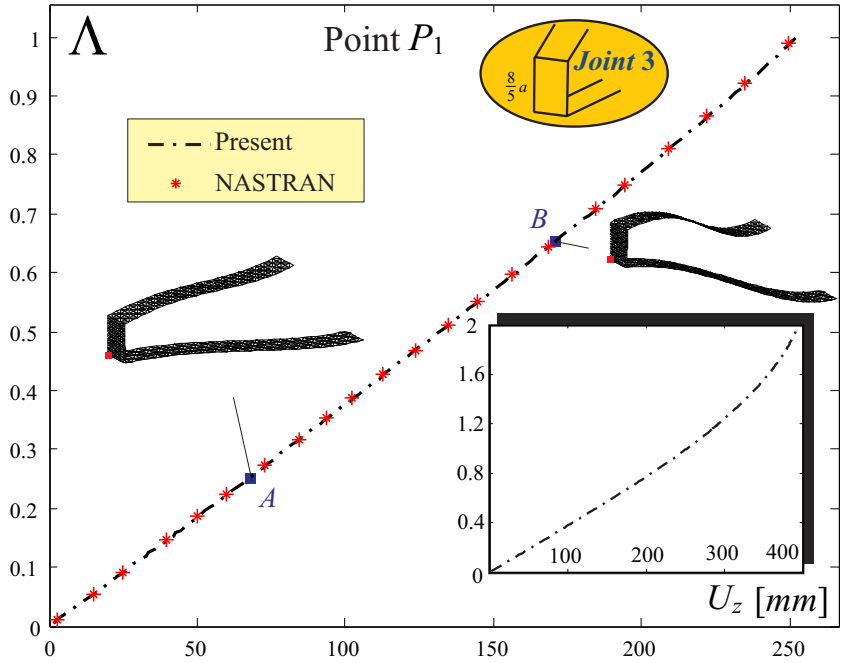

Figure 3.13: Load parameter Λ versus vertical displacement U_z for lower wing tip point P_1. Joint 3 configuration with $b = e = \frac{8}{5}\,a$. The response for the same point doubling the nominal load is also presented in the small window.

3.16) is compared with the ULSBR response (Figure 3.17) then it can be noticed how, further increasing joint's height the softening region of the load-displacement response disappears.

The natural question arises if these particular pattern is also broken in the lower end, that is, for a joint's height below a particular value. Similarly, for a configuration with joint's height smaller than the one corresponding to Joint 1 configuration it can be shown that buckling does not occur. Using the already employed nomenclature, the *Lower Limit Snap Buckling Region* (LLSBR) is then defined (see Figure 3.17). Conducting a similar investigation as the one undergone for the ULSBR, where now the joint's height is decreased, it is found that the first configuration not showing any buckling is the one with joint's height of $b = 7\ mm$ (see Figure 3.17). The stiffening branches is following the softening one without any unstable branch, and the softening-snap-stiffening pattern is no longer observed for these joint's heights.

Summarizing, the region where the response is showing a snap is bounded by the ULSBR and LLSBR curves. Incrementing or decrementing the joint's height leads to configurations where the response does not present any snap buckling phenomenon.

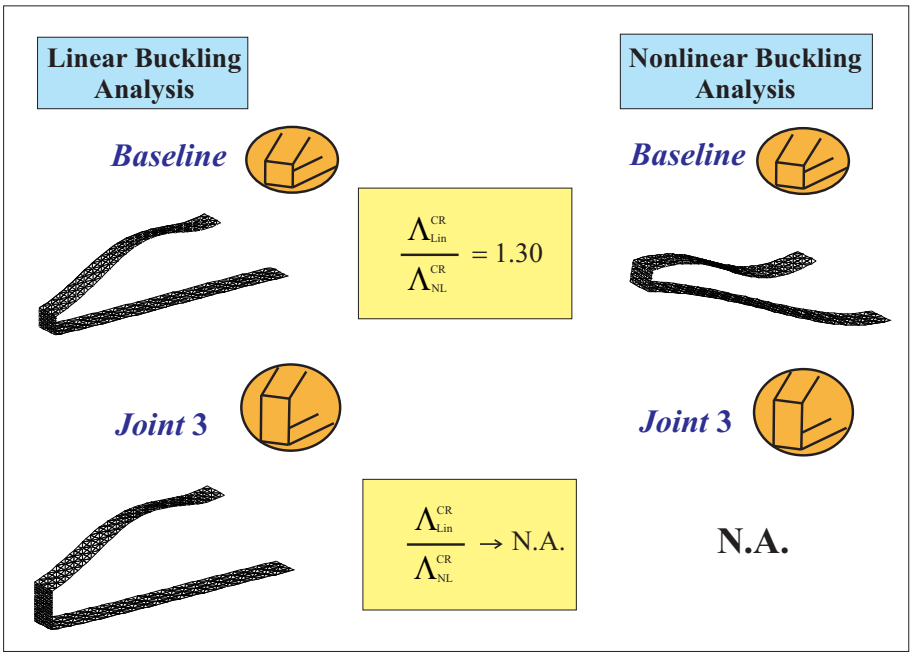

Figure 3.14: Comparison between the buckling loads assessed with the linear and nonlinear analysis, and relative mode shapes at buckling, for the Baseline and Joint 3 configurations. The nonlinear analysis does not show any buckling for Joint 3.

This is *not* a general rule: it will discussed later, when the effects of the sweep angles of the wings are introduced, that it is *not* always possible to define ULSBR and LLSBR that bound a snap buckling region. This fact demonstrates how complex the nonlinear response of a Joined Wing is in the general case.

From Figure 3.17 it can be inferred that the configurations with smaller joints than the one corresponding to LLSBR, although not presenting any snap-buckling (see the qualitative Figure 3.15 for its definition), are characterized by a much softer response than configurations whose nonlinear response curve is within the snap buckling region. From a practical perspective these configurations characterized by such significant softening effect could be hardly accepted for common design situations, even if not showing a proper mathematical defined buckling.

A configuration whose nonlinear response is beyond the ULSBR reacts in a much stiffer way and does not show any snap phenomenon. In addition, it presents important aerodynamic advantages (reduced induced drag). It is then preferable, for conventional design situations, to have configurations with joint's height equal or bigger than the one corresponding to ULSBR. More investigations with the actual structural elements of the wing (spars, ribs, composite materials etc.) will be carried out in up-coming works to

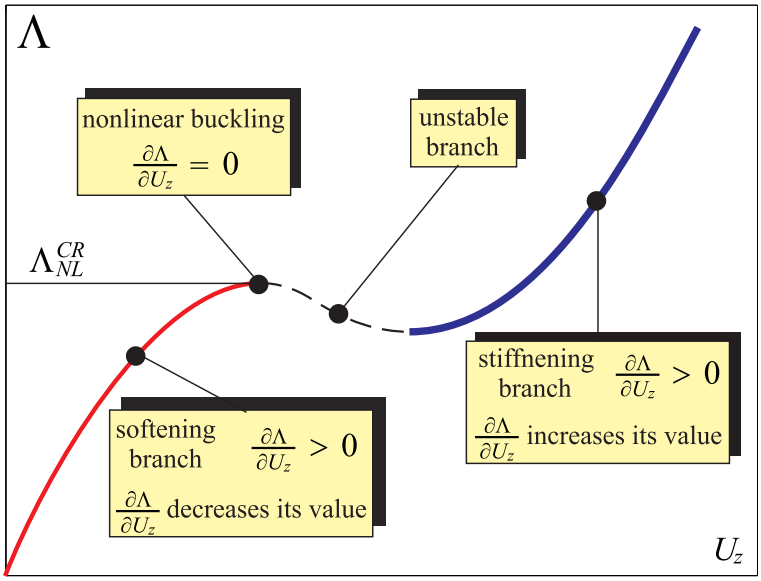

Figure 3.15: Concepts of softening branch, snap-buckling point, unstable branch, and stiffness branch in a typical load-displacement curve of a PrandtlPlane configuration (note that changing the parameters of the configuration dramatically affects the response).

assess how the present behavior is modified.

The drawn conclusions about joint's height are valid as long as the joint itself does not buckle. This is likely to happen for very slender joints.

Further observing the responses for the layout's family, Figure 3.16, it could be inferred that the responses exhibits almost the same slope and behavior for lower load levels at which the structure does not present a significant geometric nonlinearity and can be assumed to be linear. This may look counterintuitive since a smaller joint is intuitively associated with a stiffer structure. Due to the relative small values of displacement and the close-to-linear response in this area, the problem has been further investigated by a linear analysis where the two wings and the joint are represented as beams, but the sweep angle has been neglected, see Appendix A for more details. The assembly of linear beams described in Appendix A leads to the following formula for the displacement of point P_1 (see Figure 3.1):

$$U_z^{\mathrm{P}_1} = \frac{L^4\left(Ab^2(b+2L)+24JL\right)}{8EJ\left(Ab^2(b+6L)+24JL\right)}\, p_z \cdot a \tag{3.15}$$

where $A = a\,t$ is the section's area, $J = \frac{1}{12}at^3$ is the section's moment of inertia and $L = 10a$ is the wing's span. Given the geometrical and material properties of the

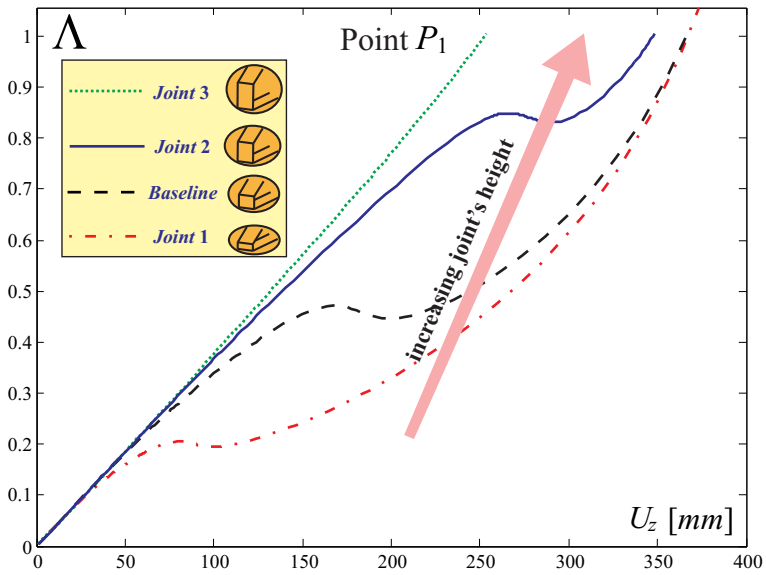

Figure 3.16: Load parameter Λ versus vertical displacement U_z for lower wing tip point P_1. Responses for different joint's heights.

example, the effects of joint's height are negligible in the range considered in the layout's family, although a sensible drop in stiffness is occurring for short joints (details omitted for brevity). This results agree with the full nonlinear responses for small applied load fractions (see Figure 3.16).

Further insight could be gained comparing the linear and nonlinear buckling analysis predictions for the different cases, Figure 3.18. Since the buckling load is properly defined only in the *Snap Buckling Region*, SBR (see Figure 3.17) and does not exist beyond the LLSBR and ULSBR bounding curves, the comparison between the linear and nonlinear responses has a practical sense only inside SBR. As a consequence, for the *Joint* 3 configuration (whose response is outside SBR) the ratio of the linear predicted buckling load to the nonlinear one is not defined.

With a deeper look, it could be inferred that both linear and nonlinear investigations show the same trend of higher buckling load with higher joints. However, the overprediction of the linear analysis is larger for shorter joints. As long as the joint's height increases, the linear predictions narrows its gap with the nonlinear one. The existence of a configuration for which both nonlinear and linear analysis agree in predicting the buckling load is an important theoretical achievement since, for that particular case, costly nonlinear analysis are not necessary to predicted the failure of the structure. However, the problem is that achieving the equality of the linear and nonlinear buckling

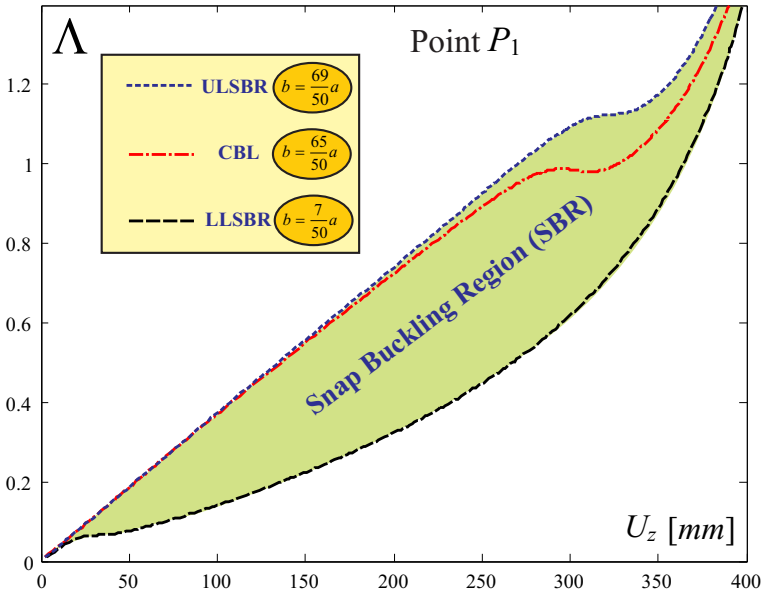

Figure 3.17: Load parameter Λ versus vertical displacement U_z for lower wing tip point P_1. The region where snap buckling occurs is bounded by the ULSBR and LLSBR curves. The CBL configuration lies in this region.

evaluations is dependent on the joined-wing configuration: it is not known a priori for which value of the joint this equality actually occurs. Thus, the nonlinear analysis cannot be avoided since it is not known in advance when the linear analysis is "accurate" (i.e., it provides the same instability point as the nonlinear analysis does).

It has been found that a configuration with joint's height of $b = 65\ mm = \frac{65}{50}a$ exhibits the coincidence of the values for the critical load evaluated with the linear and nonlinear analyses. This configuration is called the *Consistent Buckling Load* configuration, (CBL).

Notice that CBL may even not exist, but if it does, its joint's height has to be between the ones corresponding to LLSBR and ULSBR. Moreover, according to Figure 3.19, the buckling described by the linear analysis, although showing the correct load prediction, does not catch the physics underlying the real snap phenomenon.

Concluding, the linear analysis is a tool which, for the Joined Wings, is not able to model the correct physics. As a consequence, the predicted critical loads are not in accordance with the nonlinear predicted ones. They agree only for the CBL configuration.

Increasing the size of the joint corresponding to LLSBR (Figure 3.18) both the linear and nonlinear analyses predict higher buckling loads. The linear prediction is consistently

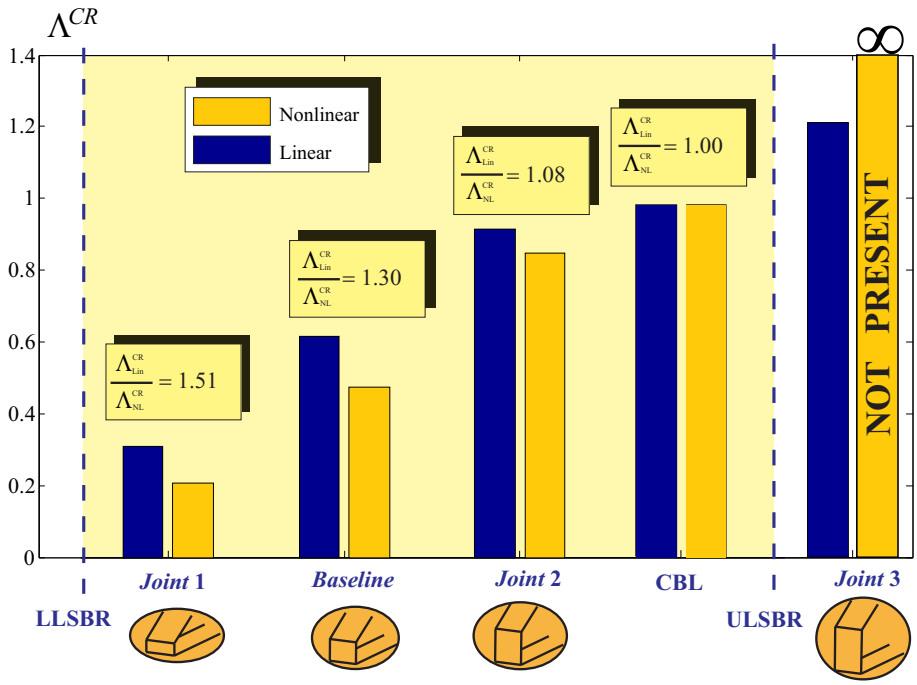

Figure 3.18: Buckling load parameter evaluated by means of linear ($\Lambda^{\mathrm{CR}}_{\mathrm{Lin}}$) and nonlinear ($\Lambda^{\mathrm{CR}}_{\mathrm{NL}}$) buckling analysis for the family of configurations obtained changing the joint's height.

higher than the nonlinear one. This gap reduces and becomes exactly equal to zero when the joint's height corresponds to the CBL case. Further increase of the joint's height still show a growing value for the buckling load. However, now the nonlinear prediction is higher than the linear one. For joint's sizes larger than the one corresponding to ULSBR the linear analysis still presents a growing buckling load, but actually, according to the nonlinear theory it no longer exists.

3.5 Effects of Sweep Angle to Post-buckling Behavior

Swept wings reduce the drag raise due to compressibility effects by increasing the critical Mach number. Moreover, swept-back angles are very beneficial since the aeroelastic divergence speed is dramatically increased. Swept-back wings are widely used in today's aeronautic world and have an important impact in the design of structures as well as in flight mechanics and dynamics of the configuration.

For a PrandtlPlane configuration the sweep angle has even a bigger impact. In fact the configuration cannot count on wing tail for fine tuning of the trim [94]. Thus,

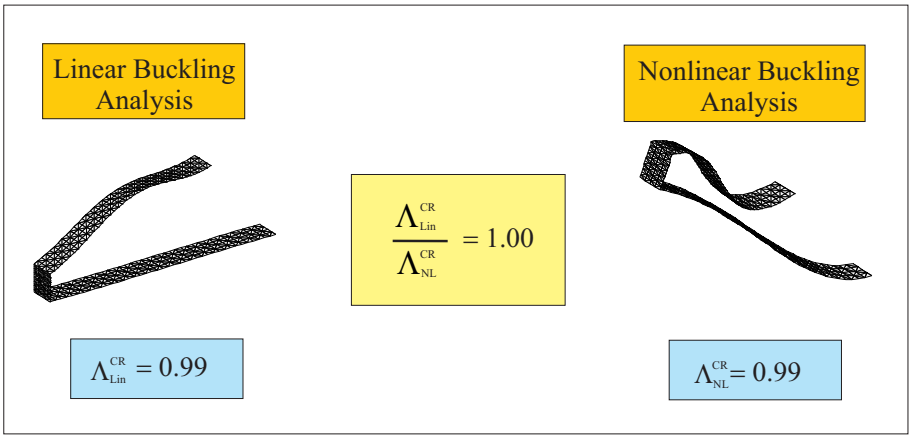

Figure 3.19: Consistent Buckling Load (CBL) configuration: the predicted buckling load assessed with linear buckling analysis, ($\Lambda^{\mathrm{CR}}_{\mathrm{Lin}}$), and nonlinear analysis, ($\Lambda^{\mathrm{CR}}_{\mathrm{NL}}$), are coincident. However, the predicted deformation shapes at buckling substantially differ.

in this complicate situation where each field has its own requirements, the constraint on a trimable configuration represents a further burden.

It should be noted that, from a theoretical point of view, the induced drag is not affected by the sweep angle. This is consequence of Munk's *stagger theorem* [143], which states that the induced drag of a lifting system does not change when elements are moved along the streamwise direction, as long as the circulation (lift) distribution is held constant.

In order to understand how sweep angle affects buckling, a family of layouts are obtained starting from the baseline configuration (Figure 3.1) and changing the parameters d and f as depicted in Figure 3.20. The wing systems obtained by altering the baseline configuration present the property that the lower and upper wing have exactly opposite values of sweep angle.

In all the analyses, the other parameters are held constant at the values corresponding to the baseline configuration. The wings are subjected to the same constant vertical pressure $p_z = 0.550125[\frac{Kg}{mms^2}]$.

3.5.1 Sweep 1 Configuration

In this first configuration both the wings are unswept, thus, according to Figure 3.1, $f = 0$ and $d = -a$. Such a layout would not be well suited for flying at high subsonic Mach numbers. Moreover, it will suffer trim and stability problems unless a further aerodynamic surface is designed for these specific purposes. In terms of structural

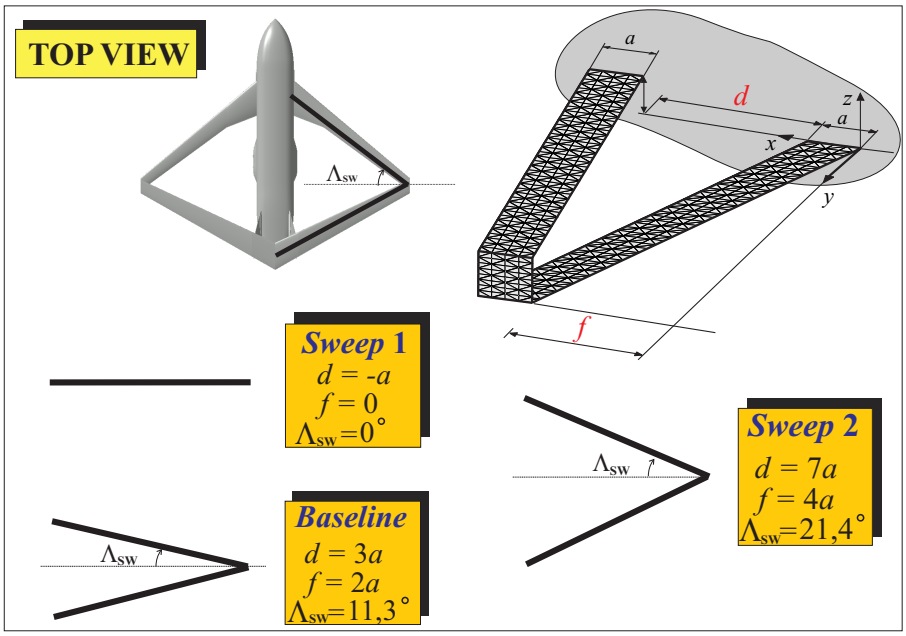

Figure 3.20: Family of configurations obtained varying d and f, or the sweep angle Λ.

response, the load displacement curves for points P_1, on the tip of the lower wing, and P_2, on the midspan of the upper wing, are depicted in Figures 3.21 and 3.22. A snapping phenomenon occurs at a load level of approximately $\Lambda^{\text{CR}}_{\text{sweep 1}} = 0.91$ (see Figure 3.21), which is almost two times the buckling load level of the baseline configuration ($\Lambda^{\text{CR}}_{\text{baseline}} = 0.47$). The unswept wings do not present the complex bending-torsion coupling typical of swept wings, and this seems to help and postpone the instability phenomenon. As a consequence, for this particular configuration and load condition, smaller sweep angles seem to be beneficial from a buckling perspective.

The analysis should not be given any physical sense after the point in the unstable branch is reached where the upper and lower wing interpenetrates. In fact, observing the deformation shapes at states B and C it is possible to show that somewhere in-between in the branch the interpenetration takes place. This does not invalidate the assessment of snap phenomenon and the consequent definition of the buckling load.

Observing in more detail the response for point P_1, a so called *snap-back* is spotted, that is, there is a region, starting from state B, in which both the load level Λ and the displacement U_z decrease. This is associated with the sharp turn of unstable branch. The question then arises, if in tracking the curve the joint's rigid rotation still monotonically increases, as seen for the baseline and other configurations previously

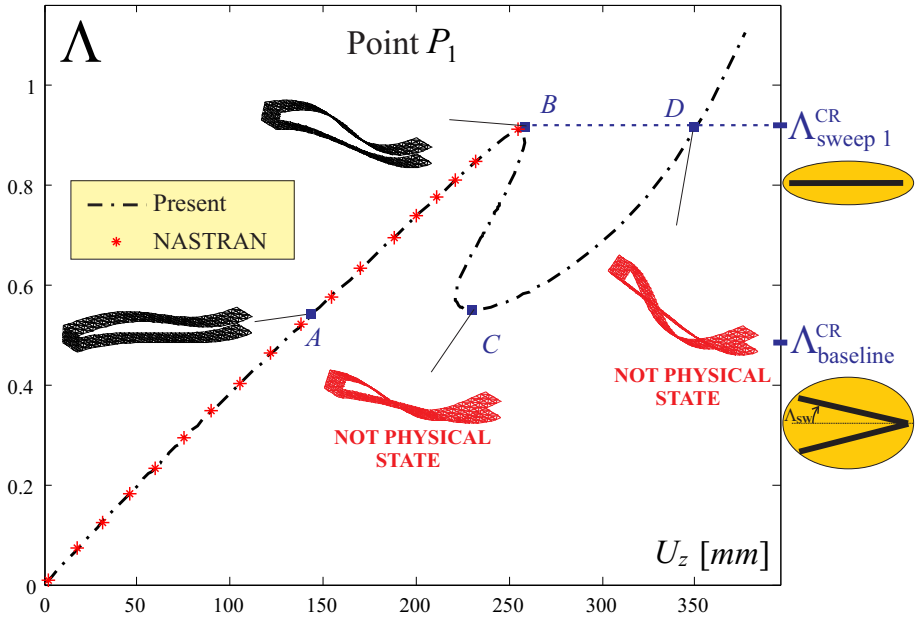

Figure 3.21: Load parameter Λ vs vertical displacement U_z for lower wing tip point P_1. Sweep 1 configuration with $d = -a$ and $f = 0$, corresponding to unswept wings case. The buckling load levels for the baseline ($\Lambda^{\text{CR}}_{\text{baseline}}$) and actual ($\Lambda^{\text{CR}}_{\text{sweep 1}}$) configurations are indicated.

investigated. This could be verified with the aid of Figure 3.23, where the parameter $\Theta_x = \frac{y_L - y_U}{z_U - z_L}$, measure of the rotation of the joint, is plotted against the load level. After state B is reached, the structure experiences a dramatic lost in the capacity of carrying any load. Carrying on, the interpenetration occurs and thus, starting from this point the analysis loses any physical sense. Monitoring the rotation of the joint is very helpful in trying to described what physically happens in the deformation, since it is not easy to detect meaningful parameters when observing the deformation shapes before and after the snap.

As a last note about the simulation, it is important to notice that NASTRAN analysis had some numerical difficulties in converging after state B. These convergence issues are not caused by the interpenetration of the two wings which, as said, occurs somewhere in the unstable branch but not immediately after the limit point B.

Results of linear analysis are also taken into consideration and compared with the corresponding ones obtained with a nonlinear analysis. As it can be inferred from Figure 3.24, the linear analysis predicts a lower buckling load than the actual one. It is also interesting to observe how strong the effects of swept wings are when comparing linear and nonlinear predicted buckling loads. In particular, for this case (which presents unswept

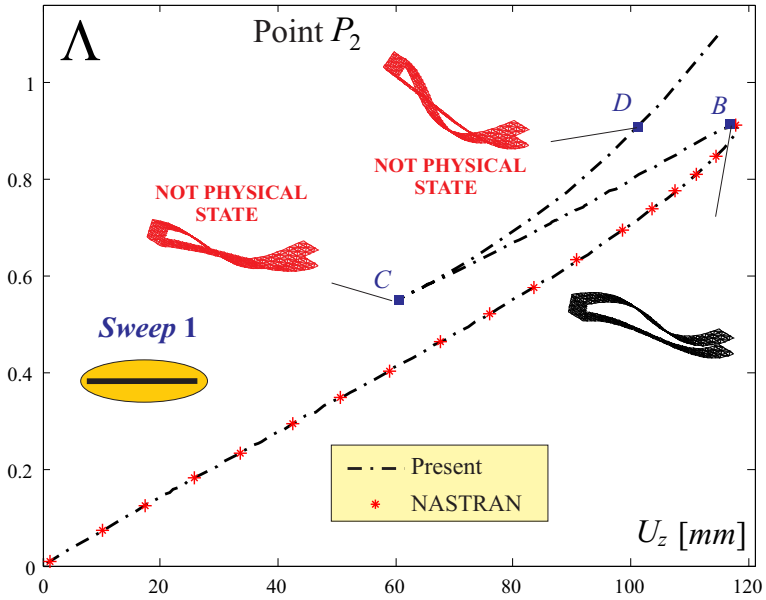

Figure 3.22: Load parameter Λ vs vertical displacement U_z for upper wing midspan point P_2. Sweep1 configuration with $d = -a$ and $f = 0$, corresponding to unswept wings case.

wings) the linear analysis underpredicts the buckling load by 14%; for the baseline configuration the linear analysis overpredicts the buckling load by 30%. Observing Figure 3.24 it can be understood that a configuration featuring sweep angle between the values corresponding to the Baseline and Sweep 1 configurations will present $\Lambda_{\text{Lin}}^{\text{CR}} = \Lambda_{\text{NL}}^{\text{CR}}$. In other words, there will be a sweep angle for which the buckling loads evaluated by the linear and nonlinear analyses are coincident (Consistent Buckling Load configuration). As discussed when the effects of the Joint's height were considered, the linear analysis is not able to predict the correct buckling mode shape (see Figure 3.24).

3.5.2 Sweep 2 Configuration

In this configuration, the parameters controlling the sweep angle of the wings are set to $d = 7a$ and $f = 4a$, for a value of $\Lambda_{\text{SW}} = 21.3°$.

The displacement of point P_1 against the load level is depicted in Figure 3.25. It could be observed that, for this configuration, no snapping phenomenon occurs. A further inspection of the load-displacement curve of Figure 3.25 shows a change of curvature at state A. Thus, the characteristic pattern composed of softening, unstable branch and hardening phases, shown in the Baseline and Sweep 1 responses, has lost the unstable branch part for this case. This instance has already been observed varying the joint's

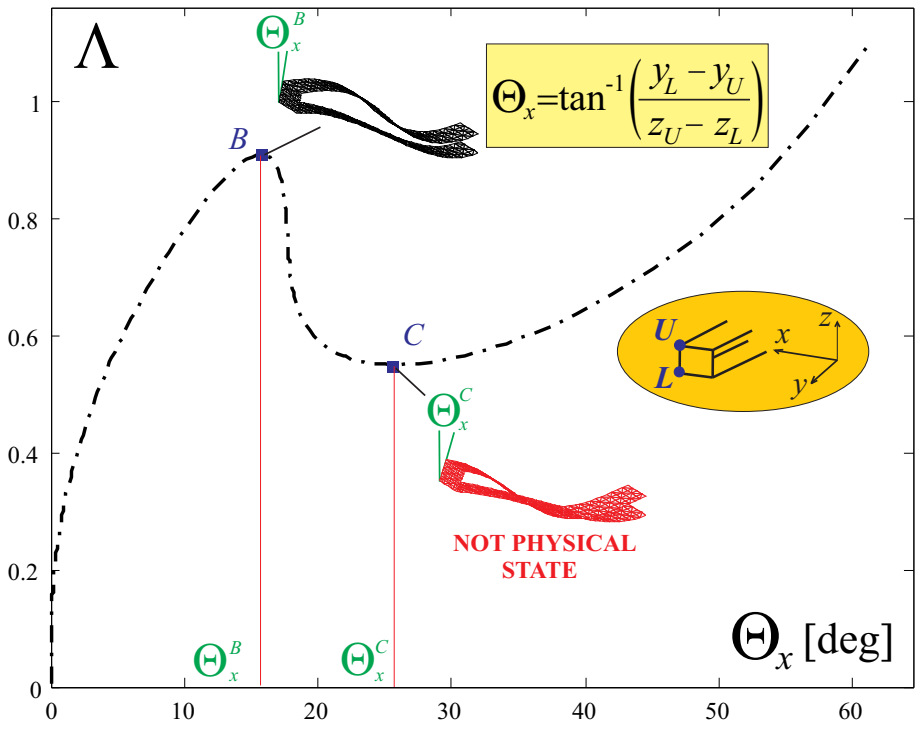

Figure 3.23: The parameter Θ_x, index of the rigid rotation of the joint along x axis is plotted against the load parameter Λ for Sweep 1 configuration.

height. Thus, in analogy with what already observed, Sweep 2 configuration presents a load-displacement curve outside of the *Snap Buckling Region*, SBR. Figure 3.26 shows the comparison between the linear and nonlinear predictions.

3.5.3 Interpretation of the Effects of Sweep Angle

As a comparative plot, the vertical displacement of point P_1 is plotted for the layouts' family, Figure 3.27. For the rest of the section only swept-back angles are considered for the lower wing, being thus the unswept wing configuration, Sweep 1 the lower limit.

It may be pointed out that, from a pure snap occurrence point of view, increasing the sweep angle leads to lower buckling loads, until a first configuration is reached, for which no buckling occurs. This configuration, in analogy to what previously discussed, corresponds to the *Lower Limit Snap Buckling Region* (LLSBR) one. For bigger sweep angles, the response does not present any snap. By means of Figure 3.27, it is easy to state that the LLSBR shows a sweep angle between the values corresponding to the Baseline and Sweep 2 configurations. Moreover, Sweep 2 configuration falls outside of

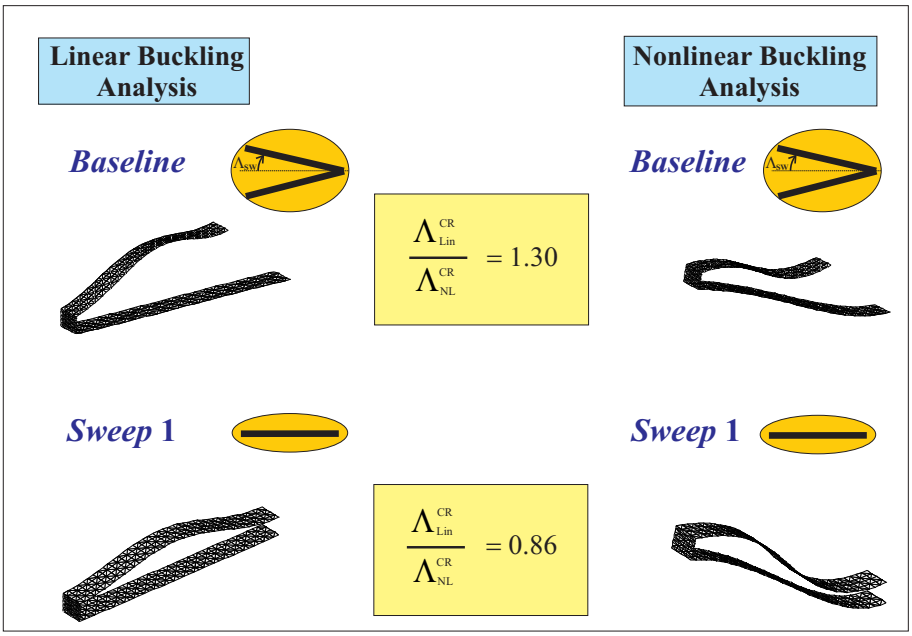

Figure 3.24: Comparison between the buckling loads assessed with the linear and nonlinear analysis, and relative mode shapes at buckling, for the Baseline and Sweep 1 configurations.

the SBR.

If it is correct to state that for configurations with bigger sweep angles than the one corresponding to LLSBR no buckling occurs in terms of snap-dynamic phenomenon, it is also misleading to consider these configurations more efficient from a structural point of view. In fact, observing Sweep 2 configuration's response, not far from the flex point on the curve, a consistent decrease of stiffness is spotted. Obviously this kind of softening could not be acceptable for most of the practical design situations. As a further observation, the slope in the first part of the response is negatively affected by sweep angle showing that highly swept wings experience a reduction in stiffness.

Increasing the sweep angles have then a detrimental effect on the buckling and stiffness of the structure. The strong bending-torsion coupling typical of swept Joined Wings may be alleviated with an appropriate choice of composite materials. See for example Reference [130].

Considering the results, the authors find that may be appropriate under some circumstances to define a *pseudo* buckling load for configurations where no dynamic instability occurs. It could be considered as the load corresponding to the flex point where the changes from a softening to a stiffening behavior. This enables to better

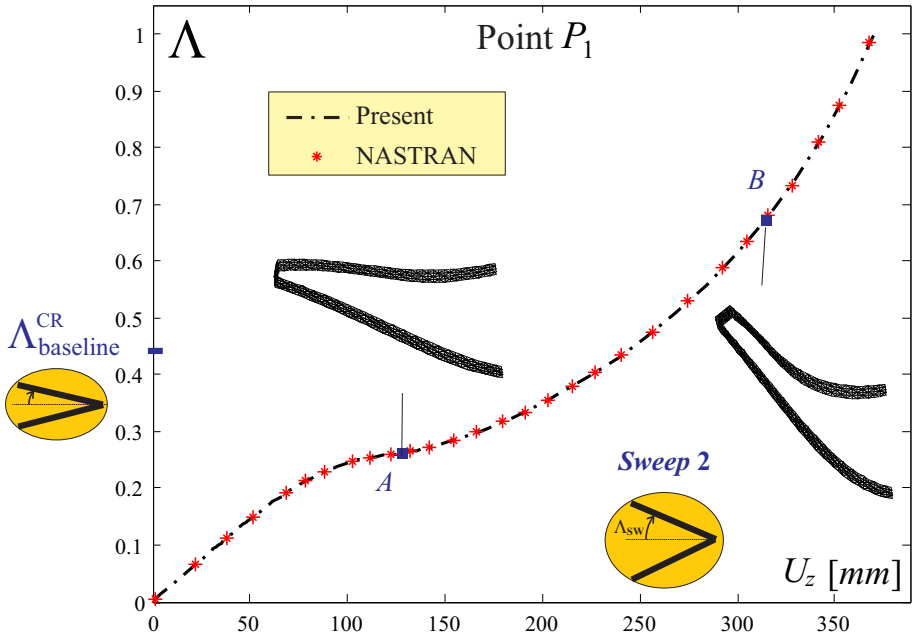

Figure 3.25: Load parameter Λ vs vertical displacement U_z for lower wing tip point P_1. Sweep 2 configuration with $d = 7a$ and $f = 4a$. The buckling load level for the baseline ($\Lambda^{\text{CR}}_{\text{baseline}}$) is indicated.

compare the efficiency of two structures, one of which is not showing a snap buckling. That definition requires a change in curvature of the response. As already previously discussed this may not happen. Thus, in order to compare the efficiency of the structures a different parameter may need to be defined.

It should be noted that the analysis performed here considered *positive* sweep angles for the *lower* wing and *negative* sweep angles for the *upper wing*. The lowest considered value for the sweep angle is zero which corresponds to a biplane with joined tips ("true" box wing configuration). The configuration with sweep angle equal to zero (unswept wings) presents a quite high snap-buckling load (see Figure 3.27) which is reduced when the wings have a non-zero sweep angle. The system presents a LLSBR but *does not show* a ULSBR: if the sweep angles are "reversed" (positive sweep angle for the upper wing and negative sweep angle for the lower wing) the system still presents a set of curves like the ones presented in Figure 3.27 (because of the symmetry) with a clear indication of the LLSBR but with a "missing" ULSBR. This is one of the main conceptual differences between a family of Joined Wings obtained by changing the sweep angles and another family of configurations obtained by changing the joint's height (see previous investigations): the first family does *not* present ULSBR whereas the second

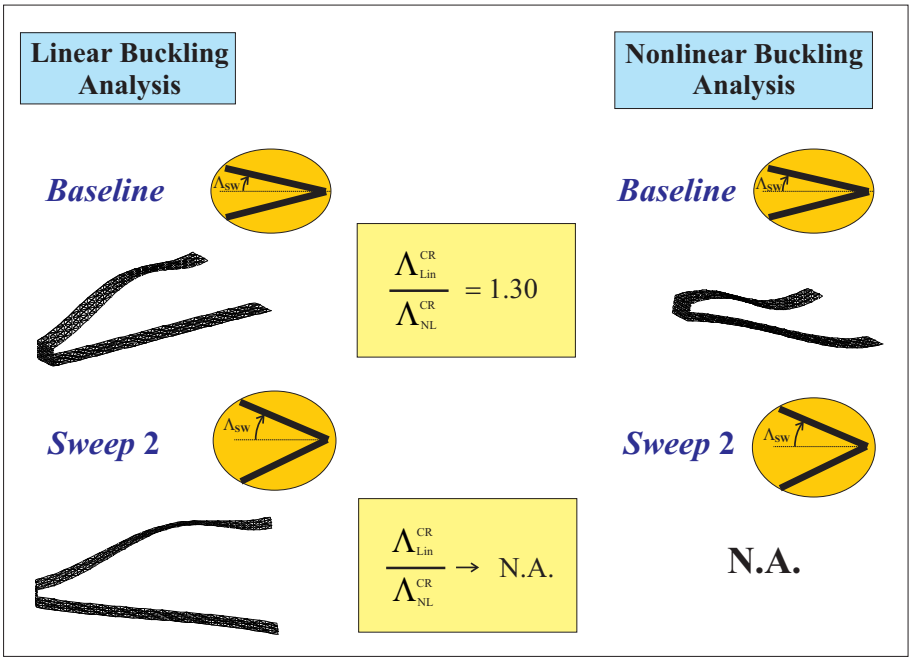

Figure 3.26: Comparison between the buckling loads assessed with the linear and nonlinear analysis, and relative mode shapes at buckling, for the Baseline and Sweep 2 configurations.

family *does* present ULSBR. Both groups of configurations present LLSBR.

Observing Figure 3.27 it is clear that for relatively large values of the applied load the response is no longer sensitive to the sweep angle (the curves are practically coincident and independent of Λ_{SW}). It should be noted that the unswept wing configuration response loses its physical meaning after a state, located in the unstable branch, corresponding to an interpenetration of the wings.

The torsional-bending coupling which is enhanced when the sweep angle is increased, is detrimental on structural performances of the configuration. This is also predicted by the linear models with a reduction of the buckling load (see Figure 3.28). In fact, within the SBR, both linear and nonlinear analyses show a decreasing of the predicted buckling load for bigger sweep angles. Where the trend is consistently predicted, the ratio of the two predictions is not.

Comparing the ratio of the linear and nonlinear predictions for the unswept and baseline configurations, it is straightforward to deduce that a configuration exists with sweep angle between the corresponding of the two configurations, for which linear and nonlinear analyses predict the same buckling load. This is the *Consistent Buckling Load*

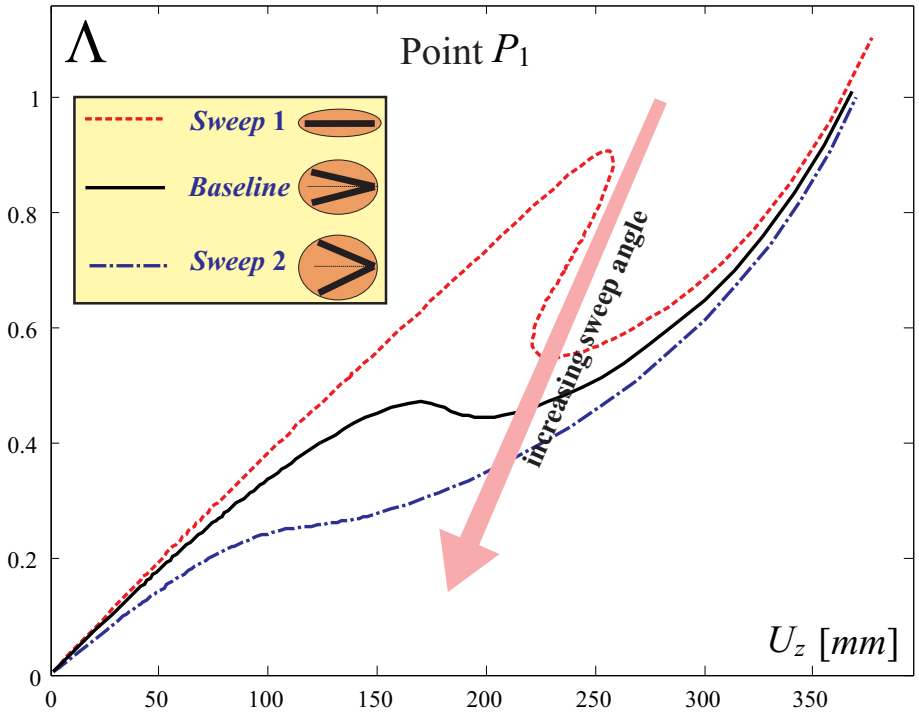

Figure 3.27: Load parameter Λ vs vertical displacement U_z for tip point P_1. Responses for configuration with different sweep angles.

CBL configuration for the sweep angle layouts' family. When moving away from this configuration, the relative difference between the linear and nonlinear predictions are expected to grow although both the predictions show the same trend. As a bottom line, the further the sweep angle value is far from the value employed in the CBL, the more is the linear prediction unreliable. If moving to a region with higher sweep angle as for the CBL configuration, the linear prediction is unreliable and non-conservative. The opposite happens when moving in the opposite region.

3.6 Effects of Lift Repartition to Post-buckling Behavior

One of the advantages related with a Box Wing airplane is the possibility of adding a constant circulation without incurring in induced drag penalties [23, 144]. As a consequence the percentage of the lifting force that is actually applied on each wing can be freely modified without increasing the induced drag. In cruise condition, the trim could be hardly maintained by equally allocating the lift between the wings [8, 94, 103]. Moreover, due to the particular architecture, the Box Wing configuration, with a proper

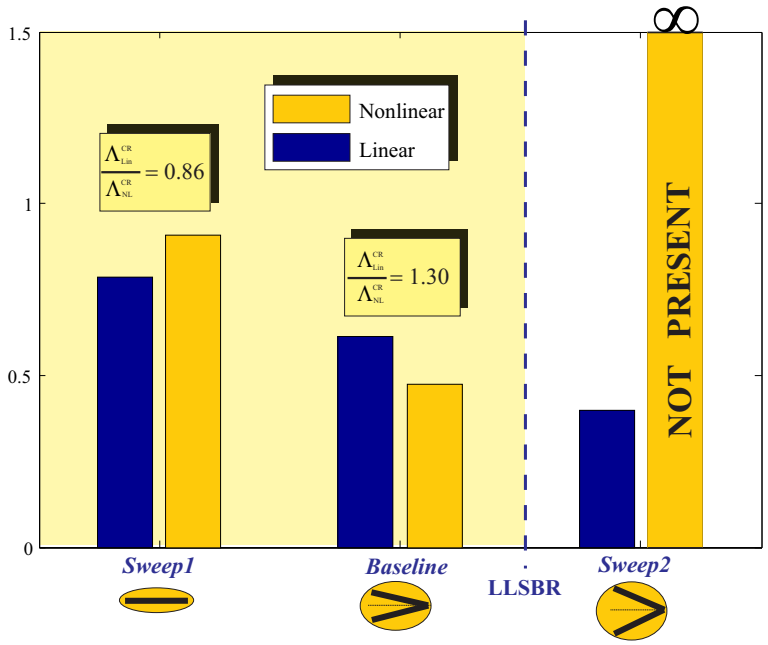

Figure 3.28: Comparison between buckling load assessed linear buckling analysis, Λ^{CR}_{Lin}, with nonlinear analysis, Λ^{CR}_{NL}, and their ratio for the family of configurations obtained changing the sweep angle.

design of the mobile surfaces, enables to start a maneuver maintaining the same total lift and reallocating it differently through the wings [6]. It is then crucial to assess the effects of this load repartition on the structural response with particular emphasis on buckling and post-critical analysis.

In order to accomplish this task, the baseline configuration (see Figure 3.1) has been considered. The reference case presents an equal repartition of the total lift on both wings (see Figure 3.29). The repartition of the load is then changed to see its effects on the structural behavior of the box wing. Mathematically, the constraint of fixed total vertical force could be expressed as

$$q_U + q_L = 2p_z \tag{3.16}$$

with p_z being the reference pressure acting on the baseline configuration on both the wings. The family of cases obtained by changing the load on both wings (with the constraint of fixed total lift) is depicted in Figure 3.29.

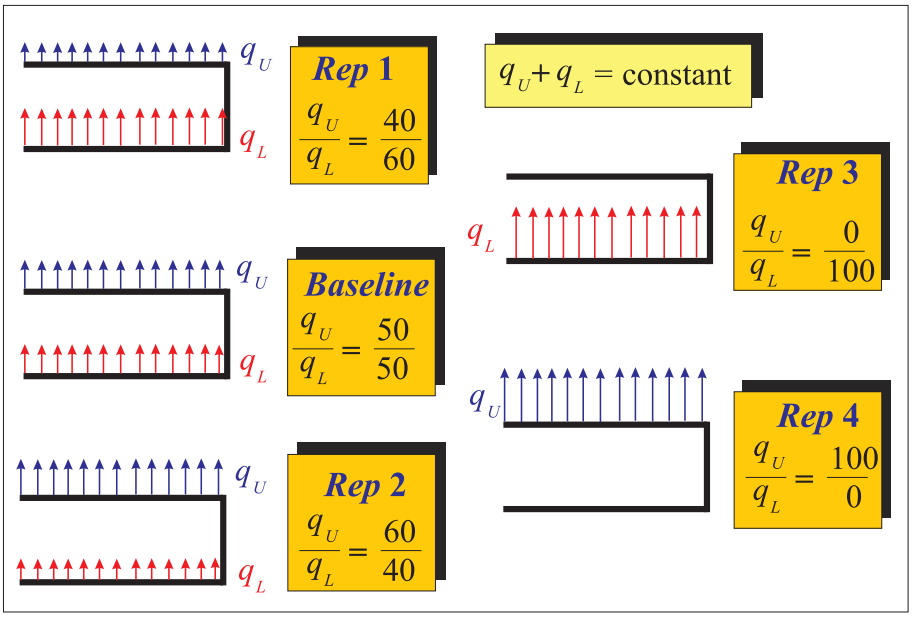

Figure 3.29: Family of load conditions obtained maintaining the *Baseline*'s geometry and varying the vertical pressures acting on the lower and upper wings. q_U and q_L represent the pressures acting on the upper and lower wing respectively.

3.6.1 *Rep* 1 Load Case

In this analysis the vertical pressures have a value of $q_L = 0.6615\ [\frac{Kg}{mms^2}]$ and $q_U = 0.441[\frac{Kg}{mms^2}]$ for the lower and upper wings respectively. The lower wing carries now 60% of the total vertical force.

Considering the same points P_1 and P_2 at the tip of the lower wing and at the midspan of the upper wing, the vertical displacements are plotted against the load level in Figures 3.30 and 3.31. The same pattern as for the equally loaded wings, Figure 3.2 and 3.3, is clearly visible. Thus, the same considerations apply regarding the nature of the snap phenomenon.

However, the buckling occurs at at slightly smaller load level, 0.43 against 0.47 (see Figure 3.30). Thus it may be inferred that, for this particular configuration, slightly overloading the lower wing has a detrimental effect on the buckling of the system.

According to Reference [103] for a typical PrandtlPlane configuration, the front wing should be slightly more loaded for trimming purposes. Moreover, the lift is allocated approximately in a 60 to 40 ratio [104]. Thus, from a pure buckling perspective the trim requirement has a negative effect, although not to a notable extent.

If a linear buckling analysis is carried out, the predicted buckling load leads to

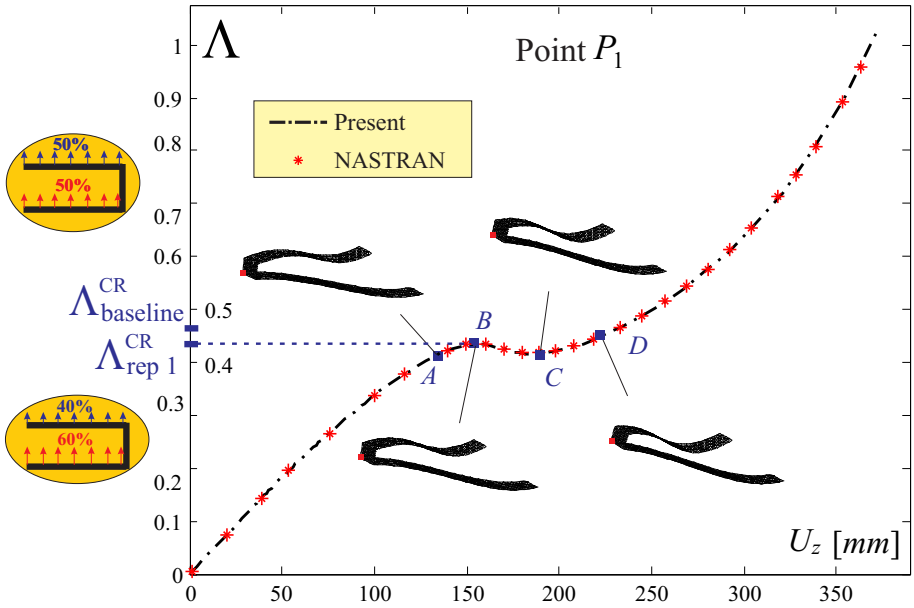

Figure 3.30: Load parameter Λ vs vertical displacement U_z for lower wing tip point P_1. *Rep* 1 load case with lower wing carrying 60% of the total load. The buckling load levels for the baseline ($\Lambda^{\text{CR}}_{\text{baseline}}$) and actual ($\Lambda^{\text{CR}}_{\text{rep 1}}$) load cases are indicated.

a bigger overprediction in respect of what happened for the baseline configuration, as shown in Figure 3.32. That is, in slightly overloading the lower wing the linear analysis is unreliable and not conservative to a bigger extent. The deformation shapes at buckling are also plotted, showing relevant differences between the linear and nonlinear results.

3.6.2 Rep 2 Load Case

This test case features exactly the inverted situation of *Rep* 1 analysis since now vertical pressures

$q_L = 0.441\ [\frac{Kg}{mms^2}]$ and $q_U = 0.6615\ [\frac{Kg}{mms^2}]$ are acting on lower and upper wing respectively.

Observing the graph showing the vertical displacements of point P_1 against the load level, Figure 3.33, the expected response is detected, where now, it is clearly visible that the buckling load is slightly higher than the one for the baseline load case. This confirms the results of the previous analysis: in the neighborhood of the equally loaded wings situation the buckling load is higher when the upper wing carries a bigger share of the total load.

The buckling analysis also confirms what observed in the previous sections, Figure

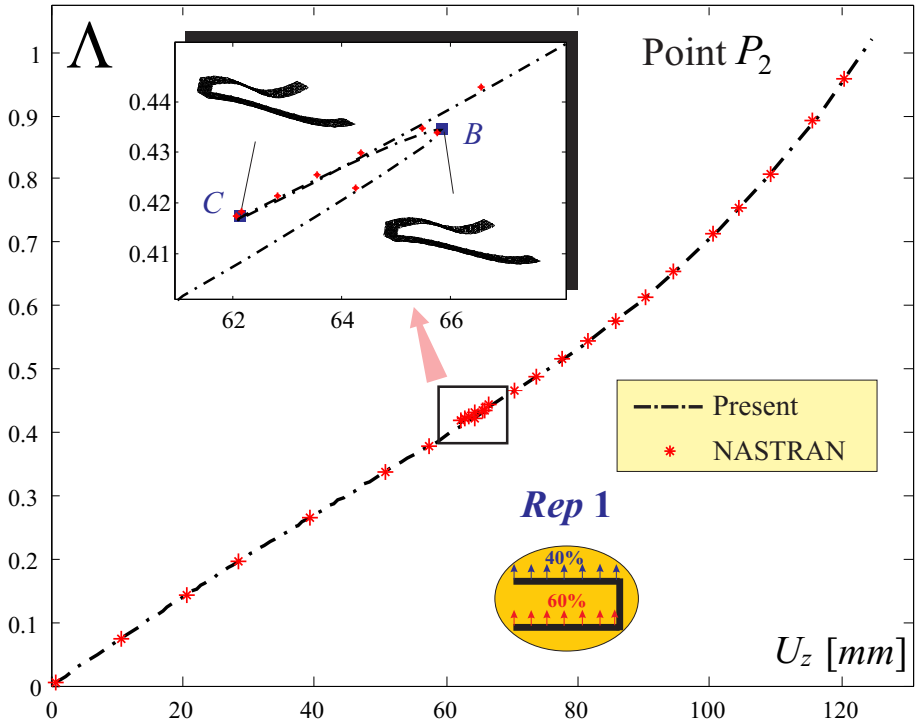

Figure 3.31: Load parameter Λ vs vertical displacement U_z for upper wing midspan point P_2. *Rep* 1 load case with lower wing carrying 60% of the total load.

3.34. That is, starting from an equally loaded wings situation and slightly increasing the share of total load carried by the upper wing, the ratio of the buckling loads evaluated with the linear and nonlinear analyses decreases.

3.6.3 *Rep* 3 Load Case

In this case the lower wing carries all the lift, being subjected to a vertical pressure
$q_L = 1.1025[\frac{Kg}{mms^2}]$. Although unrealistic, this configuration carries some interesting implications which help to reinforce the observations previously pointed out. The load-displacement responses for points P_1 and P_2, Figure 3.35 and 3.36, show a consistently lower buckling load. This was expected and predicted from the outcome of previous analyses.

Interestingly, the unstable branch almost disappeared. This is a similar phenomenon experienced by configurations whose nonlinear response is close to the limit of the *SBR*, where the response does not show any unstable branch but only the softening-stiffening pattern.

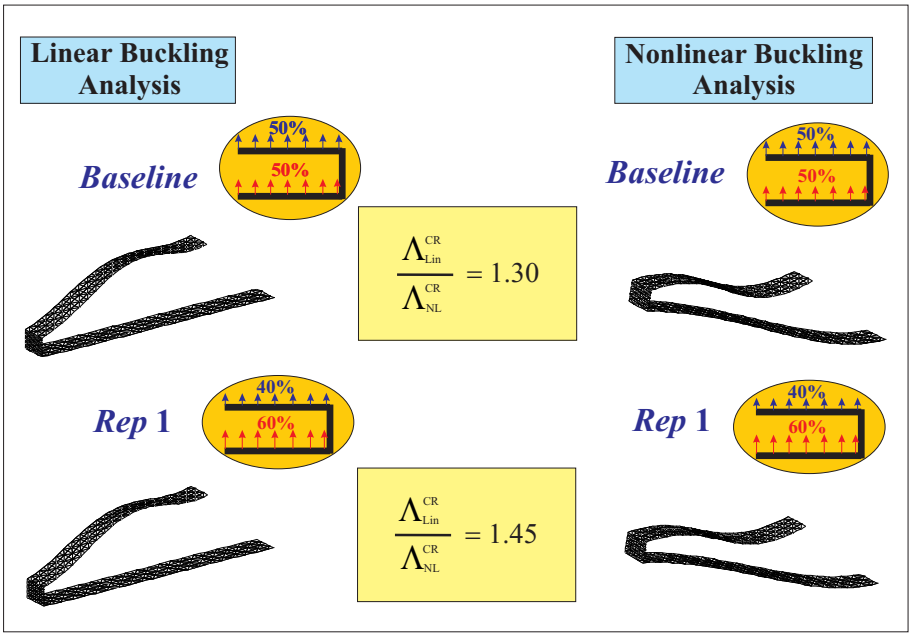

Figure 3.32: Comparison between the buckling loads assessed with the linear and nonlinear analysis, and relative mode shapes at buckling, for the Baseline and Rep 1 load cases.

From Figure 3.37 it could be inferred that for this situation the linear analysis predicts a critical load almost twice the value of the one predicted with nonlinear analysis. This confirms the trend that overprediction of the critical loads evaluated by linear buckling analysis increases if the lower wing carries a bigger share of the total load.

3.6.4 *Rep* 4 Load Case

The opposite limit situation is the one in which the upper wing is carrying all the load, being subjected to a vertical pressure of $q_U = 1.1025\ [\frac{Kg}{mms^2}]$. As for *Rep 3* case, this configuration is not realistic, being the aim of the analysis the observation and reinforcement of the concepts related to the load repartition.

As clearly shown in Figure 3.38, depicting the vertical displacement of point P_1 against the load level, no snap phenomenon occurs. After an initial quasi-linear response, a small softening region is detected, after which stiffening tendency is slowly growing. This load condition falls then outside the SBR. By means of the reasoning so far employed when dealing with the SBR concept, observing the responses of *Rep* 2 and *Rep* 4, a particular load condition with the upper wing carrying a value between 60% and 100% of the total load is expected, starting from which no unstable branch is observed in

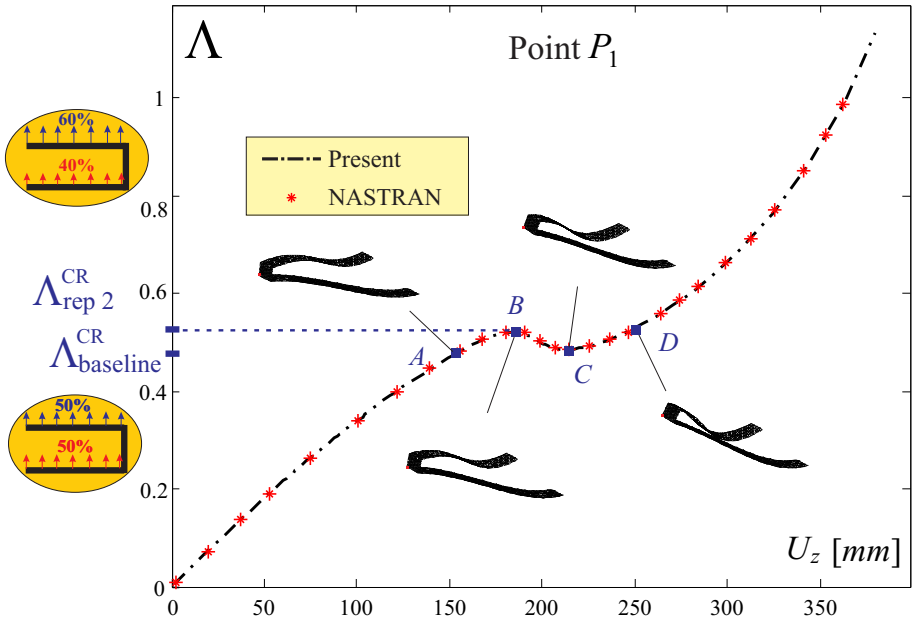

Figure 3.33: Load parameter Λ vs vertical displacement U_z for lower wing tip point P_1. Configuration *Rep* 2 with upper wing carrying 60% of the total load. The buckling load levels for the baseline ($\Lambda^{CR}_{baseline}$) and actual ($\Lambda^{CR}_{rep\ 2}$) load cases are indicated.

the response. The corresponding load-displacement curve relative to this configuration is the ULSBR.

Successive analysis undergone incrementing the share taken from the upper wing reveal that the situation where the upper wing is carrying 94.1% of the total load, and the lower wing carries the remaining 5.9%, is the ULSBR, Figure 3.41. Starting from this load share between the wing, any action further loading the upper wing will result in a response which doesn't show any buckling. It is worth to notice that in this case, although the unstable branch disappears and an abrupt stiffening is still observed across a specific point, there is any flex point as found for the studies on the joint's height.

3.6.5 Interpretation of the Effects of Load Repartition

The results about the investigation on effects of load repartition on buckling response could be summarized by Figure 3.40, where the vertical displacement is plotted for the point P_1 for the different load situations.

In the following it is assumed that the analysis is restrained to cases where only positive vertical pressures are applied, that is, *Rep* 3 and *Rep* 4 represent the limit load situations. It could be then inferred that, considering the fixed total vertical force as the

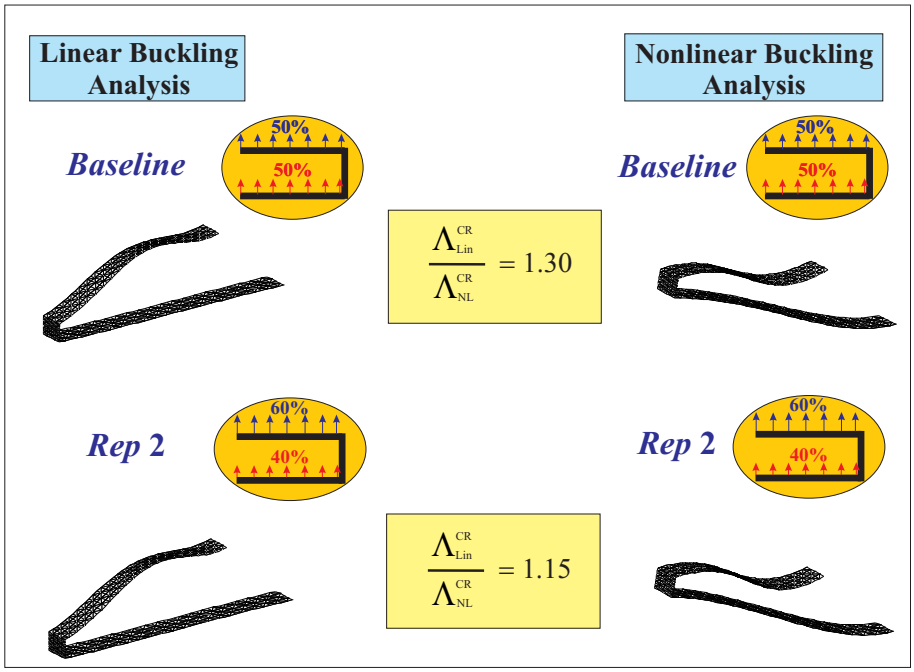

Figure 3.34: Comparison between the buckling loads assessed with the linear and nonlinear analysis, and relative mode shapes at buckling, for the Baseline and Rep 2 load cases.

one generated for the *Baseline* load case, having a more loaded upper wing is beneficial to buckling load. If the upper wing carries a percentage of total load bigger as the one corresponding to the ULSBR configuration, no snap occurs. On the contrary, unloading the upper wing and loading the lower one, the buckling load is decreased. For *Rep* 3, the snap is almost undetectable. Being *Rep* 3 the lower bound, an LLSBR configuration is not in the domain of the problem.

Just for the sake of completeness, the LLSBR is expect to exist if the analysis is further continued loading downward the upper wing, an overloading the lower wing accordingly to satisfy the fixed total lift constraint.

Also of interest is the almost identical stiffness shown in the response for very low load level which could be easily confirmed by a linear analysis as the one presented in the Appendix A.

Looking on the right end of the graph (Figure 3.40), where level load is close to the nominal one, the different response tend to coincide whatever the load is shared between the two wings.

Comparison between the linear and nonlinear predicted buckling load, Figure

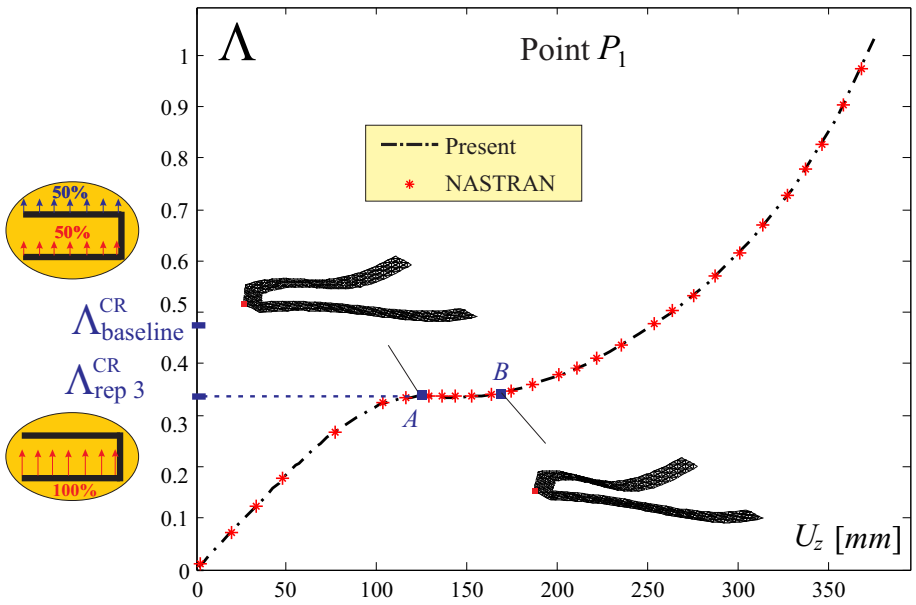

Figure 3.35: Load parameter Λ vs vertical displacement U_z for lower wing tip point P_1. Rep 3 load case with lower wing carrying all the load. The buckling load levels for the baseline ($\Lambda^{CR}_{baseline}$) and actual ($\Lambda^{CR}_{rep\ 3}$) load cases are indicated.

3.42, summarizes the results already discusses in the previous sections but adds more interesting points. For this case, the CBL configuration has been found for a load repartition of 69.1% on the upper wing and 30.9% on the lower wing. Its response is depicted in Figure 3.41.

Opposite trends between the linear and nonlinear analysis predictions are observed: when the linear analysis tends to predict higher buckling loads with a more loaded lower wing, the opposite is predicted by the nonlinear simulation. Thus, in this particular example, the inability of linear analysis to catch the right physics does not only affect the predictions, but also the trend. This contributes to amplify the error as long as moving away from the load repartition featured in the CBL case. As a bottom line, the unreliability of linear buckling analysis for joined-wing configurations, which has already been proved, turns out to be even more serious in this last case.

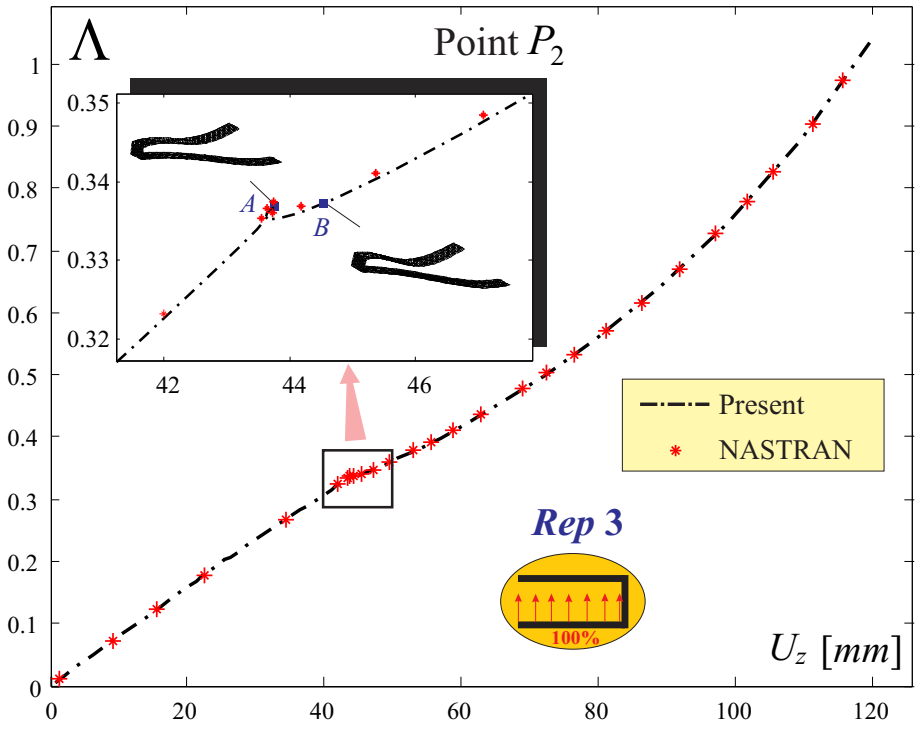

Figure 3.36: Load parameter Λ vs vertical displacement U_z for upper wing midspan point P_2. Rep 3 load case with lower wing carrying all the load.

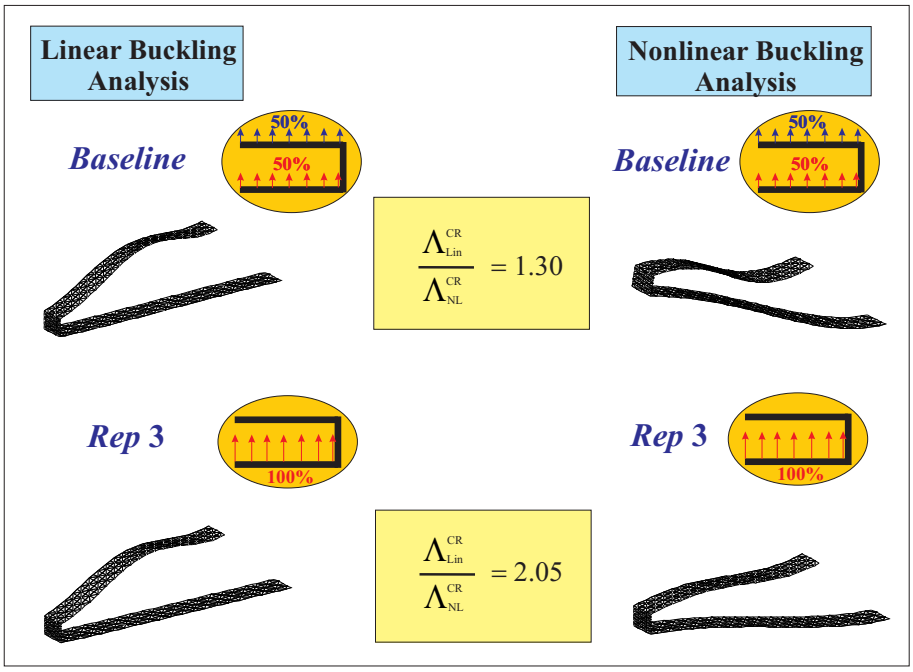

Figure 3.37: Comparison between the buckling loads assessed with the linear and nonlinear analysis, and relative mode shapes at buckling, for the *Baseline* and *Rep* 3 load cases.

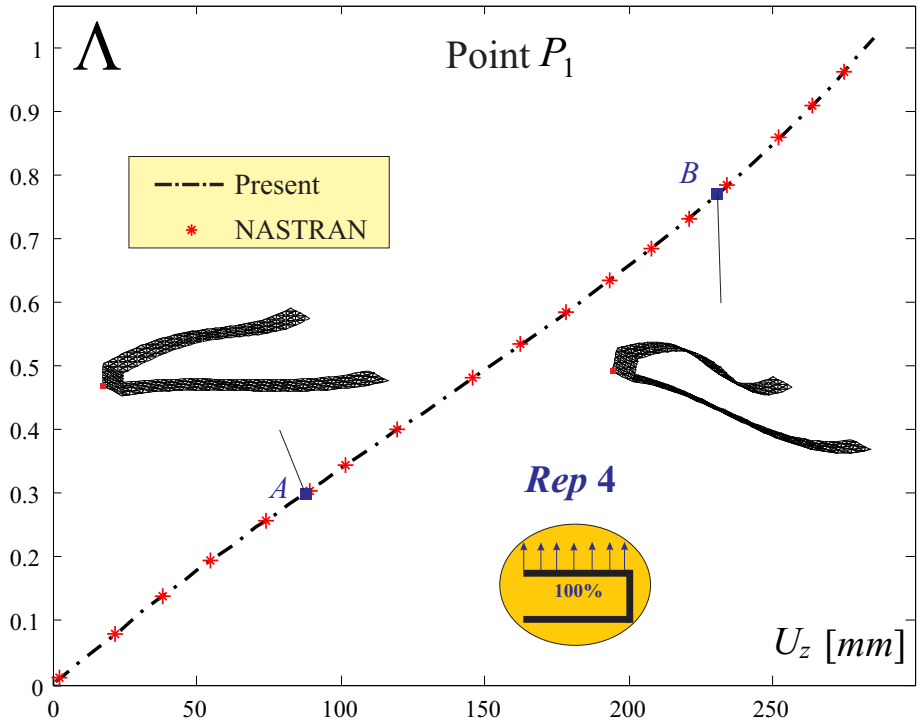

Figure 3.38: Load parameter Λ vs vertical displacement U_z for lower wing tip point P_1. *Rep* 4 load case with upper wing carrying all the load. The buckling load levels for the baseline ($\Lambda^{\text{CR}}_{\text{baseline}}$) load case is indicated.

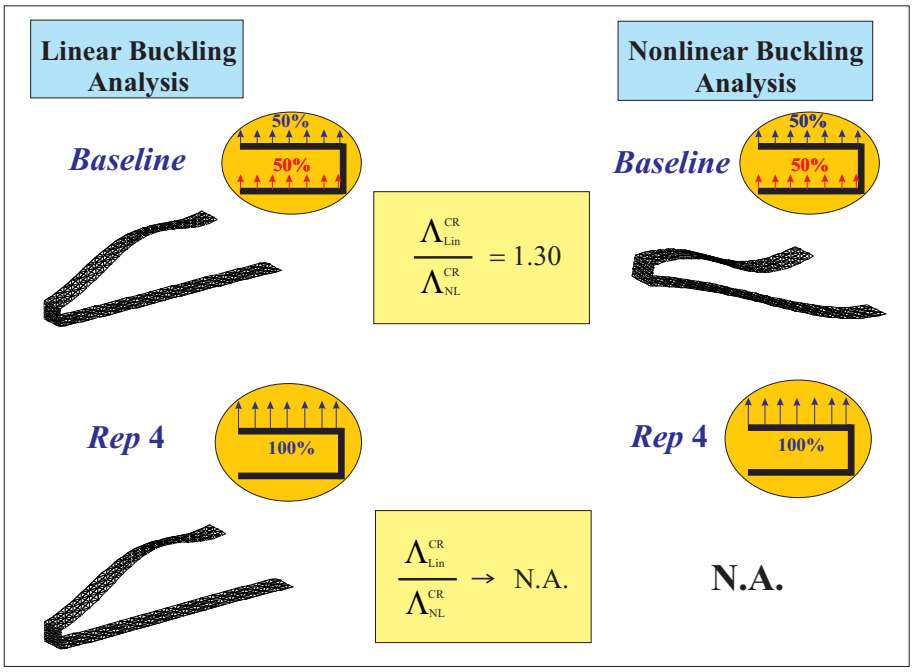

Figure 3.39: Comparison between the buckling loads assessed with the linear and nonlinear analysis, and relative mode shapes at buckling, for the *Baseline* and *Rep* 4 load cases. The nonlinear analysis does not show any buckling for *Rep* 4.

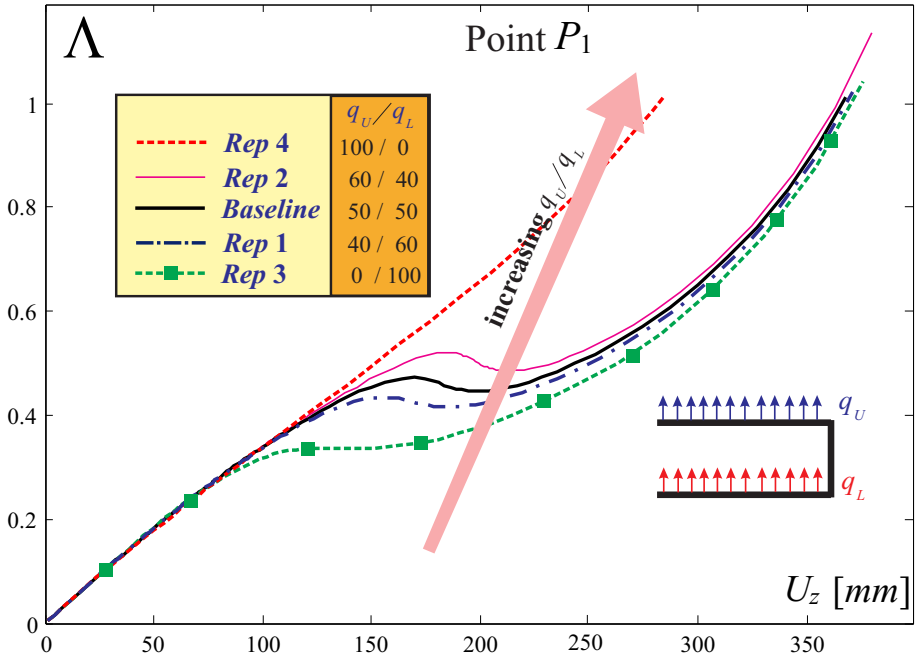

Figure 3.40: Load parameter Λ vs vertical displacement U_z for tip point P_1. Configuration with $b = e = \frac{4}{5}a$. Different load repartitions between front and rear wing.

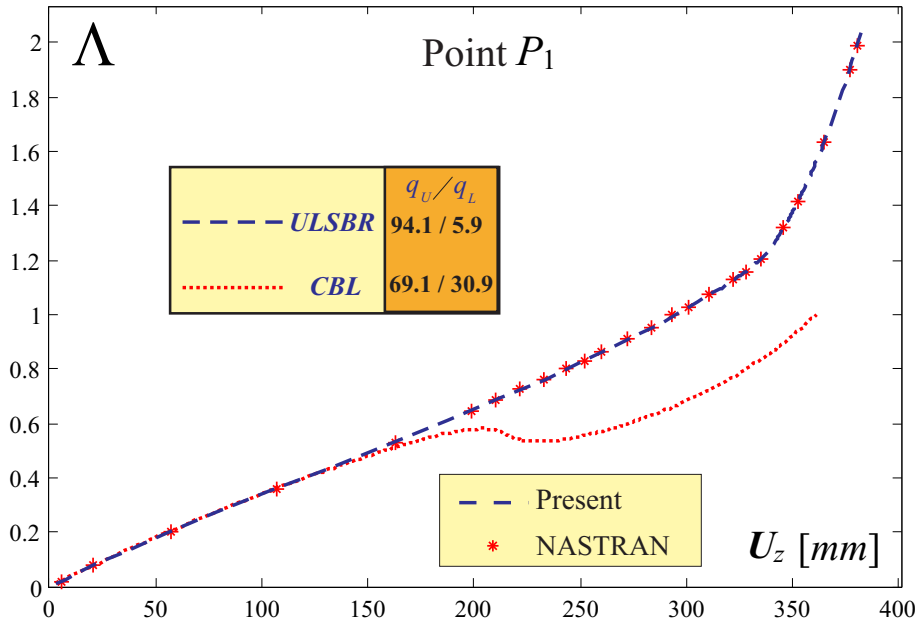

Figure 3.41: Load parameter Λ vs vertical displacement U_z for lower wing tip point P_1. Responses for the ULSBR and the CBL configurations are depicted.

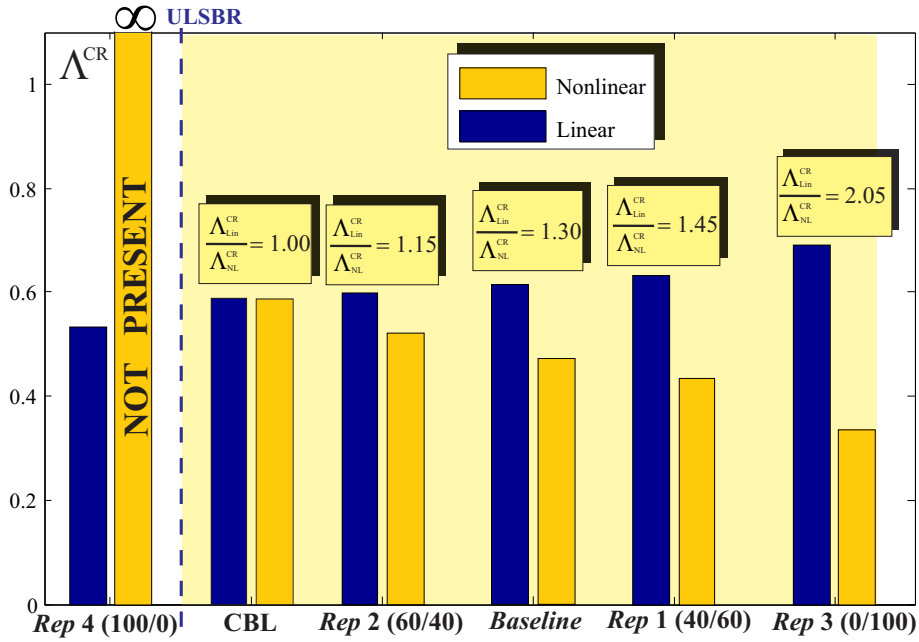

Figure 3.42: Comparison between buckling load assessed linear buckling analysis, Λ^{CR}_{Lin}, with nonlinear analysis, Λ^{CR}_{NL}, and their ratio for the family of configurations obtained changing the load repartition between the two wings. The linear analysis is not conservative and the trend is not captured.

3.7 Conclusions

A post-buckling analysis of PrandtlPlane Joined Wings has been presented for the first time. The strong nonlinear bending-torsion coupling typical of this kind of configurations is responsible of the highly nonlinear response which may first present a reduction of the stiffness of the system (softening) followed by an unstable branch and then an increase of stiffness (stiffening). The buckling load, defined here as the load which makes the structural tangent matrix singular, is often associated with a snap through type of instability: the structure is no longer able to carry more load and it immediately move to a very different state which is now capable of taking more load. This kind of instability must be avoided in the design of airplanes but it is important to understand it. For the first time it is attempted to investigate this issue for the case of PrandtlPlane Joined Wings. This is accomplished by analyzing several different configurations obtained by modifying the geometrical properties of an assigned airplane design named *baseline* configuration. The following findings can be here summarized:

- *Joint's height effects*

  Incrementing the size of the joint improves the structural response by increasing the snap-buckling load.
  In the load-displacement plane, it is possible to find the so called Snap Buckling Region (SBR). If a curve, representing the nonlinear response for a selected joint's size, is included in SBR then it is always characterized by a sequence of softening, unstable branch, and stiffening. Two response curves bound SBR. They are defined as Lower Limit Snap Buckling Region (LLSBR) and Upper Limit Snap Buckling Region (ULSBR) respectively. Thus, changing the joint's height dramatically affects the Joined Wing's structural behavior and its type of nonlinear response.
  Low height joint is not beneficial not only because of an obvious penalty on aerodynamic drag but also because of a quite substantial softening of the structure which happens even at low level of applied load.

- *Sweep angle effects*

  An increase of the sweep angle amplifies the bending-torsion coupling with dramatic reduction of the buckling load. For this case ULSBR does not exist.

- *Repartition of the lift on the wings and its effects*

In PrandtlPlane Joined Wings adding a constant circulation does not affect the induced drag. This means that the lifting force can be freely redistributed over the upper and lower wings without penalty on the induced drag. It is then important to analyze the effects of the repartition of lift on the nonlinear structural response. A higher percentage of the load on the upper wing reduces the risks of buckling.

In all of these investigations it was also shown that the linear buckling analysis is completely unreliable: in some cases it overestimates the buckling load and in others it underestimates it. The understimation/overstimation is also case-dependent. Moreover, in most of the analyzed cases the linear analysis does not capture the correct trend for the buckling load when a design parameter is changed. This has important implications in multi-disciplinary optimization codes since the buckling constraint is usually imposed by considering a linear buckling analysis. Optimizing Joined Wings without taking into account the poor quality of the buckling predictions that can be obtained with a linear analysis could lead to unsafe design or waste of computational resources if the optimized solution actually violates the "true" nonlinear buckling constraint.

Questions then arise on the type of nonlinearity that is involved in Joined Wings. Is it possible to design the Joined Wings to have a quasi-linear behavior and so to have acceptable performance for the linear buckling analysis in optimization software? The answer to this question could be in the appropriate choise of the bending-torsional coupling which could be achieved with the adoption of composite materials. This will be the subject of an upcoming work.

This paper also demonstrated the highly complex nonlinear response which makes extremely difficult the design of *reduced order models* which could save significant amount of computational cost in the aeroelastic investigations based on the frequency domain analysis and a few selected modes. Only an efficient reduced order model able to capture the main nonlinearities in the structure could be adopted. This work is only the first step towards that direction of understanding the types of nonlinearities and designing, without penalty on the actual weight of the airplane (if possible), a structure which behaves as much linearly as possible.

Acknowledgements The authors acknowledges the support by San Diego State University (College of Engineering) and by SDSU-NSF STEM Scholars Program (NSSP).

Chapter 3, in full, is a reprint of the journal paper: "*Postcritical Analysis of*

PrandtlPlane Joined-Wing Configurations, AIAA Journal, Vol. 51, No. 1, 2013." The dissertation author was the primary investigator and author of this paper. Coauthors were Luciano Demasi and Alan Márquez Razón.

Chapter 4

Nonlinear Analysis of PrandtlPlane Joined Wings: Effects of Anisotropy

This chapter is a reproduction of the following paper:
Nonlinear Analysis of PrandtlPlane Joined Wings: Effects of Anisotropy, AIAA Journal, Vol. 52, No. 5, 2014.

4.1 Introduction

JOINED Wings were proposed in the seventies [8, 10, 145] for commercial transport and supersonic fighters. Joined Wings were also the subject of US [27, 28] and European [91] patents. Many advantages are claimed compared to classical cantilevered configurations [146, 147]: improved stiffness properties, high aerodynamic efficiency [7] and superior stability and control characteristics. In addition to these theoretically significant advantages, a diamond Joined Wing can enclose a large antenna and be used for high altitude surveillance [89].

For civil transportation, the PrandtlPlane has been analyzed in terms of aerodynamic performances, flight mechanics and controls, dynamic aeroelastic stability properties and preliminary design.[28, 148]

The design of Joined-Wing type of aircraft for civil transportation was also adopted in United States with the introduction of the concept of Strut-Braced Wings

(SBW) [132] and Truss Braced Wings (TBW) [133].

The growth of interest on Joined Wings led to both experimental [82, 86] and theoretical [126, 149] studies. These studies showed that the tools developed in decades and effectively used by the industry to analyze classical cantilevered wings need to take into account structural nonlinearities [11, 150] which are significant even for small angles of attack and attached flow. The significant forces and moments transferred through the joint make the geometric structural effects particularly important and linear aeroelastic models [151] can give only a qualitative information on the instability properties but may miss important structural effects which should be taken into account [124,152]. However, the adoption of fully-nonlinear structural models is impractical for design purposes especially if several alternative configurations are explored in an optimization [151] effort. Ideally, the designer should have access to efficient reduced-order models. However, even well-established reduced order techniques [13] based on second order modes [153, 154] performed in an unsatisfactory manner when Joined Wings were considered [13, 14].

It was then realized that in order to effectively build a reduced order aeroelastic model specifically tailored for an efficient simulation with a full inclusion of the structural geometric effects, a *physical understanding* of the mechanism driving the nonlinear response of Joined Wings should be achieved. This is pursued in this work.

4.2 Contributions of the Present Work

PrandtlPlane configurations are joined-wing aircrafts designed for civil transportation. Thus, global snap-buckling instabilities are not acceptable. However, as discussed in reference [1] and in this work, a snap-buckling can take place even after a quasi-linear load-displacement response. This demonstrates the necessity of an understanding of the physics behind the instability phenomenon to avoid an abrupt change of state after a response which *appeared* to be *linear*.

For the PrandtlPlane-like configuration investigation was pursued in Reference [1]. The main results that were found could be summarized in the following main aspects. *First*, the strong nonlinear structural effects make the linear buckling analysis not very reliable as far as the static critical condition is concerned. *Second*, the system may be sensitive to snap-buckling type of instability under a certain combination of structural parameters. This led to the definition of the so-called Snap-Buckling Region which gives important indications on the design of these configurations. *Third*, it was shown that

the load repartition between the upper and lower wings has a significant impact on the stability conditions: for a typical swept-back lower wing and swept-forward upper wing configuration more load on the upper wing alleviates the risk of instability. *Fourth*, some counterintuitive effects typical of this layout were discovered. For example, increasing the joint's size may be considered a not efficient design, since it could increase the height and this would appear unfavorable: it is well known that slender columns may increase the tendency to buckle. However, for aerodynamic-like mechanical loadings it was shown that the complex nonlinear response of the Joined Wing has actually an opposite effect and the stability properties are improved when the joint's height is increased. This has also practical implications since the induced drag is significantly reduced when the gap between the upper and lower wing is increased. *Fifth*, increasing the sweep angles was shown to dramatically reduce the snap-instability load.

These findings had relevant practical implications, but several questions needed an answer. In particular, the effects of composite materials required investigation since additional couplings could be introduced because of the anisotropy. Moreover, nowadays the adoption of composites is increasingly relevant (the new *Boeing 787* and the *Airbus 350* present a large percentage of structures designed with composites) and has to be considered also for Joined Wings. In addition, even for isotropic materials but general geometries (sweep angles, dihedrals, built-in twist), a realistic PrandtlPlane would present strong anisotropic behavior from a global point of view.

In the design of these configurations, an equivalent composite plate model [155] could provide important indications. Thus, the present investigations based on plate-like models for the wings and the joint could also provide practical design information.

The JW models discussed and investigated in this work do not intend to reproduce the complex stiffness distributions of a realistic airplane configuration. The material properties and geometric dimensions are selected to be consistent with the ones typically adopted in wind tunnel models. Moreover, the materials are modified to explore how the different stiffness distributions affect the nonlinear response with particular emphasis on the snap-buckling instability.

This paper will provide contributions towards a fundamental understanding of the nonlinear response of PrandtlPlane Joined Wings. The *first contribution* concerns the role of the anisotropy (introduced by adopting composite materials) on the nonlinear response with particular emphasis on the snap-buckling instability. The *second*

contribution is about the effects of the joint-wing connection (boundary conditions) on the geometrically nonlinear structural behavior. As suggested in Reference [35], since the system is statically indeterminate, significant reaction loads can buildup in the joint area that could have important consequences on stiffness and stability. Changing the wing-to-wing connection helps to isolate and better understand the phenomenon. The *third contribution* is finding the main driving mechanism which leads to the instability. It is shown that the bending moment transferring through the joint is determinant. Interesting features peculiar of the configurations which experience buckling are discussed with particular emphasis on the inward bending of the upper wing and rigid rotation of the joint in both chord-wise and span-wise directions. The *fourth contribution* is about the importance of the differential stiffness of the two wings: it will be shown that the stiffness ratio is one of the major parameters determining the instability risks. The upper wing (usually compressed under typical load conditions) needs to have a smaller relative stiffness. A surprising result with important implications.

The present work provides indications on the physical mechanisms of the nonlinear instability for PrandtlPlane configurations and Joined Wings. This could have practical application in the development of new and efficient aeroelastic reduced order models which could effectively adopt existing and reliable tools already in use in the aerospace industry but which cannot be directly extended for the Joined Wings without a proper understanding of the nonlinear phenomena.

4.3 Nonlinear Structural Model

The geometrically nonlinear finite element [156] is based on the linear membrane constant strain triangle (CST) and the flat triangular plate element (DKT). The structural tangent matrix $\boldsymbol{K}_T$ is sum of two contributions: the elastic stiffness matrix, $\boldsymbol{K}_E$, and the geometrical stiffness matrix, $\boldsymbol{K}_G$.

The nonlinear governing equations are solved by adopting iterative methods such as *Newton-Raphson* and *arc length* techniques [139]. After each iteration a displacement vector is obtained, rigid body motion is eliminated from elements and the pure elastic rotations and strains are found [156]. Using these quantities the internal forces are updated for the next iteration.

The key relation which needs to be solved at each iteration [1, 130] involves the

structural tangent matrix $\boldsymbol{K}_T^{\text{step}\,\mu\,\text{iter}\,n} \cdot \boldsymbol{u}^{\text{step}\,\mu\,\text{iter}\,n}$, the external non-follower loads $\boldsymbol{P}_{\text{ext}}$, and the array $\boldsymbol{P}_{\text{unb}}^{\text{step}\,\mu\,\text{iter}\,n}$ containing the unbalanced loads:

$$\boldsymbol{K}_T^{\text{step}\,\mu\,\text{iter}\,n} \cdot \boldsymbol{u}^{\text{step}\,\mu\,\text{iter}\,n} = \underbrace{\left(\Lambda^{\text{step}\,\mu\,\text{iter}\,(n+1)} - \Lambda^{\text{step}\,\mu\,\text{iter}\,n}\right)}_{\lambda^{\text{step}\,\mu\,\text{iter}\,n}} \boldsymbol{P}_{\text{ext}} + \boldsymbol{P}_{\text{unb}}^{\text{step}\,\mu\,\text{iter}\,n} \tag{4.1}$$

where the displacement $\boldsymbol{u}^{\text{step}\,\mu\,\text{iter}\,n}$ and, for the arc length case, the applied load fraction $\Lambda^{\text{step}\,\mu\,\text{iter}\,(n+1)}$ are unknown. Different closing constraint equations could be employed, leading to different arc length methods, such as *Crisfield*, *Riks-Wempner* or *Ramm*'s (also called modified Riks) methods [139]. As an example, application of Crisfield's cylindrical arc length method [139] leads to the following constraint:

$$\|\boldsymbol{u}^{\text{step}\,\mu\,\text{iter}\,n} + \boldsymbol{U}^{\text{step}\,\mu\,\text{iter}\,n} - \boldsymbol{U}^{\text{step}\,\mu\,\text{iter}\,1}\|^2 = \Delta l^2 \tag{4.2}$$

where Δl has been previously fixed. Equations 4.1 and 4.2 give raise to a second order relation for the $\lambda^{\text{step}\,\mu\,\text{iter}\,n}$.

It is worth to notice that the success of one of the arc length strategies in overcoming limit points is problem dependent. In some cases some strategies perform better than others, thus it may be necessary to switch between them to track the whole response curve.

The post-critical numerical analyses are inherently difficult to be carried out. It has been the authors' experience that a satisfactory performance of the finite element formulation in the *pre-critical* region *does not* imply a satisfactory performance on the *post-critical* region. Several numerical investigations showed that the terms of the out-of-plane contribution to the geometric stiffness matrix are crucially important on this regard.

Generally, Newton-Raphson procedures are preferred for computation of states *far from limit points*, for robustness and efficiency reasons. Moreover, to effectively track the curve beyond limit points it is necessary to adopt an arc length technique and restarting of the analysis from a converged state (*restart* capability), with the adoption of different set of parameters, may be necessary. This is the reason why an efficient technique which significantly reduces the needs of restarting analyses was implemented. In particular, the capability utilized in this work can *automatically switch* from Newton-Raphson to arc length strategy when close to a limit point. The opposite capacity to

switch back to Newton-Raphson technique when far from limit points was also implemented. Furthermore, an *automatic switch* to different arc length techniques when the current one fails to overcome a limit point is also possible. More details are described in References [1, 130].

4.4 Description of the Analyzed Joined Wing Configurations

Swept wings present a significant coupling between the bending and torsional deformations with important aeroelastic consequences [157]. Due to the overconstrained nature of the Joined Wings, the sweep angle effects are even more determinant since the upper and lower wing are joined at the tip and the resulting structure is overconstrained. The bending-torsion coupling is more complex than a simple cantilevered wing and directly affects the stability properties and post-critical behavior of these configurations. Moreover, the composites can introduce some couplings which are not present in the case of isotropic materials, and with an accurate design the bending and torsional deformations may be modified to improve the overall response.

This work is mainly focused on the fundamental understanding of the geometric structural nonlinearity and the role it plays in the static instability for both unswept and swept Joined Wings. With this in mind, two configurations are discussed and analyzed. The first configuration is an unswept Joined Wing (Figure 4.1) and the second one (Figure 4.2) is a more realistic Joined Wing which presents a swept-back lower wing and a swept-forward upper wing. The loading condition is represented by a non-aerodynamic conservative vertical pressure (direction $+z$) applied to both the upper and lower wings' surfaces (the joint is unloaded). The magnitude of the pressure is $p_z = 0.55125\,[\frac{Kg}{mm \cdot s^2}]$ and corresponds to a dynamic pressure relative to a speed of $V_\infty = 30\ [m/s]$. The thickness is held constant for both the wings and the joint and is equal to 1 mm. Several materials will be adopted in this work to investigate the effects of composites on the nonlinear post-critical behavior of the Joined Wings. For a meaningful comparison of their effects, two *Baseline* configurations are defined for both the unswept and swept geometries reported in Figures 4.1 and 4.2. In particular, each baseline configuration presents a Young's modulus $E_{\text{REF}} = 6.9 \cdot 10^7 \left[\frac{Kg}{mm \cdot s^2}\right]$ and a Poisson's ratio $\nu_{\text{REF}} = 0.33$. The shear modulus is calculated from the well known relation $G_{\text{REF}} = \frac{E_{\text{REF}}}{2(1+\nu_{\text{REF}})}$. The

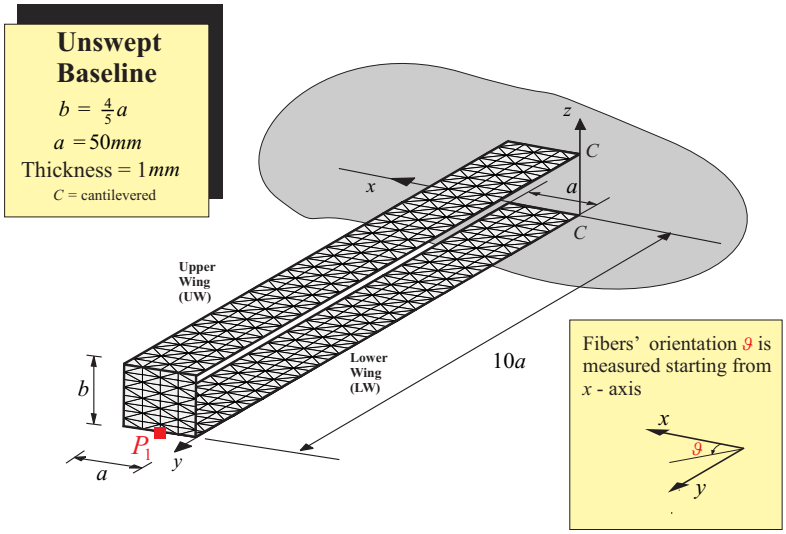

Figure 4.1: Unswept Baseline configuration, *UREF*.

baseline configurations are referred to as *UREF* and *SREF* for the unswept and swept cases respectively.

The results discussed in this work will present several investigations in which multi-layer composite materials are adopted. For these cases the laminates' thicknesses are kept constant whereas the lamination schemes are changed. Each lamina or ply is identified by a material coordinate system which is in general not coincident with the global coordinate system adopted in the solution of the problem. For that reason it is necessary to specify the fibers' orientation angle at ply level. In this work the angle is measured starting from the wing's local x-axis: in the unswept case it coincides with the global x-axis, see Figure 4.1, whereas for the swept case each wing has its own local reference x-axis (x^{UW} and x^{LW} for the upper ad lower wings respectively: see Figure 4.2). The local x-axis is always perpendicular to the wing span direction and is not parallel to x in the general case of swept Joined Wing.

A snapping phenomenon at global structural level (see also Reference [1]) as those that will be discussed here could not be accepted. It is also true that, when possible, the structures in aeronautical engineering are designed pursuing as much as possible a linear response. According to these observations, it may be stated, *incorrectly*, that a structural analysis may lose of interest well before a limit point is reached (see Reference [2] for a discussion about risks related to bi-stable regions).

It may also be argued that the configurations for which snap occurs are subjected to a

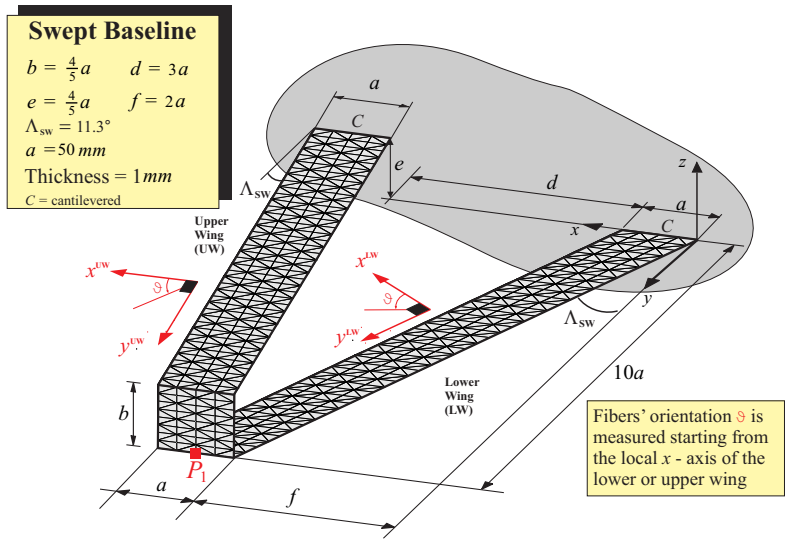

Figure 4.2: Swept Baseline configuration, *SREF*.

deformation which would not be realistic for a joined-wing aircraft.

However, the following observations could be made. *First*, the choice of the dimensions of the baseline models (see Figures 4.1 and 4.2) have been selected to be consistent with wind-tunnel scaled models. *Second*, the loads have been accordingly selected to observe the instability phenomenon, in an effort of *conceptual understanding* of the geometric nonlinearities and the effects of composite materials for both swept and unswept configurations. *Third*, HALE configurations typically undergo very large deformations, see for example Reference [60]. *Lastly*, it is very important for a thorough stability analysis the knowledge of different static equilibrium configurations at the same load level [2].

The focus is on the understanding of the snap-buckling phenomenon [1] and how the adoption of composite materials changes the strongly nonlinear structural behavior. Snap-buckling occurrence should be avoided. Composites provide a very effective option for the designer. How this can be practically achieved is extensively assessed in this work.

It should be pointed out that the efficient design of composite plate-like wings in view of achieving an optimal response (e.g., quasi-linear or snap-buckling-free response) has practical implications since a real wing-box structure could be eventually analyzed with an equivalent plate representation [155]. Thus, the analyses reported in this work could be adopted to gain directions about the design of a real snap-free joined-wing structure.

The main objective of this work is to shed some light on the physics related to the highly complex critical and post-critical behavior of composite *anisotropic* Joined Wing. Thus, the material properties used in the investigations are artificially modified to gain insights on the actual structural parameters which affect the structural response.

4.5 Unswept Joined Wing Cases

The unswept cases present the geometry shown in Figure 4.1 whereas the material properties are case-by-case changed to identify the important parameters affecting the nonlinear response. The joint transfers forces and moments between the wings. Thus, it is intuitive to expect a significant influence of the extensional and bending stiffness on the snap-buckling and post-critical responses. On this regard, if one considers the analogy with Euler's column and its instability properties when subjected to compressive forces, it could be inferred that when the two wings are loaded with a vertical pressure in the $+z$ direction the consequent compression of the upper wing is the driving mechanism to the instability. Thus, a design strategy aimed at increasing the *extensional stiffness* could be suggested. Actually, in this work a counterintuitive result will be demonstrated: the *bending stiffness* is the most relevant parameter which could not be easily predicted by simply using the joined-wing-analogue argument of Euler's column instability. Moreover, it will be shown that the *bending stiffness ratio* between the lower and upper wings is what regulates the snap-buckling for the unswept configuration reported in Figure 4.1.

4.5.1 Lower-to-Upper Wing Stiffness Ratio and its Effects on the Snap-buckling

The isotropic, orthotropic and anisotropic cases are now investigated.

Isotropic case

The Young's moduli of the upper and lower wing were varied to change the stiffness ratio, but in such a way as to maintain the linear response of point P1 of the *UREF* configuration, for details about the analytical expression see Appendix A of Reference [1]. In the process of varying the material of the wings (see Table 4.1), the joint's material has been held the same. All the analyses with the present software have

Table 4.1: Details about the materials used for the different configurations. Poisson's ratio is $\nu = 0.33$ for all cases.

Cases and relative parameters					
Case ID	Wing	Young's Modulus $E \times 10^{-7}\ \left[\frac{Kg}{mm \cdot s^2}\right]$	Ratio $E^r = \frac{E^{\mathrm{LW}}}{E^{\mathrm{UW}}}$	Snap	Critical Load Λ^{CR}
UREF	Upper	6.9	1	YES	0.91
	Lower	6.9			
UISO1	Upper	12	0.2	YES	0.81
	Lower	2.4			
UISO2	Upper	10	0.4	YES	0.84
	Lower	4.1			
UISO3	Upper	8.7	0.6	YES	0.86
	Lower	5.2			
UISO4	Upper	7.7	0.8	YES	0.88
	Lower	6.1			
UISO5	Upper	6.0	1.3	YES	0.95
	Lower	7.8			
UISO6	Upper	5.0	1.8	YES	1.07
	Lower	8.9			
UISO7	Upper	4.5	2.1	YES	1.22
	Lower	9.5			
UISO8	Upper	4.1	2.4	YES	1.52
	Lower	9.9			
UISO9	Upper	4.1	2.45	YES	1.68
	Lower	10			
UISO10	Upper	4.0	2.5	NO	∞
	Lower	10.1			

been validated with NASTRAN, and the agreement is excellent. However, in many cases it was not possible to drive to convergence the commercial tool after the limit point: this is an indication of the numerical difficulties associated with this type of simulations for the case of Joined Wings and the necessity of the automatic switching features (from Newton-Raphson to arc length and vice-versa) implemented in the in-house capability. From Table 4.1 and Figures reported in Reference [130] and omitted here for brevity, it can also be observed that the lower-to-upper wing stiffness ratio $E^r = \frac{E^{\mathrm{LW}}}{E^{\mathrm{UW}}}$ plays an important role in determining the nonlinear response and snap phenomenon occurrence: increasing E^r raises the snap load level (i.e., the first limit point encountered when tracking the response curve occurs at higher values of the load parameter Λ). Further increasing of the stiffness ratio E^r postpones the buckling occurrence to higher level loads, and eventually it disappears and the response presents a stiffening effect (increasing of the load parameter/displacement slope). As Table 4.1 suggests, a critical value E^r_{CR} could be defined, which, for this particular case, is equal to 2.5.

From the definition of E^r it is deduced that increasing the stiffness of the *lower* wing compared to the stiffness of the *upper* wing is beneficial as far as the elimination of the snap-buckling is concerned. This is apparently a counterintuitive result since it would be expected that increasing the stiffness of the upper wing (the one which is compressed under this load condition) could be beneficial. It also confirms the fact that for Joined Wings the type of response does not follow the interpretation which could be used by adopting the classical arguments of the Eulerian compressed column. For an assigned load level, comparison of the deformed shapes corresponding to different values for the parameter E^r showed [130] that the configurations on the verge of snapping (for that load level) present a deformation of the upper wing characterized by a more pronounced inward bending deformation. This property is derived here for the isotropic case, but its validity is more general, as the discussion regarding the orthotropic materials will show.

Summarizing, to avoid snap-buckling and having on the contrary a stiffening effect, the ratio E^r is one of the dominant parameters. In particular, a configuration featuring a value of this parameter larger than a critical value E^r_{CR}, does not present a snap-buckling problem.

A stiffer lower wing (or alternatively a more compliant upper wing) is then desirable for avoiding the snap-buckling problem. In a real design the different stiffness of the two wings is likely to be connected with a difference share of the load carried by each

wing. This also presents implications on the stress levels reached by the structure and has to be properly taken into account when these types of configurations are designed.

Orthotropic case

It should be observed that an isotropic material does not present a preferential direction and, thus, the nature of the nonlinear response can be fully investigated only if anisotropic materials are adopted. As a first step towards this direction, the case of orthotropic plates is here analyzed.

The first test case involves a single lamina with fibers directed along the wing span. The fibers' angle ϑ, measured counterclockwise from the x-axis is equal to 90 degrees, see Figure 4.3. This choice makes the material behavior to be orthotropic in respect of the free stream x and span-wise y directions. As done for the previously

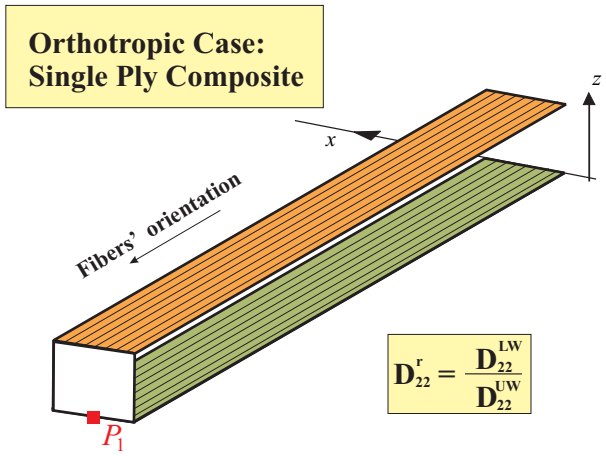

Figure 4.3: Unswept configurations for orthotropic cases and definition of lower-to-upper wing stiffness ratio.

discussed isotropic case, the material properties are changed to numerically experiment the influence of the different parameters. However, modification of the properties is performed without changing point P_1's linear static response. This choice is useful for meaningful comparison of the different responses.

The material properties are selected as follows: $E_2^{\mathrm{LW}} = E_2^{\mathrm{UW}} = E_{\mathrm{REF}}$, $G_{12}^{\mathrm{LW}} = G_{12}^{\mathrm{UW}} = G_{\mathrm{REF}}$, and $\nu_{12}^{\mathrm{LW}} = \nu_{12}^{\mathrm{UW}} = \nu_{\mathrm{REF}}$. The values of E_1^{LW} and E_1^{UW} are varied case by case.

The joint's material is fixed and is exactly the isotropic one used for the baseline case, *UREF* ($E = 6.9 \cdot 10^7$ $[Kg/(mm \cdot s^2)]$; $\nu = 0.33$). Table 4.2 presents the analyzed

Table 4.2: Details about the materials used for the different configurations. For each case it holds that $E_2 = E_{\text{REF}}$, $\nu = \nu_{\text{REF}}$, $G = G_{\text{REF}}$.

Cases and relative parameters					
Case ID	Wing	Young's Modulus $E_1 \times 10^{-7}$ $\left[\frac{Kg}{mm \cdot s^2}\right]$	Ratio $E_1^r = \frac{E_1^{\text{LW}}}{E_1^{\text{UW}}}$	Ratio $A_{22}^r = D_{22}^r = \frac{D_{22}^{\text{LW}}}{D_{22}^{\text{UW}}}$	Snap
UORTHO1	Upper	5.0	1.8	1.7	YES
	Lower	8.9			
UORTHO2	Upper	4.5	2.1	1.9	YES
	Lower	9.5			
UORTHO3	Upper	4.0	2.5	2.2	YES
	Lower	10.1			
UORTHO4	Upper	3.7	2.8	2.4	YES
	Lower	10.4			
UORTHO5	Upper	3.4	3.2	2.7	NO
	Lower	10.8			

orthotropic configurations. The parameter E_1^r still affects the stability properties: if it is increased the snap buckling is eventually eliminated (*UORTHO5*). However, there are important quantitative differences. In fact as evident from isotropic configurations UISO10 response, with a value of $E^r = 2.5 \equiv E_{\text{CR}}^r$ buckling instability was avoided. On the contrary, even if the Joined Wing's geometry, the linear response of point P_1, and stiffness ratio are kept constant (with respect to *UISO10*), the orthotropic configuration *UORTHO3* (featuring $E_1^r > E_{\text{CR}}^r$) presents buckling as seen in Table 4.2. This suggests that, although E_1^r is related to the physics of the phenomenon (increasing E^r eventually eliminates the instability as seen in Table 4.2), from a quantitative point of view it is not the best choice to identify when the instability actually occurs. To find a more representative parameter linked to the stability properties of the system and isolate the driving mechanism, the ratios of extensional and bending stiffnesses are then monitored. These ratios are indicated with the symbols A_{mn}^r and D_{mn}^r respectively. Their explicit definition is the following:

$$A_{mn}^r = \frac{A_{mn}^{\text{LW}}}{A_{mn}^{\text{UW}}} \qquad D_{mn}^r = \frac{D_{mn}^{\text{LW}}}{D_{mn}^{\text{UW}}} \tag{4.3}$$

where m and n are indicies identifying each *non-zero* term of the corresponding matrix. The superscripts "LW" and "UW" indicates that the quantities are referred to the lower wing and upper wing respectively.

It is observed that each wing is modeled with a single lamina with constant

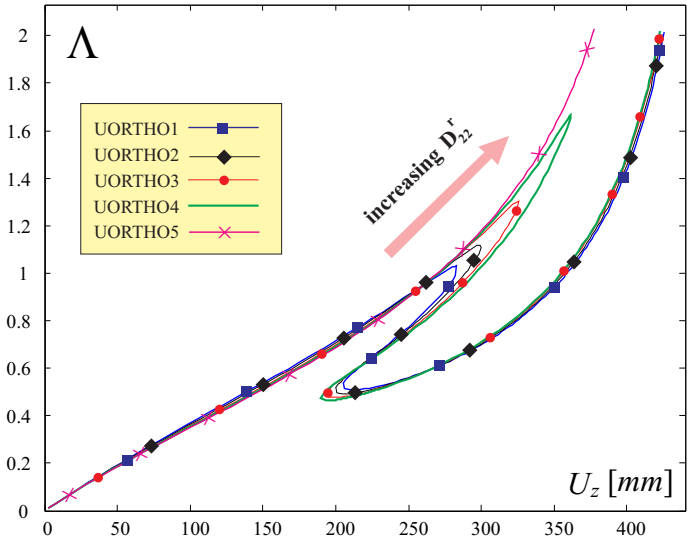

Figure 4.4: Load parameter Λ versus cumulative vertical displacement U_z of point P_1 for configurations employing different orthotropic wings. See Table 4.2 for details.

thickness and material properties. This means that the matrix $\boldsymbol{A}^r$ which contains the ratios between the extensional stiffnesses is *coincident* with the matrix $\boldsymbol{D}^r$ which contains the ratios of the bending stiffnesses.

A series of investigations correlates the snap-buckling occurrence with the ratios A^r_{22} and D^r_{22} (see Table 4.2 and Figure 4.4). This is physically expected since A^r_{22} relates the extensional stiffnesses in the wing span direction (important for example to describe the compression or tension of the wings) whereas D^r_{22} relates the flexural stiffnesses (important in the determination of the principal bending moment of the wings). Moreover, the new critical parameter $[D^r_{22}]_{\mathrm{CR}}$ ($[A^r_{22}]_{\mathrm{CR}}$) has exactly the same value as the one for the isotropic case E^r_{CR}, giving this a quantitative consistency.

Summarizing, it has been shown that the snap-buckling disappears when $A^r_{22} = D^r_{22}$ is larger than a critical value. Then the question is whether A^r_{22} is the actual parameter that needs to be investigated/monitored or if D^r_{22} is the one that needs to be considered or if both A^r_{22} and D^r_{22} are equally important. The answer represents a crucial concept in the design of a Joined Wing. For example, if A^r_{22} is the most important term then the snap-buckling is mainly driven by compressive actions. On the other hand, if D^r_{22} is the most important parameter then the snap-buckling occurs mainly because of bending actions. If the two parameters have similar relative importance, the physical mechanism is a combination of both compression and bending.

Since for a single orthotropic lamina it always is $A^r_{22} = D^r_{22}$, it is not possible to

identify what is physically relevant as far as the instability is concerned unless a larger-than-one number of plies is selected so that it is possible to separately modify $\boldsymbol{A}^r$ and $\boldsymbol{D}^r$ matrices with the consequence that $\boldsymbol{A}^r \neq \boldsymbol{D}^r$.

In particular, several test cases have been introduced with the following assumptions: the lower wing is made of the same *isotropic* material employed for the reference case; the upper wing is made of a multilayered *orthotropic* composite laminate with layers made of the same material; the thickness of two generic different layers may be different, but the total thickness of the upper wing is maintained equal to $h = 1mm$. Table 4.3 shows all the analyzed cases and the values of A^r_{22} and D^r_{22} for each configuration. For these cases a reference closed-form analytical linear solution is impractical to obtain. Thus, it is not imposed to have the same slope (linear solution) for all the nonlinear responses relative to the cases reported in Table 4.3. However, this does not pose a conceptual limitation.

Figure 4.5 summarizes the responses of all the performed analyses. As reported

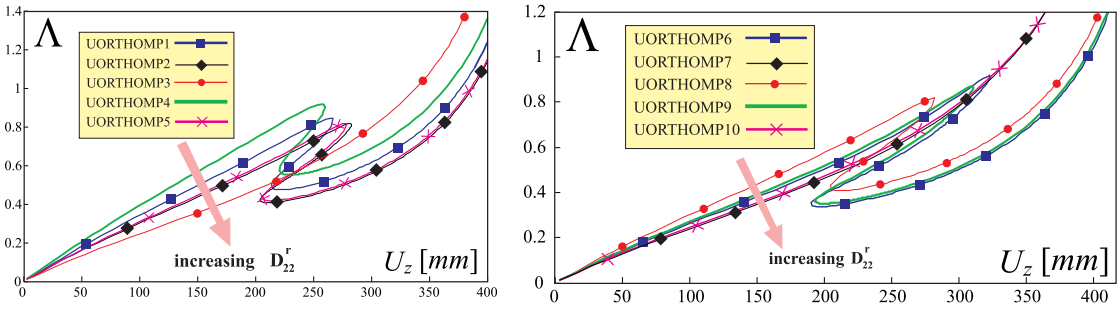

Figure 4.5: Load parameter Λ versus cumulative vertical displacement U_z of point P_1 for configurations featuring a lower wing composed of reference isotropic material ($E = E_{\text{REF}}$ and $\nu = \nu_{\text{REF}}$) and an upper wing composed of multi-ply composite material in order to have an orthotropic response. The different laminations are indicated in Table 4.3.

in Table 4.3, it is quite evident that D^r_{22} plays the leading role, since it dictates snap occurrence, where this is not the case for the A^r_{22} parameter. When A^r_{22} is held constant and equal to 1.7 and D^r_{22} is increased from 1.0 to 2.9, the snap-buckling disappears. Conversely, if D^r_{22} is held constant and A^r_{22} is varied, the response is not appreciably affected in terms of instability occurrence. Similar considerations, leading to the same conclusions, could be done for the other reported entries of A^r_{22} and D^r_{22}.

The importance of the ratio D^r_{22} is qualitatively consistent with Figure 4.6 which shows that when the snap-buckling occurs a more pronounced inward bending deforma-

Table 4.3: Details about the materials used for the different configurations. For each case the lower wing is made of an isotropic material with $E^{\mathrm{LW}} = E_{\mathrm{REF}}$, $\nu^{\mathrm{LW}} = \nu_{\mathrm{REF}}$, where the upper wing features a composite material with plies laminated as indicate above. Each ply is manufactured with the same material $E_1 = 8.5 \cdot 10^7 \left[\frac{Kg}{mm \cdot s^2}\right]$, $E_2 = 0.66 \cdot 10^7 \left[\frac{Kg}{mm \cdot s^2}\right]$, $G_{12} = 0.56 \cdot 10^7 \left[\frac{Kg}{mm \cdot s^2}\right]$, $\nu_{12} = 0.28$.

Cases and relative parameters					
Case ID	Wing	Lamination	Ratio $A^r_{22} = \frac{A^{\mathrm{LW}}_{22}}{A^{\mathrm{UW}}_{22}}$	Ratio $D^r_{22} = \frac{D^{\mathrm{LW}}_{22}}{D^{\mathrm{UW}}_{22}}$	SNAP
UORTHOMP1	Upper	$90_{0.15}/0_{0.7}/90_{0.15}$	2.5	1.3	YES
UORTHOMP2	Upper	$90_{0.1}/0_{0.35}/90_{0.1}/0_{0.35}/90_{0.1}$	2.5	1.7	YES
UORTHOMP3	Upper	$90_{0.05}/0_{0.35}/90_{0.2}/0_{0.35}/90_{0.05}$	2.5	2.7	NO
UORTHOMP4	Upper	$90_{0.25}/0_{0.5}/90_{0.25}$	1.7	1.0	YES
UORTHOMP5	Upper	$90_{0.1}/0_{0.25}/90_{0.3}/0_{0.25}/90_{0.1}$	1.7	1.7	YES
UORTHOMP6	Upper	$90_{0.05}/0_{0.25}/90_{0.4}/0_{0.25}/90_{0.05}$	1.7	2.3	YES
UORTHOMP7	Upper	$90_{0.03}/0_{0.25}/90_{0.44}/0_{0.25}/90_{0.03}$	1.7	2.9	NO
UORTHOMP8	Upper	$90_{0.1}/0_{0.8}/90_{0.1}$	3.4	1.7	YES
UORTHOMP9	Upper	$90_{0.07}/0_{0.4}/90_{0.06}/0_{0.4}/90_{0.07}$	3.4	2.2	YES
UORTHOMP10	Upper	$90_{0.05}/0_{0.4}/90_{0.1}/0_{0.4}/90_{0.05}$	3.4	2.8	NO

tion of the upper wing is present compared to cases in which instability is not observed cases. More in detail, two configurations are depicted in Figure 4.6: one is associated with the case *UORTHO1*, which has $E_1^r = 1.8$ and $D_{22}^r = A_{22}^r = 1.7$, and the other one corresponds to the case *UORTHO5*, featuring $E_1^r = 3.2$ and $D_{22}^r = A_{22}^r = 2.7$. Configuration *UORTHO1* incurs in a snap phenomenon and presents a larger inward bending for the upper wing.

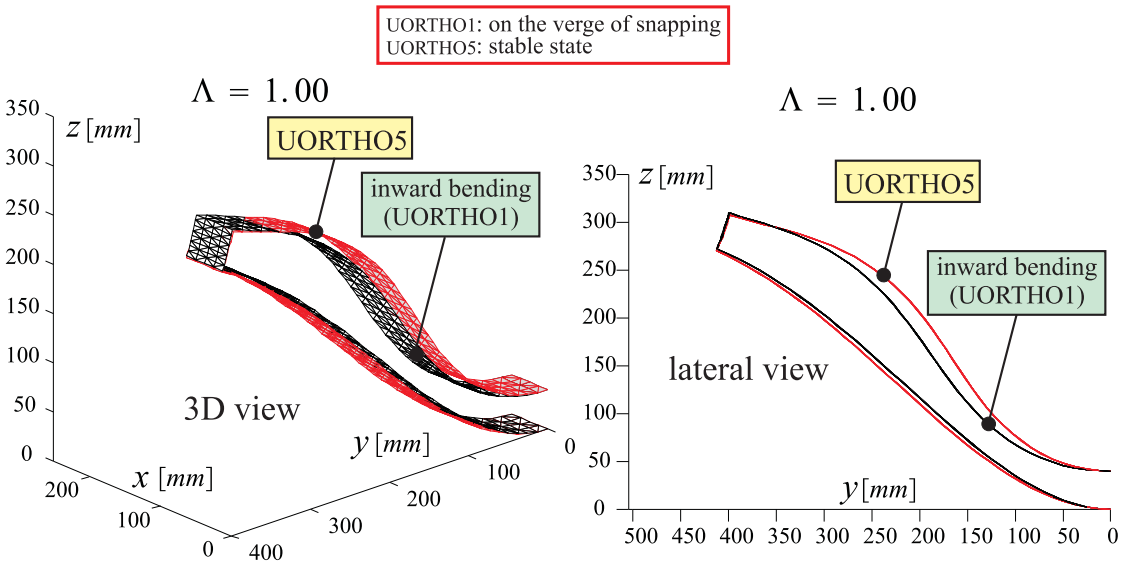

Figure 4.6: Comparison of configurations *UORTHO1* and *UORTHO5* at $\Lambda = 1$.

It is interesting to observe that, both with and without the normalization (prescribed linear displacement of point P_1, adopted for the isotropic and single lamina orthotropic cases) the critical parameter $[D_{22}^r]_{\mathrm{CR}}$ keeps almost the same value (about 2.5).

It should be also observed that the isotropic case investigated in the preceding section and in Reference 130 can be seen as a particularization of the single-lamina orthotropic case investigated here. Thus, the physics ruling the snap buckling phenomenon is the same. However, in the isotropic case changing the extensional and bending stiffnesses independently from each other was not possible and so it was not possible to identify the bending stiffness ratio as the key parameter related to the stability properties of the system.

Joint's Connection and Load Transferring Effects on the Snap-Buckling of Unswept Joined Wings

For both the cases of orthotropic and isotropic unswept Joined Wings, configurations which showed similar tip displacement for the same load level Λ but different nonlinear behavior (i.e. one configuration experienced snap-buckling and the other did not, see for example Figure 4.6) were compared. One of the main features that was noticed was the different deformation of the upper wing. In particular, the inward bending of the upper wing was more pronounced for the model that was on the verge of snapping. It is true that the curvature distribution of the upper wing depends on all the transmitted force through the joint, being this exacerbated from the large displacement characteristic of the cases. However, it is of particular interest to monitor the bending moment M_{yy} transmitted through the joint as a function of the load parameter Λ. More in detail, this is done for the configuration (see Table 4.1) which is on the verge of snapping (*UISO7*) and for the configuration (presenting different material properties than the first one but with similar load-displacement curve up to that load level) which does not present buckling (*UISO10*) [130]. Figure 4.7 shows the moment M_{yy} on a finite element on the upper wing and near the joint. Although the interest is towards general be-

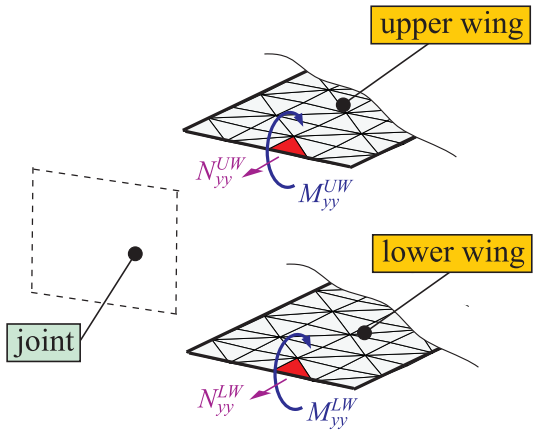

Figure 4.7: Wing span forces (N_{yy}^{UW} and N_{yy}^{LW}) per unit of length and primary bending moments (M_{yy}^{UW} and M_{yy}^{LW}) per unit of length transferred to the upper and lower wings. The forces and moments are calculated at the centroid of the finite elements shown in the figure.

havior more than specific values, to have more reliable predictions a refined model using approximately 15000 DOF (against the approximately 2600 DOF of the base model), is used for comparison purposes. These models show an almost perfect agreement in terms

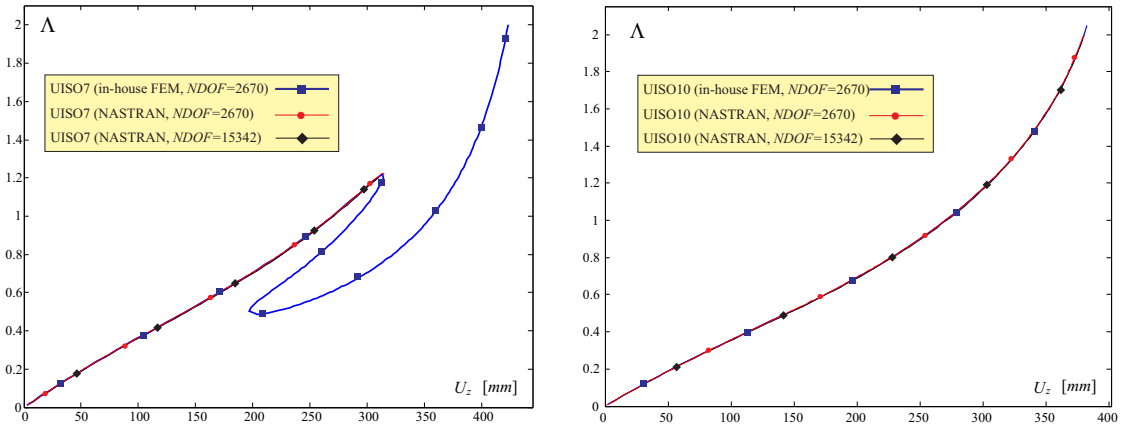

Figure 4.8: Curves of the load parameter Λ versus cumulative vertical displacement U_z of point P_1 for *UISO7*(on the left) and *UISO10*(on the right) obtained from simulations using different FE solvers and mesh sizes. Both NASTRAN solutions showed convergence problems after the first limit point.

of cumulative vertical displacement of point P_1, see Figure 4.8. As it is well known, the force and moments (see Figures 4.9 and 4.10) converge more slowly when the mesh is refined. The correlation of their trends is very good. It should also be pointed out that since the forces and moments per unit of length are evaluated at the centroid of of the elements (see Figure 4.7 for the base model) a refining of the mesh implies a calculation of these quantities on a different (but close) point. The interest of this discussion is to show the trends. Thus, this fact does not affect the following discussion.

In Figure 4.9 the value of M_{yy} is plotted for both the upper and lower wings for both the cases. Considering the upper wing, it is possible to observe that M_{yy}^{UW} shows similar trend in the pre-buckling area. However, the configuration which does not experience snap-buckling (*UISO10*) presents a larger moment M_{yy}^{UW} compared to the one corresponding to *UISO7*. At a certain load parameter, *smaller than the critical value*, the moment relative to configuration *UISO7* starts diminishing in value and eventually the snap-buckling occurs. For the lower wing the bending moments of the *UISO7* and *UISO10* configurations are practically identical. For completeness, Figure 4.10 shows the force per unit of length N_{yy} on the upper wing (see also Figure 4.7).

The different trends regarding the transmitted bending moment (see Figure 4.9 a)) suggest that the snap-buckling occurrence could be strictly tied with M_{yy}. To further demonstrate this observation, the boundary conditions between the joint and the upper (or lower) wings are now modified to *reduce the amount of moment* which is transferred.

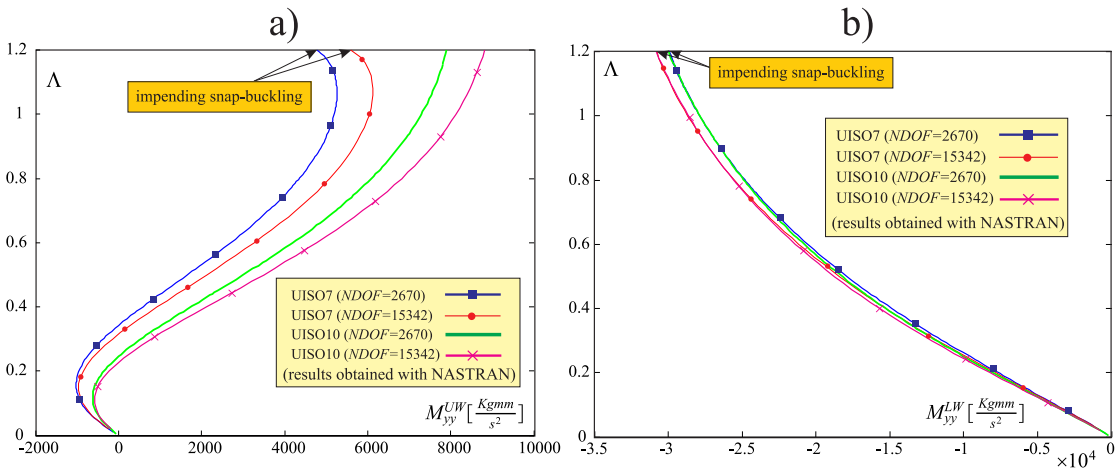

Figure 4.9: Bending moment per unit of length M_{yy} on the upper wing, a), and lower wing, b). *UISO7* and *UISO10* cases. See also Figure 4.7 for a graphical representation.

This is accomplished by the adoption of a multifreedom constraint which allows the joint-upper-wing or joint-lower-wing relative rotation. To simulate *some* stiffness of the joint a relatively small torsional spring ($k_\vartheta = 100\frac{Kg \cdot mm^2}{s^2 \cdot rad}$) has also been added at the joint-wing connection. It should be noted that a large value for the spring stiffness would correspond to a *perfect joint's connection* of the types analyzed so far, whereas a zero-value for the stiffness of the spring would correspond to a *perfect hinge connection*. Since the adopted value for the torsional stiffness is quite small compared to the stiffness of the finite elements, the simulated joint-wing connection is similar (but not equivalent) to a hinge connection. This set of boundary conditions is referred as *quasi-hinge connection* in this work.

A quasi-hinge connection reduces the amount of moment transferred by the joint to the wing. Thus, it is expected that this connection has the tendency to reduce or eliminate the buckling occurrence. To prove that, three configurations are based on *UREF* are considered: one with perfect joints, one with a *quasi-hinge connection* between the joint and upper wing, one with a *quasi-hinge connection* between the joint and the lower wing. The related nonlinear responses are plotted in Figure 4.11. It can be observed that the snap-buckling disappears in both cases in which a *quasi-hinge connection* is employed. Moreover, reducing the bending moment transmission prevents the snap to occur. Moreover, if the responses relative to these cases are superimposed, it is possible to realize that the pre-critical states for the perfect joint case show a larger value of the stiffness (i.e., higher slope of the displacement-load curve in Figure 4.11).

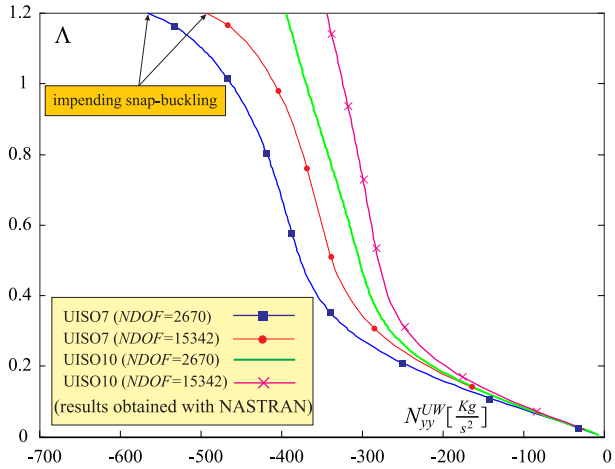

Figure 4.10: In-plane force per unit of length N_{yy} on the upper wing for the *UISO7* and *UISO10* cases. See also Figure 4.7 for a graphical representation.

Thus, the configurations featuring a quasi-hinge connection experience a reduction of stiffness, which is more pronounced when the quasi-hinge connection is located between the joint and the upper wing. Summarizing, the presented analyses lead to the conclusion that bending action transmission is one of the main sources of non-linearities when stability is concerned. When the perfect joint is considered the stiffness of the system is first increased but eventually the instability phenomena occurs (see Figure 4.11). When the bending moment is partially transmitted, the response does not present any snap-buckling phenomenon. However, there is a consistent loss of stiffness (see Figure 4.11).

Studies on the connection between wings have already been undertaken for example by Stearman, Lin, and Jhou (Reference [35]). In that work, the rigid connection was assessed as being the most favorable in terms of root bending moment alleviation and stiffness. And, at least from a stiffness perspective, the results are in agreement with the results presented in the current work. However, the analyses of Reference [35] were obtained with linear models, and thus, phenomena such as the snap-buckling could not have been predicted or included. Furthermore, it should be noted that the conclusions applies for the particular configuration (a sensorcraft/joined-wing one) and load condition. The highly complex structural response of the Joined Wings need careful investigations case by case.

The authors also like to quote a passage from Reference [35] in which it is stated that the overconstrained nature of the system could give rise to significant load transfer through the joint which could be detrimental to the structural stability of the system,

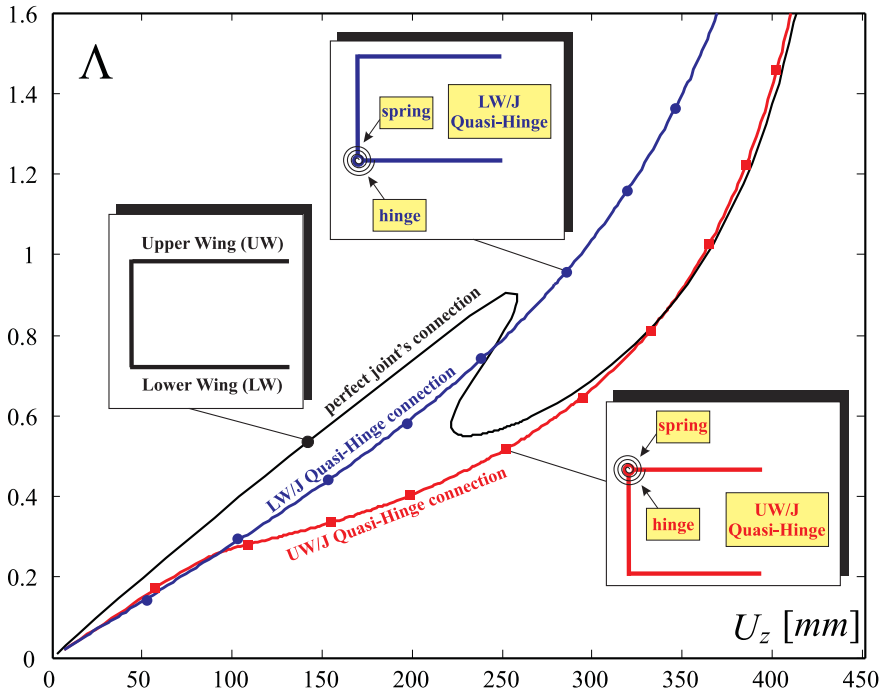

Figure 4.11: Cumulative vertical displacement (U_z) of point P_1 versus load factor (Λ) for *UREF* configurations when a rigid or quasi-hinge connection is used between the joint and the upper or lower wing. UW/J and LW/J are abbreviations for indicating a quasi-hinge connection between upper wing and joint or between lower wing and joint respectively.

and to properly take them into account a nonlinear analysis would have been needed. The present findings (see Figures 4.11 and 4.12) confirm this importance: the bending moment transfer has a primary role in snap-buckling occurrence.

Composite Materials (anisotropic case)

Previous discussions showed that for the isotropic and orthotropic cases the driving mechanism which leads to the snap-buckling is closely tied with bending effects. It was also demonstrated that the bending stiffness ratio D_{22}^r was an effective parameter to predict if the nonlinear response presents a snap-buckling instability. In particular, it was shown that the upper wing has to be more bending compliant to avoid the snap-buckling. It was found that when $D_{22}^r \equiv \frac{D_{22}^{\mathrm{LW}}}{D_{22}^{\mathrm{UW}}}$ is bigger than a critical value, then the instability disappears; $[D_{22}^r]_{\mathrm{CR}}$ does not represent an universal value, on the contrary, its magnitude is expected to be a case-dependent parameter.

For the same unswept joined-wing layout, the next step is the adoption of com-

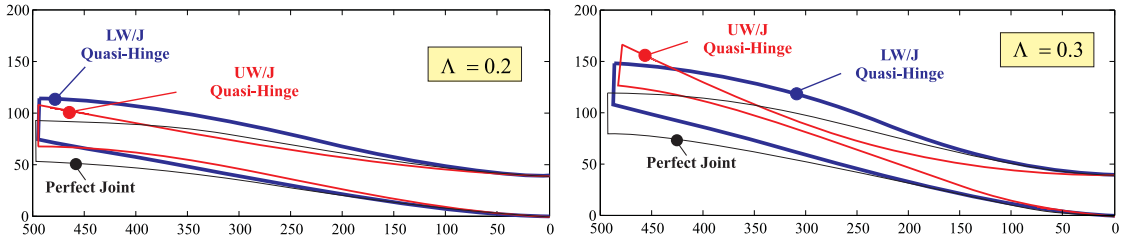

Figure 4.12: Comparison of the deformed structures for different (Λ) values, for the perfect and quasi-hinge connection cases. UW/J and LW/J are abbreviations for indicating a quasi-hinge connection between upper wing and joint or between lower wing and joint respectively.

posite materials to introduce anisotropic effects and investigate how they influence the nonlinear response. In particular, two main questions are here answered. Is D_{22}^r sufficient to describe the tendency of the structure to experience a snap-buckling? What are the effects of anisotropy on the global bending stiffness and snap-buckling?

To answer the first question, two new configurations are investigated (see Table 4.4). In the first one, named *UANIMP1*, the lower wing is isotropic and the material is the one adopted for *UREF* configuration. The upper wing is simulated with a multilayered orthotropic plate. The second configuration, named *UANIMP2*, presents a symmetric laminate for the upper wing, whereas the lower wing is made of the same isotropic reference material. Both configurations present the same value for D_{22}^r; however, the nonlinear responses are dramatically different (see Figure 4.14) and the configuration *UANIMP2* does not experience snap-buckling. This qualitative investigation shows that the new coupling between the torsional deformation and bending moment plays an important role as far as the stability properties are concerned.

Figure 4.15 shows how the anisotropy introduces torsional deformations (configuration UANIMP2) which are not present for configuration *UANIMP1*.

A series of additional configurations have been created (see Table 4.5). The lower wing is isotropic and the adopted material is the one used for the *UREF* case. The upper wing is simulated with a single lamina whose orientation is varied according to Table 4.5. Results indicate (see Figure 4.16 and Table 4.5) that the bending-torsional coupling has a major role in determining when the snap-buckling occurs. This is clearly understood if for example configurations *UANISP2* and *UANISP4* are compared. The two configurations do not present snap-buckling, although this was expected for the first one having $D_{22}^r > [D_{22}^r]_{\mathrm{CR}}$, it was not expected for the second one, for which

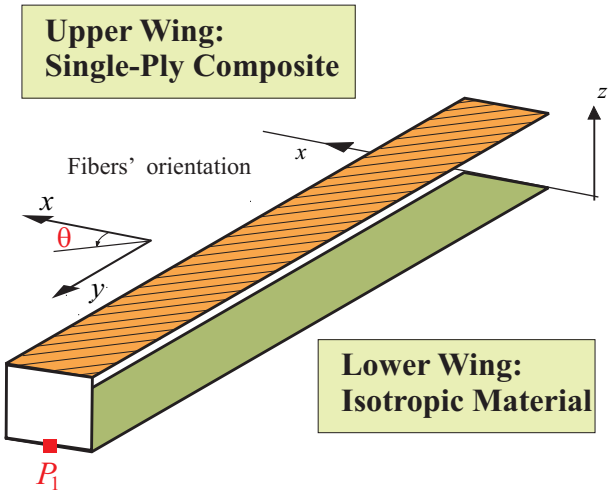

Figure 4.13: Unswept configurations for anisotropic cases.

Table 4.4: Details about the materials used for the different configurations. For each case the lower wing is composed of the reference isotropic material, where the upper wing is composed of a composite material with plies laminated as indicate above. Each ply is manufactured with the same material $E_1 = 8.5 \cdot 10^7 \left[\frac{Kg}{mm \cdot s^2}\right]$, $E_2 = 0.66 \cdot 10^7 \left[\frac{Kg}{mm \cdot s^2}\right]$, $G_{12} = 2.6 \cdot 10^7 \left[\frac{Kg}{mm \cdot s^2}\right]$, $\nu_{12} = 0.33$.

Cases and relative parameters				
Case ID	Wing	Lamination	Ratio $D^r_{22} = \frac{D^{\mathrm{LW}}_{22}}{D^{\mathrm{UW}}_{22}}$	SNAP
UANIMP1	Upper	$90_{0.049}/0_{0.25}/90_{0.402}/0_{0.25}/90_{0.049}$	2.4	YES
UANIMP2	Upper	$17_{0.1}/45_{0.8}/17_{0.1}$	2.4	NO

$D^r_{22} < [D^r_{22}]_{\mathrm{CR}}$. Analogous situation come when comparing *UANISP11* and *UANISP12*. Unexpected behaving cases present a value of D^{UW}_{26} different than zero. Since the wing system is unswept, the coupling between the torsion and bending are due only to the anisotropy of the material.

This is why for the anisotropic case understanding the mechanism which leads to the instability is more challenging.

To answer the second question (i.e., identify what are the effects of the anisotropy on global bending stiffness and snap-buckling), three different configurations (namely *UANISP15*, *UANISP4* and *UANISP12* [see Table 4.5]) are selected. None of them experiences the nonlinear buckling, and, according to Figure 4.17, they present high overall stiffness. The configurations *UANISP4* and *UANISP12* are stiffer than the configuration *UANISP15* (especially for larger values of the load step Λ) confirming that composite

Table 4.5: Details about the materials used for the different configurations. For each case the lower wing is made of the reference isotropic material, where the upper wing is composed of a single ply with the fibers oriented as indicate above (cases *UANISP1* through *UANISP14*), or of an isotropic material (*UANISP15*). The Young and shear moduli of this Table are expressed in $\left[\frac{Kg}{mm \cdot s^2}\right]$ and the values reported in the Table need to be multiplied by 10^7.

Cases and relative parameters						
Case ID	Wing	Orientation	Ratio $D^r_{22} = \frac{D^{\mathrm{LW}}_{22}}{D^{\mathrm{UW}}_{22}}$	$D^{UW}_{26} \times 10^{-7}$ $\left[\frac{Kg \cdot mm^2}{s^2}\right]$	SNAP	UW DATA
UANISP1	Upper	0°	4.5	0	NO	
UANISP2	Upper	15°	3.4	0.09	NO	
UANISP3	Upper	30°	1.9	0.18	NO	
UANISP4	Upper	32.5°	1.8	0.19	NO	$E_1 = 12.5$
UANISP5	Upper	35°	1.6	0.20	YES	$E_2 = 1.7$
UANISP6	Upper	37.5°	1.5	0.21	YES	$G_{12} = 2.7$
UANISP7	Upper	45°	1.2	0.23	YES	$\nu_{12} = 0.33$
UANISP8	Upper	60°	0.8	0.22	YES	
UANISP9	Upper	75°	0.7	0.14	YES	
UANISP10	Upper	90°	0.6	0	YES	
UANISP11	Upper	45°	2.6	0.16	NO	$E_1 = 8.5$
UANISP12	Upper	60°	1.4	0.20	NO	$E_2 = 0.66$
UANISP13	Upper	62.5°	1.3	0.20	YES	$G_{12} = 0.56$
UANISP14	Upper	65°	1.3	0.19	YES	$\nu_{12} = 0.28$
UANISP15	Upper	*Isotropic*	2.6	0	NO	$E = 2.65$ $\nu = 0.33$

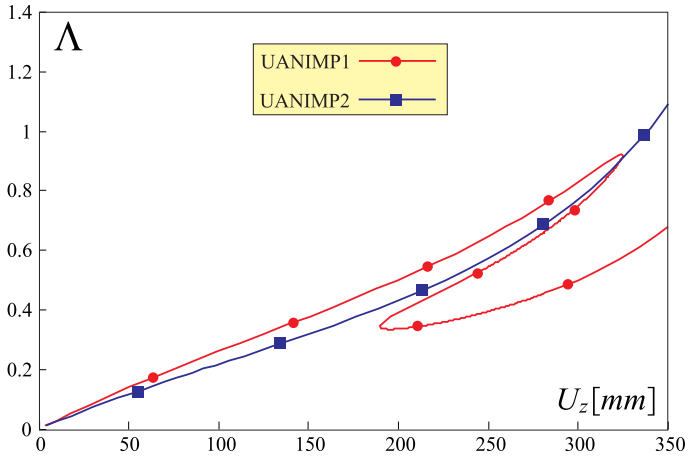

Figure 4.14: Cumulative vertical displacement of P_1 versus Λ for two different configurations featuring a lower wing composed of an isotropic material and an upper wing with an orthotropic and anisotropic behaving materials, obtained through a different disposition of plies. As a consequence of the ad-hoc lamination schemes of the plies, the ratio D^r_{22} is equal for the two cases. See Table 4.4 for details.

materials can be effectively used to change the structural behavior of the system.

In the practice, the design is more challenging since it must be taken into account the structural weight and stress levels. Moreover, the actual aerodynamic loads are of a non-conservative type and the torsional-bending coupling is then even more important: the aerodynamic forces are heavily affected by a change of angle of attack (torsion) of the wing. This study is the first step in the understanding of the difficulties and challenges associated with the nonlinear response for the case of anisotropic Joined Wings.

4.6 Swept Joined Wings and Composites

From the analysis of unswept Joined Wings two main concepts could be identified. *First*, the ratio between the bending stiffness of the wings is an important parameter to establish if the snap-buckling occurs. In particular, the upper wing has to be more bending compliant than the lower wing to remove the instability.

Second, the anisotropy introduces a coupling between the torsion and bending which is not present in isotropic unswept Joined Wing. This coupling modifies the snap-buckling occurrence.

A similar study is now attempted for the *swept* Joined Wings (see Figure 4.2). It is necessary to investigate this case since even when isotropic materials are used, a

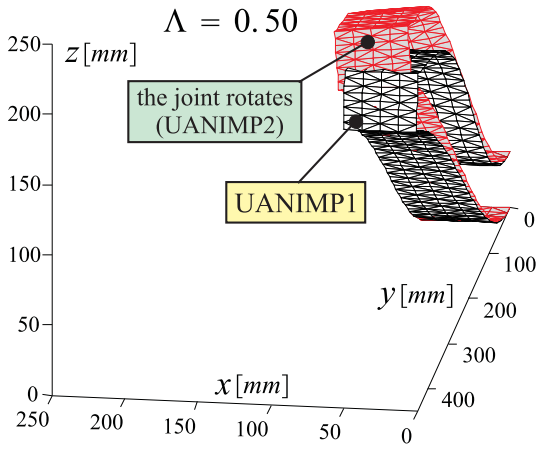

Figure 4.15: Comparison of the deformed configurations for configurations *UANIMP1* and *UANIMP2*. Notice that when the anisotropy is introduced (configuration *UANIMP2*) there is a lateral tilting of the joint.

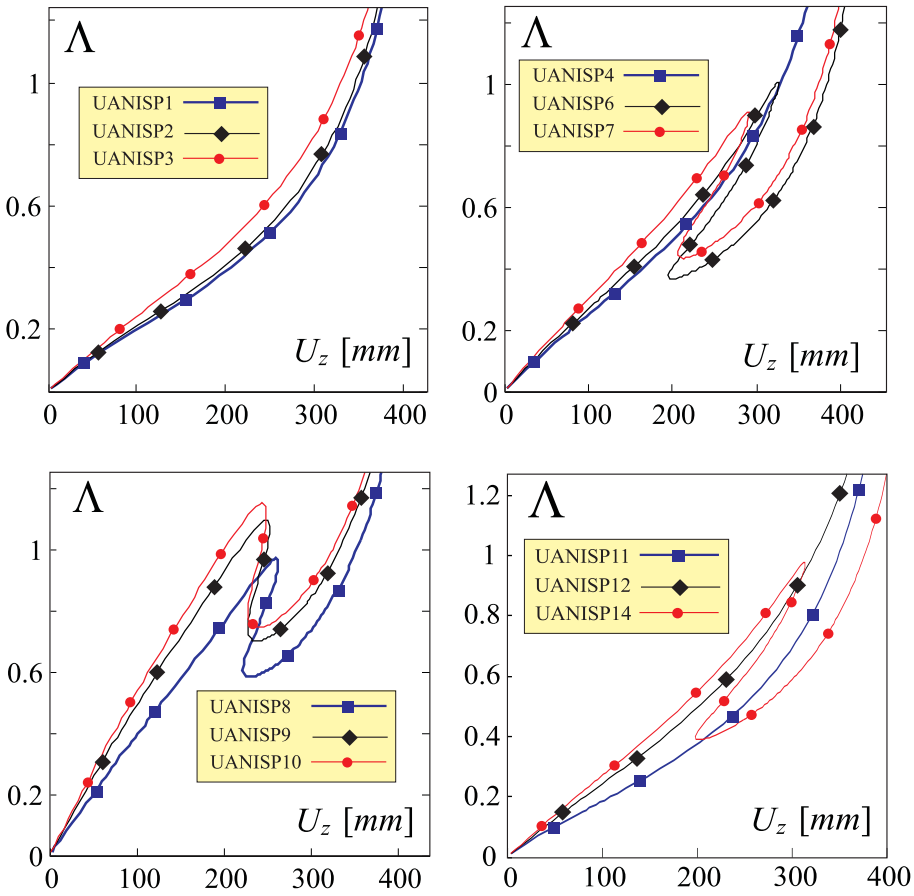

Figure 4.16: Responses for different configurations. The lower wing is composed of the reference isotropic material ($E = E_{\text{REF}}$ and $\nu = \nu_{\text{REF}}$) for all the cases, the upper wing is composed of a single layer with $E_1^{\text{UW}} = 12.5 \cdot 10^7 \left[\frac{Kg}{mm \cdot s^2}\right]$, $E_2^{\text{UW}} = 1.7 \cdot 10^7 \left[\frac{Kg}{mm \cdot s^2}\right]$, $G_{12}^{\text{UW}} = 2.7 \cdot 10^7 \left[\frac{Kg}{mm \cdot s^2}\right]$ and $\nu_{12}^{\text{UW}} = 0.33$. The orientation of the fibers for each case is specified in Table 4.5.

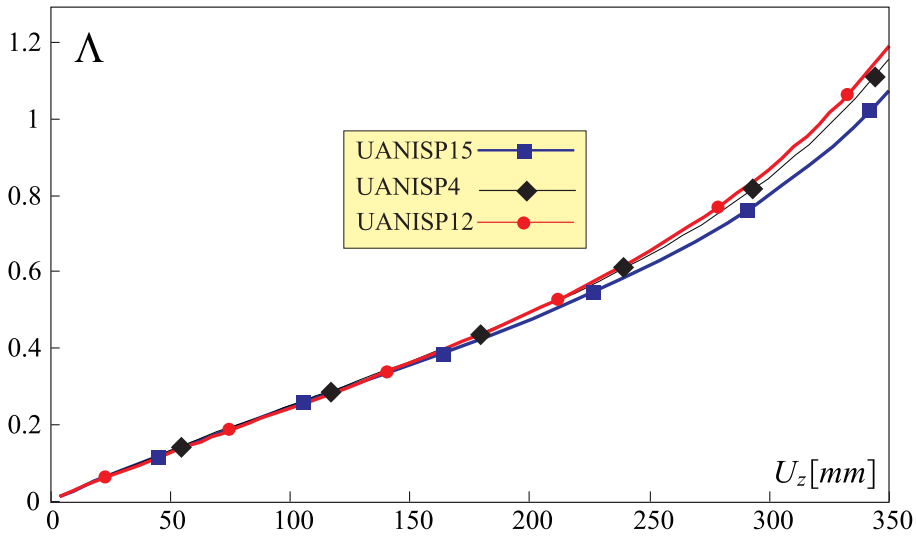

Figure 4.17: Comparison of responses for configurations *UANISP4*, *UANISP12* and *UANISP15*. All the three configurations have a lower wing composed of the isotropic reference material. Configuration *UANISP15* features an upper wing of a different isotropic material, where *UANISP4* and *UANISP12* have an upper wing composed of a single ply composite of two different materials. Details about the materials are reported in Table 4.5. Given the materials, the three configurations represent the *stiffest* responses which do not show buckling.

coupling between the bending and torsion due to the geometry of the wing system arises. It may also be observed (see Figure 4.2) that the sweep angle is moderately low. It is then reasonable to expect that the snap occurrence is still regulated by bending stiffness related parameters.

In order to better investigate the physics related to the bending, it is useful to introduce two local coordinate systems, one for each wing. The direction of the z-axis remains parallel to the global z-axis, whereas the local y-axis runs along the wing-span direction. In such a way the terms of the $\boldsymbol{D}$ matrices for the upper and lower wings maintain an immediate physical interpretation. Figure 4.2 clarifies the orientation of the lower and upper wing local axes.

4.6.1 Effects of Lower-to-Upper-Wing Stiffness Ratio

Isotropic case

The ratio of the Young's moduli of the two wings is varied. However, Young's moduli are selected so that the initial slopes of the displacements are the same (the initial slope is related to the stiffness of the linear analysis). The details about the materials of each configuration are shown in Table 4.6 and Figure 4.18, and the graphs of the cumulative vertical displacement of point P_1 are presented in Figure 4.19. It

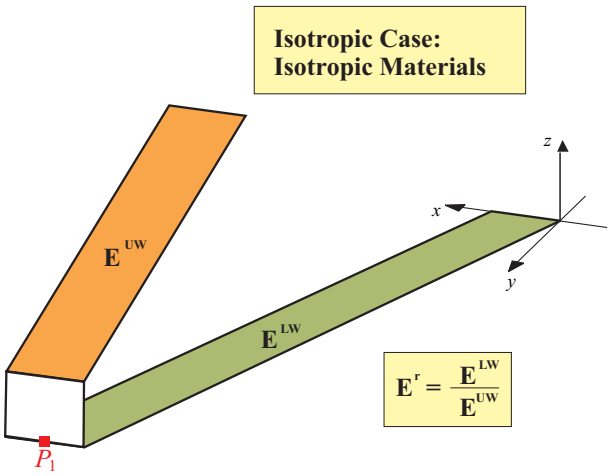

Figure 4.18: Swept configurations for isotropic cases and definition of lower-to-upper wing stiffness ratio.

can be inferred that, as in the unswept case, the ratio $E^r = \frac{E^{\mathrm{LW}}}{E^{\mathrm{UW}}}$ has an important role. However, the required value for avoiding snap is considerably larger (see Table 4.6) than

Table 4.6: Details about the isotropic materials used for the different swept Joined Wings. The Poisson ratio is $\nu = 0.33$ for each case.

Cases and relative parameters				
Case ID	Wing	Young's Modulus $E \times 10^{-7}\ \left[\frac{Kg}{mm \cdot s^2}\right]$	Ratio $E^r = \frac{E^{LW}}{E^{UW}}$	Snap
SREF	Upper	6.9	1	YES
	Lower	6.9		
SISO1	Upper	12	0.2	YES
	Lower	2.5		
SISO2	Upper	5	1.8	YES
	Lower	8.9		
SISO3	Upper	4	2.5	YES
	Lower	10.1		
SISO4	Upper	3	3.8	YES
	Lower	11.3		
SISO5	Upper	2.5	4.8	YES
	Lower	12.0		
SISO6	Upper	2.2	5.6	YES
	Lower	12.4		
SISO7	Upper	2.1	6.0	YES
	Lower	12.5		
SISO8	Upper	2.0	6.3	NO
	Lower	12.6		

the one needed for the unswept wings case (see Table 4.1). This means that the lower wing has to be much stiffer than the upper wing in order to avoid snap-buckling.

It is possible to observe that each wing of the swept configuration results to be a slightly longer and leaner (higher aspect ratio) than the previous unswept cases. However, since the sweep angle is small, the aspect ratio is not significantly affected. The consistent difference of the critical ratio E^r found for the swept case could be thought to come mainly from effects introduced by the torsion.

Analyses of two configurations [130], one incurring in snap, *SISO5*, and one not, *SISO8*, for two different load conditions are depicted in Figures 4.20 and 4.21. For the load level $\Lambda = 0.5$ *SISO5* is not very far to buckle, however, the two deformed shapes are almost superimposed (see Figure 4.20), except for the upper wings. In the *SISO5* case the upper wing experiences a more pronounced inward bending deformation, similarly with what was found for the swept cases.

The load level $\Lambda = 0.6$ represents a post-buckling situation for the configuration *SISO5*, as it could be verified in Figure 4.19(b). Besides experiencing an almost rigid rotation along $x-$axis, in this case the joint undergoes a negative rotation along global y-axis as well (see Figure 4.21).

In conclusion, the interactions between the wings are more complicated in the case of swept Joined Wings even when isotropic materials are used. This is due to the rise of forces inherent to the geometrical layout which couples the bending and torsional effects. These forces have an important role in influencing the snap phenomenon: although the span-wise bending actions drive the instability phenomenon, torsion contributes to regulate it. For example, compared to the unswept isotropic cases, the lower wing has to be significantly stiffer in order snap to be avoided. This could be intuitively explained as follows. Figure 4.21 shows that when the instability takes place a significant rigid rotation of the joint is experienced (*SISO5* configuration). Thus, the high stiffness is "required" to counteract also this joint's rotation and thus, to avoid the snap-bucking.

Orthotropic Cases

The introduction of an orthotropic material for the wings allows not only to differentiate between the relative importance of the Young's moduli E_1 and E_2, but gives also the valuable possibility to *isolate* and study more in depth the torsional effects. This was not possible for unswept layouts since, featuring the configuration geometrical

Table 4.7: Details about the orthotropic materials used for the different swept Joined Wings. The Young's Moduli and Poisson ratio are $E_1 = E_2 = E_{\text{REF}}$ and $\nu_{12} = \nu_{\text{REF}}$ for each wing of all cases. Thus, every considered configuration has the ratio D^r_{22} equal to 1.

Cases and relative parameters				
Case ID	Wing	Shear Modulus $G_{12} \times 10^{-7}\ \left[\frac{Kg}{mm \cdot s^2}\right]$	Ratio $E_1^r = \frac{E_1^{LW}}{E_1^{UW}}$	Snap
SREF	Upper	2.6	1	YES
	Lower	2.6		
SORTHO1	Upper	120	1	YES
	Lower	120		
SORTHO2	Upper	300	1	YES
	Lower	300		
SORTHO3	Upper	600	1	YES
	Lower	600		
SORTHO4	Upper	1500	1	YES
	Lower	1500		
SORTHO5	Upper	2500	1	NO
	Lower	2500		

symmetry, no torsional effects were introduced in the structure.

The stiffness parameter D_{66} is now varied to explore the effects due to the torsion but the bending stiffness ratio, extensively discussed in the preceding sections, is not modified. The use of orthotropic material gives the possibility to act on the D_{66} coefficient maintaining the same bending stiffness ratio. In fact, as it could be inferred from its well known definition, the D_{66} parameter could be fine-tuned through the adoption of different values of the material's shear modulus G_{12}. Moreover, this last material property does not influence the remaining parameters of the stiffness matrix $\boldsymbol{D}$. It is thus straightforward to selectively evaluate the importance of torsional deformation on the system response.

In this regard, *SREF* is chosen as starting configuration. Then for each wing the Young's moduli and Poisson's ratio are set such that:

$$E_1^{\text{UW}} = E_2^{\text{UW}} = E_1^{\text{LW}} = E_2^{\text{LW}} = E_{\text{REF}} \tag{4.4}$$

$$\nu_{12}^{\text{UW}} = \nu_{12}^{\text{LW}} = \nu_{\text{REF}} \tag{4.5}$$

Different values of G_{12}^{UW} and G_{12}^{LW} are chosen, with a direct effect on D_{66}^{UW} and D_{66}^{LW} respectively, as shown in Table 4.7 and Figure 4.22. The responses are depicted in

Figure 4.23. It could be inferred that torsional stiffness has an important effect on the behavior of the system. If it is increased, torsional deformations are smaller, and thus, ideally, the response is expected to be qualitatively similar to the one of the unswept case (with isotropic or orthotropic wings). This is supported noticing that *SORTHO* cases response is qualitatively similar to *UREF*'s one (see Reference [130]), showing a more abrupt snap-buckling occurrence, that is, the instability occurs without a progressive previous loss of stiffness.

As could be seen in Figure 4.23 if torsional stiffness is increased to a certain extent no instability phenomenon occurs, differently than the unswept case where it was not possible to eliminate buckling when $D_{22}^r < [D_{22}^r]_{\text{CR}}$. This difference is a consequence of the structure's layout and overconstrained nature of the system. In practice, in cases such as *SORTHO5* the torsional stiffness has a dominant role on the bending mode through the geometrical coupling, and this interaction limits the pertinence of considering the similarity between swept and unswept case.

Summarizing, in this particular overconstrained system in which bending and torsion are also coupled as a consequence of the sweep angle, it is very difficult to separate the effects on the structural response driven by one or the other deformation.

Anisotropic Effects

In this section, the lower wing is assumed to be made of the same isotropic material used for the *UREF* configuration. However, the upper wing is now composed of a single lamina. The fibers' orientation is measured starting from the upper wing local axis x^{UW}, as depicted in Figure 4.2 and 4.24. Table 4.8 reports the configurations used to assess the anisotropic effects for the swept Joined Wing. It may be inferred that the influence of torsion is now of primary importance. In fact, some configurations featuring a relatively small value of D_{22}^r do not present any snap-buckling phenomenon. It is relevant to investigate the effect of the sign for D_{26}^{UW} for practically unchanged D_{22}^r parameters. For example, configuration *SANISP16* (for which $D_{22}^r = 1.39$ and $D_{26}^{\text{UW}} = -0.20 \left[\frac{Kg \cdot mm^2}{s^2}\right]$) does not experience buckling whereas configuration *SANISP6* (for which $D_{22}^r = 1.30$ and $D_{26}^{\text{UW}} = +0.20 \left[\frac{Kg \cdot mm^2}{s^2}\right]$) does experience instability.

Not all of the configurations reported in Table 4.8 experience buckling. It is then of a practical importance to identify the conditions for which buckling occurs from a graphical point of view. In particular, the so called Snap Buckling Region *SBR* for

Table 4.8: Test cases. For each case the lower wing is made of the reference isotropic material, where the upper wing is a single ply. The material used for the upper wing presents $E_1^{\mathrm{UW}} = 8.5 \cdot 10^7 \left[\frac{Kg}{mm \cdot s^2}\right]$, $E_2^{\mathrm{UW}} = 0.66 \cdot 10^7 \left[\frac{Kg}{mm \cdot s^2}\right]$, $G_{12}^{\mathrm{UW}} = 0.56 \cdot 10^7 \left[\frac{Kg}{mm \cdot s^2}\right]$, $\nu_{12}^{\mathrm{UW}} = 0.28$. The fibers' angle is measured starting from the upper wing's local coordinate system x^{UW}. In parenthesis the same fibers' angle is referred to the global coordinate system x-axis (see Figure 4.25).

Cases and relative parameters					
Case ID	Wing	Orientation: Angle measured from x^{UW} (x)	Ratio $D_{22}^r = \frac{D_{22}^{\mathrm{LW}}}{D_{22}^{\mathrm{UW}}}$	$D_{26}^{UW} \times 10^{-7}$ $\left[\frac{Kg \cdot mm^2}{s^2}\right]$	SNAP
SANISP1	Upper	$-11.3°(0°)$	10.71	-0.01	NO
SANISP2	Upper	$33.7°(45°)$	4.60	0.10	NO
SANISP3	Upper	$48.7°(60°)$	2.22	0.18	NO
SANISP4	Upper	$53.7°(65°)$	1.80	0.20	YES
SANISP5	Upper	$58.7°(70°)$	1.51	0.20	YES
SANISP6	Upper	$63.7°(75°)$	1.30	0.20	YES
SANISP7	Upper	$78.7°(90°)$	0.97	0.11	YES
SANISP8	Upper	$-56.3°(-45°)$	1.64	-0.20	YES
SANISP9	Upper	$-86.3°(-75°)$	0.91	-0.04	NO
SANISP10	Upper	$88.7°(-80°)$	0.91	0.01	NO
SANISP11	Upper	$83.7°(-85°)$	0.92	0.07	YES
SANISP12	Upper	$-41.3°(-30°)$	3.13	-0.15	NO
SANISP13	Upper	$-71.3°(-60°)$	1.09	-0.17	NO
SANISP14	Upper	$73.7°(85°)$	1.04	0.15	YES
SANISP15	Upper	$-66.3°(-55°)$	1.21	-0.19	NO
SANISP16	Upper	$-61.3°(-50°)$	1.39	-0.20	NO
SANISP17	Upper	$-51.3°(-40°)$	1.99	-0.19	YES
SANISP18	Upper	$-46.3°(-35°)$	2.47	-0.17	YES

Joined Wings [1] can be seen in Figure 4.26. It should be noted that SBR is actually the union of two subregions which do not present symmetry with respect to the zero angle. This is expected since the Joined Wing and its materials do not present symmetries and the complex bending-torsion coupling affects the nonlinear response in a non-trivial manner.

Figure 4.25 shows the responses relative to some of the cases reported in Table 4.8.

Figure 4.27 shows graphically the connection between typical responses and fibers' orientation. Some observations could be stated. When the fibers are directed along the upper wing's chord-wise direction (local x-axis) the response is not very stiff, and snap-buckling does not occur. This is not surprising since the lower-to-upper wing bending stiffness ratio has a large value (see for example configuration *SANISP1* in Table 4.8: D^r_{22} is 10.71). It is also expected that if the fibers are rotated, the structure exhibits overall a stiffer response, since material is properly oriented to counteract the flexional actions. However, this is not always the case. If the fibers are rotated in the positive ϑ direction, the response is quite stiffer (see for example *SANISP3* in Figure 4.27), whereas if they are rotated in the opposite direction the response does not only contradict the intuition based on a stiffness perspective, but with a further decrease of ϑ a snap phenomenon occurs (see *SANISP12*, *SANISP18*, and *SANISP8* in Figure 4.27). It is not trivial to interpret and fully understand this behavior. The bending-torsion coupling at both geometrical and material level for these cases is unfavorable, and gives rise to configurations which are compliant in resisting the load and could even undergo instability.

With a further decrease of ϑ, an interesting behavior is detected. Comparing *SANISP18* and *SANISP8*, both having buckling problem, a main difference is observed: *SANISP18* corresponds to an abrupt buckling, whereas *SANISP8* has a *mild* snap, that is, in the whole neighborhood of the limit point, there is loss in stiffness. If the fibers' orientation is decreased to the point that buckling disappears, as for example happens with configuration *SANISP16*, this local softening is still observed.

Notice that the initial response has not significantly changed from the *SANISP1* case, although the fibers' orientation has varied of 50°.

The pattern showed in *SANISP16* is maintained if the angle is further decreased. But, the structural response gains progressively stiffness, until the fibers are oriented approximately along the span-wise direction, *SANISP10*. Based on the previous gained

experience about stiffness ratio influence on snap occurrence, it is unexpected that this configuration does not show a snap-buckling phenomenon, although the local loss of stiffness pattern is practically as inconvenient as an instability.

If starting from $\vartheta = 0°$ the angle is increased the behavior is somehow expected. In fact, stiffness of the response increases, *SANISP3* and snap-buckling eventually occurs, *SANISP4*. Notice that this snap has the usual behavior with the limit point occurring without having any loss of stiffness in the load-displacement curve preceding the limit point. Now, a further increase in fibers' angle leads to an initial increase in stiffness, followed however by an snap-buckling instability at a lower load level. The instability is characterized now (see *SANISP11*) by a local softening in the limit point region (*mild* snap-buckling), similar to what observed for *SANISP8* configuration.

Unexpectedly a further increase in ϑ leads to a response not showing a snap-buckling phenomenon, but, the local softening is still present (*SANISP10*).

Summarizing, starting from $\vartheta = 0$, if the angle is changed in the positive direction the response becomes stiffer and snap-buckling occurs. Then, due probably to torsional effects, local softening is introduced in the neighborhood of the limit point region. If the angle is changed in the negative direction the response experiences instability without being initially stiffer. In this case the bending-torsion coupling counteracts the typical stiffer behavior related with smaller D_{22}^{r} (and same D_{22}^{LW}), but does not avoid snap occurrence. Finally, when the fibers are oriented nearly along the span-wise direction, no instability is present, although there is a pronounced loss of stiffness.

It is the authors' opinion that further studies are needed in order to better understand the phenomenon at its basic level. In fact, although in this case the structural response is basically regulated by the bending-torsion coupling, the strong nonlinear behavior represents an added complication and makes extremely difficult and possibly unsuccessful the attempt to explain in detail the essence of the problem breaking it down in simpler cases.

4.6.2 Joint's Height Effects in the Case of Anisotropic Swept Joined Wings

In Reference [1] it was demonstrated that for the case isotropic materials the increase of the height of the joint was beneficial. This is confirmed in this work for the case of composite materials, as clearly shown in Figure 4.28 where *SANISP4* and

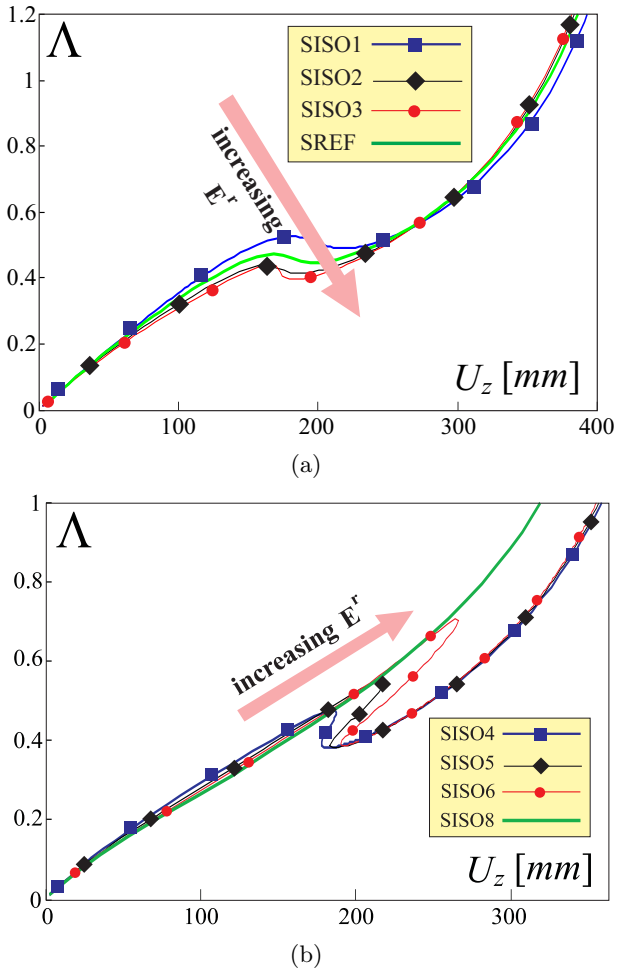

Figure 4.19: Load parameter Λ versus cumulative vertical displacement U_z of lower wing's tip point P_1 for configurations employing different isotropic materials (see Table 4.6). The ratio of Young's Modulus of the upper wing to the one of the lower wing is varied but the initial rate of change (linear case) of cumulative vertical displacement of P_1 is constant.

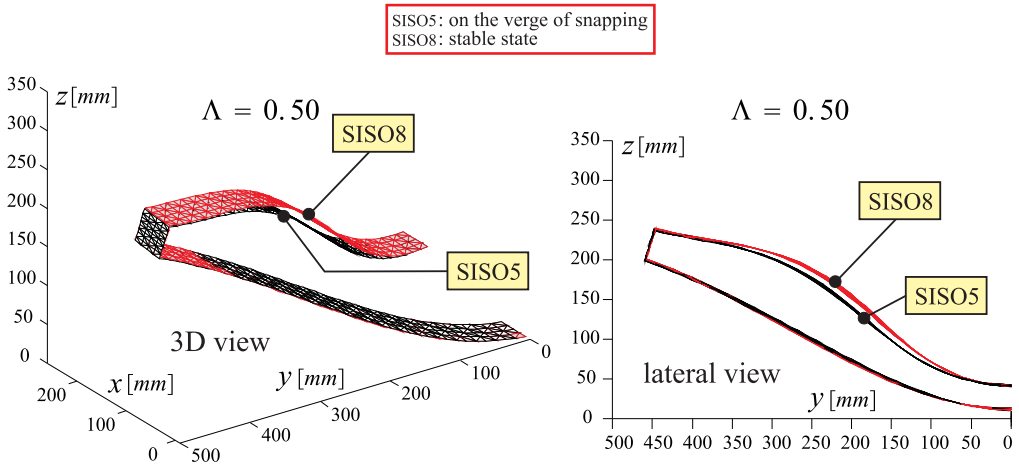

Figure 4.20: Comparison of deformed configurations *SISO5* and *SISO8* at $\Lambda = 0.5$. Tridimensional and side view.

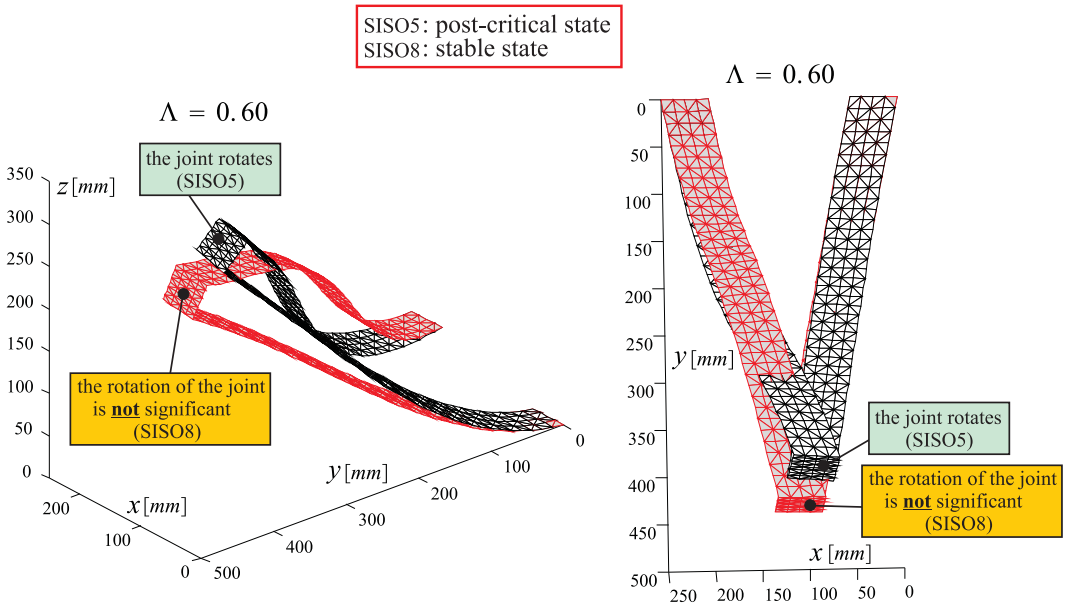

Figure 4.21: Comparison of configurations *SISO5* and *SISO8* at $\Lambda = 0.6$. Tridimensional and upper view. The *SISO5* is in its post-snap configuration.

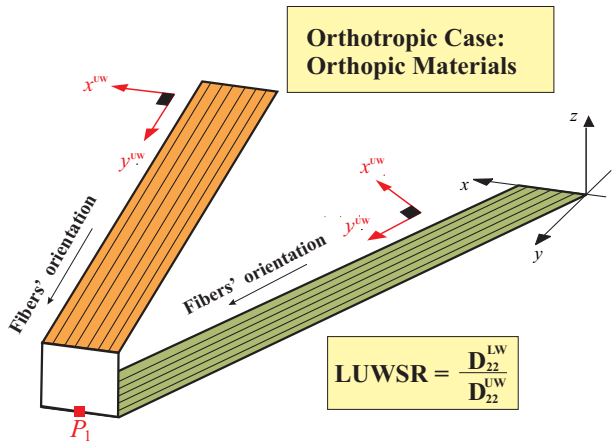

Figure 4.22: Swept configurations for orthotropic cases and definition of lower-to-upper wing stiffness ratio.

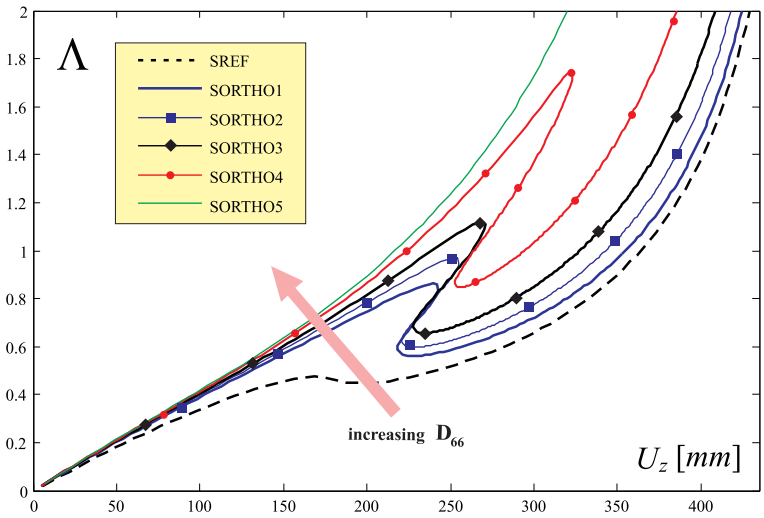

Figure 4.23: Cumulative vertical displacement (U_z) of point P_1 versus load parameter (Λ) for swept Joined Wings featuring different orthotropic wings. For each configuration upper and lower wings are manufactured with the same material. See Table 4.7 for details.

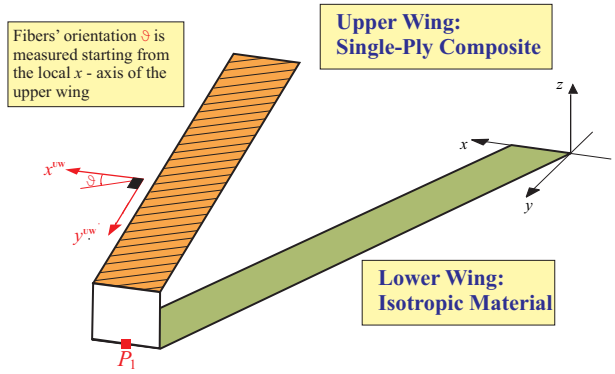

Figure 4.24: Swept configurations for anisotropic cases.

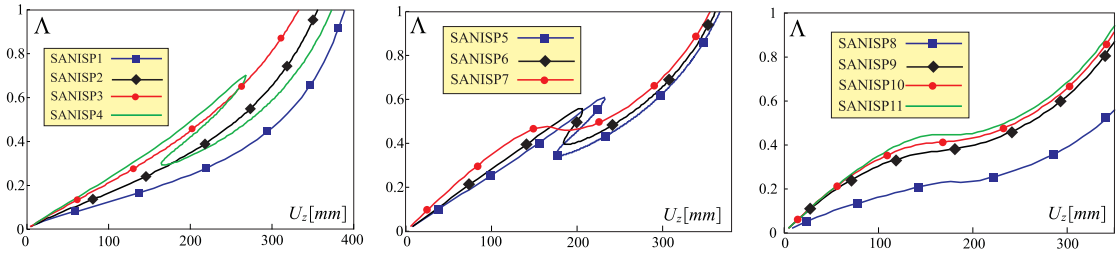

Figure 4.25: Cumulative vertical displacement (U_z) of point P_1 versus load parameter (Λ) for swept Joined Wings featuring different single-layer upper wing. See Table 4.8 for details.

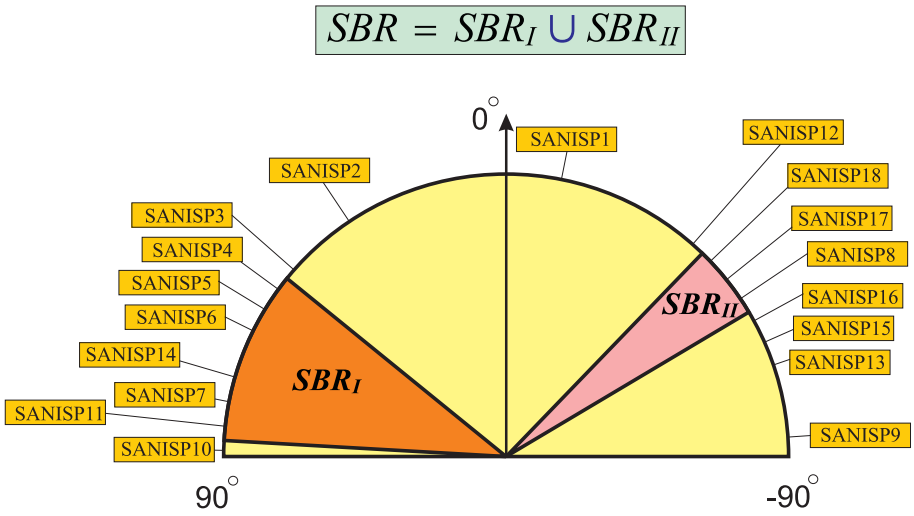

Figure 4.26: Snap Buckling Region for configurations with different orientation of the upper wing's fibers (the angles are measured in the upper wing's local coordinate system). The configurations in the *SBR* experience buckling.

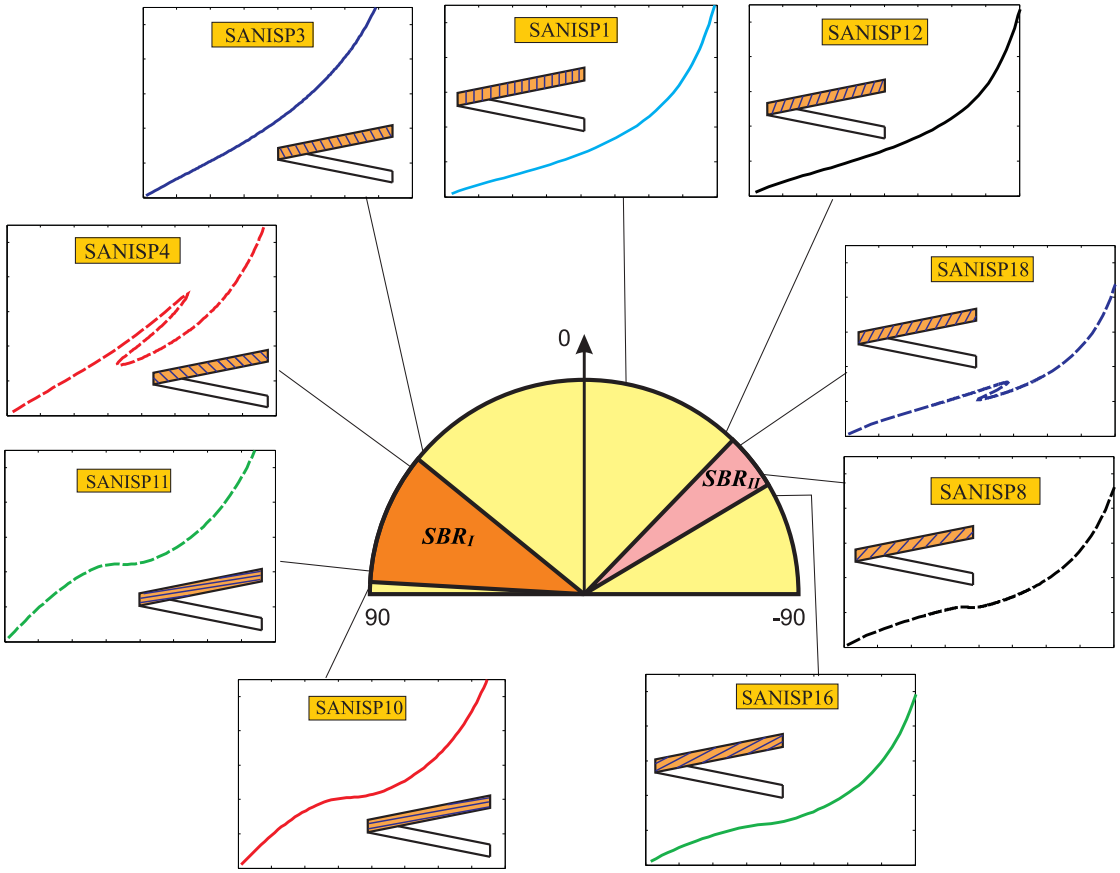

Figure 4.27: Snap Buckling Region and typical responses (vertical displacement of point P_1 versus load factor).

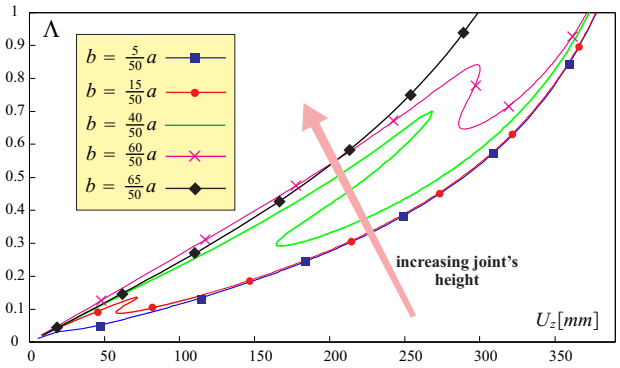

(a) SANISP4 based

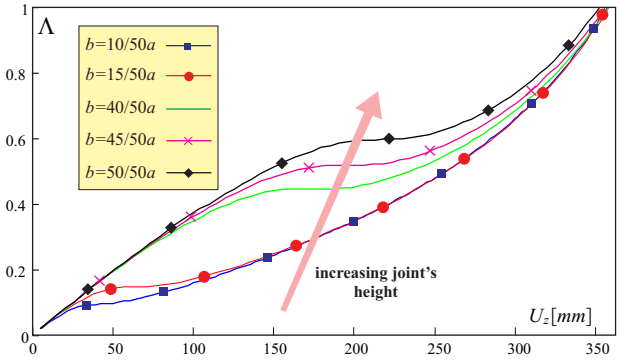

(b) SANISP11 based

Figure 4.28: Joint's effects for the *SANISP4* and *SANISP11* based configurations.

SANISP11 (see also Table 4.8) are presented. A joint's height larger than a value ($b = \frac{65}{50}a$ and $b = \frac{50}{50}a$ for the cases of Figure 4.28(a) and 4.28(b) respectively) leads to a stiffer-snap-buckling-free response. This is the concept of Upper Limit Snap Buckling Region (ULSBR) introduced in Reference [1] for the isotropic case.

4.7 Conclusions

Post-buckling investigations of *composite* PrandtlPlane Joined Wings, with particular focus on the fundamental physical aspects leading to the instability and nonlinear structural response, have been presented for the first time.

Previous analyses of this innovative configuration focused on linear structural and aeroelastic models. A first attempt towards an accurate simulation and fundamental understanding of the critical and post-critical conditions has been presented in Reference [1] where the case of *isotropic* materials was discussed. The effects of the geometrical parameters (joint's dimensions and sweep angles) showed a very complex nonlinear response which could not be predicted with the standard linear analysis but needs to be properly taken into account even at the very early stages of the design. This is particularly important since the *true* critical load can often be over predicted when a classical linear eigenvalue approach (linear buckling analysis) is adopted. Reference [1] showed that increasing the joint's height is beneficial. Moreover, it can be identified an interval of joint's heights in which the snap-buckling instability occurs. This was defined as Snap-Buckling Region (SBR). SBR could have a significant relevance in the conceptual design of PrandtlPlane configurations, since a snap-buckling type of instability must be avoided.

Reference [1] also showed that the torsional-bending coupling consequence of the *geometric* layout (swept wings) can dramatically worsen the stability properties. Finally, it was also presented that the load repartition between the upper and lower wings has a significant effect on the nonlinear response. In particular, for the common PrandtlPlane layout featuring a swept-back lower wing and a swept-forward upper wing, a higher percentage of the load on the upper wing was showed reducing the risks of buckling. However, several conceptual and theoretical aspects needed to be addressed. This was accomplished in the present work. In particular, the effect of *anisotropy* was extensively investigated by the adoption of composite materials. The following analyses have been carried out.

Unswept Case with Different Isotropic Materials for the Upper and Lower Wings

An unswept joined-wing layout was investigated. *Different isotropic* materials were selected for the upper and lower wings. The lower-to-upper-wing stiffness ratio showed to be the driving parameter as far as snap-buckling instability was concerned. In particular, a counterintuitive result was found: the main mechanism which led to the instability (under non-aerodynamic conservative loads) was *not* due to the compression. In fact, increasing the stiffness of the upper wing via incrementing the elastic modulus enhances the extensional stiffness (in theory beneficial because the upper wing is compressed), but *increases* the possibility of having buckling. From the Eulerian compressed column analogy this is a highly unexpected result. The over constrained nature of the Joined Wing (compared to the classical cantilevered wings) and the non-planar geometry are responsible of this complex behavior.

Unswept Case and Adoption of Orthotropic Materials

Additional insight on the nature of the snap-buckling was gained by the adoption of a single-lamina orthotropic plate for the upper wing. This choice was useful to detect which stiffness ratio was actually important for the snap-buckling occurrence. It was found that the ratio between the extensional stiffnesses and the ratio between the bending stiffnesses were the primary parameters affecting the Joined Wing's instability properties. As for the isotropic case, it was found that the lower wing's stiffness should be larger than the upper wing's one and the counterintuitive nature of the type of instability was confirmed. However, the single-lamina orthotropic upper wing had the drawback of presenting the lower-to-upper-wing extensional stiffness ratio equal to the lower-to-upper-wing bending stiffness ratio: it was not possible to truly separate the relative importance between the extensional and bending effects on the instability.

The problem was addressed by adopting a multilayered orthotropic laminate for the upper wing. This was very useful since for this case the lower-to-upper-wing extensional stiffness ratio is in general different than the lower-to-upper-wing bending stiffness ratio. Several investigations showed then the true driving mechanism to the instability: the snap-buckling occurrence is mainly sensitive to the lower-to-upper-wing bending stiffness ratio. In particular, it was shown that increasing the lower wing's bending stiffness was beneficial, whereas incrementing the upper wing's bending stiffness

had a negative effect on the stability of the Joined Wing.

Type of Joint's Connection and its Effects on Snap-Buckling of Unswept Joined Wings

The *bending moment transferring through the joint* is one of the leading mechanisms involved in the instability. This was demonstrated by modifying the joint-to-wing connection. In particular, a *quasi-hinge* type of connection was implemented by inserting a hinge at the joint-to-upper-wing or joint-to-lower-wing junction and a torsional spring opposing the relative rotation between the joint and the upper/lower wing. A small value of the spring stiffness was selected and the bending moment transferred to the upper wing was reduced compared to the fixed type of joint previously investigated. On a pure stability perspective, this provided a great benefit because the snap-buckling was eventually eliminated, thus, confirming the relevant importance of the bending moment transferring in the snap occurrence. As a drawback, however, the configurations with the quasi-hinge connection showed a less stiff response. Moreover, when the quasi-hinge was positioned between the joint and upper wing a softening tendency was observed in respect of the response of the configuration in which the quasi-hinge connection was established between the joint and the lower wing.

Unswept Case and Adoption of Anisotropic Materials (Composites)

While the lower wing was assumed to be isotropic, the upper wing was simulated first with a multilayered orthotropic laminate and second with a multilayered anisotropic laminate presenting identical lower-to-upper-wing bending stiffness ratio. The orthotropic case experienced a strong snap-type instability, whereas the anisotropic case did not have the instability at all in the range of explored load levels and presented a stiffening effect. Considering the fact that the geometry (unswept Joined Wings) does not introduce any bending-torsion coupling whereas the anisotropic laminate does, it was deduced that the material-induced bending-torsion coupling is important in the nonlinear response.

The bending-torsion coupling was further investigated by selecting a single-lamina with fibers generically oriented. The lower-to-upper-wing bending stiffness ratio and the primary bending-torsional deformation coupling term D_{26} was also monitored. The investigation showed that in some cases the bending-torsional coupling is beneficial

and in other cases it deteriorates the stability properties of the Joined Wing. A further insight of this coupling and its effects on the instability could be gained from the observation of the joint's rotation with respect to the wing-span direction. This rotation is heavily affected by the torsional-bending coupling. In particular, a properly designed laminate could increase or decrease the rotation of the joint with enhanced or worsened stability properties.

Swept Case with Different Isotropic Materials for the Upper and Lower Wings

The swept Joined Wing presents a torsional-bending coupling even if the same isotropic material is adopted for both the upper and lower wings. To gain further insight, the upper wing was selected to be isotropic but with different elastic modulus compared to the lower wing. Several investigations showed that to avoid snap-buckling a substantially larger lower-to-upper-wing bending stiffness ratio was necessary. A direct observation of the deformed shapes confirmed that when this type of instability occurs the rotation (with respect to the wing span axis) of the joint is significant.

Swept Case and Torsional Effects

The relative importance of torsional effects was further investigated selecting the reference swept joined-wing configuration, and changing the torsional stiffness. This was easily accomplished by adopting an orthotropic material and changing the shear modulus. When the torsional stiffness was increased, the response showed a tendency to have an abrupt snap-buckling, typical of the unswept case. This should confirm that, limiting the torsional effects introduced by the geometry, the configuration tends to behave as in the unswept case.

Swept Case and Anisotropy Effects

A physical insight on the response of PrandtlPlane Joined Wings was gained by the introduction of coupling effects associated with the anisotropy of the material. While the lower wing was maintained isotropic, the upper wing was simulated with a single-ply generically oriented material. The analyses showed a very complex bending-torsion interaction: even for a relatively simple single-ply upper wing there could be identified two distinct and unsymmetrically located regions in which the snap-buckling occurs.

In other words, the Snap Buckling Region (i.e., range of fiber orientation's angles for which the system undergoes a snap-buckling instability) is difficult to predict from pure intuitive considerations.

Joint's Height Effects in the Case of Anisotropic Swept Joined Wings

For the isotropic case examined in Reference [1] the joint's height was varied and it was found that an increase of the height was beneficial. A similar investigation has been carried out in this work with the adoption of composite materials. It was found out that the joint's height is beneficial even when the composite materials are used.

The investigations presented in this work shed some light on the very complex nonlinear response of Joined Wings. Results showed that the snap-buckling load is quite sensitive to the bending moment transferred by the joint to the upper wing. Thus, both the type of joint's connection and bending stiffness of the wings play a significant role.

When the bending-torsion coupling is introduced because of either the geometry (sweep angles) or the material (composites) or both, predicting a priori if the above mentioned effects are beneficial or not is an extremely challenging task. The simulations conducted in this work seem to suggest that the rotation of the joint about the wing span axis is an important factor for further gaining insight on instability and its properties.

Future works focusing on nonlinear effects of Joined Wings will discuss the theoretical challenges and physical implications when mechanical non-conservative loadings of a follower type and aerodynamic forces are taken into account. Specifically, in Reference [158] a Vortex Lattice Method has been used for this purpose. A further area needing some studies is the characterization of stability properties under a dynamical systems perspective [2].

Acknowledgements The authors acknowledges the support by San Diego State University (College of Engineering).

Chapter 4, in full, is a reprint of the journal paper: "*Nonlinear Analysis of PrandtlPlane Joined Wings: Effects of Anisotropy*, AIAA Journal, Vol. 52, No. 5, 2014." The dissertation author was the primary investigator and author of this paper. Coauthors were Luciano Demasi and Andrea Passariello.

Chapter 5

Risks of Linear Design of Joined Wings: a Nonlinear Dynamic Perspective in the Presence of Follower Forces

This chapter is a reproduction of the following paper:
Risks of Linear Design of Joined Wings: a Nonlinear Dynamic Perspective in the Presence of Follower Forces, CEAS Aeronautical Journal, November 2014.

5.1 Introduction

The joined-wing concept dates back to the twenties [7] as Prandtl was studying minimum induced drag of multiplane configurations. The concept was recovered and developed, and its application to aircraft was proposed in the seventies [8, 10, 145] for both commercial transport and supersonic fighters. Efforts and studies led to several patents taken out both in the US [27, 28] and Europe [91, 92]. Further rearrangements led also to designs that are far from the original joined-wing concept, such as Strut-Braced Wings (SBW) [131,132] and Truss Braced Wings (TBW) [133], both introduced in the United States. Besides the most classic aviation application as both civil [8, 9] or commercial [99] transport, in the recent years the joined-wing layout found an application in relatively new concepts as HALE [89,159] and UAV [68,160] aircraft and as amphibious

airplanes [120].

Depending on the specific field of application, many advantages on the classical cantilevered layouts are claimed, ranging from improved stiffness properties [10, 113], high aerodynamic efficiency [7, 10], superior stability and control characteristics [6] to flexible engine integration [9]. In addition to these relevant advantages, a Joined Wing with typical diamond layout can enclose a large antenna, which is of particular advantage for high altitude surveillance [89, 159]. Furthermore, the layout typical of Joined Wings enables the design of configurations capable of larger payloads [9] whose dimensions are compatible with the current airport's infrastructures: this has potential impact on the cargo transport [99]. Summarizing, other than having potential conventional advantages, Joined Wings introduce new concepts and previously unexplored possibilities.

Driven by the novelty, in the last decades many efforts have been devoted to joined-wing concepts. Unfortunately, a design which could eventually exploit these advantages is very challenging: not only is the gained experience relative to joined-wing design limited, but there are many difficulties and never-tackled-before problems. Thus, it is often not adequate to rely on old, though consolidated, design strategies developed in decades and effectively used by the industry [11].

Two of the main sources of difficulties are the typical overconstrained layout and the presence of strong structural nonlinearities [11, 60, 128], significant also for small angles of attack and attached flow. This leads to an inconsistency when it comes about sizing using linear analysis tools. The results could be misleading, as shown for example in stability and aeroelastic analyses [1, 124, 152, 158, 161]. Consequence of such not negligible effects is the need to include these nonlinearities early in the design stage. However, the adoption of fully-nonlinear structural models is impractical especially if several alternative configurations are explored in an optimization [151] effort. Ideally, one should have an efficient aeroelastic model tailored for optimization strategies.

Computational efficiency and effective inclusion of the geometric nonlinear effects is difficult to be achieved with reduced order models [13–16].

It was then realized [1, 158, 162] that a *physical insight* of the mechanism driving the nonlinear response of Joined Wings had to be gained. This information could have potential impact in the development of efficient tools for the preliminary design of these configurations.

The efforts of the present paper is in the direction of showing and studying never-

examined-before nonlinear phenomena inherent to joined-wing configurations, and which have potential impact on their design process.

5.2 Contributions of the Present Study

It has been common practice [83] to apply mechanical follower type of loads (forces acting as pressures and thus, normally to the surface) in order to more confidently try to describe the effects of aerodynamic loads. Previous efforts [1,130,162] investigated joined-wing configurations and observed that snap-buckling instabilities could eventually occur. However, in those analyses a non-follower (or conservative) mechanical loading was considered. The present work will show how *follower loading* affects the stability properties of Joined Wings: does it exacerbate or alleviate instability problems? Do follower loads change the typical patterns observed in snap-buckling phenomena?

When talking about snap phenomenon, it should not be neglected that it is *inherently a dynamic* event. However, for Joined Wings this has been examined only from a static analysis perspective [1, 130, 162]. To gain further insight it is necessary to closely follow the dynamic response involved in a snap-buckling occurrence, instead of just relying on the static configurations immediately preceding and following it. This work will tackle this issue and the correspondence between static approach and realistic dynamic analysis will be assessed.

Clearly, a snapping phenomenon at global structural level [1] could not be accepted. It is also true that, when possible, the structures in aeronautical engineering are designed pursuing as much as possible a *linear* response. According to these observations, it may be stated, *incorrectly*, that a structural analysis may lose of interest well before a *limit point* (that is, the point of snap onset) is reached.

Here comes the most important physical aspect investigated in the present paper. It will be shown that, if a structure is loaded well *under the critical load*, an adequate vanishing perturbation may cause it to assume a different equilibrium configuration after the transient has elapsed. This fact has a potential tremendous impact on the preliminary design of Joined Wings. It is potentially unsafe to avoid expensive nonlinear post-critical analyses with the argument that joined-wing structures will operate at lower-than-critical regime. If this may seem safe because the snap-buckling occurring in quasi-statical conditions is avoided, it does not guarantee against stability problems enhanced by *inertial effects* tied up with dynamic response of the system. As will be shown, one of

this kind of instabilities could be the jump to a different equilibrium configuration out of the nominal *operative* condition.

The complexity of joined-wing design is brought to a definitive higher level noticing that, in some cases, the static response shows a main branch and another isolated close branch (called *isola*). When such a situation arises, even a nonlinear static analysis comprehensive of post-critical tracking methods is *not able* to bring to light the real picture, which, on the contrary, could be depicted with the aim of ad hoc dynamic analyses. It is worth to notice that, being not possible to know a priori if an isola exists, prediction of bi-stable situations is not straightforward.

A critical discussion about how the outlined scenario, observed for simplified models, applies to real aircraft design is also given. In particular, past research on very flexible configurations, such as Unmanned Aircraft or High Altitude Long Endurance (HALE) vehicles, showed instabilities similar to the here considered ones. On the other hand, due to relatively strict regulations (stress, displacements, etc.), it can be reasonably assumed that these instabilities are less of a concern for civil aviation.

5.3 Theoretical Highlights Regarding the Present Nonlinear Structural Model

The geometrically nonlinear finite element [156, 162] is based on the linear membrane constant strain triangle (CST) and the flat triangular plate element (DKT). The structural tangent matrix $\boldsymbol{K}_T$ is sum of two contributions: the elastic stiffness matrix, $\boldsymbol{K}_E$, and the geometrical stiffness matrix, $\boldsymbol{K}_G$. Composite materials can also be modeled with the present capability.

The nonlinear governing equations are solved by adopting iterative methods such as *Newton-Raphson* and *arc length* techniques (see [2]). After each iteration a displacement array is obtained, rigid body motion is eliminated from elements and the pure elastic rotations and strains are found [163]. Using these quantities the internal forces are updated for the next iteration.

5.3.1 General approach

The residual of the discretized (in space) system is defined as the unbalance of the D'Alembert's principle. It is a measure of the quantity the Newton's law is not satisfied.

When the residual is (almost) zero, it means that the configuration is at equilibrium (either static or dynamic, depending on the problem). Since the considered problems are nonlinear both in the structural behaviour and in the forces (they are of follower type), the standard procedure to achieve a convergent state is to apply an iterative method.

When dealing with static problems, what is usually sought is a static response in terms of a parameter Λ called load level, which determines how much of the nominal (or final) load is applied. The adoption of such a strategy is important not only as a tool for achieving convergence (algorithms like Newton's one are in principle guaranteed to converge only for a relatively small region in the neighborhood of the converged point), but also to determine the local behavior of the structure, as stiffening or softening tendencies. Tracking the curve is also important to assess if the nominal condition could be safely reached: it could happen that a *snap* phenomenon arises. In other words, for a given value Λ^{CR} the structure is not able to carry any load increment in an continuously adjacent configuration (see References [1, 162] for examples of snap-instabilities). From a mathematical point of view, the tangent (or Jacobian) matrix of the system is singular when evaluated at the critical point. The mathematical approach and implementation of the iterative process applied to static analysis is documented in [2].

5.3.2 Iterative procedure for dynamic analysis

In the case of dynamic analysis, the iterative framework [2] of the static case could be easily extended, if in the residual the inertial and damping terms are considered. Let us introduce here the generalized coordinate array time derivatives $\dot{\boldsymbol{p}}$, $\ddot{\boldsymbol{p}}$.

In a continuous time setting, the residual array is defined as

$$\boldsymbol{\mathcal{R}}(t) = \boldsymbol{M}\,\ddot{\boldsymbol{p}}(t) + \boldsymbol{C}_d\,\dot{\boldsymbol{p}}(t) + \boldsymbol{F}_{\mathrm{int}}(\boldsymbol{p}(t)) - \boldsymbol{F}_{\mathrm{ext}}(\boldsymbol{p}(t), t) \tag{5.1}$$

where $\boldsymbol{M}$ is the so called mass matrix and $\boldsymbol{C}_d$ represents the structural damping matrix.

The present computational capability employs different implicit time-integration schemes, such as the generalized energy-momentum, a method that encompasses different schemes [164–169], or also a popular composite algorithm [170, 171]. However, for the sake of simplicity, only Newmark's approach is here reported. The details and derivation for the other methods are straightforward, and could be also found in the cited works. According to Reference [172], the derivative array $\dot{\boldsymbol{p}}$ and the array $\boldsymbol{p}$ evaluated at the

generic time $t + \Delta t$ could be approximated by:

$$ {}^{t+\Delta t}\dot{\boldsymbol{p}} = {}^{t}\dot{\boldsymbol{p}} + (1-\gamma)\Delta t\ {}^{t}\ddot{\boldsymbol{p}} + \gamma\,\Delta t\ {}^{t+\Delta t}\ddot{\boldsymbol{p}} \tag{5.2} $$

and

$$ {}^{t+\Delta t}\boldsymbol{p} = {}^{t}\boldsymbol{p} + \Delta t\ {}^{t}\dot{\boldsymbol{p}} + (1-2\beta)\frac{\Delta t^2}{2}\ {}^{t}\ddot{\boldsymbol{p}} + \beta\Delta t^2\ {}^{t+\Delta t}\ddot{\boldsymbol{p}} \tag{5.3} $$

In Eqs.(5.2) and (5.3), the notation ${}^{t}\boldsymbol{p}$ means that the array $\boldsymbol{p}$ is evaluated at time t. The two parameters β and γ define the inherent properties (stability, dissipation and accuracy) of the method. A common choice that ensures stability (in linear cases), second order accuracy and does not introduce numerical dissipation is the so called *trapezoidal rule*:

$$ \gamma = \frac{1}{2} \qquad \beta = \frac{1}{4} \tag{5.4} $$

It is worth to notice that the aforementioned properties of the scheme are assessed with linear analysis, see, e.g., [173]. When applied to nonlinear cases, some unwanted results may be found: in literature different situations have been studied in which theoretically stable time-integration schemes have failed when applied to nonlinear dynamics, see for example [166, 167, 174–176].

If the status of the system is known at time t, an iterative process is established to advance the system to time $t + \Delta t$. To obtain convergence for the new status, the residual evaluated at time $t + \Delta t$, or briefly ${}^{t+\Delta t}\boldsymbol{\mathcal{R}}$, is driven to zero through Newton's method. Considering a generic iteration n within a convergence process to state $t + \Delta t$, the residual is expressed as:

$$ {}^{t+\Delta t}\boldsymbol{\mathcal{R}}^{\text{iter}\,n} = \boldsymbol{M}\ {}^{t+\Delta t}\ddot{\boldsymbol{p}}^{\text{iter}\,n} + \boldsymbol{C}_d\ {}^{t+\Delta t}\dot{\boldsymbol{p}}^{\text{iter}\,n} - {}^{t+\Delta t}\boldsymbol{F}_{\text{ext}}{}^{\text{iter}\,n} + {}^{t+\Delta t}\boldsymbol{F}_{\text{int}}{}^{\text{iter}\,n} \tag{5.5} $$

Notice that, ${}^{t+\Delta t}\boldsymbol{F}_{\text{ext}}{}^{\text{iter}\,n}$ and ${}^{t+\Delta t}\boldsymbol{F}_{\text{int}}{}^{\text{iter}\,n}$ have to be considered as:

$$ {}^{t+\Delta t}\boldsymbol{F}_{\text{ext}}{}^{\text{iter}\,n} = \boldsymbol{F}_{\text{ext}}({}^{t+\Delta t}\boldsymbol{p}^{\text{iter}\,n},\, t+\Delta t) \tag{5.6} $$

$$ {}^{t+\Delta t}\boldsymbol{F}_{\text{int}}{}^{\text{iter}\,n} = \boldsymbol{F}_{\text{int}}({}^{t+\Delta t}\boldsymbol{p}^{\text{iter}\,n}) \tag{5.7} $$

A single Newton iteration reads:

$$ \boldsymbol{0} = {}^{t+\Delta t}\boldsymbol{\mathcal{R}}^{\text{iter}\,n} + {}^{t+\Delta t}\frac{\partial \boldsymbol{\mathcal{R}}}{\partial \boldsymbol{p}}^{\text{iter}\,n} \cdot\ {}^{t+\Delta t}\boldsymbol{u}^{\text{iter}\,n} \tag{5.8} $$

where the symbolism

$$ {}^{t+\Delta t}\frac{\partial \boldsymbol{\mathcal{R}}}{\partial \boldsymbol{p}}^{\text{iter } n} \tag{5.9} $$

indicates the tangent matrix evaluated at ${}^{t+\Delta t}\boldsymbol{p}^{\text{iter } n}$, and it holds:

$$ {}^{t+\Delta t}\boldsymbol{p}^{\text{iter } n+1} = {}^{t+\Delta t}\boldsymbol{p}^{\text{iter } n} + {}^{t+\Delta t}\boldsymbol{u}^{\text{iter } n} \tag{5.10} $$

In the following equation the different contributions to the tangent matrix can be identified:

$$ {}^{t+\Delta t}\boldsymbol{K}_T{}^{\text{iter } n} = {}^{t+\Delta t}\frac{\partial \boldsymbol{\mathcal{R}}}{\partial \boldsymbol{p}}^{\text{iter } n} = \frac{1}{\beta \Delta t}\left(\frac{1}{\Delta t}\boldsymbol{M} + \gamma \boldsymbol{C}_d\right) - {}^{t+\Delta t}\frac{\partial \boldsymbol{F}_{\text{ext}}}{\partial \boldsymbol{p}}^{\text{iter } n} + {}^{t+\Delta t}\frac{\partial \boldsymbol{F}_{\text{int}}}{\partial \boldsymbol{p}}^{\text{iter } n} \tag{5.11} $$

Assumption that the mass matrix $\boldsymbol{M}$ and damping matrix $\boldsymbol{C}_d$ are constant throughout the iterations has been implicitly made. The resolution of the following linear system is then required to complete each iteration:

$$ {}^{t+\Delta t}\boldsymbol{K}_T{}^{\text{iter } n} \,.\, {}^{t+\Delta t}\boldsymbol{u}^{\text{iter } n} = -{}^{t+\Delta t}\boldsymbol{\mathcal{R}}^{\text{iter } n} \tag{5.12} $$

If the new status satisfies appropriate convergence criteria, the system can be finally advanced in time.

5.3.3 Follower load contribution to the tangent matrix

Definition of follower forces

A follower force is here intended as a force which changes when a reference direction does. Both magnitude and direction can change. In the present effort the magnitude is considered to be constant and the reference *followed* direction is parallel the normal to an element vector. A case in which the magnitude only depends on the deformation could be found in [158], for example.

In the following of this contribution, the terms *array* and *vector* are differently used: when referring to the Euclidean space the terminology *vector* is used, whereas, referring to finite element degree of freedoms space the word *array* is employed.

Let $\boldsymbol{f}$ be a follower load. For example, it could be the single contribution, in array form, of a single finite element loaded with a pressure acting on one of his faces. Due to the assumption of constant magnitude (the entity of the pressure is not depending on

the element normal) it is convenient to rewrite the expression of the array by separating the magnitude and directional properties:

$$\boldsymbol{f} = |\boldsymbol{f}| \frac{\boldsymbol{f}}{|\boldsymbol{f}|} = \underbrace{|\boldsymbol{f}|}_{\text{constant}} \underbrace{\boldsymbol{n}}_{\text{unit array}} \tag{5.13}$$

The contribution $\boldsymbol{K}_F$ to the tangent matrix due to the applied follower force $\boldsymbol{f}$ can be written as:

$$\boldsymbol{K}_F = -\frac{\partial \boldsymbol{f}}{\partial \boldsymbol{p}} = -|\boldsymbol{f}| \frac{\partial \boldsymbol{n}}{\partial \boldsymbol{p}} \tag{5.14}$$

where $\frac{\partial \boldsymbol{n}}{\partial \boldsymbol{p}}$ is a matrix whose components are:

$$\left[\frac{\partial \boldsymbol{n}}{\partial \boldsymbol{p}}\right]_{ij} = \frac{\partial n_i}{\partial p_j} \tag{5.15}$$

It is straightforward to include the contribution of the pressure acting on other elements just adding them to the expression of $\boldsymbol{f}$, Eq.(5.13). The appendix shows more theoretical details on how the follower forces contribute to the tangent matrix.

5.4 Description of Analyzed Joined-Wing Configurations

5.4.1 Description of test cases

This work is mainly focused on two topics. The first one is the assessment of the different behavior of the system for non-follower (conservative) and follower load cases, with particular attention to the static instability phenomenon. The second one is the analysis of the dynamic response (for both non-follower and follower loading conditions) highlighting an inherent characteristic of this kind of systems, in which a *perturbation* may trigger the jump from a static equilibrium configuration to another one, both possible for the same loading conditions.

With this in mind, one main geometrical configuration is used. It consists in a Joined Wing which presents a swept-back lower wing and a swept-forward upper wing, see Fig. 5.1. The dimensions are selected to be consistent with the ones corresponding to wind-tunnel scaled models. The joint's height b is opportunely varied, according to the needs of the analyses. In all cases the thickness is held constant for both the wings and the joint, and is equal to 1 *mm*. The adopted material changes from case to case, and is specified when the particular configuration is analyzed. When not indicated, the material

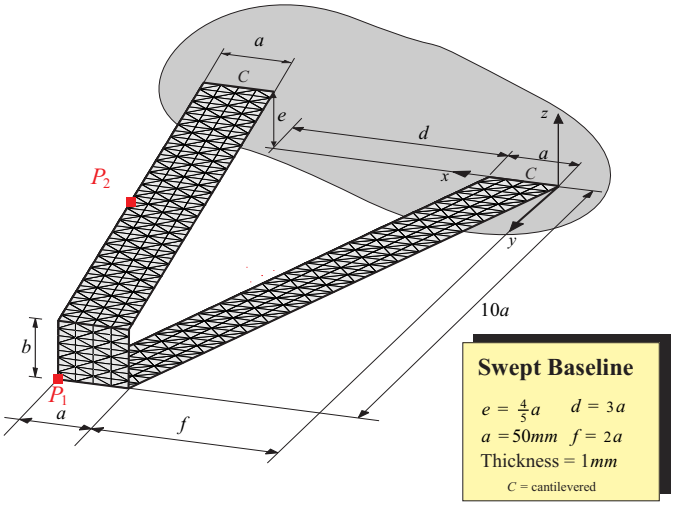

Figure 5.1: Swept Baseline configuration.

is assumed to be Aluminium featuring a Young's modulus equal to 69 GPa and Poisson's ratio $\nu = 0.33$. However, both isotropic and composite materials are considered, and, different ones may be used for different parts of the model.

All the configurations present a combination of geometry/material that have already been employed in earlier works [1, 130], for which non-follower loading only was considered.

Different class of loading conditions are employed. For the static analyses they are represented by a follower pressure acting along the surface's normal or by a non-follower (or conservative) vertical pressure (direction $+z$). This last case is used to verify the effects of the follower type of forces. In both cases the pressure is applied to both the upper and lower wing's bottom surfaces (the joint is unloaded). The pressure of $p_{\text{nom}} = 0.55125\,[\frac{Kg}{mm \cdot s^2}]$ is selected as reference value and corresponds to a dynamic pressure relative to a speed of $V_\infty = 30\ [m/s]$.

When the dynamic analyses are pursued, the loading conditions are obtained with a superposition of a fraction of the nominal static load and a portion (varying in time) of a perturbing force. The perturbing loads are forces per unit of length applied to the points lying on the mid-section of the upper wing. The entity of the perturbing forces is specified case by case.

5.5 Effects of Follower Forces on Static Response

In this section, effects of *follower loads* on the static behaviour of Joined Wings are assessed, with focus on the onset of snap-buckling instability. In particular, with reference to instabilities shown in literature [1,130,162] for structural conservative loading, the following questions are answered:

- How does follower loading influence the typical response? What are the effects compared to the conservative loading?
- How does the interval of parameter's values for which instability is observed (Snap Buckling Region concept, SBR [1,162]) change when follower loading is considered?

5.5.1 Effects on critical load

The swept joined-wing layout is considered having a joint's height $b = 40\ mm$, which is equivalent to $b = \frac{4}{5}a$, see Fig. 5.1. It is named *SREF*. Two cases are considered: in the first one the pressure always acts along the vertical direction (non-follower or conservative loading), in the latter case the pressure actions are directed along the normal to the surface direction (follower loading). How the system behavior changes in the

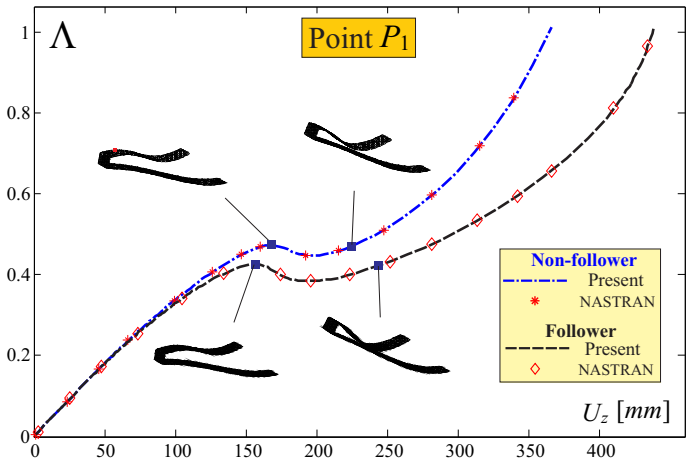

Figure 5.2: *SREF* configuration: load parameter Λ versus cumulative vertical displacement U_z of lower wing tip point P_1 for joined-wing layout featuring $b = 40\ mm$ loaded with non-follower and follower forces.

presence of follower loading is depicted in Fig. 5.2 (more cases are presented in Reference [2]). The vertical displacement of the lower wing tip (P_1 in Fig. 5.1) is chosen as measure of comparison.

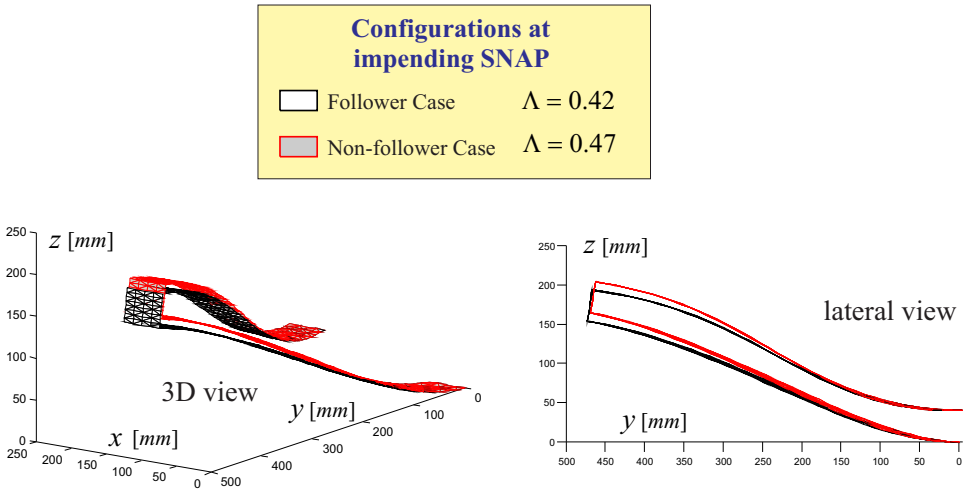

Figure 5.3: Comparison of the configurations at impending snap-buckling for the non-follower and follower loading cases.

As shown in Fig. 5.2, in the case of follower loading, *the snap occurrence is anticipated to a lower load level* and *smaller deformations*. The configurations at snap are superimposed and depicted in Fig. 5.3. In the case of follower loads, the snap occurs approximately at a load level of $\Lambda = 0.42$, where for the non-follower load case the instability occurs at $\Lambda = 0.47$. It could be observed that the deformed configurations show very similar patterns.

It may be concluded that follower loads anticipate the instability occurrence both in terms of load level and deformations.

5.5.2 Follower loads and snap-buckling region

From direct observation of the results presented above, it is logical to expect that follower loading promotes the onset of instability, not just anticipating the critical load (if an instability was also observed in the non-follower loading case), but also provoking it (if instability was not observed in the non-follower loading case).

An example that confirms this is now described. The swept joined-wing layout featuring a joint's height of $b = 80$ *mm* is considered. As shown in Fig. 5.4, if the forces are considered to be of non-follower type, the response undergoes a stiffening effect and no instability occurs (this is true also tracking the response for higher load levels, see [1]). However, for the follower loading case, snap-buckling is observed. This reinforces the negative role played by follower loading on stability of Joined Wings.

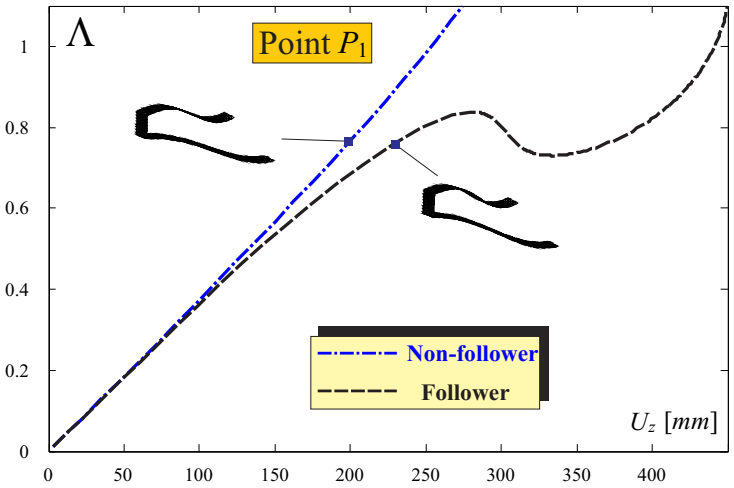

Figure 5.4: Load parameter Λ versus cumulative vertical displacement U_z of lower wing's tip point P_1 for a joined-wing layout featuring $b = 80$ mm loaded with conservative and follower forces. Snap-buckling instability is not present for the non-follower loading case.

SBR for joint's height

The concept of Snap Buckling Region (SBR) has been introduced to assess which are the limiting values of the parameters guaranteeing a snap-free behaviour.

An investigation applied on the swept baseline configuration shows an interesting result: in contrast with the case of non-follower forces (see [1]), now the SBR for the joint's height seems to be unbounded, see Fig. 5.5. The implications of this result is that, when a follower load type is considered on that particular geometry, increasing the joint's height does have beneficial effects but the snap-instability occurrence is never avoided. Although this may not look as a relevant result, the importance of not having a response featuring a snap-buckling phenomenon is crucial, as it will be clear in the next sections.

SBR for the anisotropic case

In this investigation the joint's height is fixed to $b = 40$ mm, whereas isotropic lower wing (aluminium) and a single-ply composite material ($E_1 = 85$ GPa, $E_2 = 6.6$ GPa, $G_{12} = 5.6$ GPa and $\nu_{12} = 0.28$) for the upper wing are assumed. The angle between x axis and the main direction of the composite material is varied as shown in Fig. 5.6 (see Fig. 28 of Reference [162] for more details about fibers' orientation). In the same picture responses for different angles are reported, when follower loads are

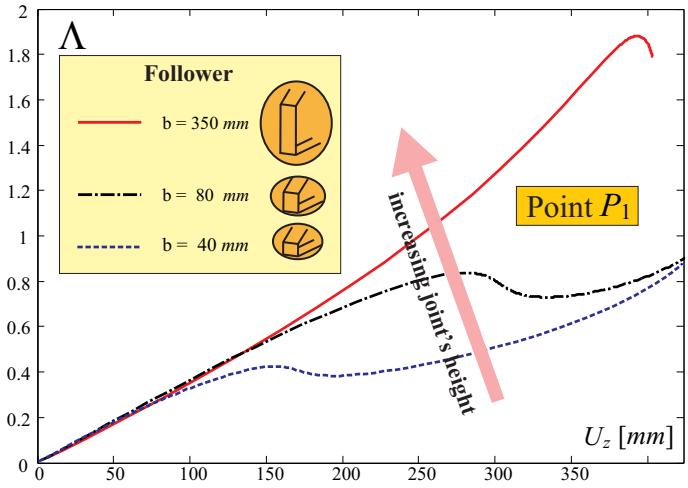

Figure 5.5: Load parameter Λ versus cumulative vertical displacement U_z of lower wing tip point P_1 for joined-wing layouts loaded with follower forces and featuring different values of joint's height. Snap-buckling is always present in the limit of higher joints.

considered. As it could be inferred, there is snap-buckling phenomenon for each possible configuration. Thus, the *SBR* extends to all the space of the angle of lamination, whereas this was not the case when conservative loading was considered, featuring two delimited SBRs [130, 162].

Summary

This section has compared the occurrence of instability phenomena of the snap-type when joined-wing models were loaded with follower forces. Only a restricted number of cases were investigated, thus general conclusions are difficult to be drawn. However, in respect of the behavior of the correspondent cases loaded with conservative loads, instability occurrence was not only anticipated (both load level- and displacement-wise), but was also induced in otherwise instability-free cases.

5.6 Study of Snap-Buckling of Joined-Wings with a Dynamic Approach

So far, snap-buckling phenomenon have been tackled on a static perspective. However, this instability is inherently dynamic, thus it is necessary to verify the physical behaviour with a dynamic analysis. In literature a similar numerical experiment has been carried out on a cylindrical shell in Reference [169], in which a dynamic analysis

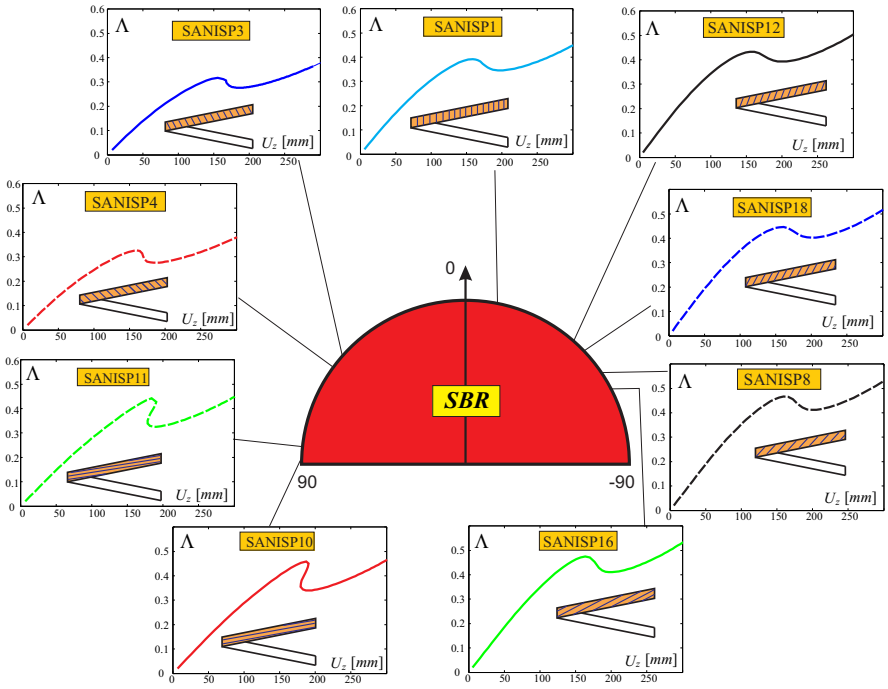

Figure 5.6: Load parameter Λ versus cumulative vertical displacement U_z of lower wing tip point P_1 for joined-wing layout featuring $b = 40$ mm loaded with follower forces.

confirmed the reliability of the static approach in predicting a snap-buckling. In the present effort, however, the characteristic times of force application have been chosen in order to simulate a quasi-static application, and thus, re-track the static response as close as possible.

Structural damping is modeled using Rayleigh approach, see, e.g. [177]. That is, the damping matrix $\boldsymbol{C}_d$ is chosen to be a combination of the mass and the tangent matrices.

$$\boldsymbol{C}_d = \alpha_M \, \boldsymbol{M} + \alpha_K \, \boldsymbol{K}_T \tag{5.16}$$

It is worth to notice that structural properties change during the nonlinear simulation, thus, damping matrix is frequently updated.

5.6.1 Dynamics/quasi-static analysis of snap-buckling with conservative loads

A configuration called *ISO6* is here considered as test case. Its layout is exactly the same as *SREF*, however, different isotropic materials are chosen for the wings: lower wing's one has a Young's modulus of 124 *GPa*, whereas for the upper wing it is 22 *GPa*. Joint is made of aluminium.

Static response, taken from Reference [162], is shown in the small boxes of Fig. 5.7. In this numerical experiment, the load level $\Lambda = 0.8$ is dynamically obtained with a ramp-type of time law. Then, after 2 seconds the load is decreased to zero as depicted in Fig. 5.7. In the same picture, the dynamic response is superimposed to the static one. For the dynamic responses the commercial codes LS-DYNA (explicit analysis in time) and ADINA (implicit analysis in time) have been used. Notice the optimum correlation.

In the *loading* phase (i.e., growing of the value of Λ in time) the snap-buckling occurs as a dynamic phenomenon (true physical behavior). The corresponding states on the static response curve are represented by B and C (see Fig. 5.7).

In the unloading phase (i.e., decreasing of the value of Λ in time), it is also possible to notice a snap (states F and G). However, this snap is *not* the same snap (in reverse direction) seen in the loading phase and occurs at lower load level Λ. After the load is completely removed the displacements return to zero with a convergent (consequence of the structural damping) oscillatory pattern.

Dynamic and static analyses are consistent with each other. Thus, static ap-

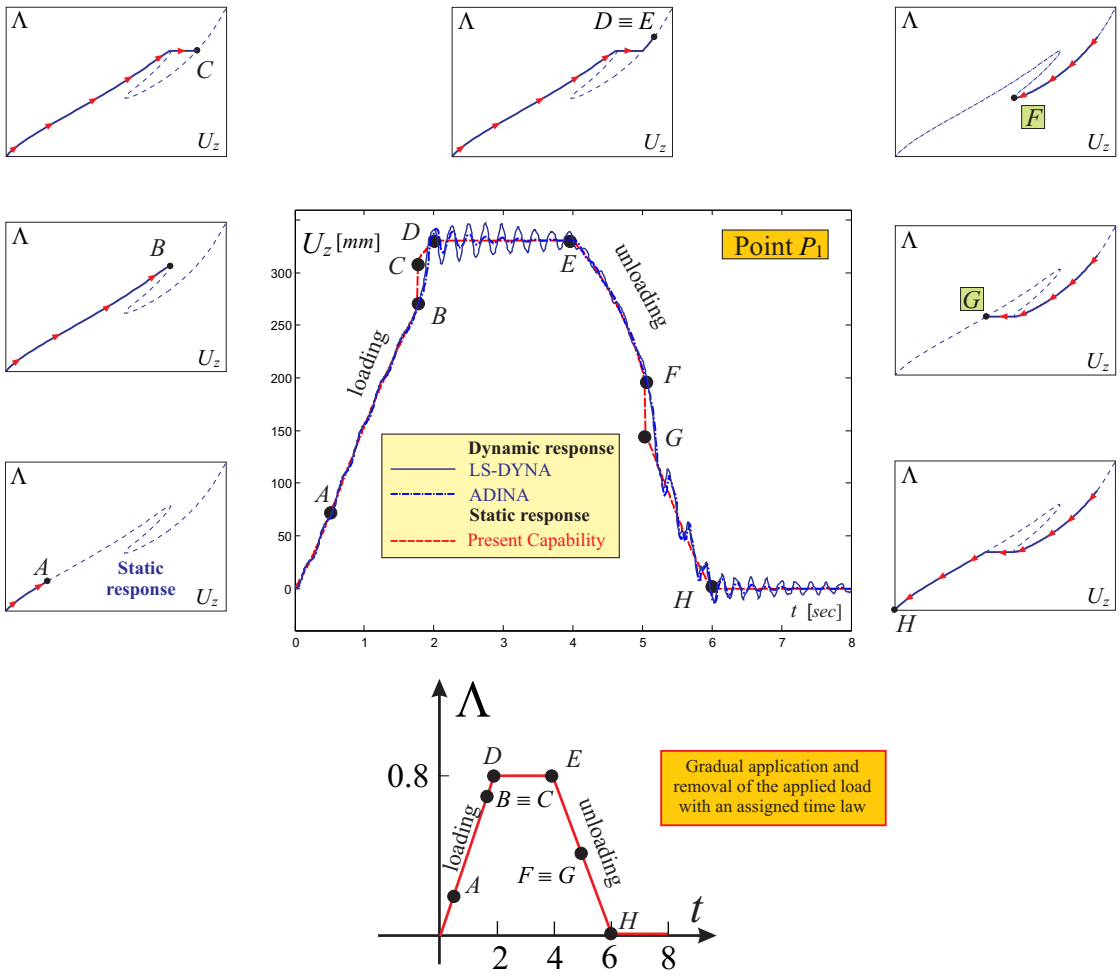

Figure 5.7: Transient quasi-static response of point P_1 at the tip of the lower wing for *SISO6* configuration. In the graph the load application is also depicted. The curves are superimposed to the static equilibrium curve (broken red line).

proach could be used as a valuable tool for describing an inherently dynamic phenomenon such as the snap-buckling.

5.7 Dynamic Nonlinear Analysis: Branch-Jumping

Next focus is on how a dynamic nonlinear analysis reveals hidden dangers related to the *bi-stable* property of the system. More in detail, it will be demonstrated that, a full post-critical nonlinear static analysis is necessary (but not sufficient) for Joined Wings, even if the structure is designed to operate in conditions far from the one relative to the critical load (Λ^{CR}).

The terminology *branch-jumping* (or more in general, *jump phenomenon*) used in the following refers to the fact that the system could start from an equilibrium configuration on a branch (denoted as main branch), and, given a vanishing dynamic perturbation, may find a static equilibrium on another branch (denoted as post critical branch). Thus, it should not be confused with the same terminology used when trying to follow a branch with a continuation method (see [178]) or with *branch-switching*.

In all the following (static or dynamic) analyses the in-house capability is used.

5.7.1 Branch-jumping for conservative loading

Consider again the *ISO6* configuration and assume that a load level $\Lambda = 0.5$ is applied, as shown in Fig. 5.8. As it could be inferred, there exist three static equilibrium configurations for that load. The state indicated with B is an unstable one, thus, it will be not observable, whereas the states A and C are both stable. For this particular choice of Λ, the system is thus bi-stable.

Assume now that the configuration is in its static equilibrium in the main branch (state A) and a vanishing perturbing force is applied. For the purposes of analysis, this perturbation is considered to be a force uniformly applied to the mid-span station of the upper wing, directed downward, and reaching a nominal entity of $805\,[Kg \cdot mm \cdot s^{-1}]$. This force corresponds to less than 6% of the overall force acting on the wings in the equilibrium configuration A. The time law of the disturbance is shown in Fig. 5.9. If Λ_{pert} represents the analogous of Λ, but for the nominal perturbing force, the disturbance is linearly increased to his nominal value in 0.1 seconds, and then linearly decreased until it vanishes, at 0.2 seconds. The response is studied for the necessary time needed to reach any stable equilibrium point.

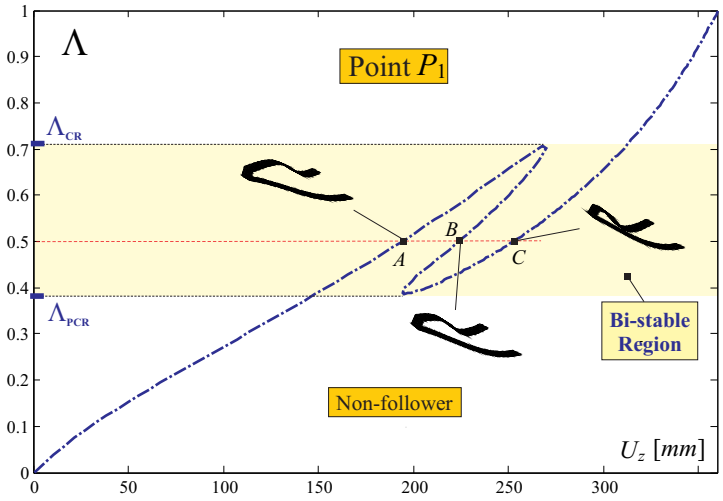

Figure 5.8: Load parameter Λ versus cumulative vertical displacement U_z of lower wing's tip point P_1 for joined-wing layout *SISO6*, featuring $b = 40$ mm, and loaded with conservative (non-follower) forces.

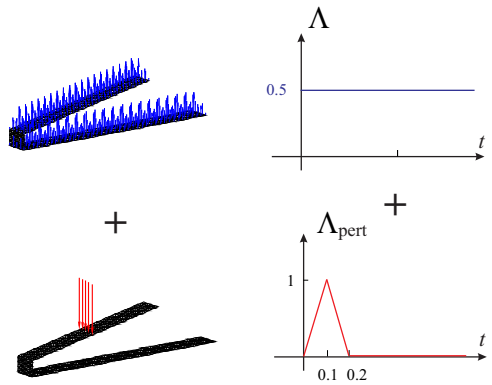

Figure 5.9: Application of the perturbation to the steady state and time evolution.

Notice that generally, from a mathematical point of view, it is not immediate to assess if a system, when perturbed, has a vanishing transient and then settles to a static equilibrium point. In fact, phenomena like limit cycle oscillations or also aperiodic motion could arise (for more details refer to works [178–180]). A physical and practical approach has been preferred instead of a mathematical rigorous study which goes beyond the scope of this work. Thus, physical sense suggests that finite perturbation would lead to vanishing transient (when damping is applied) even if the applied forces are of follower type.

In order for the oscillations to vanish, a structural viscous damping is considered, according with the Rayleigh method [177].

Output of the analysis is shown in Fig. 5.10. As it could be clearly seen, after a brief transient, the configuration does not return to the initial state (state A in the main branch), but finds an equilibrium point in the state C, which is on the post-critical branch. Fig. 5.11 summarizes the branch jumping, showing also the states A and C on the static response curve.

To better understand the phenomenon an analogy with the case shown in Fig. 5.12, adapted from [179, 180], may prove useful. Two simple dynamical systems are considered, in which a ball is constrained to move on a bowl and gravity is acting. For the first case on the left, there is only one equilibrium point (also called fixed points in dynamical systems terminology). Considering joined-wing systems, ideally, this situation could be conceptually associated to all cases outside the *bi-stable* region, i.e., in which $\Lambda > \Lambda^{\mathrm{CR}}$ and $\Lambda < \Lambda^{\mathrm{PCR}}$.

Turning the attention to the second case, on the right side, the states A and C at the bottom of the bowl, and B on the crest, are static equilibrium positions. If the ball is in equilibrium in state A, and a perturbation in terms of velocity (or vanishing force as well) is given, the ball may end up to the point C. Point B represents an unstable equilibrium configuration thus, no equilibrium would be physically observable. Given this, the system could be considered bi-stable. This picture could be conceptually associated to the *SISO6* configuration in equilibrium at a generic load fraction such that $\Lambda^{\mathrm{PCR}} < \Lambda < \Lambda^{\mathrm{CR}}$ when a perturbation is applied, as for example the case studied above and shown in Fig. 5.10.

Summarizing, equilibrium points in the bi-stable region (as A or C) are characterized by conditional stability: if a finite opportune perturbation is applied, the *jump-branching* could be triggered. The shown case underlines that this phenomenon could happen for load levels relatively smaller than the critical one (snap), and do not need an excessive magnitude of the perturbation to be triggered. This analysis suggests that it could not be a priori safe to design the configuration just relying on a pre-critical nonlinear analysis and choosing the operative condition to be far from the critical point.

In the analyses shown above, the nature of the perturbation was chosen ad hoc to be as simple as possible and to favour the deformed configuration in the post-critical branch (state C). However, there exist an infinite number of choices that will promote this instability, especially because the perturbation could be applied at different points in the structure, could have a varying spatial magnitude, and could also have a time

evolution. Considering this broad scenario, it is difficult to identify all the possible perturbations that may lead to such branch-jumping, especially recalling the strong nonlinear behaviour of the system which, somehow, undermines classical approaches.

In conclusion, if a snap-buckling phenomenon has to be avoided two strategies seem to be the most reasonable. First option is to have an *operative* static point A on a load level smaller than the second critical point, that is the critical point in the post-critical branch. Equivalently, with reference to Fig. 5.8, $\Lambda < \Lambda^{\mathrm{PCR}}$. In such a case, as the perturbation vanishes, the configuration will approach again the starting equilibrium point in the main branch. Second option is to design a snap-free structure when static response is studied. Notice that, for both cases, a nonlinear postbuckling analysis is necessary. To track all the response it may be necessary to continue the analyses also for large displacements (well larger than the ones the structure could actually carry) regions. Unfortunately, some cases may have isola centers, which are close curves in the load-displacement static response, not connected to the main branch. These structures could not be a-priori detected with a normal branch tracking methods. More on this topic is presented in Section 5.8.3.

5.7.2 Branch-jumping for follower loading

The previous analysis has been carried out when conservative loading was applied. In this section similar procedure is adopted for the case of follower loads. Configuration *SISO6* is considered and follower loads are applied (as explained in section 5.4). The static response is depicted in Fig. 5.13. Starting from the configuration relative to $\Lambda = 0.38$, a perturbation is given. The disturbance's nature follows the same indications as in the previous example. Its magnitude reads $630\,[kg \cdot mm \cdot s^{-1}]$, and it is directed in the negative z-direction. To normalize this magnitude with the forces acting at stage A the ratio of perturbing pressure (obtained dividing the magnitude of perturbing force by the wing planform surface) to the pressure acting on the wings ($0.38 \cdot p_{\mathrm{nom}}$) is calculated. Thus, the perturbation actions are about 6% of load applied at state A. The transient response is shown in Fig. 5.14. The same considerations expressed in the previous section are thus valid in presence of the follower forces.

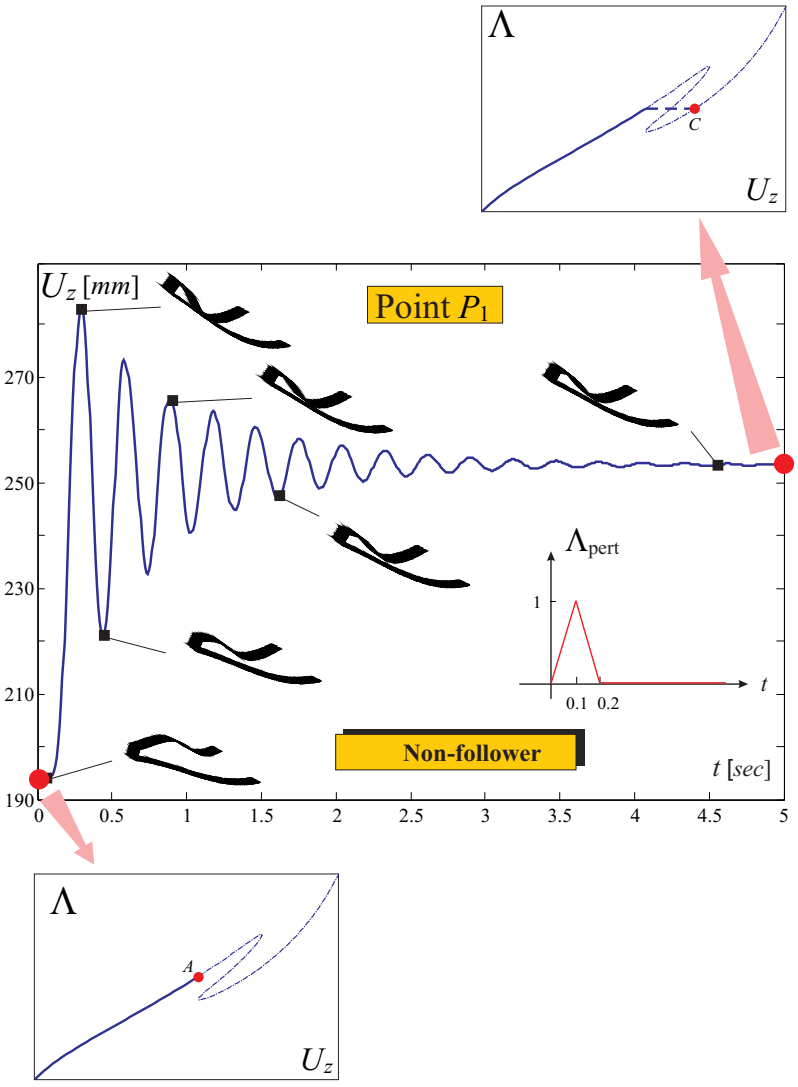

Figure 5.10: Transient response for point $P1$ at the tip of the lower wing: time versus displacement when the perturbation is applied.

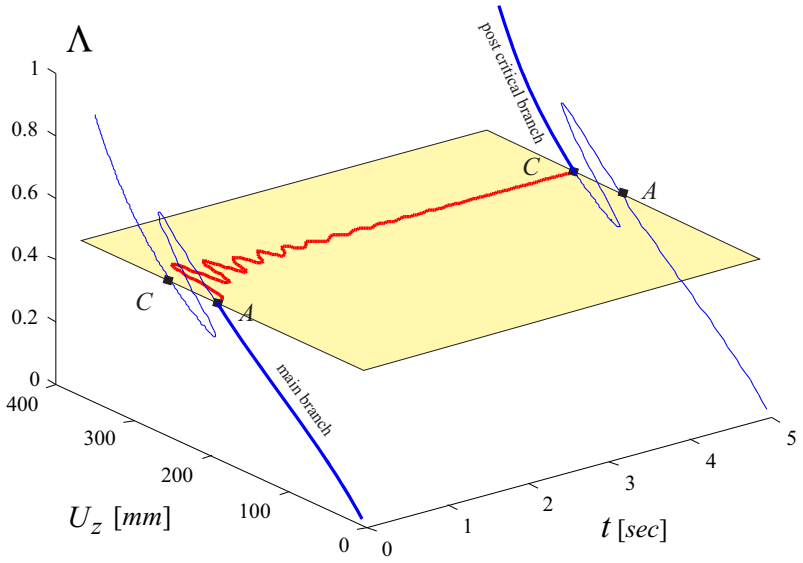

Figure 5.11: Transient response for point $P1$ at the tip of the lower wing: time evolution is represented in the $\Lambda = 0.5$ plane, static response is depicted at initial ad final times to help localize the initial and final equilibrium points.

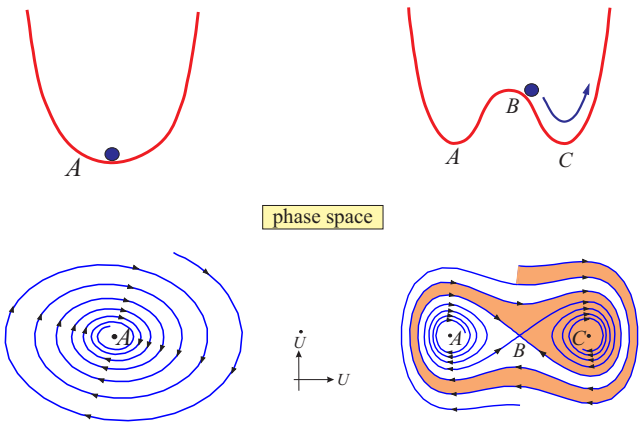

Figure 5.12: Two examples of dynamic system with one and two stable equilibrium points.

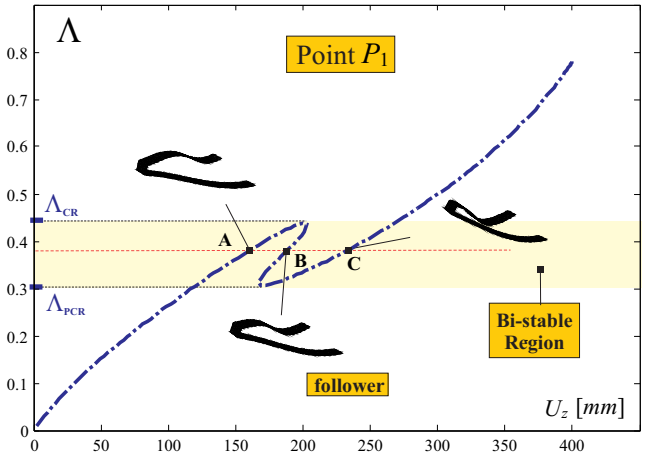

Figure 5.13: Load parameter Λ versus cumulative vertical displacement U_z of lower wing's tip point P_1 for joined-wing layout *SISO6* loaded with follower forces (pressure).

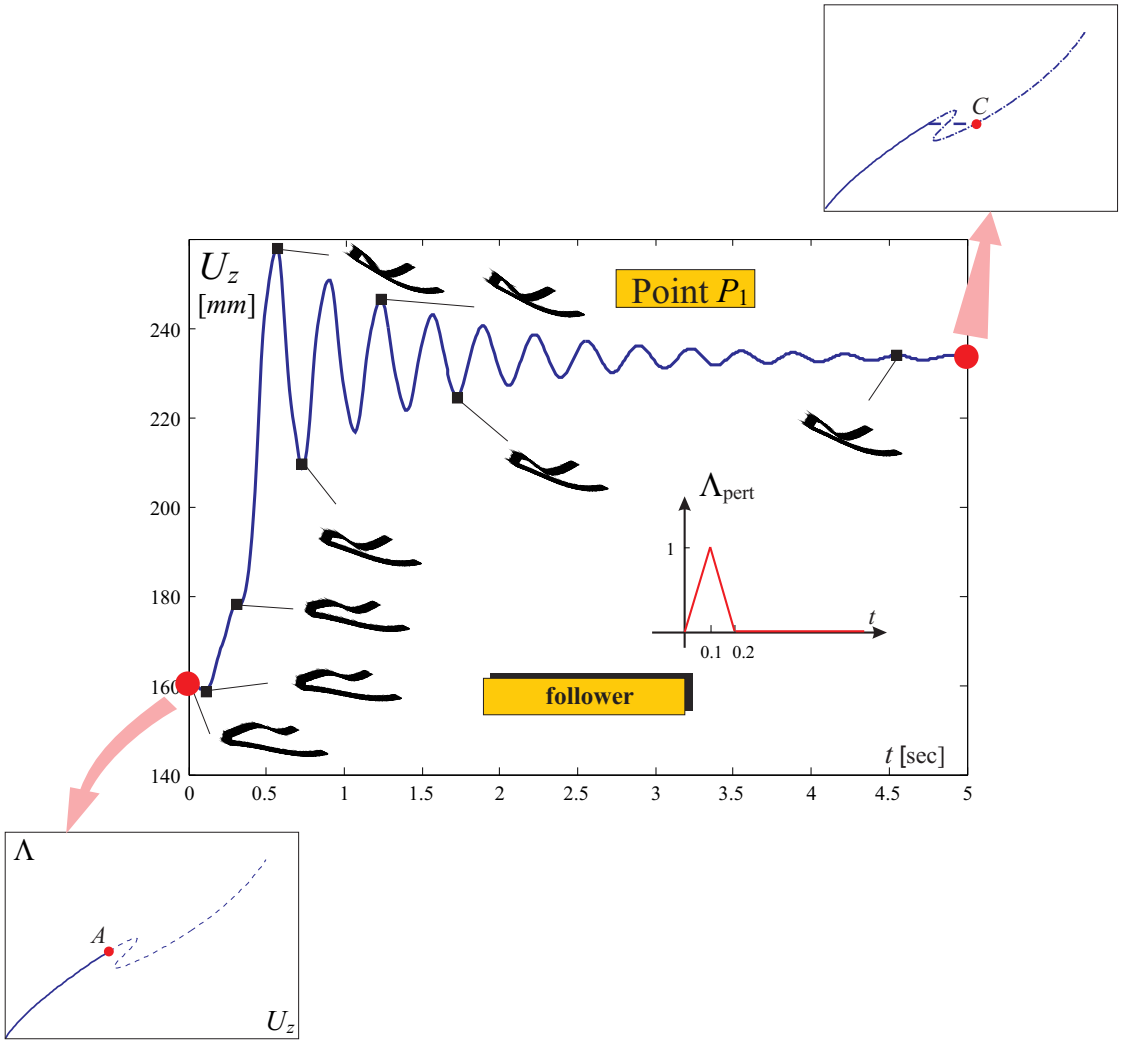

Figure 5.14: Transient response of point P_1 at the tip of the lower wing for *SISO6* configuration: time versus displacement when the perturbation is applied.

5.8 Dynamical System Characterization of Snap Phenomena in Joined Wings

In this section, the nature of the physical system is analyzed from a dynamic system perspective. It is interesting to notice how there is no unique terminology in the open literature on nonlinear dynamics. For example, with a structural engineering flavour, in [142] the critical point (associated with the snap phenomenon) are called *limit points*, and have to be differentiate from the *bifurcation points* which arise when two (or even more) branches with distinct tangents intersect. In [178] it is stated that these points are also called *turning point*, *saddle-nodes* or *fold bifurcations*. The different nomenclature is consequence of the different fields in which the same basic phenomenon was observed. However, the old bifurcation theory did not consider limit points as bifurcation points. Later, both the discover of new nonlinear phenomena and the rise of subjects as *catastrophe theory* suggested a new classification.

5.8.1 Load level and saddle-node bifurcation

If the problem is seen from a dynamical system perspective, the load level could be thought as a parameter. Considering for example the *SISO6* case loaded with conservative forces (see Figure 5.8), if the load level is varied, an interesting fact happens to the fixed points (static equilibrium points). For $\Lambda < \Lambda^{\mathrm{PCR}}$ the fixed point changes its position in the multidimensional space (where each dimension could be thought as a single degree of freedom of the system). When $\Lambda = \Lambda^{\mathrm{PCR}}$, a saddle-point bifurcation occurs: a new distinct fixed point originates (look for example at the points BC). The previous fixed points A continues to exist, changing its position. If the load level is increased, this new fixed point separates in two distinct fixed points, one unstable, B, and the other stable, C. As A, they evolve and change their position when Λ is varied. However, in the limit that Λ approaches the critical value Λ^{CR}, points A and B get closer, until, exactly when $\Lambda = \Lambda^{\mathrm{CR}}$ they are coincident and annihilates. This represents a further saddle node bifurcation. For larger load levels, only the fixed point C exists. Thus, when $\Lambda = \Lambda^{\mathrm{CR}}$ or $\Lambda = \Lambda^{\mathrm{PCR}}$ there is a topological change in the space phase of the system. This is exactly what is involved in a bifurcation. Fig. 5.15 gives a pictorial example. Notice that the concept above is actually true for the curve in the multi-dimensional space consisting of all the degrees of freedom, thus it is true also for every projection

into smaller dimensional space, e.g. the vertical displacement of point P_1.

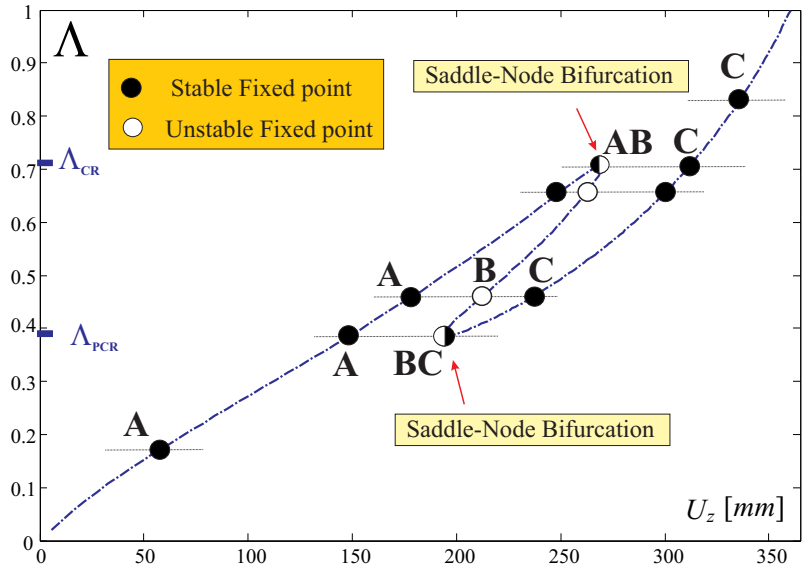

Figure 5.15: One-parameter bifurcation diagram of vertical displacement U_z of the wing tip point P_1 as function of the load level Λ. It could be observed how for $\Lambda = \Lambda^{\mathrm{PCR}}$ and $\Lambda = \Lambda^{\mathrm{CR}}$ there is a saddle-node bifurcation.

The stability of the fixed points on the branch has been suggested by physical considerations, outcome of the simulations (dynamic simulation with a perturbation) or also evaluating the sign of eigenvalues of the Jacobian (tangent matrix).

5.8.2 Joint's height and saddle-node bifurcation

Let the joint's height be considered as parameter, and refer to Fig. 5.16 (taken from Reference [1]). An analogous plot to Fig. 5.15 could be depicted, where on the y axis the joint's height is reported (Λ is now fixed). Actually, it is more meaningful to be able to consider both the joint's height and load level as parameters, and draw the so called *stability diagram* (see [179]), in which the different behaviours (regions of bi-stability) are plotted in the parameter space. The outcome is depicted in Fig. 5.17. The region enclosed by the two limit curves contains the set of parameters for which the system shows bi-stability (3 fixed-points region in Fig. 5.17). The mono-stable situations are all the points outside the region. From a practical point of view, if the joint's height falls inside the *SBR*, then the maximum allowed load level has to be under the lower limiting curve.

Close inspection of extrema of the region of bi-stability suggests the presence of

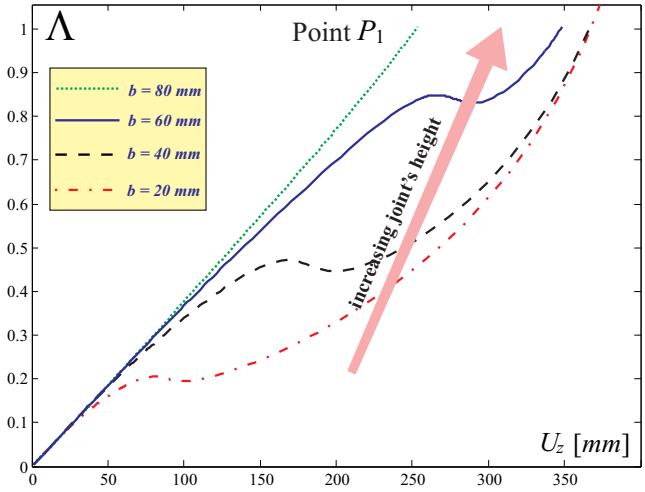

Figure 5.16: Load parameter Λ vs vertical displacement U_z for lower-wing-tip point P1. Responses for different joint's heights. This figure is taken from [1].

cusp points (further analyses are needed to verify their real nature). A three dimensional visualization of the load level, joint's height and vertical displacement of point P_1 gives the pictorial representation of the so called *cusp-catastrophe* (provided the extrema points are cusp-points). Fig. 5.18 represents the surface in the parameters space.

5.8.3 Stiffness parameter, saddle-node bifurcation and isola

Let us introduce the *stiffness ratio* (E^r) as the ratio of upper to lower wing Young's moduli. If this parameter is varied, the same bifurcation problems noticed above take place. Fig. 5.19, adapted from Reference [2], shows how the typical snap-buckling response disappears when the stiffness ratio parameter approaches a critical value, in this case $E^r = 6.3$ (details about the configurations can be found in work [162]). In the cited paper, it was thus assumed that for larger E^r the bi-stable region was disappearing, being this compatible with the so far explored scenarios (observed when joint's height was considered the free parameter).

However, this has not found to be the case after more thorough investigations, driven by physical considerations regarding the abrupt disappearing of the unstable branches, led to the discovery of an *isola*, i.e., solution branch closed in parameter space. As it is shown in Fig. 5.20, plotting all the responses for load level and displacements that go beyond practical interest (very deformed configurations) uncovers a further couple of saddle-node bifurcations (turning points C and D in the graph of *SISO6* and *SISO7*).

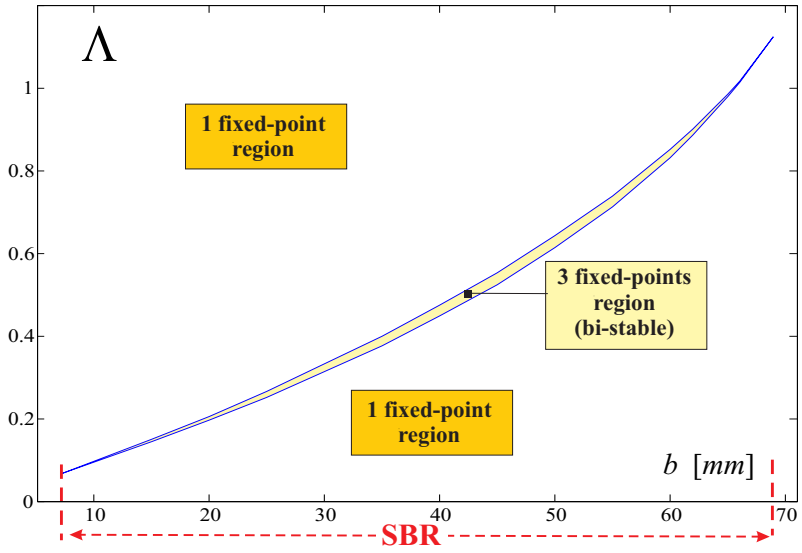

Figure 5.17: Two-parameter bifurcation diagram in the joint's height-load level (b, Λ) parameter space. The region enclosed represents a bi-stability region.

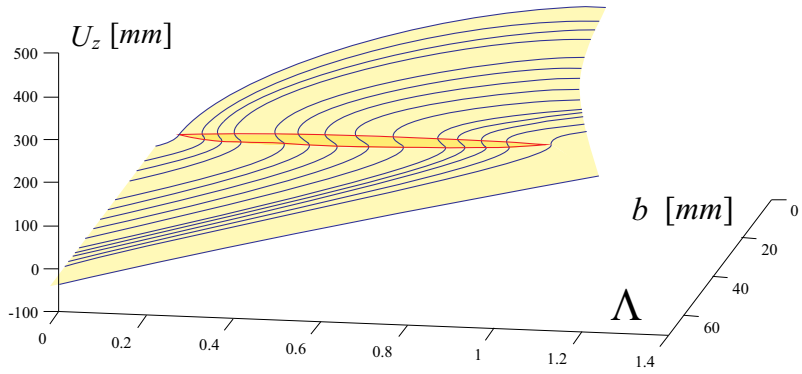

Figure 5.18: Cusp catastrophe. Load level, joint's height and vertical displacement of wing's tip.

It can then be easily conjectured, that the turning points A and D get closer when increasing E^r. Eventually they coalesce when E^r reaches a value between 6.0 and 6.3, that will here be called E^r_{IS}. For this value, a transcritical bifurcation is thus taking place (in the displacement-load level bifurcation diagram). The two branches OA and DE will touch in $A = D$, forming an unique branch OE.

On the other hand, also unstable branches AB and CD are connected through $A = D$, and thus, increasing E^r, an isola forms, detaching from the main branch. For this reason E^r_{IS} could be assessed as corresponding to an isola-type bifurcation.

It was not possible to exactly track the response for values of E^r close to the

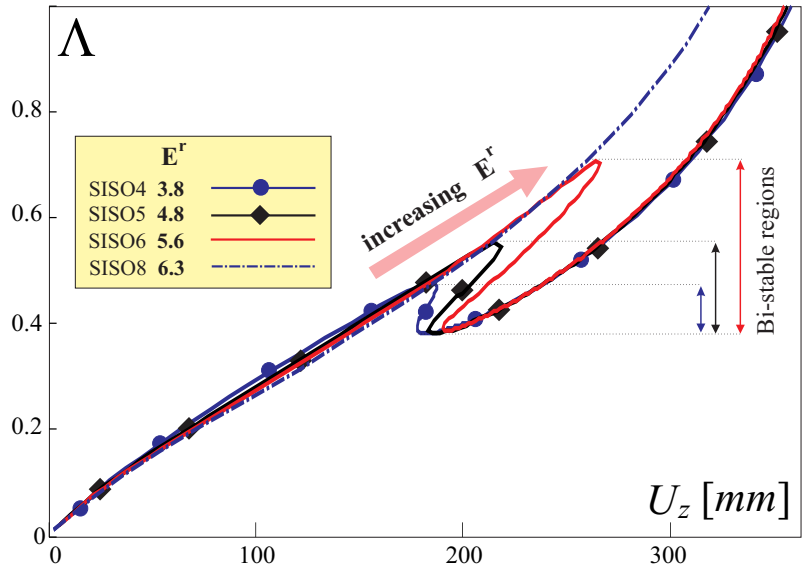

Figure 5.19: Static responses for various configurations in which the lower-to-upper wing stiffness ratio E^r is varied. This picture is adapted from [2].

bifurcation one, since the authors experienced numerical difficulties in following the unstable branches (see dashed lines in Figure 5.20). However, the shown results are enough to confidently conjecture the proposed scenario.

In order to be able to draw the isola, a static simulation was first employed and stopped to a value of Λ for which a branch of the isola was supposed to exist. Then, with a trial and error process based on intuition, an appropriate disturbance was given to the system and the response was monitored: after a transient, the system was eventually approaching a different-than-initial equilibrium state. This last configuration was taken, and thanks to the restart capabilities of the in-house code, a new static simulation with the continuation method option was launched. Thus, the isola was tracked. The investigations have been carried out up to $E^r = 7$, as shown in Fig. 5.21. Further increasing this parameter, it is plausible that the isola shrinks and finally disappears in a so called *isola center*. This investigation, however, has not been pursued here.

Isola-type bifurcations were observed in different field, see References [178, 181–185] for a more in depth treatise and some practical examples. The possible existence of isola-kind of responses for Joined Wings is one of the major contributions of this work.

The consequences of such a finding, are somehow scary. They could be summarized in saying that a path-tracking technique (inherently nonlinear) *is not enough* to ensure that bi-stable regions are not present. It is also very difficult to be aware or

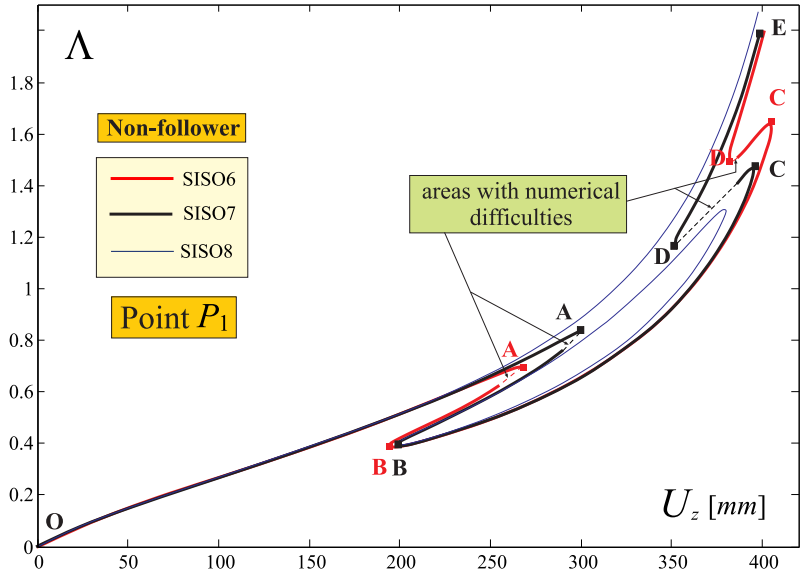

Figure 5.20: Static responses for *SISO6* ($E^r = 5.6$), *SISO7* ($E^r = 6.0$) and *SISO8* ($E^r = 6.3$) considering also high deformation regions.

expect in advance any of the typical isola behaviors. In this regard the authors like to underline that, suspect of isola behaviour were inspired by performing a wide number of analyses in a large parameter space (varying E^r, using different vanishing perturbations, etc) and by considering also the response for "practically meaningless" configurations (consider the typical pattern and the second couple of turning points C and D which arise for very large displacements in Fig. 5.20), which actually, did turn to be a key point towards understanding the physics of the response.

5.8.4 Possible effects of imperfections

In a practical design process, manufacturing problems have to be taken into account. In a setting as the one above, effects of imperfections (which could be thought as a small variation on one control parameter, as for example E^r or joint's height) may be catastrophic. One possible scenario, Fig. 5.22, is that the real operative points falls in a completely different state than the nominal one. This example may be easily obtained considering a fixed load level and two configurations differing by a small variation of one parameter (E^r, but also joint's height). Notice that the knowledge of the post-critical behaviour would not have been enough to prevent this to happen. On the contrary, a sensitivity analysis to the different parameters is necessary. It is worth a notice that the two cases display an almost identical response up to the turning point.

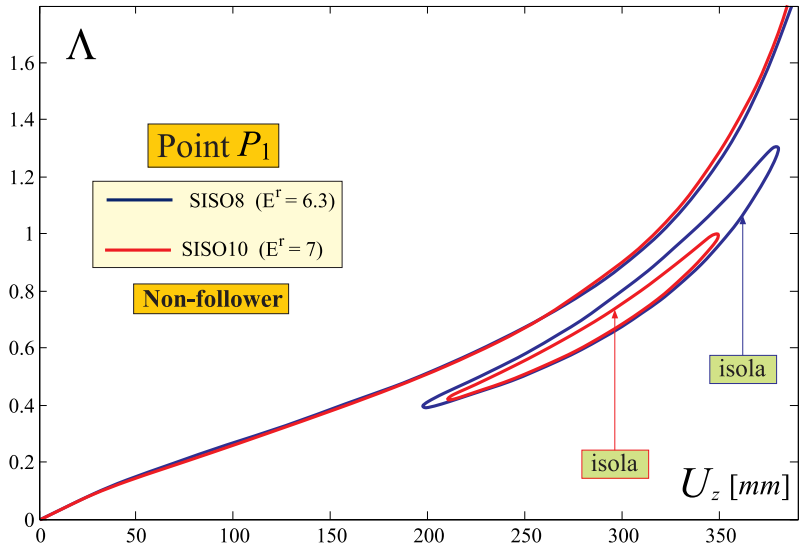

Figure 5.21: Static responses for SISO8 ($E^r = 6.3$) and SISO10 ($E^r = 7.0$) considering also high deformation regions.

A numerical example shows also a further possible scenario. Consider the configuration *SISO8*, in its stable state associated with a load level of $\Lambda = 0.5$, as depicted in Fig. 5.22. This configuration does not have any snap-buckling phenomenon, but, as seen above, two stable states exist (main branch and isola). However, the same perturbation used in Section 5.7 is not able to trigger the branch-jumping, as clearly depicted. With a *relatively small modification of the stiffness property*, driven for example by manufacturing issues, it is possible to incur in a configuration having the properties of *SISO6*. In such a case, the configuration settles in the post-critical branch after the transient. A minor perturbation which for one case leads to a negligible amplitude transient, triggers, in the other case, a branch-jumping. This completely different behaviors seem even more shocking considering that the two static analyses present an almost identical response in the main branch, and thus, show practically identical macroscopic stiffness.

5.9 Guidelines for Realistic Joined-Wing Design: a Critical Discussion

This section critically discusses how the results found on very simplified model with stiffness and mass distributions not typical of an aircraft could apply to a realistic design.

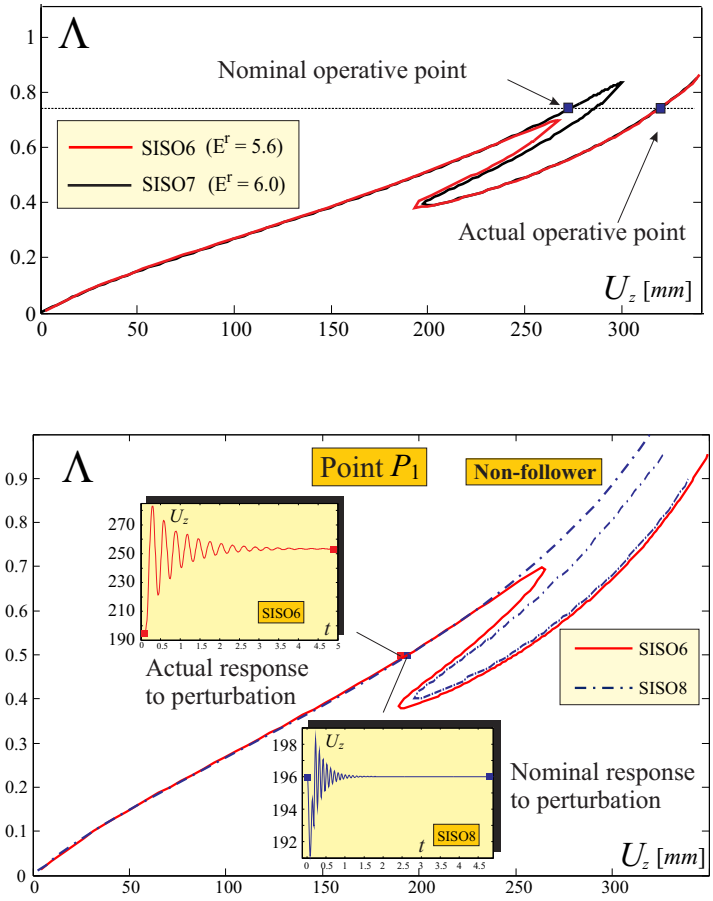

Figure 5.22: Possible effects of imperfections.

Design of an aircraft (especially Joined Wings) is a tremendously complex and multidisciplinary task, the aerodynamic loads have to be evaluated for trimmed configurations which, on their own, depend on many factors variable in time and situation (fuel and pay loads for example). On the other hand, both the model and the *real* aircraft share the same inherent overconstrained nature of the system.

Regardless of the level of displacements that can be accepted (this will be discussed later), there are in literature some documented cases in which the deformed shape was resembling very closely the deformate of the here employed simplified models, and the instability was of the snap-type. For example, Figs. 34 and 37 of Reference [186] show a snap-instability (see work [187] for a discussion of the snap-instabilites in presence of aerodynamic loads) for a beam model of the HALE *SensorCraft* in which also the flexibility of fuselage was considered. Typical snap-instabilities can also be recognized in Fig. 9 of Reference [188]: although the post-critical branch was not completely tracked, it can

be clearly recognized a converged status far from the main branch at lower-than-critical load level. Finally, the typical elastic instability of the Boeing's SensorCraft concept in Reference [85], occurring at global level rather being a buckling problem of the aft wing, closely resembles the here presented deformed shapes (see in particular Fig. 14 of the cited paper). The cases discussed in References [188] and [85] were detailed finite element models, comprehensive of the typical wing-box structure. This gives credit to the approach of conceptually studying these instabilities on relatively simple models (not taking into account a detailed wing-box): results have a practical value and are not just a pure academic exercise.

Having assessed that *realistic* highly deformable configurations may be prone to the problems shown in this paper on conceptual models, it is also true that jumps and snaps could be hardly accepted in any aeronautical design, and thus, must be avoided at all costs. Results above warn against the temptation of interrupting the structural analysis well before a limit point is reached, since, bi-stable regions may exist well below the critical load. Thus, an adequate vanishing perturbation may cause the system to assume a different equilibrium configuration after the transient has elapsed. However, it is very difficult and impractical to assess the level of stability in relation to all the possible perturbations. Thus, the most intuitive and simplest approach should completely avoid snap-buckling in the static response, or, alternatively, should design the flight envelope for load situations (speed) which do not present bi-stability. In both cases, it is necessary to evaluate the response with a nonlinear postcritical analysis, which, considered that the typical stability analysis in the early design stages relies on fast linear tools (eigenvalue approach which can be strongly nonconservative as shown in References [1,158]), dictates a large increase in computational costs.

The presence of detached equilibria branches represent a limit design burden. Typical structural analysis tools trace the nonlinear post-critical response with path-tracking continuation methods (such as the arc-length), thus, within this approach, isolas cannot be detected. Alternative systematic approaches other than a sequence of dynamic-perturbations applied to trigger the branch-jumping and discover detached branches should be employed (References cited in Section 5.8.3 may help in this regards, even though low-order models are therein studied).

Considering commercial aircraft concept (as the *PrandtlPlane*, see [9]) it is legitimate to ask to what extent may the here introduced scenario apply. In fact, regulations

limit deflections and stresses, whereas large deformation regimes are typical of the present analyses. However, this does not a-priori exclude the presence of a secondary stable configuration characterized by strain and stresses within the regulations (bi-stability). In a conservative spirit, it is necessary to ascertain this eventuality not to occur.

Furthermore, it has been recently shown [16] that reduced order modeling of Joined Wings is challenging even for small deformations, and a reduced basis augmented with modal derivatives presents better numerical performances. This indicates a nonlinearity which seems to be important already for small deformations.

An interesting last observation follows. While tracking the whole nonlinear response, a state with stresses above the material failure (or displacements above the acceptable ones) can be reached. However, stopping the simulation because of this failure would be methodologically incorrect. In fact, continuing to follow the response considering elastic material, may bring to secondary stable regions at lower load levels working in the *elastic* regimes. This bi-stability may trigger the branch-jumping.

The situation is much more complex if aerodynamic loads are considered. Nonlinear dynamic aeroelastic phenomena as limit cycle oscillation could arise (e.g., [189]), and this is not easily observable nor predictable from a static analysis, able only to predict static equilibrium conditions.

5.10 Conclusions

Recent investigations on Joined Wings have been showing a typical *snap* phenomenon for a combination of geometrical and material properties, and loading conditions. Lower-to-upper-wing bending stiffness ratio and the bending moment transferred through the joint were assessed as some of the driving factors. However, many open theoretical questions still needed an answer and the instability phenomenon and its consequences necessitated to be further studied.

The present effort contributes in unveiling the complex scenario. *First*, pressure-like loads are selected to mimic the aerodynamic loads more closely than the conservative loads were able to do. The results confirmed that snap is still present. Actually, as intuitively expected, such loading conditions exacerbate the instability phenomenon, anticipating the critical condition to smaller deformations. Follower loads eliminate buckling-free configurations and this has an obvious important impact.

Second, snap occurrence is studied with a dynamic analysis in which the load is

applied very slowly. Results show that, although inertial phenomena play an important role when abrupt dynamics is concerned, the static analysis is an excellent tool to be used.

The *third* contribution regards the real necessity of post-critical analyses of Joined Wings. In the aeronautical world, a snap would be a catastrophic event, thus, why not just design the configuration to operate well below the critical point, and avoid computationally expensive post-critical analyses? Investigations reported in this paper show a very important phenomenon: a configuration loaded well below its critical load may incur in branch-jumping problems when a vanishing perturbation is applied. That is, a jump from the equilibrium configuration on the main branch to another stable equilibrium configuration on the post-critical or secondary branch is triggered by the perturbation (whose entity may be in the order of some percentage of points of the nominal load). This seems to open a worrying scenario on a safe design of Joined Wings. In fact, if a complete analysis is not pursued, the operative conditions may fall exactly in regions where more than one equilibrium configuration is possible (bi-stable regions), and a perturbation may drive a branch-jumping.

What seemed to be a costly approach to safely design Joined Wings, found some pitfalls. In fact, studying the time-response to small vanishing perturbations, could bring to light the presence of *isolated/detached* bi-stable regions (isolas) that could not be detected otherwise with solely application of branch tracking methods. This isolated branches are very difficult to detect with an automatic process, since they need the application of ad-hoc strategies driven by the particular case (type of the perturbation, load levels for which to look for bi-stability, etc..)

The preliminary design of Joined Wings must take these aspects into account. However, the computational cost associated with the nonlinear evaluations must be overcome to have practical impact in the industry. This work goes in the direction of shedding light on the complex phenomena that must not be overlooked when Joined Wings are designed.

Acknowledgements The authors acknowledges the support by San Diego State University (College of Engineering). They also like to warmly thank Professor Antonio Palacios of the Department of Mathematics of San Diego State University for his precious suggestions about nonlinear dynamics.

Chapter 5, in full, is a reprint of the journal paper: "*Risks of Linear Design*

of Joined Wings: a Nonlinear Dynamic Perspective in the Presence of Follower Forces, CEAS Aeronautical Journal, November 2014." The dissertation author was the primary investigator and author of this paper. Coauthors were Luciano Demasi, Federica Bertuccelli and David J. Benson.

Chapter 6

Post-Critical Analysis of Highly Deformable Joined Wings: the Concept of Snap-Divergence as a Characterization of the Instability

This chapter is a partial reproduction and rearrangement of the following conference paper:
Post-Critical Analysis of Joined Wings: the Concept of Snap-Divergence as a Characterization of the Instability, AIAA 2013-1559.
Presented at the 54th AIAA/ASME/ASCE/AHS/ASC Structures, Structural Dynamics, and Materials Conference, Boston, Massachusetts, 2013.

6.1 Introduction

TYPICAL joined-wing configurations [10, 11] are characterized by significant structural geometric nonlinearities, [60, 127, 128] As a consequence, preliminary design complexity is increased [60]: existing procedures successfully adopted by the aerospace industry rely mainly on linear tools not able to correctly reproduce these effects. Employment of these lower fidelity tools is actually a practical requirement since a Multi-Disciplinary Optimization (MDO) generally involves a large amount of analyses. What has proven to be very effective in the past for classical cantilevered configurations, then,

cannot [128] be directly translated into procedures that have the same degree of computational efficiency and accuracy, when Joined Wings are considered [151]. On the other hand, neglecting structural nonlinearities in the early design stages may lead to a-posteriori-verified unacceptable solutions and can determine a significant increase of design costs.

In this scenario, reduced order models specifically tailored to retain the important nonlinearities of Joined Wings can be an ideal solution. Unfortunately, even advanced reduced order modeling techniques proved not to be very effective ([13–16]) when Joined Wings were considered. This suggests taking one step back and focusing on the nature of the involved nonlinearities, with the final goal of capturing the essential underlying physics for a more accurate and efficient design of reduced order models.

Several efforts considered mechanical loading and showed a highly complex nonlinear behavior of Joined Wings. Besides numerical approach, also experimental work [82, 83] was carried out to explore the joined-wing Sensocraft [86, 89, 159] response when subjected to follower static loads. Different works discussed theoretical aspects related to the structural nonlinearities [126] and also involved aeroelastic investigations [124, 134, 152, 161].

Only recently, see [1, 2, 130, 162], the research moved on the fundamental understanding of the peculiar nonlinear response of Joined Wings, with focus on the so called *PrandtlPlane* configurations, e.g., [9, 28, 91, 92, 94].

In particular, [1] demonstrated via nonlinear investigations that the linear buckling analysis is not very reliable as far as the static critical condition is concerned. Moreover, the wing system might be sensitive to snap-buckling type of instability for some combinations of structural parameters. The so-called Snap-Buckling Region (SBR) for Joined Wings was then introduced. Load repartition between the wings, joint size, and sweep angle had an important impact on the stability properties.

References [130, 162] presented several counter-intuitive aspects. Stiffening the compressed upper wing actually decreased the critical load; in addition, the lower-to-upper-wing bending stiffness ratio was shown to be one of the major parameters ruling the snap-buckling phenomenon. One of the most important physical aspects was the bending moment transferring through the joint: a reduction of the amount of transferred bending moment, obtained by changing the boundary conditions at the joint, significantly reduced the risk of snap-buckling instability, although at expense of the overall stiffness of the

structure.

Reference [2] discussed the effects of the non-conservative loads of the follower type on the SBR. More important, the concept of bi-stability was discussed and shown to cause branch-jumping phenomena at load levels far below the nominal critical condition (identified through the nonlinear static analysis as the snap-buckling). This has theoretically a tremendous impact on design of Joined Wings: under certain conditions an apparently safe and quasi-linear steady-state condition may actually be unsafe if the post-critical analysis is ignored. Further investigations showed also stable branches completely detached from the main branch, suggesting that path-following techniques (like the arc-length) are not sufficient to unveil the whole picture.

This work will extend the last efforts introducing aerodynamic forces and investigating the nonlinear response of the Joined Wings, with particular focus on the stability property of the system (concept of snap-divergence) and on the differences with the cases in which mechanical loads [1, 2, 130] are applied. For the first time on Joined Wings, post-divergence branches will be obtained and critically analyzed.

6.2 Contribution of the Present Study

It is common practice in the industry (e.g.., [190,191]) to calculate the divergence directly with the solution of an eigenvalue problem or via flutter analysis. The freestream velocity corresponding to the divergence is in general different than the one corresponding to the aeroelastic dynamic instability (flutter), thus, it has to be assessed which one represents the critical operative situation.

The above approaches, however, are based on an assumption that the structural properties of the system remain approximately constant. An open question is then how the divergence speed is calculated for a wing systems which experiences important geometric nonlinearity and how the divergence is precisely defined. This aspect is extensively addressed in the present work. It will also be assessed whether the eigenvalue approach, used to calculate the divergence speed, is reliable for Joined Wings.

A further contribution will be on the correlation of aeroelastic and structural static responses if mechanical conservative or nonconservative (follower type) loads are employed as a surrogate of the real aerodynamic forces. In fact, this approach is largely used as a mean of testing the structural response before more sophisticated and expensive campaigns are carried out. How reliable is this approach for Joined Wings? And, if not,

could it at least give a conservative estimate?

Starting from the above points, the *real divergence* occurrence is more critically analyzed, and physical insight is gained by means of comparisons with previous results presented in literature. In particular, aeroelastic load redistribution, overconstrained nature of Joined Wings and bending/stiffness coupling are discussed.

This work will also introduce the theoretical foundation of branch-follower numerical technique for static aeroelastic problems. These techniques are necessary to completely track the aeroelastic response, also after a critical (or turning) point is encountered.

6.2.1 On the importance of a conceptual study of Joined-Wings

One conceptual question is how the findings of this work, carried out on simplified models, relate to a real flying aircraft. On this regard, several observations can be made:

1. bi-stable regions (at macro-geometrical level) for a traditional configuration are generally not expected to be observed, whereas they are theoretically possible and shown for Joined Wing configurations. The presence of such regions impacts the design, whereas, as argued in this work, not considering the likelihood of having this phenomenon may lead to catastrophic consequences. Even for stiffness distribution typical of real wings, it is not guaranteed that such instabilities are not present, since the Joined Wings share all the same inherent properties: overconstrained nature of the system associated with significant geometric nonlinearities.

2. A real aircraft should be designed to operate within the flight envelope and should be trimmed and stable on a flight mechanics point of view. In the here presented responses, the angle of attack is fixed and the aircraft is generally not trimmed. However, as previously discussed, one of the aims of this effort is to demonstrate snap-divergence and bi-stability occurrences for Joined Wings. They are driven by specific stiffness distribution, aerodynamic load, its repartition among the wings (which encompasses aspects as trim, angle of attack etc) and overconstrained nature of the system. Thus, it is theoretically possible to observe these catastrophic phenomena also on realistic configurations operating within the flight envelope.

3. The design of a real aircraft is a significant effort, and should never be carried out on innovative joined-wing configurations without exploring the whole scenario.

Conceptual works, as the present one, are in the authors' opinion a necessity and good practice when tackling a tremendous effort like aircraft design. In fact, understanding why complex and counterintuitive phenomena eventually occur in Joined Wings is practically impossible (and expensive) when the number of design parameters/degrees of freedom is relatively large.

4. Bending/torsion coupling/aeroelastic tailoring is important in aeroelastic design. Its impact is further enhanced considering also the effects of the overconstrained nature of the system and the possibility of having multiple load paths. Since all Joined Wings feature the above properties, insight gained for one specific model (as those here presented) may have a valuable impact on the design of another one (for example, a realistic one).

6.3 Present Nonlinear Aeroelastic Capability

To investigate the role of geometric structural nonlinearities in presence of attached flow, an appropriate in-house aeroelastic framework has been selected. On the structural side, a corotational finite element based on the linear membrane constant strain triangle (CST) and the flat triangular plate element (DKT) is employed. The *structural tangent matrix* $\boldsymbol{K}_{ST}$ is sum of two contributions: the elastic stiffness matrix, $\boldsymbol{K}_E$, and the geometrical stiffness matrix, $\boldsymbol{K}_G$. The formulation is based on works presented in [135] with several corrections and improvements, e.g., [163] to the original effort.

The aerodynamic loads are evaluated through a steady incompressible VLM [192] (Vortex Lattice Method) approach. The wing is subdivided into wing surfaces, each meshed as shown in Figure 6.1. Each mesh element, called panel, is associated to a horseshoe vortex, a load point (where the aerodynamic force is applied) and a control point (where the Wall Tangency Condition -WTC- is imposed). The main assumption of the VLM is attached flow. Being geometrically nonlinear structural effects relevant for Joined Wings even for linear aerodynamics and attached flow, the current aerodynamic model is capable of capturing the main qualitative aspects of this work.

The deformation of the structure is taken into account when WTC is calculated. Splining is used to determine the slopes at the control points of the aerodynamic panels from the knowledge of the structural deflections on the structural nodes (not de-

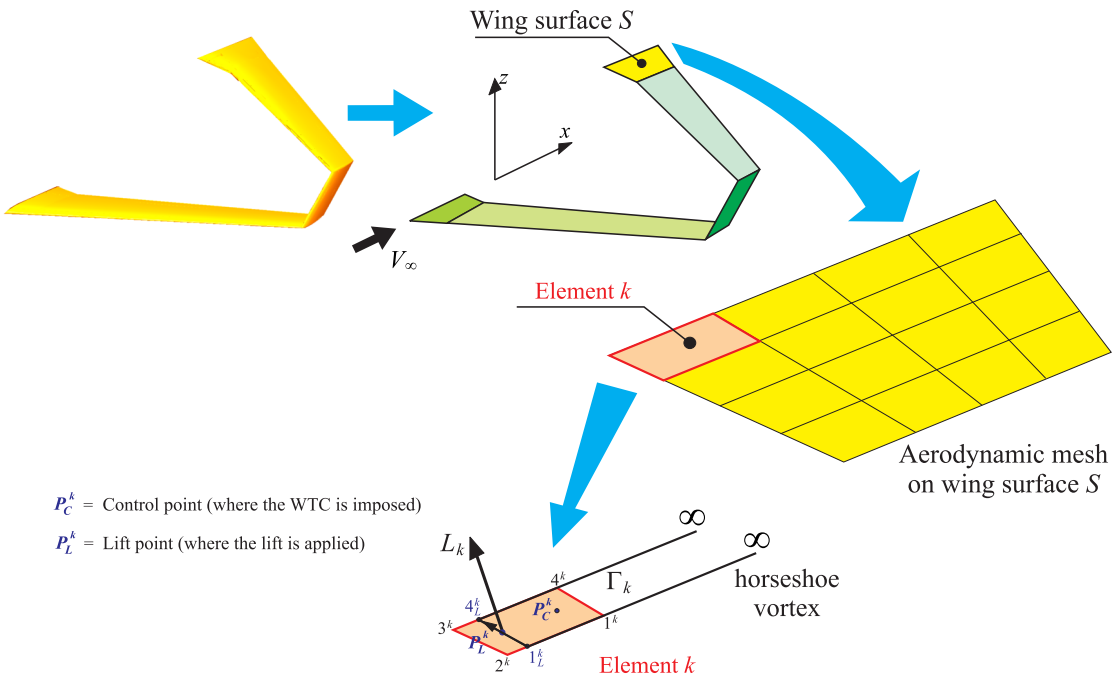

Figure 6.1: Incompressible Vortex Lattice Method: wing system, aerodynamic mesh and panel.

picted in Figure 6.1 for simplicity). A more detailed discussion of the interface technique (load/displacement transferring between the aerodynamic and structural meshes) as well as aerodynamic solver is shown in [161].

The nonlinear aeroelastic equations are solved by adopting iterative techniques discussed in Section 6.3.1. After each iteration a displacement vector is obtained, rigid body motion is eliminated and the pure elastic rotations and strains are found. Using these quantities the internal forces are updated for the next iteration. Adding the aerodynamic effects provides unique features that need to be specifically addressed. This is discussed in details in the following sections.

6.3.1 Solution of the nonlinear aeroelastic equations via arc length technique

The wings are subjected to aerodynamic loads, indicated with $\boldsymbol{L}$. A reference freestream velocity, V_∞^{ref}, and air density ρ_∞ are chosen, and corresponding dynamic pressure $p_{\text{dyn}}^{\text{ref}} = \frac{1}{2}\rho_\infty \left(V_\infty^{\text{ref}}\right)^2$ is evaluated. Two iterative procedures are employed in the static analysis: Newton-Raphson and arc length methods. Some theoretical aspects are now outlined with emphasis on the aeroelastic nature of the system under investigation.

The term *iteration* used in the following refers to the repetitive refinement of a nonlinear solution for an incremental load step μ. In nonlinear static analysis the load vector needs to be "gradually" applied to the structure for both facilitating convergence and drawing the whole curve response. This is practically achieved with the introduction of a load level Λ which represents the fraction of dynamic pressure (compared to the reference assigned value) applied to the system. Within a given load step μ several iterations take place before the numerical method converges with a prescribed tolerance.

There is a conceptual difference between the terms load step and iteration: at the beginning of a load step the equilibrium equations are "exactly" satisfied (within numerical tolerance), whereas at each iteration within a load step the static equilibrium is in general not satisfied and there is an error that needs to be reduced with additional subsequent iterations before a new load step is started. The analysis terminates when the entire reference dynamic pressure is applied.

To present the theoretical derivation, the concept of cumulative displacement vector $\boldsymbol{U}$ needs to be defined. $\boldsymbol{U}$ is a vector whose entries are the summation of all the displacements that occurred at all the previous numerical evaluations. If the undeformed structure is provided with an angle of attack (constant or variable twist) then there are aerodynamic forces even at the very first iteration of the numerical procedure. This is taken into account by defining $\boldsymbol{U}$ to be exactly a null vector only if there is no angle of attack (and so no aerodynamic forces are present). If a given incidence is provided, an appropriate initial value of $\boldsymbol{U}$ must be given so that the aerodynamic forces are correctly computed, accordingly with Eq.(6.1)).

At the *beginning* of the n^{th} iteration of a certain load step μ the aerodynamic loads are indicated with $\boldsymbol{L}_{\text{str}}^{\text{step}\,\mu\,\text{iter}\,n}$. According to the present formulation, it can be demonstrated (see [193]), that these forces have the following expression:

$$\boldsymbol{L}_{\text{str}}^{\text{step}\,\mu\,\text{iter}\,n} = p_{\text{dyn}}^{\text{step}\,\mu\,\text{iter}\,n}\, \boldsymbol{C} \cdot \boldsymbol{U}^{\text{step}\,\mu\,\text{iter}\,n} \tag{6.1}$$

where $\boldsymbol{C}$ is an aerodynamic constant matrix (this matrix would be load step dependent if the compressibility correction is added). $\boldsymbol{U}^{\text{step}\,\mu\,\text{iter}\,n}$ is the cumulative displacement array at the beginning of the n^{th} iteration. Similarly, $p_{\text{dyn}}^{\text{step}\,\mu\,\text{iter}\,n}$ represents the dynamic pressure *gradually* applied to the system evaluated before iteration n is performed. Re-

calling the definition of the load level Λ, it is possible to write:

$$p_{\text{dyn}}^{\text{step}\,\mu\,\text{iter}\,n} = \Lambda^{\text{step}\,\mu\,\text{iter}\,n} \cdot p_{\text{dyn}}^{\text{ref}} \tag{6.2}$$

When the arc length method is adopted, the unknowns are represented by the incremental displacement vector $\boldsymbol{u}^{\text{step}\,\mu\,\text{iter}\,n}$ (which is referred to the coordinates at the beginning of the current iteration, following the concept of *Updated Lagrangian Formulation*) and the load level increment $\lambda^{\text{step}\,\mu\,\text{iter}\,n}$. It holds:

$$\boldsymbol{U}^{\,\text{step}\,\mu\,\text{iter}\,(n+1)} = \boldsymbol{U}^{\,\text{step}\,\mu\,\text{iter}\,n} + \boldsymbol{u}^{\,\text{step}\,\mu\,\text{iter}\,n} \tag{6.3}$$

and

$$\Lambda^{\text{step}\,\mu\,\text{iter}\,(n+1)} = \Lambda^{\text{step}\,\mu\,\text{iter}\,n} + \lambda^{\text{step}\,\mu\,\text{iter}\,n} \tag{6.4}$$

The definiton of the aeroelastic tangent matrix, in the framework of arc length method, could be derived using the concept of *residual*. This is now presented in detail starting from the theory of generic follower forces recalled in [2].

Both the external aerodynamic loads $\boldsymbol{L}$ and the internal forces $\boldsymbol{F}_{\text{int}}$, due to the deformation of the structure, are a function of the cumulative displacement $\boldsymbol{U}$. Moreover, the aerodynamic loads are also a function of the load level Λ. The residual $\boldsymbol{\mathcal{R}}$ is defined as the difference between the aerodynamic loads and the internal forces. If convergence has been reached, then the equilibrium is satisfied and the residual is (almost) zero.

In mathematical terms the residual (or unbalanced load) is the following:

$$\boldsymbol{\mathcal{R}}\,(\boldsymbol{U}, \Lambda) = \boldsymbol{L}(\boldsymbol{U}, \Lambda) - \boldsymbol{F}_{\text{int}}(\boldsymbol{U}) \tag{6.5}$$

which, by means of equations shown in [193, 193] becomes

$$\boldsymbol{\mathcal{R}}\,(\boldsymbol{U}, \Lambda) = \Lambda \cdot p_{\text{dyn}}^{\text{ref}} \cdot \boldsymbol{C} \cdot \boldsymbol{U} - \boldsymbol{F}_{\text{int}}(\boldsymbol{U}) \tag{6.6}$$

Assume now that the starting state is identified by load step μ and iteration n and that the goal is to drive to zero the unbalanced load evaluated at the subsequent iteration. Then, a zero finding method, and in this case a Newton's method, could be applied

leading to:

$$\begin{aligned}\mathbf{0} = &\left[\frac{\partial \boldsymbol{\mathcal{R}}\left(\boldsymbol{U},\Lambda\right)}{\partial \boldsymbol{U}}\right]^{\text{step}\,\mu\,\text{iter}\,n}\left(\boldsymbol{U}^{\text{step}\,\mu\,\text{iter}\,(n+1)} - \boldsymbol{U}^{\text{step}\,\mu\,\text{iter}\,n}\right)\\ &+\left[\frac{\partial \boldsymbol{\mathcal{R}}\left(\boldsymbol{U},\Lambda\right)}{\partial \Lambda}\right]^{\text{step}\,\mu\,\text{iter}\,n}\left(\Lambda^{\text{step}\,\mu\,\text{iter}\,(n+1)} - \Lambda^{\text{step}\,\mu\,\text{iter}\,n}\right) + \boldsymbol{\mathcal{R}}^{\text{step}\,\mu\,\text{iter}\,n}\end{aligned} \tag{6.7}$$

which is more conveniently rewritten as

$$\mathbf{0} = \left[\frac{\partial \boldsymbol{\mathcal{R}}\left(\boldsymbol{U},\Lambda\right)}{\partial \boldsymbol{U}}\right]^{\text{step}\,\mu\,\text{iter}\,n}\boldsymbol{u}^{\text{step}\,\mu\,\text{iter}\,n} + \left[\frac{\partial \boldsymbol{\mathcal{R}}\left(\boldsymbol{U},\Lambda\right)}{\partial \Lambda}\right]^{\text{step}\,\mu\,\text{iter}\,n}\lambda^{\text{step}\,\mu\,\text{iter}\,n} + \boldsymbol{\mathcal{R}}^{\text{step}\,\mu\,\text{iter}\,n} \tag{6.8}$$

With $[\ ]^{\text{step}\,\mu\,\text{iter}\,n}$ it has to be intended that the derivatives are evaluated for $\boldsymbol{U}$ and Λ relative to load step μ and iteration n. The derivatives in Eq.(6.8) are calculated by using the expression for the residual (Eq.(6.6)):

$$\begin{aligned}\left[\frac{\partial \boldsymbol{\mathcal{R}}\left(\boldsymbol{U},\Lambda\right)}{\partial \boldsymbol{U}}\right]^{\text{step}\,\mu\,\text{iter}\,n} &= \Lambda^{\text{step}\,\mu\,\text{iter}\,n}\cdot p_{\text{dyn}}^{\text{ref}}\cdot\boldsymbol{C} - \left[\frac{\partial \boldsymbol{F}_{\text{int}}(\boldsymbol{U})}{\partial \boldsymbol{U}}\right]^{\text{step}\,\mu\,\text{iter}\,n}\\ \left[\frac{\partial \boldsymbol{\mathcal{R}}\left(\boldsymbol{U},\Lambda\right)}{\partial \Lambda}\right]^{\text{step}\,\mu\,\text{iter}\,n} &= p_{\text{dyn}}^{\text{ref}}\cdot\boldsymbol{C}\cdot\boldsymbol{U}^{\text{step}\,\mu\,\text{iter}\,n}\end{aligned} \tag{6.9}$$

The definitions of aerodynamic tangent matrix $\boldsymbol{K}_{A}^{\text{step}\,\mu\,\text{iter}\,n}$ and structural tangent matrix $\boldsymbol{K}_{ST}^{\text{step}\,\mu\,\text{iter}\,n}$ are now introduced:

$$\begin{aligned}-\Lambda^{\text{step}\,\mu\,\text{iter}\,n}\cdot p_{\text{dyn}}^{\text{ref}}\cdot\boldsymbol{C} &= \boldsymbol{K}_{A}^{\text{step}\,\mu\,\text{iter}\,n}\\ \left[\frac{\partial \boldsymbol{F}_{\text{int}}(\boldsymbol{U})}{\partial \boldsymbol{U}}\right]^{\text{step}\,\mu\,\text{iter}\,n} &= \boldsymbol{K}_{ST}^{\text{step}\,\mu\,\text{iter}\,n}\end{aligned} \tag{6.10}$$

Substitution of Eq.(6.10) into Eqs.(6.9) and (6.8) leads to

$$\begin{aligned}\mathbf{0} = &-\underbrace{\left[\boldsymbol{K}_{A}^{\text{step}\,\mu\,\text{iter}\,n} + \boldsymbol{K}_{ST}^{\text{step}\,\mu\,\text{iter}\,n}\right]}_{\boldsymbol{K}_{T}^{\text{step}\,\mu\,\text{iter}\,n}}\boldsymbol{u}^{\text{step}\,\mu\,\text{iter}\,n}\\ &+\lambda^{\text{step}\,\mu\,\text{iter}\,n}\cdot p_{\text{dyn}}^{\text{ref}}\boldsymbol{C}\cdot\boldsymbol{U}^{\text{step}\,\mu\,\text{iter}\,n} + \boldsymbol{\mathcal{R}}^{\text{step}\,\mu\,\text{iter}\,n}\end{aligned} \tag{6.11}$$

where $\boldsymbol{K}_{T}^{\text{step}\,\mu\,\text{iter}\,n}$ is the aeroelastic tangent matrix obtained by adding the aerodynamic and structural contributions. As apparent from Eq.(6.11) both $\boldsymbol{u}^{\text{step}\,\mu\,\text{iter}\,n}$ and the applied load fraction $\lambda^{\text{step}\,\mu\,\text{iter}\,n}$ are unknowns in the arc length method. Different closing constraint equations could be employed, leading to different arc length meth-

ods, such as *Crisfield*, *Riks-Wempner* or *Ramm*'s (also called modified Riks) methods, (e.g., [137, 139]). As an example, application of Crisfield's cylindrical arc length method (see [139]) leads to the following constraint:

$$\left|\boldsymbol{u}^{\text{step}\,\mu\,\text{iter}\,n} + \boldsymbol{U}^{\text{step}\,\mu\,\text{iter}\,n} - \boldsymbol{U}^{\text{step}\,\mu\,\text{iter}\,1}\right|^2 = \Delta l^2 \tag{6.12}$$

where Δl has been previously fixed. Eqs.(6.11) and (6.12) give raise to a second order relation for the quantity $\lambda^{\text{step}\,\mu\,\text{iter}\,n}$. It is worth to notice that the success of one of the arc length strategies in overcoming limit points is problem dependent. In some cases some strategies perform better than others, thus it may be necessary to switch between them to track the whole response curve.

6.3.2 Validation of the nonlinear aeroelastic code

The present capability has been validated comparing results with commercial software Nastran (see [152]). The arch length techniques have also been validated for the cases of mechanical loads in recent works, i.e., [1, 2, 130].

6.4 Snap-Divergence and its Mathematical Definition

To introduce the concept of snap-divergence, consider the *pure structural case* in which only mechanical forces act. In that case is possible to define a *buckling load* obtained via eigenvalue analysis. This investigation of the stability properties could be improved by linearizing about a steady state equilibrium obtained with a fully nonlinear static analysis. However, it is also possible to define (if exists for the case under investigation) the *snap-buckling load* as the one corresponding to the true critical point, in which the structural tangent stiffness matrix becomes singular.

These definitions involve a precise mathematical event (singularity of a matrix). However, nonlinear analyses may also show responses with a progressive softening (see for example [1, 130]), in which very small load increments lead to large displacements: this is, de facto, a "practical" instability. It may be then too restrictive and unsafe to base the buckling concept on the above definition (singularity of the matrix) only. It is also true that a more general definition of instability may not be easily identified, depending on the particular problem.

If the steady aeroelastic problem is now considered, the system's tangent matrix

has also the contribution of the aerodynamics. The same considerations about the stability and singularity of the matrix apply. To distinguish this same event between the structural and aeroelastic cases, the aeroelastic instability is termed "snap-divergence" (true divergence). The word "snap" is here adopted on purpose, since historically the aeroelastic divergence was typically performed with the eigenvalue analysis, and also because of the tendency to "snap" of the configuration on verge of instability.

It may be argued that the *post-divergence* regime is completely meaningless when an aeroelastic case is investigated: after the snap-divergence instability is reached the system would naturally experience a snap and *try* to reach a state on the stable post-critical branch. However, as previously discussed, the knowledge of the static post-critical regime may give indication on bistability and associated risks as the so called "branch-jumping" instability, see for example results presented in [2].

Actually, this sudden change is inherently a dynamic phenomenon and thus, inertial forces and time-dependent aerodynamic effects must be taken into consideration to properly model the response of the structure (see [194]). Limit Cycle Oscillations can develop as discussed in [161].

6.5 Linearized Divergence Speed via Eigenvalue Approach

The classic approach to evaluate divergence speed is to solve an eigenvalue problem. The starting configuration about which a linearization is carried out can be the fundamental (undeformed) one or a deformed steady state equilibrium corresponding to the dynamic pressure $p_{\text{dyn}}^{\text{ss}}$.

The structural tangent matrix corresponding to the associated steady state (i.e., after the numerical simulations are completed and the nonlinear response has been determined up to the dynamic pressure $p_{\text{dyn}}^{\text{ss}}$) is indicated with the symbol $\boldsymbol{K}_{ST}^{\text{ss}}$. Observing that the aerodynamic tangent matrix depends on the dynamic pressure, it is deduced that the matrix corresponding to the (unknown) linearized divergence condition is:

$$\boldsymbol{K}_{A}^{D} = -p_{\text{dyn}\,D}^{\text{lin}}\,\boldsymbol{C} \tag{6.13}$$

The dynamic pressure is treated as an unknown and needs to be found. Let $p_{\text{dyn}\,D}^{\text{lin}}$ be the *candidate* dynamic pressure corresponding to the instability condition (according to the linearized eigenvalue divergence analysis). The linearized divergence speed is the

non-trivial solution (i.e., $\boldsymbol{u} \neq \boldsymbol{0}$) of the following aeroelastic equation:

$$\left(\boldsymbol{K}_{ST}^{\text{ss}} + \boldsymbol{K}_{A}^{D}\right)\boldsymbol{u} = \boldsymbol{0} \tag{6.14}$$

A non-trivial solution is found when the aeroelastic matrix, obtained by adding the structural and aerodynamic contributions, is singular. This condition is now exploited by substituting Eq.(6.13) into Eq.(6.14):

$$\left(\boldsymbol{K}_{ST}^{ss} - p_{\text{dyn}\ D}^{\text{lin}}\,\boldsymbol{C}\right)\boldsymbol{u} = \boldsymbol{0} \tag{6.15}$$

This is an eigenvalue problem. The eigenvalues represent the dynamic pressure corresponding to the linearized divergence. Only *positive* eigenvalues have physical meaning and, among them, the smallest is the relevant one.

6.6 Description of the Analyzed Joined Wing Configurations

Two configurations will be analyzed in this paper. The first one, depicted in Fig. 6.2, is a Joined Wing [152] (named *JW70*) in which the joint is not located at the tip of both wings.

The second layout (Fig. 6.3) is a PrandtlPlane-like configuration [1, 130, 162] featuring a swept-back lower wing and a swept-forward upper wing. It is named *PrP40*.

For the aerodynamic analysis, the surfaces have been discretized employing 8 to 12 elements in the chordwise direction. The total number of aerodynamic panels is then approximately between 600 and 3000 for the different cases. Convergence of the aerodynamic loads has been verified already for the coarse discretization.

The adopted material is a typical Aluminium, featuring Young's modulus $E_{\text{REF}} = 6.9 \cdot 10^7 \left[\frac{Kg}{mm \cdot s^2}\right]$ and a Poisson's ratio $\nu_{\text{REF}} = 0.33$. Both models' dimensions are selected to be consistent with the ones corresponding to wind-tunnel scaled models.

The density of the air is chosen to be the standard air density ($\rho_\infty = 1.225\, kg/m^3$) whereas the geometric angle of attack is set to 1 deg. In order to get different static conditions, the onset free-stream velocity is varied (through the parameter Λ). The aerodynamic forces change during the iterative process because the deformation induces a change of local angles of attack and the freestream velocity is also changed (through Λ).

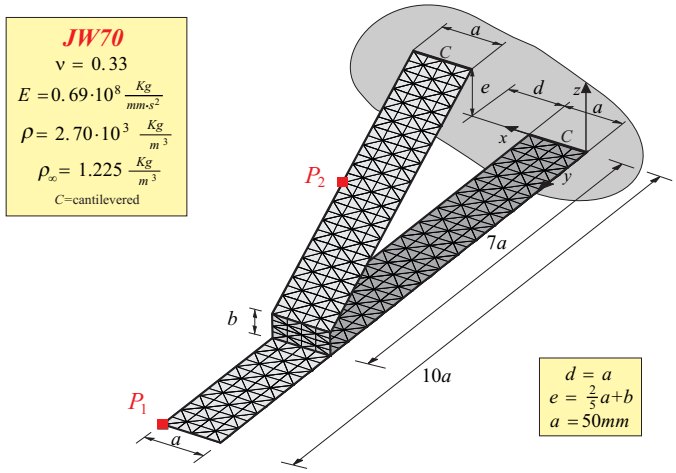

Figure 6.2: *JW70* model. The joint is located at 70% of the wing span. The thickness of the different parts of the structure is equal to 0.7 mm. The joint's height is $b = 20$ mm

.

This is taken into account by the aerodynamic tangent matrix $\boldsymbol{K}_A$ previously discussed. The aerodynamic forces are then follower forces in the sense that their magnitude depends on the structural deformation. Actual aerodynamics forces are also follower in the direction, and more refined models are widely used in literature (see [2, 161]). For a study of mechanical forces that change direction during the deformation of the Joined Wing, refer to [2].

Convergence study on the configurations has been carried out, showing that the meshes represented in Figs. 6.2 and 6.3 give results within 1% of the converged response.

6.7 Nonlinear Divergence Analysis of Configuration *JW70*

In this section the baseline configuration *JW70* is analyzed from a static nonlinear aeroelastic perspective. The stability properties are also investigated with linear capabilities (linear and linearized divergence analyses) in order to assess the reliability of classical aeroelastic computational methods. In addition to the aeroelastic simulations, pure structural investigations are also carried out. The structural response of the system subjected to both conservative and follower mechanical loads is compared with the aeroelastic analysis with the aim of providing indications on the appropriateness of using mechanical loads to mimic real aerodynamic forces (see also [195]).

The static aeroelastic response is obtained by gradually increasing the aerodynamic speed V_∞. The typical displacement-velocity curves (see Figs. 6.4 and 6.5) are

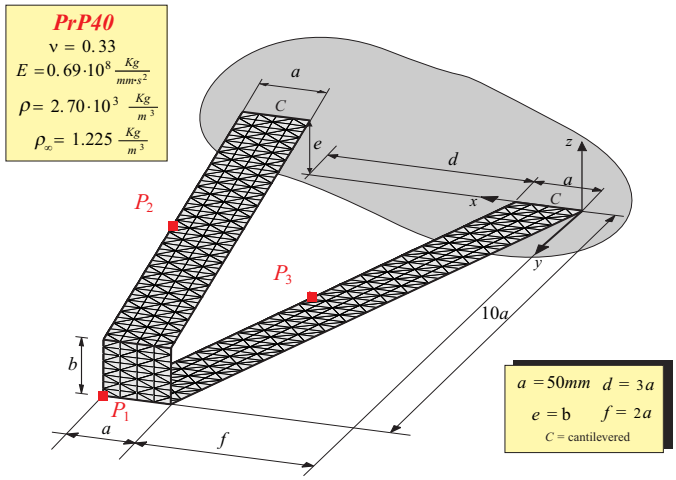

Figure 6.3: PrandtlPlane Joined Wing model *PrP40*. The joint is located at the tip of the wings. The thickness of the different parts of the structure is equal to 1.0 mm. The joint's height is $b = 40$ mm.

then obtained for point P_1 located at the tip of the lower wing and for point P_2 positioned at the mid-span of the upper wing (see Fig. 6.2 to graphically localize these points).

It is clear that a snap-divergence phenomenon occurs: with reference to Figs. 6.4 and 6.5, an infinitesimal increment of speed at state B would determine an impossibility to find a continuously adjacent static equilibrium configuration. On the contrary, the new equilibrium point would be C, characterized by the same flow speed of state B which is the *snap-divergence speed* V_∞^{CR}, equal to 34.1 m/s. Notice that, at state B the *system tangent matrix* is exactly singular, thus, the instability has a well defined mathematical characterization.

As already discussed in [2], snap instabilities are inherently dynamic phenomena. In the case of conservative mechanical forces, a snap from state B would physically lead to state C (after a transient has been extinguished through structural damping, and if the forces remain constant throughout the process). However, when aerodynamic forces are considered, this may not be the case. The dynamical system in fact, may diverge to other-than-fixed-point kind of *attractors*. An example could be the phenomenon of limit cycle oscillation (LCO), in which an infinitesimal small perturbation from a steady state (fixed point) may lead to a closed periodic pattern (see for example [161]). To check this option a linearized flutter analysis is performed with the tool described in [193, 196], and it is ascertained that flutter speed is higher than snap-divergence one's.

The configurations at impending snap-divergence (state B) and the one immedi-

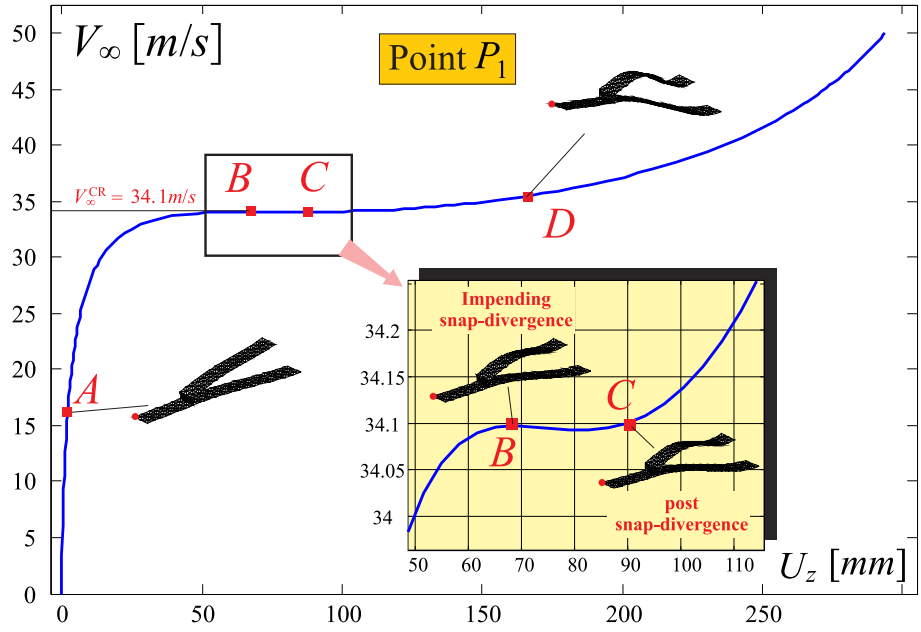

Figure 6.4: Configuration JW70: flow speed V_∞ (in m/s) versus cumulative vertical displacement U_z (in mm) for lower wing's tip point P_1. The flow is directed along x-axis, and the geometry is rotated of 1 deg in order to create an initial angle of attack. A zoom of the critical point area is provided.

ately after it (state C) are reproduced in Fig. 6.6. Moreover, Fig. 6.7 shows the span-wise distribution of lifting forces and twist distribution, for different flow speeds (corresponding to the points A through D in Figs. 6.4 and 6.5).

The sectional lifting forces of Fig. 6.7 are evaluated as the sum of the aerodynamic loads projected on the structural nodes lying on the same cross-section. The geometrical twist of each cross section is calculated considering the up- and down-stream nodes on the same station at fixed spanwise coordinate, and simply evaluating the geometrical angle between the line joining these two points and the x-axis (the deformation in the section plane may be considered of second order).

6.7.1 Physical interpretation of the aeroelastic response

Fig. 6.7 could be used to attempt a physical interpretation of the aeroelastic response as follows. Initially both the wings are producing lift, however, due to the joint connection, the upper wing experiences an increase of angle of attack (positive torsion), whereas for the inner part of the lower wing, the change in torsion is relatively

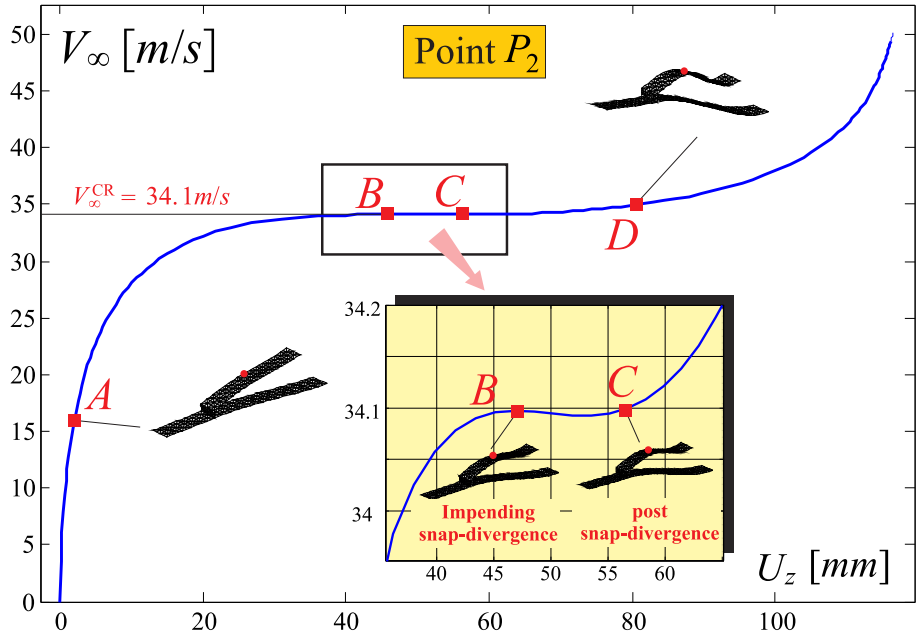

Figure 6.5: Configuration $JW70$: Flow speed V_∞ (in m/s) versus cumulative vertical displacement U_z (in mm) for upper wing's midspan point P_2. The flow is directed along x-axis, and the geometry is rotated of 1 deg in order to create an initial angle of attack.

smaller (see Fig. 6.7(a)). This coupling comes from the geometry: the upper wing has a negative sweep angle and, thus, a vertical displacement of the tip produces both a bending and a positive torsion. However, the upper wing increment of angle of attack is partially counteracted by the lower wing which shows a smaller increment in twist. This coupling is more pronounced when deformation takes place. Notice that, even for not highly deformable Joined Wings, the coupling and consequent load redistribution has a profound impact on the design since the trim conditions are affected.

When the snap-divergence velocity is reached the structural stiffness of the system

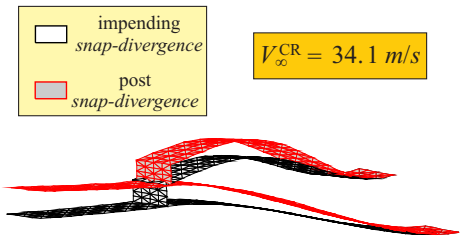

Figure 6.6: Configurations at states immediately preceding and following the snap-divergence (states B and C in Fig. 6.5).

cannot efficiently resist the aerodynamic actions. There is a general large increment of the section twist, especially localized in the upper wing, as it can be verified in Figs. 6.7(b), 6.7(c), and 6.7(d).

6.7.2 Comparison between eigenvalue and nonlinear divergence analysis

This study assesses how reliable the eigenvalue approach (as described in Section 6.5) is when geometric structural nonlinearities need to be taken into account in the calculation of the divergence conditions (V_∞^{ss}). Different starting steady states are considered when linearized eigenvalue analyses are carried out. That is, the divergence speed is calculated using the classical eigenvalue approach but the structural stiffness matrix used for the numerical evaluations is the one corresponding to a configuration relative to a flow speed between 0 and 33.5 m/s (Fig. 6.4 can be used to locate the steady states configurations in the speed-displacement response curve).

Results in terms of predicted divergence speed are depicted in Fig. 6.8. The linearized divergence speeds $V_{\infty D}^{\text{lin}}$ are plotted against the freestream velocities (V_∞^{ss}) associated with the configurations chosen for linearization. As deduced from Fig. 6.8, the linearization performed about the undeformed configuration provides a divergence speed $V_{\infty D}^{\text{lin}}$ which is about 50% larger than the true static instability condition identified by the snap-divergence speed V_∞^{CR}. More than the extent of the discrepancy, it is important to observe that the error is not conservative because the speed at which the instability occurs is overestimated.

To have more reliable results one might think to track the nonlinear response until a "reasonable" value of the speed is reached, and then linearize about that steady state configuration when doing the eigenvalue analysis. However, a higher freestream velocity about which the linearization is performed implies a higher computational cost, since a larger portion of the nonlinear response needs to be tracked. Unfortunately, from Fig. 6.8 it is clear that there are practically no accuracy improvements for the linearized divergence speed prediction, until very close to the snap-divergence speed. Notice how, graphically, there is a region, bounded by the condition $V_{\infty D}^{\text{lin}} = V_\infty^{\text{ss}}$, for which the configurations is not stable.

Summarizing, the eigenvalue approach for predicting the divergence speed appears to be *unreliable* (large errors compared to the true static instability velocity) and

unsafe (it overestimates the critical speed). It could be reliable only if all the response curve to almost the snap-divergence speed is tracked, which is meaningless since the cost would be of the same order as for a complete nonlinear analysis.

As a consequence, linear divergence analysis is not amenable to be used as a preliminary design tool (multidisciplinary design optimization) for Joined Wings.

6.7.3 Mechanical and aerodynamic forces: a comparison

The use of structural loads may be an interesting option to readily have a first guess estimate of the deformation given by the aerodynamic loads, or also to experimentally apply the forces to the structure. In this regard, past computational and experimental work on Joined Wings studied the nonlinear response due to mechanical loads (see [83, 195]). It is then important to investigate such an approach, and in particular, assess whether it is conservative.

Two mechanical types of loadings are then considered. The first class is represented by a load-per-unit-of-surface (pressure) always vertically directed (*conservative* mechanical loads). The second type is a pressure load which remains perpendicular to the structure during the deformation process (*follower* mechanical loads). In both types of load the nominal value of the pressure is $p = 0.55125\, Kg/(mm \cdot s^2)$, corresponding to the dynamic pressure of air (at sea level) with a speed of $30\, m/s$. Refer to Figs. 9-12 in [158] for the detailed responses.

To correlate the predictions of the mechanical and aerodynamic loads cases the *global vertical load* (lift) is chosen as a comparison parameter. Moreover, the resultant of a force per unit area of $0.55125\, Kg/(mm \cdot s^2)$ directed along z-axis is chosen as the nominal vertical load. The amount of lift produced/acting on the system at a given state is finally written in dimensionless form by dividing it by the lift calculated as described above. The dimensionless parameter Λ_{lift} is then defined, and plays a similar role as the one played by Λ earlier adopted. Notice that, $\Lambda_{\text{lift}} = \Lambda$ for the conservative mechanical forces because they are always directed along z.

Fig. 6.9 compares the responses when mechanical and aerodynamic loads are applied to the structure. The same trend is observed for a significant portion of graph. In other words, mechanical conservative loads may be used to assess the stiffness of the structure at least up to a certain level (here with stiffness it is qualitatively intended the ratio of the generated lift to the displacement/deformation of the structure).

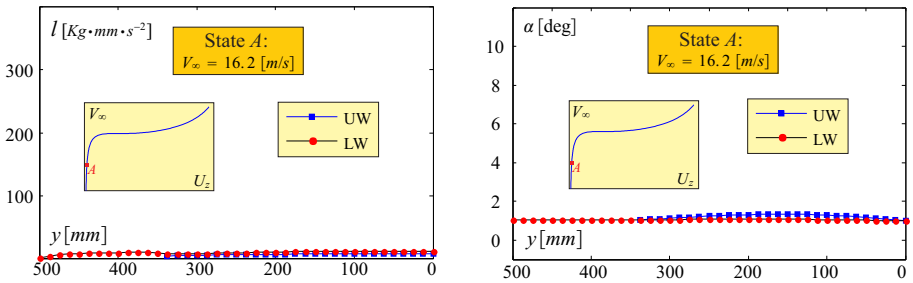

(a) Case with $V_\infty = 16.2\,m/s$ (state A in Fig. 6.4)

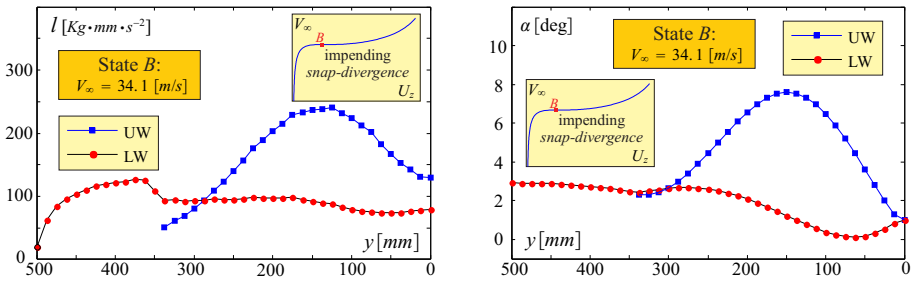

(b) Case with $V_\infty = 34.1\,m/s$, impeding snap-divergence (state B in Fig. 6.4)

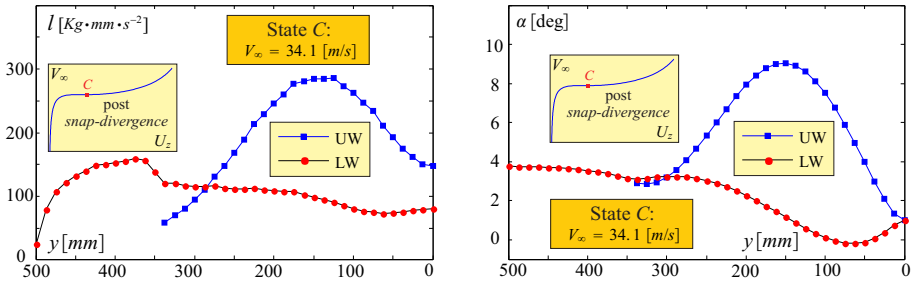

(c) Case with $V_\infty = 34.1\,m/s$, post snap-divergence (state C in Fig. 6.4)

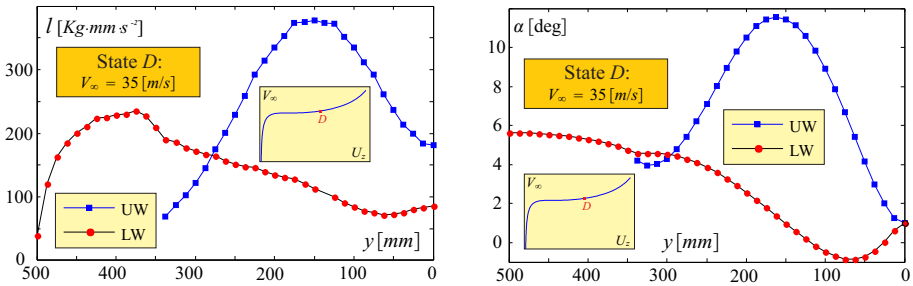

(d) Case with $V_\infty = 35\,m/s$ (state D in Fig. 6.4)

Figure 6.7: On the left column: sectional lift distribution on the wings. On the right column: geometrical twist of the sections. Results are shown for different flow speeds, as indicated in the figure. All the plots refer to both the upper (UW) and lower wings (LW).

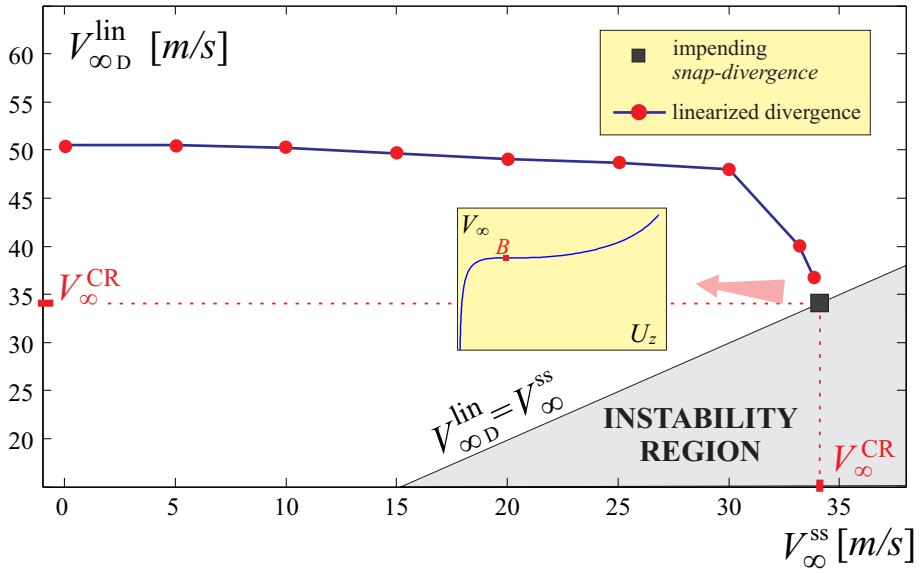

Figure 6.8: Outcome of linearized divergence analysis: on the abscissa the speeds associated with the deformed configuration chosen for linearization are depicted (i.e., V_∞^{ss}), whereas, on the ordinate, the divergence speeds obtained via eigenvalue approach are shown (i.e., $V_{\infty\,D}^{\mathrm{lin}}$). The shaded region is bounded by $V_\infty^{\mathrm{ss}} = \boldsymbol{V}_{\infty\,D}^{\mathrm{lin}}$, which is the condition for snap-divergence to occur.

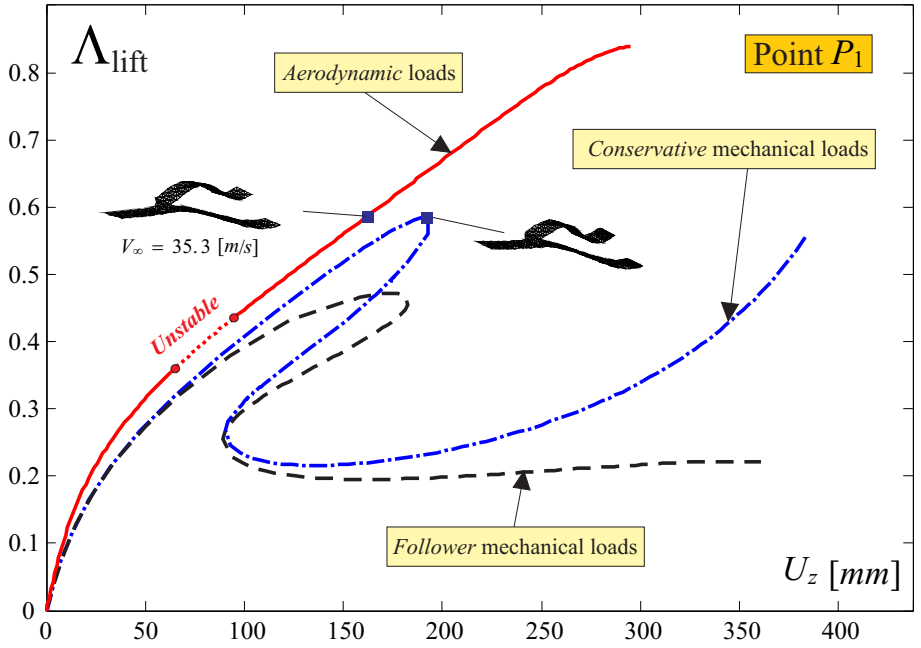

Figure 6.9: JW70 configuration: normalized load level Λ_{lift} versus cumulative vertical displacement U_z for lower wing's tip point P_1 when conservative and follower mechanical forces and aerodynamic loads are considered.

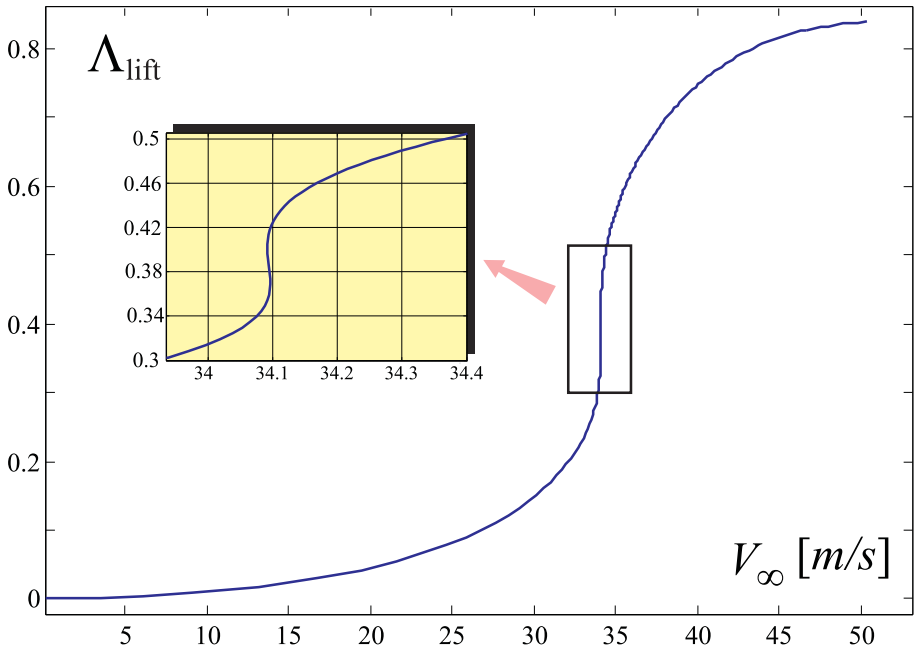

Figure 6.10: *JW70* configuration: normalized load level Λ_{lift} versus flow speed.

At first glance, the aerodynamic case may even look more favorable, since an appropriate lift may be achieved without incurring in loss of stiffness (as it happens for both the conservative and follower mechanical load cases as consequence of the snap-phenomenon). However, this graph hides an important difference between the aerodynamic and mechanical loads: the aerodynamic forces are associated to a flow speed. Although the response for the aerodynamic case looks smooth and far from any instability, actually, in practice, the region $\Lambda_{\text{lift}} = [0.3,\ 0.5]$ corresponds to an *unstable* condition (see for example Fig. 6.4 where the snap-divergence is depicted). As it could be inferred inspecting Fig. 6.10, a small perturbation/variation of the flow speed produces relatively large increments of the angle of attack of the structure with associated large increments in the lift. This emphasizes that even if mechanical forces may sometimes give good indication of load-displacement response, they cannot provide inherent information on the real stability properties of the system.

Loading the Joined Wing with follower mechanical forces represents a really penalizing test. When loaded, the structures undergoes large displacements with the effect that the surface normals have a diminishing vertical component. Acting the (follower) pressures perpendicularly to the surface, the lift begins to decrease after a critical deformation.

For a more accurate analysis, a more advanced aerodynamic model should be adopted [161]. In fact, with the present capability, the aerodynamic forces are oriented perpendicularly to the initial configuration, changing their magnitude (but not their direction) with progressive deformation of the structure [193]. The severity of a follower structural load approach is then expected when compared with the present aerodynamic capability.

6.8 Nonlinear Divergence Analysis of *PrP40* Configuration

The configuration *PrP40*, whose geometrical and material details are described in section 6.6 and depicted in Fig. 6.3, is here considered.

As for the *JW70* configuration, stability properties will be assessed with the aid of linearized divergence eigenvalue analysis. Moreover, the nonlinear aeroelastic response will be compared to results presented in [1, 2], where the same *PrP40* configuration undergoes mechanical structural conservative and follower loads respectively. As a final task a discussion about divergence, bending/torsion coupling, and overconstrained nature of Joined Wings will be given. To support the discussion, a further analysis will be introduced, i.e., the response of *PrP40* with unswept wings.

The aeroelastic response for points P_1 and P_2, on the lower wing tip and upper wing mid-span respectively (as depicted in Fig. 6.3), is shown in Fig. 6.11. It is interesting

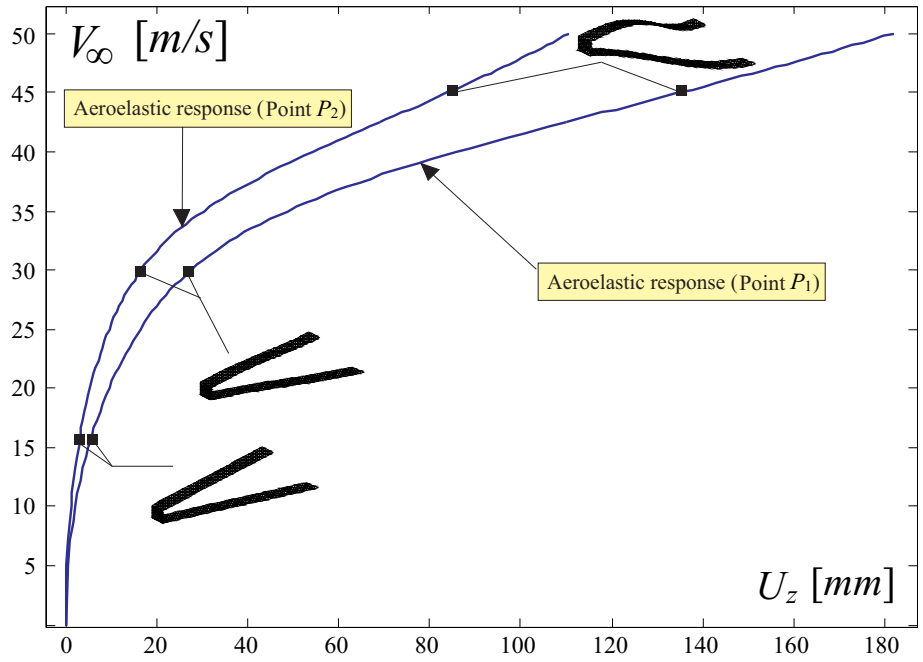

Figure 6.11: Flow speed V_∞ (in m/s) versus cumulative vertical displacement U_z (in mm) for lower wing tip point P_1 and upper wing midspan point P_2 of the joined-wing layout *PrP40*. The flow is directed along x-axis, and the geometry is rotated of 1 deg in order to create an initial angle of attack.

to observe that *no* snap-instability phenomenon is present. From a practical perspective,

however, there is a consistent loss in stiffness after the speed of $30\,m/s$.

6.8.1 Divergence analysis via eigenvalue approach

Different steady states about which the linearization is carried out, are considered. The results are reported in Fig. 6.12. If the softening tendency seen starting

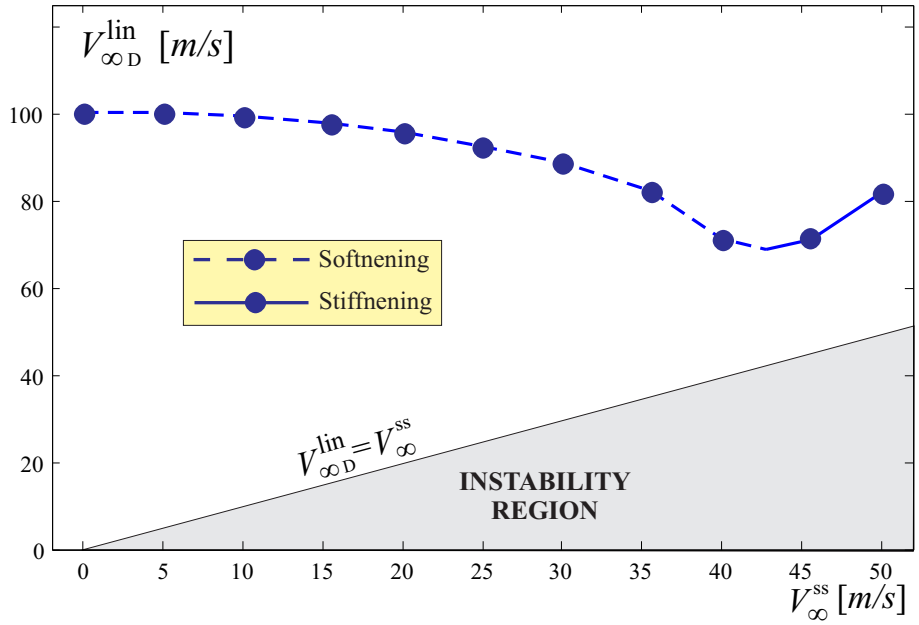

Figure 6.12: Outcome of linearized divergence analysis: on the abscissa the speeds associated with the deformed configuration chosen for linearization are depicted (i.e., V_{∞}^{ss}), whereas, on the ordinate, the divergence speeds obtained via eigenvalue approach are shown (i.e., $V_{\infty\,D}^{\mathrm{lin}}$). The shaded region is bounded by $V_{\infty}^{\mathrm{ss}} = \boldsymbol{V}_{\infty\,D}^{\mathrm{lin}}$, which is the condition for snap-divergence to occur.

from speed of $15\,m/s$ (refer to Fig. 6.11) is not considered as critical from a practical perspective, then the linearized divergence analysis correctly suggests that no stability issue would arise in the range of considered speeds. If the linearization is carried out for larger freestream velocities, then it is possible to observe a trend of decreasing predicted divergence speeds (see Fig. 6.12). This behavior suggests that a softening is in place.

6.8.2 Mechanical and aerodynamic forces: a comparison

References [1, 2] discussed the structural nonlinear analysis of the configuration *PrP40* subjected to mechanical loads and focused on the snap phenomenon. However,

such an instability was not detected in the present work when aerodynamic forces were applied. In an effort of further investigating the differences produced by the application of loads of different nature (mechanical and aerodynamic forces), it is convenient, for a quantitative comparison, to define a nominal force which will be used for normalization purposes. Following the same logics adopted for the *JW70* case, a vertical force per unit of area $p = 0.55125\, Kg/(mm \cdot s^2)$, corresponding to the dynamic pressure of air (at sea level) with a speed of $30\, m/s$, is applied and its resultant is adopted as a reference force to define a dimensionless parameter Λ_{lift}. That is, Λ_{lift} is introduced as the ratio of the global vertical (along z-axis) force due to mechanical/aerodynamic forces to the above defined reference vertical force. For the case of conservative loads presented in [1], the forces are always vertical, thus, there is equivalence between Λ and Λ_{lift}.

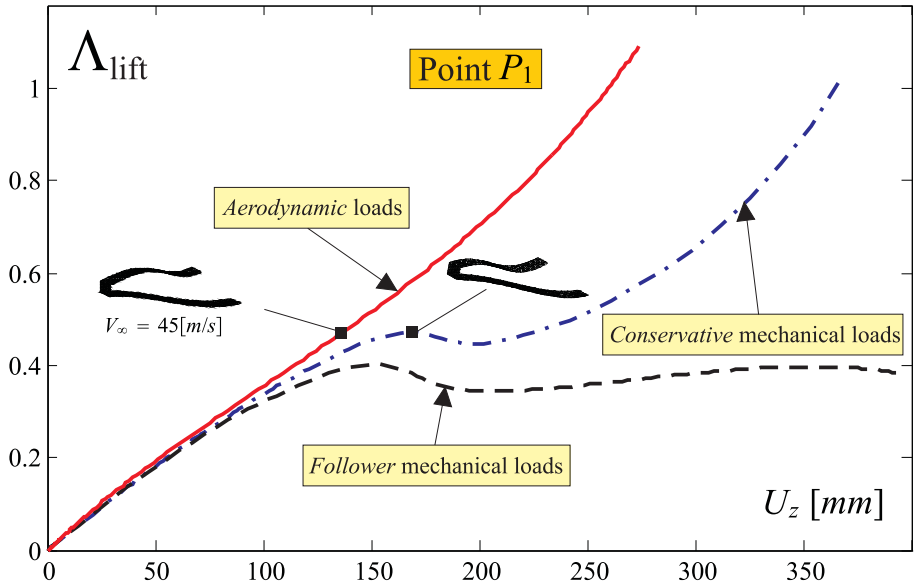

Figure 6.13: Normalized load level Λ_{lift} versus cumulative vertical displacement U_z for lower wing's tip point P_1 of the joined-wing layout *PrP40* when conservative, follower and aerodynamic loads are applied.

The normalized curves are plotted in Fig. 6.13 for the point P_1 (the tip of the lower wing) in terms of vertical displacement against the vertical load level Λ_{lift}. For the follower case (results presented in [2]) besides the snap-buckling, there is also a loss in capacity of producing vertical forces due to the progressive bending of the wing, (the normals to the finite elements assume slowly a predominant horizontal direction). On the other hand, the aerodynamic case shows an increasing ability to produce lift with

the deformation.

Effect of aerodynamic forces: physical interpretation

If the discussion reported in [1,130,162] is recalled, the configuration undergoing an instability phenomenon showed a specific deformation pattern, in which the upper wing presented a more pronounced tendency to bend downward, as opposed to the stable cases. Closely inspecting the configurations for the present case (see Fig. 6.13), it is evident that, when aerodynamic forces are acting, the upper wing has a tendency to present an upward bending of the mid-section. Thus, the aerodynamic loads are distributed in such a way to favor this pattern and this is demonstrated in Fig. 6.14, where the projections (in a variational sense) of aerodynamic forces to the structural nodes are shown. Notice that, for clarity purposes, the forces are not scaled with their actual value.

For low speed/deformations, these loads are distributed almost uniformly, however, for higher speeds they are mainly concentrated on the mid-section of the upper wing, where the bending/torsion increases the local angle of attack.

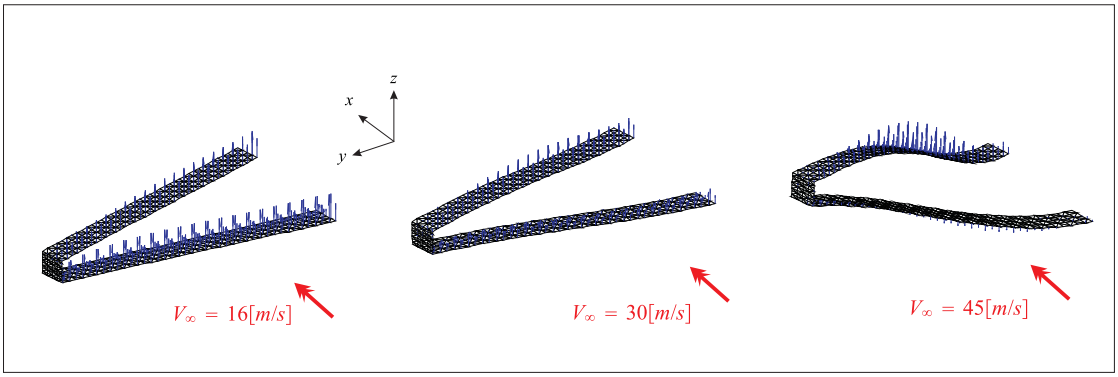

Figure 6.14: Deformations at different flow speeds. Also the correspondent aerodynamic load distributions (not scaled) are depicted.

To further investigate the underlying physics, the sectional lifting forces as well as the twist of the sections are depicted in Fig. 6.15. It could be observed the initial progressive reduction (increase) in geometrical twist for the lower (upper) wing, due to particular bending-torsion coupling associated with back (forward)-sweep angle of the wing (see Fig. 6.15(a)). This variation of twist is more pronounced in the mid-span area. The aerodynamic loads are very sensitive to variation in twist, thus this deformation

promotes a progressive reduction (increase) of loads acting on the lower (upper) wing. This effect is even larger than the mutual aerodynamic induction, which actually tends to favor an increase of lift of the lower wing (up-wash) and viceversa, a decrease for the upper wing (down-wash). In fact, in Fig. 6.15(b) it is clearly shown that the lower wing carries a smaller portion of the overall lifting forces, and undergoes a consistent decrease of the geometric twist angle. For higher speed, e.g. Fig. 6.15(c), the lower wing could even reach situations of a downforce production (no practical indications on the actual design of Joined Wings is implied on this regard; however this model gives qualitative information on the large increments of loads on the upper wing). Being the twist angle increments concentrated in the mid-span area, the lift distribution for the upper wing is approximately more concentrated in the same region, promoting then the final configuration with the upper wing presenting an upward bending.

For this particular configuration, results suggest that the usage of nonaerodynamic forces in order to study the static structural response of Joined Wings may lead to penalizing results, especially when follower mechanical forces are used.

Before further proceeding, it may be recalled that for the present aerodynamic model the direction of the loads remains fixed with the initial configuration. Thus, the deformations drive a change in the entity of the aerodynamic actions, but not in their direction. That said, a question is still posed on the opportunity to use follower mechanical loading in order to model aerodynamic forces, as it has been common practice. In this regard, a more definitive answer can be given using a higher order aerodynamic solver (see [161]).

It is indeed true that using mechanical loads has been an appropriate choice in the preliminary steps when exploratory analyses were needed and the instabilities associated with these novel configurations were first brought to light [1, 2, 130]: this approach has been crucial not only to understand as much as possible the snap phenomenon from a physical point of view, to predict it, and to understand how to avoid it, but also to reveal possible complex scenarios such as detached static equilibrium branches.

If a more decisive conclusion on the appropriateness of using mechanical loading for experimental purposes is needed, then the distribution of loads over the wings should at least qualitatively resemble the real case. This was discussed in section VIII, subsection C of reference [158], and is here not reported.

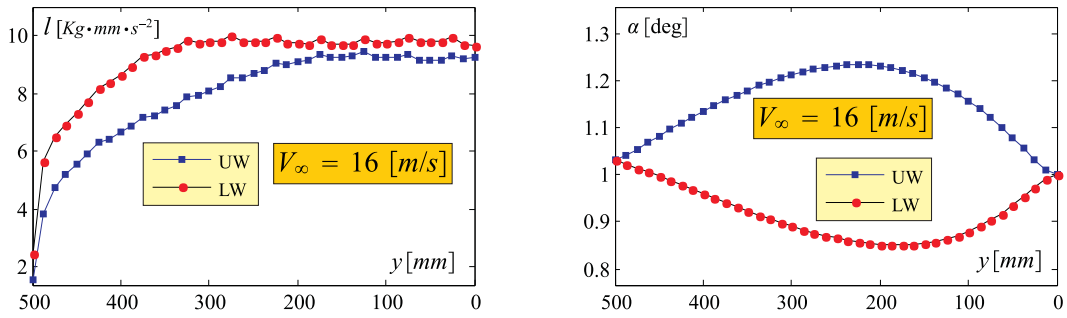

(a) Case with $V_\infty = 16m/s$

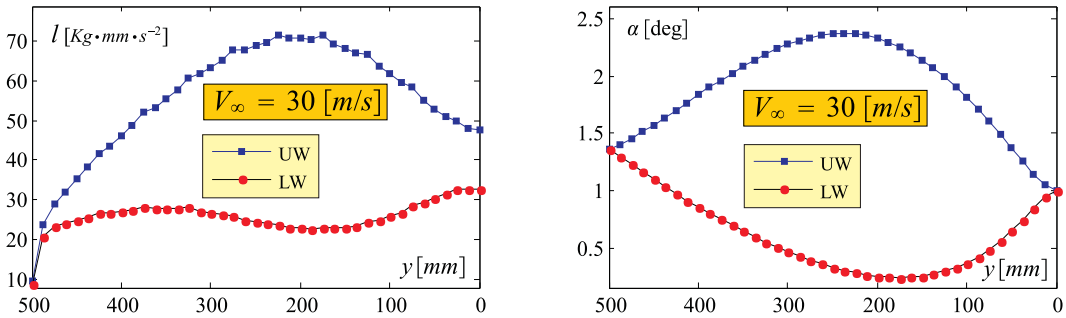

(b) Case with $V_\infty = 30m/s$

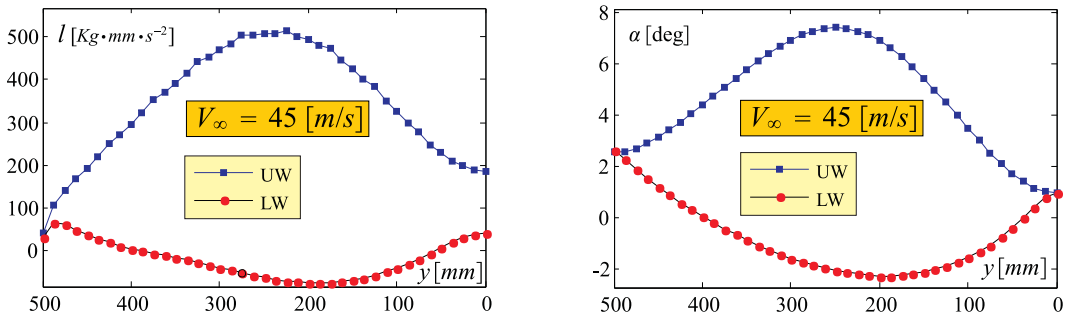

(c) Case with $V_\infty = 45m/s$

Figure 6.15: Sectional lift distribution on the wings. On the right column: geometrical twist of the sections. Results are shown for different flow speeds, as indicated in the figure. All the plots refer to both the upper (UW) and lower wings (LW).

6.8.3 Effects of bending/torsion coupling and overconstrained nature of Joined Wings: physical interpretation

Effects of the bending/torsion coupling were tackled in [130, 162] for the case of pure structural loading. With reference to those works, both geometrical (sweep angle) and material (composites) coupling were examined, observing a very strong effect on the stability. Furthermore, in the most complicated cases it was difficult to make any prediction and fully understand the underlying physics. For example, changing fibers direction, and thus acting on the coupling at material level, it was possible to have responses having or not snap-buckling phenomena.

In the presence of aerodynamic forces, there is a very strong dependence on the shape of the configuration, especially on the twist distribution. Thus the overall sensitivity to the deformation is now enhanced. As a consequence, bending/torsion coupling plays a key-role in determining the response.

Traditionally, one of the use of composite materials (aeroelastic tailoring) has aimed to exploit the advantage of this coupling in order to avoid instability phenomena as, for example, aeroelastic divergence. However, when Joined Wings are considered, the situation is more complicated by the overconstrained nature of the system, which opens the door to a new scenario.

In the previous sections it was observed that the coupling due to the geometry (sweep angle) was responsible of a tendency of concentrating the lifting actions in the mid-span region of the upper wing. In fact, a negative (positive) sweep angle promotes an increase (decrease) of twist as consequence of a bending action. Since the system is overconstrained (the wings are joined at the tip) the two different tendencies are mitigated, in the sense that having the twist angle to be approximately the same at the tip (this is true because the joint is small and could be thought as rigid), the relative increase (decrease) of twist is counteracted, especially in that region, see e.g. Fig. 6.15.

This particular redistribution of twist and loads was thought as being the main *anti-snap* mechanism. To demonstrate it, a particular configuration employing the same geometrical and material properties of *PrP40* but having unswept wings is now studied. Results of the investigation are shown in Fig. 6.16. The graphs clearly show a snap-divergence occurrence. The analysis completely supports the role played by bending/torsion coupling in preventing snap-divergence through a redistribution of the loads.

Consider now the swept *PrP40* layout, and suppose a more uniform load distri-

bution is sought. One may think to exploit the anisotropic properties of a composite material (coupling at material level). An immediate action would be to design/fine-tune each wing separately. Within this perspective, the coupling introduced through the composite material should ideally counteract the geometric coupling, thus, a positive (negative) coupling is sought for the lower (upper) wing. In other words, to avoid a local decrease in lift on the lower wing, a tendency that favours a positive twist for a bending deformation is needed. And viceversa for the upper one. However, this is where effects of the overconstrained system come into play: the joint transfers the actions, and the wanted/expected result may not be easily achieved.

Summarizing, the importance of structural geometric nonlinearities and the over-constrained nature of the system turns the design in a really challenging one, since actions that may arise spontaneously for addressing a particular issue in a *wanted* direction on a particular wing, may end up creating other unexpected consequences. More investigations on this regard will be presented in future works.

6.9 Conclusions

In the framework of Joined Wings and for the first time, this work introduced the concept of *snap-divergence* as the condition at which the aeroelastic tangent matrix becomes singular, and compared the results with linearized divergence speeds obtained via eigenvalue analysis.

Two types of Joined Wings were investigated. The first one (named $JW70$) had the joint located at 70% of the wing span. The second one (named $PrP40$) was a PrandtlPlane-like wind tunnel model with the joint located at the tip of the wing.

Numerical analyses showed that $JW70$ experienced snap-divergence. Linearized divergence evaluations, about steady states corresponding to different freestream velocities, were also conducted, showing that for the $JW70$ the eigenvalue approach is not reliable and overestimates the speed at which the instabilities occur (unsafe). The linearized divergence speed was close to the actual snap-divergence speed only for steady states near to the true unstable (snap-divergence) point.

A comparison of the response of the system subjected to aerodynamic, conservative, and follower loads was also carried out for the configuration $JW70$. The response obtained with aerodynamic loads was not showing any abrupt loss in lifting capacity, as it happened for the two mechanical cases (for these last cases this loss in load carrying

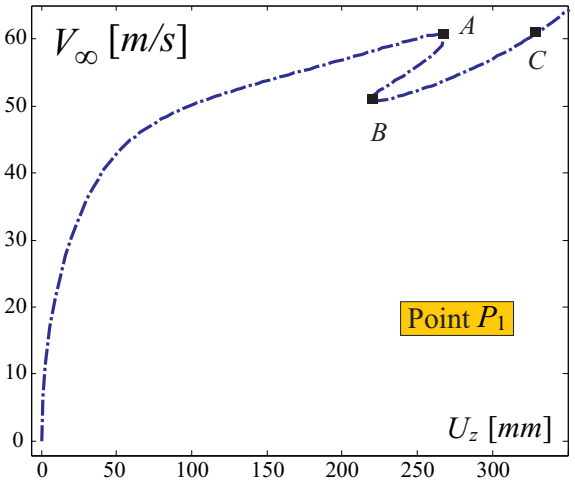

(a) Speed vs Vertical displacement of the tip.

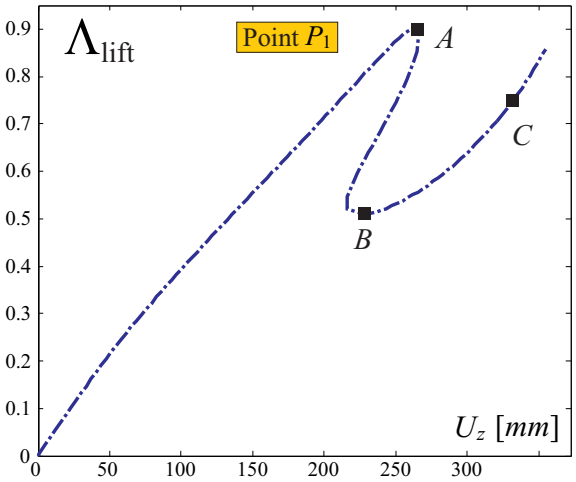

(b) Lift load level vs speed.

Figure 6.16: Flow speed V_∞ (in m/s) versus cumulative vertical displacement U_z (in mm) for lower wing tip point P_1 of the unswept version of joined-wing layout *PrP40*. The flow is directed along x-axis, and the geometry is rotate of 1 deg in order to create an initial angle of attack.

coincides with the snap condition). Thus, in contrast with what verified above about snap-divergence, one may have erroneously concluded that the aeroelastic response was not associated to any form of instabilities. The conceptual error is that, trying to quantify the static deflections to an applied load, aeroelastic instabilities cannot be taken into account. Thus, mimicking aeroelastic loads with mechanical forces should be carefully meditated upon.

The second analyzed joined-wing configuration, the $PrP40$, did not experience snap-divergence. However, from the system's response it was possible to notice a softening followed by a stiffening without a true mathematical snap-divergence occurrence. The corresponding linearized divergence, obtained with an eigenvalue approach, showed its minimum value at the end of the softening region.

Aerodynamic load distributions due to the aeroelastic deformation promoted an upward bending of the upper wing, a pattern that was noticed in [1,130] for PrandtlPlane-like configurations not incurring in buckling instability. This last example demonstrated that the overconstrained and nonlinear response of a Joined Wing can also have positive effects on the stability properties, if properly understood. This cannot be conclusive because of the simplified wind tunnel-like models presented in the study and the focus on static analysis. But the study gave indications on what the challenges and opportunities that these Joined Wings configurations represent.

Chapter 6, in part, is a reprint of the conference paper: "*Post-Critical Analysis of Joined Wings: the Concept of Snap-Divergence as a Characterization of the Instability*, AIAA 2013-1559." The dissertation author was the primary investigator and author of this paper. Coauthors were Luciano Demasi and Federica Bertuccelli.

Chapter 7

Phenomenology of Nonlinear Aeroelastic Responses of Highly Deformable Joined-wings Configurations

This chapter is a partial reproduction of the following paper:
Phenomenology of Nonlinear Aeroelastic Responses of Highly Deformable Joined Wings, Advances in Aircraft and Spacecraft Science, An International Journal, *In press*, 2014.

7.1 Introduction

THERE is currently great interest in innovative aircraft configurations. Among them, joined-wing concept [9, 10] has captured the attention as a possible candidate for the airplane of the future. However, it was argued and also demonstrated that a reasonably accurate conceptual/preliminary design is hard to be pursued due to inherent structural nonlinearities that may invalidate the results obtained with fast lower-fidelity tools, which are a necessity when exploring the large parameter's space typical of the early design stages. For example, references [1, 60, 130] showed non-negligible differences when comparing structural responses obtained with linear and nonlinear capabilities. As a consequence, consolidated design strategies and tools developed in decades, and effectively used by the industry, have to be reviewed. This represents one of the major

barriers to the development of Joined Wings [11].

The need to include these structural nonlinearities early in the design has pushed the researchers to try to achieve computational efficiency with reduced order models [13, 14]. However, results in this direction have not been quite encouraging. Some recent results are shown in references [15, 16].

The situation outlined in reference [2] goes well beyond a bad prediction of the critical condition. It is in fact shown that, bi-stability is possible and thus, catastrophic branch-jumping may eventually arise well before the static limit condition is reached. The only tool to detect such regions is a nonlinear full post-critical analysis (branch tracking). Actually, this may not be enough to plot the complete static equilibrium diagram: in reference [197] *isola*-type of bifurcations are shown.

When assessing joined-wing behaviour from a static aeroelastic perspective, similar problems were noticed [158] in terms of presence of bi-stable regions, and the snap-divergence concept was introduced. The strong structural nonlinearities have demonstrated to be dominant also for small angles of attack and attached flow, which can be considered linear.

However, a complete scenario of the aeroelastic properties may be sketched only by nonlinear dynamic investigations. To the best of authors' knowledge, nonlinear aeroelastic dynamic analysis was pursued only in a few efforts, i.e. references [152, 198]. The first of these preliminary studies showed how the flutter speed prediction varied when using a nonlinear modelling of the structure, whereas the second studied a limit cycle oscillation.

The effort of the present paper is in the direction of showing, studying and gaining insight into the dynamic aeroelastic phenomena inherent to these configurations, and which have potential impact on the design of Joined Wings.

7.2 Contribution of the Present Study

The numerical investigations presented in references [1, 2, 130, 158, 162] characterized the response of Joined Wings on a conceptual level. In particular, a snap-instability was first found when statically loading the structure with mechanical forces. The occurrence of such kind of instability (saddle-node bifurcation, refer to [178] for more details) was also observed when mechanical forces of a follower type or aerodynamic loads were considered. For the true aeroelastic case, the static instability was named

snap-divergence, in order to resemble the true snap-phenomenon that was arising in the pure mechanical case, even if a real snap may practically not occur due to the nonconservative nature of aerodynamic forces. One of the contributions of this paper is the study of this phenomenon from a dynamic point of view: after assessing, by means of a series of linearized frequency-domain analyses, that the flutter speed is higher than the snap-divergence one, the true dynamic response will be shown.

In reference [158] the *snap-divergence* was compared to the traditional divergence analysis, performed through an eigenvalue analysis about particular configurations (usually the undeformed one). Discrepancy between the critical speeds predicted by these two approaches was substantial. Moreover, the traditional eigenvalue approach was overpredicting the divergence speed. It is then expected a mismatch also between flutter speeds evaluated by means of linear and nonlinear flutter analyses. This will be shown to be important and to have a similar trend as the one found for the divergence analysis: linear tools overpredict the flutter speed, at least for the considered configurations. The above comparison is further augmented by considering different damping ratios and by incorporating time domain analyses.

Assessment of flutter speed gives a local information about loss of stability (Hopf's bifurcation), however, does not provide a picture of what happens in the post-critical region (see the works cited in reference [194] for a comprehensive literature review). With the aid of different time-domain capabilities LCOs are shown. For the Sensorcraft-like case, it is found an asynchronous motion between the outer and inner part of the lower wing: while the inner part moves in a wave-like pattern, the outer part has a small localized oscillation during the ascending or descending portion of the periodic motion.

A peculiarity of some joined-wing configurations is that, for higher speed, further bifurcation phenomena as *period doubling* [178–180,194] occur. Moreover, loss of periodicity can also be observed when speed is further increased, suggesting that a transition to chaos may be in place. On the other hand, for other joined-wing layouts experiencing an LCO, increasing the speed may have the opposite effect, leading to a stable state.

A very important and often neglected fact is the level of confidence that should be given to solvers employed for investigating the aeroelastic problem. A first differentiation is made by frequency domain and time domain tools. In some of the present numerical experiments both of these techniques are used. For the time domain approach, different options are provided. However, some preliminary theoretical discussions are

necessary. For example, studies on delta wings showed that when the structural nonlinearities are important they may also drive the limit cycle oscillation much more than the aerodynamic effects do. References [199–201] are a good example: the response was mainly driven by the structural nonlinearities. Considering the strongly nonlinear (on the structural side) response of Joined Wings, it is then natural to investigate under which conditions the structural geometric nonlinearities play an important role in the development of limit cycle oscillation, which may appear even for a completely attached flow and linear aerodynamics. Even within these reasonable assumptions there are different level of approximations. In this paper effects of load/displacements transferring methods (splining, [202], meshless [203]), different way of distributing the aerodynamic singularities (on an undeformable reference plane or attached to the body) as well as modelling of the wake (rigid or free) are evaluated. It will be shown that solvers implementing different assumptions may lead to considerably different results. This is especially true for PrandtlPlane configurations, for which aerodynamic load redistribution have a major impact on aeroelastic performances: wake deformation is then a factor to take account of.

It is important to collocate this effort in an historical and bibliographical context. Flutter analysis of Joined Wings was first performed in reference [8], for a box-wing layout [27]. It was found that the flutter instability was a limitation to the design of the configuration. Later, [5, 114] the so called *PrandtlPlane* [28, 91, 92] configuration was studied on an aeroelastic perspective and the encountered flutter problems were alleviated with the introduction of a double fin. In the above references linear flutter prediction methods were used. Moreover, the analyses were carried out on a *realistic* (i.e, inertial and stiffness distributions were assessed considering real-like operative conditions) aircraft, whereas conceptual investigations on wind-tunnel-like models will be pursued in this paper.

However, as shown in reference [158] for the static aeroelastic case and in this paper for the dynamic aeroelastic one, linear results could be non-conservative since higher critical speeds may be predicted. If a large discrepancy between the linear and nonlinear predicted aeroelastic instability speeds is found on the conceptual models, then a qualitative indication on the actual aircraft is implicitly provided.

Very few results have been proposed for different layouts of Joined Wings [198], and a lack of understanding of the physics of the phenomenon is evident: additional

studies are then necessary.

7.3 Theoretical Highlights of the Present Computational Tools

In a generic aeroelastic code the basic aerodynamic and structural solvers need to interact, passing to each other the information regarding the deformations (which directly influence the aerodynamic forces) and the forces (which deform the structure). It goes well beyond the goals of this paper to present a summary of all the possible strategies that could be adopted. The authors refer the reader to excellent works as [204–206] and the herein cited references.

In the following, the *components* of the in-house aeroelastic capabilities are described separately. They consist in a finite element method for the computational structural dynamics (CSD) and an unsteady vortex lattice method (UVLM) for the time domain aerodynamic simulations. A doublet lattice method (DLM) for the frequency domain unsteady aerodynamics calculations is also employed: details about this particular solver could be found in literature, see references [193, 196, 207].

Hereinafter, different interface (load/displacement transferring) strategies are analyzed.

Finally, the coupling is treated, and the different aeroelastic solvers are discussed.

7.3.1 Structural Finite Element Model

The geometrically nonlinear finite element [135, 136, 156, 208] is based on the linear membrane constant strain triangle (CST) and the flat plate discrete Kirchhoff triangle (DKT). The capability has also embedded the calculation of the structural tangent matrix $\boldsymbol{K}_T$, which is the sum of two contributions: the elastic stiffness matrix, $\boldsymbol{K}_E$, and the geometric stiffness matrix, $\boldsymbol{K}_G$. Composite materials are implemented. A corotational approach is used, and thus, rigid body motion is eliminated from elements and the pure elastic deformations are found.

The post-critical capability of the structural, and also aeroelastic code, are here omitted for brevity. The reader is referenced to [2, 158] for details.

7.3.2 Dynamic Solver

Newton's Law and Definition of the Residual

According to the second Newton's law, at each time dynamic equilibrium has to be satisfied. Let $\boldsymbol{s}$ be the generalized coordinate array (arising from the FE discretization) and $\dot{\boldsymbol{s}}$, $\ddot{\boldsymbol{s}}$ its time derivatives. Assume $\boldsymbol{M}$ to be the mass matrix, and that the damping forces, related to the structural damping, are proportional to $\dot{\boldsymbol{s}}$ through the damping matrix $\boldsymbol{C}_d$, constant with time. The internal structural forces are indicated with $\boldsymbol{F}_{\text{int}}$. Since only elastic materials are considered, these forces are function of the deformation only. The external loads are here specialized to be the aerodynamic forces acting on the body, and are a generical function of t, $\boldsymbol{s}$, $\dot{\boldsymbol{s}}$ and $\ddot{\boldsymbol{s}}$. These dependencies are related to the history (wake evolution), current configuration (steady production of aerodynamic forces), velocity of deformation (which changes the local angle of attack) and acceleration of deformation, respectively.

The dynamic equilibrium law reads as follows:

$$\boldsymbol{M}\,\ddot{\boldsymbol{s}} + \boldsymbol{C}_d\,\dot{\boldsymbol{s}} = \boldsymbol{P}_{\text{ext}}(\boldsymbol{s}, \dot{\boldsymbol{s}}, \ddot{\boldsymbol{s}},\, t) - \boldsymbol{F}_{\text{int}}(\boldsymbol{s}) \tag{7.1}$$

The residual is then defined as:

$$\boldsymbol{\mathcal{R}}(\boldsymbol{s}, \dot{\boldsymbol{s}}, \ddot{\boldsymbol{s}}, t) = \boldsymbol{M}\ddot{\boldsymbol{s}} + \boldsymbol{C}_d\dot{\boldsymbol{s}} - (\boldsymbol{P}_{\text{ext}}(\boldsymbol{s}, \dot{\boldsymbol{s}}, \ddot{\boldsymbol{s}},\, t) - \boldsymbol{F}_{\text{int}}(\boldsymbol{s})) \tag{7.2}$$

In order to obtain the dynamic equilibrium the residual has to be zero at each generic time t. However, when the problem is discretized in respect to the time, it is possible to enforce the dynamic equilibrium only at some temporal points. In literature several methods exist for the time discretization of dynamic structural problems, see for example [166, 209, 210].

In the following, the framework of the Newmark's $\beta-$Method and successive improvements leading to the *Generalized α-Method* (GAM) are introduced. The reasons that led to the introduction of the so called *Generalized Energy-Momentuum Method* (GEMM) and its implementation are then presented (see reference [169] for more details).

From Newmark β-Method to the Generalized α-Method

Before further proceeding, the notation used to state the evaluation of the quantity $\boldsymbol{A}$ at the generic time t is introduced:

$$ {}^{t}\boldsymbol{A} = \boldsymbol{A}|_{t} \tag{7.3} $$

If the generic quantity $\boldsymbol{A}$ has both a direct and indirect dependence on time, for example $\boldsymbol{A}(\boldsymbol{s}(t), t)$, then the notation is the following:

$$ {}^{t}\boldsymbol{A} = \boldsymbol{A}|_{(\,\boldsymbol{s}|_{t}, t)} \tag{7.4} $$

In reference [172], to advance in time from t to $t + \Delta t$, Newmark proposed the following relation between acceleration, velocity and displacement vectors:

$$ \begin{aligned} {}^{t+\Delta t}\dot{\boldsymbol{s}} &= {}^{t}\dot{\boldsymbol{s}} + (1-\gamma)\,\Delta t\,{}^{t}\ddot{\boldsymbol{s}} + \gamma\,\Delta t\,{}^{t+\Delta t}\ddot{\boldsymbol{s}} \\ {}^{t+\Delta t}\boldsymbol{s} &= {}^{t}\boldsymbol{s} + \Delta t\,{}^{t}\dot{\boldsymbol{s}} + (1-2\beta)\,\frac{\Delta t^2}{2}\,{}^{t}\ddot{\boldsymbol{s}} + \beta\,\Delta t^2\,{}^{t+\Delta t}\ddot{\boldsymbol{s}} \end{aligned} \tag{7.5} $$

The process was driven by Taylor's expansion and mean value theorem. The choice of γ and β determines important characteristics as accuracy, rate of convergence, stability and the alternatively explicit or implicit nature of the scheme [209]. Common choice is to take:

$$ \gamma = \frac{1}{2} \qquad \beta = \frac{1}{4} \tag{7.6} $$

which gives an unconditionally stable (irrespective of the size of the time step Δt) and quadratic convergent scheme (this has been proven for linear problems [173]).

With reference to eq.(7.2), it is straightforward to impose the dynamic equilibrium at the generic time $t + \Delta t$,

$$ {}^{t+\Delta t}\boldsymbol{\mathcal{R}} = \boldsymbol{M}\,{}^{t+\Delta t}\ddot{\boldsymbol{s}} + \boldsymbol{C}_d\,{}^{t+\Delta t}\dot{\boldsymbol{s}} - \left({}^{t+\Delta t}\boldsymbol{P}_{\text{ext}} - {}^{t+\Delta t}\boldsymbol{F}_{\text{int}}\right) = \boldsymbol{0} \tag{7.7} $$

and apply the scheme proposed in eq.(7.5).

It is desirable in structural dynamic problems solved through step-by-step time integration algorithms to possess *algorithmic damping*. Particularly, it is necessary to control the dissipation on the high frequency modes since using standard FEM to discretize the spatial domain, the spatial resolution of these modes is poor. Thus, spurious

high frequency modes should be damped out, and this should affect neither the low frequency modes nor the accuracy of the scheme. For example, the Newmark β-method family algorithms provide high-frequency dissipation if a different choice of the parameters in eq.(7.6) is made, with the drawbacks of an only first-order accuracy in time and too much dissipation on the low frequency modes [164]. This has driven the formulation of improved methods that enable to overcome these limitations, mantaining second-order accuracy: the HHT-α [211] and the WBZ-α [212] methods are just some examples. All these schemes are particular cases of the more general *Generalized α-method* (GAM), which represents a family of implicit time-integration schemes, and has been introduced in reference [164].

The scheme giving the relationships between the values of $\boldsymbol{s}$, $\dot{\boldsymbol{s}}$ and $\ddot{\boldsymbol{s}}$ is the same carried out in eq.(7.5), but now the additional equation needed to close the problem is a modified version of the standard choice of eq.(7.7): the idea is to force the dynamic equilibrium using convex combinations of these variables. Defining the following quantities:

$$\begin{cases} {}^{t+\alpha_f\Delta t}\boldsymbol{s} = (1-\alpha_f)\ {}^{t}\boldsymbol{s} + \alpha_f\ {}^{t+\Delta t}\boldsymbol{s} \\ {}^{t+\alpha_f\Delta t}\dot{\boldsymbol{s}} = (1-\alpha_f)\ {}^{t}\dot{\boldsymbol{s}} + \alpha_f\ {}^{t+\Delta t}\dot{\boldsymbol{s}} \\ {}^{t+\alpha_m\Delta t}\ddot{\boldsymbol{s}} = (1-\alpha_m)\ {}^{t}\ddot{\boldsymbol{s}} + \alpha_m\ {}^{t+\Delta t}\ddot{\boldsymbol{s}} \end{cases} \tag{7.8}$$

where, differently from the previously adopted notation, the superscripts are here used to indicate a convex combination of the values at the beginning (t) and at the end ($t+\Delta t$) of the time step and not values evaluated at time $t+\alpha\Delta t$. Clearly, α_m=α_f=1 gives rise to the Newmark family of methods.

The task is now to determine the relations between the algorithmic parameters α_m, α_f, γ and β to gain the desired numerical features. It can be demonstrated [164] that the generalized α-method is second-order accurate, provided that

$$\begin{aligned} \gamma &= \frac{1}{2} + \alpha_m - \alpha_f \\ \beta &= \frac{1}{4}\left(1 + \alpha_m - \alpha_f\right)^2 \end{aligned} \tag{7.9}$$

The stability property of an algorithm applied to linear problems depends upon the eigenvalues of its amplification matrix, in particular on spectral radius ϱ (defined as the largest of the eigenvalues). The spectral radius is also important because it is a measure of the numerical dissipation, that is a smaller spectral radius value corresponds to a

larger numerical dissipation; to obtain a numerical algorithm which gives the desired numerical damping at the high frequencies without an excessive dissipation in the low frequency region, its spectral radius should then be close to unity in the low frequency domain and smoothly decrease as the frequency increases. Summarizing, see [164] for details, it is possible to have a second order (in time) accurate unconditionally stable (for linear problems) scheme, which has a user-defined dissipation on the high frequencies and minimizes the dissipation on lower frequencies if, along with eq.(7.9), the following is also satisfied:

$$\begin{aligned} \alpha_f &= \frac{1}{1+\varrho_\infty} \\ \alpha_m &= \frac{2-\varrho_\infty}{1+\varrho_\infty} \end{aligned} \tag{7.10}$$

where ϱ_∞ denotes the value of the spectral radius in the high-frequency limit (ϱ_∞ is then the user-specified value to control high-frequency dissipation).

Application of this method to eq.(7.2) is not straightforward. In fact, in literature [164, 166], this procedure has been developed mainly for linear cases in which the forces were depending on time or displacements only. Thus, using the convex combination of eq.(7.8) would be completely identical to the case in which the convex combination is used for the different term of the residual. However, in the present case, there is a force term depending nonlinearly from the displacement ($\boldsymbol{F}_{\text{int}}$) and one term depending on t, $\boldsymbol{s}$, $\dot{\boldsymbol{s}}$ and $\ddot{\boldsymbol{s}}$ ($\boldsymbol{P}_{\text{ext}}$).

Focus is now on the external forces. One option is to remain consistent with the evaluation in time dictated by eq.(7.8), i.e., to set the external/aerodynamic forces evaluated at different convex combinations of the displacement and derivatives vectors:

$$\boldsymbol{P}_{\text{ext}}\big|_{\left({}^{t+\alpha_f\Delta t}\boldsymbol{s},\, {}^{t+\alpha_f\Delta t}\dot{\boldsymbol{s}},\, {}^{t+\alpha_m\Delta t}\ddot{\boldsymbol{s}},\, t+\alpha_f\Delta t\right)} \tag{7.11}$$

A peculiarity of such an approach is that, in cases for which an explicit linear dependence of the external forces on the displacements, velocities, accelerations, and a dependence (not necessarily linear) on time is found, the residual (eq.(7.2)) could be written as:

$$\boldsymbol{\mathcal{R}}(\boldsymbol{s},\dot{\boldsymbol{s}},\ddot{\boldsymbol{s}},t) = \left(\boldsymbol{M}-\boldsymbol{M}^A\right)\,\ddot{\boldsymbol{s}} + \left(\boldsymbol{C}_d-\boldsymbol{C}_d^A\right)\,\dot{\boldsymbol{s}} - \boldsymbol{K}^A\,\boldsymbol{s} - \left(\boldsymbol{P}_{\text{ext}}^A(t)-\boldsymbol{F}_{\text{int}}(\boldsymbol{s})\right) = \boldsymbol{0} \tag{7.12}$$

where $\boldsymbol{M}^A$, $\boldsymbol{C}_d^A$ and $\boldsymbol{K}^A$ express the linear dependence of the aerodynamic forces, and $\boldsymbol{P}_{\text{ext}}^A(t)$ represents the time dependence. Thus, except for the internal forces, the appli-

cation of the GAM closely matches what explained in reference [164]. Applying this first approach also to the internal forces, the discrete equation for the residual can be written as:

$$
{}^{t+\Delta t}\boldsymbol{\mathcal{R}} = \boldsymbol{M}\,{}^{t+\alpha_m \Delta t}\ddot{\boldsymbol{s}} + \boldsymbol{C}_d\,{}^{t+\alpha_f \Delta t}\dot{\boldsymbol{s}} - \boldsymbol{P}_{\text{ext}}\big|_{\left({}^{t+\alpha_f \Delta t}\boldsymbol{s},\, {}^{t+\alpha_f \Delta t}\dot{\boldsymbol{s}},\, {}^{t+\alpha_m \Delta t}\ddot{\boldsymbol{s}},\, t+\alpha_f \Delta t\right)} + \boldsymbol{F}_{\text{int}}\big|_{\left({}^{t+\alpha_f \Delta t}\boldsymbol{s}\right)} \tag{7.13}
$$

Consider now the internal forces. If the structural model is linear, then

$$
\boldsymbol{F}_{\text{int}}\big|_{\left({}^{t+\alpha_f \Delta t}\boldsymbol{s}\right)} = {}^{t+\alpha_f \Delta t}\boldsymbol{F}_{\text{int}} \qquad \text{(for linear structures)} \tag{7.14}
$$

which is equivalent to consider a convex combination of the terms of the residual equation or the displacement. This no longer holds if the forces are nonlinear. Thus the question arises as to which form should be considered.

Generalized Energy-Momentum Method

To apply a convex combination directly to the edge values of the internal and external loads and not to the displacements, proves to be very important for the properties of the numerical scheme, in particular the stability one. In fact, algorithms which are unconditionally stable for linear dynamics often lose this stability in the non-linear case, see for example references [166–168, 173–176]. This is also true if algorithmic damping, as evaluated with linear approach (like in [164]) is introduced. A further criterion for the stability of time-integration algorithms (other than the eigenvalue analysis shown earlier for the Generalized α-method) is the conservation of energy, motivated by the theorem presented in reference [213] which states that, when applied to Hamiltonian systems, a numerical algorithm is stable in energy if the sum of kinetic and internal energies are bounded within each time step relative to the external work, kinetic and internal energies in the previous time step.

The first algorithm which guaranteed unconditional stability in nonlinear dynamics of three-dimensional elastic bodies was the Energy-Momentum Method [165]. Actually, its appeal has been redimensioned by some numerical experiments, see [167,168,214]. In fact, convergence problems were observed, and small time steps were needed to obtain a stable and converged solution. These difficulties have been put in relation to high modes which are responsible of numerical collapse driven by an unphysical highly oscil-

latory response. It seems then advisable to introduce some form of damping in order to keep under control difficult cases [167].

A strategy to introduce controllable numerical dissipation to the Energy Momentum Method, denoted as Generalized Energy-Momentum Method was presented in refences [168, 169], applied to three-dimensional truss element and nonlinear dynamics of shells. It includes numerical dissipation adopting the Generalized α-method to advance the solution within time and guarantees the energy conservation or decay using the convex combination of the internal forces at the beginning and at the end of the time interval, ${}^{t+\alpha_f \Delta t}\boldsymbol{F}_{\text{int}}$ instead of considering it applied at the generalized midpoint, $\boldsymbol{F}_{\text{int}}\big|_{({}^{t+\alpha_f \Delta t}\boldsymbol{s})}$.

Unfortunately, is it not possible to automatically extend this approach to the aerodynamic forces, since the simultaneous dependence on acceleration, velocity and displacement does not make straightforward the use of a unique convex combination: it would be an open question which value between α_f and α_m should be used on this regard. In this effort, both the option ${}^{t+\alpha_f \Delta t}\boldsymbol{P}_{\text{ext}}$, namely:

$$ {}^{t+\alpha_f \Delta t}\boldsymbol{P}_{\text{ext}} = (1-\alpha_f)\, {}^{t}\boldsymbol{P}_{\text{ext}} + \alpha_f\, {}^{t+\Delta t}\boldsymbol{P}_{\text{ext}} \tag{7.15} $$

and the one previously introduced in eq.(7.11), have been used. Notice also that, in other works like [215], different convex combinations were suggested for the external forces. Summarizing, the strategy adopted to discretize in time the equations of motion is the GEMM, whereas the aerodynamic term is evaluated with a GAM or also a GEMM-like approach. Notice that, for the particular considered cases, no appreciable differences were noticed between the two approaches.

In the following, the derivation of the Newton process for convergence is shown for the GEMM-like approach only. The residual equation becomes:

$$ \begin{aligned} {}^{t+\Delta t}\boldsymbol{\mathcal{R}} = \boldsymbol{M}\, \left((1-\alpha_m)\, {}^{t}\ddot{\boldsymbol{s}} + \alpha_m\, {}^{t+\Delta t}\ddot{\boldsymbol{s}}\right) + \boldsymbol{C}_d\, \left((1-\alpha_f)\, {}^{t}\dot{\boldsymbol{s}} + \alpha_f\, {}^{t+\Delta t}\dot{\boldsymbol{s}}\right) - \\ (1-\alpha_f)\, {}^{t}\boldsymbol{P}_{\text{ext}} - \alpha_f\, {}^{t+\Delta t}\boldsymbol{P}_{\text{ext}} + (1-\alpha_f)\, {}^{t}\boldsymbol{F}_{\text{int}} + \alpha_f\, {}^{t+\Delta t}\boldsymbol{F}_{\text{int}} \end{aligned} \tag{7.16} $$

It is important to notice that, considering a generic time t in which all the quantities are known, and wishing to advance in time to $t + \Delta t$, it is possible, by means

of eqs.(7.5), to reduce the residual to a function of only one variable. Thus,

$$^{t+\Delta t}\boldsymbol{\mathcal{R}} = \boldsymbol{\mathcal{R}}\left(^{t+\Delta t}\boldsymbol{s}\right) \tag{7.17}$$

Newton's Method Applied to the Residual

A generic zero finding methods could be applied to eq.(7.16) (or alternatively, eq.(7.13)) in order to drive to zero the residual and thus obtain the dynamic equilibrium. If Newton's method is used then the residual is locally approximated with an affine model and the new linearly predicted zero is considered. A single Newton's iteration reads:

$$\mathbf{0} = {}^{t+\Delta t}\boldsymbol{\mathcal{R}}^{\text{iter } n} + {}^{t+\Delta t}\left[\frac{\mathrm{d}\boldsymbol{\mathcal{R}}}{\mathrm{d}\boldsymbol{s}}\right]^{\text{iter } n} \cdot {}^{t+\Delta t}\boldsymbol{u}^{\text{iter } n} \tag{7.18}$$

where the superscript "iter n" specifies the iteration at which the quantities are considered. The symbolism

$$^{t+\Delta t}\left[\frac{\mathrm{d}\boldsymbol{\mathcal{R}}}{\mathrm{d}\boldsymbol{s}}\right]^{\text{iter } n} \tag{7.19}$$

indicates the tangent matrix evaluated at ${}^{t+\Delta t}\boldsymbol{s}^{\text{iter } n}$, and it holds:

$${}^{t+\Delta t}\boldsymbol{s}^{\text{iter } n+1} = {}^{t+\Delta t}\boldsymbol{s}^{\text{iter } n} + {}^{t+\Delta t}\boldsymbol{u}^{\text{iter } n} \tag{7.20}$$

The tangent matrix for the system is:

$$^{t+\Delta t}\left[\frac{\mathrm{d}\boldsymbol{\mathcal{R}}}{\mathrm{d}\,\boldsymbol{s}}\right] = \frac{\alpha_m}{\beta\,\Delta t^2}\boldsymbol{M} + \frac{\alpha_f\,\gamma}{\beta\Delta t}\boldsymbol{C}_d - \alpha_f\left(\frac{\mathrm{d}\,{}^{t+\Delta t}\boldsymbol{P}_{\text{ext}}}{\mathrm{d}\,{}^{t+\Delta t}\boldsymbol{s}} - \frac{\mathrm{d}\,{}^{t+\Delta t}\boldsymbol{F}_{\text{int}}}{\mathrm{d}\,{}^{t+\Delta t}\boldsymbol{s}}\right) \tag{7.21}$$

where the iteration superscript has been dropped for clarity. Notice that eq.(7.21) changes during iterations only if the internal structural forces $\boldsymbol{F}_{\text{int}}$ or the external (aerodynamic) loads $\boldsymbol{P}_{\text{ext}}$ are nonlinear with ${}^{t+\Delta t}\boldsymbol{s}$. Notice also the contribution of the structural tangent matrix and force (aerodynamic) tangent matrix to the system's/global tangent one.

Once the iterative process reaches a convergent state, then a new time step could be taken and the iterative sequence repeated.

Structural Damping

The structural model provides the possibility to reproduce more consistently the dynamic behaviour taking into account the presence of structural damping, represented by the damping matrix $\boldsymbol{C}_d$; the approach consists in the extrapolation of structural modal damping from the system. Considering a problem with one degree of freedom, the free spring-damping-mass system is described by the equation

$$m\,\ddot{s} + 2c\,\dot{s} + k\,s = 0 \tag{7.22}$$

being s the generic coordinate describing the motion, m the mass, c the damping coefficient and k the spring constant. Rearranging the equation, the canonical form is easily obtained:

$$\ddot{s} + 2\,\zeta\,\omega_n \dot{s} + \omega_n^2\,s = 0 \tag{7.23}$$

where ω_n represents the natural frequency of the system and ζ the damping ratio (common values are in the range of $0.01 \div 0.05$). Once eq.(7.22) is stated in canonical form and ζ is chosen, the damping coefficient c is automatically set.

If the system has more than one degree of freedom, and the differential equations of motion are *linear*, it is possible, by means of the so called light damping approximation [216], to describe the evolution of the system decoupling the evolution of each natural mode. Thus, for the generic i-th mode the following relation holds:

$$\ddot{q}_i + 2\zeta_i \omega_{n_i} \dot{q}_i + \omega_{n_i}^2 q_i = 0 \tag{7.24}$$

which in matrix form is written as

$$\ddot{\boldsymbol{q}} + \boldsymbol{C}_\Delta\,\dot{\boldsymbol{q}} + \boldsymbol{\Omega}\,\boldsymbol{q} = \boldsymbol{0} \tag{7.25}$$

The introduction of damping to the lower frequencies influences the solution so it is necessary only to model a physical phenomenon and in this sense eq.(7.24) represents a convenient strategy that gives the possibility to set this damping factor for each mode independently.

The next step is to be able to relate the modal form of the equation (where the modal damping ratio ζ_i could be set) to the generic n-dimensional system which

describes the dynamic behaviour of the degrees of freedom of the structure ($\boldsymbol{s}$):

$$\boldsymbol{M}\,\ddot{\boldsymbol{s}} + \boldsymbol{C}_d\,\dot{\boldsymbol{s}} + \boldsymbol{K}\,\boldsymbol{s} = \boldsymbol{0} \tag{7.26}$$

The matrices are constant, and it is possible to write the response as a superposition of elementary solutions through the modal coordinates $\boldsymbol{q}$:

$$\boldsymbol{s} = \boldsymbol{\Phi}\,\boldsymbol{q} \tag{7.27}$$

where $\boldsymbol{\Phi}$ is the modal matrix. Substituting eq.(7.27) into eq.(7.26) and pre-multiplying by $\boldsymbol{\Phi}^T$, it holds

$$\hat{\boldsymbol{M}}\,\ddot{\boldsymbol{q}} + \hat{\boldsymbol{C}}\,\dot{\boldsymbol{q}} + \hat{\boldsymbol{K}}\,\boldsymbol{q} = \boldsymbol{0} \tag{7.28}$$

where, using the properties of the modal coordinates, it is possible to show that the modal mass $\hat{\boldsymbol{M}}$ and stiffness $\hat{\boldsymbol{K}}$ matrices are diagonal. The aim is to define $\boldsymbol{C}_d$ through $\hat{\boldsymbol{C}}$. The first step is to assume that $\hat{\boldsymbol{C}}$ is diagonal, so that it is straightforward to write eq.(7.24) for the generic i-th generalized coordinate. It is then possible to define the damping ratios for each mode in this form, and reconstruct the matrix $\boldsymbol{C}_d$ using the inverse of relation eq.(7.27) and left-multiplying by $\boldsymbol{\Phi}^{-T}$, namely:

$$\boldsymbol{C}_d = \boldsymbol{\Phi}^{-T}\,\hat{\boldsymbol{C}}\,\boldsymbol{\Phi}^{-1} \tag{7.29}$$

Actually the dynamic behaviour of a system is ruled by the most meaningful modes that are associated with the low natural frequencies, so it can be preferable both from a computational and (numerical) accuracy point of view to consider the process for just n modes on which it is significant to apply the damping, see reference [193]. If N is the total number of degrees of freedom of the structure, $\boldsymbol{\Phi}$ is now an $N \times n$ matrix; eq.(7.29) could not be used since $\boldsymbol{\Phi}$ is not a square matrix. To perform a similar equivalence, but in a least square sense, the following operations are performed starting from eq.(7.27):

$$\begin{aligned}
&\boldsymbol{\Phi}^T\boldsymbol{s} = \boldsymbol{\Phi}^T\boldsymbol{\Phi}\,\boldsymbol{q}\\
&\boldsymbol{T} = [\boldsymbol{\Phi}^T\boldsymbol{\Phi}]^{-1}\boldsymbol{\Phi}^T\\
&\boldsymbol{T}\boldsymbol{s} = \boldsymbol{q}\\
&\boldsymbol{C}_d = \boldsymbol{T}^T\hat{\boldsymbol{C}}\boldsymbol{T}
\end{aligned} \tag{7.30}$$

7.3.3 Aerodynamic model

Introduction

The present section introduces the aerodynamic model adopted in the study. The hypotheses of potential and incompressible flow are assumed to be valid.

Geometry Definition and Evaluation of Induced Velocity

Unsteady Vortex Lattice Method (UVLM) is used as aerodynamic solver: the main advantage of such a formulation is the required simple programming effort, which makes it preferable when operating with thin wings; for a detailed treatise refer to [192].

The singularities are vortex ring elements, each of which is composed by four constant-strength vortex line segments with the same value of circulation Γ. The wing is discretized by an arbitrary user selected number of quadrilateral aerodynamic panels as shown in Fig. 7.1. The vortex ring associated with each panel is shift downstream along each lateral edge of one fourth of the same edges. The velocity induced at an arbitrary

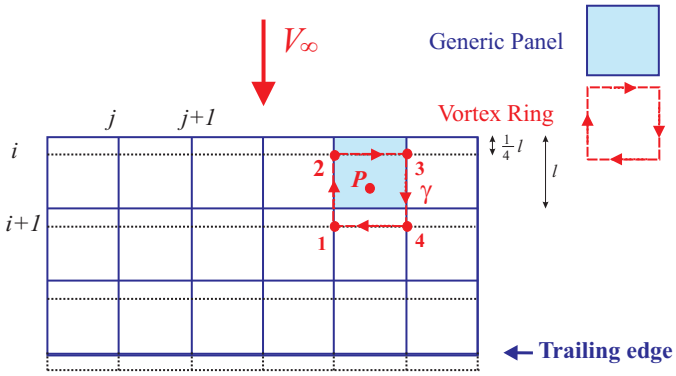

Figure 7.1: Location of the vortex rings in the aerodynamic grid.

point P by the generic vortex segment of circulation Γ is obtained from the Biot-Savart law. In particular, assume $\boldsymbol{V}_{\mathrm{SI}_{\mathrm{km}}}$ to be the velocity induced in the k-th collocation (or control) point by m-th ring of unitary circulation. Moreover, consider that the generic k-th collocation point (where the wall tangency condition has to be enforced), lies on the *center* of the k-th vortex ring, whose local direction is $\boldsymbol{n}_k$. Then, it is possible to define the generic km-the term of matrix of body influence coefficients $\boldsymbol{A}$:

$$\boldsymbol{A}_{\mathrm{km}} = \boldsymbol{V}_{\mathrm{SI}_{\mathrm{km}}} \cdot \boldsymbol{n}_k \tag{7.31}$$

Wake Model

For an unsteady flow a key role is played by the modelling of the wake. The most accurate model prescribes that each vortex moves with the local stream velocity since the vortex wake is force free, obtaining the so called *wake roll-up*. However this approach is quite time consuming and so often a simpler one, consisting in assuming a prescribed shape for the wake, is adopted. The effects of wake modelling on the aeroelastic responses will be discussed later.

In both cases, the wake is modelled with several rows of vortex rings of different strength, each shed at a certain time-step. When impulsively starting from a rest condition, only wing bound vortex rings exist. Consequently, there are no wake panels and the solution is easily found by specifying the zero normal flow boundary condition on the collocation points. During the second time step, the wing moves along its flight path and each trailing edge vortex panel sheds a wake ring with a vortex strength equal to its circulation in the previous time step (automatically satisfying the Kelvin condition). For the case of prescribed wake, it is enough to impose that each wake's point is convected by the free-stream velocity and so the procedure can be continued at each successive time step determining in such a way a wake of known geometry. Notice that, a wake vortex ring does not change its circulation (consequence of Helmholtz theorem). If the free wake is modelled, at the end of each timestep, once the problem is solved and the unknown intensity of the circulation Γ of every ring of the body is known, the evaluation of the induced velocity (u,v,w) at each vortex ring corner point l is performed in order to move the vortex elements by:

$$(\Delta x, \Delta y, \Delta z)_l = (u, v, w)_l \cdot \Delta t \tag{7.32}$$

This is the only difference between the two methods, because once the wake geometry is defined, the calculation of influence matrices and thus, the solution of the problem at the next time step are established in an identical manner. The modelling of the wake is completed and so it is possible to evaluate the contribution of each wake ring r-th to the local velocity in the k-th control point and store it in the $\boldsymbol{A}_w$ matrix of wake influence coefficients, where

$$\boldsymbol{A}_{w_{kr}} = \boldsymbol{V}_{\mathrm{WI}_{kr}} \cdot \boldsymbol{n}_{\mathrm{k}} \tag{7.33}$$

with $\boldsymbol{V}_{\mathrm{WI}_{kr}}$ being the wake-induced velocity from wake ring r at the collocation point k.

Before further proceeding with the description of the model, it is worth to highlight a few important aspects concerning the roll-up modelling. The use of discrete vortex segments to account for the vorticity in the shed wake originates accuracy issues due to the singularity that arises from a straight application of the Biot-Savart law when the induced point is located very close to the vortex line, leading to nonphysical values of the local velocity assigned to it. This usually occurs when a wake encounters another body or when the wake has an intense roll-up causing self-intersections. Aeroelastic response of a highly deformable wing seems to emphasize this aspect, since the trailing edge of the body changes position with time and so the position where the wake is shed, calling for a more complicated roll-up of the wake compared to the pure aerodynamic case. To prevent this kind of numerical problems and lack of accuracy, many techniques have been introduced, as for example the vortex-core model. The basic idea, as shown in [217], is that the formation of the wake behind any lifting surface must be considered as a viscous phenomenon, with the vorticity contained in the vortex core diffused radially outward with time. This observation is corroborated, for example, by experimental measurements of the distribution of tangential velocity surrounding a tip vortex shed from a blade at various wake ages [218]. According to a potential theory, this region is infinitesimal because all the vorticity is concentrated along the axis of each vortex filament and this leads to singularity in the evaluation of the Biot-Savart law near the vortex. In a more realistic model, this line should have an inner part, that is a finite core, where the flow rotates almost as a rigid body, whereas in the outer part behaves almost as a potential flow. With this line of reasoning, it is possible to define the core radius r_c both as the radial location where the tangential speed induced by the vortex has a maximum and as the boundary from the inner rotational flow field and the outer potential flow. Now that the physical meaning of the sought de-singularization of the induction estimate is pointed out, a revisited version of the Biot-Savart law is presented:

$$\boldsymbol{V} = \frac{\Gamma}{4\pi} \frac{h}{(r_c^{2n} + h^{2n})^{\frac{1}{n}}} (\cos\theta_1 - \cos\theta_2) \cdot \boldsymbol{e} \tag{7.34}$$

where the reader is referred to [218] for the notation and a plausible choice of the size of core radius.

The other important aspect is related to the issue of reducing as much as possible the time needed to evaluate at each timestep the influence of the *far* vortex rings. With this aim, thanks to the equivalence between vortex ring and doublet panels [219],

application of the far field formulas of point-doublet may be employed [192].

Another option to reduce the computational costs is the truncation of the wake domain: a threshold is defined so that beyond that distance the contribution of the wake on the local velocity on the control points over the body is assumed negligible. As a consequence, the *far wake panels* could be neglected. This wake truncation is thought to be sufficiently reliable because there is only interest in the wake influence over the body.

Boundary Condition

In order to be able to write the wall tangency condition, which states the *no normal velocity* condition on the control points over the body, all the contributions have to be taken into account: the velocity induced by the body rings $\boldsymbol{V}_{\mathrm{SI}}$, and wake rings $\boldsymbol{V}_{\mathrm{WI}}$, the kinematic velocity $\boldsymbol{V}_{\mathrm{KIN}}$, which is the velocity of wind on the surface (in particular it is of interest the one at the collocation points) due to relative motion of the wing, as viewed in the body frame of reference. This last contribution depends on the free-stream velocity, the rigid motion of the body but also on the elastic deformation of the body $\boldsymbol{V}_{\mathrm{rel}}$ (this is relevant in aeroelastic problems). The terms $\boldsymbol{V}_{\mathrm{WI}}$ and $\boldsymbol{V}_{\mathrm{KIN}}$ contribute to the right hand side, whereas $\boldsymbol{V}_{\mathrm{SI}}$ is unknown (byproduct of the multiplication of matrix $\boldsymbol{A}$ of eq.(7.31) with the unknown intensity of the body vortex rings). Thus, it is possible to write in a matrix form the following system

$$\boldsymbol{A} \cdot \boldsymbol{\Gamma} = \boldsymbol{RHS} \tag{7.35}$$

where $\boldsymbol{\Gamma}$ is the array containing the unknowns (strength of the vortex rings), and

$$RHS_k = -(\boldsymbol{V}_{\mathrm{WI}_k} + \boldsymbol{V}_{\mathrm{KIN}_k}) \cdot \boldsymbol{n}_k \tag{7.36}$$

is the vector containing the known part of the normal velocity components.

Evaluation of Loads

Once solved the linear set of equations, next step is the evaluation of the pressure over each body panel and subsequently the applied loads. The Bernoulli equation for incompressible and irrotational flow with the hypothesis of negligible body forces states

that the sum of the left-hand side terms of eq.(7.37) are a function of time only

$$\frac{p}{\rho} + \frac{v^2}{2} + \frac{\partial \phi}{\partial t} = C(t) \tag{7.37}$$

where p is the pressure, ρ is the density, v is the local fluid velocity and ϕ its potential. Evaluating the left-hand side of eq.(7.37) in two points of the fluid, an arbitrary point and a reference point at infinity (where $\phi = 0$ and $\boldsymbol{v} = \mathbf{0}$ having chosen the wind reference system), eq.(7.38) is obtained:

$$\frac{p_\infty - p}{\rho} = \frac{v^2}{2} + \frac{\partial \phi}{\partial t} \tag{7.38}$$

It is then possible to integrate the pressure and, with aid of Kutta-Joukowsky theorem, assess the lift produced by each panel.

7.3.4 Interface Algorithms

Infinite Plate Splines

Theory The Infinite Plate Spline concept was introduced in reference [202] and is the basis of several of the interpolation schemes used in today's commercial software. This method is based on a superposition of the solutions of the equilibrium equation describing an infinite plate subjected to small deflections. The key idea is to consider a set of discrete points (x_i,y_i) lying within a two-dimensional domain, each of them has associated a deflection w_i that defines the *vertical* position of the surface on which both structural and aerodynamic points are presumed to be. Using a superposition of solutions it is possible to calculate the values of a set of *fictitious* concentrated loads acting at the known set of points that give rise to the required deflection w. In this way, given the deflections of the structural grid points the concentrated forces are obtained and it is possible, by an interpolation process, to calculate the values on a set of aerodynamic grid points. The interpolated function is differentiable everywhere.

The main drawback of the method is that it is inherently 2-D and so it is limited to interpolate out-of-plane displacement only. Moreover, a piecewise flat planform for the wing has to be assumed, also when the wing is deformed. In the following, the entire mathematical procedure to gain the desired results is omitted and just the major features are outlined; for details about the derivation of the scheme the reader is referred

to reference [220].

The governing equation for a plate (bending case) that extends to infinity in both directions is:

$$D_{11}\frac{\partial^4 w}{\partial x^4} + 2\left(D_{12} + 2D_{66}\right)\frac{\partial^4 w}{\partial x^2 \partial y^2} + D_{22}\frac{\partial^4 w}{\partial y^4} = p \tag{7.39}$$

where p is the applied pressure. Then, a series of hypotheses are considered. First, the material is assumed to be isotropic, giving this a specific value for the D_{11}, D_{12}, D_{22}, D_{66} stiffness terms. Then, radial symmetry is imposed, and a concentrated load is applied at the origin. After that, with the argument that no singular displacement is acceptable at the origin, some terms in the closed form of the solution w are set to zero. Final adjustments are done to avoid oscillations. With all these hypotheses, the final form for the vertical displacement w is:

$$w\left(x, y\right) = a_0 + a_1 x + a_2 y + \sum_{i=1}^{\tilde{N}} \tilde{F}_i r_i^2 \ln r_i^2 \tag{7.40}$$

with:

$$\begin{aligned} a_0 &= \sum_{i=1}^{\tilde{N}} \left[A_i + B_i\left(x_i^2 + y_i^2\right)\right] \\ a_1 &= -2\sum_{i=1}^{\tilde{N}} B_i x_i \\ a_2 &= -2\sum_{i=1}^{\tilde{N}} B_i y_i \end{aligned} \tag{7.41}$$

where $\tilde{N}$ is the number of fictitious loads (or alternatively, the number of known value w_i), A_i, B_i and r_i are known quantities and $\tilde{F}_i$ are the fictitious concentrated loads used to reconstruct the shape of the plate, given the actual position of the set of known points.

Application to the displacement and load transfer The goal of this interface algorithm is to provide both a relation between structural and aerodynamic mesh displacements and to aerodynamic and structural loads. In other word, it consists in two phases: given a displacement vector $\boldsymbol{U}$ (and also its derivatives), representing the unknowns associated with the structural nodes, it extrapolates the displacement at the aerodynamic mesh points, so that the aerodynamic forces, may be evaluated by the aerodynamic solver; given the aerodynamic forces, it projects them to the structural nodes, so that the computational mechanics capability can calculate the structural dis-

placements. The way these phases are arranged depends on the way the aeroelastic coupling is performed. In the present effort, the goal is to get an explicit expression of the aerodynamic loads applied at the structural nodes, given a structural deformation $\boldsymbol{U}$.

Before further proceeding, the interface algorithm is specialized. The reference planes where the splines are specified are planar, and have the local x-axis (x^S) along the (initial) free-stream direction. The local vertical displacements (which are then perpendicular to the spline plane but not necessarily coincident with the vertical displacement in the global coordinates z) are denoted with Z^S and $\mathcal{Z}^S$ for the generic structural node and aerodynamic control point, respectively.

Eq.(7.40) shows how IPS are employed to evaluate the z^S coordinate of a generic point of the system once both its position through the local coordinates x^S and y^S and the required coefficients are given. The expression of the aerodynamic loads is calculated starting from the boundary condition applied on the *control points* and the involved quantities are thus related to the derivative of the vertical displacement with respect to the x^S direction $\dfrac{\mathrm{d}\mathcal{Z}^S}{\mathrm{d}x^S}$ (which, as it will be shown in the following is related to the changes of relative angle of attack), the speed $\dot{\mathcal{Z}}^S$ and the acceleration $\ddot{\mathcal{Z}}^S$ of this set of points, so that the sought algorithm should provide relations between them and the degrees of freedom in the structural nodes. Eq.(7.40) can be advantageously applied to the structural points in matricial form, it can be written as

$$\boldsymbol{Z}^S = \boldsymbol{G}\,\tilde{\boldsymbol{F}} \tag{7.42}$$

Inverting this expression, the unknown array $\tilde{\boldsymbol{F}}$ containing the fictitious concentrated loads is obtained; now the coefficients that have to be used for the spline interpolation (see eq.(7.41)) are known.

In order to avoid the time consuming task of obtaining the vector $\tilde{\boldsymbol{F}}$ at each timestep, the assumption that during the deformation process the original local coordinates x_i^S and y_i^S of the generical point i do not change is made, i.e. the vertical projection is always corresponding (or at least in good approximation) to the initial position of the structural point considered. If this hypothesis is not satisfied, $\boldsymbol{G}$ changes during the simulation and has to be continuously evaluated.

Carrying on the interpolation for the desired variables, the following relations

are obtained

$$\begin{aligned}\dot{\boldsymbol{\mathcal{Z}}}^S &= \boldsymbol{H}\dot{\boldsymbol{Z}}^S \\ \ddot{\boldsymbol{\mathcal{Z}}}^S &= \boldsymbol{H}\ddot{\boldsymbol{Z}}^S \\ \frac{\mathrm{d}\boldsymbol{\mathcal{Z}}^S}{\mathrm{d}x^S} &= \boldsymbol{H}^D\boldsymbol{Z}^S\end{aligned} \tag{7.43}$$

where $\boldsymbol{H}$ easily derives from eq.(7.42) now applied to the vertical displacement field $\boldsymbol{\mathcal{Z}}^S$ of the aerodynamic mesh (the constant expression of the spline's matrices allows one to use them to interpolate also the time derivatives); $\boldsymbol{H}^D$ is the interface matrix for the spatial derivative of the displacement and can be gained differentiating eq.(7.41) with respect to the local x direction and specializing it for the control points.

The last task to be performed to complete the interfacing for the aerodynamic-structural coupling originates from the following issue: for a correct application of the Kutta-Joukowsky theorem, the aerodynamic loads have to be applied in the load points of the vortex ring. In order to use a FEM structural solver, the loads are thought to act on the structural nodes and thus, given an external concentrated load, its transferring to the FE nodes of the triangle shell element has to be performed. The problem, depicted in Fig. 7.2 can be tackled with an energy conserving approach imposing that the virtual work done by the external force is equal to the virtual work done by the nodal forces of the element. The expression of the forces acting on the three vertices of the triangle

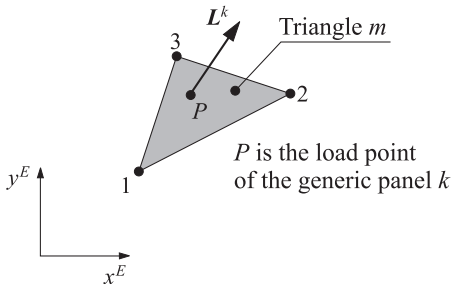

Figure 7.2: Applied load in a triangular element

equivalent to the aerodynamical load applied in the point P with coordinates (x^E, y^E) is given by

$$\begin{aligned}\boldsymbol{L}_1^m &= h_1^m\left(x_P^E, y_P^E\right)\boldsymbol{L}^k \\ \boldsymbol{L}_2^m &= h_2^m\left(x_P^E, y_P^E\right)\boldsymbol{L}^k \\ \boldsymbol{L}_3^m &= h_3^m\left(x_P^E, y_P^E\right)\boldsymbol{L}^k\end{aligned} \tag{7.44}$$

where the shape functions relative to the nodes 1, 2 and 3 of the triangle m are indicated respectively as $h_1^m\left(x^E, y^E\right)$, $h_2^m\left(x^E, y^E\right)$ and $h_3^m\left(x^E, y^E\right)$ and can be evaluated making use of the area coordinates [221].

Interface with Moving Least Square derived algorithm

The present interface algorithm has the purpose to solve the typical aeroelastic problem of coupling the aerodynamic and structural meshes granting important features [222]. It is in fact possible to interface both non-matching surfaces or non-matching topologies. Cases in which a control point falls outside the range of the source mesh are also naturally tackled. There is also a relative insensitiveness to the node density variations in the source mesh. A very important feature is the conservation of exchanged quantities, in particular momentum and energy: this is a keypoint since in literature [223] it has been shown how nonconservartive interfaces may lead to wrong results. In spite of these valuable advantages, the computationally efficiency of interface computation is really high. A further very desirable feature is the relative independence from the numerical formulation of the solvers of the two fields.

Problem Statement Thanks to *meshless* approach it is possible to achieve the previously listed goals. Traditionally, meshless methods were introduced as a method of numerical resolution of partial differential equations different than finite element method (FEM), finite difference method (FDM) and finite volume method (FVM). In these last approaches, spatial domain is often discretized into meshes: the set of differential equations are approximated by a set of algebraic equations for each mesh and then, by assembling in the proper way the contribution of all of them, the final system of algebraic equations for the whole problem is obtained. On the contrary, in mesh free method [203], this system of algebraic equations for the whole problem is obtained using a set of nodes scattered in the domain which do not form a mesh because no information on the relationship between the nodes (e.g., connectivity of an element) is required.

These methods seem to solve some issues of the classical approaches which are here briefly listed. First, the creation of an adequately discretized mesh is notoriously a bottleneck in the process since it is both manpower and computer time consuming. Second, the classical approaches have a limited regularity of the solution, especially in its derivatives, at the elements' boundaries (although approaches using higher order continuous basis function like *NURBS* were already proposed in [224]). Moreover, with

lagrangian grids/meshes there is a lost of accuracy when large deformations are investigated because of the element distortions. A close examination of these difficulties shows that the root of the problem is the necessity to use elements (mesh); on the contrary a meshless method does not have these limitations, and could add or delete nodes when they are needed, providing a great flexibility to the analysis.

In the present effort what is adopted from the meshless method is one of its central features: the shape functions. A number of ways to construct shape functions have been proposed in literature, here the choice falls on Moving Least Square approximation (MLS), which belongs to the family of finite series representation methods. This family of shape functions were originally introduced for data fitting and surface reconstruction [225], while in [226] they were used for the first time to build shape functions for the Diffuse Element Method (DEM), which was among the first ones properly called mesh free method and had a strong impact on the field. The two main features of MSL are the continuity and smoothness in the entire problem domain of the approximated field function, and the ability to produce the desired order of consistency (a method is said to have k-th order consistency if can reproduce polynomials of up to the k-th order). The procedure of constructing shape functions using MLS approximation is fully presented in appendix C, while in this section just the main features are outlined.

Moving Least Square The basic idea is to compute the value of a function $u(\boldsymbol{x})$ on a set of nodes $\{\boldsymbol{\eta}_1, \boldsymbol{\eta}_2, ..., \boldsymbol{\eta}_{\hat{N}}\}$ from its values $\hat{u}(\boldsymbol{\xi}_1)$, $\hat{u}(\boldsymbol{\xi}_2)$, ..., $\hat{u}(\boldsymbol{\xi}_{\hat{n}})$ on scattered centers (or sources) $\{\boldsymbol{\xi}_1, \boldsymbol{\xi}_2, ..., \boldsymbol{\xi}_{\hat{n}}\}$ without deriving an analytical expression. This extrapolation is denoted $\hat{u}^h$ and is built as a sum of $\hat{m}$ basis functions $\hat{p}_i(\boldsymbol{\eta})$

$$\hat{u}^h(\boldsymbol{\eta}) = \sum_{i=1}^{\hat{m}} \hat{p}_i(\boldsymbol{\eta})\, a_i^{\boldsymbol{\xi}}(\boldsymbol{\eta}) = \hat{\boldsymbol{p}}(\boldsymbol{\eta}) \cdot \boldsymbol{a}^{\boldsymbol{\xi}}(\boldsymbol{\eta}) \tag{7.45}$$

where $a_i^{\boldsymbol{\xi}}$ are the unknown coefficients of the basis functions which depend on the point $\boldsymbol{\eta}$ where the value is sought and on the set of scattered centers $\boldsymbol{\xi}$ where the function is known (this dependence, denoted by the superscript in eq.(7.45), will be omitted in the following for clearness). The array $\hat{\boldsymbol{p}}$ of basis functions consists often of monomials of the lowest order such to form polynomial basis with minimum completeness but particular functions can be added to reproduce a particular behaviour of the investigated variables.

In the present study linear and quadratic polynomials are adopted. The neigh-

bourhood of the point $\boldsymbol{\eta}$, its *support domain*, is given by a subset of $\boldsymbol{\xi}$, namely $\boldsymbol{\xi}^s$, made of $\hat{n}_s$ nodes which are the only ones used locally to approximate the field function. Each node $\boldsymbol{\eta}$ has a different set $\boldsymbol{\xi}_s$ with in general a different number of nodes $\hat{n}_s$, that is $\hat{n}_s$=$\hat{n}_s(\boldsymbol{\eta})$. The $\hat{m}$ coefficients a_i describing (as shown in eq.(7.45)) the function in the point $\boldsymbol{\eta}$ are obtained minimizing the functional weighted residual (a weighted discrete L_2 norm) $J(\boldsymbol{\eta})$:

$$J(\boldsymbol{\eta}) = \sum_{i=1}^{\hat{n}} W(\boldsymbol{\eta} - \boldsymbol{\xi}_i) \left[\tilde{u}(\boldsymbol{\xi}_i, \boldsymbol{\eta}) - \hat{u}(\boldsymbol{\xi}_i)\right]^2 \tag{7.46}$$

where

$$\tilde{u}(\boldsymbol{\xi}_i, \boldsymbol{\eta}) = \hat{\boldsymbol{p}}(\boldsymbol{\xi}_i) \cdot \boldsymbol{a}(\boldsymbol{\eta}) \tag{7.47}$$

is the approximated value of the the field function in the generical center of the set $\boldsymbol{\xi}$ obtained by means of the same extrapolation process pointed out in eq.(7.45). The weight function W used in eq.(7.46) is positive for all the $\boldsymbol{\xi}_i$ centers in the support of node $\boldsymbol{\eta}$ and zero outside, and has two important roles in constructing the MLS shape functions: it provides weighting for the residual at different nodes in the support domain (small weights are wanted for centers far from $\boldsymbol{\eta}$); it ensures a smooth manner for centers to leave and enter the support domain of the considered node. Here comes out the important difference with the FEM shape functions, which are obtained minimizing the residual J in eq.(7.46) assuming a unitary constant weight function and repeating this operation element by element (which coincides with the support domain of the nodes). By replacing the discontinuous weights of FEM approach with continuous weighting functions evaluated in the centers of the nodes the smoothness of the approximate function is granted. Solving the minimization problem

$$\frac{\partial J(\boldsymbol{\eta})}{\partial \boldsymbol{a}} = 0 \tag{7.48}$$

an expression for the coefficient vector $\boldsymbol{a}(\boldsymbol{\eta})$ is obtained, allowing to rewrite eq.(7.45)

$$\hat{u}^h(\boldsymbol{\eta}) = \boldsymbol{\Phi}(\boldsymbol{\eta}) \cdot \hat{\boldsymbol{u}} \tag{7.49}$$

where $\boldsymbol{\Phi}(\boldsymbol{\eta})$ is the array containing the coefficients of the MLS shape function corresponding to the node $\boldsymbol{\eta}$, while $\hat{\boldsymbol{u}}$ has the value of the field function on the centers. For more details on the derivation refer to appendix C.

It can be observed that the shape functions in eq.(7.49) do not satisfy the Kronecker delta criterion $\Phi_i(\boldsymbol{\xi}_j) = \delta_{ij}$ resulting in $\hat{u}^h(\boldsymbol{\xi}_i) \neq \hat{u}(\boldsymbol{\xi}_i)$, that is, the nodal parameters $\hat{u}(\boldsymbol{\xi}_i)$ are not coincident with the nodal values $\hat{u}^h(\boldsymbol{\xi}_i)$; this means that they are not interpolants, but rather approximates of a function; this property can represents a drawback when the imposition of essential boundary conditions is requested, but it is possible to overcome it as shown in appendix C.

As stated, the MLS approximation is able to reproduce the desired order of consistency, depending on the complete order of the monomial basis $\hat{\boldsymbol{p}}$: if the complete order of the base is k, it can be demonstrated that the shape function will possess k consistency.

The calculation of spatial derivatives of the function $\hat{u}$ requires to derive eq.(7.45):

$$\frac{\partial u}{\partial x} \simeq \frac{\partial u^h}{\partial x} = \frac{\partial \hat{\boldsymbol{p}}}{\partial x} \cdot \boldsymbol{a} + \hat{\boldsymbol{p}} \cdot \frac{\partial \boldsymbol{a}}{\partial x} \tag{7.50}$$

The second term of eq.(7.50) is not trivial to evaluate and a straight procedure is showed in [203]; it is not an expensive task itself, however it requires the knowledge of the cloud of particles surrounding each point $\boldsymbol{\eta}$ and, thus, it depends on the point where the information is evaluated; on the contrary, the first term can be evaluated *a priori*. Work [226] proposed the concept of diffusive derivative, which consists in approximating the derivative only with the first term on the right hand side of eq.(7.50), and it proved convergence at optimal rate.

The great advantage of the problem expressed in this form is the possibility to preserve the local character of the MLS approximation choosing a compact support weight function W, that is supposed to satisfy the following requirements:

- W is a monotonically decreasing function that depends only on a scalar parameter r that represents the Euclidean distance from the two considered points;
- W has a compact support, so

$$\begin{cases} W(r) > 0 \text{ if } r < \overline{r} \\ W(r) = 0 \text{ if } r > \overline{r} \end{cases} \tag{7.51}$$

- W enjoys normal property such that

$$\int_{\Omega} W(\boldsymbol{\eta} - \boldsymbol{x})\, d\Omega = 1 \tag{7.52}$$

  where $\overline{r}$ is the radius delimiting Ω, the local support of node $\boldsymbol{\eta}$.

Examples of functions that satisfy these requirements are the Radial Basis Function (RBF) family, which can be found in different forms as Multiquadratics, Gaussian, Thin Plate Spline and Logarithmic. In this study the adopted functions possess the lowest possible degree among all piecewise polynomial compactly supported radial functions of a given order of smoothness [227]: this is an important property since the approximate functions are as smooth as the involved weight function.

After the dimension of the local support is chosen, the last operation of the preliminary phase is the determination of the centers which belong to each node $\boldsymbol{\eta}$; several strategies exist to solve this task and a suitable choice from the computational point of view is to rely on *nearest neighbor searching algorithms* [228]: given a set S of n data points in a metric space X in real d-dimensional space, the idea is to preprocess these points so that, given any query point $q \in X$, the k nearest points to q can be efficently reported. These algorithms perform the geometric preprocessing of building the structure at $O(d)$ cost and the subsequent operation to get the nearest neighbor from the data set with an $\mathrm{O}(k \cdot \log d)$ cost.

As previously stated, an important property sought in the present interface algorithm is the conservation of momentum and energy; using eq.(7.49) to exchange the information of displacement and velocity from the structure to the aerodynamic field, conservation (although not in a strictly mathematical sense) is achieved because a minimization process is performed and so a limited amount of information can be transmitted [222]. While the conservation of momentum transmitted is taken in account with the definition of the $\boldsymbol{\Phi}$ interface matrix, other considerations lead to conservation of energy. As demonstrated in appendix C, to ensure the balance of the energy exchanged bewteen fluid and structure, the loads on the structural nodes $\boldsymbol{f}_i$ have to be evaluated by multiplying the loads $\boldsymbol{F}_i$ on the aerodynamic grid by the transpose of the interpolation matrix $\boldsymbol{H}$ (same as $\boldsymbol{\Phi}$ of eq.(7.49)) that matches the two displacement fields.

7.3.5 Aeroelastic Coupling

In this section the goal is to express the aerodynamic loads so that they can be combined with the dynamic model presented in section 7.3.2 in order to formulate the aeroelastic problem.

Boundary Condition

The starting point to obtain the sought expression is the boundary condition (enforced at the control points). Recalling the matrix formulation from eq.(7.35), it is worth to highlight the various contributions to the $\boldsymbol{RHS}$ vector. The *first* contribution can be written as

$$\boldsymbol{RHS}_1 = -\boldsymbol{A}_w \cdot \boldsymbol{\Gamma}_w \tag{7.53}$$

where $\boldsymbol{A}_w$ is the wake influence coefficients matrix and $\boldsymbol{\Gamma}_w$ is the vector with the strength of the wake singularities, both completely defined from the previous time steps calculations.

The *second* term is the free-stream contribution

$$\boldsymbol{RHS}_2 = -\boldsymbol{V}_\infty^n \tag{7.54}$$

where $\boldsymbol{V}_\infty^n$ is the component of the free-stream velocity along the normal to the ring. In order to evaluate this term, it is useful to consider Fig. 7.3, in which the k-th body ring as well as the position of the control point and a sketch of both the deformed and undeformed configurations are depicted. Unit vector $\boldsymbol{i}$ is parallel to the free stream, while $\boldsymbol{i}^S$ is the direction of the free stream projected to the undeformed ring plane. By definition, the k-th element of $\boldsymbol{V}_\infty^n$ is given by $V_\infty \boldsymbol{i} \cdot \boldsymbol{n}_k$, where $\boldsymbol{n}_k$ is the normal to the ring in its *actual* configuration, and the following holds:

$$\boldsymbol{i} \cdot \boldsymbol{n}_k = \cos\left(\frac{\pi}{2} - \alpha^k\right) = \sin\alpha^k = \sin\left(\overline{\alpha}^k + \beta^k\right) = \sin\overline{\alpha}^k \cos\beta^k + \cos\overline{\alpha}^k \sin\beta^k \tag{7.55}$$

being $\overline{\alpha}^k$ the angle of attack of ring k in the undeformed configuration and the angles

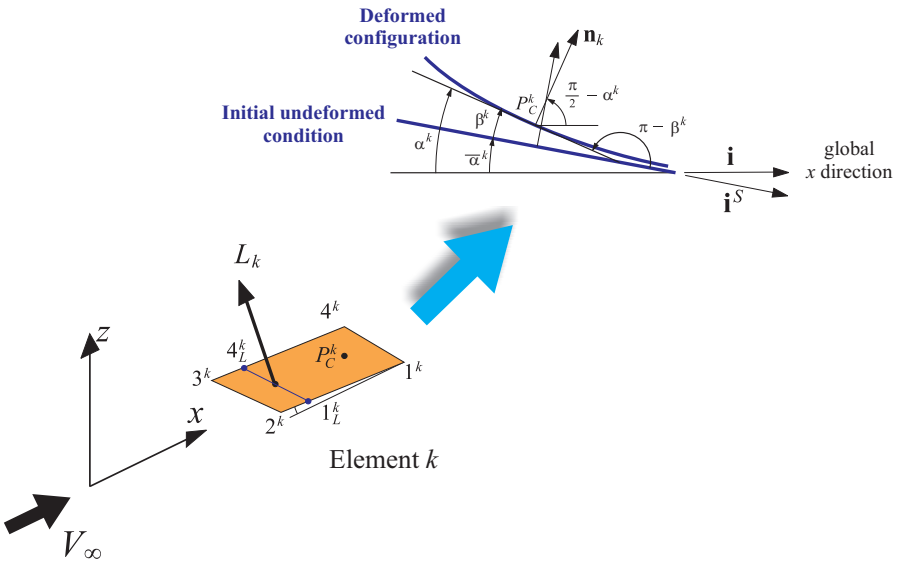

Figure 7.3: Geometry and local normal of the body ring

α^k and β^k the ones reported in Fig. 7.3. Under the assumption of small angles:

$$\begin{aligned} &\cos\overline{\alpha}^k \approx 1 \\ &\cos\beta^k \approx 1 \\ &\sin\beta^k \approx \tan\beta^k = -\tan\left(\pi - \beta^k\right) \end{aligned} \tag{7.56}$$

A synthetic expression of eq.(7.55) can be given, discerning the different meanings of the involved terms:

$$V_\infty \boldsymbol{i} \cdot \boldsymbol{n}_k = V_{\infty,0}^{n_k} + V_{\infty,d}^{n_k} \tag{7.57}$$

where $V_{\infty,0}^{n_k} = V_\infty \sin\overline{\alpha}^k$ is the k-th element of $\boldsymbol{V}_{\infty,0}^{n}$, and is related to just the change in the rigid angle of attack (*rigid aoa*); it is thus a function of the time only. The second term $V_{\infty,d}^{n_k}$ is the contribution of the free stream due to the deformation of the wing (*elastic aoa*) and is a function of the deformed shape. Observing that $\tan\beta^k$ is equal to the opposite of the derivative of the displacement of the control point in the direction of the *undeformed* normal in respect to the direction $\boldsymbol{i}^S$ (*undeformed* x direction), it can be written:

$$V_{\infty,d}^{n_k} = -V_\infty \frac{\mathrm{d}\hat{Z}_k}{\mathrm{d}x_k^S} \tag{7.58}$$

where the vector $\hat{\boldsymbol{Z}}$ collects the displacements of the control points along the undeformed aerodynamic rings' normals. This contribution can be directly related to the slope of

the normal component of displacement of the control point k.

The third term depends on the strain rate of the structure: it originates from the relative body-flow velocity that is established as the body changes its shape, giving a contribution to the effective flow speed that has to be taken into account for a correct evaluation of eq.(7.35). This is an important source of aerodynamic damping. It holds:

$$\boldsymbol{RHS}_3 = \dot{\boldsymbol{Z}} \tag{7.59}$$

The generic $\dot{\boldsymbol{Z}}$ can be evaluated extrapolating the deformation velocity on the control points from the vector $\dot{\boldsymbol{U}}$, which contains the generalized velocity of the structural nodes, and multiplying it by the normal to the k-th ring $\boldsymbol{n}_k$, in its *actual* configuration.

Now that all the RHS terms have been conveniently treated, eq.(7.35) can be re-written as:

$$\begin{aligned} \boldsymbol{A} \cdot \boldsymbol{\Gamma} &= \boldsymbol{RHS}_1 + \boldsymbol{RHS}_2 + \boldsymbol{RHS}_3 \\ &= -\boldsymbol{A}_w \cdot \boldsymbol{\Gamma}_w - \boldsymbol{V}_\infty^n + \dot{\boldsymbol{Z}} \end{aligned} \tag{7.60}$$

and inverting $\boldsymbol{A}$, this final form is obtained:

$$\boldsymbol{\Gamma} = \boldsymbol{\Gamma}_1 + \boldsymbol{\Gamma}_2 \cdot \boldsymbol{U} + \boldsymbol{\Gamma}_3 \cdot \dot{\boldsymbol{U}} \tag{7.61}$$

$\boldsymbol{\Gamma}_1$ is the known contribution due to the wake and to the *rigid aoa*, i.e., the first term in eq.(7.57)

$$\boldsymbol{\Gamma}_1 = -\boldsymbol{A}^{-1}\boldsymbol{A}_w \cdot \boldsymbol{\Gamma}_w - \boldsymbol{A}^{-1}\boldsymbol{V}_{\infty 0}^n \tag{7.62}$$

$\boldsymbol{\Gamma}_2$ is the matrix that multiplies the displacement field $\boldsymbol{U}$; it features a matrix performing the interpolation between the aerodynamic and structural meshes in order to get the derivative in respect to x^S ($\boldsymbol{H}_{\mathrm{dx}}$) of the displacement. This matrix is multiplied by the matrix ($\boldsymbol{N}_0$) in order to sample correctly just the component parallel to the *undeformed* normal of the ring:

$$\boldsymbol{\Gamma}_2 = -V_\infty \boldsymbol{A}^{-1}\boldsymbol{N}_0\boldsymbol{H}_{\mathrm{dx}} \tag{7.63}$$

$\boldsymbol{\Gamma}_3$ multiplies the given velocity field $\dot{\boldsymbol{U}}$. The matrix ($\boldsymbol{H}_{\mathrm{disp}}$) performs the interpolation between the two meshes, and is multiplied by ($\boldsymbol{N}_{\mathrm{d}}$) in order to sample correctly just the component parallel to the *actual* normal of the ring.

$$\boldsymbol{\Gamma}_3 = \boldsymbol{A}^{-1}\boldsymbol{N}_{\mathrm{d}}\boldsymbol{H}_{\mathrm{disp}} \tag{7.64}$$

Aeroelastic Loads

Starting from the Bernoulli equation for an incompressible, irrotational and unsteady flow, and following reference [192] it is possible to evaluate the aerodynamic actions. These relations can be advantageously expressed in matrix form as

$$\boldsymbol{p} = \rho \boldsymbol{\Delta} \cdot \boldsymbol{\Gamma} + \rho \frac{\partial \boldsymbol{\Gamma}}{\partial t} \tag{7.65}$$

where p is the array containing the difference between upper and lower pressure for each panel, $\boldsymbol{\Delta}$ is the matrix that, for each ring of the body, applies the finite difference derivative scheme to $\boldsymbol{\Gamma}$ and multiplies it with the suitable coefficients. To finally obtain the expression of the lift acting on the load points of the aerodynamic mesh, the direction $\boldsymbol{r}_L^k$ of the force over the k-th ring is chosen accordingly to the Kutta-Joukowsky theorem as:

$$\boldsymbol{r}_L^k = \boldsymbol{i} \times \boldsymbol{r}_{4_L^k - 1_L^k} \tag{7.66}$$

where $\boldsymbol{r}_{4_L^k - 1_L^k}$ connects the projections of the load point P_L^k along the segments $3^k - 4^k$ and $2^k - 1^k$ (as depicted in Fig. 7.4) and has a modulus equal to the width of the ring panel. Calling c_k the chord of the ring and ($\boldsymbol{i}$, $\boldsymbol{j}$, $\boldsymbol{k}$) the axes direction in the

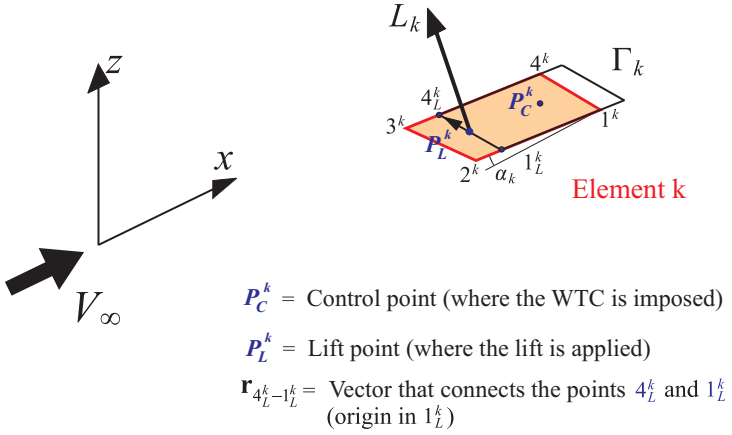

Figure 7.4: Direction of the lift over the ring k

global coordinate system, it is finally possible to give a general expression of the three

components of the lift force acting on the k^{th} ring:

$$\begin{aligned} L_{\text{x}}^k &= c_k \boldsymbol{i} \cdot \boldsymbol{r}_{4_L^k - 1_L^k}\, p_k \\ L_{\text{y}}^k &= c_k \boldsymbol{j} \cdot \boldsymbol{r}_{4_L^k - 1_L^k}\, p_k \\ L_{\text{z}}^k &= c_k \boldsymbol{k} \cdot \boldsymbol{r}_{4_L^k - 1_L^k}\, p_k \end{aligned} \tag{7.67}$$

which in matrix form becomes:

$$\boldsymbol{L} = \boldsymbol{S}\,\boldsymbol{p} \tag{7.68}$$

If N is the number of body rings, $\boldsymbol{S}$ is a $3N \times N$ matrix such that when multiplied by $\boldsymbol{p}$ gives rise to the vector $\boldsymbol{L}$, whose dimensions are $3N \times 1$, and is assembled repeating the pattern of eq.(7.67) for each element k.

As it can be seen from eq.(7.65), the unsteady part of the pressure depends on the derivative of $\boldsymbol{\Gamma}$ with respect to time. The derivation can be carried out using eq.(7.61), leading to

$$\frac{\partial \boldsymbol{\Gamma}}{\partial t} = \frac{\partial \boldsymbol{\Gamma}_1}{\partial t} + \boldsymbol{\Gamma}_2 \cdot \dot{\boldsymbol{U}} + \boldsymbol{\Gamma}_3 \cdot \ddot{\boldsymbol{U}} \tag{7.69}$$

where the derivatives of $\boldsymbol{\Gamma}_2$ and $\boldsymbol{\Gamma}_3$ are considered negligible. Now eq.(7.65) combined with eqs.(7.61) and (7.69) lead to the sought expression for the aerodynamic loads

$$\boldsymbol{L}^{\text{LP}} = \boldsymbol{L}_1^{\text{LP}} + \boldsymbol{L}_2^{\text{LP}} \cdot \boldsymbol{U} + \boldsymbol{L}_3^{\text{LP}} \cdot \dot{\boldsymbol{U}} + \boldsymbol{L}_4^{\text{LP}} \cdot \ddot{\boldsymbol{U}} \tag{7.70}$$

with

$$\begin{aligned} \boldsymbol{L}_1^{\text{LP}} &= \rho \boldsymbol{S} \cdot \boldsymbol{\Delta} \cdot \boldsymbol{\Gamma}_1 + \rho \boldsymbol{S} \cdot \frac{\partial \boldsymbol{\Gamma}_1}{\partial t} \\ \boldsymbol{L}_2^{\text{LP}} &= \rho \boldsymbol{S} \cdot \boldsymbol{\Delta} \cdot \boldsymbol{\Gamma}_2 \\ \boldsymbol{L}_3^{\text{LP}} &= \rho \boldsymbol{S} \cdot \boldsymbol{\Delta} \cdot \boldsymbol{\Gamma}_3 + \rho \boldsymbol{S} \cdot \boldsymbol{\Gamma}_2 \\ \boldsymbol{L}_4^{\text{LP}} &= \rho \boldsymbol{S} \cdot \boldsymbol{\Gamma}_3 \end{aligned} \tag{7.71}$$

The superscript LP is used to outlined how these are forces applied on the load points of the ring. As for the matrices $\boldsymbol{H}_{\text{dx}}$ and $\boldsymbol{H}_{\text{disp}}$, the interface algorithm will provide the way to transfer this quantities on the structural nodes.

Residual and Tangent Matrix Expression

It us assumed that the aerodynamic forces have been projected to the nodes of the structural solver trough one of the load transferring techniques: the previously

defined $\boldsymbol{L}_1^{\mathrm{LP}}$, $\boldsymbol{L}_2^{\mathrm{LP}}$, $\boldsymbol{L}_3^{\mathrm{LP}}$ and $\boldsymbol{L}_4^{\mathrm{LP}}$ are now named as $\boldsymbol{L}_1^S$, $\boldsymbol{L}_2^S$, $\boldsymbol{L}_3^S$ and $\boldsymbol{L}_4^S$ because they are quantities related to the structural nodes. Recalling section 7.3.2, there were different options for the time integration, leading to different options for the evaluation of the aerodynamic contribution, namely eqs.(7.15) and (7.11). With the expression outlined in eq.(7.71), and recalling that $\boldsymbol{s}$ was expressing the generalized structural coordinates whereas $\boldsymbol{U}$ represents the displacement from an initial reference configuration, it is then immediately possible to give the appropriate value of the aerodynamic loads in the expression of the residual.

Also the derivation of the aerodynamic tangent matrix is trivial. With reference to eq.(7.21)

$$\frac{\mathrm{d}\,{}^{t+\Delta t}\boldsymbol{L}^S}{\mathrm{d}\,{}^{t+\Delta t}\boldsymbol{s}} = \frac{\partial\,{}^{t+\Delta t}\boldsymbol{L}^S}{\partial\,{}^{t+\Delta t}\boldsymbol{s}} + \frac{\partial\,{}^{t+\Delta t}\boldsymbol{L}^S}{\partial\,{}^{t+\Delta t}\dot{\boldsymbol{s}}}\,\frac{\partial\,{}^{t+\Delta t}\dot{\boldsymbol{s}}}{\partial\,{}^{t+\Delta t}\boldsymbol{s}} + \frac{\partial\,{}^{t+\Delta t}\boldsymbol{L}^S}{\partial\,{}^{t+\Delta t}\ddot{\boldsymbol{s}}}\,\frac{\partial\,{}^{t+\Delta t}\ddot{\boldsymbol{s}}}{\partial\,{}^{t+\Delta t}\boldsymbol{s}} \tag{7.72}$$

Recalling eqs.(7.5) and (7.70), and observing that derivatives with respect to the generalized coordinates are identical to derivatives in respect to displacements, i.e.,

$$\frac{\mathrm{d}}{\mathrm{d}\boldsymbol{s}} = \frac{\mathrm{d}}{\mathrm{d}\boldsymbol{U}} \tag{7.73}$$

then, it can be inferred that:

$$\frac{\mathrm{d}\,{}^{t+\Delta t}\boldsymbol{L}^S}{\mathrm{d}\,{}^{t+\Delta t}\boldsymbol{s}} = \boldsymbol{L}_2^S + \frac{\gamma}{\beta\Delta t}\,\boldsymbol{L}_3^S + \frac{1}{\beta\Delta t^2}\,\boldsymbol{L}_4^S \tag{7.74}$$

7.3.6 Aeroelastic Solvers

In the present study three solvers have been used. Each of them is characterized by using different options both on the pure aerodynamic side (but within the model of incompressible potential flow), and on the aeroelastic coupling. The three solvers, called *Solver1*, *Solver2* and *Solver3* have increasing computational cost. Their properties are graphically presented in Fig. 7.5. A solver based on the *doublet lattice method* (DLM) [196, 207] method is occasionally employed for comparison purposes.

Solver1

This model adopts the IPS as interface algorithm and, as outlined in section 7.3.4, this implies simplified hypotheses, inherent both to the limits of the algorithm itself (as the 2D assumption) and to simplifications needed to preserve low computational costs.

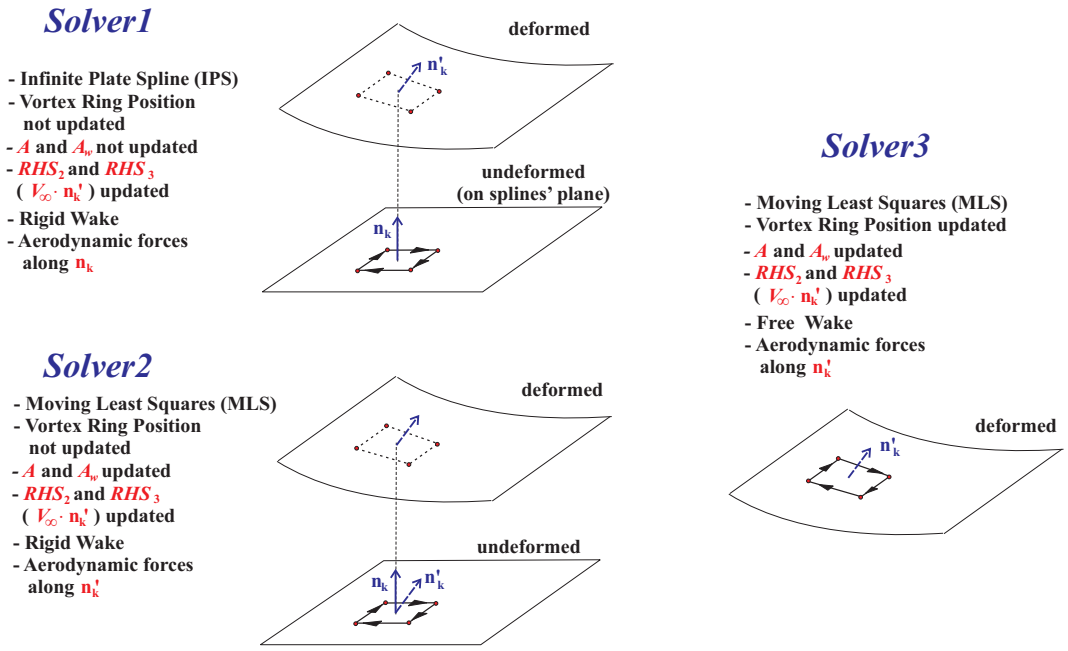

Figure 7.5: Differences between the time-domain aeroelastic solvers.

As a consequence in this model the aerodynamic mesh does not follow the structure, i.e., the coordinates of inducing rings and the inducted control points that are employed in the evaluation of the coefficients of the matrices $\boldsymbol{A}$ and $\boldsymbol{A}_w$ in section 7.3.3 do not depend on the deformation process of the body. However, body's deformation still influences the boundary condition (and thus the aerodynamic load) with the terms $\boldsymbol{RHS}_2$ and $\boldsymbol{RHS}_3$ discussed in section 7.3.5. Such a choice implies that a prescribed wake model is adopted, as it appears an useless computational task to consider a free-wake model shed from an aerodynamic mesh that does not occupy the real position of the body.

Solver2

In *Solver2* the IPS is substituted with the MLS interpolation algorithm. Everything is linked with the coupling of aerodynamic and structural fields, which removes the obstacle of passing information between two sets of points occupying the same planar surface, as necessary with IPS. This allows to build up for each time step the real aerodynamic mesh. However, in this case a mixed approach is chosen: the *velocity vector* used for the matrices $\boldsymbol{A}$ and $\boldsymbol{A}_w$ is still evaluated ignoring the new position of the body, but the *aerodynamic coefficients* of these matrices (i.e. the normal components of the velocities) are updated at each timestep because in eqs.(7.31) and (7.33) it is considered

the actual normal direction $\boldsymbol{n}_k$ of the ring where the k-th control point is placed.

The reason of this choice is the assumption that for a correct estimate of the *velocity vector* the important aspect is the relative distance between the vortex line and the induced point and this is still in good agreement with the initial one when the body is deformed. On the contrary, what is mainly changed during the dynamic evolution, especially for very deformed configurations as the ones under investigations, is the direction along which the boundary condition should be written. Thus, there is a lack of accuracy to keep projecting the induced velocity vector on the initial normal direction.

Thanks to the MLS is possible to evaluate the updated $\boldsymbol{r}_L^k$, which gives the direction of lift produced from the k-th ring, see eq.(7.66). This is accomplished by means of evaluation of the actual position of the points 4_L^k and 2_L^k in Fig. 7.4. It is worth to notice that now the aerodynamic load is *follower both in direction and intensity.*

Since the aerodynamic mesh still remains attached to the *undeformed* configuration, free-wake approach has been not considered to be meaningful, thus, *Solver2* represents an improvement in the accuracy comparing to the *Solver1* without an excessive drawback in simulation run time.

Solver3

Solver3 adopts the MLS interpolation algorithm and considers the aerodynamic mesh in its actual position, enabling the free-wake model and the *correct* (without further assumptions as the ones made before) expression of all the quantities involved in the evaluation of the aerodynamic loads.

7.4 Validation of the Computational Capability

Validation of the in-house computational capabilities is here demonstrated. Some components or even some full aeroelastic solvers have already been validated in previous works. For example, nonlinear structural finite element code, both in the static and dynamic versions, has been already employed in some previous efforts, i.e. [1, 2, 158, 162, 229]. Moreover, also the *DLM* capability has been already described and checked in references [193, 196]. However, some other components have been newly implemented. For example, even if the *VLM* implant was already used in the *DLM*, the new *UVLM* was not yet tested.

7.4.1 Validation of the Aerodynamic Solvers

Validation of the pure aerodynamic solvers is here demonstrated. A few words are necessary to introduce the results. Referring to section 7.3.6, two of the several features that distinguish the aeroelastic solvers are the locations of the vortex rings and the treatment of the wake. From a pure aerodynamic perspective, then, the different modelling concerns the wake only. Thus, to validate the unsteady behaviour, the wake is treated both as rigid or deformable.

A common validation mean, popular as the *Wagner*'s test case, consists in an impulsive start of an airfoil. There is an analytical expression, see [3] that describes the evolution of the lift coefficient in respect of τ, known as reduced time, which is the covered distance expressed in semi-chords of the airfoil, i.e., $\tau = 2\,V_\infty\,t/c$. Here t represents the time and c the chord of the airfoil. If C_L is the lift coefficient, it holds that $C_L(\tau) = C_L(\infty)\,\Psi(\tau)$, where:

$$\Psi(\tau) = 1 - 0.165\,e^{-0.0455\tau} - 0.335\,e^{-0.3\tau} \tag{7.75}$$

Since this test case is a bi-dimensional one, to validate the solvers a wing with large aspect-ratio in considered ($AR = 30$) and the evaluation of the lift coefficient is done at its mid-station. The simulation is run considering $\Delta t\,V_\infty/c = 1/8$. Results are shown in Fig. 7.6, where the lift coefficient normalized to the steady lift coefficient is plotted against the reduced time, for both the rigid and deformable wake approaches. Results are in satisfying agreement.

7.4.2 Validation of the Meshless Transferring Capability

Validation of meshless capability has been carried out whereas this is not pursued here for the spline interface (validations were already performed in previous works using the same framework). Since *Solver1* relies on IPS, a modified version of this solver has been implemented featuring the meshless for the load and displacements transferring. Then, a joined-wing configuration is considered, as the one depicted in Fig. 7.7. Notice that, this same configurations will be a test case geometry for this paper. A freestream speed of 55 m/s is considered, and the angle of attack α, measured in the symmetric xz plane, has the evolution depicted in the same graph. The results are in an excellent agreement, especially considering that at these large displacements the infinite spline

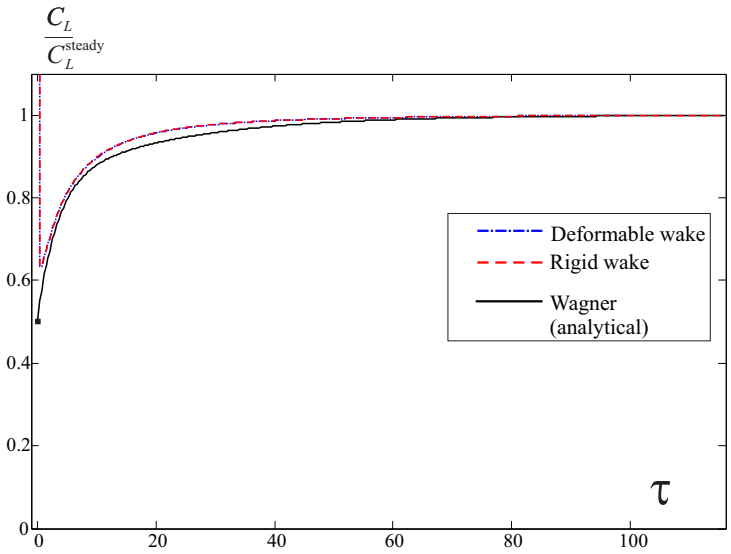

Figure 7.6: Results of Wagner's test case using a rigid and a deformable wake: lift coefficient normalized to the steady lift coefficient plotted against the reduced time. The analytical solution is obtained from [3].

method may begin to have issues related to its formulation, i.e., the assumption of constant projection of the points is no longer exactly satisfied. This results, beside other cases not reported here for brevity, may be considered as a valuable validation for the meshless method.

7.4.3 Final Validation of the Time Domain Aeroelastic Codes Capabilities

In this final subsection the three time domain solvers are validated against experimental results which are proposed in reference [4]. It consists of a delta wing plate model tested in a low-speed wind tunnel showing limit cycle oscillations. For the geometry and details about the configuration the reader is referred to the original work. This experiment is also performed numerically by the solvers, and results are directly compared with the reference experiment, as well as computational results reported in [193], obtained with a technique that transforms the frequency domain DLM results in time domain response.

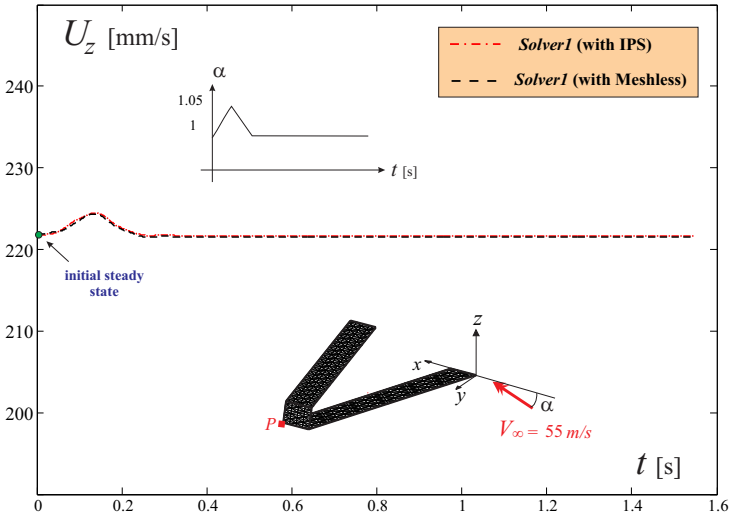

Figure 7.7: Aeroelastic transient analysis of a Joined Wing configuration studied the *Solvber1* when employing both IPS and Meshless transfers method.

Solver1

Numerical results obtained with *Solver1* are shown in Table 7.1. To favour the comparisons, the first two columns report reference results, where as the third and forth show the performances of *Solver1* with two different values of structural damping. Maximum vertical speed of the tip for LCO established at different wind speed are also represented in Fig. 7.8.

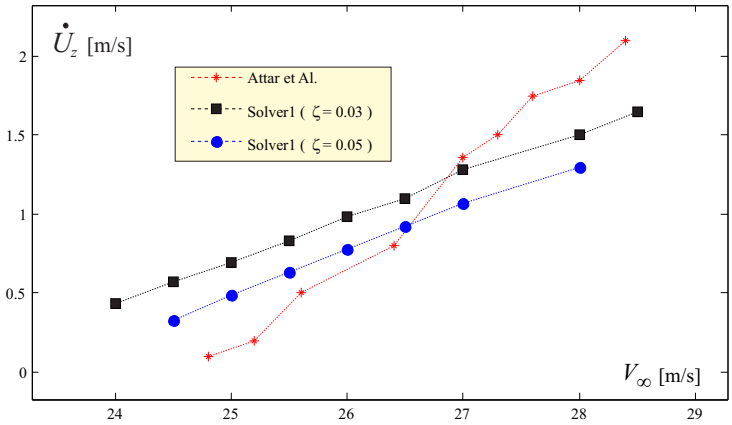

Figure 7.8: Results of Delta Wing test case: experimental [4] *Solver1*. The maximum vertical speed of the wing's tip is plotted against the wind speed.

Solver2

Numerical data for *Solver2* are now shown in Table 7.2. Maximum vertical speed of the tip for LCO established at different wind speeds is also represented in Fig. 7.9.

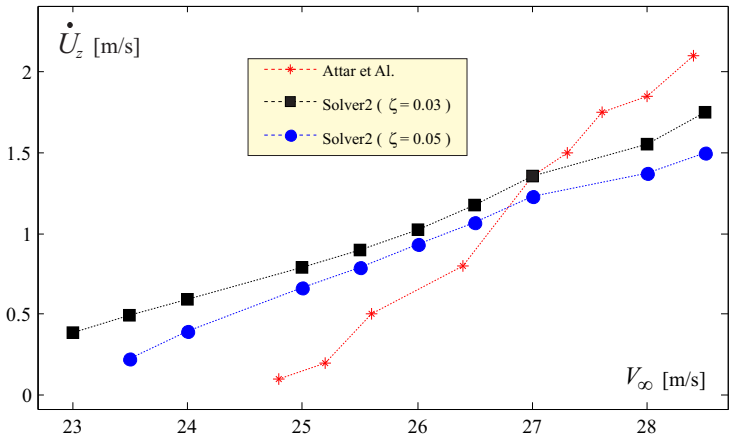

Figure 7.9: Results of Delta Wing test case: experimental [4] and *Solver2*. The maximum vertical speed of the wing's tip is plotted against the wind speed.

Solver3

The same process is repeated for *Solver3*. See Table 7.3. Maximum vertical speed of the tip for LCO established at different wind speed are also represented in Fig. 7.10.

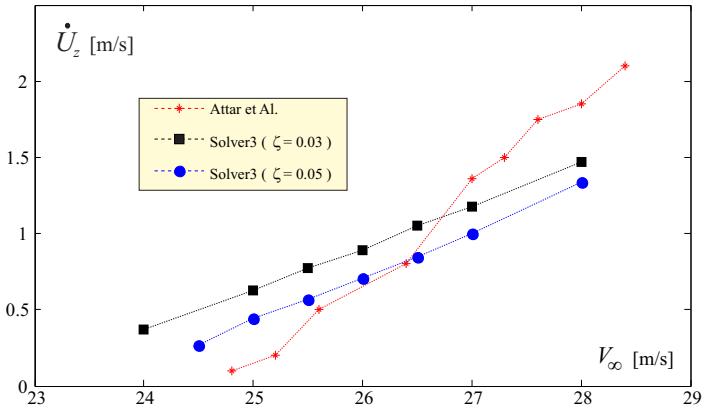

Figure 7.10: Results of Delta Wing test case: experimental [4] and *Solver3*. The maximum vertical speed of the wing's tip is plotted against the wind speed.

Table 7.1: Validation of *Solver1* with Delta Wing test case. $\dot{U}_{z_{\text{tip}}}$ is the maximum vertical speed of the tip of the wing.

	Attar et Al. [4] (experimental)	Demasi et Al. [193]	*Solver1* ζ=3%	*Solver1* ζ=5%
Flutter velocity	24 m/s	22,7 (ζ= 1%)	24 m/s	24,5 m/s
$\dot{U}_{z_{\text{tip}}}$ (V_∞=25,5 m/s)	0,5 m/s		0,69 m/s	0,63 m/s
$\dot{U}_{z_{\text{tip}}}$ (V_∞=27 m/s)	1,36 m/s	1 m/s (ζ= 5%)	1,28 m/s	1,07 m/s
LCO frequency (V_∞=27 m/s)	14,5 Hz	14.92 Hz (ζ= 5%)	15,3 Hz	14,8 Hz
$\dot{U}_{z_{\text{tip}}}$ (V_∞=28 m/s)	1,85 m/s	1,55 m/s (ζ= 3%)	1,5 m/s	1,3 m/s

Table 7.2: Validation of *Solver2* with Delta Wing test case. $\dot{U}_{z_{\text{tip}}}$ is the maximum vertical speed of the tip of the wing.

	Attar et Al. [4] (experimental)	Demasi et Al. [193]	*Solver2* ζ=3%	*Solver2* ζ=5%
Flutter velocity	24 m/s	22,7 (ζ= 1%)	23 m/s	23,5 m/s
$\dot{U}_{z_{\text{tip}}}$ (V_∞=25,5 m/s)	0,5 m/s		0,9 m/s	0,66 m/s
$\dot{U}_{z_{\text{tip}}}$ (V_∞=27 m/s)	1,36 m/s	1 m/s (ζ= 5%)	1,36 m/s	1,23 m/s
LCO frequency (V_∞=27 m/s)	14,5 Hz	14.92 Hz (ζ= 5%)	16 Hz	15,3 Hz
$\dot{U}_{z_{\text{tip}}}$ (V_∞=28 m/s)	1,85 m/s	1,55 m/s (ζ= 3%)	1,55 m/s	1,37 m/s

Table 7.3: Validation of *Solver3* with Delta Wing test case. $\dot{U}_{z_{\text{tip}}}$ is the maximum vertical speed of the tip of the wing.

	Attar et Al. [4] (experimental)	Demasi et Al. [193]	*Solver3* ζ=3%	*Solver3* ζ=5%
Flutter velocity	24 m/s	22,7 (ζ= 1%)	24 m/s	24,5 m/s
$\dot{U}_{z_{\text{tip}}}$ (V_∞=25,5 m/s)	0,5 m/s		0,77 m/s	0,57 m/s
$\dot{U}_{z_{\text{tip}}}$ (V_∞=27 m/s)	1,36 m/s	1 m/s (ζ= 5%)	1,18 m/s	1 m/s
LCO frequency (V_∞=27 m/s)	14,5 Hz	14.92 Hz (ζ= 5%)	15,6 Hz	15,1 Hz
$\dot{U}_{z_{\text{tip}}}$ (V_∞=28 m/s)	1,85 m/s	1,55 m/s (ζ= 3%)	1,47 m/s	1,34 m/s

7.5 Description of the Analyzed Joined-Wing Configurations

There are different configurations that will be analyzed in this paper. The first one, depicted in Fig. 7.11, is a Joined Wing (named *JW70*) in which the joint is not located at the tip of both the wings. The thickness of the wings and the joint is 0.7 mm.

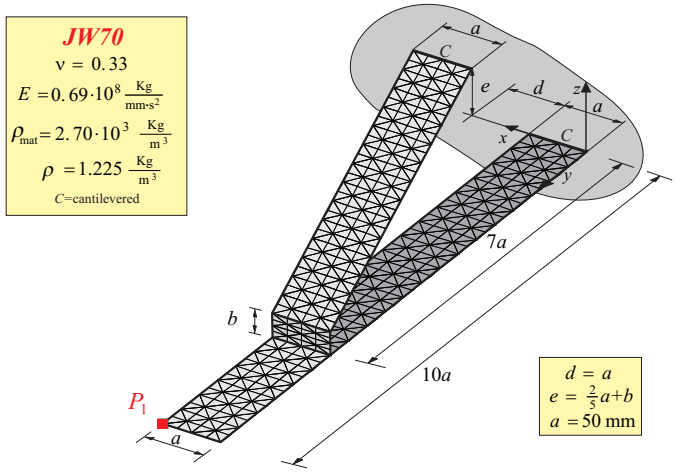

Figure 7.11: JW70 model. The joint is located at 70% of the wing span. The thickness of the different parts of the structure is equal to 0.7 mm.

The second configuration (Fig. 7.12) is a PrandtlPlane-like [9] configuration featuring a swept-back lower wing and a swept-forward upper wing. It is designated *PrP40*. For this layout, the thickness of the wings is varied and specified case by case. Both *JW70* and the *PrP40* have been chosen for reference reasons, see [1, 2, 158, 162]. The models' dimensions are selected to be consistent with the ones corresponding to wind-tunnel scaled models.

The last layout (Fig. 7.13) is the typical *Sensorcraft* [12]. The geometrical details are taken from reference [134], a part from the thickness which has been set to 0.7 mm. In this configuration the aft wing is directly joined to the front wing, to act like a strut.

For all the layouts the adopted material is a typical Aluminium, featuring a Young's modulus $E = 6.9 \cdot 10^7 \left[\frac{\text{Kg}}{\text{mm}\cdot\text{s}^2}\right]$, a Poisson's ratio $\nu = 0.33$ and a density $\rho_{\text{mat}} = 0.69 \cdot 10^3\,\text{kg/m}^3$.

For the aerodynamic analysis, the surface is discretized employing different (usu-

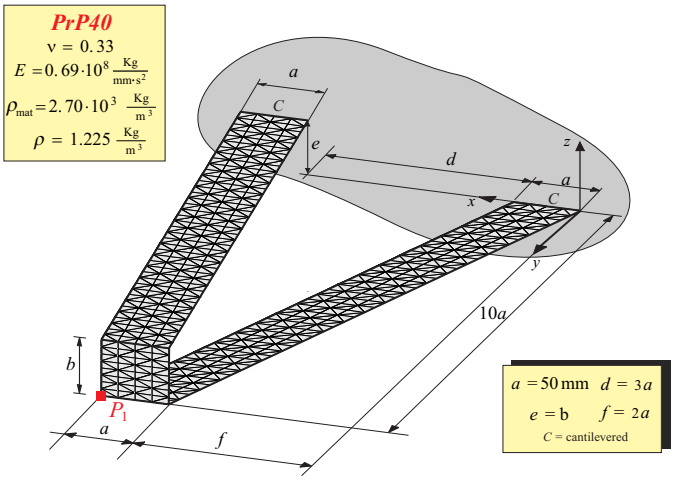

Figure 7.12: PrandtlPlane Joined Wing model PrP40. The joint is located at the tip of the wings.

ally about 12) elements in the chordwise direction. The overall number of rectangular elements is then between approximately 600 and 3000 for the different cases.

The density of the air is chosen to be the standard air density ($\rho = 1.225\,\mathrm{kg/m^3}$).

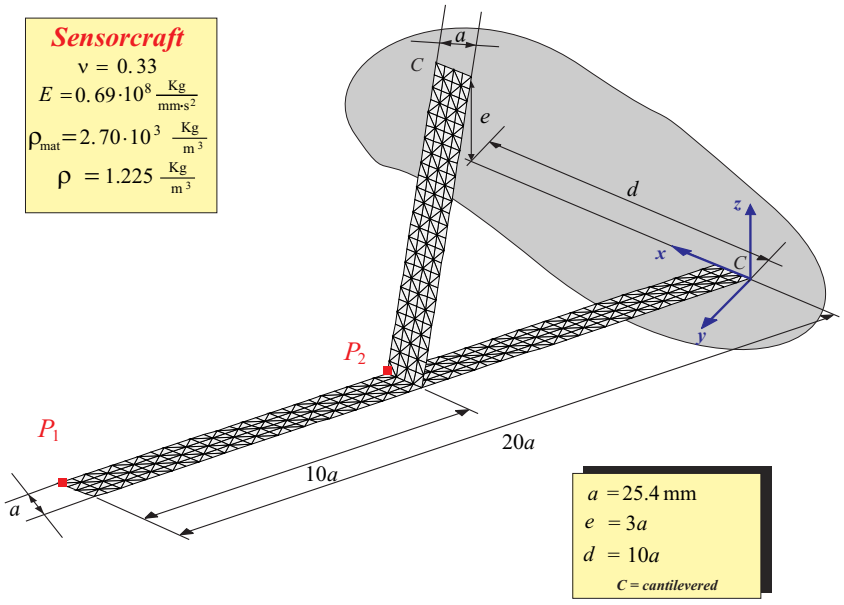

Figure 7.13: *Sensorcraft*. The aft wing is connected to the front one at the midspan. The thickness of the wings is equal to 0.7 mm.

7.6 Snap Divergence

The concept of *snap divergence* was first introduced in references [158, 187]. It was related to a precise mathematical event, which was the singularity of the aeroelastic tangent matrix. For that critical condition an infinitesimal increment in the onset flow speed was determining an equilibrium not continuously adjacently to the previous one. In other words, a jump phenomenon (from which the word *snap*) was expected. This jump phenomenon could be theoretically demonstrated to happen if the acting forces are of the conservative type, and this actually is pursued and shown in [2,197]. However, aerodynamic forces are not of the conservative type and the scenario could be much more complicated. First of all, for the case here investigated it has been verified (and will be reported in next sections) that flutter speed is larger than snap-divergence one, thus, the stability (in a local sense) of the equilibrium points could be assessed with static aeroelastic analysis. Moreover, different-than-fixed points type of attractors may theoretically exist, with the consequence that snap may even induce the system to settle, for example, to a limit cycle oscillation.

In this section the snap-divergence response will be shown. The time-domain capability is used, in particular *Solver1*. This choice is dictated by the necessity to keep the aeroelastic modelling consistent to the one used in references [158, 187].

7.6.1 Time response on Snap-divergence Occurence

Consider the static aeroelastic response reported in Fig. 7.14 (taken and adapted from Refs. [158, 187]). Starting from the steady state A, a perturbation in the onset velocity is applied.

Before describing the perturbation application, it is worth to explain how the simulation was started. The steady state aeroelastic solver was using horse shoe singularities to represent the bound vorticity, whereas in the time domain dynamic capability a vortex ring representation is used. Equivalence has been imposed on the aerodynamic loads, determining thus the circulation of the vortex rings. A further point is the fact that static solutions were considered converged after a tolerance on the residual was reached. Of course, in a real numerical setting it is not possible to reach the perfect equilibrium. Thus, it has been checked that the numerical unbalance was negligible.

With the starting condition (state A in Fig. 7.14, corresponding to a free-stream speed of $V_\infty = 33$ m/s), the flow speed is first increased to reach $V_\infty = 34.3$ m/s (state

B), then decreased to its initial value. This is process a quasi-static process, as could be inferred from the box in Fig. 7.14, where the wind speed in respect of time is plotted.

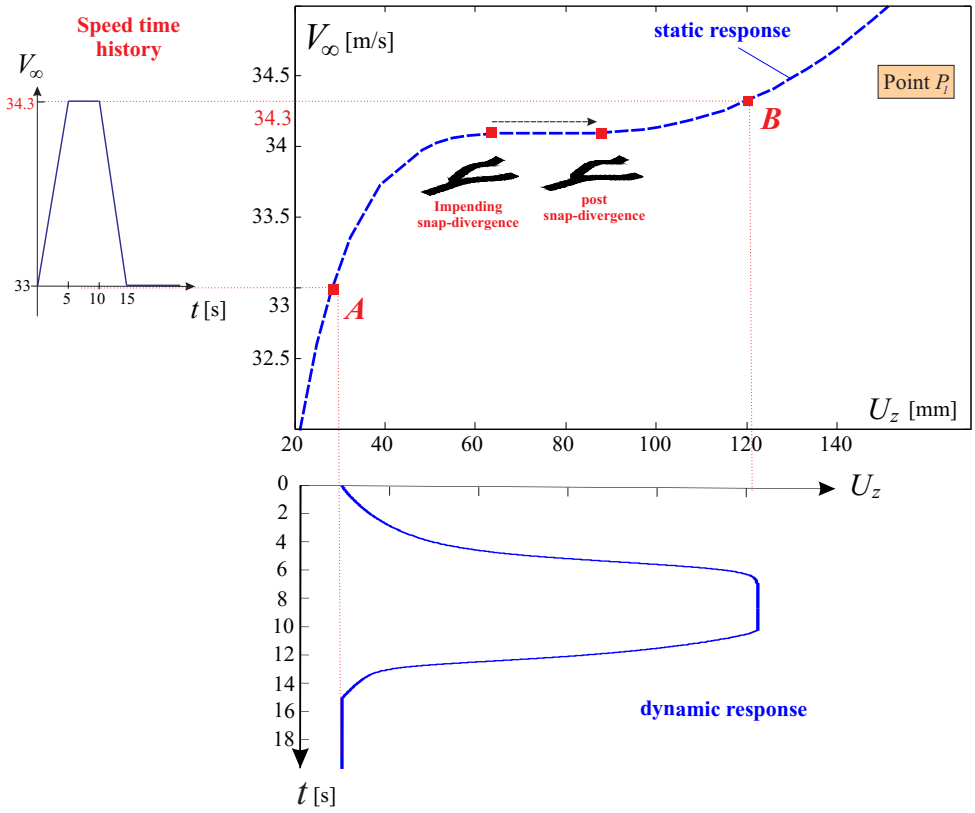

Figure 7.14: Aeroelastic static response of *JW70*, speed perturbation in time, and aeroelastic dynamic response to the perturbation. U_z refers to the vertical displacement of the wing tip, point P_1 of Fig. 7.11.

Tracking the dynamic response, as long as the speed approaches values close to the one of *snap-divergence*, there is an abrupt increase in the displacement of the wing tip (measure of the deformation of the structure). Comparing the displacements for the static and dynamic cases, the snap-divergence phenomenon may be well recognized. In the inverse phase, where the speed is decreased to its initial value, similar trend is observed and the initial static equilibrium condition is obtained at the end of the transient. Further looking at the response, the inertial effects seem to be of secondary importance in this specific case, in fact no oscillation is observed.

Summarizing, the dynamic response matches closely the static one.

7.7 Flutter Evaluated with Linear and Nonlinear Analyses

This section shows how linear and nonlinear tool may predict notably different flutter speeds. As already outlined in section 7.3, the here considered nonlinearity is relative to the large displacement of the configurations (geometric nonlinearity). This comparison was already pursued in [1, 158, 187], for mechanical loading and static aeroelastic conditions, respectively. It was assessed that linear analysis may give unreliable and nonconservative predictions. In some cases linear tools were not even able to correctly evaluate trends when one or more parameters were varied.

In this section the difference between the two approaches from an aeroelastic dynamic point of view is pursued by means of the frequency domain (DLM) solver, see [193]. This solver requires the modes of the structures as an input. Thus, as it will be shown, the process of running different analyses with modes representative of the undeformed or deformed structure is the keypoint in which nonlinear effects are introduced.

7.7.1 PrP40

The already introduced configuration *PrP40* is first taken into consideration. As said, the DLM method requires the modes of the structures as an input. Thus, evaluating the modal properties of the structures at different point on the static aeroelastic response (the static aeroelastic equilibrium states can be found in [158] and are presented also in the next session), it is possible to have a progressively more refined estimate of the flutter speed (Hopf's bifurcation).

Results are relative to different structural damping values: a chosen value of damping ratio is applied to the considered modes, in the process explained in section 7.3.2.

Flutter speeds are 51.5 m/s for the zero damping case, 52.2 when $\zeta = 0.01$, 53.7 when $\zeta = 0.02$ and 54.9 when $\zeta = 0.03$. Discrepancy of the flutter speed evaluated for the undeformed configuration (which is the common practice) and the real one is about 22%. Unfortunately, in this case the discrepancy is in the nonconservative side (overprediction of the critical condition). Actually, increasing the linearization speed enhances this mismatch, at least for a large portion of the response. Interestingly enough, an overprediction of the divergence speed was also found for the aeroelastic static case (see [158, 187]).

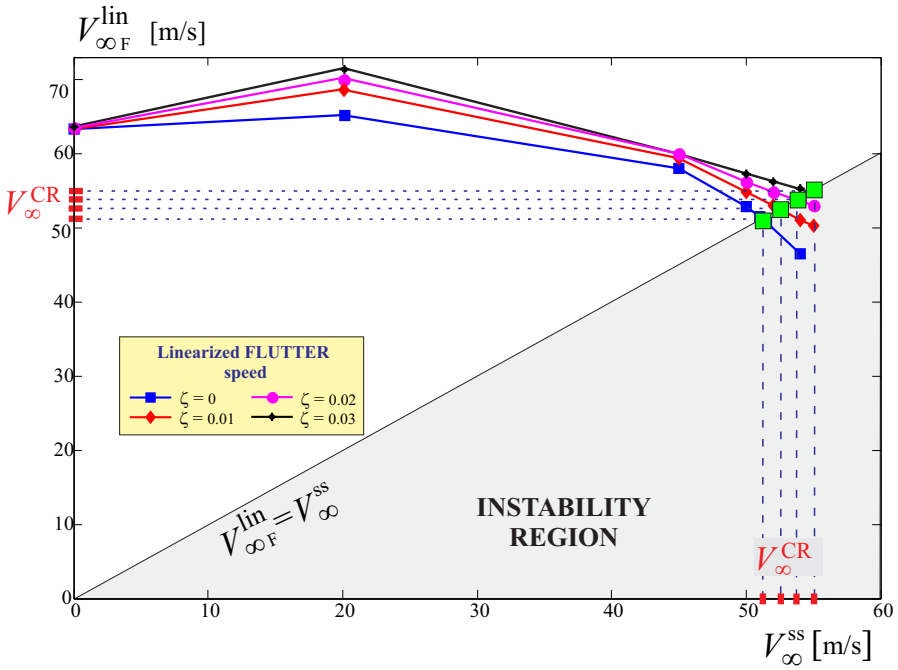

Figure 7.15: Flutter speed predicted linearizing about steady state relative to different flow speeds for *PrP40*. The real critical condition (*nonlinear flutter*) happens when these two speeds coincide.

In literature it is claimed [230] that DLM model lacks in precision when used for cases in which wake roll-up plays an important role, or for case in which the structural deformation is conspicuous. In other works, e.g. [4], the real wake geometry was judged to be not influent for the specific aeroelastic case under examination. In this regard, next section which will focus more on the LCO, will also present a comparison among flutter speeds predicted with different approaches (frequency vs time domain) and models.

7.7.2 Sensorcraft

Here the *Sensorcraft* is considered. Results are shown in Fig. 7.16. The interesting property of this configuration is the relatively smaller deformation consequences of the chosen geometric properties (this will be better characterized in next section). However, as it could be appreciated, there is still a non-negligible overprediction of the linear tool. In fact, considering the zero-damping case, the linear prediction gives 59.1 m/s against the 51.6 m/s, with a difference of approximately 15%.

A further aspect to underline is the relative insensitiveness of the flutter speed in respect of the structural damping. This was not the case for the previously examined

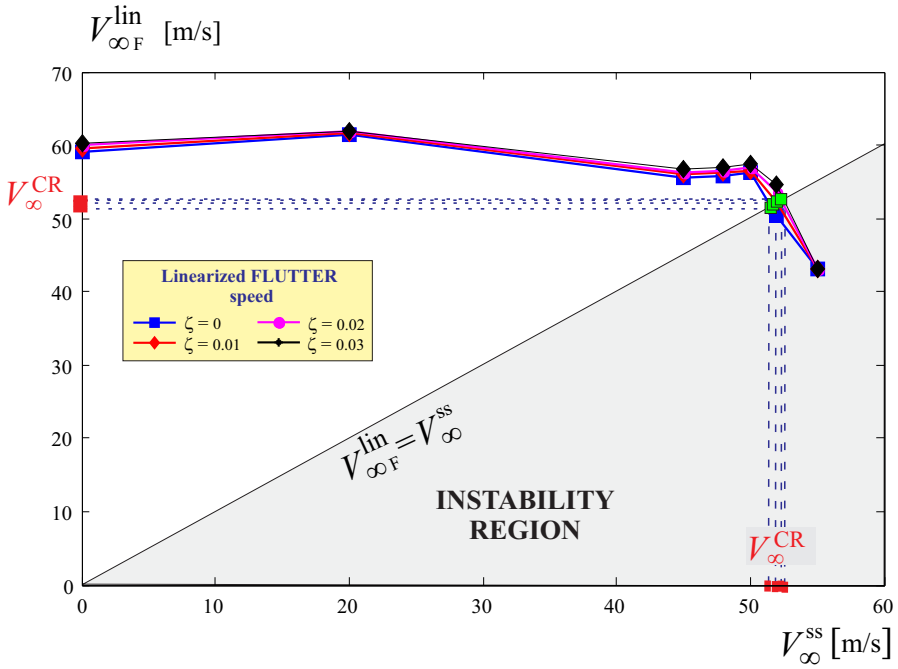

Figure 7.16: Flutter speed predicted linearizing about steady state relative to different flow speeds for *Sensorcraft*. The real critical condition (*nonlinear flutter*) happens when these two speeds coincide.

configuration.

It is interesting to observe that, linearizing about a speed other than the fundamental (zero) one, the flutter prediction instead of being more precise, may actually lead to larger errors. This was observed also for the *PrP40* case, suggesting that, evaluation done with immediate successive linearization may give misleading trends and even more inaccurate predictions, unless the linearization speed is close to the real critical one. These results stress out the big role played by the nonlinearities in Joined Wings configurations.

7.8 Postcritical Dynamic Aeroelastic Analysis

In this section different results are shown. Flutter speed as predicted by the time- and frequency-domain solvers are compared, for different values of the damping ratio. For the post-flutter, different dynamic responses, in particular Limit Cycle Oscillations (LCO), are observed for the baseline configurations. These LCOs are obtained perturbing the steady state, or, alternatively, increasing the angle of attack until the target value is reached. The sophistication of the analyses is mitigated by the use of all the solvers as an important mean of comparison and validation. The discrepancies observed when different solvers are employed is discussed in more depth and a physical interpretation of these differences is also attempted, when possible. The outcome of this analysis has important consequences since it suggests which solver should be used to reach a good balance between reliability and computational costs.

7.8.1 Limit Cycle Oscillation for JW70

The previous sections gave both a static and dynamic evaluation of the aeroelastic properties of the joined-wing configurations under examination. In particular, flutter speed was assessed with frequency domain solver. In this regard, a time domain solver may be used to assess if the flutter speed was consistently predicted, and, also, to show the post-critical response. Moreover, solvers based on different modelling are used to provide an insight in what are the important requirements for this kind of problem, so that simpler and computationally less expensive solutions may be used with confidence.

Solver1

Fig. 7.17 shows the dynamic response of the *JW70* configuration evolving from an equilibrium state as the ones depicted in the graph. For each case, a vanishing angle of attack perturbation is given to provoke a more observable transient, and eventually induce more rapidly a post-flutter behaviour. This perturbation consists in a linear increase in the angle formed by the onset flow direction and the x-axis, followed by a symmetric decrease to the unperturbed value (which is 1°). The peak is reached at 0.1 seconds, and at its value it holds that $\alpha_x = 1.01$ (this is shown in the box in Fig. 7.17).

All the results have been obtained considering no structural damping. The simulations have been carried out for different speeds, so that both the typical subcritical and supercritical responses could be appreciated. In particular, with this approach, it

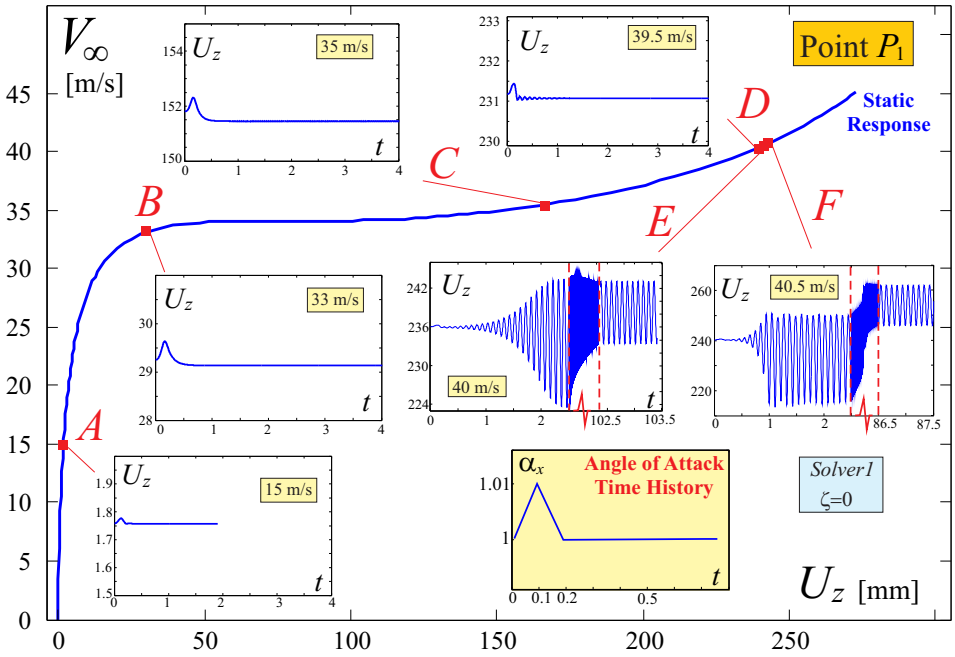

Figure 7.17: *Solver1*. Aeroelastic dynamic response of *JW70* starting from steady states relative to different velocities when a vanishing perturbation in angle of attack of the onset flow is given.

is possible to locate a small interval in which the flutter speed lies (according to this solver). For the present case, the flutter speed falls in the interval $39,5 \div 40$ m/s. These results are analyzed and discussed in more depth in section 7.8.1.

For speed larger than flutter, an LCO is observed. The properties of the LCOs are depicted in Fig. 7.18. Very interesting is the transient of system before settling to an LCO. Not only the path described in the space phase is long before it is finally attracted from the LCO orbit. But, for a wind speed of $V_\infty = 40.5$ m/s it has also an abrupt change in the oscillatory trend. It is the authors' opinion, and actually, it may be supported by physical sense, that this behaviour is largely due to the overconstrained nature of the joined-wing layout. The mutual loads transferred through the joints give raise to a complicated response. This could be easily verified comparing the transient to the LCO shown above with the ones of the Delta Wing case (see reference [193]).

Solver2

The same process outlined in the previous section is now repeated using a different aerodynamic solver. The difference with the previous case is concentrated in a

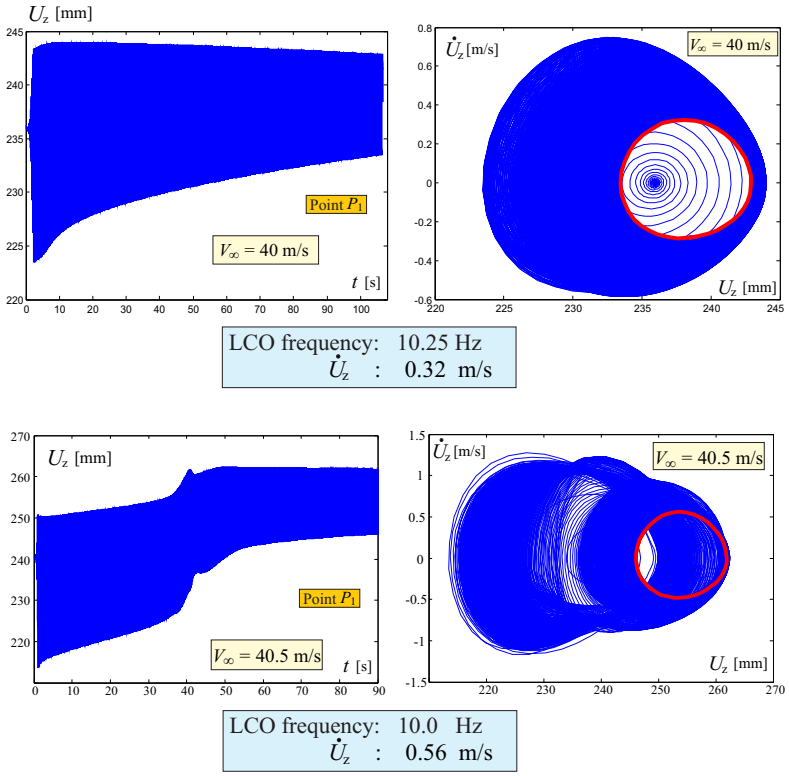

Figure 7.18: Time response and Phase-space trajectory for *JW70* configuration, for different flow speeds. *Solver1* is employed. No structural damping is considered.

more consistent application of the boundary condition (which requires the re-evaluation of the aerodynamic tangent matrix at each timestep) and also the application of the Kutta-Joukowsky formula on the real deformed structure. Moreover, all the aerodynamic/structural information are passed thanks to a meshless method. Refer to section 7.3.6 for more details.

The static response, used to start a simulation from a steady state condition, is depicted in Fig. 7.19. It is obtained with a static aeroelastic tool consistent with the above employed hypotheses. It may be well noticed that the snap-divergence has now a more pronounced connotation.

In the same figure and in Fig. 7.20, the dynamic responses obtained starting from different steady velocity and applying the above described perturbation are given. It may be observed how, with this more realistic modelling, the flutter speed sensibly decreases if compared with the outcome of the above analyses. In fact, even for structural damping ratio of ζ different than zero, and speeds that were subcritical (in term of flutter) when the case was analyzed with the *Solver1*, an LCO is observed.

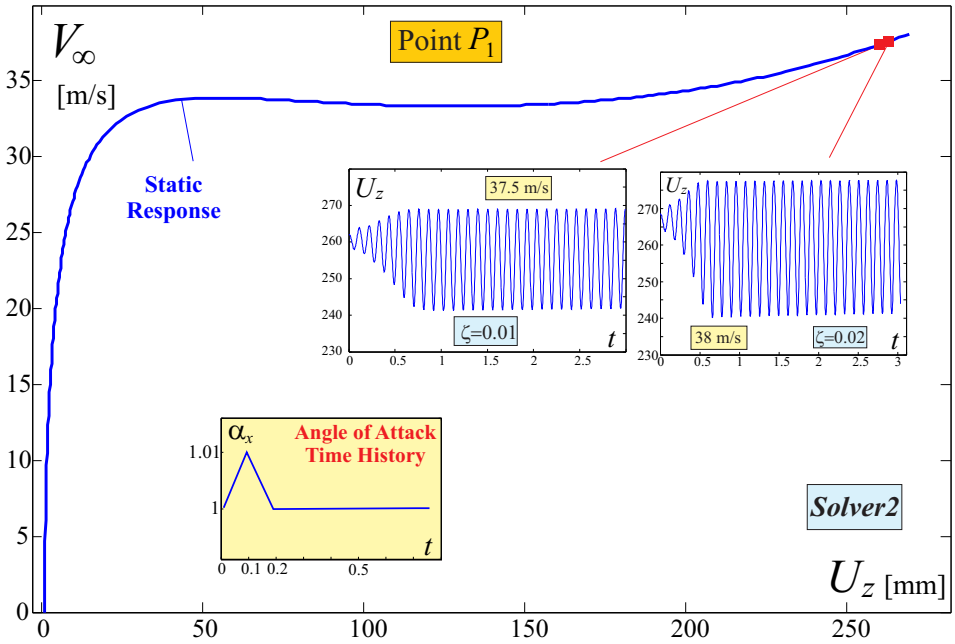

Figure 7.19: *Solver2*. Aeroelastic dynamic response of *JW70* starting from steady states relative to different velocities when a vanishing perturbation in angle of attack of the onset flow is given. Different structural damping are considered.

Solver3

The capability of free wake is considered in *Solver3*. The vortex rings are now considered attached to the structure. Thus, differently than *Solver2*, there is a perfect consistency between the control point where boundary condition is applied and inducing singularities panels. Refer again to section 7.3.6 for more details.

To consistently compare the results with the the ones presented above, it is necessary to find a suitable steady state condition. There are two generic ways to achieve a steady state. One method is based on an iterative process starting from an initial first guess wake geometry, moving it accordingly with the induced velocity components parallel to a plane perpendicular to the free-stream velocity (see [192]). A further way to proceed, is just to start from a rest condition and follow the transient until a steady state is reached.

Here, an approach similar to the second one is employed. In fact, an impulsive start is given to the configuration, and the angle of attack is slowly increased until it reaches the sought value (in Fig. 7.21 is depicted the time history of the nominal angle of attack). When these simulations are carried out for larger speeds than the flutter one,

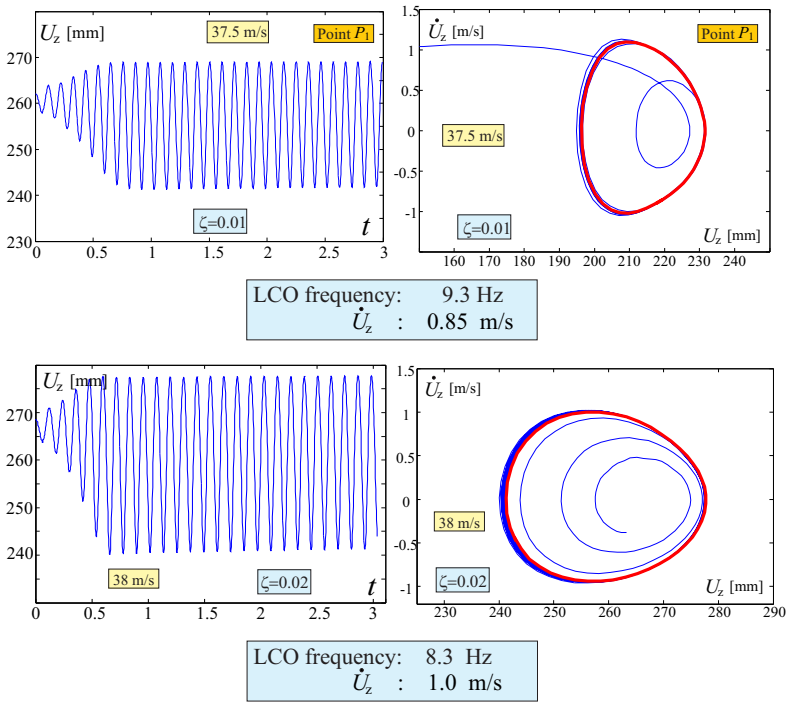

Figure 7.20: Time response and Phase-space trajectory for *JW70* configuration, for different flow speeds. *Solver2* is employed.

then, obviously, a steady state is not observed. Results are summarized in Fig. 7.21. The time histories suggest that the flutter speed lies in the $36 \div 38$ m/s range, probably closer to 38 m/s. In fact, the LCO observed at this speed has a very limited amplitude, indicating that the state is one immediately following a Hopf's bifurcation. With a small increase in speed, the LCO has a larger amplitude. With a further increment of speed, the response does not seem to have any periodicity, suggesting a transition toward chaos. A in depth analysis is needed to affirm and demonstrate the above possible chaotic behaviour.

It is very interesting to notice how a relatively small variation in speed (see Fig. 7.21) significantly changes the kind of response.

Effects of Solver's Choice and Structural Damping on Flutter Speed

In Fig. 7.22 it is plotted the flutter speed, as evaluated with the different solvers, with respect to the structural damping ratio. The critical speeds evaluated with the time domain solvers are obtained by considering the two successive speeds for which the response was showing and was not showing an LCO. In the graph, the DLM overestimates

the flutter speed in respect with all other methods. In particular, *Solver1* uses the same aerodynamic and load transferring of the DLM one, thus, to prove that this difference is not an artifact of numerics, the number of natural modes, aerodynamic panels and structural elements have been verified to be enough to give convergent results (the details are here omitted for brevity).

Solver2 gives lower flutter speeds. Applying the lift in the appropriate direction and consider the real normal in the application of the boundary condition exacerbates the bending actions. However, in general, even if in agreement with intuition, this may not always hold. For example, it will be shown for the *PrP40* layout that this is not the case.

With *Solver3*, the singularities are bound to the structure, and the wake is free to deform and evolve. Especially this last features has a relevant role in increases the critical speed.

All the solvers show a similar trend of the flutter speed with the structural damping.

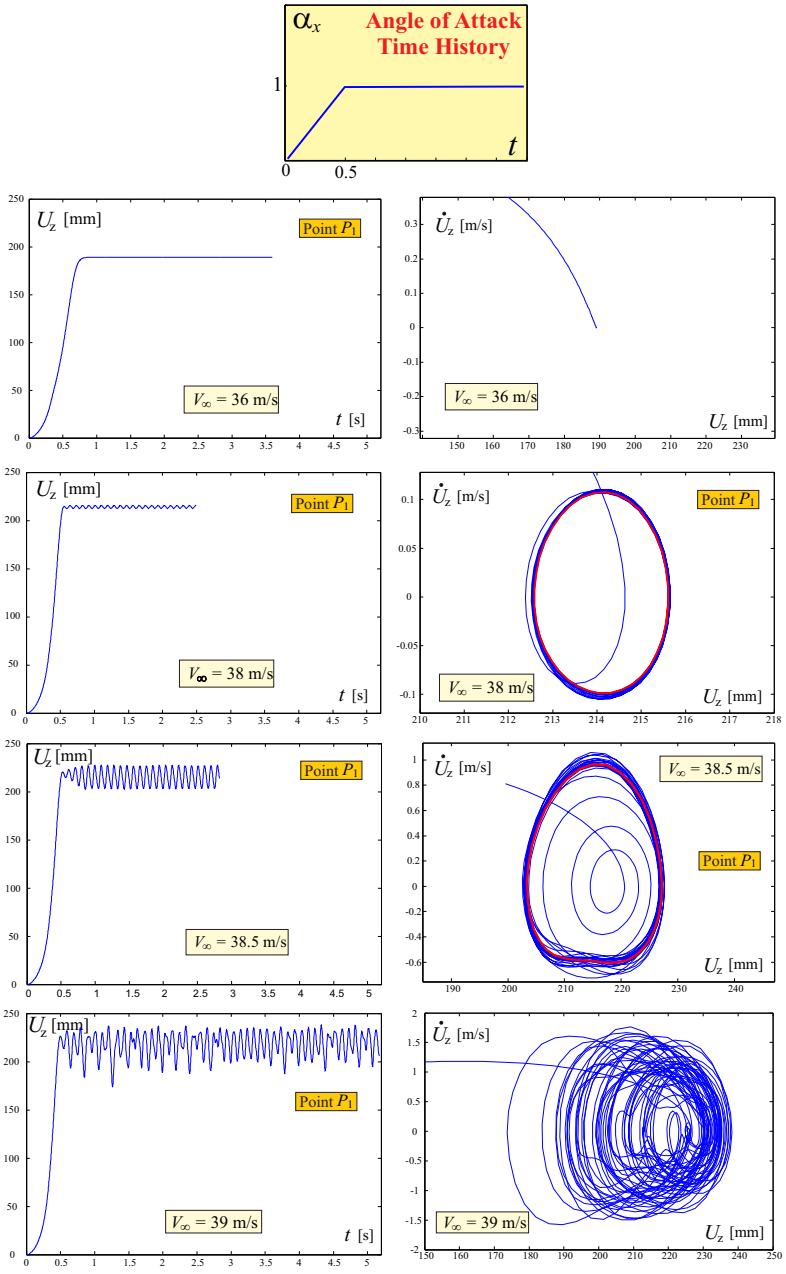

Figure 7.21: Time response and Phase-space trajectory for *JW70* configuration, for different flow speeds. *Solver3* is employed. The angle of attack is increased linearly from 0° to 1° in 0.5 seconds. No structural damping is considered. The *LCO* observed at a speed of $V_\infty = 38$ m/s has a frequency of 10.8 Hz. The one at $V_\infty = 38.5$ m/s has a frequency of 10.5 Hz.

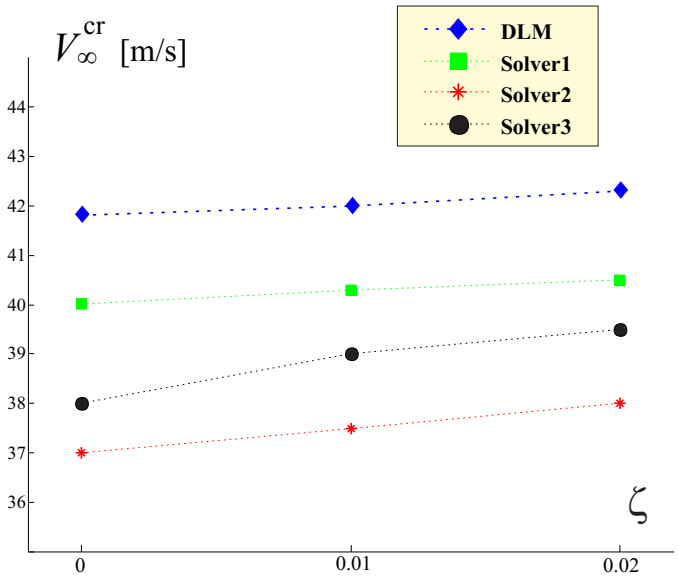

Figure 7.22: Flutter speeds for *JW70* configuration, evaluated with the different solvers and for different structural damping ratio values.

7.8.2 Limit Cycle Oscillation for PrP40

This section retraces the logics of the previous part. However, the configuration under examination is now the *PrP40*. See Fig. 7.12 for details about the geometry. For this specific test case, the thickness of the wings is set to $t = 1$ mm. The modality of application of the perturbation strictly follows what done in the previous section.

Solver1

Fig. 7.23 shows both the aeroelastic static response, andd the time evolution of the *PrP40* configuration starting from an equilibrium state depicted in the graph and experiencing a vanishing perturbation. This disturbance consists in a linear increase in the angle formed by the onset flow direction and the x-axis, followed by a symmetric decrease to the unperturbed value (which is 1°). The typical times are the same described in the *JW70* case. For all cases the structural damping is set to zero. Both configurations relative to subcritical and supercritical speeds are chosen.

The outcome of the simulations suggests that the flutter speed is in the $58 \div 59$ m/s range. Observing the response for speed larger than the flutter's one, it may be noticed how, differently than the *JW70* case, the response is not settling to his final LCO with the typical pattern observed before, in which the oscillating motion was very slowly cutting its amplitude and shifting its mean value before reaching the asymptotic behaviour. On the contrary, after a very brief peak, the response immediately sets to the asymptotic mean value, and the amplitude of the oscillation rapidly reaches the regime one. This could be observed with the aid of Fig. 7.24.

Repeating the simulation with a value of the damping ratio $\zeta = 0.03$ the critical speed increases, however, the time response reminds the ones of the undamped system. Thus, this cases are not shown here for brevity.

Solver2

The static aeroelastic response is first obtained in a way consistent with the hypothesis of the aerodynamic solver. Then, picking a speed, the initial configuration is automatically chosen, the perturbation is applied and the response is studied. Results are shown in Fig. 7.25, whereas the LCOs in the phase-space diagram are given in Fig. 7.26.

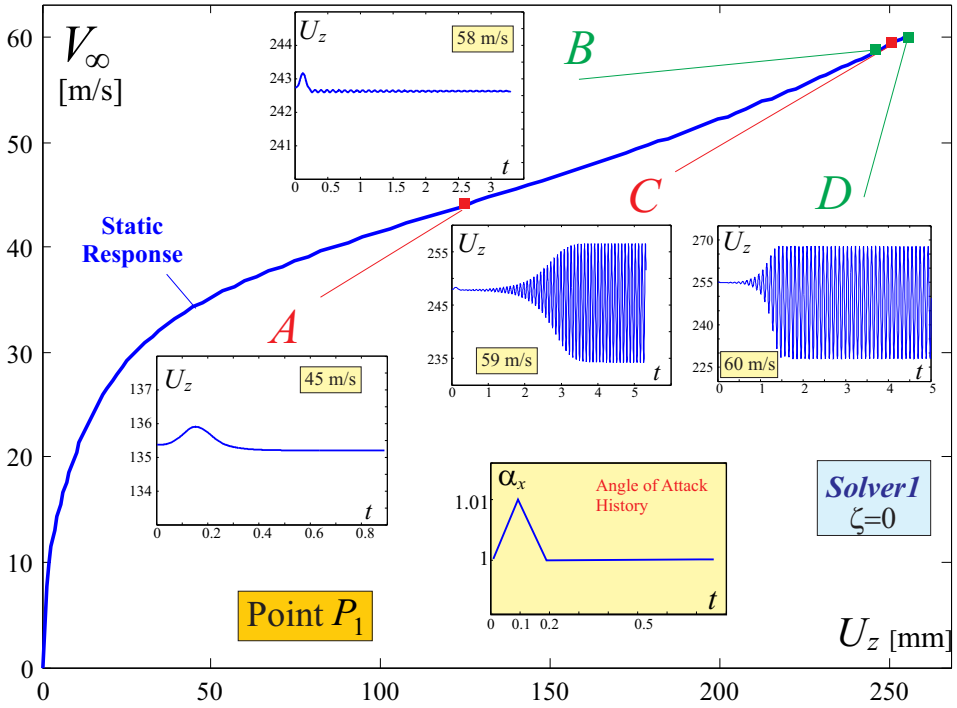

Figure 7.23: *Solver1*. Aeroelastic dynamic response of *PrP40* starting from steady states relative to different velocities when a vanishing perturbation in angle of attack of the onset flow is given.

An interesting direct comparison of the LCO properties at a fixed speed (59 m/s) when choosing two different solvers is shown in Fig. 7.27. Exploiting the geometrical follower nature of the aerodynamic forces (taken into account with *Solver2*) has an important effect on the amplitude of the LCO, and also on the frequency: both of them increase by a considerable extent. Although it is always difficult to rely on intuition when studying flutter, the increase in amplitude "is expected" in the sense that a follower force tends to exacerbate the deformation.

Solver3

Time responses and phase spaces of the limit cycle oscillations found by means of the *Solver3* are not reported. However, the performances of this tool in predicting flutter speed are analyzed in the next section.

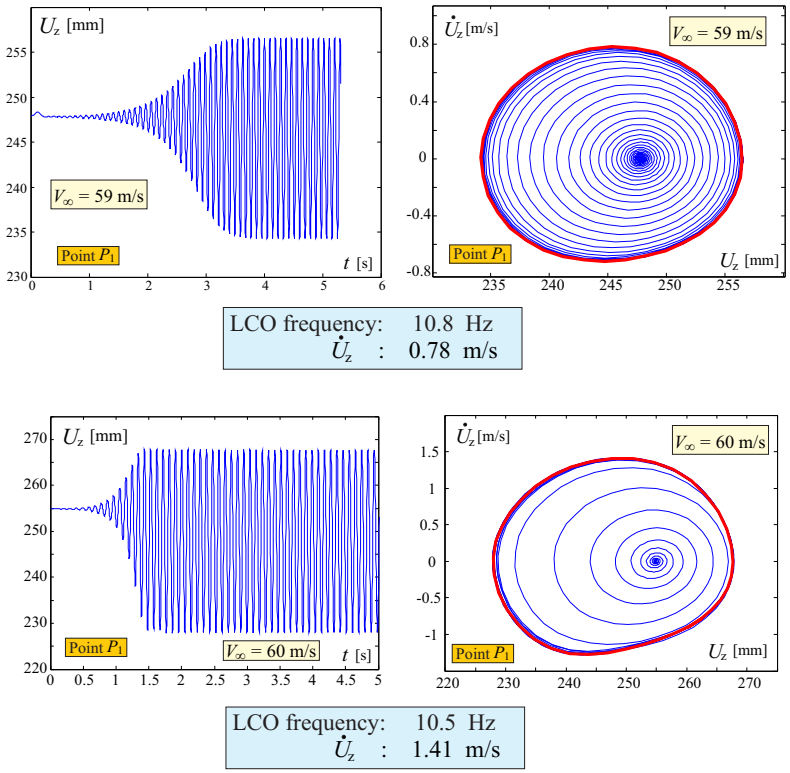

Figure 7.24: Time response and Phase-space trajectory for *PrP40* configuration, for different flow speeds. *Solver1* is employed. No structural damping is considered.

Effects of Solver's Choice and Structural Damping on Flutter Speed

In Fig. 7.28 it is plotted the flutter speed, as evaluated with the different solvers, with respect to the structural damping ratio. Considering the undamped case, the DLM solver found a flutter speed of approximately 51.5 m/s, whereas, *Solver1* predicts a critical speed of 58.5 m/s. The relative error is in the order of 12%, definitely larger than the discrepancy observed for the *JW70* case. Further analyses are needed to explain this difference. A further comment is that, differently than previous case, now the DLM predicts the lowest speed, giving thus a conservative estimation of the flutter speed.

Another difference from the *JW*70 case is the higher flutter speeds predicted by *Solver2* when compared to *Solver1*, for nonzero damping ratios.

However, the most relevant observation is the discrepancy of *Solver3* with all other solvers. Here, an explanation is tempted based on physical arguments. Comparing *Solver3* with *Solver2* the most significant source of differences is the treatment of the wake. To isolate this effect, a pure aerodynamic case is introduced.

An impulsive start of an undeformable *PrP40*, immersed in a flow with an angle

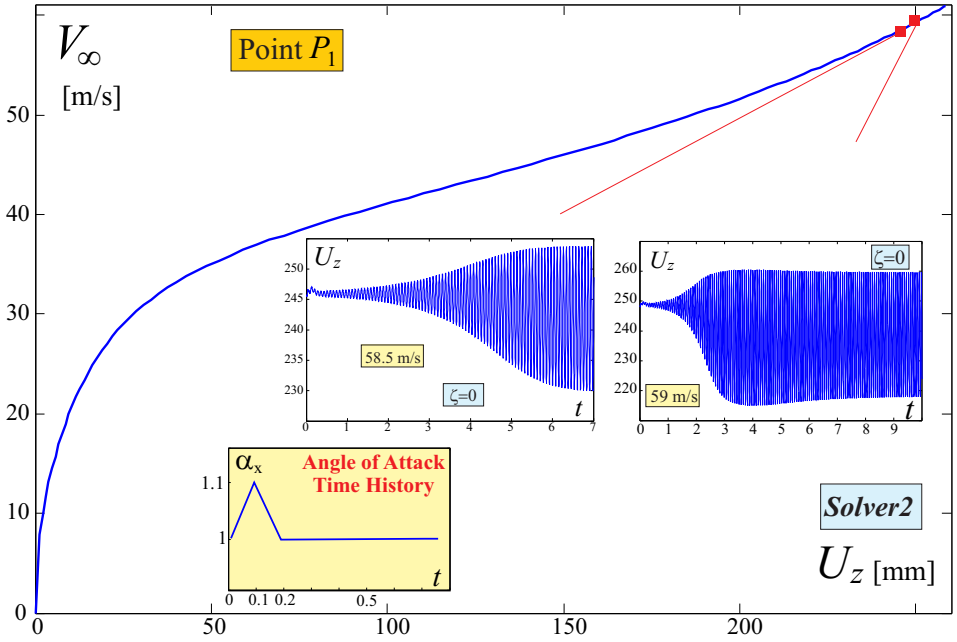

Figure 7.25: *Solver2*. Aeroelastic dynamic response of *PrP40* starting from steady states relative to different velocities when a vanishing perturbation in angle of attack of the onset flow is given.

of attack of 5° is now considered. Both a rigid wake and a flexible (free) wake model are used. The lift coefficient evolution in time is depicted in Fig. 7.29. In the immediate transient there is a small difference between the lift coefficient which vanishes when evolving in time. If, for a time in which the global lift coefficients are identical, the lift distribution along the wingspan is compared, effects of the different modelling of the wake could be better appreciated. When free wake is modeled, there is a decrease, especially concentrated on the outer part of the upper wing, of the lift; on the other hand on the front wing there is an almost uniformly distributed increase.

A similar aerodynamic study was repeated for an unstaggered *PrandtlPlane*-like configuration: it was deduced that the large load redistribution due to wake deformation was not just strictly connected with the stagger of the *PrP40* configuration. Thus, it is expected that also the other joined-wing layouts experience a considerable load redistribution when a free-wake model is adopted. The question has still to be answered regarding why the *PrandtlPlane*-like configuration is much more sensitive to the wake modelling. The following speculative explanation could be attempted. It may be noticed that in this configuration both of the wings extend spanwise to the same amount, and the redistribution of loads on the wing-tip area has large bending moment effects due to

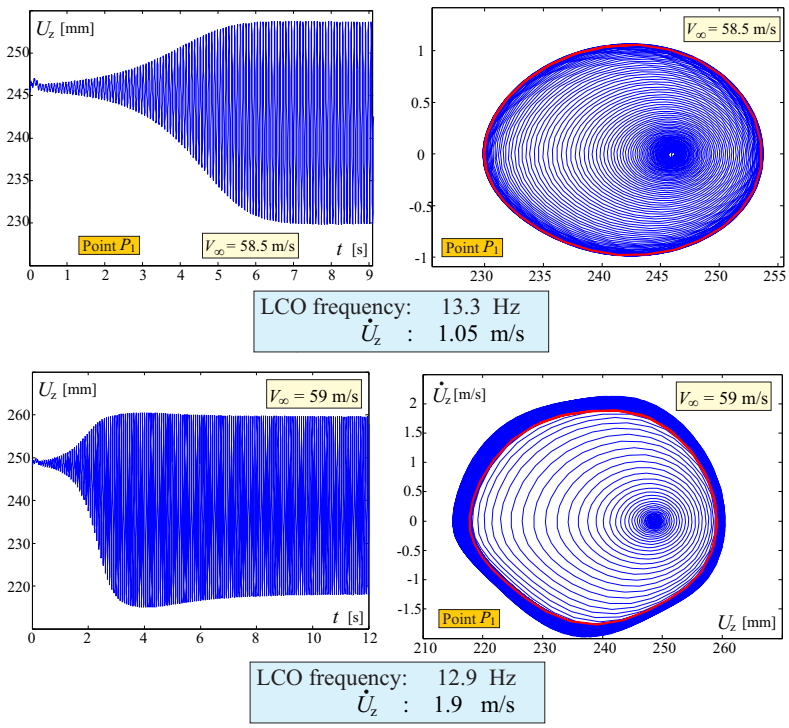

Figure 7.26: Time response and Phase-space trajectory for *PrP40* configuration, for different flow speeds. *Solver2* is employed. No structural damping is considered.

the large moment arm with respect to the wing root. Thus, it seems reasonable to link these actions to a consistently different aeroelastic response. However, as said, this has to be demonstrated, especially considering that this redistribution is of course particular of the specific case under examination (undeformed wings), thus it is not immediate to extend these results to the real deformed case.

A further note about the redistribution is that, it would affect the induced drag of the configuration. This was already shown in reference [231], where a free-wake modelling was shown to predict a lower induced drag whereas the lift coefficient was not experiencing differences. It is then suggested that, application of classic formulae [7, 18, 20, 21] for a first evaluation of the induced drag may be slightly penalizing.

7.8.3 Sensorcraft

Now the *Sensorcraft* configuration is considered. The undisturbed flow forms with the x-axis an angle of 3°, and this enables to track an aeroelastic static response as shown in Fig. 7.30. The dynamic response is studied applying a vanishing perturbation in angle of attack, as described for the previous cases.

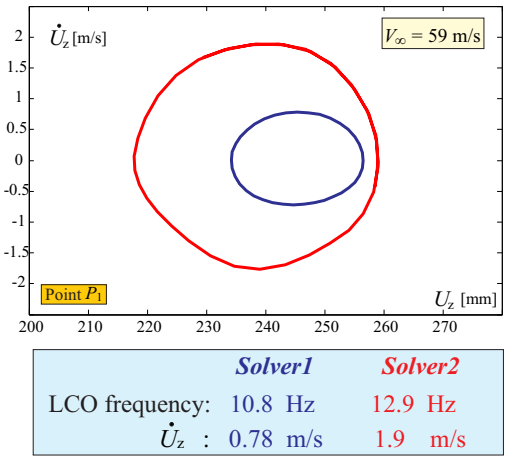

Figure 7.27: LCOs of *PrP40* at a speed of $V_\infty = 59$ m/s as predicted by *Solver1* and *Solver2*.

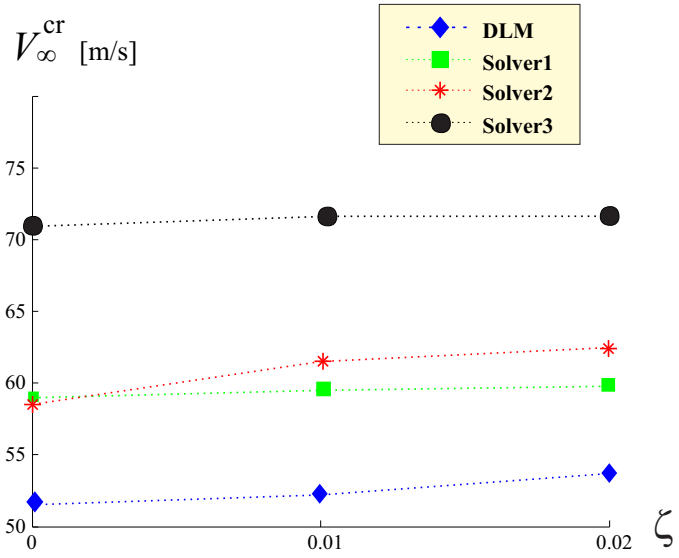

Figure 7.28: Flutter speeds for *PrP40* configuration, evaluated with the different solvers and for different structural damping ratio values.

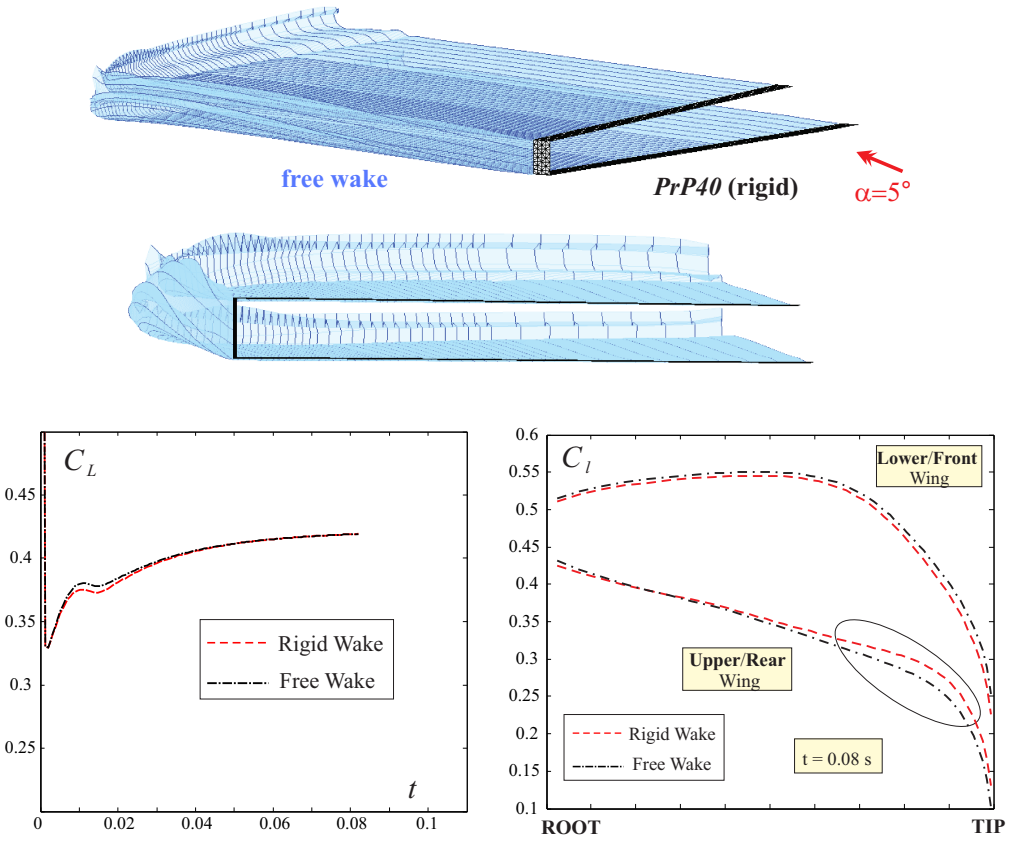

Figure 7.29: Wake models and their effects on the lift coefficients of the PrP40's wings.

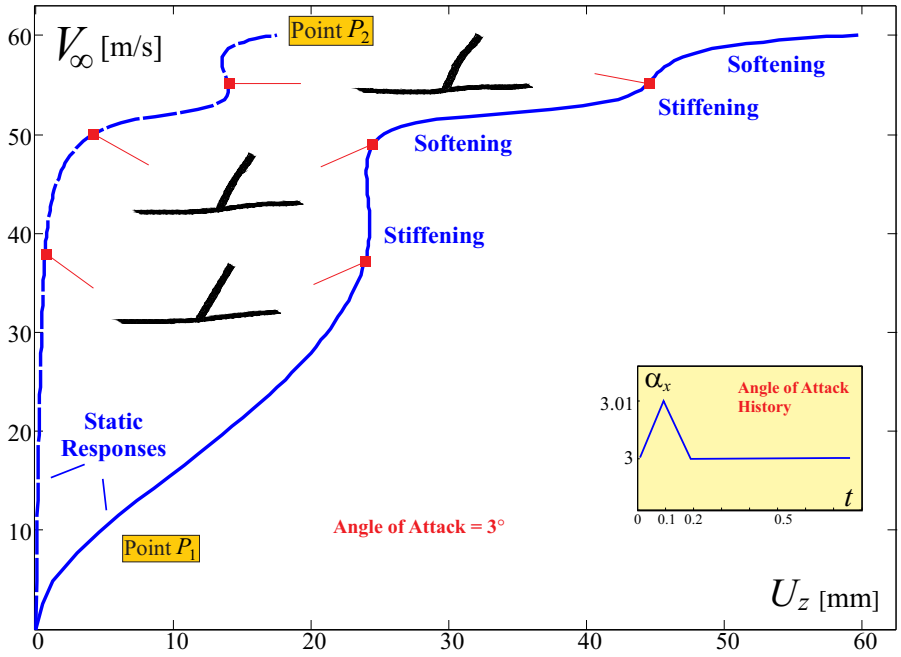

Figure 7.30: Aeroelastic static response of *Sensorcraft*. Vertical displacements of points $\boldsymbol{P}_1$ and $\boldsymbol{P}_2$ are taken into consideration (see Fig. 7.13). Angle of attack is 3°. The vanishing perturbation that is applied to track the dynamic response is also represented.

Solver1

Solver1 is here used to track the response. However, before further proceeding, it is interest to comment the aeroelastic static response of this configuration, as shown in Fig. 7.30. It features the vertical displacement of both point $\boldsymbol{P}_1$, lying on the wing tip, and $\boldsymbol{P}_2$, at the midspan, as depicted in Fig. 7.13. The extreme nonlinear response presents a sequence of softening and stiffening. In the first stiffening region (for wing's tip), the deformation of the upper wing produces a bending moment transmitted directly to the lower wing, such that the tip of the wing does not experience any vertical displacement for a wide range of speeds.

Dynamic responses are presented in Fig. 7.31 for different speeds. Focus is first on the LCO for a speed of $V_\infty = 52.5$ m/s. Considering the midspan point $\boldsymbol{P}_2$, the trajectory described by this point when a limit cycle oscillation is established is the usual wave-like response. However, this does not hold for wing tip $\boldsymbol{P}_1$. In fact, considering a period, during the ascending part the motion is temporary reversed and some higher frequency oscillations of smaller amplitude establish before continuing again the ascending motion. The descending motion does not show such a pattern. This response has been observed also when structural damping (algorithmic damping as explained in section 7.3.2, has always been used in the present simulations) was considered (not shown here) suggesting thus, that this phenomenon is not an artifact of numerics but rather real expression of the physics.

If the speed is slightly increased to $V_\infty = 53.5$ m/s, the same pattern is observed, however now the oscillation observed within the ascending motion increases its amplitude. It is natural then to repeat this process for higher speeds and observe what happens. A speed of $V_\infty = 59$ m/s is considered, and the response is depicted in Fig. 7.32. The response does not show any aeroelastic instability, although the speed is increased from the previous cases showing LCOs. This result is unexpected and underlines, once again, the difficulties inherent to the design of such a configuration. With the aid of Fig. 7.33 this property is shown: starting from a stable situation, the speed is slowly decreased until a critical condition is reached. It can be appreciated that, for $V_\infty = 57$ m/s the response immediately loses its stability (in the static sense) and an LCO is developed after the transient.

Solver2

Use of *Solver2* does not seem to give large differences from what previously observed. What can be noticed is a small decrease of the frequency, as shown in Fig. 7.34 when compared with the previous results. Also the same oscillating pattern during the ascending motion is observed. In order to better visualize this phenomenon, it is interesting to plot the *snapshots* of the configuration during a period, Fig. 7.35. As it can be easily verified, the states c, d and e describe the small oscillation during the ascending motion. Focusing then on the upper wing, it can be observed a unique smooth wave-like pattern identified by a compression and an extension, whereas for the outer portion of the wing this does not hold. It is not trivial to understand why the portions of the wing system have different dynamics, since different sources of difficulties are present: nonlinear structure, coupled aerodynamic structural and inertial effects, and also overconstrained nature of the system. As it will be shown in the next section, adding a further source of nonlinearity (wake roll up) also influences the above mentioned pattern.

Solver3

Results obtained with *Solver3* are presented in Fig. 7.36. The speed is selected so that it was possible to observed the small oscillation pattern of the tip of the wing (point $\boldsymbol{P}_1$). The angle of attack is increased until the value of 3° is obtained. It is interesting to observe that the high frequency oscillation pattern earlier observed is now present in the descending portion of the LCO. To visualize this pattern, *snapshots* of the configuration during a period are presented in Fig. 7.37. States f, g and h describe the small oscillation during the descending motion. It can be verified how, even if the midspan point $\boldsymbol{P}_2$ is monotonically descending in this window of time, the outer portion of the wing inverts its motion bending upward before restarting its descend.

Effects of Solver's Choice and Structural Damping on Flutter Speed

In Fig. 7.38, it is plotted the flutter speed, as evaluated with the different solvers, with respect to the structural damping ratio. The predictions are now much closer, and the differences are negligible. This is related both to the particular layout and to the smaller deformations involved, which do not enhance the modelling differences of the solvers.

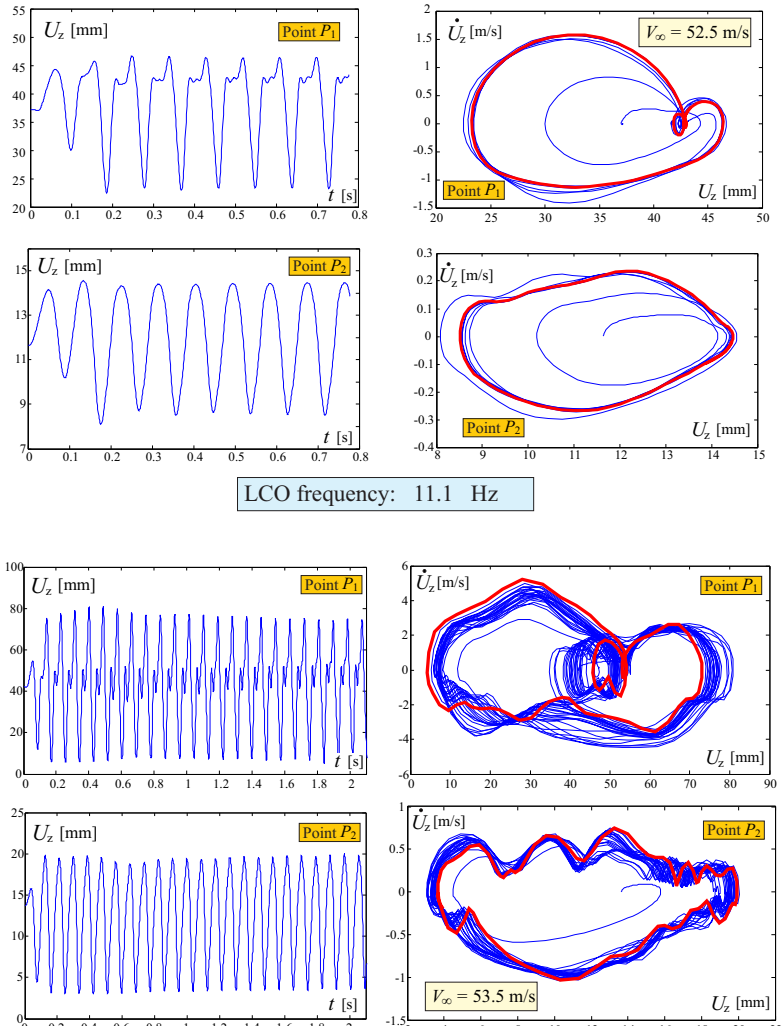

Figure 7.31: Time response and Phase-space trajectory for *Sensorcraft* configuration, for different flow speeds. *Solver1* is employed. No structural damping is considered. Vertical displacements of both points $\boldsymbol{P}_1$ and $\boldsymbol{P}_2$ are considered (see Fig. 7.13).

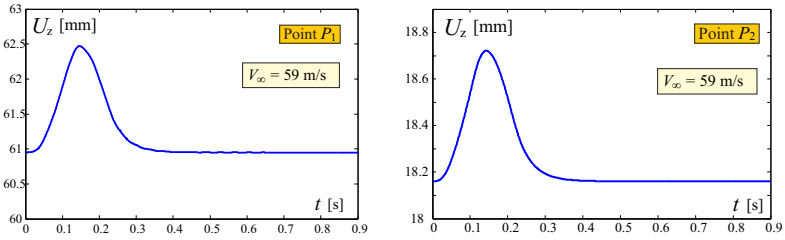

Figure 7.32: Time response for *Sensorcraft* configuration, for $V_\infty = 59$ m/s. *Solver1* is employed. No structural damping is considered. Vertical displacements of both points $\boldsymbol{P}_1$ and $\boldsymbol{P}_2$ are considered (see Fig. 7.13).

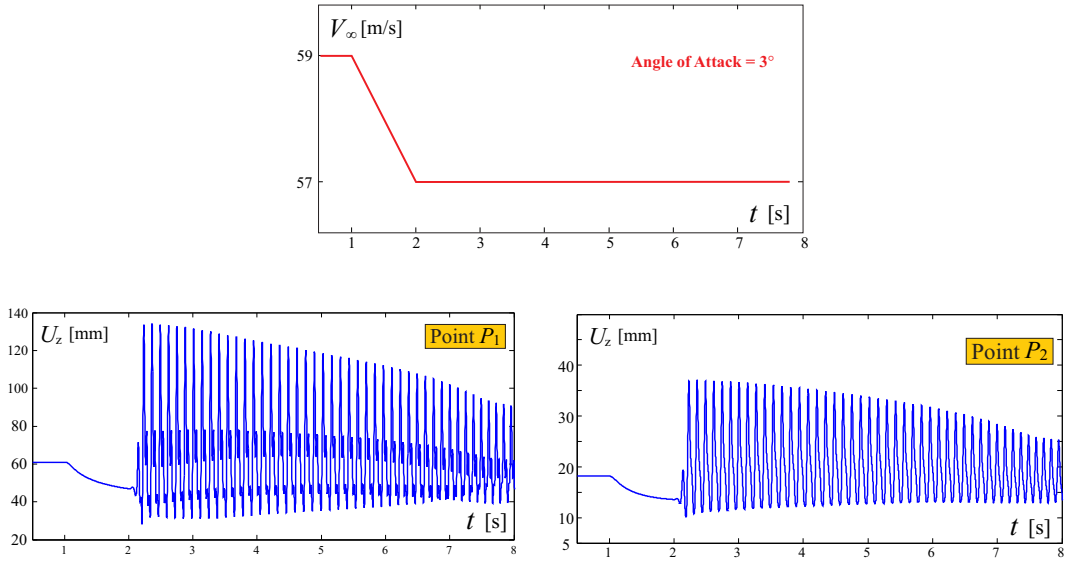

Figure 7.33: Time response for *Sensorcraft* configuration, when the speed is decreased from $V_\infty = 59$ m/s to $V_\infty = 57$ m/s, and the angle of attack is maintained to 3°. *Solver1* is employed. No structural damping is considered. Vertical displacements of both points $\boldsymbol{P}_1$ and $\boldsymbol{P}_2$ are considered (see Fig. 7.13).

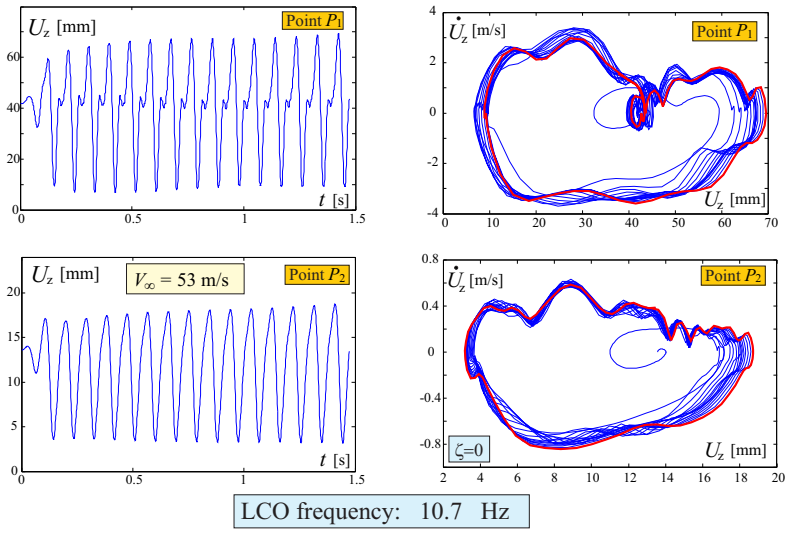

Figure 7.34: Time response and Phase-space trajectory for *Sensorcraft* configuration at a speed $V_\infty = 53$ m/s. *Solver2* is employed. Vertical displacements of both points $\boldsymbol{P}_1$ and $\boldsymbol{P}_2$ are considered (see Fig. 7.13).

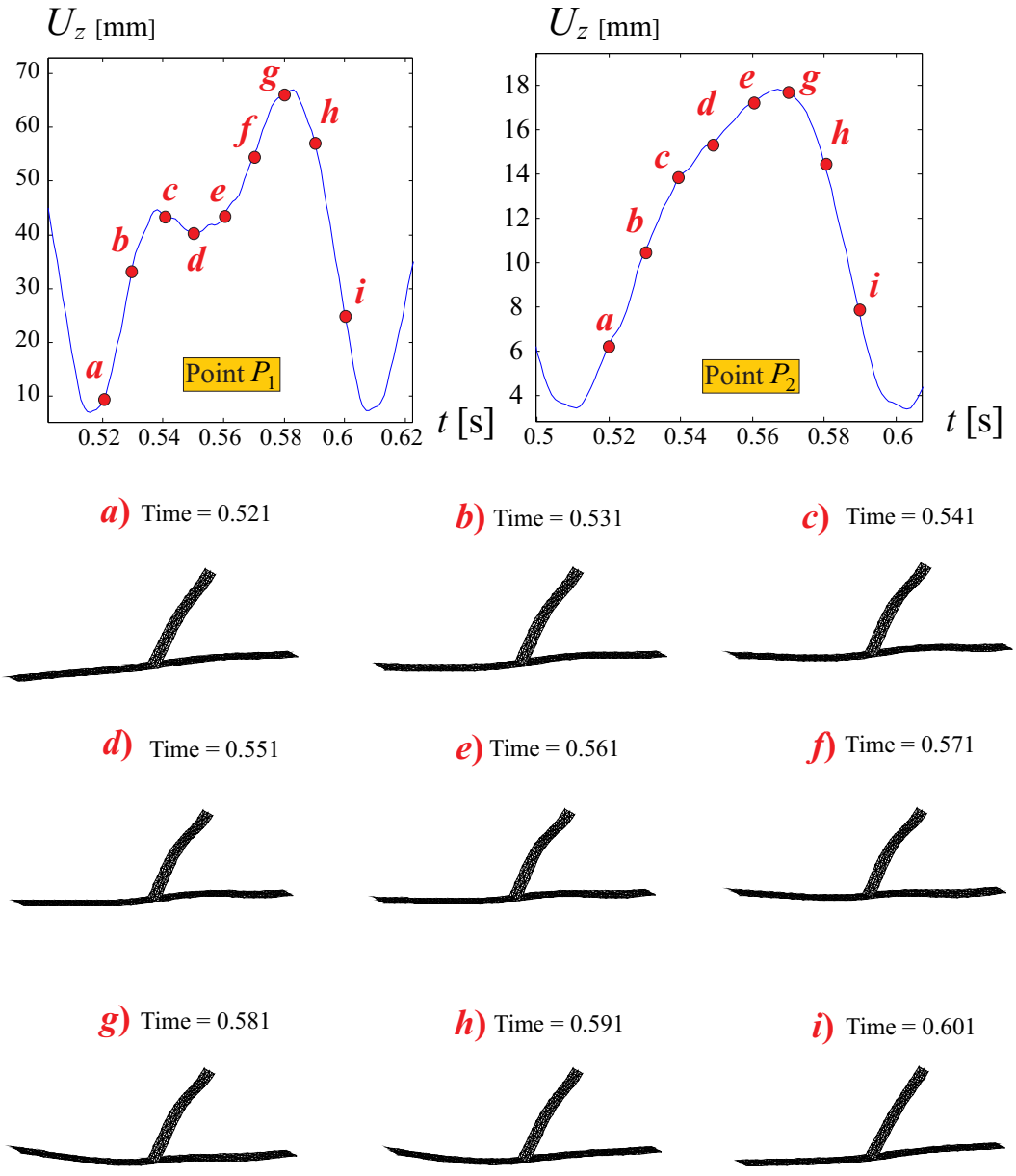

Figure 7.35: Sequence of snapshots of the deformed configuration during one period (LCO). *Solver2* is employed and $V_\infty = 53$ m/s. The points c, d and e represent the small oscillation in the ascending motion.

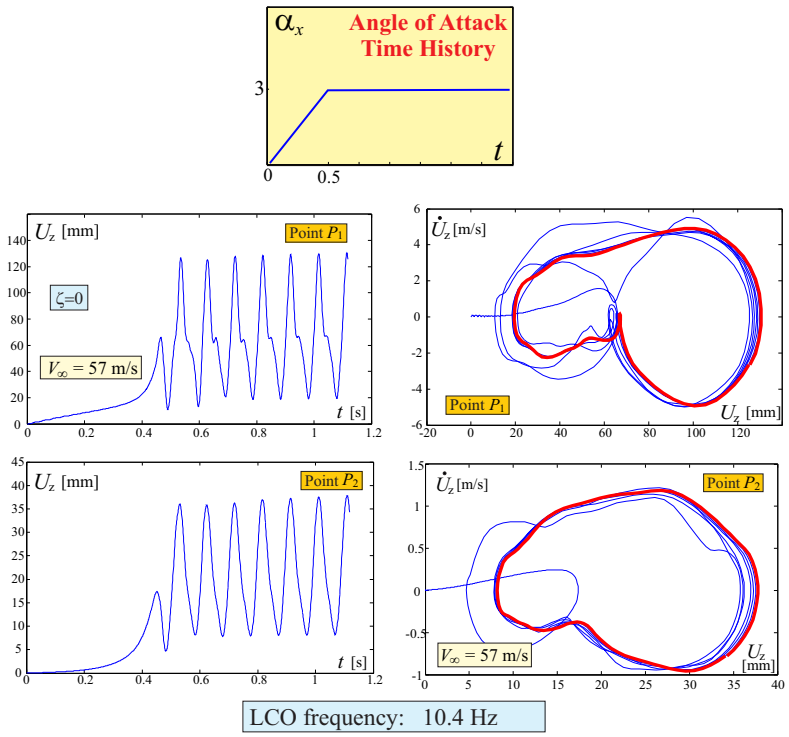

Figure 7.36: Time response and Phase-space trajectory for *Sensorcraft* configuration, for $V_\infty = 57$ m/s. *Solver3* is employed. Vertical displacements of both points $\boldsymbol{P}_1$ and $\boldsymbol{P}_2$ are considered (see Fig. 7.13).

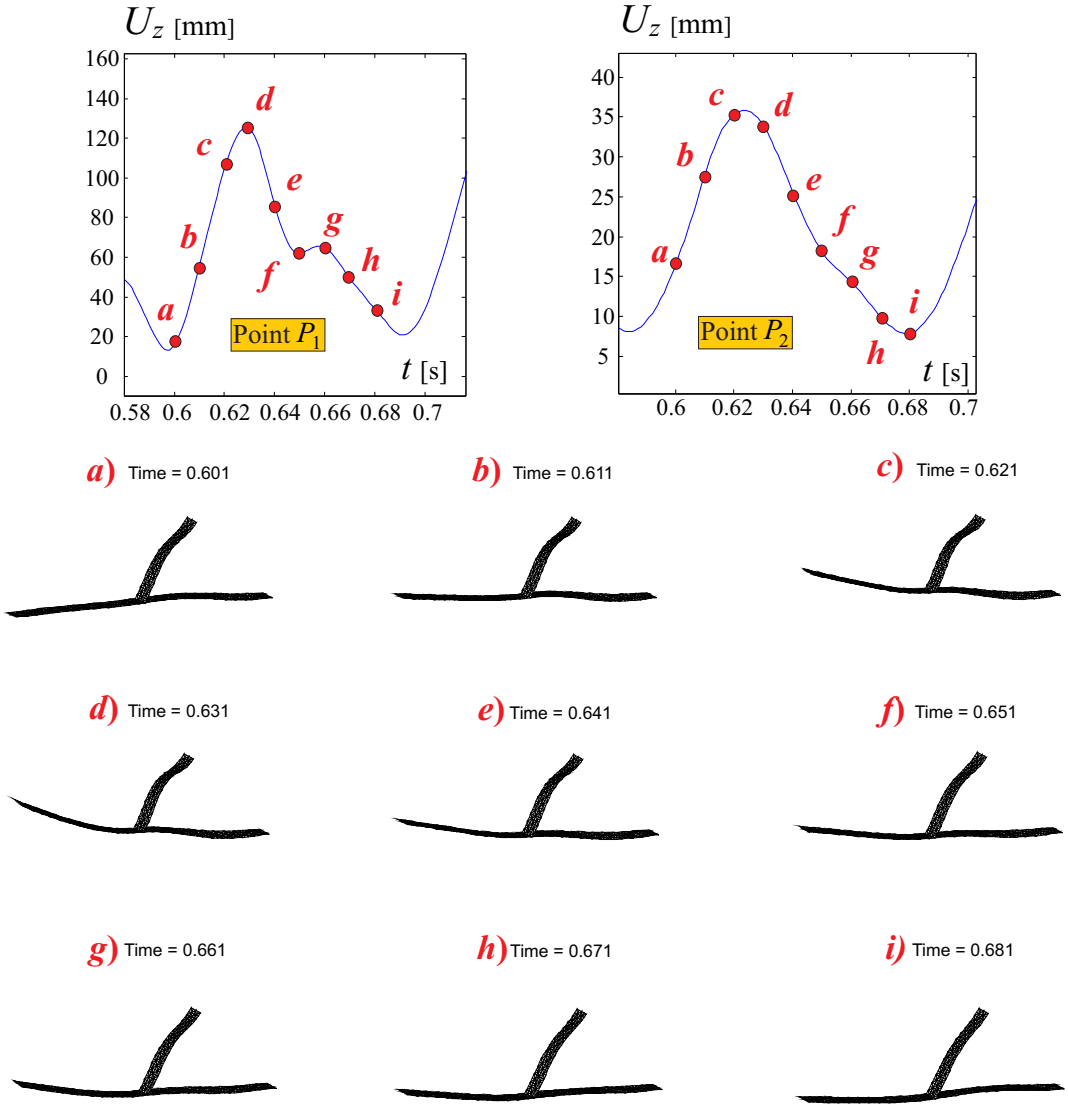

Figure 7.37: Sequence of snapshots of the deformed configuration during one period (LCO). *Solver3* is employed and $V_\infty = 57$ m/s. The points f, g and h represent the small oscillation in the descending motion.

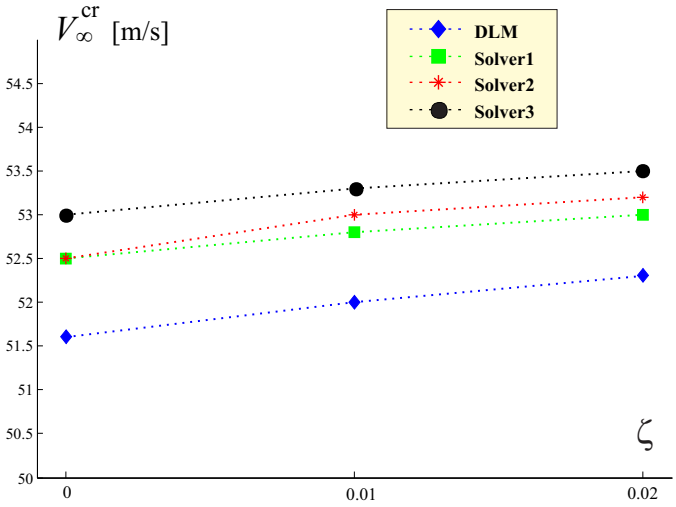

Figure 7.38: Flutter speeds for *Sensorcraft* configuration, evaluated with the different solvers and for different structural damping ratio values.

7.9 Joined Wings: a Dynamical System Perspective

This section shows the complicate picture of Joined Wings responses described from a dynamical system perspective. Different kinds of bifurcations are detected when tracing the *stability diagram*, and the situation appears very complex.

Before further going into details, the test case is here described. Consider the *PrP40* layout, shown in Fig. 7.12. The thickness is now selected to be 0.6 mm. The freestream velocity is along the x axis. *Solver1* is used to study the dynamic response. As it will be clear in the following, also aeroelastic static tool with continuation capabilities (arc-length methods) are used.

Being the angle of attack zero, there are no aerodynamic forces in the undeformed (basic) configuration. Thus, it is an equilibrium (fixed point) configuration for all velocities. With reference to the bifurcation diagram of Fig. 7.39, in which the vertical displacement of the tip of the lower wing (point P_1 in Fig. 7.12) has been chosen as representative displacement variable and the parameter is the flow speed, these fixed points lie on the ordinate. If the speed is increased, V^{sd} is reached. This speed is associated with saddle node bifurcations occurring on branches far from the fundamental one. What occurs is the inception of two fixed node points on each of the non-fundamental branches. That is, if the speed falls between V^{sd} and V^{bf}, there are *five possible equilibrium configurations*, and three of them are *stable*, see Fig. 7.39. Thus, a so called *tri-stability* situation is in place. With aid of Fig. 7.40, a speed in this range has been chosen, i.e. $V_\infty = 29.5$ m/s, and the equilibrium points are represented with a small circles, full (empty) if they are stable (unstable). Consequence of multi-stability have been already explored and discussed for joined-wing layouts in references [2, 197]. This property is demonstrated in Fig. 7.41 by giving different vanishing perturbations in angle of attack, and observing that after the transient the configuration could settle to the three different equilibrium states on the branches. When speed approaches V^{bf}, there is a bifurcation that leads to change of stability of the main branch: the undeformed configuration looses its stability. What happens in the negative part of U_z is here not studied, thus, any fixed point that may exist in that part of the plane has not been taken into consideration. The typical phase-space diagram for $V_\infty = 33.7$ m/s, which is in the range $V^{\mathrm{bf}} \div V^{\mathrm{hb}}$ is depicted in Fig. 7.40. There is a bi-stability, being the stable states on the branch I and II. There are also two unstable poles, the first being on the undeformed configuration and the other one on the branch II. Responses showing this behaviour are

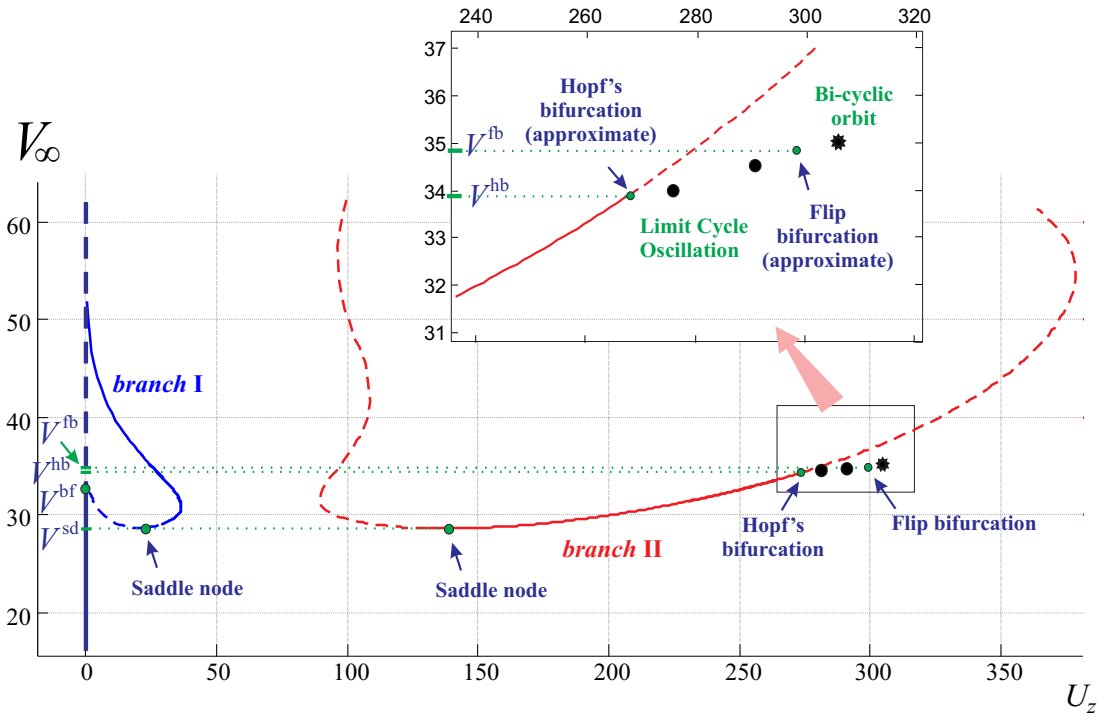

Figure 7.39: Bifurcation diagram for the test case. *Solver1* is employed. Solid(dashed) lines represent stable (unstable) fixed points, full circles stand for stable limit cycle oscillations (the largest value is depicted) and the full complex star stand for stable bi-cyclic periodic closed orbit (largest value is depicted in the graph).

represented in Fig. 7.42.

Increasing the speed, it is finally found an Hopf's bifurcation, V^{hb}. This bifurcation pertains the branch II only. The fixed static solution becomes unstable, and, on the contrary, a stable limit cycle oscillation is developed. The properties of the points on the other branches do not change. Thus, as it is shown for a speed $V_\infty = 34.0$ m/s, which is in the range $V^{hb} \div V^{fb}$, perturbations lead to the response shown in Fig. 7.43.

The largest bifurcation speed found in this analysis is V^{fb}, for which a flip bifurcation (also called period doubling) occurs. For speeds slightly larger than V^{fb}, then, considering that the only stable point lies on the branch I, there is still a bi-stability. This is shown also in Fig. 7.44. It is important to notice that, to mathematical assess a flip-bifurcation occurrence the eigenvalues of the so called *Monodromy Matrix* (known also as Floquet characteristic multipliers) [178, 232] have to be studied. However, this analysis is not trivial when relatively large (in terms of number of DOFs) systems are considered. Thus, this was not pursued in this study. On the contrary, period doubling was assessed noticing that, immediately after the bifurcation point, the period of the

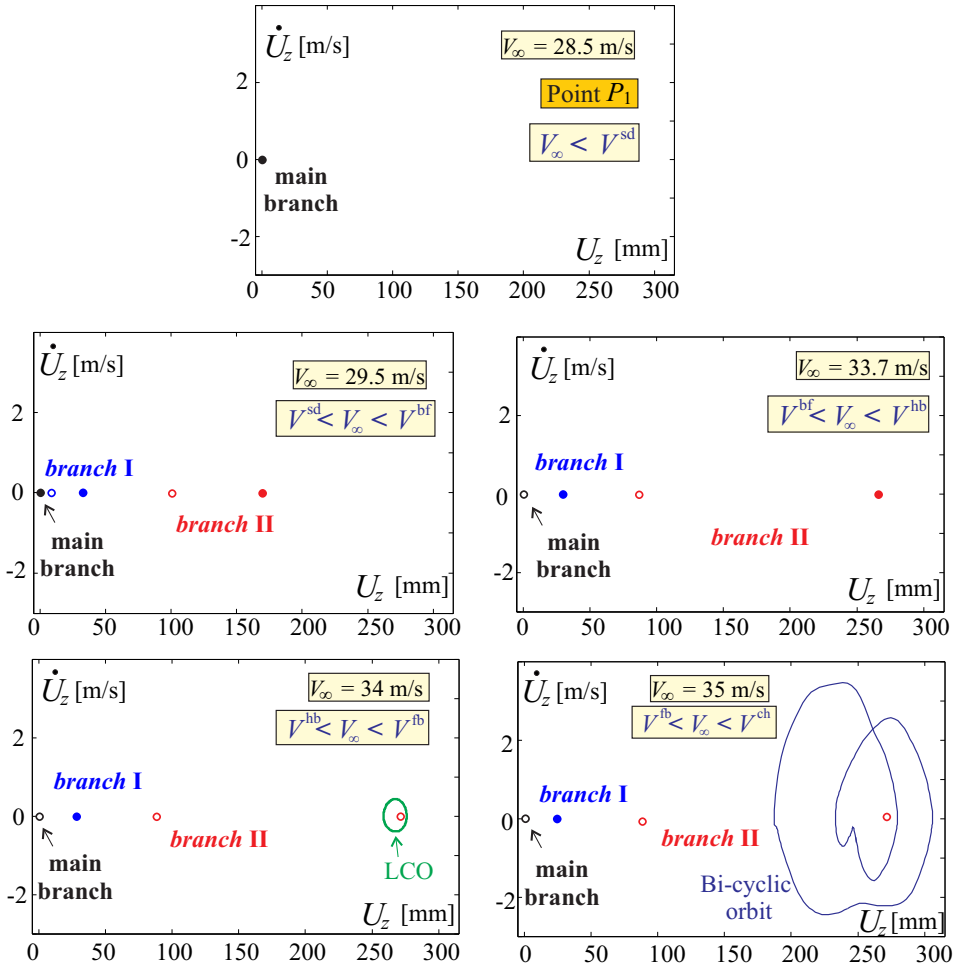

Figure 7.40: Phase space for different speeds.

closed orbit was doubling compared to the one of the limit cycle oscillation established at a speed lower than the period doubling one. Fig. 7.45 clearly shows the doubling of the period. The closer orbit described after period doubling occurrence is here assessed to as bi-cyclic periodic orbit. It is presented more in detail in Fig. 7.45. The time responses as well as the state spaces are plotted considering now three degrees of freedom. Other than the point P_1, now also vertical displacements of points P_2 and P_3, shown in Fig. 7.12, are considered.

When speed is further increased, the response associated with the branch detached from the period doubling bifurcation seems to have a chaotical response, as shown in Fig. 7.46. In depth analyses are needed to confirm transition to chaos. The branch I stable fixed point is still present (Fig. 7.39).

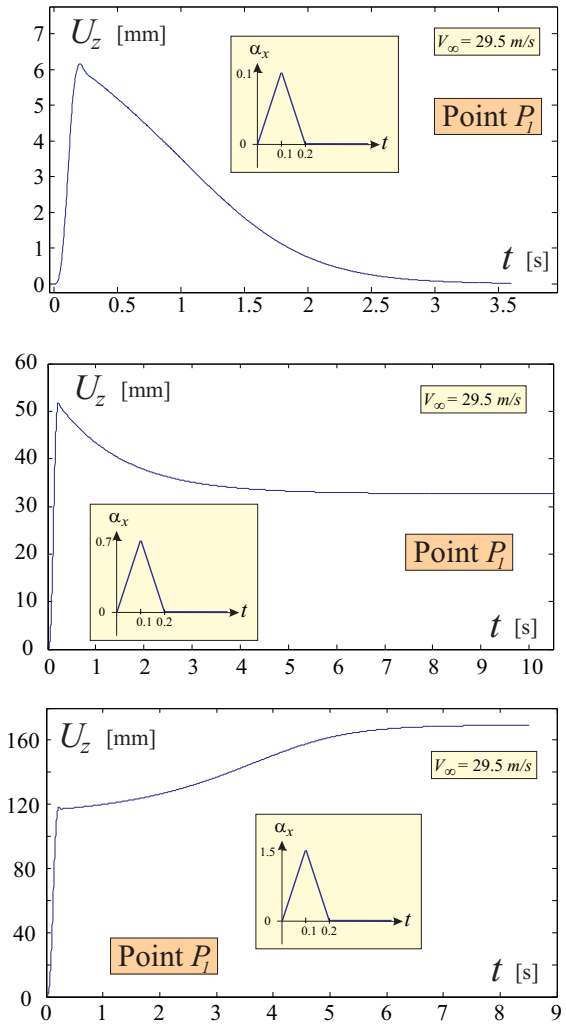

Figure 7.41: Tri-stability region, at $V_\infty = 29.5$ m/s. Starting from the initial undeformed configuration different vanishing perturbations in angle attack are given, and the response is tracked.

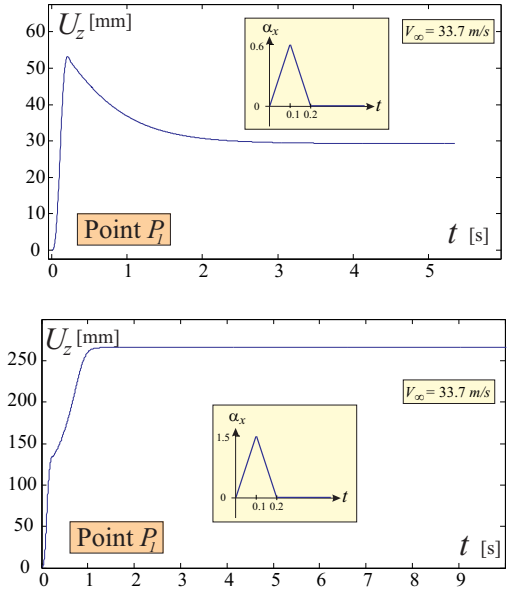

Figure 7.42: Bi-stability region, at $V_\infty = 33.7$ m/s. Starting from the initial undeformed configuration different vanishing perturbations in angle attack are given, and the response is tracked. The systems could settle down to both static equilibrium on branches I and II.

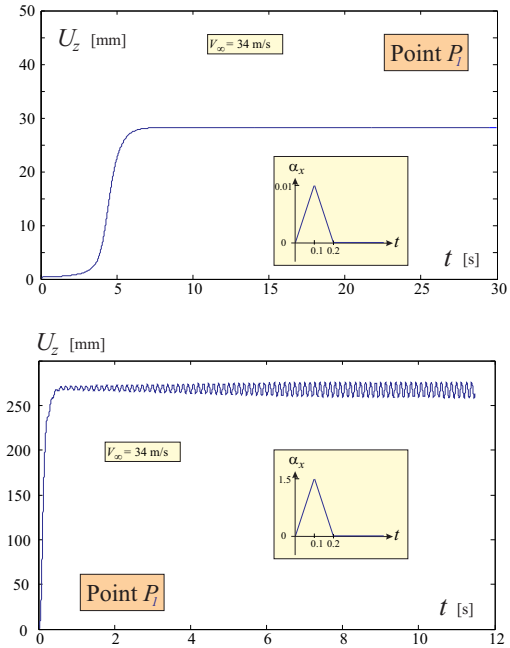

Figure 7.43: Bi-stability region. Starting from the initial undeformed configuration different vanishing perturbations in angle attack are given, and the response is tracked. Either the static solution on branch I or the limit cycle oscillation are approached after a transient.

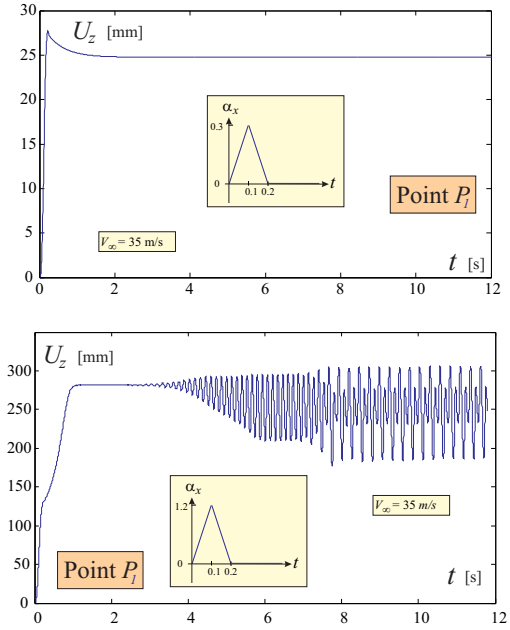

Figure 7.44: Bi-stability region. Starting from the initial undeformed configuration different vanishing perturbations in angle attack are given, and the response is tracked. Either the static solution on branch I or the bi-cyclical closed orbit are approached after a transient.

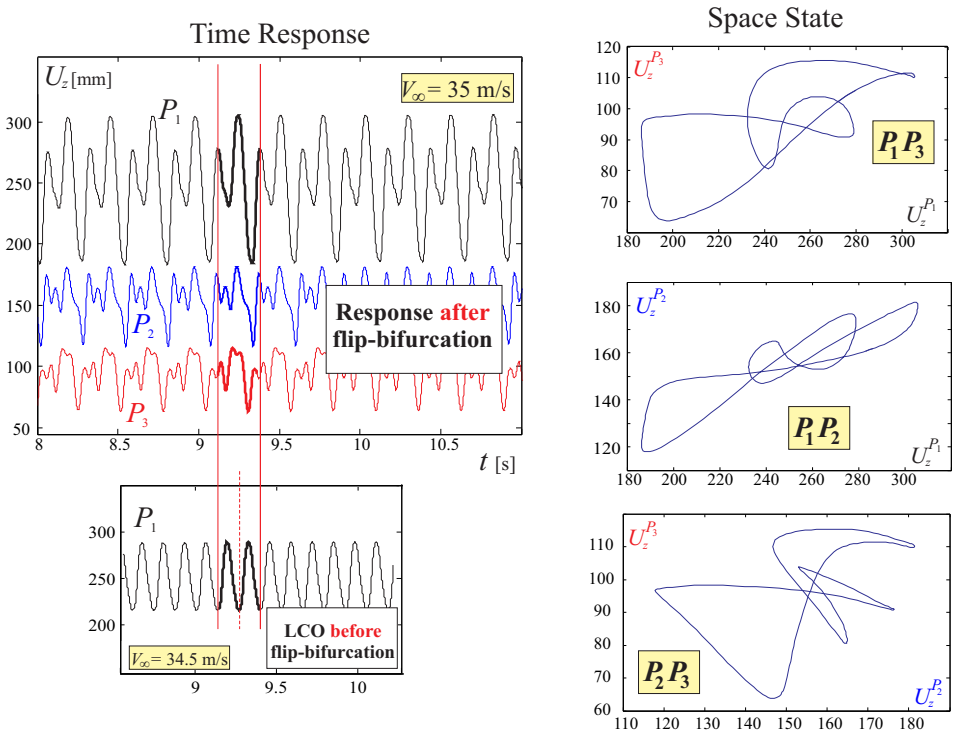

Figure 7.45: Closed orbit for higher than flip bifurcation speeds. Time response for points P_1, P_2, P_3, and state spaces for their combinations. The time responses are also compared to a subcritical one to assess the doubling of the period.

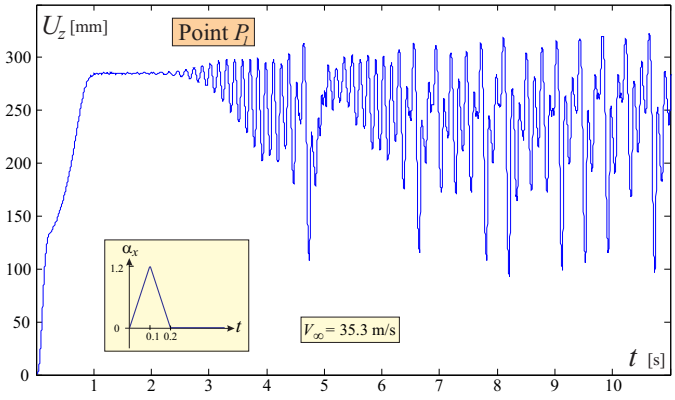

Figure 7.46: Time response for $V_\infty = 35.3$ m/s when a vanishing perturbation in angle attack is given: the response does not show any periodicity.

7.10 Conclusions

Aeroelastic dynamic phenomena of Joined Wings have been here presented. Previous efforts assessed Joined Wings response for mechanical loads and post-critical conditions in static [1, 2, 162], and dynamic [158] regimes. The true aeroelastic post-critical condition was also studied. As a logical continuation this paper analyzed the aeroelastic dynamic response. The effort was directed towards different perspectives.

First, a dynamic characterization of the *snap-divergence* concept was achieved. In fact, its occurrence was first found in reference [158], and examinated by means of an aeroelastic static analysis. The question was then to assess its existence and the behaviour of the system. Results showed that the static predictions were correct, and the characteristic *snap* was observed.

Second, flutter analysis undergone with a linear frequency-domain tool was compared to a nonlinear one, obtained as a sequence of linearizations performed about deformed configurations. These investigations continued what previously assessed in efforts [1, 158] for mechanical instability and divergence. It was found that the linear tools were giving nonconservative predictions.

Third, the impact of different modelling of the aeroelastic problem (as the interface method or as the wake description) on flutter speed was assessed for time-domain solvers. Comparisons with the above frequency-domain capability were also given. It was shown that, free-wake modelling was increasing flutter speed (at least for the configurations under examination), and this was put in relation with the particular architecture of the layout. Other differences in the prediction were not enough clear to be assessed.

Fourth, aeroelastic dynamic post-critical regime was explored. Limit cycle oscillations were found. For some combinations of solvers and configurations, the transient to the LCO showed unusual trends: phase-space transient trajectories were not resembling the final periodic orbit and the transient time was relatively long. It was however difficult to give any further physical interpretation without having the support of experimental data. Moreover, for the Sensorcraft-like configuration, at certain speeds, the limit cycle oscillation was showing within a period different patterns between the outer and inner parts of the wing system.

Fifth, the joined-wing behaviour was studied in more depth on a dynamical system perspective. Bi-stability and tri-stability were observed, in analogy with what discovered in reference [2]. For a certain speed, one branch was experiencing an Hopf's

bifurcation (flutter), followed by a flip bifurcation (or period doubling). These are common symptoms predicting transition to chaos.

A contribution that this paper aims to give is also represented by the detailed treatise of theory of implementation of the aeroelastic solvers. This has been accomplished describing problems inherent to the time-discretization of the dynamic equation. Moreover, the aeroelastic coupling is presented in detail, with emphasis on the different contributions giving raise to the aerodynamic unsteady forces. And, finally, application and specialization of the meshless method was tackled in depth.

Acknowledgements The authors acknowledges the support by San Diego State University (College of Engineering). They also like to warmly thank Professor Antonio Palacios of the Department of Mathematics of San Diego State University for his precious suggestions about nonlinear dynamics.

Chapter 7, in part, is a reprint of the journal paper: "*Phenomenology of Nonlinear Aeroelastic Responses of Highly Deformable Joined Wings*, Advances in Aircraft and Spacecraft Science, An International Journal, *In press*, 2014." The dissertation author was the primary investigator and author of this paper. Coauthors were Andrea Iannelli, Luciano Demasi and Alan Márquez Razón.

Part III

Aeroelastic Analysis of a Realistic PrandtlPlane Configuration

Chapter 8

Aeroelastic Studies Applied to a PrandtlPlane Configuration

This chapter is a partial reproduction of the following conference paper:
PrandtlPlane Joined Wing: Body Freedom Flutter, Limit Cycle Oscillation and Freeplay Studies.
It will be presented at the 56th AIAA/ASMe/ASCE/AHS/SC Structures, Structural Dynamics, and Materials Conference, AIAA Science and Technology Forum and Exposition (SciTech2015) Orlando, Florida, January 2015.

8.1 Introduction

It is a recurring circumstance, in aircraft design, to re-size layout after a preliminary assessment of a solution outcome of a conceptual design stage. For cantilevered classical configurations, after years of practice and experience this problem has been mitigated and does not represent an insurmountable issue. For Joined Wings there is no similar industrial experience. Thus, attempts to conceptually design such a configuration using handbook or very low fidelity tools have always resulted in non-competitive layouts. For example, using standard structural design tools calibrated on traditional configurations may lead to considerably heavier configurations than a reference optimized traditional one, with *consequent non-demonstrated claims about non-competitiveness* of the joined-wing aicraft. An interesting discussion about the need of an ad-hoc design practice in order to exploit the potential benefits is given in Refs. [10, 11]. However, the situation is

actually even more challenging. Due to the geometrical layout of a typical Joined Wing, there is an unavoidable coupling of the different disciplines. Being this true also for traditional configurations, for Joined Wings this is pushed to the limit. For example, the flight mechanics requirements on low speed conditions may not be completely satisfied with a fine-tuning of the flap/slats design, and this constraint may completely change the layout in terms of twist distribution and sweep angle. In other words, a multidisciplinary optimization seems to be unavoidable. An example of *PrandtlPlane* applied optimization process (although structural constraints were not considered) is presented in Refs. [102, 103].

One of the major challenges in the design of Joined Wings is represented by important structural nonlinearities which are significant even at very low incidence and attached (linear) flow. Moreover, as already shown in the literature [1, 60, 130, 158, 197] the typical joined-wing layout, featuring an overconstrained system at global level, is responsible of introducing strong structural nonlinearities and counterintuitive behaviors. This high complexity implies that at early design phases of the configuration, even adopting a multidisciplinary optimization, but relying on linear tools, may lead to far-from-optimal or even impossible-to-fly configurations.

Several theoretical studies [13–16,233] tried to address this difficulty by employing reduced order models. However, their efficiency was found to be unsatisfactory.

Given this scenario, efforts to better understand possible problems of geometrical nonlinearities at structural level were made [130, 158, 197]. The results were obtained on conceptual wind-tunnel-like models, and snap-types of instabilities were observed. Aeroelastic static analyses showed that eigenvalue approach for aeroelastic divergence speed assessment was overpredicting the true instability speed. In Ref. [161, 189] nonlinear aeroelastic dynamic responses were shown: not only the *true* critical speed was found to be lower than the one predicted considering the undeformed structure, but several phenomena as flip-bifurcation, multi-stability and eventually chaos were observed. When a source of *nonlinearity* of aerodynamic origin (wake roll-up) was incorporated, the effects were noticeable.

Natural extension of these efforts is to apply the gained knowledge and the in-house computational tools to study the nonlinear aeroelastic response of a more *realistic* layout, obtained through preliminary optimization and fine-tuning, as the ones presented in Refs. [5, 6, 114, 116]. This design features a commercial aircraft application and thus,

differently than previously investigated cases, is characterized by smaller displacements.

8.2 Contribution of the Present Study

Considering the literature on Joined Wings design, with emphasis on *Box Wing* [27] and *PrandtlPlane* [28, 91, 92] configurations, a significant amount of work has been carried out, see for example Ref. [148]. Thus, a *realistic* reference configuration based on these works is available for thorough aeroelastic analysis: it is well known [157, 234] that the stiffness and inertial distributions play a primary role in the occurrence of flutter.

More in details, this paper will feature a *PrandtlPlane* layout *similar* to the one studied in Refs. [5, 6, 114, 116]. This configuration was obtained through a partial MDO and then progressively fine-tuned [112, 113, 115, 148, 235].

Given also the studies on *flight mechanics* and control surfaces [6,116], this configuration represents an interesting starting point for studying nonlinear aeroelasticity and freeplay effects. *Impact of control surface freeplay on flutter* [194, 236] has never been studied before for Joined Wings. Differently than traditional configurations, for the PrandtlPlane Joined Wings there are multiple mobile surfaces located on both wings. Thus, the response of the system will be the result of a complicated interaction of each control surface freeplay. The contributions of this paper are outlined below.

- Starting from the joined-wing model presented in Ref. [114], a structurally "equivalent" model is designed. The mobile surfaces are considered being perfectly connected to the wing around the hinge line (no freeplay), and flutter analysis is carried out. However, a further step is taken: the post-flutter response is tracked with a time-domain capability, showing the limit cycle oscillation. Aerodynamic-structure energy transfer is also investigated and discussed.

- The second contribution, is on the impact of control surface freeplay on flutter response of this configuration. Mobile surfaces have been previously designed for this specific configurations complying with handling qualities requirements at various flight conditions, see Refs. [6, 116, 117] for details. Thanks to these efforts, and assuming a reasonable law describing a realistic freeplay of mobile surfaces, it is possible to study that effect on the aeroelastic response of the overconstrained system represented by the PrandtlPlane. This is carried out both on the frequency domain, in which the rigid modes associated with the free surfaces are interacting

with the elastic modes changing flutter properties, and on the time domain, where the nonlinear response of freeplay and its effects on limit cycle oscillation amplitude and frequency are observed.

- The flutter analysis are repeated when also rigid body modes are considered. In fact, in literature several Joined Wings presented low frequencies of the first natural modes (e.g., [8, 114, 151]), favouring a possible interaction between elastic and rigid modes. Other than pursuing such an investigation (commonly referred to as free-free or free-flying aeroelastic analysis), a sensitivity analysis is carried out by changing fuselage weight and (pitching) moment of inertia.

The present effort, based on a qualitatively *realistic* layout, is logically part of conceptual analyses [1, 158, 161, 162, 197]. Moreover, it represents a step towards a full trimmed (structurally) nonlinear aeroelastic analysis of the PrandtlPlane configuration, in which also freeplay effects of mobile surfaces are considered.

8.3 Theoretical Highlights Regarding the Present Computational Tool

The in-house computational capabilities are here briefly outlined. They consists in a finite element method for the computational solid dynamics (CSD), a doublet lattice method (DLM) for the frequency domain unsteady aerodynamic and an unsteady vortex lattice method (UVLM) for the time domain aerodynamics. The coupling (time integration) and interfacing (load and displacement transferring) are described in detail in Refs. [161, 189]. Briefly, an implicit integration scheme is used to advance in time, being the nonlinear problem at each time-step solved by means of a Newton approach. Moreover, the interface information is passed through *moving least squares* (MLS) approach.

It this interesting to point out that these tools are prospectively sufficient to capture the physics of the here sought phenomenon (see Ref. [189]). In fact, experimental and numerical works have clearly shown how, in many cases, the structural nonlinearities drive the limit cycle oscillation much more than the aerodynamic ones do. Ref. [236] showed a limit cycle oscillation on a wing in which freeplay was taken into account. When the numerical results were not in good agreement with the experiments, this was a consequence of the neglected structural geometric nonlinearities [199–201].

A brief description of the in-house capability is presented in the following.

8.3.1 Structural finite element model

The geometrically nonlinear finite element [135,136,156,208] is based on the linear membrane constant strain triangle (CST) and the flat triangular plate element (DKT). The capability has also embedded the calculation of the structural tangent matrix $\boldsymbol{K}_T$, which is sum of two contributions: the elastic stiffness matrix, $\boldsymbol{K}_E$, and the geometrical stiffness matrix, $\boldsymbol{K}_G$. Composite material composed of several and differently oriented layers (theoretically these layers could also be of different materials) are implemented. A corotational approach is used, and thus rigid body motion is eliminated from elements and the pure elastic rotations and strains are found.

In order to tackle the freeplay problem, and simulate the play of the control surfaces, the present computational tool was further added the capability of specifically modeling nonlinear springs. The ad-hoc formulation is very briefly presented below. Multifreedom constraint (MFC) capability will complete the set of the tools needed to properly model mobile surface devices behavior. Both the springs and the MFC give a contribution to the structural tangent matrix $\boldsymbol{K}_T$. The freeplay springs contribution is presented in detail in Appendix C.1.

For the free-free analysis, rod and lumped mass elements are needed to model rigid connections and concentrated masses located in the space to model fuselage inertial contributions. The first ones give a contribution to the tangent matrix, whereas the second ones contribute to the system's mass matrix.

Freeplay springs

A generic connection between two finite elements sharing a common part of the hinge line is presented in Fig. 8.1. Nodes H1 (H2) and H3 (H4) are connected through translational MFCs, which force them to be (almost) coincident in space. The "freeplay spring" is a rotational spring acting on the hinge line, reacting to relative rotations between the two elements (called for reference Master and Slave). Defining a direction on the hinge line, $\boldsymbol{e}^A$, the relative rotation $\Delta\theta$ can be measured, accordingly with the axis direction. This enables the evaluation of the moment exerted by the spring once the law $M(\Delta\theta)$ is defined. This moment acts on the elements, with the appropriate sign: for the master element $\boldsymbol{M} = M(\Delta\theta)\,\boldsymbol{e}^A$, whereas for the slave the opposite holds.

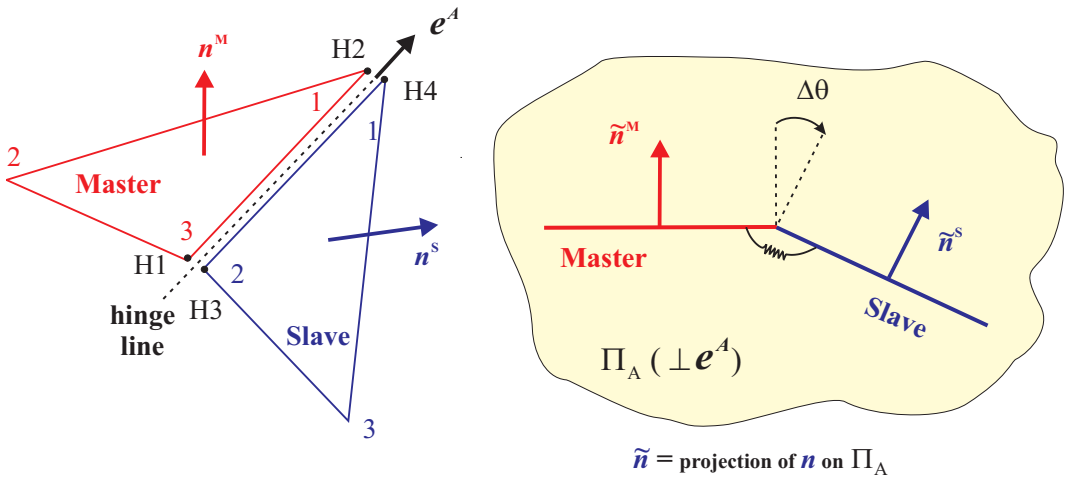

Figure 8.1: Freeplay spring acting on the hingeline connecting two finite elements.

Final step consists in projecting the rotational actions, thought on the hinge line, on the hinge nodes. This is simply accomplished by equally distributing the moment between the nodes. Summarizing:

$$\begin{cases} \boldsymbol{M}^{H1} = -\dfrac{\boldsymbol{M}}{2} & \boldsymbol{M}^{H2} = -\dfrac{\boldsymbol{M}}{2} \\ \boldsymbol{M}^{H3} = \dfrac{\boldsymbol{M}}{2} & \boldsymbol{M}^{H4} = \dfrac{\boldsymbol{M}}{2} \end{cases} \tag{8.1}$$

where $\boldsymbol{M} = M(\Delta\theta)\, \boldsymbol{e}^A$.

As said, angle $\Delta\theta$ is the relative rotation of the two elements along the hinge line, and thus is evaluated in the perpendicular plane $\boldsymbol{\Pi}_A$. Then, the relative rotation can be expressed (in radiants) as:

$$\Delta\theta = \sin^{-1}((\boldsymbol{n}^M \times \boldsymbol{n}^S) \cdot \boldsymbol{e}^A) \tag{8.2}$$

where $\boldsymbol{n}^M$ and $\boldsymbol{n}^S$ are the normals of the master and slave element, respectively. This equation is representative of the relative rotation about the hinge line.

Freeplay affects directly the law relating the reaction moment and the relative angle. A mobile surface freeplay could be reproduced using a piecewise value of the spring stiffness K_θ (which could ideally represents the reaction of aileron actuator). As shown in Fig. 8.2, it exists a region delimited by the angle 2δ in which the aileron is free to rotate.

Outside of this region the spring (actuator) has a non-zero stiffness. For a numerical point

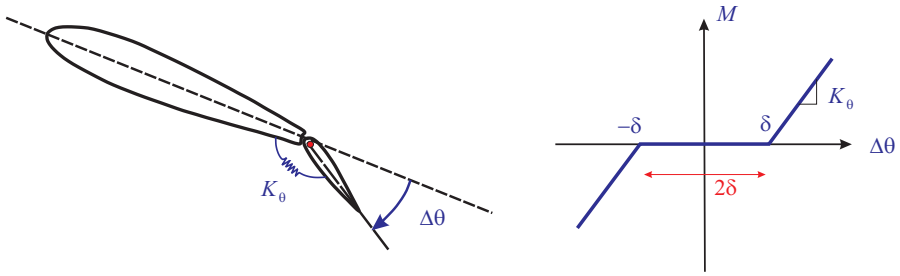

Figure 8.2: Freeplay concept: in the region delimited by the angle δ the surface is free to move without encountering any resistance.

of view, however, it may not be convenient to use such a description, since it does not fit well solution strategies based on Newton's iterations. On the contrary, continuity of the derivative (spring stiffness) has been guaranteed smoothly connecting the different value with one of the several options described in the literature. In particular, Fig. 8.3 shows

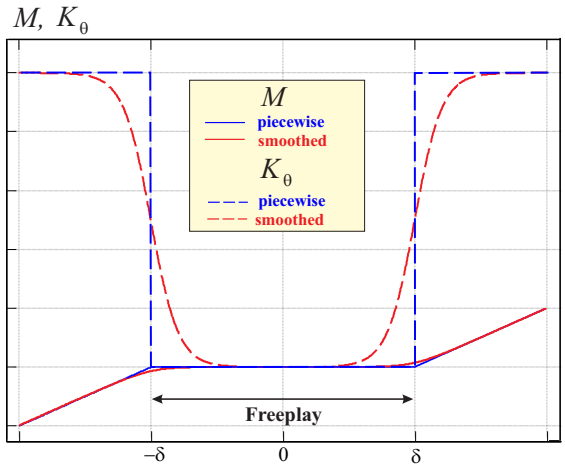

Figure 8.3: Smoothed piecewise freeplay law.

the smoothed law, when a sigmoid-like function is used to approximate the derivative. Small numerical timesteps are needed to guarantee convergence. A more robust and less computationally demanding approach is outlined in [237].

8.3.2 Aerodynamic models

The computational tools used for the evaluation of the aerodynamic forces are based on the hypothesis of potential flow (non-viscid and irrotational). As said before, the interest of this effort is to evaluate the effect of the structural nonlinearities,

thus, complicated nonlinear aerodynamic phenomena such as shockwave-boundary layer interaction, flow separation, etc, are not considered. Considering the hypothesis of attached flow the potential flow theory underlying the computational method is adequate to simulate the aerodynamic field with very low computational costs.

For the flutter velocity prediction a frequency domain approach (the Doublet Lattice Method, DLM [191]) is used. For the time domain simulations, necessary to simulate the evolution of the aeroelastic system, an unsteady vortex lattice method (UVLM) (see [192]) is adopted. The in-house capability has also built-in the aerodynamic tangent matrix $\boldsymbol{K}_A$, which is useful when using an implicit time-integration approach. For more details the reader is referred to following efforts: [158, 161, 189].

As far as load and displacement transfers are considered, an *MLS* approach is chosen [222]. In this way, it is possible to project a force acting on the aerodynamic grid onto the structural one, and vice versâ, project the displacements (deformations) of the structural grid onto the aerodynamic ones. A more thorough treatise on this topic is also shown in [161].

8.4 Description of the Analyzed *PrandtlPlane* Configuration

The chosen configuration is a typical *PrandtlPlane*, an artistic view is given in Fig. 8.4 (reproduction from Ref. [5]). It is a 250 passenger mid-long range (6000 nm) design with a MTOW of 230 tons. It will be addressed throughout this section with the name *PrP250*. The external surface and general layout shape were designed also with

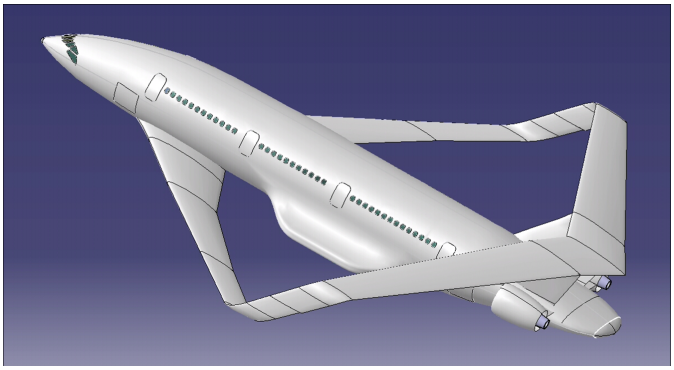

Figure 8.4: Artistic view of the *PrP250*, taken from [5].

the aid of an MDO software, presented in Refs. [102,103]. Later, the structures were fine-

tuned [5,112] taking into account different constraints as maximum stress, local buckling of stiffened panels, aileron efficiency, static aeroelasticity and flutter. The structural model used for linear flutter analysis is shown in Fig. 8.5.

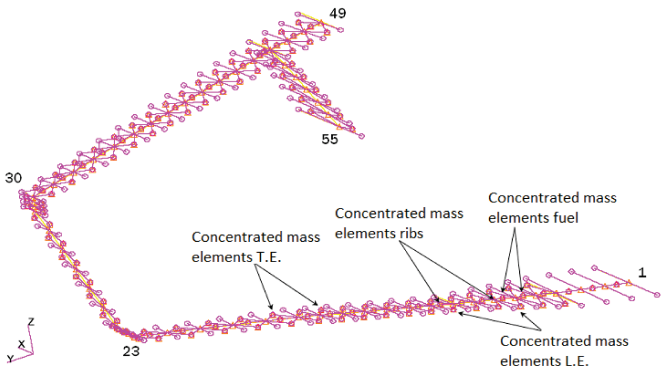

Figure 8.5: Structural model used for flutter analysis of *PrP250*. Taken from [5].

Further work has been carried out optimizing the structure and, finally, employing composite materials [113, 235], although in the present work the focus will be the one built with *aluminium alloy*. Flutter analysis was also the focus of parallel works [114, 115].

The mobile surfaces have been sized in Refs. [6, 116, 117]. An excerpt of the layout is shown in Fig. 8.6. According to these last references, the design of the flight

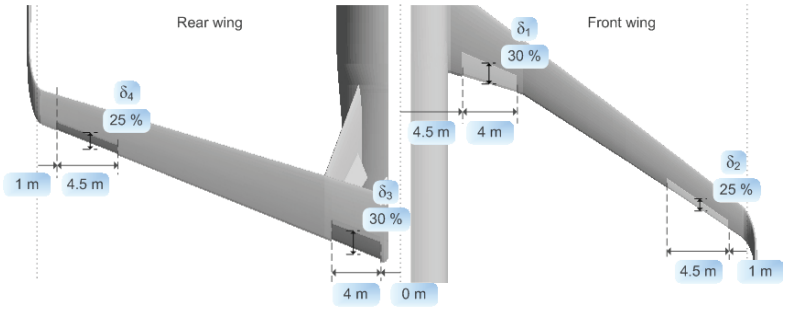

Figure 8.6: Control surfaces layout for *PrP250*. Taken from [6].

controls was complying with a set of handling qualities requirements at various flight conditions (low speed, high speed, crosswind, high altitude and low altitude). The handling qualities requirements were involving maneuvers as push pull, minimum time to bank, aircraft trim with one engine out, take-off rotation and steady turn. A linear stability analysis indicated that the aircraft had good longitudinal handling qualities and was stable. Moreover, the aircraft configuration made it possible to have pure torque

control in pitch.

8.4.1 Baseline model

Equivalence process

Since the original structural configuration was modeled with beam elements first, and later a detailed full wing-box model was designed (as shown in Ref. [235]), and since the focus of the present effort is towards a conceptual work, it has been decided to build an "equivalent" shell structure describing only a medium surface. In order to match the properties of the structures in terms of modes, different preliminary approaches have been investigated. In particular, the following options have been explored:

- equivalent model through analytical static stiffness approach and dynamic mass equivalence;
- modal equivalence following the process shown in Ref. [238];
- modal equivalence through an optimization process.

The last approach has been proven to be the most successful. The inherent overconstrained nature of the system has put a remarkable difficulty in the matching process, consequence of the coupling of primary bending, torsion and secondary bending, with the consequence that the modes were all showing, at different extent, some level of deformations inherent to the above described features.

Although slightly different, aeroelastic scaling shares commonalities with the present problem. It was pursued in literature in different efforts, and did show to be an unexpectedly difficult task to be accomplished on Joined Wings, see for example Refs. [67, 76].

The first natural modes of the beam model were considered. By means of an extrapolation, the target mode shapes were obtained for the surface described by shell elements. Some physical reasoning suggested to use a multi-layer structure, in which the different layers' fibers were oriented perpendicularly to each other in order to easier decouple, for example, the bending and torsional effects. In particular, after testing different solutions, a five-layer laminate, with a $0/90/0/90/0°$ (the local direction about which the angle were measured was the axis of the beam model) pattern was employed: the second and fourth layer were *mainly* regulating the torsional stiffness, the ones on the

sides were *mainly* controlling the bending stiffness, whereas the central layer had most of the impact in *fine tuning* the extensional stiffness. This choice was also confirmed to be an appropriate one with preliminary numerical experiments carried out for validation purposes on simpler wing layouts.

The structure has been then divided in 23 different segments, each of which had a direct correspondence to the different geometrical segments of the real wing (kink, different dihedral, joint, fin, etc...). For each segment, layers' material properties as well as thickness and density were chosen as the design variables. The objective function to be minimized was containing a mismatch on the natural frequencies. Moreover, the minimization process had some inequality constraints on the thicknesses and density of the layers. This has proven to be a quite successful approach, within the limit set by the different physical models.

Within the optimization approach, different methodologies were tested. Initially, a global optimization process (based on work [239]) was tested, with the local optimization carried out with the tools offered by the commercial software *Matlab Optimization Toolbox*. However, due to the large required computational resources (caused by the model complexity), it was chosen to run a local optimization process, starting from a reasonable configuration found with previous equivalence procedures (see above) as "first guess".

A crucial step was the capability of correctly associate the modes with the target ones for correct identification of the frequencies to be used for the objective function.

Matching was carried out for the first 5 modes only. This choices was consequence of the following facts:

- Optimization process was time consuming. More design variables were eventually needed for reasonable matching with higher frequency modes, with a relevant increase in the costs of the optimization process.

- The overall sense of the equivalence was in giving a more realistic stiffness and distribution mass, rather than perfectly matching a structure, like the beam one, which is inherently not the "exact" model.

Matching the first five modes was not a trivial problem. After several numerical test it was found that the "best" fitting was obtained by relaxation of the matching of the fourth mode. Summarizing, the following results were achieved in terms of mismatch on

the natural frequencies of the modes:

0.02%	first mode
5.06%	second mode
0.01%	third mode
24.33%	fourth mode
0.87%	fifth mode

Results showed that the laminate where all presenting symmetric layup, giving credit to the initial assumptions on the fibers' direction.

The matching was pursued on the structure without the fuel. This configuration represented the departure moment from the original beam model of [115] and the authors made different choices. For example, the fuel was uniformly distributed on the structural (coincident with the aerodynamic) surface, in particular on the two wings, and not on the joint and vertical empennage. With uniform, the authors mean that an equivalent surface density was used to match the same quantity of fuel allocated in the different wing segments. For the beam model the fuel was allocated a little bit behind the elastic beam axis. This certainly affects flutter occurrence and nature. However, as already stated, the aim of this research is not to reproduce the exact flutter scenario of the reference model, but to use its geometry, stiffness and mass distribution as a starting point and later perform conceptual investigations.

Although the first five modes were thought to dynamically (not necessarily from an aeroelastic point of view) retain most of the physics, this was not the case for the static point of view. A small mismatch on tip deflection for a mechanical pressure load was observed. The material stiffness and density were slightly scaled, conserving thus the same modal properties, and pursuing thus a better static matching. As a consequence, the total mass of the original model was restored (within limits) by scaling the total amount of allocatable fuel.

In order to better reproduce loss in stiffness consequence of the mobile surface presence without modeling any sort of freeplay, the model was "cut" in correspondence of lateral edges of mobile surfaces. Moreover, the fuel mass was not distributed on the mobile areas, as will be better explained in the next section. In other words, this model had control surfaces perfectly clamped on the theoretical hinge line.

Hereinafter, the configuration obtained with the equivalence process outlined above will be considered as the *baseline configuration*.

Constraints

First let us introduce the coordinate system. x is directed along the streamwise direction and z vertically. $y = 0$ (plane xz) represents a symmetry plane.

Sections on the symmetry plane are allowed to translate in the plane, and rotate perpendicularly to it. Root section of the fin is clamped. The section slightly inboard of the elevator on the front wing where ideally intersection with the fuselage take place is only free to rotate in the stream direction x.

8.4.2 Mobile surfaces

Mobile surfaces had to be modeled in order to study freeplay effects. This was done following works presented in Refs. in [6,116,117]. Since cutting the mobile surfaces intuitively implies a change of the stiffness properties, it was checked that this process was not significantly changing the natural frequencies and also the flutter speed and properties of the model. The mobile surface's mass was set unloading it from the fuel part (diminishing the density of the material). Actually, also the option of regulating their weight with handbook procedures, as shown in [240] was explored. Once again, use of such tools on a unconventional configuration is strongly debatable, and is here justified by the conceptual character of this effort.

Location of mobile surfaces, as designed in Fig. 8.6, are pictorially shown in Fig. 8.7. In the following of this section, the model in which the mobile surfaces are

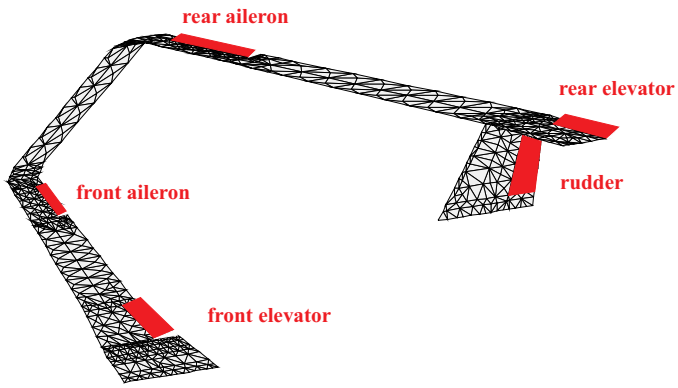

Figure 8.7: Location of control surfaces.

designed are identified with 5 digits string, being each digit 0 or 1 whether the surface is perfectly constrained or not, and following the sequence: front elevator, front aileron, rear aileron, rear elevator and rudder. For example, 01010 refers to a configuration with fixed front elevator, rear aileron and rudder.

8.5 Flutter Properties of the PrandtlPlane

Flutter analysis has been carried out on *PrP250*. As explained, the control surfaces have been considered perfectly-rigidly connected (clamped) to their upstream wing-part. The frequency domain in-house code, based on *DLM* and root-locus [161] has been validated against the commercial code *NASTRAN*. The nominal aerodynamic and structural meshes are represented in Fig. 8.8. The choice of the discretization was driven by convergence analysis: the in-house finite element capability has proven to be converged with the mesh shown in the picture, whereas a little more refined model (non depicted in the figure) was needed for *NASTRAN* in order to achieve convergence.

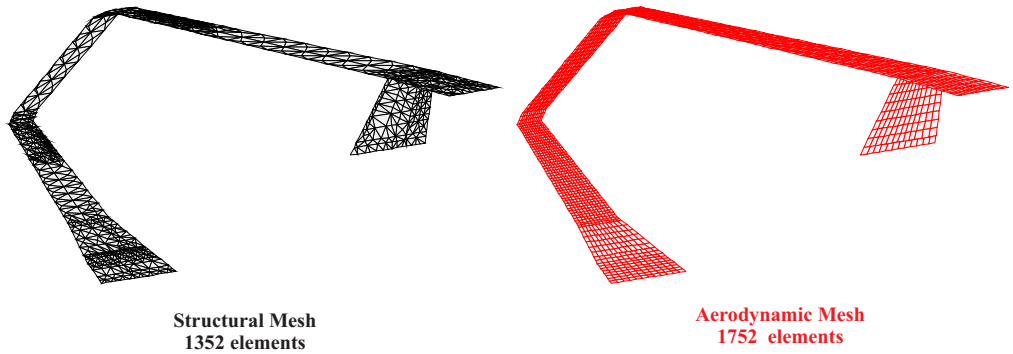

Figure 8.8: Nominal structural and aerodynamic meshes used for the aeroelastic analysis.

The first five natural modes and associated frequencies are represented in Fig. 8.9. Due to the overconstrained nature of the layout bending/torsion coupling of both wings is enhanced. The *first mode* is characterized by a vertical deflection of the wings, with an (almost) rigid vertical translation of the joint. Having the wings almost opposite sweep angle values, and being connected trough the joint, a complicated torsional deformation can be observed. In the *second mode* the joint tilting is dominating the deformation, inducing the characteristic wing bending and torsion. Moreover, the joint itself bends. On the contrary, in the *third mode* the joint (almost) rigidly translates horizontally and vertically and slightly tilts inward/outward. The *fourth* mode has a prominent torsional

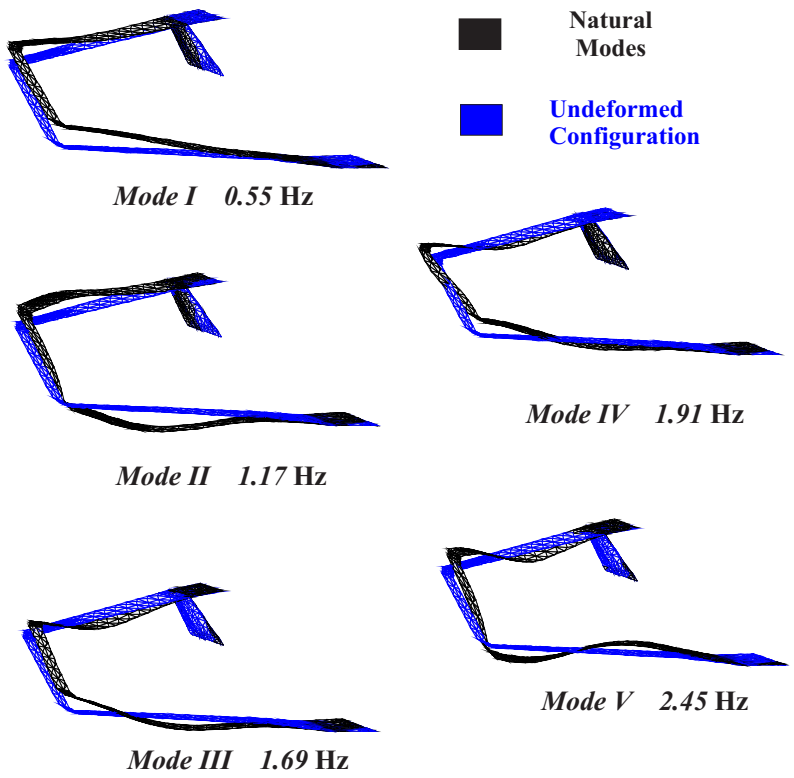

Figure 8.9: First five natural modes and associated frequencies.

deformation of the joint. *Fifth mode* resembles the second one, however, for a very similar joint displacement and deformation, opposite wing bending are present. In particular, the lower wing presents a more complex bending deformation when compared to mode II.

The frequencies of the modes are not high, and this suggests that interaction with rigid body motion can be non-neglibile. This will be investigated in a dedicated section of this effort (namely section 8.7), however, for the moment, the fixed (cantilevered) system is considered.

Results of flutter analysis are shown in Figs. 8.10 and 8.11 in terms of real and imaginary part of the eigenvalues of the system for different wind speeds. How it can be easily inferred, the second mode becomes unstable (flutter) for a speed of approximately 257 m/s. Moreover, coalescence of the frequencies of the first two modes is observed before flutter occurs. The associated root locus is shown Fig. 8.11.

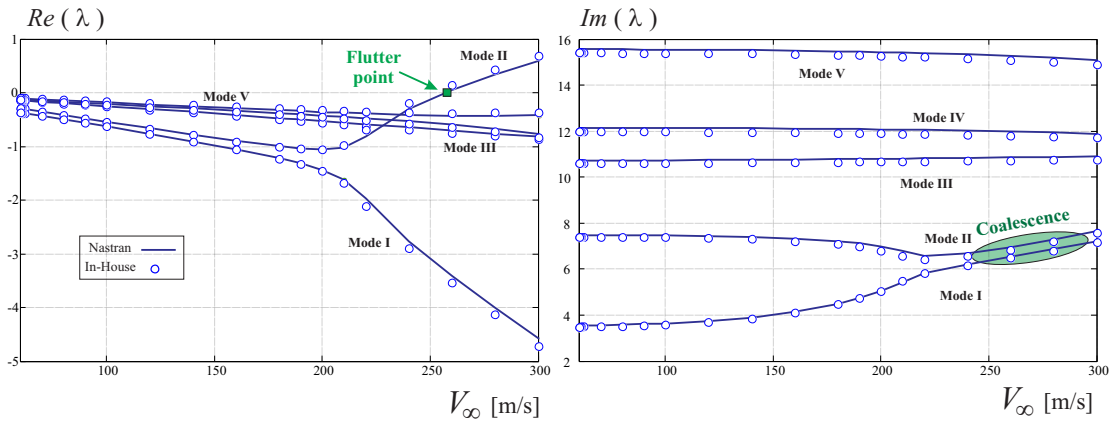

Figure 8.10: Real and Imaginary parts of the eigenvalue of the system at different speeds.

8.5.1 Time domain analysis and energy transferring

A nonlinear dynamic aeroelastic analysis is performed at the speed of 260 m/s, which is a post-flutter regime. The undeformed configuration is considered, and a vanishing perturbation in angle of attack is given to accelerate the transition to the limit cycle oscillation. Note that the previous flutter analysis was performed using the modes at the undeformed state; thus it is expected that including structural nonlinearities changes the flutter point with respect to Fig. 8.10; also please note that this is not a matched flutter analysis for simplicity of the theoretical conceptual discussion.

The response for the lower and upper wing's tip (named FT and RT) is presented in Fig. 8.12. If the deformed configurations are plotted within a wave (between time 16 s and 17.1 s), the pattern shows (see Fig. 8.13) that the deformation resembles mainly a superposition of the first and second natural modes. Interestingly enough, the first and second modes are also the ones that coalesce for a wide range of speeds relatively close to the flutter one. In Fig. 8.13 it is possible to observe a shorter or longer joint. However, this graphical representation is only a projection of the joint and the change in length is mainly due to a rigid rotation (tilting).

In Fig. 8.14, successive plots of the deformed configuration colored according to the *power of the aerodynamic forces* are shown within the same time window. When the power is positive (negative) fluid is transferring (extracting) energy to (from) the structure. Being the response preceding a LCO a positive quantity of energy is absorbed by the structure in one cycle. However, it is interesting to observe that lower wing almost always extracts energy, whereas different parts of the upper wing alternate between

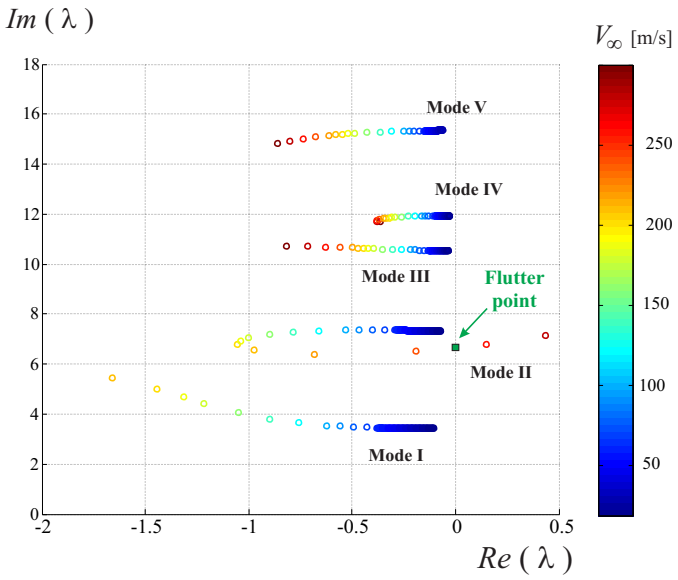

Figure 8.11: Root locus of the system. The different colors identify the associated speed.

transferring and absorbing.

8.5.2 Post-flutter response and LCO

Focus is now on the limit cycle oscillation that develops after the transient has elapsed. A procedure similar to the one proposed above is here again used, at the same wind speed of 260 m/s. In Fig. 8.15 the time-displacement of the lower and upper wing's tip are depicted. Moreover, to better characterize the LCO, also the phase spaces are shown. The displacements and velocities are larger for rear wing's tip.

Effects of modeled wake's length In all above cases, wake was modeled without allowing for roll-up. Although in some case in literature this has been shown to have a non-negligible impact on aeroelastic response (see Refs. [161, 189]), it is generally a widely used an well accepted approximation. Within a boundary element approach (BEM), modeling of the wake may be computationally intense for unsteady simulations. In particular, without a free wake modeling is important to keep the timestep constant in order to avoid to recalculate the aerodynamic influence coefficients of the wake. On the other hand, time step needs to be small enough to appropriately track the unsteady phenomena and avoid convergence problems (in nonlinear approaches).

In literature a wake's length of about 20 times a reference value (usually the

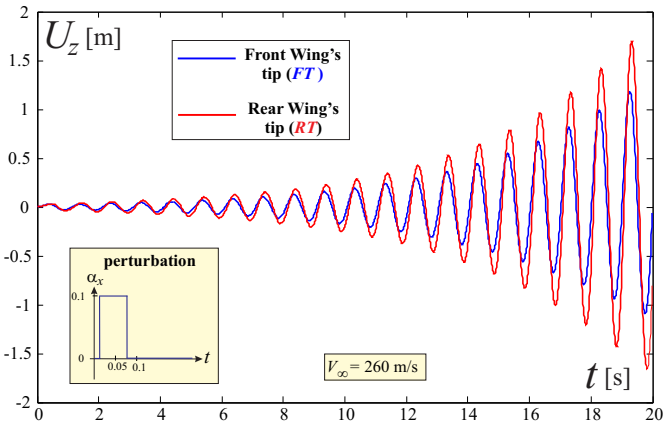

Figure 8.12: Time response of the system for $V_\infty = 260$ m/s: vertical displacement of the lower (FT) and upper (RT) wing's tip.

wing's chord) was showing converged results (in terms of steady forces), see for example Ref. [241]. However, considering computational costs, the authors did a preliminary analysis with the aim of reducing wake's length while retaining the aeroelastic transient and asymptotic behaviour. Wake's length slightly larger than ten times a reference dimension (root chord), was proven to be enough.

The following simulation limits wake's length to a very short value (slightly larger than the chord reference), with the spirit of observing the different aeroelastic behavior. As depicted in Fig. 8.16, when a very short wake is modeled, time to reach the LCO is larger, its amplitude and frequency are smaller. Wake carries the *previous history*, and cutting it discards previous deformation patterns. Moreover, also for steady state cases, short wakes do not represent correctly the physical (and mathematical) problem and the interaction of the vorticity shed by a wing with the same wing or, in the present case, with other wings.

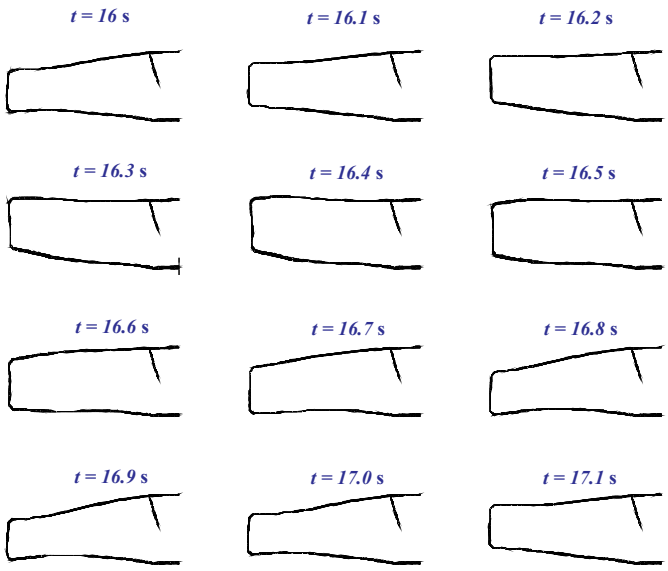

Figure 8.13: Time response of the system for $V_\infty = 260$ m/s: magnified (2x) deformations at different snapshots taken in the interval $16 \div 17.1$ s.

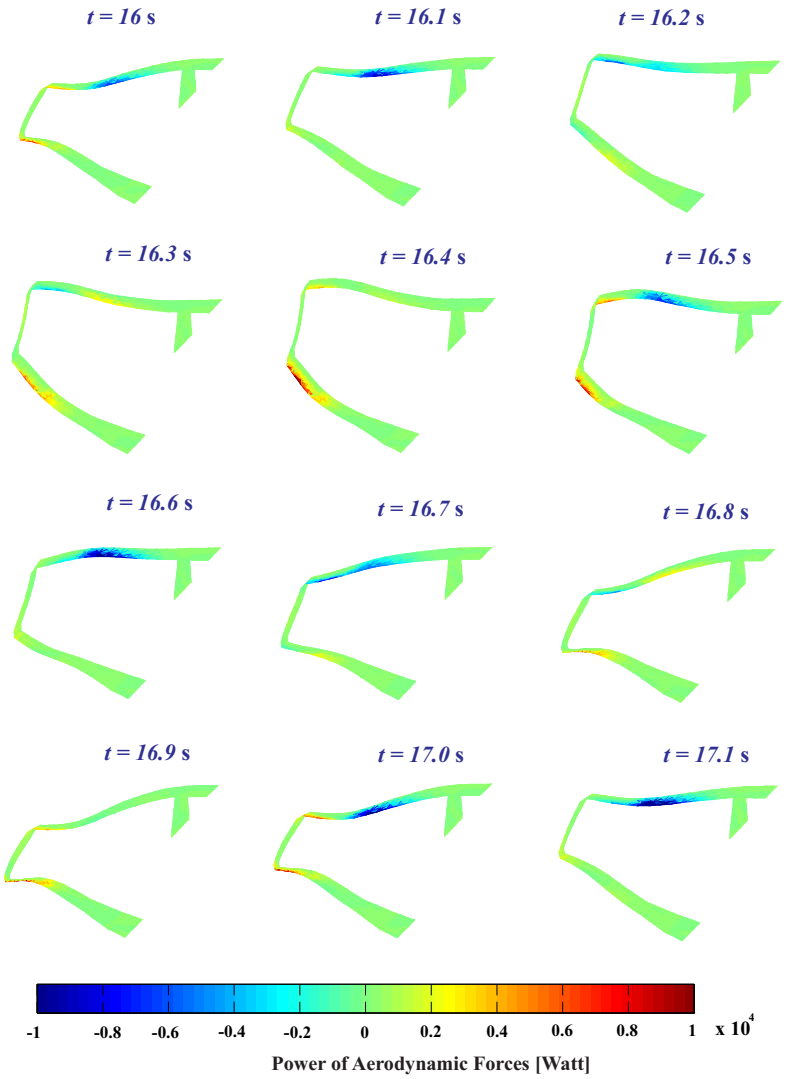

Figure 8.14: Time response of the system for $V_\infty = 260$ m/s: magnified (5x) deformations and power of aerodynamic forces at different snapshots taken in the interval $16 \div 17.1$ s.

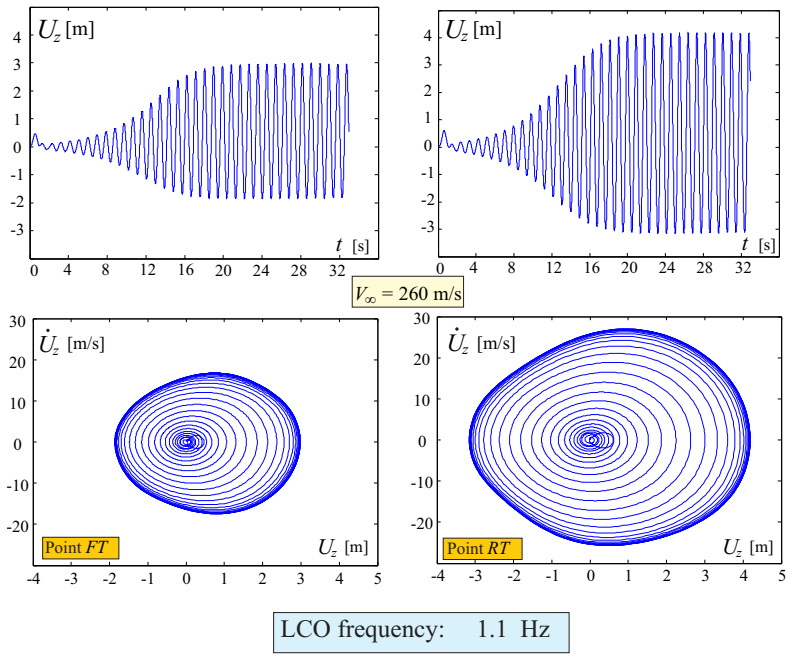

Figure 8.15: Time response of the system for $V_\infty = 260$ m/s: vertical displacement of lower and upper wing's tips FT and RT, and phase-space diagrams.

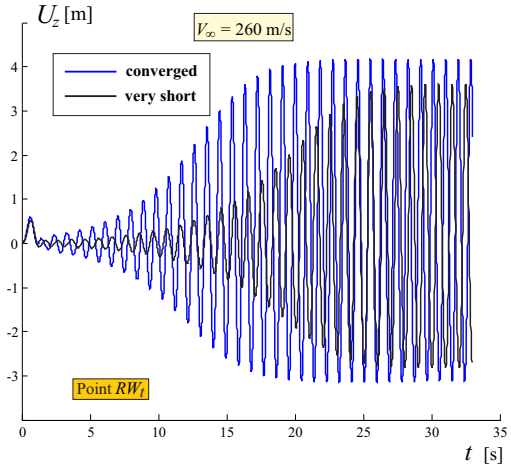

Figure 8.16: Responses (vertical displacement of upper wing's tips RW_t) for different modeled wake's lengths.

8.6 Flutter of the PrandtlPlane with Freeplay

In this section, effects of freeplay of mobile surfaces will be studied. Freeplay is complicated to be precisely assessed and controlled in real situations. This is explained, for example in [242], where it is also stressed out how design can initially fulfill freeplay regulations, but, over aircraft's lifetime variations in parameters may lead to different aeroelastic response than the nominal one. This is shown in the paper as a strong sensitivity of LCO amplitude and frequency to freeplay angles.

Typically, freeplay is modeled considering a nonlinear rotational spring acting on the hinge line, and connecting the mobile surface to the wing. The response of such a spring in the *Moment-Angle* diagram, is usually described by a piecewise response: a linear dependence is chosen outside the freeplay interval, and a null response inside it. This model in inherently nonlinear. Slope outside the freeplay and interval of null reaction depend strongly on the actuation architecture.

When performing frequency-domain analyses about undeformed configurations, the angle is zero and thanks to the piecewise stiffness of the springs, the stiffness is zero (see Fig. 8.2). In other words, such a flutter analysis (*linearized stability analysis* of the aeroelastic system) is performed on a system in which locally the mobile surfaces can freely rotate.

In this section, different mobile surfaces are selectively and alternatively considered to have a freeplay. When the flutter calculations are performed in the frequency domain the system is studied assuming it in the reference (undeformed) state. Thus, being the system linearized, the rotational stiffness of the springs is zero and the surface will be free to rotate. It will be observed that, in most cases, the same fundamental instability mechanism as when no freeplay is modeled, is still present at approximately the same speed. For some specific combinations of mobile surfaces having freeplay, the flutter speed could even increase.

Besides this main instability, *additional modes may become unstable* at relatively low speeds. These additional instabilities, however, persist for a limited range of speed values, and disappear when structural or other sources of damping are modeled. In some other cases, even after modeling the structural damping, a "persisting" instability associated to a higher mode and occurring at speed lower than the fundamental one is observed. To validate the frequency-domain analyses, the same approach of the previous section is pursued, i.e., both in-house and commercial tools are compared, and also a

time-domain analysis is adopted to observe the response.

Effect of freeplay on LCO are also studied for a specific case. This exploits the full nonlinearity of the freeplay, showing how its amplitude is related to time-response of the system, in particular to LCO's amplitude and frequency.

Note that the present capability models both the *distributed* nonlinearity (structural geometric) and the *concentrated* one (piecewise description of the spring stiffness at the hinge of the control surface).

8.6.1 Freeplay of a single mobile surface

The goal of this work is to provide physical insights on the freeplay of the different surfaces. Thus, it is now investigated the case in which only a single surface (among all) presents the freeplay. All the other surfaces are considered "fixed".

Front wing's elevator

Freeplay is modeled for the front wing's elevator (see Fig. 8.6) only. Flutter analysis is given in Fig. 8.17 in terms of eigenvalues' real and imaginary parts. It can

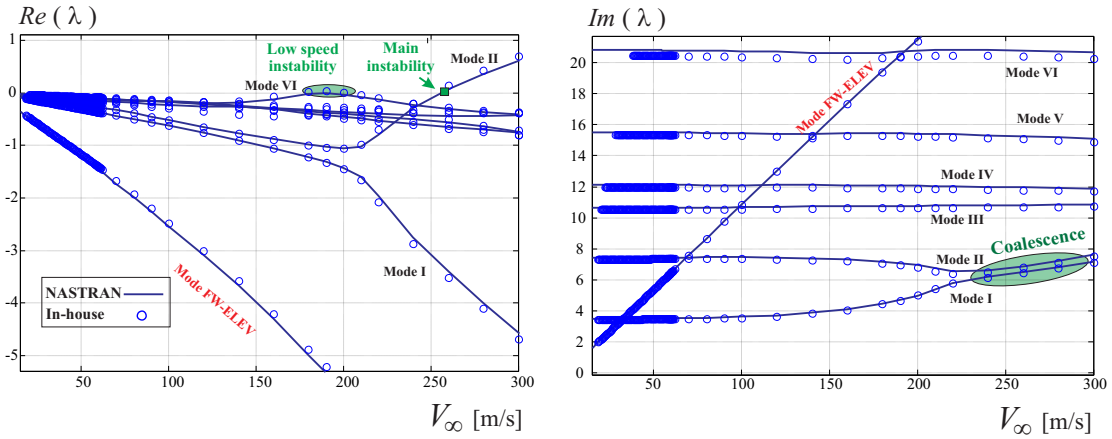

Figure 8.17: Real and Imaginary parts of the eigenvalue of the system at different speeds. Free-play of the front wing (inboard) elevator (case *10000*).

be inferred that the fundamental flutter mode (see the "main" instability", mode II, in Figs. 8.10 and 8.17) becomes unstable at approximately the same speed as the case with no mobile surfaces. However, effects of the free elevator induce an instability of the sixth elastic mode, for which a flutter is observed at smaller speeds (see "Low speed instability", mode VI, in Fig. 8.17).

Before further proceeding it is important to stress out that this case has been verified with a convergence study by using refined aerodynamic meshes, refined structural grids and both simultaneously. Also the number of considered modes for the frequency-domain analysis has been increased and the effect on the results assessed. This approach was pursued for all the cases in which a relatively high-frequency mode was observed to become unstable.

The sixth mode is depicted in Fig. 8.18. Overall, the situation does not look very

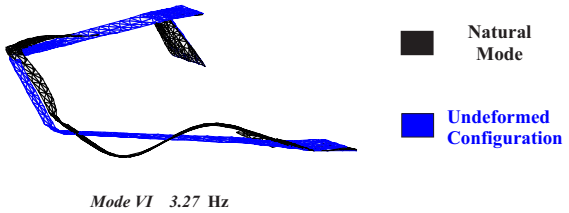

Figure 8.18: Sixth elastic natural mode for the configuration with freeplay on the front elevator.

unfavourable. In fact, the "main" flutter speed (see the crossing of mode II in Fig. 8.17) has not dropped as it can actually happen in several situations (see reference [242]), and the instability of the sixth mode is limited to a very small range of speeds, suggesting that it can be easily "dominated".

Actually, the above analysis is on the conservative side since no structural damping was modeled. Considering a 1% damping ratio ($\zeta = 0.01$) changes the scenario to the one depicted in Fig. 8.19. It is evident how the high frequency instability (mode

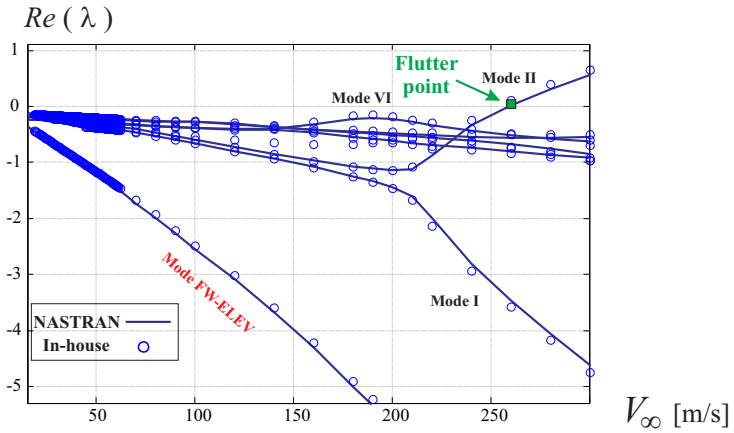

Figure 8.19: Real parts of the eigenvalue of the system at different speeds. Free-play of the front wing (inboard) elevator (case *10000*), structural damping $\zeta = 0.01$.

VI, "Low speed instability" in Fig. 8.17) is eliminated: the sixth mode's real part of the

eigenvalue does not cross the zero value for all the considered velocities.

Front wing's aileron

All control surfaces are now fixed except the front wing's aileron (configuration 01000). Flutter analysis is given in Fig. 8.20 in terms of eigenvalues' real and imaginary parts (structural damping is not considered). The scenario is similar to the previous case

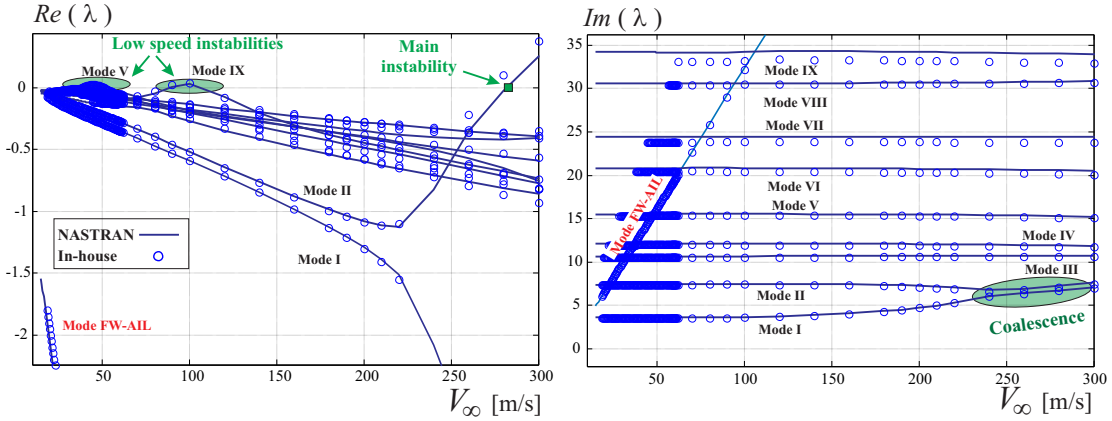

Figure 8.20: Real and Imaginary parts of the eigenvalue of the system at different speeds. Free-play of the front wing (outboard) aileron (case *01000*).

in which the front elevator was considered. Some high-frequency modes become unstable for a window of speeds in the low range. Again, considering a 1% of structural damping removes these instabilities, as shown in Fig. 8.21

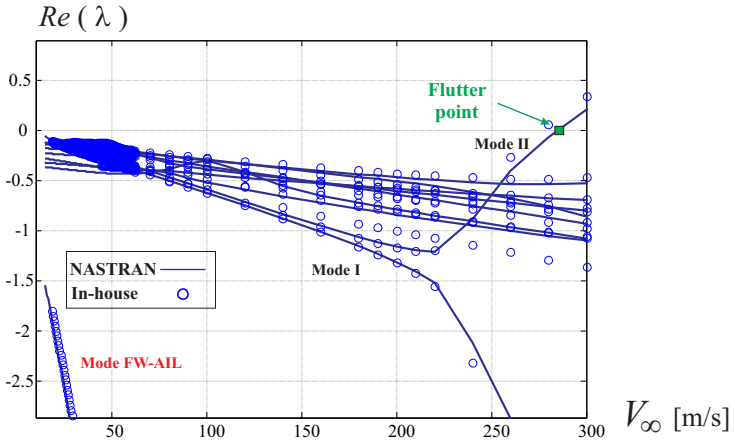

Figure 8.21: Real parts of the eigenvalue of the system at different speeds. Free-play of the front wing (outboard) aileron (case *01000*), structural damping $\zeta = 0.01$.

An interesting point regarding this case is the increase in the "fundamental"

flutter speed of about 10% when compared to the case without any freeplay, Fig. 8.10. In other words, having a freeplay on the front aileron posticipates the main flutter occurrence compared to the case without freeplay. This can be easily observed comparing Figs. 8.20 and 8.10. A time-domain analysis at the speed of $V_\infty = 260$ m/s supports the above finding. In fact, with reference to Figs. 8.22 and 8.12, the response to the same perturbation is strongly damped when the outboard aileron is left free. It is interesting to

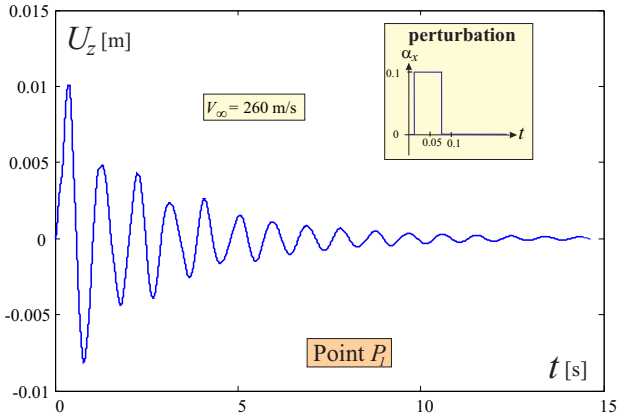

Figure 8.22: Free front wing's (outboard) aileron. Time response of the system for $V_\infty = 260$ m/s: vertical displacement of the lower wing's tip (P_1).

notice how the same mechanism of flutter, coalescence of the first and second frequencies is *posticipated* (see Fig. 8.23) when the front aileron is free to rotate. Thus, it may be inferred that the later occurrence of flutter is consequence of the interaction of the elastic modes with the rigid one concerning the aileron.

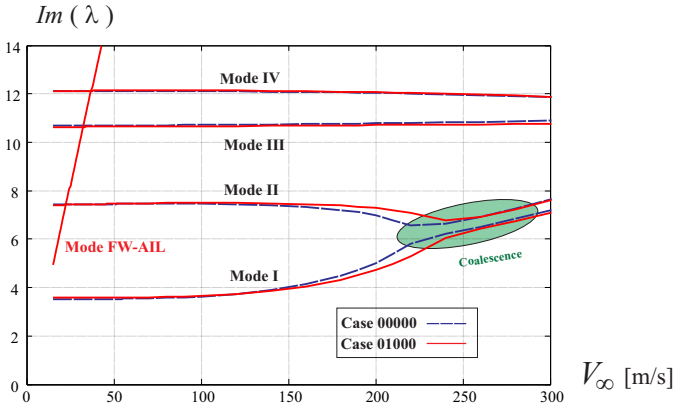

Figure 8.23: Imaginary parts of the eigenvalue of the system at different speeds for the 00000 (all mobile mobile surfaces perfectly blocked) and 01000 (front aileron free).

Trying to understand in depth flutter phenomena is always a formidable task.

Dynamic response and energy exchange between the fluid and the structure can provide useful information regarding the flutter mechanism as will now be shown. With reference to the previous discussion presented in section 8.5.8.5.1 and Fig. 8.14, it was observed that lower wing was almost always extracting energy from the fluid. A more in depth inspection reveals that the tip region, in correspondence of the aileron, is where this exchange of energy is concentrated. It can be then speculated that, the presence of the aileron free to oscillate about the hinge line, interferes with this extraction mechanism, reducing it.

These findings can provide useful indications regarding passive *flutter suppression* methodologies specifically tailored for this airplane configuration. More in general, understanding the *energy transfer mechanism* between the structure and the flow provides valuable insight helping designing passive or active devices to suppress flutter.

This energy transfer may also suggest additional insights. In a previous study [189], different wake aerodynamic models were influencing by a large extent flutter speed of a box-wing layout. It was observed that different models were responsible of a load redistribution, especially in the tip region. In the light of the importance of the tip region for energy exchange, in particular, energy extraction from the fluid, it may be speculated that having a sensible mismatch on the aerodynamic forces in such a critical area can lead to consistent discrepancies in the flutter speed prediction. Obviously, this observation needs to be supported with more investigations to be conclusive.

Effects of aileron length The observed rise of the flutter speed is intuitively not expected since, as well known in literature (see for example Refs. [242, 243]), usually the aileron and elastic modes interact to anticipate the instability at lower speeds. With reference to one of the first studies in this regard, [243], the span width of the aileron in respect of the wing was varied and flutter characteristics were investigated. In effort [242] the aileron had larger span-extension when compared with the present one. This effect is here reproduced, modifying the span-wise length of the aileron, as shown in Fig. 8.24. Aeroelastic analysis on this configuration shows a dramatic drop in flutter speed when the aileron is free to rotate. See the real eigenvalue versus speed diagram in the same picture, and notice how the aileron's mode becomes unstable at relatively lower speed when compared to the shorter aileron version (case depicted in Fig. 8.21).

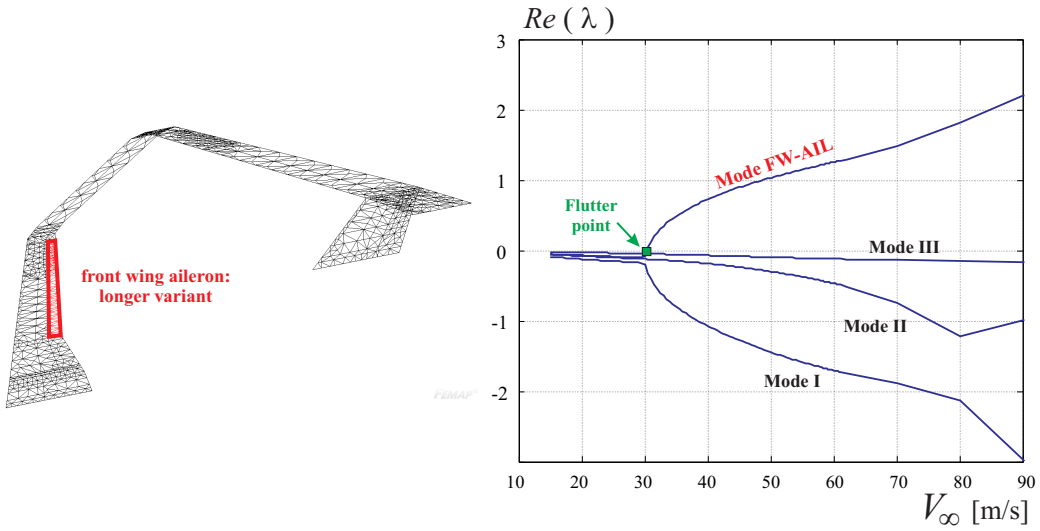

Figure 8.24: Configuration with an enlarged front wing (outboard) aileron, used for demonstrating the drop in flutter speed. Real part of the eigenvalue of the aeroelastic system are plotted at different speeds.

Rear wing's elevator

Considering the elevator on the rear wing free to oscillate (case 00010) leads to a completely different scenario than the one seen for the elevator on the front wing. Results of flutter analysis for this case are given in Fig. 8.25 in terms of eigenvalues' real and imaginary parts. Depending on the solver (in-house or NASTRAN), the 8th

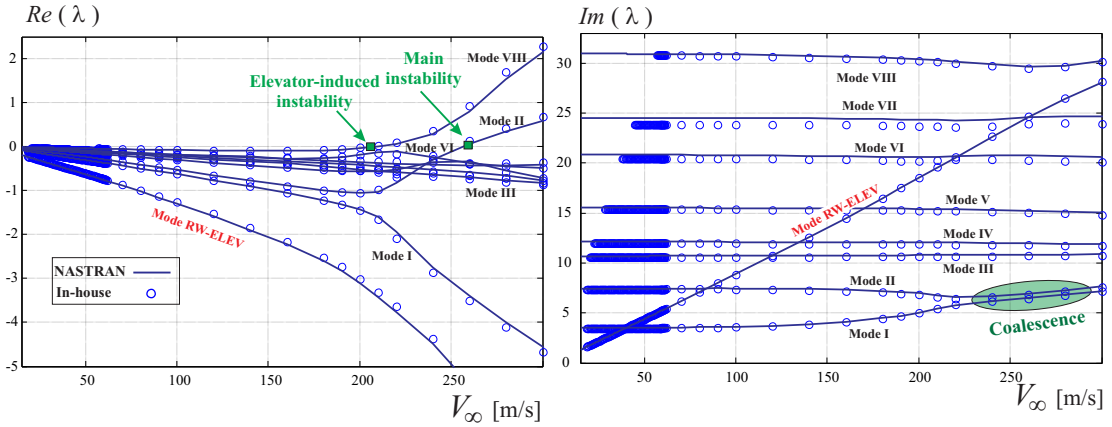

Figure 8.25: Real and Imaginary parts of the eigenvalue of the system at different speeds. Freeplay of the rear wing (inboard) elevator (case *00010*).

mode becomes unstable at a speed between 205 – 210 m/s. This instability though, has different connotations than the previous observed non-fundamental ones. In fact,

its instability persists and is not limited to a small windows of speeds. Moreover, the use of structural damping or nodal rotational dampers can't avoid its presence but, at most, postpone it to higher speed. Notice also that the same fundamental instability with coalescence of the first and second mode still takes place.

As shown in Fig. 8.26 the 8th elastic mode mainly presents deformations of the aft wing: the bending of the wing is coupled with pitching induced by an in plane deformation of the vertical stabilizer. The front wing mainly presents in plane deformation.

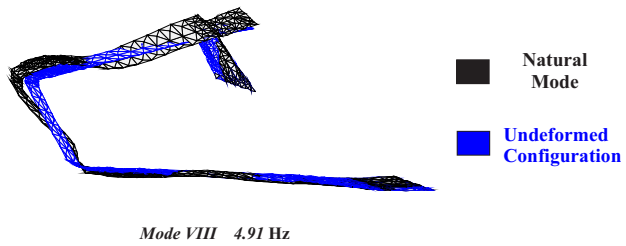

Figure 8.26: Eighth elastic natural mode for the configuration with freeplay on the rear elevator.

A time domain response showing the dynamic instability is offered in Fig. 8.27, where vertical displacement of the points lying on the xz plane ($y = 0$), on the hinge line and trailing edge (HL and TE in the figure, respectively) of the elevator are depicted. This figure is obtained by performing the transient analysis for a speed larger than the flutter speed (post-flutter regime).

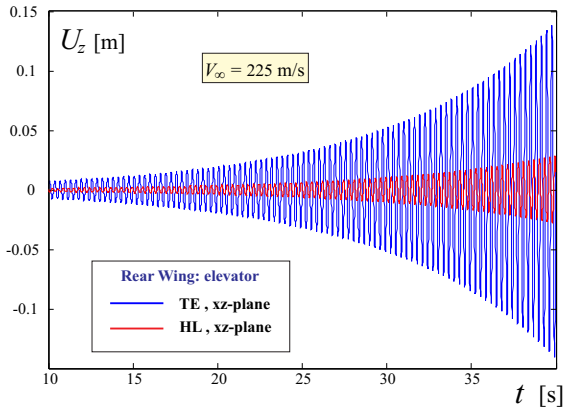

Figure 8.27: Time domain response for the configuration with free rear elevator at a speed of $V = 225$ m/s.

Fig. 8.28 shows snapshots (displacements are magnified by a factor of 5) at dif-

ferent times. Rear elevator area is responsible of energy transferring, and is where most of the displacements are located. However, also a front wing deformation can be appreciated.

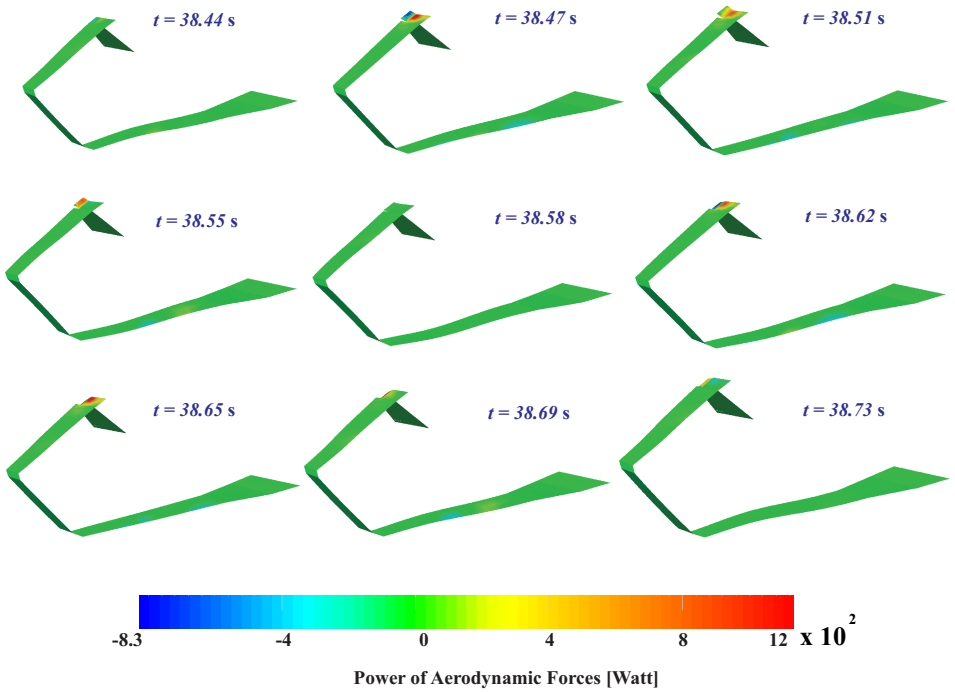

Figure 8.28: Time response of the system with free rear elevator for $V_\infty = 225$ m/s: magnified (5x) deformations and power of aerodynamic forces at different snapshots taken in the interval $38.4 \div 38.7$ s.

Rear wing's aileron

Flutter analysis is given in Fig. 8.29 in terms of eigenvalues' real and imaginary parts. It is possible to notice that several modes (both lower and higher frequency ones) become unstable for a window of speeds in the low region. Moreover, the second mode looses stability at higher speed again ($V_\infty = 257$ m/s), and the fundamental flutter mechanism is then recovered. Structural damping ($\zeta = 0.03$) is considered in Fig. 8.30. Differently than the previous cases modeling structural damping does not eliminate the low speed flutter. Increasing the damping ratio may not be a conceptual sound approach, since damping modeling is per-se an art, and uncertainties in this regard need always to be considered.

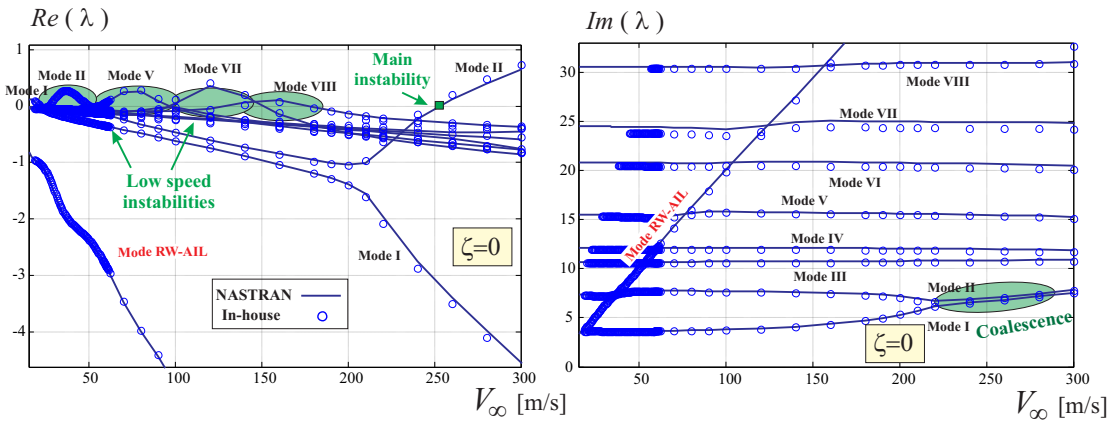

Figure 8.29: Real and Imaginary parts of the eigenvalue of the system at different speeds. Free-play of the rear wing (outboard) aileron (case *00100*). The real part is plotted for different values of structural damping and dampers.

Effects of dampers One option to eliminate the low speed instabilities is then to add dampers to the hinge line. This is, of course, a conceptual modeling approach, since in a real situation damping needs to be added to the complex actuator mechanism. Moreover, other means, like mass balancing, can be pursued. However, the aim of this study is to give an exploratory analysis showing that adding a "reasonable" source of damping will stabilize the system against low speed flutter.

As said, on the aileron hinge line rotational dampers are added. A value of specific damping of approximately 11.7 $\mathrm{N \cdot s \cdot rad^{-1}}$ is considered. This value is the result of applying 5 N·m/(rad/sec) concentrated dampers on each finite element node lying on the hinge line. Although in a real scenario it is unlikely this means to be used as damping source, it is interesting to notice that devices with such performances are available on the market. As shown in the frequency domain analysis, Fig. 8.30, using rotatory dampers eliminates the low speed instabilities.

A time-domain analysis is carried out at the speed of $V_\infty = 37$ m/s and $\zeta = 0.03$ with and without dampers, to show the different responses and confirm the frequency domain results. Results are summarized in Fig. 8.31.

It is worth to be noticed that this low speed instability induces very small deformations, which, in a real scenario may or may not produce appreciable effects. However, design needs always to comply with official regulations.

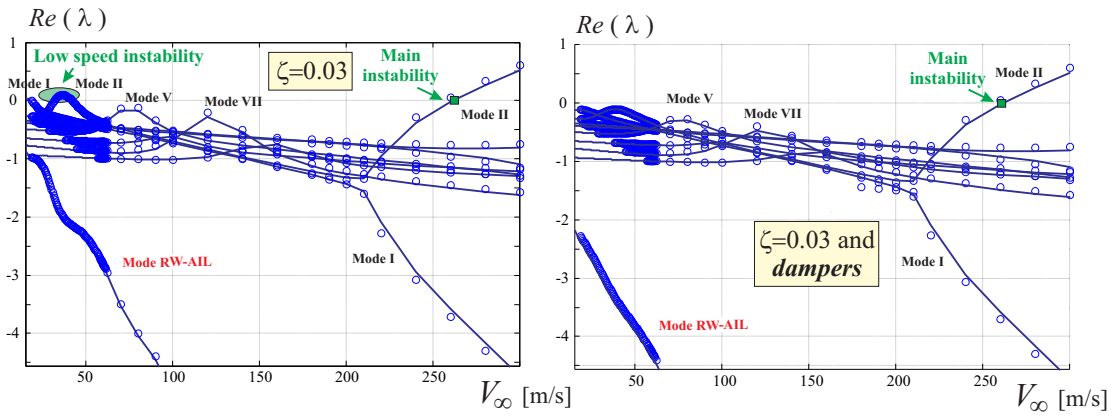

Figure 8.30: Real parts of the eigenvalues of the system at different speeds. Free-play of the rear wing (outboard) aileron (case *00100*). Structural modal damping coefficient is $\zeta = 0.03$. On the diagram on the right, rotatory dampers are added along the hinge line.

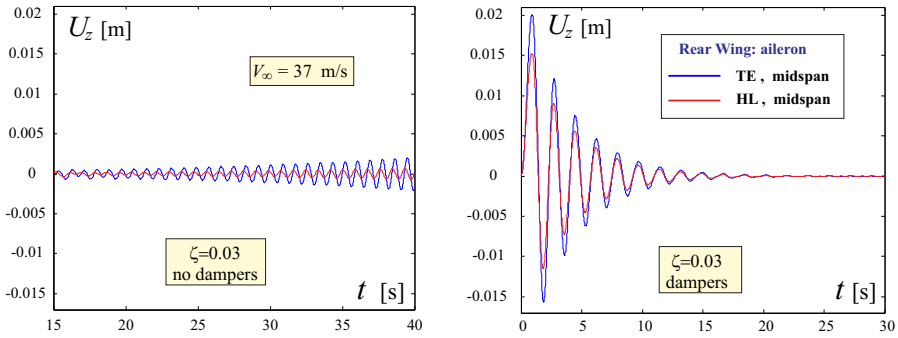

Figure 8.31: Time response (after a perturbation is given) of the system with free rear aileron for $V_\infty = 37$ m/s: vertical displacement time history of the points on the hinge line (HL) and trailing edge (TE), at midspan aileron.

8.6.2 Concurrent freeplay of two mobile surfaces

Rear wing's elevator and aileron

When freeplay is considered on both rear wing's elevator and aileron, the stability properties of the system are summarized in Fig. 8.32. Figs. 8.25 and 8.29, depicting stability properties when freeplay of the mobile surfaces was selectively considered, help understanding the combined presence of freeplay. Instabilities in short windows of low speed are typical of the free rear wing outboard aileron case, whereas a "persistent" instability of the mode VIII was observed for the free elevator case. However, when the freeplay is modeled for the two mobile surfaces mode VIII becomes unstable at much lower speed.

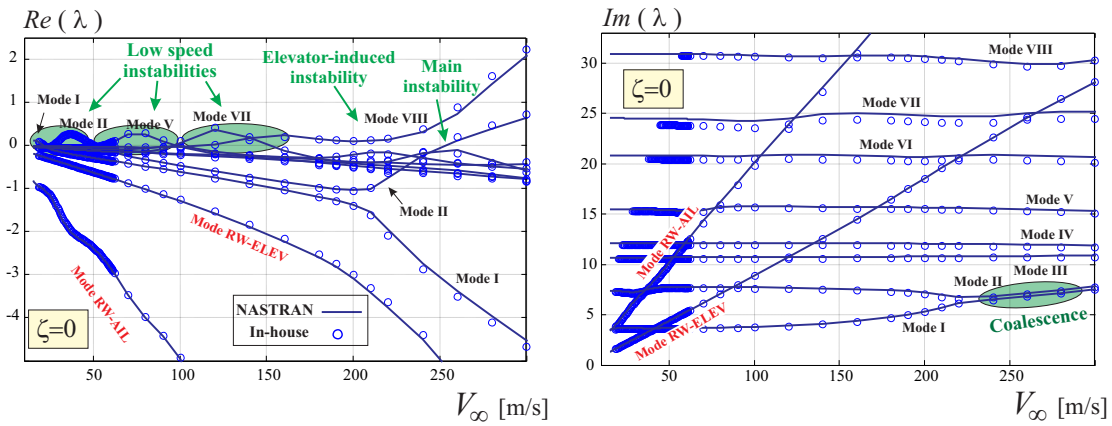

Figure 8.32: Real and Imaginary parts of the eigenvalue of the system at different speeds. Free-play of the rear wing's elevator and aileron (case *00110*).

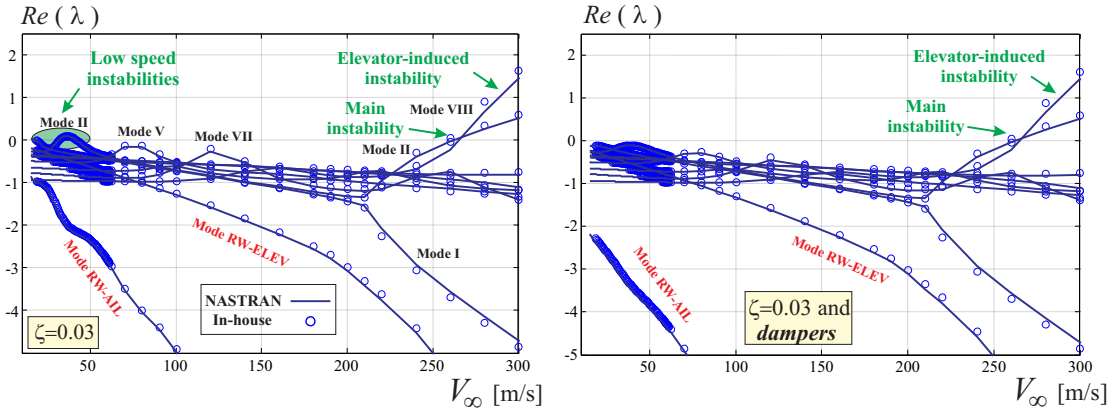

Figure 8.33: Real and Imaginary parts of the eigenvalue of the system at different speeds. Free-play of the rear wing's elevator and aileron(case *00110*) when structural damping and dampers on the hinge line are modeled.

In Fig. 8.33 the stability of the system (only real part of the eigenvalue) is depicted considering a structural damping, and eventually rotational dampers placed on the hinge line. A reasonable structural damping (damping ratio $\zeta = 0.03$) eliminates most of the low speed instabilities, moreover, it makes the fundamental instability (second mode) occur before the mode VIII's one. If rotational dampers are added on the hinge line of both the aileron and elevator (for the same amount of specific damping indicated above) then the low speed instabilities disappear. It is interesting to notice that 8th mode is not affected to an appreciable effect by the dampers.

8.7 Body-freedom Flutter Analysis of the Baseline Configuration

In this section free-flying flutter analyses on baseline configuration is carried out. Differently than a real trimmed aeroelastic investigation, the flutter is evaluated about the undeformed configuration. Since no geometrical twist inducing any geometrical angle of attack is included in the aerodynamic description, the undeformed configuration carries no lift when asymptotic angle of attack is zero, i.e., the undisturbed flow is parallel to x-axis.

A further issue to take into account is the static stability (on a flight mechanics perspective), which was guaranteed by the preliminary design of the layout carried out in Refs. [6, 114]. Since the here used equivalent model relies on the same aerodynamic surface and the difference in the position of the center of gravity is negligible, the margin of stability remains approximately the same.

Historically, the most notable cases of interaction between rigid body and elastic modes in aeroelastic applications go back until the pre World War II, on Flying Wings-like configurations (see work [244] for a nice historical background). Such an interaction was named *Body Freedom Flutter* (BFF). Example of early experimental investigations involving BFF are [245, 246].

For Joined Wings, low frequencies of the first elastic modes have been observed in different cases (see effort [8] for a Box Wing case, [85] for "Diamond Wing"). For this reason, Joined Wings have been considered potentially prone to interaction between the elastic and rigid body modes [147,151], changing the flutter properties from the idealized fixed (cantilevered) case. Notice, that these low frequency values do not guarantee, per se, the above prospected interaction, playing the relative fuselage/wing mass and inertia, and also the configuration flight mechanics properties a relevant role [245]. This section aims to characterize the *Prandtlplane* behavior in this regard.

8.7.1 Modeling approach

In order to take into account the rigid-body modes of the aircraft, the fuselage effects have to be modeled. If it is true that an acceptable inertia and stiffness distributions are needed in order to give conclusive results, it is also true that fuselage models for this configuration are very complicated (see for example Ref. [111]) to be described with

the similar level of fidelity characterizing the wings. Thus, as a first preliminary step, the fuselage has been considered as completely rigid. Moreover, its inertial properties are extrapolated considering the real position of the center of gravity of the whole configuration (see Refs. [6, 107, 117]), deducing the fuselage overall weight (comprehensive of payload) and evaluating its moment of inertia with arguments based on similarity. It holds that nominal fuselage mass is $M_{\text{fus}}^{\text{ref}} = 9.1 \cdot 10^4$ Kg, and (pitching) moment of inertia $I_{\text{fus}}^{\text{ref}} = 1.2 \cdot 10^7$ Kg·m^2. The fuselage inertial properties may change to a large extent the response of the system. For this reason, investigations carried out with the above reference values may be of limited value if not augmented with a sensitivity analysis, as pursued in the following sections.

To model the above target inertia properties, concentrated masses have been appropriately placed on the front wing- and fin-fuselage connections. To avoid local unrealistic in-plane deformations, these sections have been reinforced connecting the nodes with rigid links. See Fig. 8.34 for a conceptual representation. The same elements were used to rigidly connect the front wing and fin, guaranteeing rigid body motions of the aircraft. The connections represented in the same picture do not represent the real arrangement, which was pursued carefully avoiding relative rigid motions between some nodes.

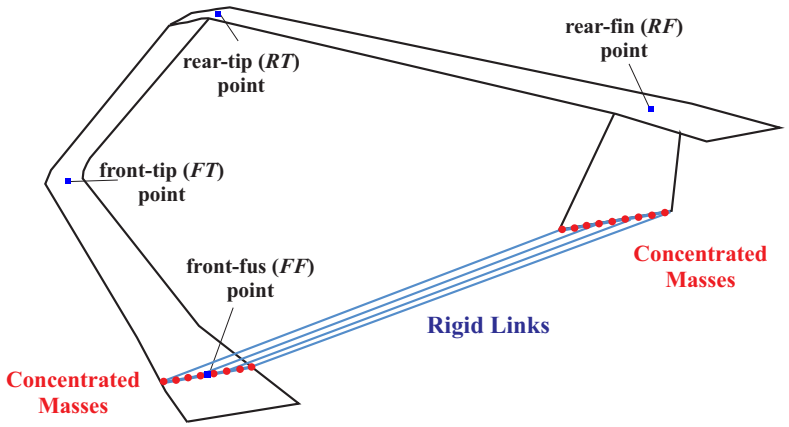

Figure 8.34: Free-flying conceptual model. Notice the concentrated masses and the rigid links. In the FEM model the rod elements rigidly connecting the nodes have been arranged to carefully avoid rigid rotations and translations.

The above modeling is consistent with the objective of conducing symmetric free-flying analyses, where with symmetric is intended that only plunging and pitching motions are considered. A full free-flying analysis should also consider the antisymmetric

modes, and in this case the above placements of the concentrated masses has to be revisited since it does not describe the proper inertial moment in the latero-directional plane.

To specifically assess the value of concentrated nodal masses (modeling inertial effects of the fuselage), an algorithm was written able to comply with these three constraints:

a) fuselage's target mass;

b) fuselage's target moment of inertia;

c) position of the of center of gravity projection on the symmetry plane.

8.7.2 Preliminary results on a front-wing-only layout

To assess the capability of such modeling procedure to capture body-freedom flutter, the configuration composed of the front-wing and a lighter version of fuselage is first considered. Analyses carried out with NASTRAN are shown in Fig. 8.35, where only the two rigid body modes and the first three elastic ones are depicted. As clearly shown, the rigid modes do not *significantly* interact with the elastic ones.

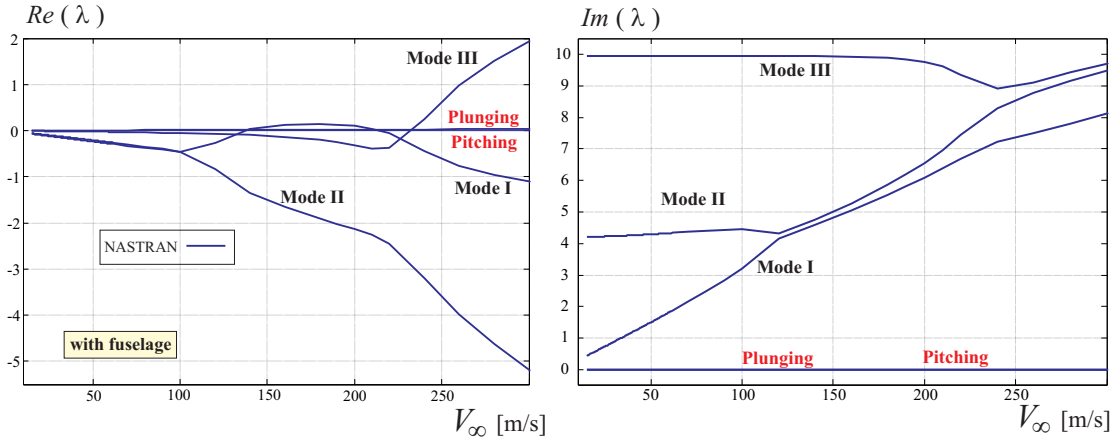

Figure 8.35: Real and Imaginary parts of the eigenvalue of the front wing plus scaled fuselage system, at different speeds.

However, when the fuselage is not modeled (or, equivalently, it has a negligible mass and inertia), there is an interaction between the first (elastic) mode and the pitching (rigid) mode, see Fig. 8.36. This same strong interaction between rigid and (first) elastic (bending) mode was the one usually observed for flying wings, for which the notion of

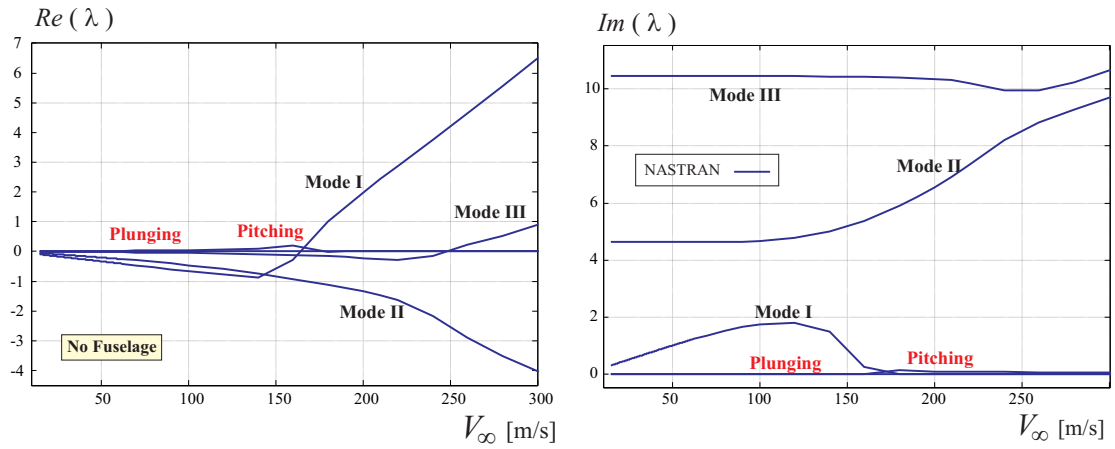

Figure 8.36: Real and Imaginary parts of the eigenvalue of the front wing without fuselage system, at different speeds.

BFF was introduced. Obviously this example has been carried out only with the purpose of validating a model and procedure, and does not carry any quantitative information (the configuration might even be unstable from a flight mechanics point of view).

8.7.3 Results for the PrandtlPlane

The natural modes of the system are first depicted in Fig. 8.37. Results of the

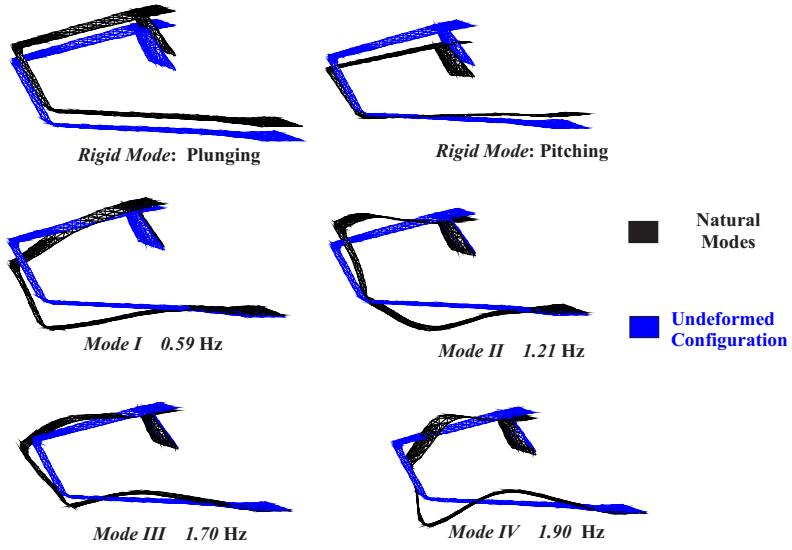

Figure 8.37: Two rigid modes (plunging and pitching) and first four elastic modes with associated frequencies.

flutter analysis with the in-house code and NASTRAN present an excellent correlation,

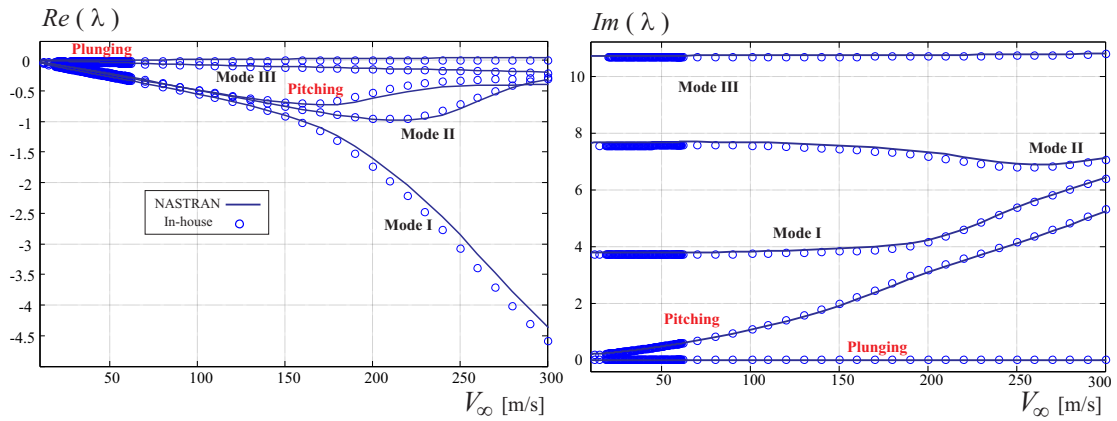

Figure 8.38: Real and Imaginary parts of the eigenvalue of the PrandtlPlane plus fuselage system, at different speeds.

see Fig. 8.38. The flutter occurrence is not represented because the analyses were carried out for incompressible cases ($M = 0$), whereas, as far as speed is increased the approximation of neglecting compressibility effects is progressively less justified (even at sea level).

The fact that a free-flying analysis would not, according to the frequency-domain analyses, experience flutter within the considered speed domain, whereas the constrained model is (compare Figs. 8.10 and 8.38), poses some questions that need to be addressed. First, it should be again remarked that a thorough analysis needs also to consider the real fuselage design, the aircraft (aeroelastically) trimmed at different flight conditions within the flight envelope. However, the present effort represents a first step in this direction and may give some important preliminary indications. The question is then, how sensitive are the aeroelastic stability properties of the system to inertial parameters? How do they change with fuselage mass and pitching moment of inertia?

Time response

A time-domain analysis of the response of the free-flying model to a vanishing perturbation is here presented. This is carried out both for low and high speeds.

It is important to remark that these analyses are intended to help interpreting results obtained with the frequency domain analyses, and not as independent real trimmed aeroelastic analyses. In fact, the initial (linearization) configuration is undeformed, the angle of attack is zero, and null are also the lifting forces.

The here-used time-domain aeroelastic solver employs vortex-rings, the interface

algorithms rely on a moving least squares (MLS) approach, as described in Refs. [161, 189]. The rings are located on the undeformed surface, and they do not follow the structure in its displacement. Conversely, the deformation is taken into account updating the normal used both in the tangency-wall condition and in the Kutta-Joukowsky force formula.

Lower speed case The air speed is set to $V_\infty = 50$ m/s. A vanishing perturbation in angle of attack α_{flow} is given, as depicted in the box of Fig. 8.39. This particular

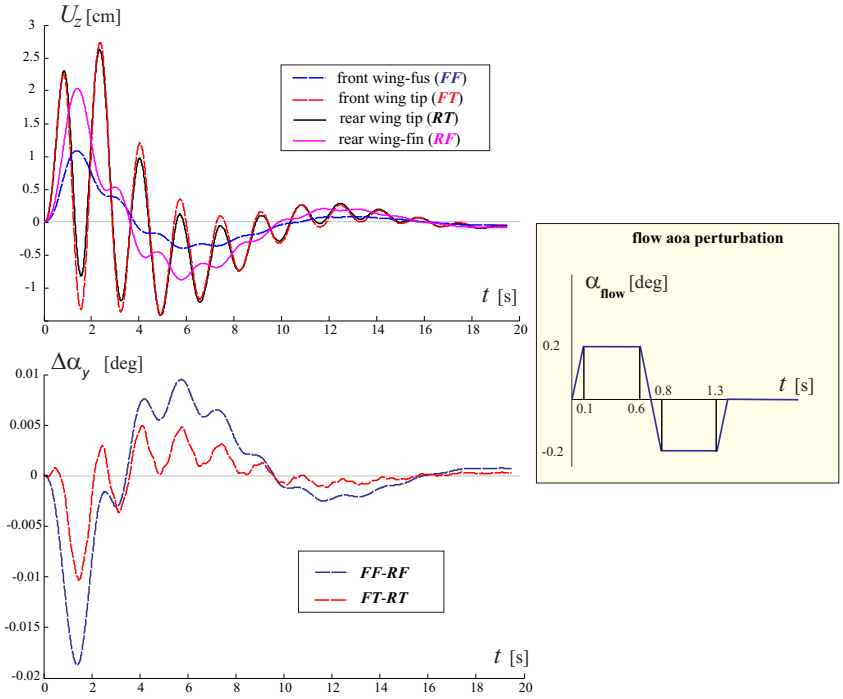

Figure 8.39: Time response for $V_\infty = 50$ m/s. The perturbation in flow angle of attack is depicted in the box. Above, vertical displacement of the four points on the mid-chord (front and rear wing's tips - FT and RT, front wing-fuselage and rear wing-fin connection - FF and RF) are depicted. Below, the geometrical rigid rotations of the fuselage/fin (FF-RF) and tip/tip (FT-RT) segments along axis-y are given.

symmetric shape is adopted in an effort of avoiding a strong tendency to depart too much from the planes where aerodynamic singularities are positioned. Due to the adopted load-displacement interface (where singularities maintain their position regardles of wing's deformation), this guarantees an acceptable precision.

Time-response of the different test points is also shown. The test points are all lying on the mid-chord of different span locations, and on different wings. Point FF lies on the front wing, at the hypothetical intersection with the fuselage, FT and RT are on

the wing's tip, whereas RF lies on the connection between the rear wing and the fin (see Fig. 8.34 for a pictorial representation of the points). On the same figure, below, it is depicted the evolution of values of two angles. The first one is the variation of the angle (measured in the plane XZ) of the segment connecting the points FF-RF and FT-RT. Since the point on the fuselage and the one on the fin's root are rigidly connected, it can be assessed as the geometrical angle of attack of the aircraft.

As it can be inferred from Fig. 8.39, after a transient the displacements settle to zero. This means that the elastic deformations and also the rigid body motion slowly vanish.

Higher speed case A larger speed is here considered, namely $V_\infty = 260$ m/s. The same vanishing perturbation is here adopted (although the peeks are smaller, namely 0.01°). This case is interesting because it can be compared directly to investigation carried out at the same speed for cantilevered aircraft, see Fig. 8.12 and section 8.5.8.5.1, showing an unstable behaviour.

Fig. 8.40 depicts the response. From an aeroelastic point of view, the oscillations

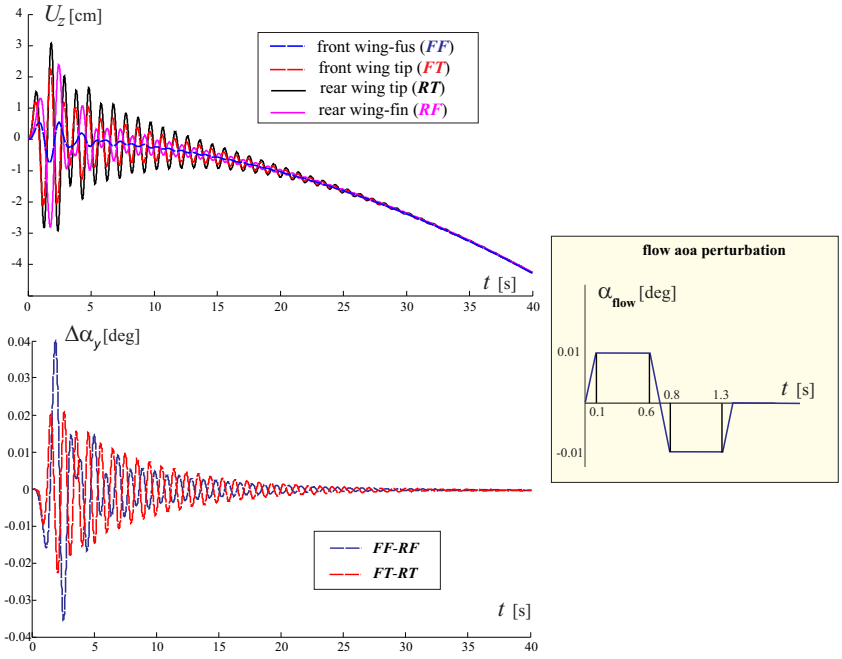

Figure 8.40: Time response for $V_\infty = 260$ m/s. The perturbation in flow angle of attack is depicted in the box. Above, vertical displacement of the four points on the mid-chord (front and rear wing's tips - FT and RT, front wing-fuselage and rear wing-fin connection - FF and RF) are depicted. Below, the geometrical rigid rotations of the fuselage/fin (FF-RF) and tip/tip (FT-RT) segments along axis-y are given.

vanish, whereas at the same speed the cantilevered model was unstable. A very small (notice the scale in Fig. 8.40) rigid vertical translation is noticed. Current investigations are aiming to understanding this point, and assess if it is an artifact of numerics or is related to the plunging mode.

Sensitivity to fuselage's mass and moment of inertia

As stated, effects of uncertainties in the determination of the fuselage moment of inertia need to be carefully assessed. For this reason, some sensitivity analyses are here presented, in which the mass of the fuselage and/or its moment of inertia are changed. However, the same position of the center of gravity is maintained to keep the same margin of stability.

Fuselage Mass variation If the *mass of the fuselage is increased, the flutter speed drops*. In particular, when its value is increased of an 80% of the original weight, flutter is observed for a speed of $V_\infty = 253$ m/s. However, this drop in instability onset speed should carefully be understood. In fact, it does not represent the limit toward the clamped case. This can better argued with aid of Fig. 8.41, showing the stability properties of the system when two heavier fuselages are considered. Comparing the

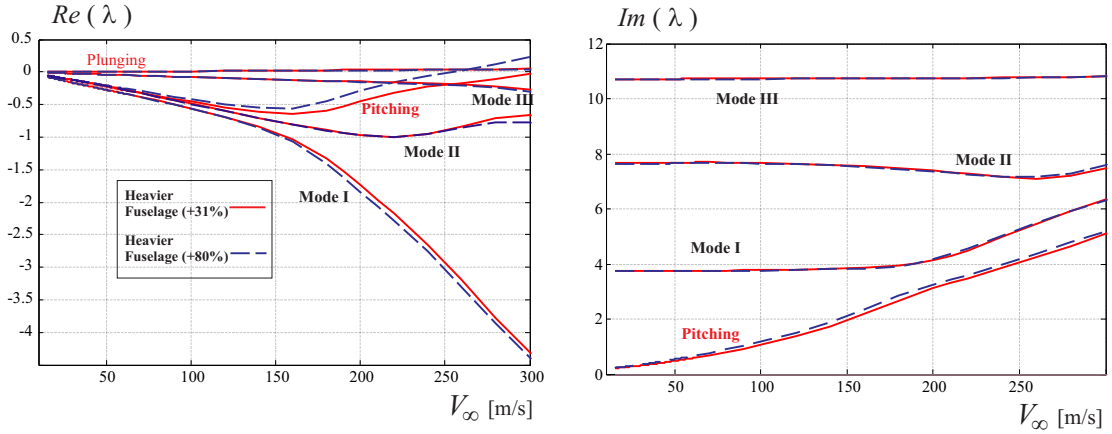

Figure 8.41: Real and Imaginary parts of the eigenvalue of the PrandtlPlane with heavier fuselages (moment of inertia of the fuselage and location of system's center of gravity are kept to the reference values).

diagram with the one of the cantilevered system, Fig. 8.10, now the the pitching mode is the one turning unstable (and not the second one). Mode II, on the contrary, is stable. Coalescence of the pitching and first elastic mode is noticed, whereas the classic

coalescence characterizing the fundamental flutter of the fixed configuration, involving first and second elastic modes, seem to be posticipated.

Fuselage Moment of Inertia Variation Now, the mass of the fuselage is kept constant to its nominal value, whereas the inertia is increased. With reference with Fig. 8.42, it can be inferred that second mode becomes critical at lower speeds when the moment of inertia increases. As expected, the frequency domain suggests that now interaction of the pitching mode with the elastic ones is weaker, and coalescence of the mode I and II is anticipated. This picture shows how, *in the limit of increasing pitch inertia, the*

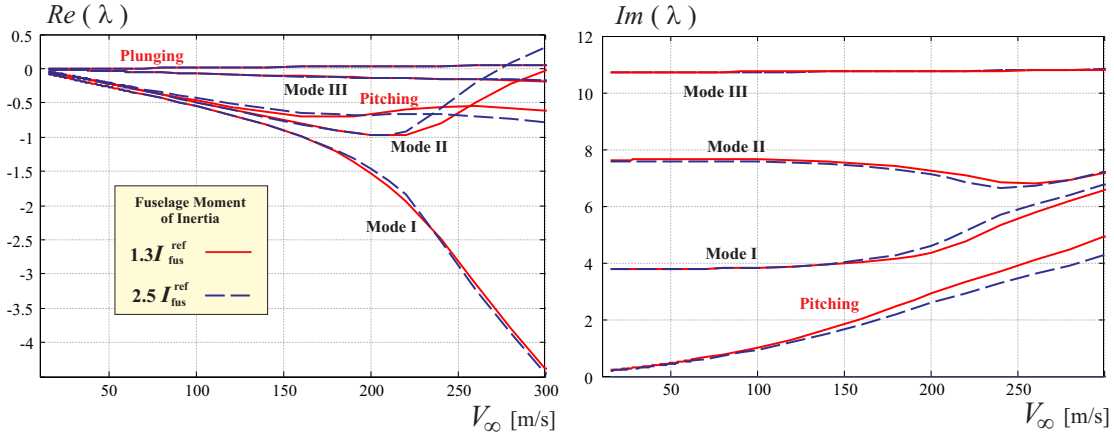

Figure 8.42: Real and Imaginary parts of the eigenvalue of the PrandtlPlane with fuselages with larger moment of inertia (fuselage weight and location of system's center of gravity are kept to the reference values).

cantilevered system stability properties are recovered.

Discussion Results above can be reinterpreted to show how there is a passage from BFF to cantilevered flutter type when the fuselage pitch inertia- increases (for a fixed weight). With cantilevered flutter it is intended the flutter occurring when mode II becomes unstable and a coalescence between frequencies modes I and II is observed: this is exactly the mechanism observed in the previous sections for the cantilevered system.

The pitching inertia is varied from $0.1 \cdot I_{\text{fus}}^{\text{ref}}$ to $4.3 \cdot I_{\text{fus}}^{\text{ref}}$. With reference to Fig. 8.43, in the lower pitching inertia case (dashed lines), the flutter is of the BFF type, involving pitching mode (depicted in green). On the contrary, mode II (in red) is well in the stable region. There is also a coalescence of the pithing and first elastic mode.

In the nominal case (thin continuous lines), within the speed range, all the modes

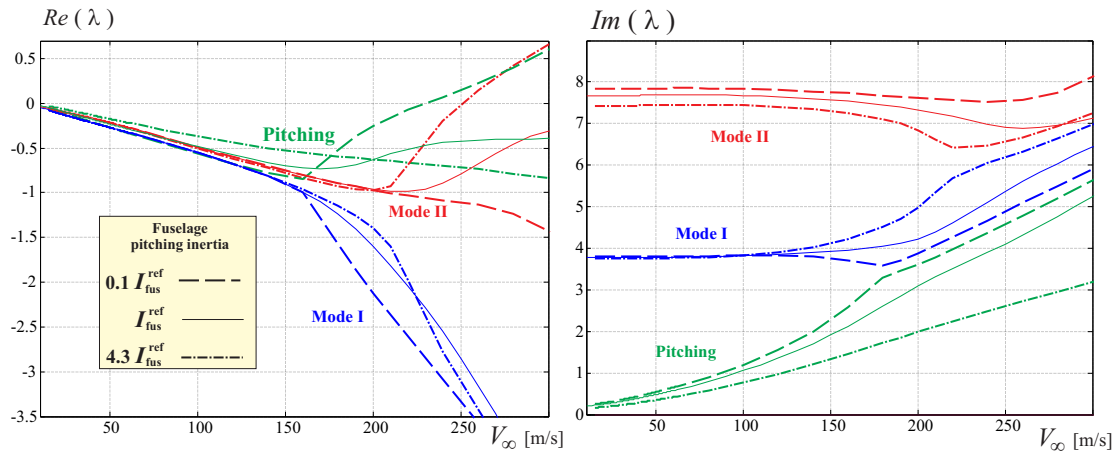

Figure 8.43: Real and Imaginary parts of the eigenvalue of the PrandtlPlane when pitching inertia is varied (location of system's center of gravity is kept fixed).

are stable. Thus, no flutter is observed for this case. For mode II (in red), the margin of stability (here intended as the distance of the real part of the associated eigenvalue from 0) decreases. Frequencies of pitching (green) and first (blue) modes do not get as close as before. The opposite trend is observed for the frequencies of mode I and II. This is the prelude to a change in the stability properties.

When pitching inertia is further increased (dotted-dashed lines), flutter is observed, associated with the same properties of the cantilevered system case: mode II (red) becomes unstable. Coalescence of modes I and II is observed in the frequency-speed diagram, whereas pitching mode frequencies keep far from the ones of the first mode.

Summarizing, for a fixed mass, for lower pitching inertia the aeroelastic stability properties is characterized by BFF, whereas, for large values, cantilevered flutter is observed. For some values of the moment of inertia between the above limiting cases (like the nominal chosen one) flutter won't be observed within the speeds of interest.

As stated in different literature efforts [147, 151, 244], BFF can also be favoured by a relative small separation between the elastic modes and short-period frequency. Short period frequency increases when pitching moment decreases, reducing thus the gap from the elastic modes frequencies (which for Joined Wings are inherently small) and promoting the interaction.

8.8 Conclusions

This effort has contributed to shed light on the dynamic aeroelastic behaviour of a joined-wing configuration called *PrandtlPlane*. The *first* contribution was the study of the flutter phenomenon also from a post-critical perspective. A limit cycle oscillation was observed, and its pattern, strongly involving tilting of the joint, depicted. Time domain response was very useful to study the power transferred from the fluid to the structure. It was highlighted that, the front wing had a destabilizing aeroelastic effect since it extracts energy from the fluid. The most active region in this energy exchange was the tip.

In the framework of Joined Wings and for the first time, this work also studied effects of freeplay of mobile surfaces on aeroelastic properties. It was found that in some cases, a few modes were unstable for a small range of speeds in the low spectrum, however, the same "fundamental" flutter mechanisms was observed at high speed. Adding a structural source of damping (structural damping or rotational concentrated dampers on the hinge line) was showing to eliminate the low speed issues.

Freeplay on some specific mobile surface (front wing's aileron) was found to have impact also in this "fundamental" instability. In particular, flutter speed was observed to be consistently increased. With reference to the energy diagram, this phenomenon was attributed to a "disturbance" of energy-transfer mechanism in an area mainly extracting energy from the fluid.

In some other cases, freeplay was inducing an higher-mode instability, occurring before the "fundamental" flutter. Contrary with the previous situations, the instability was persisting and not confined to a small window of speeds. Thus, addition of damping and dampers had the effect of only slightly posticipating its occurrence, but not eliminating it.

The *third* contribution concerned the flutter analysis when rigid body modes were considered, i.e., a free-flying flutter analysis. For the baseline configuration, the interaction between the rigid and elastic modes proved to be beneficial, since no instability was occurring within the range of considered speeds. For having a clearer picture, a parametric study was carried out varying fuselage mass and (pitching) moment of inertia. When pitching inertia was fixed, increasing fuselage mass was promoting a body freedom flutter (BFF). Conversely, fixing fuselage weight and varying moment of inertia showed an interesting scenario: for low pitching inertia BFF was the instability mech-

anism, accompanied by a coalescence of pitching and first elastic mode frequencies. As progressively increasing the inertia, the flutter speed associated with BFF progressively increased and the instability eventually disappeared. However, second mode instability was experiencing the opposite trend. Thus, for a sufficiently large value of the inertia, the classic cantilevered flutter, with a coalescence of first and second elastic modes' frequencies was recovered.

This effort represents a first step toward a complete free-flying trimmed analysis of a PrandtlPlane configuration.

Acknowledgements The authors acknowledges the support by San Diego State University (College of Engineering) and University of California San Diego (Graduate Student Association). They also like to warmly thank Professor Aldo Frediani of the Aerospace Engineering Department of Università di Pisa for his valuable suggestions and for providing us the original PrandtlPlane model, Professor Mark Voskuijl of the Aerospace Engineering Department of Delft Institute of Technology, Daan Van Ginneken and Nicolas Divoux for sharing their material and clarifying and summarizing their previous work, starting point for this effort.

Chapter 8, in part, is a reprint of the conference paper that will be soon presented (AIAA SciTech 2015): "*PrandtlPlane Joined Wing: Body Freedom Flutter, Limit Cycle Oscillation and Freeplay Studies.*" The dissertation author was the primary investigator and author of this paper. Coauthors were Rocco Bombardieri, Luciano Demasi and Andrea Iannelli.

Chapter 9

Conclusions

This effort offers and in-depth study of the aeroelastic behavior of Joined Wings, with particular emphasis on *nonlinear* (at structural geometric level) regime. Phenomenological and conceptual approaches have been favoured to unveil the complicated scenario, and different original interpretations about consequences and practical implications of these nonlinearities have been given, both for purely mechanical and aeroelastic loading cases.

To provide a picture of these contributions, they are presented in the following thematic areas.

Review A review of past works on joined Wing is given. No effort was made in the last thirty years to have a unique vision about Joined Wings. Moreover, American and European researches were not completely and in-depth aware of each other, leading to some independent results that needed to be associated one with the other one.

The present extensive review is a first step in that direction.

Computational tools In-house aeroelastic code has been developed for carrying out the analyses. Although fundamental modules (structural, aerodynamics, etc) rely on well-known ad accepted methods (finite and boundary element methods), the particular pursued coupling between aerodynamics and structures, although not theoretically novel, is not widely used and has never been shown in detail in previous works.

Within the same framework different levels of fidelity were achieved with different submodeling approaches. The merit of this effort was presenting in detail some theoretical parts and discussing issues related to the different formulations.

Structural conceptual work This work showed for the first time snap-buckling phenomena observed on simplified models of Joined Wings when loaded with mechanical forces. A first parametric investigations concerning macro-geometrical properties (sweep angle, joint's height) and load repartition between the wings was conducted. For each case, eigenvalue approach and nonlinear analysis were compared, showing that the first one was not able to retain the physics of the instability. As a consequence, predictions of the critical load were not reliable and not able to capture the correct *trend*. These findings promote a new interpretation of the instability as a global phenomenon rather than a *buckling of the aft wing*, expression used in literature for almost a decade to characterize this occurrence. More recent studies conducted by other researchers on a HALE configuration indirectly observed and supported this new interpretation.

A step further in the direction of gaining insights was then made. Other than tracking the post-critical response, a study on possible parameters driving the instability was performed, proving valuable indications. In particular, importance of bending stiffness, bending/torsion coupling and the moment transferred through the joint was critically analyzed. However, when bending/torsion coupling was relevant and simultaneously originated at geometrical and material levels, the behavior was not possible to be "reasonably" predicted. Examination of the deformed shapes, showing particular traits for the configurations incurring in stability problems, contributed to gain a deeper understanding.

Presence of snap-buckling, however, introduced issues that manifested well before the critical load was reached. So called bi-stable regions were in fact found. They represented a potential danger for promoting branch-jumping in presence of appropriate perturbations. In general, to identify such regions, post-critical analyses tracking the response also in *non-feasible regions* are necessary. Besides, operative conditions need to be out of bi-stable areas. These considerations represent *important design indications* regarding Joined Wings.

More complicate scenario may arise: a so-called *isola* (fully detached and close equilibrium branch) was found for particular values of the parameters. Such a picture is very worrying in terms of design perspective, since it implies multi-stable regions that cannot be detected through the common path-tracking continuation methods.

Finally, within this complex bifurcation scenario, the sensitivity to the (unavoidable) manufacturing defects is enhanced. A small change in parameters (joint's height,

material stiffness, etc) was able to induce sudden shifts in behavior. Although never investigated with such level of depth, some efforts found a strong sensitivity to joint's stiffness in terms of flutter and divergence occurrences (evaluated with linear approaches).

Static aeroelastic conceptual work The same instability phenomena observed for the mechanical case had an equivalent counterpart in the aeroelastic case. This led to the formulation of the *snap-divergence* concept, as opposed to the classic definition of aeroelastic divergence evaluated thorough eigenvalue analysis. Thus, the same concerns expressed above apply also for the aeroelastic case.

The eigenvalue approach was found to give unreliable trends, also if enhanced by successive linearizations. Good estimates of the real critical speed were possible only after tracking most of the nonlinear response, jeopardizing the computational advantages inherent to the method.

Thanks to the experience matured during the preliminary stages, it was possible to understand and explain why some configurations were not incurring in stability problems even in the presence of aerodynamic loads. However, in general, the dependence of aerodynamic actions on deformations, the strong sensitivities to torsion further complicated the interactions between bending/torsion coupling and overconstrained nature of the system.

Some previous experimental works carried out by the AFRL and collaborators tried to mimic the aerodynamic actions with mechanical follower loads. However, reliability of this surrogate models needed to be assessed, and an answer in this direction is given by the present effort, showing that this approach can hide important instabilities: although the structure might show very similar stiffness (to be intended as load versus deformation ratio), an infinitesimal increase in wind speed might cause a finite variation of aerodynamic loads, de-facto, an instability.

Dynamic aeroelastic conceptual work Aeroelastic dynamic phenomena were then observed, using multi-fidelity approaches. As for the previous settings, classic flutter analysis carried out on initial/undeformed configurations did not provide accurate results. Which, on turn, were possible only updating the initial configuration to one relative to almost the critical speed.

Post-flutter (post Hopf's bifurcation) responses were shown. Strong sensitivity to the speed was observed, and the transients before settling to the limit cycle oscillation

(LCO) were dominated by features consequences of the transferring of loads through the joint. A further increase in speed was, in some cases, leading to a so called *flip bifurcation* (or period doubling). In some other cases the LCO was extinguishing and static equilibrium found.

Modeling techniques played an important role: for some joined-wing layouts results were strongly sensitive to modeling of the wake shed by the wing. This was the case for flutter speed for example. Traditionally, effects of neglecting wake roll-up are considered to be of the second order.

A stability diagram, traced for one particular configuration, showed the rich picture: multi-stability in static regimes, multi-stability in mixed static/dynamic regimes, Hopf's and flip's bifurcations and possible route to chaos gave an idea of the complexity of the nonlinear behaviour.

Dynamic aeroelasticity: effects induced by freeplay of control surfaces Effects of freeplay of mobile surfaces were investigated for a typical *PrandtlPlane*, a civil aviation realization of the joined-wing (box-wing) concept. The original model was provided from a partner University (Università di Pisa), and was the result of an MDO. An optimization process was carried out to retain the original aeroelastic properties while changing it to satisfy requirements of the analyses.

Low speed flutter occurrences were observed. However, these instabilities were usually appearing only for a small speed interval, and were generally dominated with dampers. Such instabilities involved high frequency modes, whereas, the main dynamic instability was observed to preserve in all cases its mechanism (involving low frequency modes) as in the configuration without any freeplay.

In some cases freeplay of some mobile surfaces (front aileron) increased this main instability speed, providing possible design indication for passive flutter suppression. On the contrary, in some other cases (rear elevator), a different violent flutter mechanism was triggered by the freeplay at lower-than-reference critical speed.

Dynamic aeroelasticity: free flying analysis The first natural frequencies showed relative low values on the above PrandtlPlane configuration. Thus, the elastic modes might theoretically interact with the rigid body motion, giving rise to so called *body-freedom* flutter. In order to assess this eventuality, a free-flying flutter analysis was carried out modeling the inertial effects of the fuselage. Interestingly, flutter issues were

alleviated by a large extent for the particular configuration under examination.

Design directions The conceptual work carried out on simplified models, predicted instabilities which were practically observed (although never studied) in literature efforts on detailed HALE models employing realistic stiffness distributions and also a detailed structural description (spars, ribs, etc). Thus, all the difficulties and complexities shown for the models presented in this thesis might have a practical impact on real design of Joined Wings, at least for the highly flexible cases. Design directions were then formulated, as summarized by the following list:

- Stability analysis should not be pursued with linear eigenvalue analysis. In fact, such an approach can lead to unsafe predictions and costly re-design computations.
- The static analysis should not be stopped when the maximum load is reached. On the contrary, it should be continued to track the response also in the *non-feasible* regions to assess if a snap-instability (with consequent bi-stable region) occurs.
- The operative conditions should be designed to avoid bi-stable regions.
- Even if no snap-instability is observed with path tracking techniques (arc length methods), there is no guarantee that branch jumping does not occur: a detached branch (*isola*) can exist.
- Joined Wings should be approached with a *global* perspective, and be thought as a unique whole system. Local actions or modifications may have a strong effect at large scales.
- Sensitivity to manufacturing defects needs to be carefully assessed.
- Even within the same modeling approach, different approximations and submodeling that are demonstrated not to be important (e.g., wake shape for aeroelastic studies) for traditional configurations, can lead to different results.

Appendix A

Analytical Frame Calculation

For a better understanding and analysis of the Joined Wins, an analytical solution of the frame depicted in Figure A.1 proves to be useful. This over constrained frame could be considered as a rough approximation of the joined-wing systems, and enables a closed form solution. To further simplify the problem, the structure lies on the yz plane, thus this schematization applies better for the unswept joined-wing configuration, Sweep 1, although the results could be eventually apply for configurations with sweep angle different than zero.

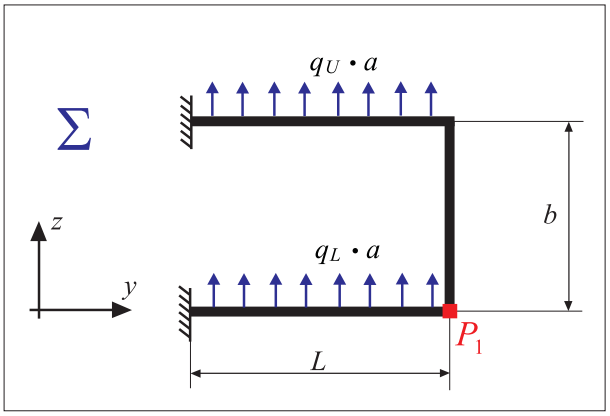

Figure A.1: Frame taken as a simplified structure of the proposed Joined Wings.

By means of classic resolution method of overconstrained beams [247], the following closed form solution is found for the vertical displacement of point P_1 where

$q_U \cdot a = q_L \cdot a = p_z \cdot a$:

$$U_z^{\mathrm{P}_1} = \frac{L^4 \left(Ab^2(b+2L) + 24JL\right)}{8EJ \left(Ab^2(b+6L) + 24JL\right)} p_z \cdot a \tag{A.1}$$

and E is the Young modulus, A and J are the area and the moment of inertia of the cross section respectively.

Calculating the derivative of the vertical displacement of P_1 in respect of the joint's height, and considering the case in which the load is equally partitioned between the two beams:

$$\frac{\partial U_z^{\mathrm{P}_1}}{\partial b} = \frac{AbL^5 \left(Ab^3 - 48JL\right)}{2EJ \left(Ab^2(b+6L) + 24JL\right)^2} p_z \cdot a \tag{A.2}$$

Substituting the values of $L = 10a$, $A = a\,t$, $J = \frac{a}{12}t^3$ and $p_z a = 0.55125a$, which are consistent with the geometry of Sweep 1, it is possible to show that $\frac{\partial U_z^{\mathrm{P}_1}}{\partial b}$ is practically unchanged if b, the height of the joint, is modified. In other words, the displacement is practically unaffected by changing the size b of the joint in the range of interest. This explains why the curves of Figure 3.16, obtained by changing the joint's height b are practically superimposed in the linear region (small displacements).

Appendix B

Appendix: Follower forces and contribution to the tangent matrix

B.1 From global to element level

In Eq.(5.14) the array representation is used, that is, $\boldsymbol{n}$ and $\boldsymbol{p}$ are arrays in the nodal degree of freedom representation. On the other hand, for a intuitive treatise it is necessary to refer to the element's level, that is, to consider the cartesian vector representing the generic normal to the element direction and the coordinate vector of the nodes forming that element. In order to enhance clarity, the cartesian vector are always indicated with an underscore. Fig. B.1 shows a force, applied at node M_2, whose direction *follows* the normal vector relative to element m.

The process of associating a cartesian vector applied to a node to his array representation has to be formally defined: for the array $\boldsymbol{n}$ indicating the normal to the element m direction applied at the generic node N_i, it could be written

$$\boldsymbol{n} = \boldsymbol{\mathcal{I}}_{N_i} \boldsymbol{\mathcal{L}} \underset{\sim}{\boldsymbol{k}}_m \tag{B.1}$$

where $\boldsymbol{\mathcal{L}}$ is a matrix that transforms the cartesian vector in an opportune array in which also the rotational dofs are considered, and $\boldsymbol{\mathcal{I}}_{N_i}$ represents a matrix that positions the array in the corresponding nodal array's layout. It is also necessary to specify a relation

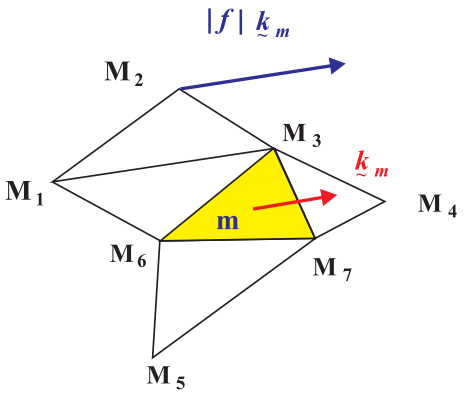

Figure B.1: A generic follower force, applied at node M_2, and following element m normal, $\boldsymbol{k}_m$.

between the array $\boldsymbol{p}$ and the position vector $\underset{\sim}{\boldsymbol{x}}^{M_i}$ relative to the generic node M_i. Using the same formalism adopted in the writing of Eq.(B.1), it can be inferred that

$$\boldsymbol{p} \leftarrow \boldsymbol{\mathcal{I}}_{M_i} \boldsymbol{\mathcal{L}}\, \underset{\sim}{\boldsymbol{x}}^{M_i} \tag{B.2}$$

where the symbol $\leftarrow$ is used instead of the equality because not just the node M_i contributes to form the array $\boldsymbol{p}$ (linear and rotational coordinates of all the nodes are listed in it). It could be demonstrated that the matrix $\frac{\partial \boldsymbol{n}}{\partial \boldsymbol{p}}$ (see its use in the definition of $\boldsymbol{K}_F$ in Eq.(5.14)) can be calculated as follows:

$$\frac{\partial \boldsymbol{n}}{\partial \boldsymbol{p}} = \boldsymbol{\mathcal{I}}_{N_i} \boldsymbol{\mathcal{L}}\, \frac{\partial \underset{\sim}{\boldsymbol{k}}_m}{\partial \underset{\sim}{\boldsymbol{x}}^{M_i}} \boldsymbol{\mathcal{I}}_{M_i}^T\, \boldsymbol{\mathcal{L}}^T \tag{B.3}$$

where matrix representation of $\frac{\partial \underset{\sim}{\boldsymbol{k}}_m}{\partial \underset{\sim}{\boldsymbol{x}}^{M_i}}$ is:

$$\left[\frac{\partial \underset{\sim}{\boldsymbol{k}}_m}{\partial \underset{\sim}{\boldsymbol{x}}^{M_i}}\right]_{rs} = \frac{\partial \left(\underset{\sim}{\boldsymbol{k}}_m \cdot \underset{\sim}{\boldsymbol{e}}_r\right)}{\partial \left(\underset{\sim}{\boldsymbol{x}}^{M_i} \cdot \underset{\sim}{\boldsymbol{e}}_s\right)} \tag{B.4}$$

and $\underset{\sim}{\boldsymbol{e}}_r$, $\underset{\sim}{\boldsymbol{e}}_s$ are the generic unit vectors directed along the rth and sth cartesian components respectively. The evaluation of the term above is carried out at element level.

B.2 Follower Forces at Element Level

Focus is on the generic element m and its normal vector, $\underset{\sim}{\boldsymbol{k}}_m$. Consider also the following unit vectors associated with this element, as depicted in Fig. B.2:

$$\underset{\sim}{\boldsymbol{i}}_m = \frac{\underset{\sim}{\boldsymbol{x}}^{M_2} - \underset{\sim}{\boldsymbol{x}}^{M_1}}{|\underset{\sim}{\boldsymbol{x}}^{M_2} - \underset{\sim}{\boldsymbol{x}}^{M_1}|} \qquad \underset{\sim}{\boldsymbol{j}}_m = \frac{\underset{\sim}{\boldsymbol{x}}^{M_3} - \underset{\sim}{\boldsymbol{x}}^{M_1}}{|\underset{\sim}{\boldsymbol{x}}^{M_3} - \underset{\sim}{\boldsymbol{x}}^{M_1}|}$$

where $\underset{\sim}{\boldsymbol{x}}^{M_1}$, $\underset{\sim}{\boldsymbol{x}}^{M_2}$, $\underset{\sim}{\boldsymbol{x}}^{M_3}$ represent the coordinate vector of the nodes. The unit normal

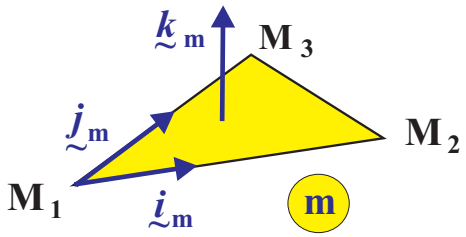

Figure B.2: The generic element m, nodes M_1, M_2, M_3, unit vectors $\boldsymbol{i}_m$ connecting nodes M_1 and M_2, $\boldsymbol{j}_m$ connecting nodes M_1 and M_3, $\boldsymbol{k}_m$ normal to the plane.

vector of the element is then:

$$\underset{\sim}{\boldsymbol{k}}_m = \frac{\underset{\sim}{\boldsymbol{i}}_m \times \underset{\sim}{\boldsymbol{j}}_m}{\left|\underset{\sim}{\boldsymbol{i}}_m \times \underset{\sim}{\boldsymbol{j}}_m\right|} \tag{B.5}$$

In the following the subscript m is dropped for the sake of brevity. Consider the derivative of $\boldsymbol{k}$ in respect of the sth component of coordinate vector of node M_i, that is:

$$\frac{\partial \underset{\sim}{\boldsymbol{k}}}{\partial \left(\underset{\sim}{\boldsymbol{x}}^{M_i} \cdot \underset{\sim}{\boldsymbol{e}}_s\right)} = \frac{\partial \underset{\sim}{\boldsymbol{k}}}{\partial x_s^{M_i}} \tag{B.6}$$

where $\underset{\sim}{\boldsymbol{e}}_s$ represents the unit vector directed along the sth cartesian component. By means of Eq.(B.5):

$$\frac{\partial \underset{\sim}{\boldsymbol{k}}}{\partial x_s^{M_i}} = \left(\frac{\partial \underset{\sim}{\boldsymbol{i}}}{\partial x_s^{M_i}} \times \underset{\sim}{\boldsymbol{j}} + \underset{\sim}{\boldsymbol{i}} \times \frac{\partial \underset{\sim}{\boldsymbol{j}}}{\partial x_s^{M_i}}\right) \left|\underset{\sim}{\boldsymbol{i}} \times \underset{\sim}{\boldsymbol{j}}\right|^{-1} + \left(\underset{\sim}{\boldsymbol{i}} \times \underset{\sim}{\boldsymbol{j}}\right) \left[-\left|\underset{\sim}{\boldsymbol{i}} \times \underset{\sim}{\boldsymbol{j}}\right|^{-2} \left(\frac{\partial}{\partial x_s^{M_i}} \left|\underset{\sim}{\boldsymbol{i}} \times \underset{\sim}{\boldsymbol{j}}\right|\right)\right] \tag{B.7}$$

Using the fact that $\underset{\sim}{\boldsymbol{i}}$ and $\underset{\sim}{\boldsymbol{j}}$ are unit vectors and adopting some identities valid for vectors, it is possible to demonstrate that

$$\frac{\partial \underset{\sim}{\boldsymbol{k}}}{\partial x_s^{M_i}} = \left(\frac{\partial \underset{\sim}{\boldsymbol{i}}}{\partial x_s^{M_i}} \times \underset{\sim}{\boldsymbol{j}} + \underset{\sim}{\boldsymbol{i}} \times \frac{\partial \underset{\sim}{\boldsymbol{j}}}{\partial x_s^{M_i}}\right) \left|\underset{\sim}{\boldsymbol{i}} \times \underset{\sim}{\boldsymbol{j}}\right|^{-1} + \frac{\left(\underset{\sim}{\boldsymbol{i}} \times \underset{\sim}{\boldsymbol{j}}\right)\left(\underset{\sim}{\boldsymbol{i}} \cdot \underset{\sim}{\boldsymbol{j}}\right)}{\left|\underset{\sim}{\boldsymbol{i}} \times \underset{\sim}{\boldsymbol{j}}\right|^3} \left(\frac{\partial \underset{\sim}{\boldsymbol{i}}}{\partial x_s^{M_i}} \underset{\sim}{\boldsymbol{j}} + \underset{\sim}{\boldsymbol{i}} \frac{\partial \underset{\sim}{\boldsymbol{j}}}{\partial x_s^{M_i}}\right) \tag{B.8}$$

The derivatives of the unit vectors $\underset{\sim}{\boldsymbol{i}}$ and $\underset{\sim}{\boldsymbol{j}}$ can be shown to have the following expressions (see Appendix of Reference [2]):

$$\frac{\partial \underset{\sim}{\boldsymbol{i}}}{\partial x_s^{M_i}} = -\frac{\delta_{1i} - \delta_{2i}}{|\underset{\sim}{\boldsymbol{x}}^{M_2} - \underset{\sim}{\boldsymbol{x}}^{M_1}|} \left[\mathbf{e}_s - (\underset{\sim}{\boldsymbol{i}} \cdot \mathbf{e}_s)\, \underset{\sim}{\boldsymbol{i}}\right] \tag{B.9}$$

and

$$\frac{\partial \underset{\sim}{\boldsymbol{j}}}{\partial x_s^{M_i}} = -\frac{\delta_{1i} - \delta_{2i}}{|\underset{\sim}{\boldsymbol{x}}^{M_3} - \underset{\sim}{\boldsymbol{x}}^{M_1}|} \left[\mathbf{e}_s - \left(\underset{\sim}{\boldsymbol{j}} \cdot \mathbf{e}_s\right) \underset{\sim}{\boldsymbol{j}}\right] \tag{B.10}$$

where δ is Kronecker's delta operator. At this point, Eq.(B.8) is totally defined in terms of $\underset{\sim}{\boldsymbol{i}}$ and $\underset{\sim}{\boldsymbol{j}}$. By means of Eq.(B.3), the contribution of the following forces to the tangent matrix, Eq.(5.14), is completely defined.

Appendix C

Meshless Interface Algorithm

The procedure of constructing shape functions using MLS approximation and the way to apply them in order to obtain the coupling between aerodynamic and structural field with the desired properties is here presented. The values of the function $\hat{u}(\boldsymbol{x})$ on a set of nodes $\{\boldsymbol{\eta}_1, \boldsymbol{\eta}_2, ..., \boldsymbol{\eta}_{\hat{n}}\}$ are obtained from its values $\hat{u}(\boldsymbol{\xi}_1)$,$\hat{u}(\boldsymbol{\xi}_2)$,...,$\hat{u}(\boldsymbol{\xi}_{\hat{n}})$ on scattered centers (or sources) $\{\boldsymbol{\xi}_1, \boldsymbol{\xi}_2, ..., \boldsymbol{\xi}_{\hat{n}}\}$ without deriving an analytical expression. This extrapolation is denoted by $\hat{u}^h(\boldsymbol{\eta})$ and is built as a sum of $\hat{m}$ basis functions $\hat{p}_i(\boldsymbol{\eta})$

$$\hat{u}^h(\boldsymbol{\eta}) = \sum_{i=1}^{\hat{m}} \hat{p}_i(\boldsymbol{\eta})\, a_i^{\boldsymbol{\xi}}(\boldsymbol{\eta}) = \hat{\boldsymbol{p}}(\boldsymbol{\eta}) \cdot \boldsymbol{a}^{\boldsymbol{\xi}}(\boldsymbol{\eta}) \tag{C.1}$$

where a_i are the unknown coefficients of the basis functions which depend on the point $\boldsymbol{\eta}$ where the value is sought; the vector $\hat{\boldsymbol{p}}$ of basis functions consists often of monomials of the lowest order such to form polynomial basis with minimum completeness but particular functions can be added to reproduce a particular behaviour of the variables investigated. In the present study linear and quadratic polynomials are adopted:

$$\begin{aligned} \hat{\boldsymbol{p}} &= \{1, x, y, z\} \\ \hat{\boldsymbol{p}} &= \{1, x, y, z, x^2, xy, y^2, yz, z^2, zx\} \end{aligned} \tag{C.2}$$

The $\hat{m}$ coefficients a_i describing (as shown in eq.(C.1)) the function in the point $\boldsymbol{\eta}$ are obtained minimizing the weighted residual functional (a weighted discrete L_2 norm) $J(\boldsymbol{\eta})$

$$J(\boldsymbol{\eta}) = \sum_{i=1}^{\hat{n}} W(\boldsymbol{\eta} - \boldsymbol{\xi}_i)\, [\tilde{u}(\boldsymbol{\xi}_i, \boldsymbol{\eta}) - \hat{u}(\boldsymbol{\xi}_i)]^2 \tag{C.3}$$

where

$$\tilde{u}(\boldsymbol{\xi}_i, \boldsymbol{\eta}) = \hat{\boldsymbol{p}}(\boldsymbol{\xi}_i) \cdot \boldsymbol{a}(\boldsymbol{\eta}) \tag{C.4}$$

is the approximated value of the the field function in the generical center of the set $\boldsymbol{\xi}$ obtained by means of the same extrapolation process pointed out in eq.(C.1). A useful matrix form of eq.(C.3) can be given as follow:

$$J(\boldsymbol{\eta}) = (\hat{\boldsymbol{P}}\,\boldsymbol{a}(\boldsymbol{\eta}) - \hat{\boldsymbol{u}}) \cdot \Big(\boldsymbol{W}\,(\hat{\boldsymbol{P}}\,\boldsymbol{a}(\boldsymbol{\eta}) - \hat{\boldsymbol{u}}) \Big) \tag{C.5}$$

where the following vectors and matrices are introduced:

$$\hat{\boldsymbol{u}} = \{\hat{u}(\boldsymbol{\xi}_1), \hat{u}(\boldsymbol{\xi}_2), ..., \hat{u}(\boldsymbol{\xi}_{\hat{n}})\}$$

$$\hat{\boldsymbol{P}} = \begin{bmatrix} \hat{p}_1(\boldsymbol{\xi}_1) & \hat{p}_2(\boldsymbol{\xi}_1) & ... & \hat{p}_{\hat{m}}(\boldsymbol{\xi}_1) \\ \hat{p}_1(\boldsymbol{\xi}_2) & \hat{p}_2(\boldsymbol{\xi}_2) & ... & \hat{p}_{\hat{m}}(\boldsymbol{\xi}_2) \\ ... & ... & ... & ... \\ \hat{p}_1(\boldsymbol{\xi}_{\hat{n}}) & \hat{p}_2(\boldsymbol{\xi}_{\hat{n}}) & ... & \hat{p}_{\hat{m}}(\boldsymbol{\xi}_{\hat{n}}) \end{bmatrix} \tag{C.6}$$

$$\boldsymbol{W} = \begin{bmatrix} W(\boldsymbol{\eta} - \boldsymbol{\xi}_1) & 0 & ... & 0 \\ 0 & W(\boldsymbol{\eta} - \boldsymbol{\xi}_2) & ... & 0 \\ ... & ... & ... & ... \\ 0 & 0 & ... & W(\boldsymbol{\eta} - \boldsymbol{\xi}_{\hat{n}})) \end{bmatrix} \tag{C.7}$$

Solving the minimization problem

$$\frac{\partial J(\boldsymbol{\eta})}{\partial \boldsymbol{a}} = \boldsymbol{0} \tag{C.8}$$

an expression for the coefficient vector $\boldsymbol{a}(\boldsymbol{\eta})$ is obtained

$$\boldsymbol{a}(\boldsymbol{\eta}) = \hat{\boldsymbol{A}}^{-1} \hat{\boldsymbol{B}}\,\hat{\boldsymbol{u}} \tag{C.9}$$

where $\hat{\boldsymbol{A}}$ is called the *moment matrix* and is given by

$$\hat{\boldsymbol{A}} = \hat{\boldsymbol{P}}^T\,\boldsymbol{W}\,\hat{\boldsymbol{P}} \tag{C.10}$$

and $\hat{\boldsymbol{B}}$ is given by

$$\hat{\boldsymbol{B}} = \hat{\boldsymbol{P}}^T\,\boldsymbol{W} \tag{C.11}$$

It is now possible to give a definitive expression of eq.(C.1) as:

$$\hat{u}^h(\boldsymbol{\eta}) = \sum_{i=1}^{\hat{n}} \Phi_i(\boldsymbol{\eta})\, \hat{u}_i \tag{C.12}$$

where $\Phi_i(\boldsymbol{\eta})$ is the coefficient of the MLS shape function of node $\boldsymbol{\eta}$ corresponding to the center i, which is given by

$$\Phi_i(\boldsymbol{\eta}) = \sum_{j=1}^{\hat{m}} \hat{p}_j(\boldsymbol{\eta}) \left[\hat{\boldsymbol{A}}^{-1}\hat{\boldsymbol{B}}\right]_{ji} \tag{C.13}$$

Eq.(C.12) can also be written in the following matrix form, suitable for applications to the aeroelastic model

$$\hat{u}^h(\boldsymbol{\eta}) = \boldsymbol{\Phi}(\boldsymbol{\eta}) \cdot \hat{\boldsymbol{u}} \tag{C.14}$$

where $\boldsymbol{\Phi}(\boldsymbol{\eta})$ is the array containing the coefficients of the MLS shape function of node $\boldsymbol{\eta}$.

The Radial Basis Functions (RBF) that can be adopted for the three-dimensional cases [227] are

$$\begin{aligned}
&W^0(r) = (1-r)^2 && \mathcal{C}^0 \\
&W^2(r) = (1-r)^4(4\,r+1) && \mathcal{C}^2 \\
&W^4(r) = (1-r)^6(\frac{35}{3}r^2 + \frac{18}{3}r + 1) && \mathcal{C}^4 \\
&W^6(r) = (1-r)^8(32\,r^3 + 25\,r^2 + 8r + 1) && \mathcal{C}^6
\end{aligned} \tag{C.15}$$

where r represents the Euclidean distance between the two considered points. The degree of smoothness $\mathcal{C}^n$ of the RBF bounds the maximum number of continuous derivatives of the approximant function $\hat{\boldsymbol{u}}^h$, as can be argued from the expression of the shape functions in eq.(C.13). Usually the weight functions in eq.(C.15) are written using as independent variable r/δ instead of r, where δ is a scaling factor that allows one to change the function support for different centers, making more appropriate the determination of the local support dimension in those cases where there is a great variation in the data density or when it is requested to exactly enforce structural constraints on the aerodynamic mesh.

The minimization problem has a unique solution if the symmetric matrix $\hat{\boldsymbol{A}}$ is positive definite; this matrix may become singular when the interface is not a well-posed problem, as for example when the number of terms of polynomial basis m is bigger than the number $\hat{n}$ of nodes used in the support domain or when nodes and relative centers

are such that the basis functions vanish in the local support. Especially the latter case can often represent an issue if, for example, planar or piecewise planar configurations are analyzed and it is thus useful to resort to the concept of Moore-Penrose pseudoinverse for evaluation of $\boldsymbol{a}$ in eq.(C.9). The so-called Moore-Penrose pseudoinverse of matrices [248] is a concept that generalizes the usual notion of inverse of a square matrix, but that is also applicable to singular square matrices or even to non-square matrices. For this reason it proved to be particularly useful in dealing with certain least squares problems, when an approximation for solutions of linear equations like $\hat{\boldsymbol{A}}\boldsymbol{z} = \boldsymbol{c}$ is sought, where $\hat{\boldsymbol{A}}$ is a given $\hat{m} \times \hat{n}$ matrix and $\boldsymbol{c}$ is a column vector with $\hat{m}$ components; the solution is expressed as the set of all vectors $\boldsymbol{z}^\star$ such that the Euclidean norm $||\hat{\boldsymbol{A}}\boldsymbol{z}^\star - \boldsymbol{c}||$ has the least possible value, called the minimizing set of the linear problem, and it can be demonstrated that this set is obtained through a matrix $\hat{\boldsymbol{A}}^+$, named the Moore-Penrose pseudoinverse of $\hat{\boldsymbol{A}}$ and satisfying the following properties:

$$\begin{aligned} &\hat{\boldsymbol{A}}\hat{\boldsymbol{A}}^+\hat{\boldsymbol{A}} = \hat{\boldsymbol{A}} \\ &\hat{\boldsymbol{A}}^+\hat{\boldsymbol{A}}\hat{\boldsymbol{A}}^+ = \hat{\boldsymbol{A}}^+ \\ &\hat{\boldsymbol{A}}\hat{\boldsymbol{A}}^+ \text{ and } \hat{\boldsymbol{A}}^+\hat{\boldsymbol{A}} \text{ are self-adjoint} \end{aligned} \tag{C.16}$$

For the Singular Value Decomposition Theorem [249] a matrix $\hat{\boldsymbol{A}}$ can always be written as

$$\hat{\boldsymbol{A}} = \boldsymbol{V}\boldsymbol{S}\boldsymbol{W}^\star \tag{C.17}$$

where $\boldsymbol{V}$ and $\boldsymbol{W}$ are unitary matrices given by the *Polar Decomposition Theorem* and $\boldsymbol{S}$ is a diagonal matrix whose diagonal elements are the singular values of $\hat{\boldsymbol{A}}$, i.e., the square root of the eigenvalues of $\hat{\boldsymbol{A}}^T\hat{\boldsymbol{A}}$. Eq.(C.17) shows the so-called singular value decomposition of the matrix $\hat{\boldsymbol{A}}$. It can be demonstrated that the Moore-Penrose pseudoinverse is given by

$$\hat{\boldsymbol{A}}^+ = \boldsymbol{W}\boldsymbol{S}^+\boldsymbol{V}^\star \tag{C.18}$$

where $\boldsymbol{S}^+$ is a diagonal matrix whose diagonal elements are the reciprocal of the singular values of $\hat{\boldsymbol{A}}$. The crucial point is the choice of which diagonal elements have to be retained in $\boldsymbol{S}^+$, because this is the way an inverse matrix of a singular one is given, i.e, just the *invertible* part is inverted. In the present effort, the following strategy is chosen: the singular values of $\hat{\boldsymbol{A}}$ are normalized dividing them by the maximum one and a cut off value is adopted such that all the smaller ones are replaced with 0 in $\boldsymbol{S}^+$

(where the reciprocal would be requested). It should be observed that when the matrix $\hat{\boldsymbol{A}}$ is singular, it has at least one of its singular values equal to zero and so a cut off of 0 could be enough, but it can happen that although $\hat{\boldsymbol{A}}$ is non singular from a mathematical point of view (no zero eigenvalues) it has a high condition number and eq.(C.18) without further modifications wouldn't be enough to obtain good results.

The final issue is the conservation of energy [222]. To present the problem and its solution in the most general way, the following coupling conditions are considered

$$\begin{aligned} &\boldsymbol{\sigma}^s\,\boldsymbol{n} = -p\,\boldsymbol{n} + \boldsymbol{\sigma}^f\,\boldsymbol{n} \\ &\boldsymbol{\eta}^s = \boldsymbol{\eta}^f \\ &\dot{\boldsymbol{\eta}}^s = \dot{\boldsymbol{\eta}}^f \quad \text{or} \quad \frac{\partial \dot{\boldsymbol{\eta}}^s}{\partial n} = \frac{\partial \dot{\boldsymbol{\eta}}^f}{\partial n} \end{aligned} \tag{C.19}$$

where $\boldsymbol{\eta}^s$ denotes the structural boundary position, $\boldsymbol{\eta}^f$ is the aerodynamic counterpart, p is the pressure, $\boldsymbol{\sigma}^s$ and $\boldsymbol{\sigma}^f$ are respectively the structure stress tensor and the fluid viscous stress tensor, and $\boldsymbol{n}$ is the normal vector to either a newly defined virtual interface surface or the surface of the fluid. The first relation expresses the dynamic equilibrium between stresses on the two fields, whereas the others are kinematic compatibility conditions on displacement and speed; for the latter one, just the normal component can be used if an inviscid flows is considered (wall tangency condition). As these conditions are valid for continuous systems and the two fields are discretized to solve the problem, conservation properties have to be assured: the change of energy in the fluid-structure system need to be equal to the energy supplied by external forces. In the following it is demonstrated how this property can be retained enforcing the coupling conditions in a weak sense through the use of Virtual Work. Calling $\delta\boldsymbol{\eta}^f$ and $\delta\boldsymbol{\eta}^s$ the admissible displacements for the two respective fields, the relation between nodal quantities (i and j are respectively the generical aerodynamic and structural node) is

$$\delta\boldsymbol{\eta}_i^f = \sum_{j=1}^{j_s} \Phi_j(\boldsymbol{\eta}_i^f)\,\delta\boldsymbol{\eta}_j^s \tag{C.20}$$

where i^f and j^f are respectively the number of aerodynamic and structural nodes considered. The resulting virtual displacement of the aerodynamic surface Γ^f is obtained assuming N_i base functions belonging to the aerodynamic field discretization space cor-

responding to the i^f nodes of the same surface; in this way, the following relation holds

$$\delta\boldsymbol{\eta}^f = \sum_{i=1}^{i_f} N_i \sum_{j=1}^{j_s} \Phi_j(\boldsymbol{\eta}_i^f)\, \delta\boldsymbol{\eta}_j^s \tag{C.21}$$

The virtual work of the aerodynamic load is equal to

$$\delta W^f = \int_{\Gamma^f} (-p\boldsymbol{n} + \boldsymbol{\sigma^f}\boldsymbol{n}) \cdot \delta\boldsymbol{\eta}^f \, d\Gamma \tag{C.22}$$

Calling $\boldsymbol{f}_j$ the load on the structural node j induced by the fluid, the virtual work of the forces acting on the structure is

$$\delta W^s = \sum_{j=1}^{j^s} \boldsymbol{f}_j \, \delta\boldsymbol{\eta}_j^s \tag{C.23}$$

Imposing equivalence of the virtual works and rearranging eq.(C.22) through eq.(C.20) and eq.(C.21) the following holds

$$\boldsymbol{f}_j = \sum_{i=1}^{i^f} \boldsymbol{F}_i \, \Phi_j(\boldsymbol{\eta}_i^f) \tag{C.24}$$

where $\mathbf{F}_i$ is given by

$$\boldsymbol{F}_i = \int_{\Gamma^f} (-p\,\boldsymbol{n} + \boldsymbol{\sigma^f}\boldsymbol{n})\, N_i \, d\Gamma \tag{C.25}$$

Consider now $\boldsymbol{f}$ ($\boldsymbol{F}$) to be the matrix whose rows are the forces evaluated at the generic aerodynamic (structural) j-th (i-th) node, $\boldsymbol{f}_j$ ($\boldsymbol{F}_i$). Thus eq.(C.24) may be written in the matrix form:

$$\boldsymbol{f} = \boldsymbol{\Psi}^T \boldsymbol{F} \tag{C.26}$$

being $\boldsymbol{\Psi}$ the interpolation matrix that matches the two displacement's fields, that is, Ψ_{ij}=$\Phi_j(\boldsymbol{\eta}_i^f)$. Eq.(C.26) shows the sought result: to ensure the balance of the energy exchanged between fluid and structure, the loads on the structural nodes $\boldsymbol{f}$ have to be evaluated multiplying the loads $\boldsymbol{F}$ on the aerodynamic grid by the transpose of the interpolation matrix.

C.1 Contribution of Freeplay Springs to the Tangent Matrix

It is necessary to recall few mathematical definitions which will be necessary to develop the spring's contribution to the tangent matrix:

- $\boldsymbol{U}$, called the *displacement array* refers to the generalized displacements. It is then an *array* with 3 translational and 3 rotational components for each node. Thus, for a model with N nodes, $\boldsymbol{U}$ has $6N$ components.
- $\boldsymbol{x}$ refers to the translational (cartesian) coordinates of a node.
- If $\boldsymbol{a}$ and $\boldsymbol{b}$ are arrays
$$\left[\frac{\mathrm{d}\boldsymbol{a}}{\mathrm{d}\boldsymbol{b}}\right]_{ij} = \frac{\mathrm{d}a_i}{\mathrm{d}b_j}$$
- If $\boldsymbol{a}$ and $\boldsymbol{b}$ are arrays, *dyadic operator* is defined as:
$$[\boldsymbol{a} \otimes \boldsymbol{b}]_{ij} = a_i b_j$$

The keypoint to asses the freeplay spring contributions to the tangent matrix consists in evaluating the derivatives of the spring reaction (not yet projected to the nodes) in respect of the nodal displacements, i.e:

$$\frac{\mathrm{d}(M\ \boldsymbol{e}^A)}{\mathrm{d}\boldsymbol{U}} = \underbrace{\boldsymbol{e}^A \otimes \frac{\mathrm{d}M}{\mathrm{d}\boldsymbol{U}}}_{\text{term1}} + \underbrace{M\frac{\mathrm{d}\boldsymbol{e}^A}{\mathrm{d}\boldsymbol{U}}}_{\text{term2}} \tag{C.27}$$

Term1 The first term of eq.(C.27) is evaluated exploiting a chain rule, and evaluating the derivatives:

$$\text{term1} = \boldsymbol{e}^A \otimes \left(\frac{\mathrm{d}M}{\mathrm{d}\Delta\theta}\ \frac{\mathrm{d}\Delta\theta}{\mathrm{d}\boldsymbol{U}}\right) \tag{C.28}$$

The first term inside the parenthesis depends on the freeplay spring law relating the deflection and the reaction of the spring, $M = M(\Delta\theta)$. The last term depends on the expression of $\Delta\theta$ given in Eq.(8.2):

$$\text{term1b} = \frac{\mathrm{d}\Delta\theta}{\mathrm{d}\boldsymbol{U}} = \frac{\mathrm{d}}{\mathrm{d}\boldsymbol{U}}\left(\sin^{-1}(\underbrace{(\boldsymbol{n}^M \times \boldsymbol{n}^S) \cdot \boldsymbol{e}^A}_{y^*})\right) = \frac{1}{\sqrt{1-y^{*2}}}\frac{\mathrm{d}y^*}{\mathrm{d}\boldsymbol{U}} \tag{C.29}$$

where:

$$\frac{\mathrm{d}y^*}{\mathrm{d}U_i} = \left[\frac{\mathrm{d}\boldsymbol{n}^M}{\mathrm{d}U_i}\times\boldsymbol{n}^S + \boldsymbol{n}^M\times\frac{\mathrm{d}\boldsymbol{n}^S}{\mathrm{d}U_i}\right]\cdot\boldsymbol{e}^A + \left[\frac{\mathrm{d}\boldsymbol{e}^A}{\mathrm{d}U_i}\right]\cdot(\boldsymbol{n}^M\times\boldsymbol{n}^S) \tag{C.30}$$

To evaluate the derivatives of the element's normal, with reference to Fig. C.1, it holds:

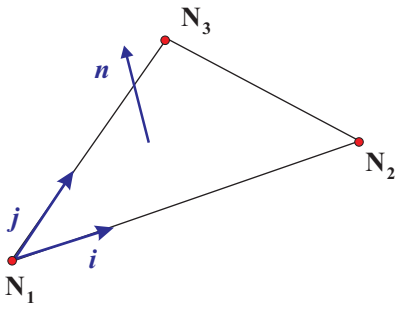

Figure C.1: Generic triangular finite element, nodes N_1, N_2, N_3, unit vectors $\boldsymbol{i}$ and $\boldsymbol{j}$ connecting the nodes as shown, and normal to the plane unit vector $\boldsymbol{n}$.

$$\boldsymbol{n} = \frac{\boldsymbol{i}\times\boldsymbol{j}}{\|\boldsymbol{i}\times\boldsymbol{j}\|} \tag{C.31}$$

Considering the derivative of $\boldsymbol{n}$ in respect of the i-th component of the coordinate vector of node N_j (both $i, j = 1, 2, 3$), that is:

$$\frac{\partial\boldsymbol{k}}{\partial(\boldsymbol{x}^{N_j}\cdot\boldsymbol{e}_i)} = \frac{\partial\boldsymbol{k}}{\partial x_i^{N_j}} \tag{C.32}$$

where $\boldsymbol{e}_i$ represents the unit vector directed along the i-th cartesian component. By means of eq.(C.31) it is possible to demonstrate that:

$$\frac{\partial\boldsymbol{n}}{\partial x_i^{N_j}} = \left(\frac{\partial\boldsymbol{i}}{\partial x_i^{N_j}}\times\boldsymbol{j} + \boldsymbol{i}\times\frac{\partial\boldsymbol{j}}{\partial x_i^{N_j}}\right)\|\boldsymbol{i}\times\boldsymbol{j}\|^{-1} + \frac{(\boldsymbol{i}\times\boldsymbol{j})(\boldsymbol{i}\cdot\boldsymbol{j})}{\|\boldsymbol{i}\times\boldsymbol{j}\|^3}\left(\frac{\partial\boldsymbol{i}}{\partial x_i^{N_j}}\cdot\boldsymbol{j} + \boldsymbol{i}\cdot\frac{\partial\boldsymbol{j}}{\partial x_i^{N_j}}\right) \tag{C.33}$$

Term2 The second term of eq.(C.27), enters also eq.(C.30). Hinge line direction is expressed by the unit vector defined as (see Fig. 8.1):

$$\boldsymbol{e}^A = \frac{\boldsymbol{x}^{H2} - \boldsymbol{x}^{H1}}{\|\boldsymbol{x}^{H2} - \boldsymbol{x}^{H1}\|} \tag{C.34}$$

After some calculations it is found that:

$$\frac{\partial\boldsymbol{e}^A}{\partial x_i^{Hj}} = \frac{\delta_{j2} - \delta_{j1}}{\|\boldsymbol{x}^{H2} - \boldsymbol{x}^{H1}\|}\left[\boldsymbol{e}_i + (\boldsymbol{e}^A\cdot\boldsymbol{e}_i)\,\boldsymbol{e}^A\right] \tag{C.35}$$

Once the expression of eq.(C.27) has been explicitated, the contribution to the tangent matrix can be easily assessed remembering to equally distribute the moment (with the appropriate sign) between the two hinge nodes on the master and slave elements.

Bibliography

[1] Demasi, L., Cavallaro, R., and Razón, A., "Postcritical Analysis of PrandtlPlane Joined-Wing Configurations," *AIAA Journal*, Vol. 51, No. 1, 2013, pp. 161–177.

[2] Cavallaro, R., Demasi, L., and Bertuccelli, F., "Risks of Linear Design of Joined Wings: a Nonlinear Dynamic Perspective in the Presence of Follower Forces," No. AIAA 2013-1558, 54th AIAA/ASME/ASCE/AHS/ASC Structures, Structural Dynamics, and Materials Conference, Boston, Massachusetts, American Institute of Aeronautics and Astronautics, 8-11 April 2013.

[3] Kier, M. T., "Comparison of Unsteady Aerodynamic Modelling Methodologies with Respect to Flight Loads Analysis," *AIAA Atmospheric Flight Mechanics Conference and Exhibit Guidance, Navigation, and Control and Co-located Conferences*, No. AIAA 2005-6027, August 2005.

[4] Attar, P. J., Dowell, E. H., and White, J., "Modeling the LCO of a delta wing using a high fidelity structural model," Vol. 3, 2004, pp. 1986 – 2000.

[5] Dal Canto, D., Frediani, A., Ghiringhelli, G. L., and Terraneo, M., "The Lifting System of a PrandtlPlane, Part 1: Design and Analysis of a Light Alloy Structural Solution," *Variational Analysis and Aerospace Engineering: Mathematical Challenges for Aerospace Design*, edited by G. Buttazzo and A. Frediani, Vol. 66 of *Springer Optimization and Its Applications*, Springer US, 2012, pp. 211–234, 10.1007/978-1-4614-2435-2_9.

[6] Ginneken, D. A. J., Voskuijl, M., Van Tooren, M. J. L., and Frediani, A., "Automated Control Surface Design and Sizing for the PrandtlPlane," No. AIAA 2010-3060, 2010, Presented at the 51st AIAA/ASME/ASCE/AHS/ASC Structures, Structural Dynamics & Materials Conference, Orlando, Florida, 12-15 April 2010.

[7] Prandtl, L., "Induced Drag of Multiplanes," Tech. Rep. TN 182, NACA, March 1924.

[8] Lange, R. H., Cahill, J. F., Bradley, E. S., Eudaily, R. R., Jenness, C. M., and Macwilkinson, D. G., "Feasibility Study of the Transonic Biplane Concept for Transport Aircraft Applications," 1974, NASA CR–132462, Lockheed–Georgia Company.

[9] Frediani, A., Cipolla, V., and Rizzo, E., "The PrandtlPlane Configuration: Overview on Possible Applications to Civil Aviation," *Variational Analysis and Aerospace Engineering: Mathematical Challenges for Aerospace Design*, edited by G. Buttazzo and A. Frediani, Vol. 66 of *Springer Optimization and Its Applications*, Springer US, 2012, pp. 179–210, 10.1007/978-1-4614-2435-2_8.

[10] Wolkovitch, J., "The Joined Wing Aircraft: an Overview," *Journal of Aircraft*, Vol. 23, No. No. 3, March 1986, pp. 161–178.

[11] Chambers, J. R., *Innovation in Flight: Research of the NASA Langley Research Center on Revolutionary Advanced Concepts for Aeronautics*, No. 39 in Monograph in Aerospace History, NASA, November 2005, NASA SP 2005-4539.

[12] Lucia, D., "The SensorCraft Configurations: A Non-Linear AeroServoElastic Challenge for Aviation," No. AIAA 2005-1943, 46th AIAA/ASME/ASCE/AHS/ASC Structures, Structural Dynamics and Materials Conference, American Institute of Aeronautics and Astronautics, 18-21 April 2005.

[13] Demasi, L. and Livne, E., "The Structural Order Reduction Challenge in the Case of Geometrically Nonlinear Joined-Wing Configurations," 2007, Presented at the 48th AIAA/ASME/ASCE/AHS/ASC Structures, Structural Dynamics & Materials Conference, Honolulu, Hawaii, 23-26 April 2007.

[14] Demasi, L. and Palacios, A., "A Reduced Order Nonlinear Aeroelastic Analysis of Joined Wings Based on the Proper Orthogonal Decomposition," 2010, Presented at the 51st AIAA/ASME/ASCE/AHS/ASC Structures, Structural Dynamics & Materials Conference, Orlando, Florida, 12-15 April 2010.

[15] Phlipot, G., Wang, X., Mignolet, M., Demasi, L., and Cavallaro, R., "Nonintrusive Reduced Order Modeling for the Nonlinear Geometric Response of Some Joined Wings," No. AIAA 2014-0151, 55th AIAA/ASMe/ASCE/AHS/SC Structures, Structural Dynamics, and Materials Conference, AIAA Science and Technology Forum and Exposition (SciTech2014) National Harbor, Maryland, American Institute of Aeronautics and Astronautics, 13-17 January 2014.

[16] Teunisse, N., Tiso, P., Demasi, L., and Cavallaro, R., "A Computational Method for Structurally Nonlinear Joined Wings Based on Modal Derivatives," No. AIAA 2014-0494, 55th AIAA/ASMe/ASCE/AHS/SC Structures, Structural Dynamics, and Materials Conference, AIAA Science and Technology Forum and Exposition (SciTech2014) National Harbor, Maryland, American Institute of Aeronautics and Astronautics, 13-17 January 2014.

[17] Montanari, A. F. and Pappalardo, M., "Sul problema di Prandtl della minima resistenza indotta di un sistema portante," AIDAA, November 1999, pp. 267–278, translated: "On Prandtl's problem about minimization of induced drag of a lifitng system".

[18] Frediani, A. and Montanari, G., "Best wing system: an exact solution of the Prandtl's problem," *Variational Analysis and Aerospace Engineering*, Vol. 33 of

Springer Optimization and Its Applications, Springer New York, 2009, pp. 183–211.

[19] Demasi, L., Monegato, G., Dipace, A., and Cavallaro, R., "Minimum Induced Drag Theorems for Joined Wings, Closed Systems, and Generic Biwings: Theory," AIAA, 2015, To be presented at SciTech 2015.

[20] Demasi, L., Monegato, G., Rizzo, E., Cavallaro, R., and Dipace, A., "Minimum Induced Drag Theorems for Joined Wings, Closed Systems, and Generic Biwings: Results," AIAA, 2015, To be presented at SciTech 2015.

[21] Demasi, L., Dipace, A., Monegato, G., and Cavallaro, R., "Invariant Formulation for the Minimum Induced Drag Conditions of Nonplanar Wing Systems," *AIAA Journal*, Vol. 52, No. 10, October 2014, pp. 2223–2240.

[22] Von Kármán, T. and Burgers, J., *Aerodynamic Theory: General aerodynamic theory : Perfect fluids / [By] Th. von Kármán ; J. M. Burgers*, No. v. 2, J. Springer, 1935.

[23] Kroo, I. M., "Nonplanar Wing Concepts for Increased Aircraft Efficiency," *Innovative configurations and advanced concepts for future civil aircraft*, edited by E. Torenbeek and H. Deconinck, Lecture series of Von Karman Institute of Fluid Dynamics, Jun 2005, p. [661] p. in various pagings, ISBN: 2-930389-62-1.

[24] Henderson, W. P. and Huffman, J. K., "Aerodynamic Characteristics of a Tandem Wing Configuration at a Mach Number of 0.30," Technical Memorandum TM X-72779, NASA, NASA Langley Research Center, 1975.

[25] Cahill, J. F. and Stead, D. H., "Preliminary Investigation at Subsonic and Transonic Speeds of the Aerodynamic Characteristics of a Biplane Composed of a Sweptback and Sweptforward Wing Joined at the Tips," Research Memorandum RM L53L24b, NACA, March, 12 1954.

[26] Muhlpacher and Bruti, "Prandtl Box Wing Layout Application to UAV configuration: wind tunnel computational data comparison," Aerospace Aerodynamics Research Conference, Royal Aeronautical Society, London (UK), June 10-12 2003.

[27] Miranda, L. R., "Boxplane Wing and Aircraft," September 1974.

[28] Frediani, A., "Swept-wing box-type aircraft with high flight static stability," Feb. 2004, WO Patent App. PCT/IT2004/000,071.

[29] Wolkovitch, J., "Joined wing aircraft," March 1976.

[30] Samuels, M. F., "Structural Weight Comparison of a Joined Wing and a Concentional Wing," *Journal of Aicraft*, Vol. 19, No. No. 6, June 1982, pp. 485–491, AIAA 81-0366R.

[31] Miura, H., Shyu, A. T., and Wolkovitch, J., "Parametric Weight Evaluation of Joined Wings by Structural Optimization," *Journal of Aircraft*, Vol. 25, No. No. 12, December 1988, pp. 1142–1149.

[32] Hajela, P. and Chen, J. L., "Optimum structural sizing of conventional cantilever and joined wingconfigurations using equivalent beam models," Vol. Aircraft Systems, Design and Technology Meeting, AIAA/AHS/ASEE, Dayton, Ohio, October 20-22 1986.

[33] Hajela, P. and Chen, J. L., "Preliminary weight estimation of conventional and joined wings using equivalent beam models," *Journal of Aircraft*, Vol. 25, No. 6, 1988, pp. 574–576.

[34] O'Banion, J., Jhou, J., Stearman, R., and Smith, S., "A Study of Joint Fixativity in a Joined-Wing Aircraft," Tech. Rep. 97N72033, NASA, 1987, 19970021285.

[35] Lin, H.-H., Jhou, J., and Stearman, R., "Influence of Joint Fixity on the Aeroelastic Characteristics of a Joined Wing Structure," No. AIAA-90-0980-CP, AIAA/ASME/ASCE/AHS/ASC Structures, Structural Dynamics and Materials Conference, 31st, Long Beach, CA, American Institute of Aeronautics and Astronautics, Washington, DC, April 2-4 1990, pp. 1442–1454.

[36] Wolkovitch, J. and Bettes, W., "Low Speed Wind Tunnel Test on Joined Wing and Monoplane Configurations. Vol. I: Analysis of Results. Vol II: Test Data," Navy Contract N00014-79-C-0953 ACA Report 82-1 and 82-2, ACA Industries, Inc., 28603 Trailriders Dr., Rancho Palos Verdes, CA 90274, February 1982, Navy Contract N00014-79-C-0953.

[37] Clyde, J., Bonner, E., Goebel, T., and Spacht, L., "Joined Wing Transonic Design and Test Validation," Tech. Rep. Navy Contract N00014-82-C-0601, AD-A148-355, NA-84-134, Rockwell International, June 22nd 1984, Prepared for Office of Naval Research.

[38] Smith, S. C. and Stonum, R. K., "Experimental Aerodynamic Characteristics of a Joined-wing Research Aircraft Configuration," Technical Report NASA-TM-101083, NASA, Apr 1989, 19890014914.

[39] Smith, S., Cliff, E., and Kroo, I., "The Design of a Joined-Wing Flight Demonstrator Aircraft," No. AIAA-87-2930, AIAA/AHS/ASEE Aircraft Design, Systems and Operations Meeting, St. Louis, Missouri, September 14-16 1987.

[40] Wolkovitch, J., "Application of the Joined Wing to Cruise Missiles," Contractor Report ONR-CR212-266-1, Navy Contract N00014-79-C-0953, AD-A096450, NASA, November 1980.

[41] Wolkovitch, J., Wainfan, B., Ben-Harush, Y., and Johnson, W., "Application of the Joined Wing to Tiltrotor Aircraft," Contractor Report CR-177543, NASA, ACA Industries, November 1989.

[42] Wolkovitch, J., "The joined wing - An overview," 23rd Aerospace Sciences Meeting, Reno, Nevada, January 14-17 1985.

[43] Cavallaro, R. and Demasi, L., "Challenges, Ideas, and Innovations of Joined-Wing Configurations: A Concept from the Past, an Opportunity for the Future," *Progress in Aerospace Sciences*, 2015, To appear.

[44] Gall, P., "An experimental and theoretical analysis of the aerodynamic characteristics of a biplane-winglet configuration," Technical Memorandum 85815, NASA, 1984, N84-28779.

[45] Sterk, F., Torenbeek, E., of Aeronautical Engineers, N. A., and of Technology. Students Society 'Leonardo da Vinci'., D. U., *Unconventional Aircraft Concepts: Papers Presented at a Symposium*, Delft University Press, 1987.

[46] Gallman, J. W., Kroo, I. M., and Smith, S. C., "Design Synthesis and Optimization of Joined-Wing Transports," AIAA/AHS/ASEE Aircraft Design, Systems and Operations Conference, Dayton, OH, September 17-19 1990, AIAA-90-3197.

[47] Gallman, J., Smith, S., and Kroo, I., "Optimization of joined-wing aircraft," *Journal of Aircraft*, Vol. 30, No. No 6, Nov.-Dec. 1993, pp. 897–905.

[48] Gallman, J. W. and Kroo, I. M., "Structural optimization for joined-wing synthesis," *Journal of Aircraft*, Vol. 33, No. No. 1, January-February 1996, pp. 214–223.

[49] Bhatia, M., Kapania, R. K., Gur, O., Schetz, J., Mason, W., and Haftka, R. T., "Progress Towards Multidisciplinary Design Optimization of Truss Braced Wing Aircraft with Flutter Constraints," No. AIAA 2010-9077, 13th AIAA/ISSMO Multidisciplinary Analysis Optimization Conference, 13-15 September, 2010, Forth Worth, Texas, September 2010.

[50] Carrier, G., Atinault, O., Dequand, S., Hantrais-Gervois, J., Liauzun, C., Paluch, B., Rodde, A. M., and Toussaint, C., "Investigation of a Strut-Braced Wing Configuration for Future Commercial Transport," No. Paper ICAS2012-1.10.2, 28th Congress of the International Council of the Aeronautical Sciences, 23-28 September, 2012, Brisbane, Australia, September 2012.

[51] Callus, P. J., "Conformal Load-Bearing Antenna Structure for Australian Defense Force Aicraft," *DSTO-TR-1963*, 2007.

[52] Johnson, F. P., "Sensor Craft - Tomorrow's eyes and ears of the Warfighter," No. AIAA 2001-4370, AIAA Modeling and Simulation Technologies Conference and Exhibit, Montreal, Canada, 6-9 August 2001.

[53] Blair, M. and Canfield, A. R., "A Joined-Wing Structural Weight Modeling Study," 43rd AIAA/ASME/ASCE/AHS/ASC Structures, Structural Dynamics, and Materials Conference, 2002.

[54] Roberts, R., Canfield, R., and Blair, M., "SensorCraft Structural Optimization and Analytical Certification," No. AIAA 2003-1458, 44th AIAA/ASME/ASCE/AHS/ASC Structures, Structural Dynamics, and Materials Conference, Norfolk, Virginia, 7-10 April 2003.

[55] Roberts, R., Canfield, R., and Blair, M., "Sensor-Craft Structural Optimization and Analytical Certification," No. AIAA 2005-2015, 46th AIAA/ASME/ASCE/AHS/ASC Structures, Structural Dynamics and Materials Conference, Austin, Texas, 18-21 April 2005.

[56] Pettit, C. L., Canfield, R. A., and Ghanem, R., "Stochastic Analysis of an Aeroelastic System," No. EM-2002, 15th ASCE Engineering Mechanics Conference, Columbia University, New York, NY, June 2-5 2002.

[57] Roberts, R. W., *Sensor-Craft Analytical Certification*, Master's thesis, Air Force Institute of Technology, 2003.

[58] Schwartz, J., Canfield, R., and Blair, M., "Aero-Structural Coupling and Sensitivity of a Joined-Wing SensorCraft," No. AIAA 2003-1580, 44th AIAA/ASME/ASCE/AHS/ASC Structures, Structural Dynamics, and Materials Conference, Norfolk, Virginia, 7-10 April 2003.

[59] Robinson, J., "Structural Testing and Analysis of a Joined Wing Tehcnology Demonstrator," AFRL-VA-WP-TR-2004-3048.

[60] Blair, M., Canfield, R. A., and Roberts Jr., R. W., "Joined-Wing Aeroelastic Design with Geometric Nonlinearity," *Journal of Aircraft*, Vol. 42, No. No. 4, July 2005, pp. 832–848.

[61] Rasmussen, C. C., Canfield, R. A., and Blair, M., "Optiomization Process for Configuration of Flexible Joined-Wing," No. AIAA 2004-4330, 10th AIAA/ISSMO Multidisciplinary Analysis and Optimization Conference, Albany, New York, 30 August-1 September 2004.

[62] Rasmussen, C. C., Canfield, R. A., and Blair, M., "Joined-wing Sensor-Craft Configuration Design," *Journal of Aircraft*, Vol. 43, No. No. 5, September-October 2006, pp. 1470–1478.

[63] Rasmussen, C., Canfield, R., and Blair, M., "Optimization process for configuration of flexible joined-wing," *Structural and Multidisciplinary Optimization*, Vol. 37, No. 3, 2009, pp. 265–277.

[64] Lee, H., Kim, Y., Park, G., Kolonay, R., Blair, M., and Canfield, R., "Structural Optimization of a Joined-Wing Using Equivalent Static Loads," No. AIAA 2006-7009, 11th AIAA/ISSMO Multidisciplinary Analysis and Optimization Conference, Portsmouth, Virginia, 6-8 September 2006.

[65] Lee, H., Kim, Y., Park, G., Kolonay, R., Blair, M., and Canfield, R., "Structural Optimization of a Joined-Wing Using Equivalent Static Loads," *Journal of Aicraft*, Vol. 44, No. 4, July-August 2007, pp. 1302–1308.

[66] Pereira, P., Almeida, L., Suleman, A., Bond, V., Canfield, R., and Blair, M., "Aeroelastic Scaling and Optimization of a Joined-Wing Aircraft Concept," No. AIAA 2007-1889, 48th AIAA/ASME/ASCE/AHS/ASC Structures, Structural Dynamics, and Materials Conference, Honolulu, Hawaii, 23-26 April 2007.

[67] Blair, M., Garmann, D., Canfield, R., Bond, V., Pereira, P., and Suleman, A., "Non-Linear Aeroelastic Scaling of a Joined-Wing Concept," No. AIAA 2007-1887, 48th AIAA/ASME/ASCE/AHS/ASC Structures, Structural Dynamics, and Materials Conference, Honolulu, Hawaii, 23-26 April 2007.

[68] Richards, J., Aarons, T., Garnand-Royo, J., Suleman, A., Canfield, R., and A.Woolsey, "Airworthiness Evaluation of a Scaled Joined-Wing Aircraft," No. AIAA-2012-1721, 53rd AIAA/ASME/ASCE/AHS/ASC Structures, Structural Dynamics, and Materials Conference, Honolulu, Hawaii, 23-26 April 2012.

[69] Ricciardi, A. P., Canfield, R. A., Patil, M., and Lindsley, N., "Nonlinear Aeroelastic scaling of a Joined-Wing Aircraft," No. AIAA 2012-1454, 53rd AIAA/ASME/ASCE/AHS/ASC Structures, Structural Dynamics, and Materials Conference, Honolulu, Hawaii, 23-26 April 2012.

[70] Eger, C. A., Ricciardi, A., Canfield, R. A., and Patil, M., "Design of a Scaled Flight Test Vehicle Including Linear Aeroelastic Effects," No. AIAA 2013-1563, 54th AIAA/ASME/ASCE/AHS/ASC Structures, Structural Dynamics, and Materials Conference, Boston, Massachusetts, 8-11 April 2013, SDM Student Papers Competition.

[71] Richards, J., Garnand-Royo, J. S., Suleman, A., Canfield, R. A., and Woolsey, C. A., "Design and Evaluation of Aeroelastically Tuned Joined-Wing SensorCraft Flight Test Article," No. AIAA 2013-1786, 8-11 April, 54th AIAA/ASME/ASCE/AHS/ASC Structures, Structural Dynamics, and Materials Conference, Boston, Massachusetts 2013, SDM Student Papers Competition.

[72] Richards, J., Suleman, A., Canfield, R., and Blair, M., "Design of a Scaled RPV for Investigation of Gust Response of Joined-Wing Sensorcraft," No. AIAA 2009-2218, 50th AIAA/ASME/ASCE/AHS/ASC Structures, Structural Dynamics, and Materials Conference, Palm Spings, 4-7 May 2009.

[73] Richards, J., Suleman, A., Aarons, T., and Canfield, R., "Multidisciplinary Design for Flight Test of a Scaled Joined Wing SensorCraft," No. AIAA 2010-9351, 13th AIAA/ISSMO Multidisciplinary Analysis Optimization Conference, Fort Worth, texas, 13-15 September 2010.

[74] Richards, J., Aarons, T., Suleman, A., Canfield, R., Woolsey, C., Lindsley, N., and Blair, M., "Design for Flight Test of a Scaled Joined Wing SensorCraft," No. AIAA-2011-2011, 52rd AIAA/ASME/ASCE/AHS/ASC Structures, Structural Dynamics, and Materials Conference, Denver, Colorado, 4-7 April 2011, SDM 2011 Student Papers Competition.

[75] Ricciardi, A., Canfield, R. A., Patil, M., Eger, C. A., and Lindsley, N. J., "Nonlinear Aeroelastic Scaled Model Optimization Using Equivalent Static Loads," No. AIAA 2013-1785, 54th AIAA/ASME/ASCE/AHS/ASC Structures, Structural Dynamics, and Materials Conference, Boston, Massachusetts, 8-11 April 2013.

[76] Ricciardi, A. P., Eger, C. A. G., Canfield, R. A., and Patil, M. J., "Nonlinear Aeroelastic-Scaled-Model Optimization Using Equivalent Static Loads," *Journal of Aicraft*, 2014.

[77] Ricciardi, A. P., Patil, M. J., and Canfield, R. A., "Utility of Quasi-Static Gust Loads Certification Methods for Novel Configurations," No. AIAA 2011-2043, 52nd

AIAA/ASME/ASCE/AHS/ASC Structures, Structural Dynamics, and Materials Conference, Denver, Colorado, 4-7 April 2011.

[78] Ricciardi, A. P., Patil, M. J., Canfield, R. A., and Lindsley, N., "Evaluation of Quasi-Static Gust Loads Certification Methods for High-Altitude Long-Endurance Aircraft," *Journal of Aircraft*, Vol. Vol. 50, No. No. 2, 2013, pp. pp. 457–468.

[79] Bond, V. L., Canfield, B., Matos, M., Suleman, A., and Blair, M., "Wind Tunnel Testing of a Twisted Wing for Longitudinal Control in a Joined-Wing Aicraft," No. AIAA 2007-1772, 2007, Presented at the 48th AIAA/ASME/ASCE/AHS/ASC Structures, Structural Dynamics & Materials Conference, Honolulu, Hawaii, 23-26 April 2007.

[80] Bond, V. L., Canfield, R. A., Matos, M. D. L. M. S., Suleman, A., and Blair, M., "Joined-Wing Wind-Tunnel Test for Longitudinal Control via Aftwing Twist," *Journal of Aircraft*, Vol. 47, No. 5, September-October 2010, pp. 1481–1489.

[81] Boston, J., Swenson, E., Kunz, D., Yu, W., and Blair, M., "Experiments with Geometric Non-Linear Coupling for Analytical Validation," No. AIAA 2010-3018, 2010, Presented at the 51st AIAA/ASME/ASCE/AHS/ASC Structures, Structural Dynamics & Materials Conference, Orlando, Florida, 12-15 April 2010.

[82] Boston, J., Swenson, E., Kunz, D., Yu, W., and Blair, M., "Experiments with Geometric Nonlinear Coupling for Analytical Validation," *Journal of Aircraft*, Vol. 48, No. 4, July-August 2011, pp. 1136–1146.

[83] Kim, T., Swenson, E., Kunz, D., Lindsley, N., and Blair, M., "Follower-Force Experiments with Geometric Nonlinear Coupling for Analytical Validation," No. AIAA 2011-1978, 52nd AIAA/ASME/ASCE/AHS/ASC Structures, Structural Dynamics, and Materials Conference, Denver, Colorado, 4-7 April 2011.

[84] LeDoux, S., Vassberg, J., Dehaan, M., and Fatta, G., "Aerodynamic Cruise Design of a Joined Wing SensorCraft," No. AIAA 2008-7190, 26th AIAA Applied Aerodynamics Conference, Honolulu, Hawaii, 18-21 August 2008.

[85] Reichenbach, E., "Aeroservoelastic Design and Test Validation of the Joined Wing Sensorcraft," No. AIAA 2008-7189, 26th AIAA Applied Aerodynamics Conference, Honolulu, Hawaii, 18-21 August 2008.

[86] Reichenbach, E., Castelluccio, M., and Sexton, B., "Joined Wing Sensorcraft Aeroservoelastic Wind Tunnel Test Program," No. AIAA 2011-1956, 52nd AIAA/ASME/ASCE/AHS/ASC Structures, Structural Dynamics and Materials Conference, Denver, Colorado, 4-7 April 2011.

[87] Sharma, V. and Reichenbach, E., "Development of an Innovative Support System for SensorCraft Model," No. AIAA 2011-1958, 52nd AIAA/ASME/ASCE/AHS/ASC Structures, Structural Dynamics and Materials Conference, Denver, Colorado, 4-7 April 2011.

[88] Scott, R., Castelluccio, M., Coulson, D., and Heeg, J., "Aeroservoelastic Wind-Tunnel Tests of a Free-Flying, Joined-Wing SensorCraft Model for Gust Load Alleviation," No. AIAA 2011-1960, 52nd AIAA/ASME/ASCE/AHS/ASC Structures, Structural Dynamics and Materials Conference, Denver, Colorado, 4-7 April 2011.

[89] Scott, M., Enke, A., and Flanagan, J., "SensorCraft Free-Flying Aeroservoelastic Model Design and Fabrication," No. AIAA 2011-1957, 52nd AIAA/ASME/ASCE/AHS/ASC Structures, Structural Dynamics and Materials Conference, Denver, Colorado, 4-7 April 2011.

[90] Frediani, A., "Large dimension aircraft," May 4 1999, US Patent 5,899,409.

[91] Frediani, A., "New Large Aircraft," 2002, European Patent EP 0716978B1, 20 March 2002.

[92] Frediani, A., "Velivolo Biplano ad Ali Contrapposte," 2003, Italian Patent FI 2003A000043, 19 February 2003.

[93] ACARE, "Strategic Research Agenda," October 2002, Vol.1.

[94] Frediani, A., "The Prandtl Wing," *Innovative Configurations and Advanced Concepts for Future Civil Aircraft*, VKI Lecture Series 2005-2006, Von Karman Institute, June 2005, p. [661] p. in various pagings, ISBN: 2-930389-62-1.

[95] Frediani, A., Crema, L. B., Chiocchia, G., Ghiringhelli, G., and Morino, L., "Development of an innovative configuration for transport aircraft; A project of five italian universities," XVII Congresso Nazionale AIDAA (17th National Congress AIDAA), Rome, 2003, pp. 2089–2104.

[96] Frediani, A., Gasperini, M., Saporito, G., and Rimondi, A., "Development of a PrandtlPlane Aircraft Configuration," XVII Congresso Nazionale AIDAA (17th National Congress AIDAA), Rome, 2003, pp. 2089–2104.

[97] Morino, L., Bernardini, G., and Mastroddi, F., "Multi-Disciplinary Optimization for the Conceptual Design of Innovative Aircraft Configurations," *CMES: Computer Modeling in Engineering & Sciences*, Vol. Vol. 13, No. No. 1, 2006, pp. pp. 1–18.

[98] Catapano, A., *Dimensionamento preliminare di una sezione di fusoliera di un velivolo da oltre 1000 passeggeri*, Msc thesis, Università di Pisa, Department of Aerospace Engineering, 2010.

[99] Oliviero, F. and Frediani, A., "Conceptual Design of a Very Large PrandtlPlane Freighter," *Variational Analysis and Aerospace Engineering: Mathematical Challenges for Aerospace Design*, edited by G. Buttazzo and A. Frediani, Vol. 66 of *Springer Optimization and Its Applications*, Springer US, 2012, pp. 305–321, 10.1007/978-1-4614-2435-2_13.

[100] Oliviero, F., *Conceptual design of a large PrandtlPlane freighter*, Master's thesis, Univeristá di Pisa, 2010.

[101] Frediani, A., Rizzo, E., Cipolla, V., Chiavacci, L., Bottoni, C., Scanu, J., and Iezzi, G., "Development of ULM PrandtlPlane Aircraft and Flight Tests on Scaled Models," XIX AIDAA Congress, Forlí, Italy, 17-21 September 207.

[102] Rizzo, E. and Frediani, A., "Application of Optimisation Algorithms to Aircraft Aerodynamics," *Variational Analysis and Aerospace Engineering*, edited by G. Buttazzo and A. Frediani, Vol. 33 of *Springer Optimization and Its Applications*, Springer New York, 2009, pp. 419–446.

[103] Rizzo, E., *Optimization Methods Applied to the preliminary design of innovative non conventional aircraft configurations*, Edizioni ETS.

[104] Chiavacci, L., *Progetto Aerodinamico Preliminare di un Velivolo Ultraleggero tipo PrandtlPlane*, Ms thesis, Università di Pisa, 2006, Advisors: Prof Frediani A., Prof. Casarosa C., PhD Rizzo E. In Italian.

[105] Cipolla, V. and Giuffrida, S., *Utilizzo di codici a pannelli nel progetto preliminare di velivoli prandtlplane ultraleggeri; applicazione a nuove configurazioni*, Master's thesis, Univeristá di Pisa, October 2006, In Italian.

[106] Iezzi, G., *PrandtlPlane High Lift System Preliminary Aerodynamic Design*, Master's thesis, Università di Pisa, 2006.

[107] Frediani, A., Rizzo, E., Bottoni, C., Scanu, J., and Iezzi, G., "A 250 Passenger PrandtlPlane Transport Aircraft Preliminary Design," *Aerotecnica Missili e Spazio (AIDAA)*, Vol. 84, 2005.

[108] Bottoni, C. and Scanu, J., *Preliminary design of a 250 passenger PrandtlPlane aircraft*, Master's thesis, University of Pisa, 2004, Advisors: Prof. Aldo Frediani, Prof. Dieter Schmitt, Dr. Ing. Eric Maury.

[109] Bernardini, M., *Dimensionamento strutturale preliminare di un segmento di fusoliera di un velivolo PrandtlPlane*, Msc thesis, University of Pisa, 2004, Main Advisor: Aldo Frediani. In Italian. Title translation:" Preliminary Structural Sizing of a PrandtlPlane's Fuselage Segment".

[110] Pierotti, F., *Progetto e dimensionamento strutturale preliminari del tronco posteriore di fusoliera di un velivolo PrandtlPlane*, Msc, University of Pisa, 2004, Advisor: Aldo Frediani. In Italian. Title translation:"Preliminary design and structural sizing of a PrandtlPlane fuselage end segment.".

[111] Dimartino, C. and Baldini, M., *Analisi agli elementi finiti di un tronco di fusoliera di un velivolo PrandtlPlane sottoposto a carichi limite di pressurizzazione e di massa.*, Master's thesis, Università di Pisa, 2009.

[112] Dal Canto, D., *Progetto preliminare del cassone alare di un velivolo di tipo PrandtlPlane mediante l'applicazione di un metodo di ottimizzazione strutturale*, Master's thesis, Dipartimento di Ingegneria Aerospaziale, Università di Pisa, December 2009, Advisor: Alfo Frediani.

[113] Frediani, A., Quattrone, F., and Contini, F., "The Lifting System of a PrandtlPlane, Part 3: Structures Made in Composites," *Variational Analysis and Aerospace Engineering: Mathematical Challenges for Aerospace Design*, edited by G. Buttazzo and A. Frediani, Vol. 66 of *Springer Optimization and Its Applications*, Springer US, 2012, pp. 269–288, 10.1007/978-1-4614-2435-2_11.

[114] Divoux, N. and Frediani, A., "The Lifting System of a PrandtlPlane, Part 2: Preliminary Study on Flutter Characteristics," *Variational Analysis and Aerospace Engineering: Mathematical Challenges for Aerospace Design*, edited by G. Buttazzo and A. Frediani, Vol. 66 of *Springer Optimization and Its Applications*, Springer US, 2012, pp. 235–267, 10.1007/978-1-4614-2435-2_10.

[115] Divoux, N., *Preliminary Study on Flutter Characteristics of a PrandtlPlane Aircraft*, Master's thesis, TU Delft, 2008.

[116] Voskuijl, M., Klerk, J., and Ginneken, D., "Flight Mechanics Modeling of the PrandtlPlane for Conceptual and Preliminary Design," *Variational Analysis and Aerospace Engineering: Mathematical Challenges for Aerospace Design*, edited by G. Buttazzo and A. Frediani, Springer Optimization and Its Applications, Springer US, 2012, pp. 435–462.

[117] Ginneken, D. V., *Automated Control Surface Design and Sizing for the PrandtlPlane*, Master's thesis, TU Delft, April 2009.

[118] Beccasio, N., Tesconi, M., and Frediani, A., "PrandtlPlane Propelled with Liquid Hydrogen: A Preliminary Study," *Variational Analysis and Aerospace Engineering: Mathematical Challenges for Aerospace Design*, edited by G. Buttazzo and A. Frediani, Springer Optimization and Its Applications, Springer US, 2012, pp. 1–25.

[119] Frediani, A., Lucchesi, M., and Lippi, T., "CFD Hydrodynamic Analysis of an Ultralight Amphibious PrandtlPlane," 3rd CEAS 3rd Air and Space Conference - XXI AIDAA Congress, Venice, Italy, 17-21 October 2011.

[120] Cipolla, V., Frediani, A., Oliviero, F., Pinucci, M., Rizzo, E., and Rossi, R., "Ultralight Amphibious PrandPrandtl: The Final Design," Italian Association of Aeronautics and Astronautics, XXII Conference, Napoli (Italy), 9-12 September 2013.

[121] Cipolla, V., Frediani, A., Oliviero, F., and Gibertini, G., "Ultralight Amphibious PrandPrandtl: Wind Tunnel Tests," Italian Association of Aeronautics and Astronautics, XXII Conference, Napoli (Italy), 9-12 September 2013.

[122] Cipolla, V., Di Ció, F., Frediani, A., Oliviero, F., Roccaldo, M., and Rossi, R., "A Ultralight Amphibious PrandPrandtl: Towing Tank Tests on a Scaled Model," Italian Association of Aeronautics and Astronautics, XXII Conference, Napoli (Italy), 9-12 September 2013.

[123] Livne, E., "Aeroelasticity of Joined-Wing Airplane Configurations: Past Work and Future Challenges - A Survey," April 16-19 2001, Presented at the 42nd

AIAA/ASME/ASCE/AHS/ASC Structures, Structural Dynamics & Materials Conference, Seattle, WA, 16-19 April 2001.

[124] Demasi, L. and Livne, E., "Exploratory Studies of Joined Wing Aeroelasticity," April 18-21 2005, Presented at the 46th AIAA/ASME/ASCE/AHS/ASC Structures, Structural Dynamics & Materials Conference, Austin, Texas, 18-21 April 2005.

[125] Green, N. S., Canfield, R. A., Swenson, E. D., Yu, W., and Blair, M., "Structural Optimization of Joined-Wing Beam Model with Bend-Twist Coupling Using Equivalent Static Loads," , No. AIAA 2009-2644, Presented at the 50$^{\text{th}}$ AIAA/ASME/ASCE/AHS/ASC Structures, Structural Dynamics & Materials Conference, Palm Springs, California, May. 4-7, 2009.

[126] Sotoudeh, Z. and Hodges, D. H., "Incremental Method for Structural Analysis of Joined-Wing Aircraft," *Journal of Aircraft*, Vol. 48, No. No. 5, September 2011, pp. 1588–1601.

[127] Liu, S., Wickert, D. P., and Canfield, R. A., "Fluid-Structure Transient Gust Response Sensitivity for a Nonlinear Joined Wing Model," No. AIAA 2010-3118, 51st AIAA/ASME/ASCE/AHS/ASC Structures, Structural Dynamics and Materials Conference, Orlando, Florida, 12 - 15 April 2010.

[128] Kim, Y. I., Park, G. J., Kolonay, R. M., Blair, M., and Canfield, R. A., "Nonlinear Response Structural Optimization of a Joined Wing Using Equivalent Loads," *AIAA Journal*, Vol. 46, 2008.

[129] Su, W., *Coupled Nonlinear Aeroelasticity and Flight Dynamics of fully Flexible Aircraft*, Phd thesis, University of Michigan, 2008.

[130] Cavallaro, R., Demasi, L., and Passariello, A., "Nonlinear Analysis of PrandtlPlane Joined Wings - Part II: Effects of Anisotropy," No. AIAA 2012-1462, 53rd AIAA/ASME/ASCE/AHS/ASC Structures, Structural Dynamics, and Materials Conference, Honolulu, Hawaii, 23-26 April 2012.

[131] Sulaeman, E., "Effect of Compressive Force on Aeroelastic Stability of a Strut-Braced Wing," PhD dissertation, November 26, 2001, Blacksburg, Virginia.

[132] Gern, F. H., Ko, A., Sulaeman, E., Gundlach, J., Kapania, R. H., and Haftka, R. T., "Multidisciplinary Design Optimization of a Transonic Commerical Transport with Strut-Braced Wing," *Journal of Aircraft*, Vol. 38, No. No. 6, November 2001, pp. 1006–1014.

[133] Gur, O., Bhatia, M., Schetz, J. A., Mason, W. H., Kapania, R. K., and Mavris, D. N., "Design Optimization of a Truss-Braced-Wing Transonic Transport Aircraft," *Journal of Aircraft*, Vol. 47, No. 6, 2010, pp. 1907–1917.

[134] Patil, M. J., "Nonlinear Aeroelastic Analysis of Joined-Wing Aircraft," No. AIAA 2003-1487, Presented at the 44$^{\text{th}}$ AIAA/ASME/ASCE/AHS/ASC Structures, Structural Dynamics & Materials Conference, Norfolk, Virginia, April 7-10 2003.

[135] Levy, R. and Spillers, W., *Analysis of geometrically nonlinear structures*, No. v. 1, Kluwer Academic Publishers, 2003.

[136] Gal, E. and Levy, R., "The Geometric Stiffness of Triangular Composite-Materials Shell Elements," *Computers and Structures*, Vol. 83, 2005, pp. 2318–2333.

[137] Riks, E., "An incremental approach to the solution of snapping and buckling problems," *International Journal of Solids and Structures*, Vol. 15, No. 7, 1979, pp. 529 – 551.

[138] Crisfield, M., "A Fast Incremental/Iterative Solution Procedure that Handles Snap-Through," *Computers & Structures*, Vol. 13, 1981.

[139] Crisfield, M., *Non Linear Finite Element Analysis of Solid and Structures*, Vol. 1, John Wiley & Sons, 1991.

[140] Felippa, C., "Nonlinear Finite Element Methods," 2011, http://www.colorado.edu/engineering/CAS /courses.d/NFEM.d/Home.html.

[141] Ramm, E., "Strategies for tracing the nonlinear response near limit points," *Nonlinear Finite Element Analysis in Structural Mechanics*, edited by W. Wunderlich, E. Stein, and K. J. Bathe, Springer-Verlag, 1981, pp. 63–89.

[142] Riks, E., "The Application of Newton's Method to the Problem of Elastic Stability," *Journal of Applied Mechanics*, Vol. 39, No. 4, 1972, pp. 1060–1065.

[143] Munk, M., *Isoperimetrische Aufgaben aus der Theorie des Fluges*, Dieterichsche Universitäts-Buchdruckerei, 1919.

[144] Demasi, L., "Induced Drag Minimization: A Variational Approach Using the Acceleration Potential," *Journal of Aircraft*, Vol. 43, May-June 2006.

[145] Letcher, J., "V-Wings and Diamond-Ring Wings of Minimum Induced Drag," *Journal of Aircraft*, Vol. 9, No. No. 8, August 1972, pp. 605–607.

[146] Livne, E., "Future of Airplane Aeroelasticity," *Journal of Aircraft*, Vol. 40, No. No. 6, November 2003, pp. 1066–1092.

[147] Livne, E. and Weisshaar, T. A., "Aeroelasticity of Nonconventional Airplane Configurations-Past and Future," *Journal of Aircraft*, Vol. 40, No. No. 6, November 2003, pp. 1047–1065.

[148] Buttazzo, G. and Frediani, A., editors, *Variational Analysis and Aerospace Engineering: Mathematical Challenges for Aerospace Design Contributions from a Workshop held at the School of Mathematics in Erice, Italy*, Springer US, 2012.

[149] Paletta, N., Belardo, M., and Pecora, M., "Load Alleviation on a Joined-Wing Unmanned Aicraft," *Journal of Aircraft*, Vol. 47, No. No. 6, November 2010, pp. 2005–2016.

[150] Kim, Y.-I., Park, G.-J., Kolonay, R., Blair, M., and Canfield, R., "Nonlinear Dynamic Response Structural Optimization of a Joined-Wing Using Equivalent Static Loads," No. AIAA 2008-2159, 49th AIAA/ASME/ASCE/AHS/ASC Structures, Structural Dynamics, and Materials Conference, 16th AIAA/ASME/AHS Adaptive Structures Conference, Schaumburg, IL, 7-10 April 2008.

[151] Weisshaar, T. A. and Lee, D. H., "Aeroelastic Tailoring of Joined-Wing Configurations," 43nd AIAA/ASME/ASCE/AHS/ASC Structures, Structural Dynamics and Materials Conference, Denver, CO„ 22-25 April 2002.

[152] Demasi, L. and Livne, E., "Contributions to Joined-Wing Aeroelasticity," 2009, Presented at the International Forum on Aeroelasticity and Structural Dynamics Conference, Seattle, Washington, 21-25 June 2009.

[153] Tiso, P. and Jansen, E., "A Finite Element Based Reduction Method for Nonlinear Dynamics of Structures," Presented at the 46$^{\text{th}}$ AIAA/ASME/ASCE/AHS/ASC Structures, Structural Dynamics & Materials Conference, Austin, Texas, 18-21 April 2005.

[154] Tiso, P. and Rixen, D., "Reduction methods for MEMS nonlinear dynamic analysis," *Nonlinear Modeling and Applications, Volume 2*, edited by T. Proulx, Conference Proceedings of the Society for Experimental Mechanics Series, Springer New York, 2011, pp. 53–65.

[155] Giles, L. G., "Equivalent Plate Modeling for Conceptual Design of Aircraft Wing Structures," Tech. Rep. NASA-TM-111263, NASA, Septemeber 1995.

[156] Levy, R. and Gal, E., "Triangular Shell Element for Large Rotations Analysis," *AIAA Journal*, Vol. 41, No. No. 12, December 2003, pp. 2505–2508.

[157] Bisplinghoff, R. and Ashley, H., *Principles of Aeroelasticity*, Dover Phoenix Editions, Dover Publications, 2002.

[158] Demasi, L., Cavallaro, R., and Bertuccelli, F., "Post-Critical Analysis of Joined Wings: the Concept of Snap-Divergence as a Characterization of the Instability," No. AIAA 2013-1559, 54th AIAA/ASME/ASCE/AHS/ASC Structures, Structural Dynamics, and Materials Conference, Boston, Massachusetts, American Institute of Aeronautics and Astronautics, 8-11 April 2013.

[159] Heeg, J. and Morelli, E., "Evaluation of Simultaneous-Multisine Excitation of the Joined Wing SensorCraft Aeroelastic Wind Tunnel Model," 2011, Presented at the 52$^{\text{nd}}$ AIAA/ASME/ASCE/AHS/ASC Structures, Structural Dynamics & Materials Conference, Denver, Colorado, 4-7 April 2011.

[160] Cipolla, V. and Frediani, A., "Design of Solar Powered Unmanned Biplanes for HALE Missions," *Variational Analysis and Aerospace Engineering: Mathematical Challenges for Aerospace Design*, edited by G. Buttazzo and A. Frediani, Vol. 66 of *Springer Optimization and Its Applications*, Springer US, 2012, pp. 141–177, 10.1007/978-1-4614-2435-2_7.

[161] Cavallaro, R., Iannelli, A., Demasi, L., and Razón, A. M., "Phenomenology of Nonlinear Aeroelastic Responses of Highly Deformable Joined-wings Configurations," No. AIAA 2014-1199, 55th AIAA/ASMe/ASCE/AHS/SC Structures, Structural Dynamics, and Materials Conference, AIAA Science and Technology Forum and Exposition (SciTech2014) National Harbor, Maryland, 13-17 January 2014.

[162] Cavallaro, R., Demasi, L., and Passariello, A., "Nonlinear Analysis of PrandtlPlane Joined Wings: Effects of Anisotropy," *AIAA Journal*, Vol. 52, No. 5, May 2014, pp. 964–980.

[163] Rankin, C. and Nour-Omid, B., "The use of projectors to improve finite element performance," *Computers & Structures*, Vol. 30, No. 1–2, 1988, pp. 257 – 267.

[164] Chung, J. and Hulbert, G. M., "A Time Integration Algorithm for Structural Dynamics With Improved Numerical Dissipation: The Generalized-alpha Method," *Journal of Applied Mechanics*, Vol. 60, No. 2, 1993, pp. 371–375.

[165] Simo, J. C. and Tarnow, N., "The discrete energy-momentum method. Conserving algorithms for nonlinear elastodynamics," *Zeitschrift für Angewandte Mathematik und Physik (ZAMP)*, Vol. 43, 1992, pp. 757–792, 10.1007/BF00913408.

[166] Crisfield, M., *Non Linear Finite Element Analysis of Solid and Structures*, Vol. 2, John Wiley & Sons, 1991.

[167] Kuhl, D. and Ramm, E., "Constraint Energy Momentum Algorithm and its application to non-linear dynamics of shells," *Computer Methods in Applied Mechanics and Engineering*, Vol. 136, No. 3–4, 1996, pp. 293 – 315.

[168] Kuhl, D. and Crisfield, M. A., "Energy-conserving and decaying Algorithms in non-linear structural dynamics," *International Journal for Numerical Methods in Engineering*, Vol. 45, No. 5, 1999, pp. 569–599.

[169] Kuhl, D. and Ramm, E., "Generalized Energy–Momentum Method for non-linear adaptive shell dynamics," *Computer Methods in Applied Mechanics and Engineering*, Vol. 178, No. 3–4, 1999, pp. 343 – 366.

[170] Bathe, K.-J. and Baig, M. M. I., "On a composite implicit time integration procedure for nonlinear dynamics," *Computers & Structures*, Vol. 83, No. 31–32, 2005, pp. 2513 – 2524.

[171] Bathe, K.-J., "Conserving energy and momentum in nonlinear dynamics: A simple implicit time integration scheme," *Comput. Struct.*, Vol. 85, No. 7-8, April 2007, pp. 437–445.

[172] Newmark, N. M., "A method of computation for structural dynamics," *Journal of Engineering Mechanics, ASCE*, Vol. 85 (EM3), 1959, pp. 67–94.

[173] Hughes, T. J., "Stability, convergence and growth and decay of energy of the average acceleration method in nonlinear structural dynamics," *Computers & Structures*, Vol. 6, No. 4–5, 1976, pp. 313 – 324.

[174] Park, K. C., "An Improved Stiffly Stable Method for Direct Integration of Nonlinear Structural Dynamic Equations," *Journal of Applied Mechanics*, Vol. 42, No. 2, 1975, pp. 464–470.

[175] Hughes, T. J. R., "A note on the stability of Newmark's algorithm in nonlinear structural dynamics," *International Journal for Numerical Methods in Engineering*, Vol. 11, No. 2, 1977, pp. 383–386.

[176] Wood, W. L. and Oduor, M. E., "Stability properties of some algorithms for the solution of nonlinear dynamic vibration equations," *Communications in Applied Numerical Methods*, Vol. 4, No. 2, 1988, pp. 205–212.

[177] Clough, R. and Penzien, J., *Dynamics of Structures*, Computers & Structures, 2003.

[178] Seydel, R., *Practical Bifurcation and Stability Analysis*, Interdisciplinary Applied Mathematics, Springer, 2009.

[179] Strogatz, S. H., *Nonlinear Dynamics And Chaos: With Applications To Physics, Biology, Chemistry, And Engineering (Studies in Nonlinearity)*, Studies in nonlinearity, Perseus Books Group, 1st ed., Jan. 1994.

[180] Thompson, J. and Stewart, H., *Nonlinear Dynamics and Chaos: Geometrical Methods for Engineers and Scientists*, A Wiley-Interscience publication, Wiley, 1986.

[181] Kubíček, M., Stuchl, I., and Marek, M., ""Isolas" in solution diagrams," *Journal of Computational Physics*, Vol. 48, No. 1, 1982, pp. 106 – 116.

[182] Dellwo, D., Keller, H. B., Matkowsky, B. J., and Reiss, E. L., "On the Birth of Isolas," *SIAM Journal on Applied Mathematics*, Vol. 42, No. 5, 1982, pp. pp. 956–963.

[183] Dellwo, D., "A Constructive Theory of Isolas Supported by Parabolic Cusps, Centers and Bifurcation Points," *SIAM Journal on Applied Mathematics*, Vol. 46, No. 5, 1986, pp. 740–764.

[184] Ganapathisubramanian, N. and Showalter, K., "Bistability, mushrooms, and isolas," *The Journal of Chemical Physics*, Vol. 80, No. 9, 1984, pp. 4177–4184.

[185] Avitabile, D., Desroches, M., and Rodrigues, S., "On The Numerical Continuation Of Isolas Of Equilibria," *International Journal of Bifurcation and Chaos*, Vol. 22, No. 11, 2012, pp. 1250277.

[186] Cesnik, C. and Su, W., "Nonlinear Aeroelastic Modeling and Analysis of Fully Flexible Aircraft," No. AIAA 2005-2169, 46th AIAA/ASME/ASCE/AHS/ASC Structures, Structural Dynamics and Materials Conference, Austin, Texas, 18-21 April 2005.

[187] Demasi, L., Cavallaro, R., and Bertuccelli, F., "Post-Critical Analysis of Highly Deformable Joined Wings: the Concept of Snap-Divergence as a Characterization of the Instability," 2013, Submitted for Publication.

[188] Kaloyanova, V. B., Ghia, K. N., and Ghia, U., "Structural Modeling and Optimization of the Joined Wing of a High-Altitude Long-Endurance (HALE) Aircraft," No. AIAA 2005-1087, 43rd AIAA Aerospace Sciences Meeting and Exhibit, Reno, Nevada, 10-13 January 2005.

[189] Cavallaro, R., Iannelli, A., Demasi, L., and Razón, A. M., "Phenomenology of Nonlinear Aeroelastic Responses of Highly Deformable Joined Wings," *Advances in Aircraft and Spacecraft Science, An International Journal*, , No. AAS47174E, 2014, In press.

[190] ZONA Thechnology Inc., *ZAERO*, 2004, Theoretical Manual, Version 7.1.

[191] Rodden, W. P. and Johnson, E. H., *User Guide V 68 MSC/NASTRAN Aeroelastic Analysis*, MacNeal-Schwendler Corporation, 1994.

[192] Katz, J. and Plotkin, A., *Low-Speed Aerodynamics*, Cambridge Aerospace Series, Cambridge University Press, 2001.

[193] Demasi, L. and Livne, E., "Dynamic Aeroelasticity of Structurally Nonlinear Configurations Using Linear Modally Reduced Aerodynamic Generalized Forces," *AIAA Journal*, Vol. 47, 2009, pp. 71–90.

[194] Dowell, E., Edwards, J., and Strganac, T., "Nonlinear Aeroelasticity," *Journal of Aircraft*, Vol. 40, No. 5, September 2003, pp. 857–874.

[195] Bond, V., Canfield, R. A., Cooper, E. J., and Blair, M., "Experimental Nonlinear Static Deflection of a Subscale Joined Wing," *Journal of Aircraft*, Vol. 49, No. 1, January-February 2012, pp. 329–333.

[196] Demasi, L. and Livne, E., "Aeroelastic coupling of geometrically nonlinear structures and linear unsteady aerodynamics: Two formulations," *Journal of Fluids and Structures*, Vol. 25, No. 5, 2009, pp. 918 – 935.

[197] Cavallaro, R., Demasi, L., Bertuccelli, F., and Benson, D. J., "Risks of Linear Design of Joined Wings: a Nonlinear Dynamic Perspective in the Presence of Follower Forces," *CEAS Aeronautical Journal*, November 2014, pp. 1–20.

[198] Bhasin, S., Chen, P., Wan, Z., and Demasi, L., "Dynamic Nonlinear Aeroelastic Analysis of the Joined Wing Configuration," No. AIAA 2012-1791, 53rd AIAA/ASME/ASCE/AHS/ASC Structures, Structural Dynamics, and Materials Conference, Honolulu, Hawaii, 23-26 April 2012.

[199] Gordnier, R. E. and Melville, R. B., "Numerical Simulation of Limit-cycle Oscillations of a Cropped Delta Wing Using the Full Navier-Stokes Equations," *International Journal of Computational Fluid Dynamics*, Vol. 14, No. 3, 2001, pp. 211–224.

[200] Gordnier, R. E., "Computation of Limit-Cycle Oscillations of a Delta Wing," *Journal of Aircraft*, Vol. 40, No. 6, 2003, pp. 1206–1208.

[201] Attar, P. and Gordnier, R., "Aeroelastic prediction of the limit cycle oscillations of a cropped delta wing," *Journal of Fluids and Structures*, Vol. 22, No. 1, 2006, pp. 45 – 58.

[202] Harder, R. L. and Desmarais, R. N., "Interpolation using surface splines," *Journal of Aircraft*, Vol. 9, No. 2, 1972, pp. 189–191.

[203] Liu, G., *Mesh Free Methods: Moving Beyond the Finite Element Method*, Taylor & Francis, 2010.

[204] Felippa, C. and Geers, T. L., "Partitioned analysis for coupled mechanical systems," *Engineering Computations*, Vol. 5, No. 2, 1988, pp. 123 – 133.

[205] Deparis, S., Discacciati, M., Fourestey, G., and Quarteroni, A., "Fluid–structure algorithms based on Steklov–Poincaré operators," *Computer Methods in Applied Mechanics and Engineering*, Vol. 195, No. 41–43, 2006, pp. 5797 – 5812, John H. Argyris Memorial Issue. Part II.

[206] Küttler, U. and Wall, W. A., "Fixed-point fluid–structure interaction solvers with dynamic relaxation," *Computational Mechanics*, Vol. 43, 2008, pp. 61–72.

[207] Rodden, W. P., Taylor, P. F., and McIntosh, S. C., "Further Refinement of the Subsonic Doublet-Lattice Method," *Journal of Aircraft*, Vol. Vol. 35, No. No. 5, September 1998, pp. pp. 720–727.

[208] Gal, E., Levy, R., Abramovich, H., and Pavsner, P., "Buckling analysis of composite panels," *Composite Structures*, Vol. 73, No. 2, 2006, pp. 179 – 185, International Conference on Buckling and Postbuckling Behavior of Composite Laminated Shell Structures.

[209] Hughes, T. J. R., *The Finite Element Method: Linear Static and Dynamic Finite Element Analysis*, Prentice-Hall, 1987.

[210] Belytschko, T., Liu, W., and Moran, B., *Nonlinear finite elements for continua and structures*, Wiley, 2000.

[211] Hilber, H. M., Hughes, T. J. R., and Taylor, R. L., "Improved numerical dissipation for time integration algorithms in structural dynamics," *Earthquake Engineering & Structural Dynamics*, Vol. 5, No. 3, 1977, pp. 283–292.

[212] Wood, W. L., Bossak, M., and Zienkiewicz, O. C., "An alpha modification of Newmark's method," *International Journal for Numerical Methods in Engineering*, Vol. 15, No. 10, 1980, pp. 1562–1566.

[213] Belytschko, T. and Schoeberle, D. F., "On the Unconditional Stability of an Implicit Algorithm for Nonlinear Structural Dynamics," *Journal of Applied Mechanics*, Vol. 42, No. 4, 1975, pp. 865–869.

[214] Dong, S., "BDF-like methods for nonlinear dynamic analysis," *Journal of Computational Physics*, Vol. 229, No. 8, 2010, pp. 3019 – 3045.

[215] Krenk, S., "Energy conservation in Newmark based time integration algorithms," *Computer Methods in Applied Mechanics and Engineering*, Vol. 195, No. 44-47, 2006, pp. 6110 – 6124.

[216] Ginsberg, J., *Mechanical and Structural Vibrations: Theory and Applications*, Wiley, 2001.

[217] Leishman, J. G. and Bhagwat, M. J., "Generalized viscous vortex model for application to free-vortex wake and aeroacoustic calculations," 58th Annual Forum and Technology Display of the american Helicopter Society International, Montreal, Canada, 11-13 June 2002.

[218] Leishman, J. G., *Principles of helicopter aerodynamics*, Cambridge aerospace series, Cambridge University Press, Cambridge, New York, 2000.

[219] Hess, J. and Smith, M., "Calculation of Potential Flows about Arbitrary Bodies," 1967.

[220] Smith, M. J., Hodges, D. H., and Cesnik, C. E. S., "An Evaluation of Computational Algorithms to Interface Between CFD and CSD Merhodologies," 1995.

[221] Bathe, K. J., "Finite Element Procedures," 1996, Prentice Hall, Englewood Cliffs, NJ, USA.

[222] Quaranta, G., Masarati, P., and Mantegazza, P., "A conservative mesh-free approach for fluid structure problems in Coupled Problems," *International Conference for Coupled Problems in Science and Engineering, Santorini, Greece*, 23-29 May 2005, pp. 24–27.

[223] Cebral, J. R. and Lohner, R., "Conservative Load Projection and Tracking for Fluid-Structure Problems," *AIAA Journal*, Vol. Vol. 35, No. No. 4, 1997, pp. pp. 687–692.

[224] Celniker, G. and Gossard, D., "Deformable Curve and Surface Finite-elements for Free-form Shape Design," *SIGGRAPH Comput. Graph.*, Vol. 25, No. 4, July 1991, pp. 257–266.

[225] Lancaster, P. and Salkauskas, K., "Surfaces Generated by Moving Least Squares Methods," *Mathematics of Computation*, Vol. 37, No. 155, 1981, pp. 141–158.

[226] Nayroles, B., Touzot, G., and Villon, P., "Generalizing the finite element method: Diffuse approximation and diffuse elements," *Computational Mechanics*, Vol. 10, 1992, pp. 307–318.

[227] Wendland, H., "Piecewise polynomial, positive definite and compactly supported radial functions of minimal degree," *Advances in Computational Mathematics*, Vol. 4, 1995, pp. 389–396.

[228] Arya, S., Mount, D. M., Netanyahu, N. S., Silverman, R., and Wu, A. Y., "An optimal algorithm for approximate nearest neighbor searching fixed dimensions," *J. ACM*, Vol. 45, No. 6, Nov. 1998, pp. 891–923.

[229] Demasi, L., Gordnier, R. E., Santarpia, E., and Dipace, A., "High-Fidelity Simulations of a Flexible Flapping Wing in Forward Flight," No. AIAA 2013-1648, 54th AIAA/ASME/ASCE/AHS/ASC Structures, Structural Dynamics, and Materials Conference, Boston, Massachusetts, American Institute of Aeronautics and Astronautics, 8-11 April 2013.

[230] Murua, J., Palacios, R., and Graham, J. M. R., "Applications of the unsteady vortex-lattice method in aircraft aeroelasticity and flight dynamics," *Progress in Aerospace Sciences*, Vol. 55, No. 0, 2012, pp. 46 – 72.

[231] Bernardini, G., *Problematiche Aerodinamiche Relative alla Progettazione di Configurazioni Innovative*, Ph.D. thesis, Politecnico di Milano, Nov 1999.

[232] Quaranta, G., Mantegazza, P., and Masarati, P., "Assessing the local stability of periodic motions for large multibody nonlinear systems using POD," *Journal of Sound and Vibration*, Vol. 271, 2003, pp. 1015–1038.

[233] Teunisse, N., Tiso, P., Demasi, L., and Cavallaro, R., "Computational Reduced Order Methods for Structurally Nonlinear Joined Wings"," 2th SciTech2015, Kissimmee, Florida, 5-9 January 2015.

[234] Clark, R., Cox, D., Jr., H. C. C., Edwards, J. W., Hall, K. C., Peters, D. A., Scanlan, R., Simiu, E., Sisto, F., and Strganac, T. W., *A Modern Course in Aeroelasticity*, Vol. 116 of *Solid Mechanics and Its Applications*, Springer Netherlands, 2005.

[235] Quattrone, F. and Contini, F., *Preliminary design and FEM analysis of a new conception non-standard wing structure: the PrandtlPlane 250 wing structure*, Master's thesis, Dipartimento di Ingegneria Aerospaziale, Università di Pisa, October 2010, Advisor: Alfo Frediani.

[236] Tang, D. and Dowell, E. H., "Flutter and Limit-Cycle Oscillations for a Wing-Store Model with Freeplay," *Journal of Aircraft*, Vol. 43, No. 2, 2006, pp. 487–503.

[237] Liu, L. and Dowell, E. H., "Harmonic Balance Approach for an Airfoil with a Freeplay Control Surface," *AIAA journal*, Vol. 43, No. 4, April 2005, pp. 802–815.

[238] Karaağaçli, T., Yildiz, E. N., and Özgüven, H. N., "Determination of Dynamically Equivalent FE Models of Structures from Experimental Data," *Structural Dynamics, Volume 3*, edited by T. Proulx, Conference Proceedings of the Society for Experimental Mechanics Series, Springer New York, 2011, pp. 785–799.

[239] Addis, B., Locatelli, M., and Schoen, F., "Local Optima Smoothing for Global Optimization," *OPTIMIZATION METHODS AND SOFTWARE*, Vol. 20, 2005, pp. 437.

[240] Torenbeek, E., *Synthesis of Subsonic Airplane Design: An Introduction to the Preliminary Design of Subsonic General Aviation and Transport Aircraft, with Emphasis on Layout, Aerodynamic Design, Propulsion and Performance*, Springer, 1982.

[241] Bramesfeld, G., *A Higher Order Vortex-Lattice Method with a Force-Free Wake*, Ph.D. thesis, The Pennsylvania State University, August 2006.

[242] Bansal, P. and Pitt, D. M., "Uncertainties in control surface free-play and structural properties and their effect on flutter and LCO," No. AIAA 2014-0679, 55th AIAA/ASMe/ASCE/AHS/SC Structures, Structural Dynamics, and Materials Conference, AIAA Science and Technology Forum and Exposition (SciTech2014) National Harbor, Maryland, 13-17 January 2014.

[243] Theodorsen, T. and Garrick, I. E., "Flutter calculations in three degrees of freedom," naca-report-741, NACA, 1942.

[244] Love, M. H., Zink, P. S., Wieselmann, P. A., and Youngren, H., "Body Freedom Flutter of High Aspect Ratio Flying Wings," No. AIAA 2005-1947, 46th AIAA/ASME/ASCE/AHS/ASC Structures, Structural Dynamics and MMaterial Conference, Austin, Texas, 18-21 April 2005.

[245] Lambourne, N., "An Experimental Investigation on the Flutter Characteristics of a Model Flying Wing," Aeronautical Research Council. Reports and Memoranda. No. 2626, 1952.

[246] Chipman, R., Rauch, F., Rimer, M., and Muñiz, B., "Body-freedom Flutter of a 1/2 Scale Forward-Swept-Wing Model, an Experimentwal and Analytical Study," Contract Report NASA CR-172324, NASA, April 1984, by Grumman Aerospace Corporation.

[247] Algostino, A., Faraggiana, G., and Perino, A. S., *Scienza Delle Costruzioni*, 2006, ISBN 978-88-251-7291-1.

[248] Moore, E. H., "On the reciprocal of the general algebraic matrix," *Bulletin of the American Mathematical Society*, Vol. 26, pp. 394–395.

[249] Barata, J. C. A. and Hussein, M. S., "The Moore-Penrose Pseudoinverse. A Tutorial Review of the Theory," 2011.